Technical Progress Report for:

$\overline{\mathrm{P}}$ANDA

(Anti<u>P</u>roton <u>An</u>nihilations at <u>Da</u>rmstadt)

Strong Interaction Studies with Antiprotons

$\overline{\mathrm{P}}$ANDA Collaboration

We propose to study fundamental questions of hadron and nuclear physics in interactions of antiprotons with nucleons and nuclei, using the universal $\overline{\mathrm{P}}$ANDA detector. Gluonic excitations and the physics of strange and charm quarks will be accessible with unprecedented accuracy thereby allowing high-precision tests of the strong interaction. The proposed $\overline{\mathrm{P}}$ANDA detector is a state-of-the-art internal target detector at the HESR at FAIR allowing the detection and identification of neutral and charged particles generated within the relevant angular and energy range. This task will be shared by the combination of a central and a forward spectrometer of modular design where both are optimized for the specific kinematics of the antiproton-nucleon annihilation process.

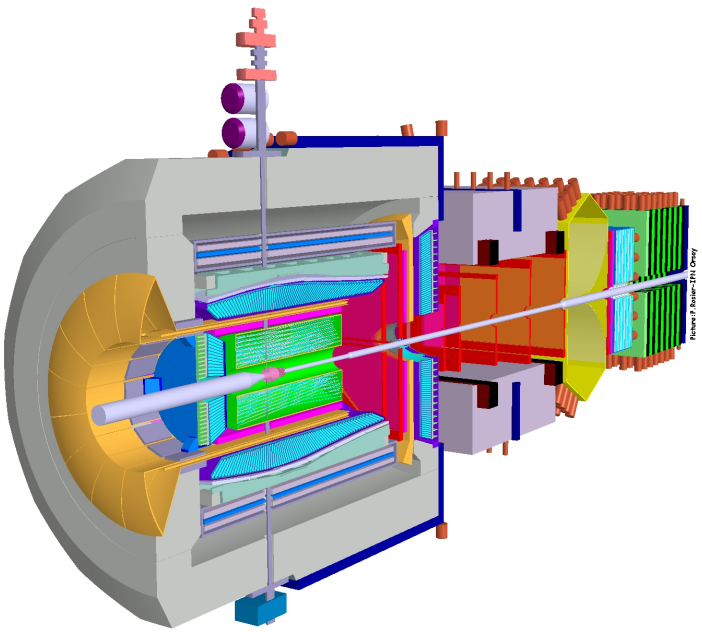

The $\overline{\text{P}}$ANDA Collaboration

Universität Basel, Switzerland
M. Kotulla, B. Krusche, F. Zehr

Institute of High Energy Physics, Chinese Academy of Sciences, Beijing, China
J.J. Xie, B.S. Zou

Universität Bochum, I. Institut für Experimentalphysik, Germany
A. Golischewski, K. Götzen, T. Held, H. Koch, B. Kopf, B. Lewandowski, H. Nowak, H. Schmücker, M. Steinke, P. Wieczorek, A. Wilms, J. Zhong

Helmholtz-Institut für Strahlen- und Kernphysik, Bonn, Germany
F. Hinterberger

Università di Brescia, Italy
A. Zenoni

Dipartimento di Fisica e Astronomia dell'Università di Catania and INFN, Sezione di Catania, Italy
M. De Napoli, G. Raciti, E. Rapisarda

Instytut Fizyki, Uniwersytet Jagiellonski, Cracow, Poland
P. Hawranek, B. Kamys, St. Kistryn, A. Magiera, P. Moskal, B. Piskor-Ignatowicz, C. Piskor-Ignatowicz, Z. Rudy, P. Salabura, J. Smyrski, M. Wojciechowski

Gesellschaft für Schwerionenforschung mbH, Darmstadt, Germany
U. Lynen, J. Lühning, H. Orth, K. Peters, T.R. Saitoh, C. Schwarz, C. Sfienti

Technische Universität Dresden, Germany
K.-T. Brinkmann, H. Freiesleben, R. Jäkel

Veksler-Baldin Laboratory of High Energies (VBLHE), Joint Institute for Nuclear Research ([a]), Laboratory of Particle Physics (LPP) ([b]), Laboratory of Information Technologies (LIT) ([c]), Laboratory of Nuclear Problems (LNP) ([d]), Dubna, Kabardian-Balkarian State University ([e]) and Institute of Applied Mathematics and Automation ([f]), Nal'chik, Russia
V.M. Abazov[d], G. Alexeev[d], A. Arefiev[a], M.Yu. Barabanov[a], B.V. Batyunya[a], D. Bogoslovski[a], T.Yu. Bokova[a], V.V. Borisov[a], V.A. Budilov[a] Yu.V. Bugaenko[a], V.Kh. Dodokhov[a], A.A. Efremov[a], O.I. Fedorov[a], A.A. Feshchenko[b], A.S. Galoyan[b], G. Ivanov[a], E. Jafarov[a], V.I. Kaplin[a], A. Karmokov[e], E.K. Koshurnikov[a], V.Ch. Kudaev[f], V.I. Lobanov[a], A.F. Makarov[a], L.V. Malinina[a], V.L. Malyshev[d], K.V. Mikhailov[a], B. Morosov[a], G.A. Mustafaev[e], A.M. Nakhushev[f], P.V. Nomokonov[a], I.A. Oleks[a], V. Pismennaya[a], T.A. Pocheptsov[a], A. Polanski[c], G. Pontecorvo[d], A. Povtoreyko[a], Yu.N. Rogov[b], I.A. Rufanov[a], S. Ryabtsun[b], Z.Ya. Sadygov[a], R.A. Salmin[b], A.G. Samartsev[d], M.G. Sapozhnikov[b], T. Sereda[a], G.S. Shabratova[a], A.A. Shishkin[d], A.N. Skachkova[d], N.B. Skachkov[d], E.A. Strokovsky[b], R.Sh. Teshev[e], V. Tikhomirov[a], V.V. Tokmenin[d], E.P. Ustenko[a], V.V. Uzhinsky[c], N.V. Vlasov[b], A.S. Vodopianov[a], S.A. Zaporozhets[a], N.I. Zhuravlev[d] A.I. Zinchenko[a]

University of Edinburgh, United Kingdom
M. Aliotta, D. Branford, K. Föhl, D. Watts, P. Woods

Friedrich Alexander Universität Erlangen-Nürnberg, Germany
W. Eyrich, A. Lehmann

Northwestern University, Evanston, U.S.A.
K. Seth

Università di Ferrara and INFN, Sezione di Ferrara, Italy
D. Bettoni, R. Calabrese, P. Dalpiaz, E. Luppi, M. Savriè

Johann Wolfgang Goethe-Universität Frankfurt, Germany
R. Dörner, R. Grisenti, M. Kaesz

INFN-Laboratori Nazionali di Frascati, Italy
P. Gianotti, C. Guaraldo, O.N. Hartmann, M. Iliescu, V. Lucherini, E. Pace, C. Petrascu, D. Sirghi, F. Sirghi

INFN, Sezione di Genova, Italy
R. Ballantini, M. Macri, R. Parodi, A. Pozzo

Justus Liebig-Universität Gießen, II. Physikalisches Institut, Germany
M.G. Destefanis, W. Döring, P. Drexler, M. Düren, I. Fröhlich, D.G. Kirschner, W. Kühn, K. Makonyi, V. Metag, M. Nanova, R. Novotny, F. Ottone, C. Salz, J. Schneider, B. Seitz, G.-C. Serbanut, H. Stenzel, U. Thöring M. Thiel

University of Glasgow, United Kingdom
J. Annand, A. Borissov, D. Ireland, R. Kaiser, J. Kellie, K. Livingston, C. McGeorge, D. Protopopescu, G. Rosner

Institut für Kernphysik ([a]), Zentralinstitut für Elektronik ([b]), Forschungszentrum Jülich, Germany
M. Drochner[b], W. Gast[a], A. Gillitzer[a], D. Grzonka[a], V. Hejny[a], G. Kemmerling[b], H. Kleines[b], W. Oelert[a], D. Prasuhn[a], J. Ritman[a], S. Schadmand[a], A. Sibirtsev[a], A. Sokolov[a], T. Stockmanns[a], H. Ströher[a], A. Ucar[a], P. Vlasov[a], P. Wintz[a], P. Wüstner[b]

Uniwersytet Slaski, Katowice, Poland
J. Holeczek, J. Kisiel, B. Kłos,

Institute of Modern Physics, the Chinese Academy of Science, Lanzhou, P.R. China
R. Chen, L. Duan, Z. Hu W. Li, Z. Sun, G. Xiao, Z. Xiao, H. Xu, H. Xu

Institut für Kernphysik, Johannes Gutenberg-Universität Mainz, Germany
P. Achenbach, J. Pochodzalla, A. Sanchez-Lorente

Politecnico di Milano ([a]), Physics Department, Università di Milano ([b]) and INFN, Sezione di Milano ([c]), Italy
P. Alberto[b,c], R. Bassini[c], C. Boiano[c], I. Iori[b,c], S. Riboldi[a,c]

Research Institute for Nuclear Problems, Belarus State University, Minsk, Belarus
V.I. Dormenev, G.Y. Drobychev, A.A. Fedorov, A.E. Korneev M.V. Korzhik, A.R. Lopatik, O.V. Missevitch

Technische Universität München, Germany
B. Ketzer, I. Konorov, A. Mann, S. Neubert, S. Paul, L. Schmitt, Q. Weitzel

Westfälische Wilhelms-Universität Münster, Germany
D. Frekers, A. Khoukaz, A. Täschner, J. Wessels

Budker Institute of Nuclear Physics (BINP), Novosibirsk, Russia
E. Baldin, V. Malyshev, A. Maslennikov, S. Peleganchyk, G. Pospelov, A. Sukharev, Yu. Tikhonov

Institut de Physique Nucléaire, Orsay, France
M. Guidal, T. Hennino, M. Mac Cormick, S. Ong, B. Ramstein, J. Van de Wiele, J. Pouthas, P. Rosier, T. Zerguerras

Dipartimento di Fisica Nucleare e Teorica, Università di Pavia ([a]), INFN, Sezione di Pavia ([b]), Italy
G. Bendiscioli[a,b], G. Boca[a,b], A. Fontana[a,b], P. Genova[a,b], L. Lavezzi[a,b], P. Montagna[a,b], A. Panzarasa[a,b], A. Rotondi[a,b], P. Salvini[b]

Institute for High Energy Physics (IHEP)([a]), Protvino;
Tomsk State University (TSU)([b]), Tomsk, Russia;
and National Center of Particle and High Energy Physics (NCPHEP)([c]), Minsk, Belorussia
E. Ardashev[a], Yu. Arestov[a], G. Ayzenshtat[b], G. Britvich[a], B. Chuiko[a], S. Golovnya[a], S. Gorokhov[a], A. Kholodenko[a], V. Lishin[a], V. Parakhin[a] V. Pikalov[a], V. Shelikhov[a], N. Shumeiko[c], A. Solin[c], O. Tolbanov[b], A. Tyazhev[b], A. Vorobiev[a]

Petersburg Nuclear Physics Institute of Academy of Science (PNPI), Gatchina, St. Petersburg, Russia
S. Belostotski, G. Gavrilov, Y. Naryshkin, O. Miklukho, A. Sarantsev, V. Vikhrov

Kungliga Tekniska Högskolan (KTH), Stockholm, Sweden
B. Cederwall, A. Johnson

Stockholms Universitet, Sweden
C. Bargholtz, K. Lindberg, P.E. Tegnér, I. Zartova

Università del Piemonte Orientale Alessandria, Torino and INFN, Sezione di Torino, Italy
M.L. Colantoni, L. Fava, D. Panzieri

Dipartimento di Fisica Generale 'A. Avogadro', Università di Torino and INFN, Sezione di Torino, Italy
M. Alexeev, A. Amoroso, F. Balestra, R. Bertini, M.P. Bussa, O. Denisov, A. Ferrero, L. Ferrero, V. Frolov, R. Garfagnini, A. Grasso, A. Maggiora, M. Maggiora, G. Pontecorvo, G. Piragino, F. Tosello, G. Zosi

Dipartimento di Fisica Generale Università di Torino (^{a}), Dipartimento di Fisica Sperimentale, Università di Torino (^{b}), INFN, Sezione di Torino (^{c}), IFSI, Sezione di Torino (^{d}) and Politecnico di Torino (^{e}), Italy
M. Agnello[c,e], E. Botta[b,c], T. Bressani[b,c], L. Busso[a,c], D. Calvo[b,c], P. De Remigis[c], A. Feliciello[b,c], F. Ferro[c,e], A. Filippi[b,c], F. Iazzi[c,e], S. Marcello[b,c], G. Mazza[c], O. Morra[c,d], A. Rivetti[c], R. Wheadon[c]

INFN, Sezione di Trieste and Università di Trieste, Italy
R. Birsa, F. Bradamante, S. Dalla Torre, M. Giorgi, A. Martin, P. Schiavon, F. Tessarotto

Physikalisches Institut, Universität Tübingen, Germany
H. Clement, E. Doroshkevitch, K. Ehrhardt, P. Gonser

The Svedberg Laboratory, Uppsala, Sweden
H. Calén, C. Ekström, K. Fransson, A. Kupsc, P. Marciniewski

Institutionen för Strålningsvetenskap, Uppsala Universitet, Sweden
F. Cappellaro, B. Höistad, T. Johansson, I. Lehmann, A. Lundborg, Y.-N. Rao, Ö. Nordhage, J. Nyberg, H. Pettersson, K. Schönning, P. Thörngren Engblom, U. Wiedner, J. Zlomanczuk

Universitat de Valencia, Dpto. de Física Atómica, Molecular y Nuclear, Spain
J. Diaz

Stefan Meyer Institut für Subatomare Physik, Österreichische Akademie der Wissenschaften, Vienna, Austria
M. Cargnelli, H. Fuhrmann, P. Kienle, J. Marton, E. Widmann, J. Zmeskal

Soltan Institute for Nuclear Studies, Warsaw, Poland
Z. Guzik, M. Kisielinski, T. Kozlowski, D. Melnychuk, J. Wojtkowska, B. Zwieglinski

Warsaw University of Technology, Institute of Atomic Energy, Otwock-Swierk, Poland
B. Slowinski

Spokesperson: Ulrich Wiedner Email: ulrich.wiedner@tsl.uu.se
Deputy: Paola Gianotti Email: paola.gianotti@lnf.infn.it

Preface

This document is intended to show progress that the international $\overline{\mathrm{P}}$ANDA collaboration made in the design of the detector. It is clear that six months after the approval of the $\overline{\mathrm{P}}$ANDA Letter of Intent not all detectors are defined and specified in detail.
Nevertheless, with ongoing R&D, significant progress has been made since in the hardware design and is reported here together with the expected physics performance.

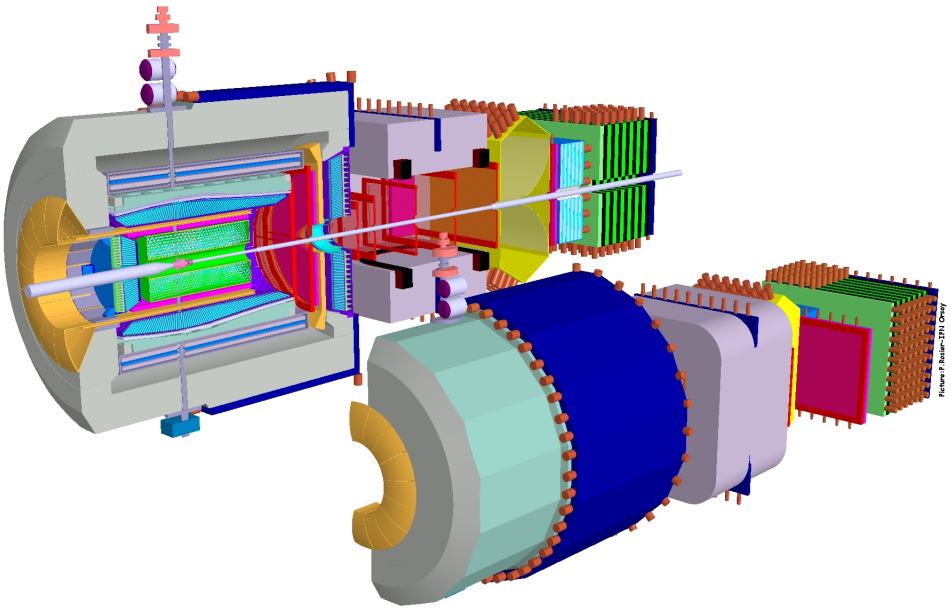

Contents

Introduction

The $\overline{\text{P}}$ANDA collaboration proposes to build a state-of-the-art universal detector for strong interaction studies at the high-energy storage ring HESR at the international FAIR facility. The detector is designed to take advantage of the extraordinary physics potential which will be available utilizing high intensity, phase space cooled antiproton beams.

Spectroscopy has been a prime tool for physics in the last century and has played a leading role in the development of quantum mechanics and the standard model of physics. Quantum Chromo Dynamics (QCD) is generally accepted to be the correct underlying theory of the strong interaction. However, our knowledge of the behavior at large distances is still rather primitive. Spectroscopy experiments within hadron physics are the tool to investigate both in the dynamics governing the interaction of fundamental particles and the existence of new forms of matter. The latter could consist of gluonic degrees of freedom, like glueballs and hybrids, previously undiscovered charmonium states, the extension of the nuclear chart into the strangeness dimension, or particles produced inside nuclear matter. Only when we can predict, confirm, and explain the physical states of the theory, we can hardly claim that we understand the strong interaction. The deep understanding might have further reaching implications in particle physics. For example, it is quite possible that the weak interactions becomes strong at high energies and field theories of the strong interaction may be relevant to the mechanism of the electroweak symmetry breaking. In strong-interaction studies based on QCD we have the ideal laboratory to test our understanding of theory against experimental results.

Significant progress beyond the present understanding can only be made if the statistics and precision of the data and their analysis exceeds past efforts by several orders of magnitude. The $\overline{\text{P}}$ANDA detector will be optimized for the physics goals as discussed above. At the same time, the detection system should be able to accommodate additional physics aspects, like Drell-Yan and $\mathcal{CP}$-violating processes. The $\overline{\text{P}}$ANDA program carries outstanding discovery potential and excellent opportunities for the investigation of additional physics topics. In this report, we aim to demonstrate the detector's intrinsic ability to cover a broad variety of physics processes.

Placing a detector inside a storage ring allows for optimal use of precious antiprotons but poses severe experimental challenges. The number of antiprotons is limited and the required high-luminosity can only be achieved by an appropriately attuned target. Triggering on decaying charm particles requires precise micro vertex tracking close to the target or lepton identification, dependent on the final state. The $\overline{\text{P}}$ANDA detector has an advanced particle identification system. Charged particle tracking together with a high-resolution electromagnetic calorimeter are mandatory for spectroscopy experiments. The almost full coverage of the solid angle in $\overline{\text{P}}$ANDA is achieved by a combination of a target spectrometer with a forward spectrometer. The complex detector arrangement is to assure the measurement of complete sets of parameters and signatures. The procedure warrants a robust and redundant physics reconstruction which is considered particularly important in a high-luminosity environment.

The design of $\overline{\text{P}}$ANDA is based on previous experience in antiproton experiments and takes advantage of ongoing detector developments performed at the high-energy laboratories for experiments. A first sketch of the detector that fulfils the physics requirements was laid out in the Letter of Intent (LoI). In the meantime, an extensive R&D program for detector and cost optimization has started in certain areas which settles open options in the detector design. Within the growing $\overline{\text{P}}$ANDA collaboration assignments for the different tasks have been distributed among the different institutions. The aim of the Technical Progress Report is a description of the detector and the expected physics performance.

1 Executive Summary

1.1 Physics Motivation

The strong force governs the microscopic structure of matter. It dominates the interaction between the nucleons, i.e. the protons and neutrons within the atomic nucleus, and it is the key force that determines the interaction between the quarks within the nucleon and within other hadrons (strongly interacting particles). Achieving a fully quantitative understanding of matter at this level is one of the most challenging and fascinating areas of modern physics. During the last two decades hadronic physics has moved from phenomenological to fundamental understanding. The theory of Quantum Chromodynamics (QCD) is regarded as the basic theory of the strong interaction. While being elegant and deceptively simple, the theory generates a most remarkable richness and complexity of phenomena. The possible forms of matter range from the spectrum of strongly interacting hadrons and nuclear species to compact stars of extreme density and to the quark-gluon plasma, a state of matter in the early universe and, possibly, in the interior of very heavy stars.

The fundamental building blocks of QCD are the quarks which interact with each other by exchanging particles, the gluons. QCD is simple and well understood at short-distance scales, much shorter than the size of a nucleon ($< 10^{-15}$ m). In this regime, the basic quark-gluon interaction is sufficiently weak. Here, perturbation theory can be applied, a calculation technique of high predictive power yielding accurate results when the coupling strength is small. In fact, many processes at high energies can quantitatively be described by perturbative QCD within this approximation.

The perturbative approach fails when the distance among quarks becomes comparable to the size of the nucleon, the characteristic dimension of our microscopic world. Under these conditions, the force among the quarks becomes so strong that they cannot be further separated, in contrast to the electromagnetic and gravitational forces which fall off with increasing distance. This unusual behavior is related to the self-interaction of gluons: gluons do not only interact with quarks but also with each other, leading to the formation of gluonic flux tubes connecting the quarks. As a consequence, quarks have never been observed as free particles and are confined within hadrons, complex particles made of 3 quarks (baryons) or a quark-antiquark pair (mesons). Baryons and mesons are the relevant degrees of freedom in our environment. An important consequence of the gluon self-interaction and – if found – a strong proof of our understanding of hadronic matter is the predicted existence of hadronic systems consisting only of gluons (glueballs) or bound systems of quark-antiquark pairs and gluons (hybrids).

In the evolution of the universe, some microseconds after the big bang, a coalescence of quarks to hadrons occurred associated with the generation of mass. The elementary light quarks, the up and down quarks, that make up the nucleon have very small masses amounting to only a few percent of the total mass of the nucleon. Most of the nucleon mass, and of the visible universe stems from the QCD interaction. The generation of mass is associated with the confinement of quarks and the spontaneous breaking of chiral symmetry, one of the fundamental symmetries of QCD in the limit of massless quarks.

The phenomena of the confinement of quarks, the existence of glueballs and hybrids, and the origin of the mass of strongly interacting, composite systems related to confinement and the breaking of chiral symmetry are long-standing puzzles and represent the intellectual challenge in our attempt to understand the nature of the strong interaction and of hadronic matter. GSI has a distinguished history of having made important contributions to the physics of strong interactions, in particular nuclear physics. The proposed $\overline{\text{P}}$ANDA experiment will enable the new FAIR facility to play a significant role in strong interaction physics, providing a link between nuclear physics and hadron physics.

1.2 Research Program

The proposal demonstrates that antiproton beams of unprecedented intensity and quality in the energy range of 1 GeV to 15 GeV, as provided by the new FAIR facility together with $\overline{\text{P}}$ANDA, will be an excellent tool to address fundamental questions. Antiproton beams in this energy regime, stored in the High-Energy Storage Ring (HESR) for in-ring experiments, will provide access to the heavier strange and charm quarks and to copious production of gluons. As illustrated in Fig. 1.1, the physics program

offers a broad range of investigations that extend from the study of Quantum Chromodynamics to the test of fundamental symmetries. The key components of the antiproton program are summarized as follows:

The determination of the interaction potential through precision spectroscopy has been a successful tool at all levels of the structural hierarchy of matter, as for example in atoms and molecules. The charm quark is sufficiently heavy to lend itself to non-relativistic perturbative treatment far more reliably than the light up, down, and strange quarks. Thus, an optimal testing ground for a quantitative understanding of confinement is provided by charmonium spectroscopy, i.e. the spectroscopy of mesons built of charmed quark-antiquark pairs ($c\bar{c}$). The proposed program, using resonant antiproton-proton annihilation, is a quantitative and qualitative extension of successful experiments performed recently at the antiproton accumulator at FNAL, USA. However, the studies (which ended in 2 000) were limited in scope by lower antiproton energies ($< 9\,\text{GeV}$), lower luminosities ($\leq 2.5 \cdot 10^{31}\text{cm}^{-2}s^{-1}$) and a detector only capable of detecting electromagnetic reaction products. At FAIR, advanced antiproton cooling techniques will enable high energy resolution and a more versatile detector setup will be employed allowing for the first time a measurement of both electromagnetic and hadronic decays with high precision. The goal is to achieve comprehensive precision spectroscopy of the charmonium system for a detailed study, particularly of the confinement part of the QCD potential. This in turn will help to understand the key aspects of gluon dynamics which are being investigated and quantitatively predicted in the framework of Lattice QCD.

Recent experiments at LEAR/CERN have demonstrated that particles with gluonic degrees of freedom are produced copiously in proton-antiproton annihilation in the light quark sector. A central part of the antiproton program presented in this proposal is the first search for gluonic excitations, glueball and hybrids, in the charmonium mass range where they are expected to be less mixed with the multitude of normal mesons. The unambiguous determination of the gluonic modes would establish an important missing link in the confinement problem of hadrons.

GSI has an active ongoing program on the modification of the properties (masses, widths, *etc.*) of light mesons (pions and kaons) by the nuclear medium and the relation to the partial restoration of chiral symmetry. The proposed experimental program at the HESR will address the open problem of interactions and in-medium modifications of hadrons with charm quarks in nuclei. On the one hand, this is an extension of the present GSI research program. On the other hand, the program will provide the first insight into the gluonic charmonium-nucleon and charmonium-nucleus interaction. A quantitative knowledge of charmonium-nucleon cross sections is considered to be of crucial importance in the identification of the formation of the quark-gluon plasma in ultra-relativistic heavy-ion collisions.

A new and largely unexplored dimension in the chart of nuclides is introduced by replacing an up or down quark by a strange quark in a nucleon bound in a nucleus, leading to the formation of a hypernucleus. Here, the strangeness quantum number is introduced into the nucleus. Antiproton beams at the proposed facility will allow efficient production of hypernuclei with more than one strange hadron. The program opens new perspectives for nuclear structure studies and is a novel complement to the proposal to study the structure of nuclei with radioactive beams. The nucleon with the strange quark (hyperon) is not restricted in the population of nuclear states as neutrons and protons are. These exotic nuclei offer a variety of new and exciting perspectives in nuclear spectroscopy and for studying the forces among hyperons and nucleons.

One of the most important symmetries of physics is $\mathcal{CP}$ symmetry (charge conjugation $\mathcal{C}$ times spatial parity $\mathcal{P}$). $\mathcal{CP}$ symmetry implies that the laws of physics apply to a system after the combined action of exchanging particles by their antiparticles and by reflection of the system in a spatial mirror. However, if $\mathcal{CP}$ symmetry was perfectly obeyed, none of the matter in the universe, neither stars nor human beings, would exist since matter and antimatter would have annihilated each other. The observed dominance of matter in the universe may be attributed to $\mathcal{CP}$ violation, an effect directly observed in the decay of neutral kaons and, very recently, in B mesons. $\mathcal{CP}$ violation can be studied in the charm meson sector and in hyperon decays, with the HESR storage ring running at full luminosity. An observation of significant $\mathcal{CP}$ violation would indicate physics beyond the Standard Model.

Two of the research areas with antiprotons, the in-medium properties of charmed hadrons and the structure of atomic nuclei with one or more strange hadrons, are examples of the close intellectual connection between the physics with antiprotons and two other major thrusts of the current proposal, relativistic nucleus-nucleus collisions and nuclear structure physics with radioactive beams. They

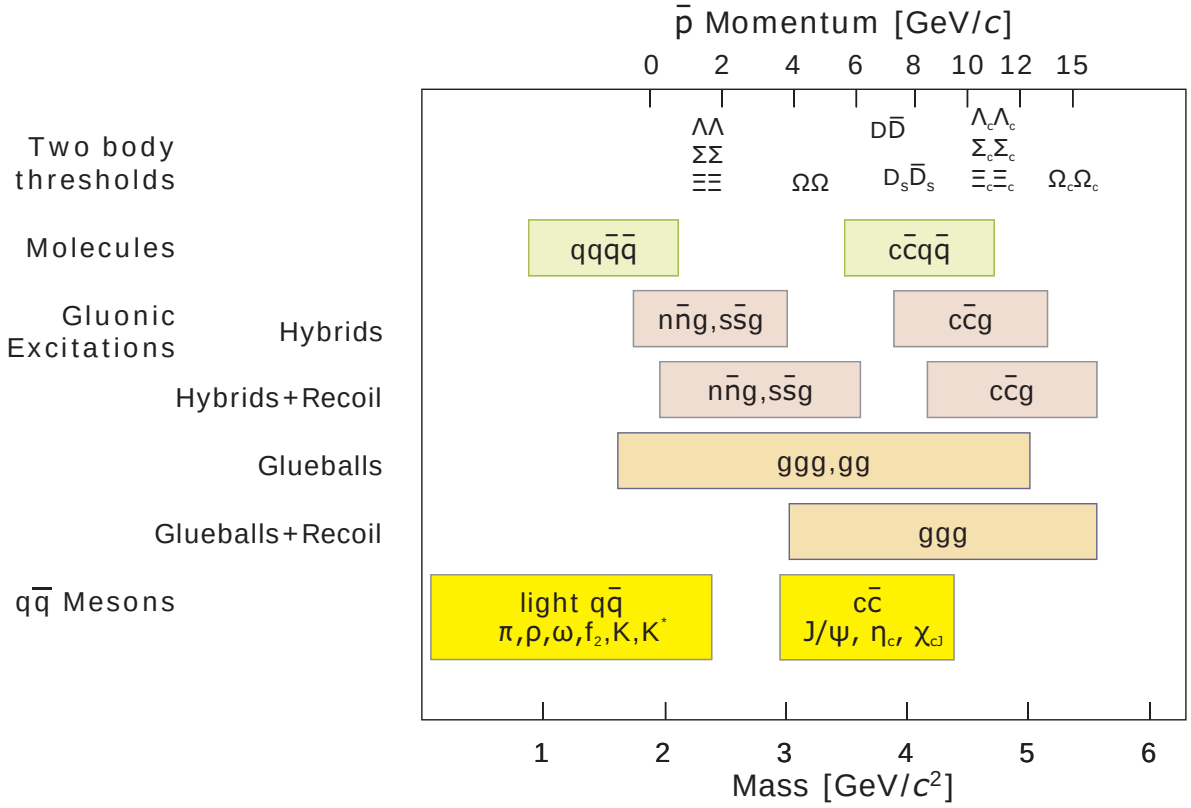

Figure 1.1: Mass range of hadrons accessible at the HESR with antiproton beams. The figure indicates the antiproton momenta required for charmonium spectroscopy, the search for charmed hybrids and glueballs, the production of D meson pairs and the production of Σ baryon pairs for hypernuclear studies. The energy range covered by the former Low Energy Antiproton Ring (LEAR) at CERN is indicated by the arrow.

contribute in a synergetic way to the broader goal of a deeper understanding of the structure of hadronic matter in all its forms. Finally, the close connection between the various components of the present proposal is evident in the pursuit of symmetry tests and symmetry breaking effects, which are the key for our understanding of how the world is built from the fundamental building blocks.

1.3 Instrumentation and Detector

The technical capabilities and the uniqueness of the proposed facility are of great importance in the realization of the research objectives. Fig. 1.2 shows the High-Energy Storage Ring (HESR) for antiprotons with its key components: a high energy electron cooling section that will provide beams of unprecedented quality and precision and the internal target facility with an advanced detector system. The high energy electron cooling is a genuine technological challenge. Therefore, a detailed research and development project and a collaborative effort has been initiated with experts from Fermilab and Novosibirsk.

The detector design incorporates the most recent technologies in order to reach the required performance criteria with regard to mass, momentum and energy resolution, hit resolution, particle identification, and solid angle coverage. The combination of the high-quality antiproton beam and the detec-

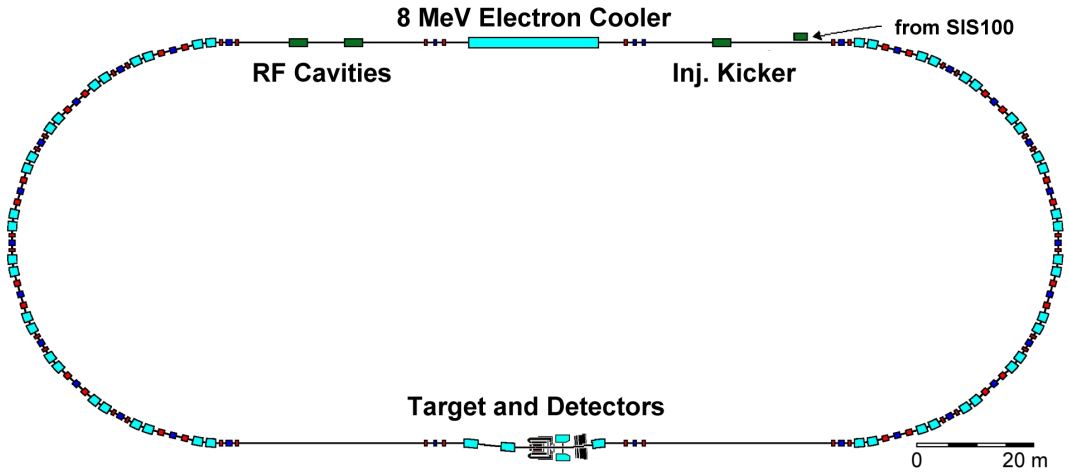

Figure 1.2: Layout of HESR.

tor system provides a powerful and unique facility, unparalleled worldwide, to carry out the research discussed in the main section of the report.

The goal is to achieve almost full hermiticity. The detector has to be able to track particles down to momenta of 100–200 MeV/c and up to a maximum of 8 GeV/c. A vertex detector is required since many channels include charm mesons. A key component is electromagnetic calorimetry with excellent resolution. Furthermore, particle identification of kaons, protons, and muons is mandatory.

The general layout of $\overline{\text{P}}$ANDA is based on two magnetic spectrometers and is shown in Fig. 1.3. The *target spectrometer* surrounds the interaction region and has a superconducting solenoid as momentum analyzer. A forward opening of 5–10° (depending on the respective axis) allows high momentum tracks to enter the *forward spectrometer* with a large gap dipole magnet.

1.3.1 Interaction region

Various targets are considered for the different physics programs within $\overline{\text{P}}$ANDA. Most of the measurements require a proton target which can be realized in two alternative ways:

- A pellet target device produces a stream of small pellets of frozen hydrogen falling through and interacting with the antiproton beam. This type of target is able to achieve average densities in the order of up to $10^{16}\,\text{cm}^{-2}s^{-1}$. That would match the desired luminosity of $2 \cdot 10^{32}\,\text{cm}^{-2}s^{-1}$ at a gas load compatible with a low cross section for pumping around the interaction region. Furthermore, by having several hundred interactions within one pellet, it is possible to track its flight path and determine the individual interaction points precisely.

- The second option is a cluster jet target which sends an ultra-dense hydrogen jet through the beam. It provides a homogeneous stream of gas which is easy to handle from the accelerator point of view. Currently, the R&D work is focussing on improving the densities such that the design luminosity of $\overline{\text{P}}$ANDA can be reached.

As the requirements on a target for different types of experiments are manifold, it is not clear, whether one target will be able to fulfill all of them. Thus currently both targets are foreseen on equal footing and would fit into the detector. A cluster jet target or a pellet target can also be used for reactions with nuclei. However, higher luminosities and a better definition of the interaction point are provided by using wire or strip targets (see Sec. 4.5). The use of an internal gas storage cell, e.g. a target of polarized ^{3}He, is proposed (see Sec. 4.3).

1.3.2 Target Spectrometer

The defining element of the target spectrometer is the superconducting solenoidal magnet. It has a length of 2.5 m, a diameter of 1.9 m and an axial field of 2 T. It has to accommodate a gap for pipes of the target device. The target spectrometer is made up of the following components:

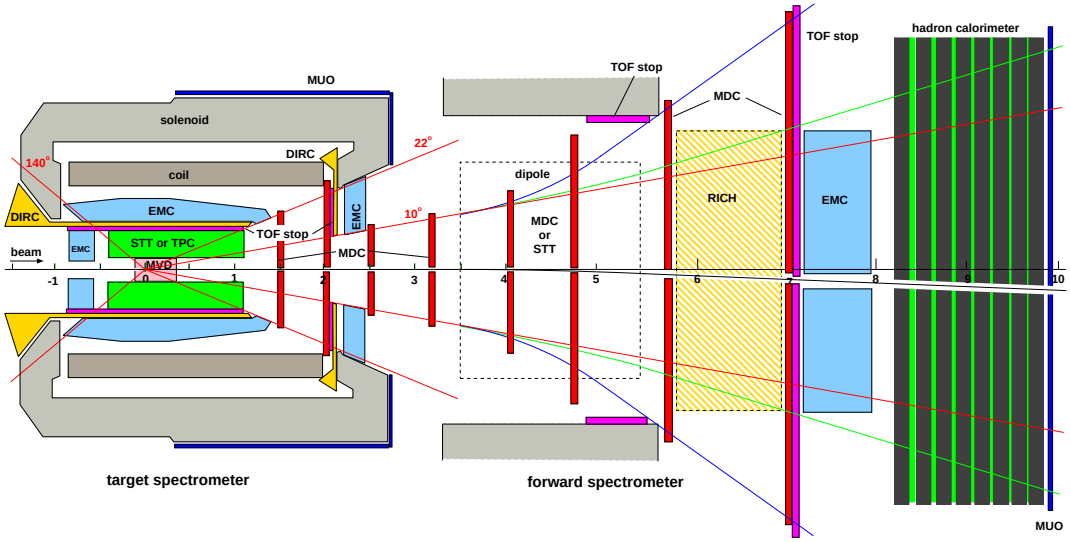

Figure 1.3: Setup of the $\overline{\text{P}}$ANDA detector.

- The interaction point is surrounded by a micro vertex detector (MVD) which has five barrel shaped layers plus five disk-shaped detectors in forward direction. The three innermost layers are composed of pixel detectors to achieve best resolution and to be able to easily detect decay vertices displaced from the interaction point. The outer layers are composed of microstrip detectors which are easier to handle.

  The baseline technology chosen for the pixel detectors are hybrid active pixel sensors as used by several LHC experiments. The electronics still has to be modified to accommodate continuous readout. As alternatives to silicon pixels, GaAs based detectors are considered as well as much thinner monolithic pixel sensors where the problem of radiation hardness would have to be solved.

- The MVD is surrounded by a cylindrical tracker. Two options are currently discussed, a straw tube tracker (STT) consisting of a set of double layers of self-supporting straws and a time projection chamber (TPC) with continuous readout.

  The TPC is the technically more challenging option since it requires an ungated charge collection based on a GEM readout. However it has the benefit of less material and offers in addition particle identification via $\mathrm{d}E/\mathrm{d}x$.

  On the other hand, the STT is seen as a safe fall-back solution which should still fulfil the basic tracking requirements.

  In the forward direction circular or octagonal mini drift chambers are used to track particles with higher momenta before they enter the forward spectrometer.

- The next detector is a Cherenkov counter based on the DIRC principle as used in BaBar at SLAC. It consists of quartz rods in which Cherenkov light is internally reflected to an array of photon detectors in the backwards direction. The readout can be either done by imaging a 2D pattern of reflections with a large number of PMTs or APDs or by measuring just one coordinate and the time of light propagation inside the quartz very precisely.

  In forward direction a disk-shaped Cherenkov counter with quartz radiator and detectors for internally reflected light similar as for the barrel DIRC is planned. Its readout should be located between the solenoid coil and the return yoke to allow the calorimeter end cap to be as close as possible.

- An electromagnetic calorimeter is placed outside the DIRC. It consists of a barrel part with 11 360 crystals, a forward end cap with 6 864 crystals and a backward end cap with 816 crystals. As detector material $PbWO_4$ is foreseen,

since it is fast and has a reasonable resolution. As alternative BGO with still higher light yield albeit slower signals is considered.

- Finally, outside the superconducting magnet and its iron return yoke, drift tubes track muons exiting the spectrometer.

The necessity of a time-of-flight detector in the target spectrometer is still under discussion. Although the flight path is short, low momentum particles could still be identified.

1.3.3 Forward Spectrometer

The heart of the forward spectrometer is a dipole magnet with a large opening and a field integral of 2 Tm. This will provide the required momentum resolution for forward tracks with momenta up to 8 GeV/*c*.

One problem of the dipole magnet is the deflection of the beam. If included in the beamline design it can be countered by a magnet chicane. Otherwise the beam could be shielded from the magnetic field, introducing some material in the acceptance. A completely different option would be the usage of a toroidal magnet in the forward spectrometer. Although providing an azimuthal symmetry nicely matching to the target spectrometer it reduces the acceptance at small angles and requires the instrumentation of a larger area with trackers and calorimeters.

The detector systems in the forward spectrometer are summarized in the following:

- Tracking is provided by mini drift chambers. Before the magnet, they have the same octagonal shape as in the end cap of the target spectrometer. After the magnet, a rectangular shape matches is more suitable for the spread of tracks. The use of straw tube trackers inside the dipole field is considered for better momentum resolution.

- The option of a third Cherenkov counter, based on gas or aerogel is still under investigation. In addition, a time-of-flight detector is considered for charged particle identification.

- An electromagnetic calorimeter based on lead/scintillator sampling and WLS fibre readout (Shashlyk type) is foreseen in the forward spectrometer. It should have 276 channels to cover the acceptance and will reach a resolution in the range of 3–5%/$\sqrt{E}$[GeV].

- After the electromagnetic calorimeter, the MIRAC detector from WA80 at CERN is under investigation as a hadron calorimeter after refurbishing its readout.

- The last piece of equipment is a muon detector based on drift tubes.

1.3.4 Data Acquisition and Trigger

The selected readout and trigger concept foresees continuous digitization of all detector channels. Special trigger hardware is not foreseen. The readout electronics has to be fully pipelined and has to perform autonomously the detection of valid hits as well as intelligent data reduction by clusterization, signal shape analysis, and time reconstruction to transfer only the physically relevant minimum of information. All data are marked by a synchronous timestamp by which event building can be performed at a later stage.

The data are fed into a configurable network. Attached computer nodes with the required bandwidth digest the full rate of certain sub-detectors used for the first selection level. Other detectors transfer data only for time slices selected on some level. Parallel selections are possible and several levels will bring the data rate down to the required 100–200 MB/s to mass storage. The clear advantage of this scheme is its flexibility: Any conceivable physics signature of an interesting process measurable by the $\overline{\text{P}}$ANDA detector could be converted into a sequence of selection algorithms. Typical signatures are the decays of J/ψ to leptons, decay vertices of charm or strange hadrons, identified kaons or electromagnetic showers, *etc.*. The level of complexity is only limited by the required processing power and can be scaled up by attaching more nodes.

The trigger system and the universality of the detector make $\overline{\text{P}}$ANDA a unique tool in hadron physics, ready for future challenges.

2 Physics Case

2.1 Overview

Experimentally, studies of hadron structure can be performed with different probes such as electron, pion, kaon, proton or antiproton beams, each of which have its specific advantages. In antiproton-proton annihilation, particles with gluonic degrees of freedom as well as particle-antiparticle pairs are copiously produced, allowing spectroscopic studies with unprecedented statistics and precision. Therfore, antiprotons of 1–15 GeV/c will be an excellent tool to address the open problems. The following experiments are foreseen:

- Charmonium ($c\bar{c}$) spectroscopy: precision measurements of mass, width, decay branches of all charmonium states, especially for extracting information on the quark-confining potential. The unequaled resolution in the $\bar{\mathrm{p}}\mathrm{p}$ formation process and small systematic uncertainties give the unique opportunity to improve dramatically our knowledge which cannot be achieved elsewhere.
- Firm establishment of the QCD-predicted gluonic excitations (charmed hybrids, glueballs) in the charmonium mass range (3–5 GeV/c^2) using high statistics in combination with sophisticated spin-parity analysis in fully exclusive measurements.
- Search for modifications of meson properties in the nuclear medium and the possible relationship to the partial restoration of chiral symmetry for light quarks. Particular emphasis is placed on mesons with open and hidden-charm, extending ongoing studies in the light quark sector to heavy quarks and adds information on contributions of the gluon dynamics to hadron masses.
- Precision γ-ray spectroscopy of single and double hypernuclei for extracting information on their structure and on the hyperon-nucleon and hyperon-hyperon interaction.

Further physics opportunities will open up as soon as the HESR facility reaches the full design luminosity:

- Extraction of generalized parton distributions from $\bar{\mathrm{p}}\mathrm{p}$ annihilation
- D meson decay spectroscopy (rare leptonic and hadronic decays)
- Search for $\mathcal{CP}$ violation in the charm and strangeness sector (D meson decays, $\Lambda\bar{\Lambda}$ system)

Selected topics of the science case will be discussed in the following sections. For topics not mentioned here, please refer to the CDR [1] and previous work on the physics and a potential detector [2, 3]. It is an important feature of the $\overline{\mathrm{P}}$ANDA detector that for a specfific antiproton momentum and target selection, different physics aspects can be studied simultaneously.

2.2 Charmonium

The fundamental understanding of strong interactions in terms of QCD was greatly stimulated by the discovery of the J/ψ in 1974. This and other systems of a charm and anti-charm quark (charmonium) turned out to be a powerful tool in the understanding of the strong interaction. They are the results of $c\bar{c}$ spectroscopy which help tuning potential models of mesons. This is the place where the gluon condensate, closely related to the charmonium masses, is determined. The gluon condensate together with the $q\bar{q}$ condensate represent the energy density of the QCD vacuum. The charmonium system offers unique advantages for understanding quarkonia since the low density of states and their narrowness reduces mixing among them while below the corresponding open-charm thresholds.

The best understanding has been achieved for the ψ states. These can be formed directly at electron-positron colliders. With an antiproton beam charmonium states of all quantum numbers could be formed directly and the precision of the mass and width measurement depends on the beam quality only. In this case, the detector resolution is less important and the detector response is optimized for an efficient background rejection. Important data on the excited non-ψ states, the D states of charmonium, will be extremely helpful to further develop theoretical understanding.

2.2.1 Narrow Charmonium

The comparison of the hadronic decays of the J/ψ and the ψ' [4] shows that radial excitations of charmonium are far from being simple recursions of the ground states. Therefore, it is a necessity to identify and study the first radial excitation of the charmonium ground state η_c'. It was discovered by the Belle-Experiment in hadronic B decays [5] and was confirmed by CLEO and BaBar [6, 7] in $\gamma\gamma$-collisions. Its properties are incompatible with earlier findings by Crystal Ball [8] and is only marginally consistent with most model calculations. The accuracy for the width ($\Gamma = (19\pm10)\,\text{MeV}/c^2$) is only 50 %. In contrast to the limited statistics and the systematic limitations of e^+e^- machines, including the measurements at the B-factories, a $\overline{\text{p}}$p scan will finally settle these questions, also for the ground state of charmonium, the η_c. Here, five precise measurements of the η_c properties were performed in the past two years which disagree strongly among each other [9, 10, 11].

The precision of the measurements will take advantage of the high yield of charmonium production in $\overline{\text{p}}$p annihilations (e.g. BR($\overline{\text{p}}\text{p} \rightarrow \eta_c$)= $(1.2\pm0.4)\cdot10^{-3}$). By detecting hadronic final states ($KK\pi\pi$, $4K$, 4π, $K\overline{K}\pi$, $\eta\pi\pi$, ...) with branching fractions two orders of magnitude higher than in the $\gamma\gamma$ decay mode used so far, high-statistics samples can easily be collected.

The singlet-P resonance of charmonium, h_c, is of extreme importance in determining the spin dependent components of the $q\bar{q}$ confinement potential. The h_c was first observed and positively identified by E760 in the process $\overline{\text{p}}\text{p} \rightarrow h_c \rightarrow J/\psi\pi^0$ [12]. The value of the mass measured by E760 was $M(h_c) = (3526.2\pm0.3)\,\text{MeV}/c^2$ whereas, due to the limited statistics, only an upper value for the width at 1.1 MeV could be set. The h_c has subsequently been observed by the E835 collaboration in the process $\overline{\text{p}}\text{p} \rightarrow h_c \rightarrow \eta_c\gamma \rightarrow \gamma\gamma\gamma$ [13] and by the CLEO collaboration in the decay mode $h_c \rightarrow \eta_c\gamma$, with the η_c decaying to hadrons [14]. The mass values of E835 and CLEO agree with each other and with the E760 result. It should be pointed out that due to the narrow width ($\leq 1\,\text{MeV}/c^2$) and expected low yields, only a $\overline{\text{p}}$p formation experiment like $\overline{\text{P}}$ANDA will be able to measure the h_c width and to carry out a systematic study of its decay modes. The proposed experiment could provide a substantial improvement of the determination of this state and is an important part of the charmonium program.

Many other aspects are worth measuring, like the radiative de-excitation of the χ_{cJ} states (^3P_J). The decays are dominated by the dipole term E1. Higher multipoles arise in the relativistic treatment of the interaction between the electromagnetic field and the quarkonium system, and can be studied by measuring the angular distributions of both χ_{c1} and χ_{c2}. A discrepancy with theory has been observed by the FNAL experiments E760 and E835 [15, 16] at the $2.5\,\sigma$ level. Further high-statistics measurements are needed to increase the significance of the result.

2.2.2 Charmonium above Open Charm Threshold

Above the $D\overline{D}$ breakup threshold at $3.73\,\text{GeV}/c^2$ the charmonium spectrum is poorly known since e^+e^- experiments have only measured $R = \sigma(e^+e^- \rightarrow \textit{hadrons})/\sigma(e^+e^- \rightarrow \mu^+\mu^-)$ in large energy steps. Here, rather washed-out structures were observed. The latest, much more accurate measurements by BES [19] do not confirm the sharp states reported by [20]. It is an open question whether the higher vector states at 4040, 4160, and $4415\,\text{MeV}/c^2$ are realistic. It is of critical importance to investigate this mass region in small energy steps. E760/E835 were not able to study any physics above the $D\overline{D}$ threshold because of their energy limitation.

Yet, this is the region in which narrow $^1D_2$, $^3D_2$ states (which are narrow because they cannot decay to $D\overline{D}$) and the first radial excitation of the h_c and the χ_{cJ} are expected to exist. A first evidence for such a state comes from the Belle collaboration which in 2003 reported the discovery of a new, narrow resonance in the decay mode $J/\psi\pi^+\pi^-$ with a mass of $3872.0\,\text{MeV}/c^2$ [21]. This new state, called $X(3872)$, has subsequently been observed by CDF [22], DØ [23] and BaBar [24]. The mass measurements by the four experiments are in very good agreement but the mass value does not fit in the current models. Therefore, alternative interpretations, like a $D^0\overline{D}^{*0}$ molecule, have been discussed. A precision measurement of all ^1D and ^3D states is mandatory in order to distinguish between various models.

Apart from the unexpected discovery of the $X(3872)$ there are numerous other narrow charmonium states expected above the open charm threshold. The narrowness usually arises from forbidden decay channels and/or nodes in the wave functions inhibiting the day. A list of narrow charmonium is provided in Table 2.1. The calculation is based on a potential ansatz with Coulomb, linear confinement,

	Mass [MeV/c^2]		Width [MeV/c^2]	
	predicted	measured	predicted	measured
$\psi(1D)$		3770	43	23.6±2.7
$\psi(3S)$		4040	74	52±10
$\psi(2D)$		4159	74	78±20
$\eta_c(3S)$	≈4070		67	
$\chi_{c0}(2P)$	≈3870		29	
$\psi_3(1D)$	≈3800		0.6	
$\chi_{c4}(1F)$	≈4100		9.0	
$h_{c3}(1F)$	≈4030		64	

Table 2.1: Predictions for narrow charmonia ($\Gamma < 70\,\mathrm{MeV}/c^2$) above the open charm threshold from potential and $^3P_0$ models. Details can be found in [17]. Measured values are taken from PDG [18].

smeared hyperfine and spin-orbit terms

$$\begin{aligned} V(r) &= -\frac{4}{3}\frac{\alpha_s}{r} + br + \frac{32\pi}{9m^2}\alpha_s\delta_\sigma(r)S_1\cdot S_2 \\ &+ \left[\frac{2\alpha_s}{m^2r^3} + \frac{b}{2m^2r}\right]L\cdot S \\ &+ \frac{4\alpha_s}{m^2r^3}T \end{aligned} \quad (2.1)$$

The values for a, b, and δ_σ have been fitted to match known resonances. The $^3P_0$ model has been used to calculate partial decay widths for all open charm decays. In addition to the topics discussed above, exclusive charmonium decays represent a crucial testing ground for QCD predictions. Hadron helicity non-conserving processes, $\mathcal{G}$-parity violating decays, radiative ψ' decays and hadronic χ_{cJ} decays are of particular interest.

To test the ability to detect charmonium decays in formation mode the channels

- $\overline{\mathrm{p}}\mathrm{p} \rightarrow \eta_c \rightarrow \phi\phi, \rightarrow K^+K^-K^+K^-$,
- $\overline{\mathrm{p}}\mathrm{p} \rightarrow \eta_c \rightarrow K^0_S K^\pm\pi^\mp$,
- $\overline{\mathrm{p}}\mathrm{p} \rightarrow, \eta_c \rightarrow \gamma\gamma$,
- $\overline{\mathrm{p}}\mathrm{p} \rightarrow \psi(3770) \rightarrow D\overline{D}$, and
- $\overline{\mathrm{p}}\mathrm{p} \rightarrow \psi(4040) \rightarrow D^*\overline{D^*}$

have been chosen for validation.

2.3 Gluonic Excitations

The QCD spectrum is richer than that of the naive quark model because the gluons, mediating the strong force between quarks, can act as principal components of entirely new types of hadrons. These "gluonic hadrons" fall into two categories: glueballs and hybrids. Glueballs are predominantly excited states of glue while hybrids are resonances consisting largely of a quark, an antiquark, and excited glue. The additional degrees of freedom carried by gluons allow glueballs and hybrids to have spin-exotic quantum numbers J^{PC} that are forbidden for normal mesons and other fermion-antifermion systems. Exotic quantum numbers (e.g. $J^{PC} = 0^{--}$, 0^{+-}, 1^{-+}, 2^{+-}) provide the best opportunity to distinguish between gluonic hadrons and $q\overline{q}$ states. However, even non-exotic glueballs and hybrids can be identified by measuring an overpopulation of the experimental meson spectrum and by comparing properties, like masses, quantum numbers, and decay channels, with predictions from models or Lattice Quantum Chromodynamics (LQCD). The properties of glueballs and hybrids are determined by the long-distance features of QCD and their study will yield fundamental insight into the structure of the QCD vacuum.

The most promising results for gluonic hadrons have come from antiproton annihilation experiments. Two particles, first seen in πN scattering [25, 26] with exotic $J^{PC} = 1^{-+}$ quantum numbers, $\pi_1(1400)$ [27] and $\pi_1(1600)$ [28] are clearly seen in $\overline{\mathrm{p}}\mathrm{p}$ annihilation at rest. Table 2.2 shows a summary of all reported resonances with exotic quantum numbers. In the search for glueballs, a narrow state at $1500\,\mathrm{MeV}/c^2$, discovered in antiproton annihilations by Crystal Barrel [37, 38, 39, 40, 41], is considered the best candidate for the glueball ground state ($J^{PC} = 0^{++}$). However, the mixing with nearby conventional scalar $q\overline{q}$ states makes the unique interpretation as a glueball difficult.

2.3.1 Hybrid Charmonium

The search for glueballs and hybrids has mainly been restricted to the mass region below $2.2\,\mathrm{GeV}/c^2$. Experimentally, it would be very rewarding to go to

Experiment	Exotic	J^{PC}	Mass [MeV/c^2]	Width [MeV/c^2]	Decay	Refs.
E852	$\pi_1(1400)$	1^{-+}	1359 $^{+16}_{-14}$ $^{+10}_{-24}$	314 $^{+31}_{-29}$ $^{+9}_{-66}$	$\eta\pi$	[29]
Crystal Barrel	$\pi_1(1400)$	1^{-+}	1400 $\pm20\pm20$	310 ±50 $^{+50}_{-30}$	$\eta\pi$	[27]
Crystal Barrel	$\pi_1(1400)$	1^{-+}	1360 ±25	220 ±90	$\eta\pi$	[30]
Obelix	$\pi_1(1400)$	1^{-+}	1384 ±28	378 ±58	$\rho\pi$	[31]
E852	$\pi_1(1600)$	1^{-+}	1593 ±8 $^{+29}_{-47}$	168 ±20 $^{+150}_{-12}$	$\rho\pi$	[32]
E852	$\pi_1(1600)$	1^{-+}	1597 ±10 $^{+45}_{-10}$	340 $\pm40\pm50$	$\eta'\pi$	[32]
Crystal Barrel	$\pi_1(1600)$	1^{-+}	1590 ±50	280 ±75	$b_1\pi$	[33]
Crystal Barrel	$\pi_1(1600)$	1^{-+}	1555 ±50	468 ±80	$\eta'\pi$	[28]
E852	$\pi_1(1600)$	1^{-+}	1709 $\pm24\pm41$	403 $\pm80\pm115$	$f_1\pi$	[34]
E852	$\pi_1(1600)$	1^{-+}	1664 $\pm8\pm10$	185 $\pm25\pm28$	$\omega\pi\pi$	[35]
E852	$\pi_1(2000)$	1^{-+}	2001 $\pm30\pm92$	333 $\pm52\pm49$	$f_1\pi$	[34]
E852	$\pi_1(2000)$	1^{-+}	2014 $\pm20\pm16$	230 $\pm32\pm73$	$\omega\pi\pi$	[35]
E852	$h_2(1950)$	2^{+-}	1954 ±8	138 ±3	$\omega\pi\pi$	[36]

Table 2.2: Light states with exotic quantum numbers. The experiment E852 at BNL was performed with a pion beam on a hydrogen target, while Crystal Barrel was a $p\bar{p}$ spectroscopy experiment and LEAR.

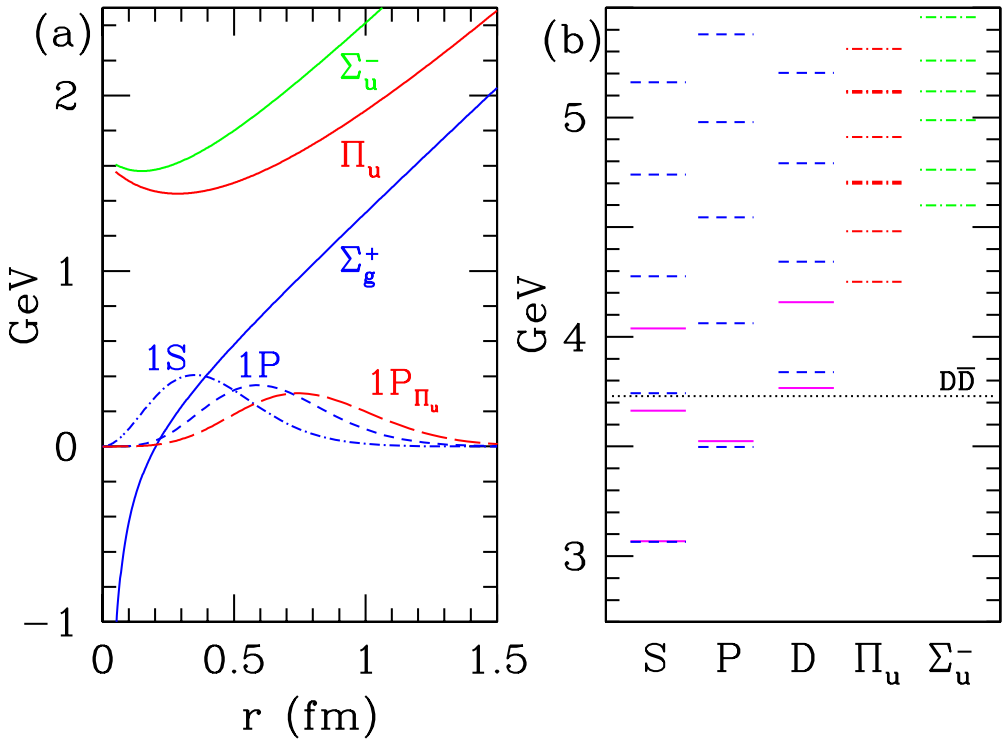

Figure 2.1: (a) Heavy quarkonium potentials and wave functions for different excitation levels from LQCD. Σ denotes normal one gluon exchange while the excited Π potentials are the lowest lying hybrid potentials. In that case, the attraction is not mediated by a single gluon but a string of gluons which carry angular momentum. (b) shows the charmonium spectrum from LQCD. The conventional charmonium states are on the right while the hybrids are found in column Π_u and Σ_u^-. See [42] for details.

higher masses because of the unavoidable problems due to the high density of normal $q\bar{q}$ mesons below 2.5 GeV/c^2. Here, the light quark states form a structure-less continuum and heavy quark states are far fewer in number and can easily be resolved. This is particularly true for the charmonium region. Exotic charmonia are expected to exist in the 3–5 GeV/c^2 mass region where they could be resolved

(a) m($c\bar{c}$g), 1^{-+}	Group	Ref.	
	4 390±80±200	MILC97	[43]
	4 317±150	MILC99	[44]
	4 287	JKM99	[45]
	4 369±37±99	ZSU02	[46]

(b) m($c\bar{c}$g,1^{-+})-m($c\bar{c}$,1^{--})	Group	Ref.	
	1 340±80±200	MILC97	[43]
	1 220±150	MILC99	[44]
	1 323±130	CP-PACS99	[47]
	1 190	JKM99	[45]
	1 302±37±99	ZSU02	[46]

Table 2.3: Masses differences (a) and masses (b) from quenched LQCD. The results for the lightest J^{PC} exotic cluster around the threshold for $D\overline{D}^{**}$ + *c.c.* production.

and identified unambiguously.

Predictions for hybrids come mainly from calculations based on the bag model, flux tube model, and constituent gluon model and, recently, with increasing precision, from LQCD [48, 49]. For hybrids, the theoretical results qualitatively agree, lending support to the premise that the predicted properties are realistic. Charmonium hybrids can be expected since the effect of an extra gluonic degree of freedom in meson-like systems is evident in the confining potentials for the $c\bar{c}g$ system (e.g. as derived from LQCD calculations in the Born-Oppenheimer approximation [49]).

The discussions have only been centered around the lowest-lying charmonium hybrids. Four of these states ($J^{PC} = 1^{--}$, 0^{-+}, 1^{-+}, 2^{-+}) correspond to a $c\bar{c}$ pair with $J^{PC} = 0^{-+}$ or 1^{--}, coupled to a gluon in the lightest mode with $J^{PC} = 1^{--}$. The other four states ($J^{PC} = 1^{++}, 0^{+-}, 1^{+-}, 2^{+-}$) with the gluon mode $J^{PC} = 1^{-+}$ are probably heavier. Three of the eight charmonium hybrids have spin-exotic quantum numbers ($J^{PC} = 0^{+-}$, 1^{-+}, 2^{+-}). Thus, mixing effects with nearby $c\bar{c}$ states are excluded and experimental identification is particularly simple. Compared to light hybrid candidates with reported widths of 200 to 400 MeV/c^2 [25, 26, 27, 28], charmonium hybrids are likely to be narrower since open-charm decays are forbidden or suppressed below the $D\overline{D}^*_J$ + *c.c.* (often referred to as DD^{**}) threshold. From experiments at LEAR we know that production rates of such $q\bar{q}$ states are similar to those of states with exotic quantum numbers. Thus, we estimate that the cross sections for the formation and production of charmonium hybrids will be similar to those of normal charmonium states which is in the order of 120 pb ($\overline{\mathrm{p}}\mathrm{p} \rightarrow J/\psi\pi^0$ [50]), in agreement with theoretical predictions [51].

Formation experiments would generate non-exotic charmonium hybrids with high cross sections while production experiments would yield a charmonium hybrid together with another particle, such as a π or an η. In $\overline{\mathrm{p}}\mathrm{p}$ annihilation, production experiments are the only way to obtain charmonium hybrids with exotic quantum numbers. It is envisaged that the first step of exploring charmonium hybrids would consist of production measurements at the highest antiproton energy available ($E_{\overline{\mathrm{p}}} = 15$ GeV, $\sqrt{s} = 5.46$ GeV/c^2) and studying all possible production channels available to cover exotics and non-exotic states. The next step would consist of formation measurements by scanning the antiproton energy in small steps in the regions where promising hints of hybrids have been observed in the production measurements, thus having a second check on the static properties like the J^{PC} assignment as well as mass and width.

The discovery of such a reaction would necessitate a very good charmonium reconstruction efficiency. Thus, apart from the benchmark channels used for conventional charmonium, the charmed hybrid production in the mode $\overline{\mathrm{p}}\mathrm{p} \rightarrow \psi_g\eta \rightarrow \chi_{cJ}\pi^0\pi^0\eta$ has also been used to study the detector performance in multibody charmonium reactions (see Sec. 13.5.9).

2.3.2 Glueballs

LQCD calculations make rather detailed predictions for the glueball mass spectrum in the quenched approximation disregarding light quark loops [52]. For example, the calculated width of approximately 100 MeV/c^2 [53] for the ground-state glueball matches the experimental results. LQCD predicts the presence of about 15 glueballs, some with exotic quantum numbers in the mass range accessible to the HESR.

Glueballs with exotic quantum numbers are called oddballs which cannot mix with normal mesons. As a consequence, they are predicted to be rather narrow and easy to identify experimentally [54]. It is conceivable that comparing oddball properties with those of non-exotic glueballs will reveal deep insight into the presently unknown glueball structure since the spin structure of an oddball is different [54]. The lightest oddball, with $J^{PC} = 2^{+-}$ and a predicted mass of 4.3 GeV/c^2, would be well within the range of the proposed experimental program. Like charmonium hybrids, glueballs can either be formed directly in the $\bar{p}p$-annihilation process, or produced together with another particle. In both cases, the glueball decay into final states like $\phi\phi$ or $\phi\eta$ would be the most favorable reaction below 3.6 GeV/c^2 while $J/\psi\eta$ and $J/\psi\phi$ are the first choice for the more massive states.

The indication for a tensor state around 2.2 GeV/c^2 was found in the experiment of Jetset collaboration at LEAR [55]. The acquired statistics was not sufficient for the complementary reactions to be determined. We plan to measure the $\bar{p}p \to \phi\phi$ channel with statistics of two orders of magnitude higher than in the previous experiments. Moreover, other reactions of two vector particle production, such as $\bar{p}p \to \omega\omega, K^*\overline{K^*}, \rho\rho$ will be measured. However, the best candidate for the pseudo-scalar glueball ($\eta_L(1440)$), studied comprehensively at LEAR by the Obelix collaboration [56, 57, 58, 59, 60], is not widely accepted to be a glueball signal because the calculations of LQCD predict its mass above 2 GeV/c^2. Therefore, new data on many glueball states are needed to make a profound test of different model predictions.

It is worth stressing again that $\bar{p}p$-annihilations present a unique possibility to search for heavier glueballs since alternative methods have severe limitations. The study of glueballs is a key to understanding long-distance QCD. Every effort should be made to identify them uniquely.

The six photon channel $\bar{p}p \to \pi^0\pi^0\eta \to 6\gamma$ is investigated in the simulation chapter (see Sec. 13.5.1) in order to compare the well known performance of existing detectors (Crystal Barrel, E760/E835) with the performance of the PANDA setup. Other channels of interest are open and hidden charm final states which are already used for the validation of charmonium production.

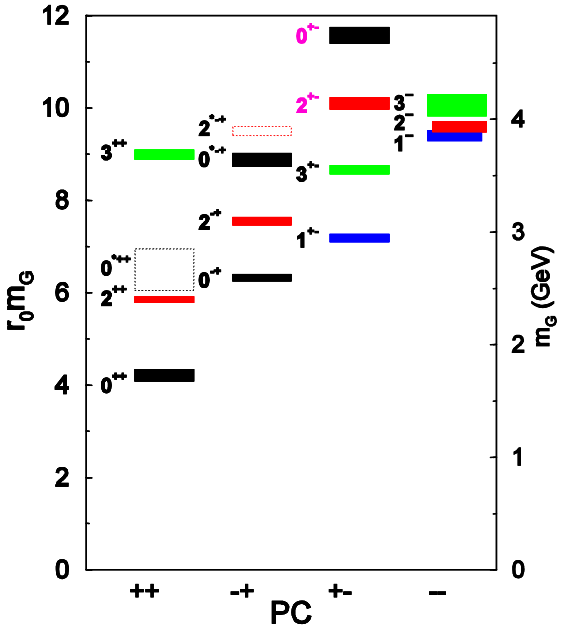

Figure 2.2: Glueball prediction from LQCD calculations. See [61, 52] for details. While the region of the ground-state glueball was investigated in the LEAR era (in particular by Crystal Barrel) are the tensor glueball and the spin exotic glueballs with $J^{PC} = 0^{+-}$ and 2^{+-} important research topics for PANDA.

2.3.3 Other Exotics

Other exotics like tetra- and pentaquark systems (up to $\approx$2.7 GeV/c^2) are accessible in this energy range. Charmed pentaquarks would require an antiproton beam of at least 20 GeV/c and have consequently not been considered. Tetra-quark production can be investigated by Drell–Yan-like tagged events where one $q\bar{q}$ pair creates a lepton pair while the other four may produce a bound state of four quarks. The pentaquark production could be studied near threshold (e.g. $\bar{p}p \to \Theta^+\Theta^-$) where low partial waves dominate.

2.4 Charm in Nuclei

Presently, the investigation of medium modifications of hadrons embedded in hadronic matter is one of the main research activities at GSI. The physics goal is to understand the origin of hadron masses in the context of spontaneous chiral symmetry breaking in QCD and their modification due to chiral dynamics and partial restoration of chiral symmetry in a hadronic environment. The studies have been focused on the light quark sector due to the limitations in available energy. The in-medium potential of pions has been deduced from spectroscopic information obtained in the study of deeply bound pionic states [62, 63, 64]. Studies of K^+ production in proton-nucleus collisions [65, 66] and of K^+ and K^- production in heavy-ion collisions [67, 68, 69, 70, 71] are consistent with repulsive and attractive mass shifts of these particles, respectively, in nuclear matter. The study of medium modifications of the light vector mesons (ρ, ω, ϕ), for which substantial changes of spectral functions in the medium are predicted to occur already at normal nuclear matter density [72], is the main research goal of the Hades experiment.

The high-intensity $\overline{\mathrm{p}}$ beam up of to 15 GeV/c will allow an extension of this program to the charm sector, both for hadrons with hidden and with open charm. The short-distance interaction of charmonium states, consisting of charm quarks only, with color singlet hadrons is governed by the exchange of two or more gluons. As the masses of charmonia are dominated by the large mass of the charm quark pair, only little sensitivity to changes in the quark condensate is expected for charmonium states. Consequently, the in-medium mass of these states would be affected primarily by a modification of the gluon condensate. Therefore, investigating the interaction of $c\bar{c}$ mesons with nucleons and nuclei is one way to explore fundamental aspects of gluon dynamics in QCD. However, recent calculations [73] indicate only small in-medium mass reductions of the order of 5–10 MeV/c^2 for the low lying charmonium states J/ψ and η_c. The situation may be different for excited charmonium states as this effect is expected to scale with the volume occupied by the $c\bar{c}$ pair. Large attractive mass shifts of 40 MeV/c^2 for χ_{cJ}, 100 MeV/c^2 for ψ', and 140 MeV/c^2 for $\psi(3770)$ were recently predicted by modelling a QCD 2^{nd} order Stark-effect [74, 75]. An experimental verification of the in-medium mass shifts will give access to the strength of the gluon condensate inside nuclei.

For D mesons, the situation is different. Built of a heavy c quark and a light antiquark, the D meson is the QCD analogue to the hydrogen atom. Hence, D mesons provide the unique opportunity to study the in-medium dynamics of a system with a single light quark. Recent theoretical work agrees in the prediction of a mass splitting for D mesons in nuclear matter but disagrees in the predicted size of the splitting (50 MeV/c^2 in Ref. [76, 77], 160 MeV/c^2 in Ref. [78]) and in the sign of the D^- mass shift (attractive in Ref. [76, 77], repulsive in Ref. [78]). A smaller in-medium mass shift but a broad D meson spectral distribution is obtained in Ref. [79].

It should be noted that the availability of $\overline{\mathrm{p}}$ beams opens completely new opportunities to investigate the nuclear potential of strange hadrons. Apart from the formation of hypernuclei as discussed in Sec. 2.5, the production of slow K^- or $\overline{\Lambda}$ inside nuclei and the possible existence of nuclear bound states may be studied in $\overline{\mathrm{p}}$-nucleus collisions.

2.4.1 Charmonium Absorption

Experimental information on charm propagation in nuclear matter is scarce and theoretical predictions are highly model dependent. In order to form a basis for a better understanding of the properties of charmed hadrons in nuclear matter, first studies within this research program should concentrate on the measurement of J/ψ and D meson production cross sections in $\overline{\mathrm{p}}$ annihilation on a series of nuclear targets. The comparison of the resonant J/ψ yield obtained from $\overline{\mathrm{p}}$ annihilation on protons and different nuclear targets allows to reliably deduce the J/ψ nucleon dissociation cross section [80]. This is particularly important for the understanding of J/ψ suppression in ultra-relativistic heavy-ion collisions, interpreted as a signal for a transition to a quark-gluon phase.

In particular, an exclusive measurement of the final states populated in $\overline{\mathrm{p}}$d collisions would allow to determine the coupling between different channels with charmed hadrons and to study the interaction of charmed hadrons with nucleons and mesons in the final state. For example, the reaction $\overline{\mathrm{p}}\mathrm{d} \rightarrow J/\psi\gamma\mathrm{n}$ [81] provides the possibility to measure the elastic $J/\psi + N$ cross section down to low relative momenta.

2.4.2 Mass Shift of Charmed Mesons in Nuclei

The experimental access to medium modifications of charmed hadrons is more difficult. Whereas the

in-medium mass of charmonia can be reconstructed from their decay into di-leptons or photons, different signals have been proposed for the detection of the in-medium mass shifts of D mesons. A reduction of the $D\overline{D}$ threshold would result in an increased D and $\overline{D}$ production in $\overline{\text{p}}$ annihilation on nuclei, in particular at sub-threshold energies [78]. D and $\overline{D}$ mesons can be identified via their hadronic decays with $\overline{K}$ and K mesons in the final state. Cross sections of typically 1 nb near threshold lead to about 100 events registered per day at a luminosity of $10^{31}\,\text{cm}^{-2}\text{s}^{-1}$ which would allow a substantial D meson physics program.

Moreover, a lowering of the $D\overline{D}$ threshold in the nuclear medium could open this decay channel or increase its partial width for the decay of the excited charmonium states lying close to the free $D\overline{D}$ mass ($\psi(3770)$, ψ', χ_{c2}) [77, 82], provided the reduction of the in-medium masses of the charmonium states is sufficiently small. Recent model calculations [83] indicate that a dropping of the $D\overline{D}$ threshold in the nuclear medium by $\sim 50\,\text{MeV}/c^2$ could be seen in a suppression of low-mass di-leptons from the decay of the $\psi(3770)$.

An observable modification of the excited charmonium spectral distribution due to the $D\overline{D}$ decay is not expected if the states exhibit substantial attractive in-medium mass shifts [74, 75] of similar size as the $D\overline{D}$ threshold. However, according to Refs. [74, 75] the mass shifts of the charmonium states may be deduced from their in-medium decay which is enhanced relative to the decay in the vacuum due to the collisional width along the path inside the nucleus.

In Sec. 13.5.10, the $\overline{\text{P}}$ANDA detector performance for finding a J/ψ signal in a $\overline{\text{p}}$Cu reaction is discussed in further detail.

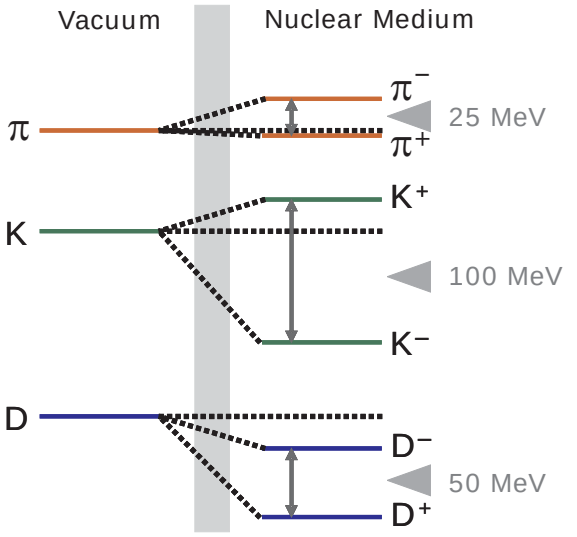

Figure 2.3: Shift of D mesons in the nuclear medium. The shift of pions and kaons have been discovered already before at GSI.

2.5 Hyperon-Hyperon and Quark-Quark Forces

2.5.1 Hypernuclei

Replacing an up or a down quark with a strange quark in a nucleon, which is bound in a nucleus, leads to the formation of a hypernucleus. A new quantum number, strangeness, is introduced into the nucleus, adding a third axis to the nuclear chart. Due to experimental limitations the third dimension has only scarcely been explored in the past.

Single and double Λ-hypernuclei were discovered 50 [84] and 40 years ago [85], respectively. However, only 6 double Λ-hypernuclei are presently known, in spite of a considerable experimental effort during the last 10 years. Thanks to the use of $\overline{\text{p}}$ beams and the skilful combination of experimental techniques, copious production at $\overline{\text{P}}$ANDA is expected, with even higher numbers than at (planned) dedicated facilities. A new chapter of strange nuclear physics will be opened whose first result will be the determination of the ΛΛ strong interaction strength, not feasible with direct scattering experiments.

The hyperon – usually a Λ particle – is not restricted by the Pauli principle in populating all possible nuclear states, in contrast to neutrons and protons. The description of hyperons occupying the allowed single-particle states is without the complications encountered in ordinary nuclei, like pairing interactions. The strength of the Λ-N strong interaction may be extracted with a description of the pure single-particle states by well known wave functions. Furthermore, the decomposition into the different spin-dependent contributions may be analyzed. For these contributions, significantly different predictions exist from meson exchange current and quark models. At the same time, the Λ-N weak interaction can be studied where the Pauli principle acts in the opposite way: the decay of the Λ into $N\pi$ is suppressed, since all nucleon states in the nucleus are occupied. In contrast, the process $\Lambda N \rightarrow NN$ is allowed, opening a unique window for four-baryon, strangeness non-conserving interaction.

2.5.2 Di-Baryons

The possible existence of an $S = -2$ six-quark ($uuddss$) H-di-baryon [86, 87] represents another challenging topic of $\Lambda\Lambda$ hypernuclear physics. The experimental search for this lightest strangelet has been inconclusive. Moreover, even a strongly bound H-particle cannot be excluded [88]. In fact, the short time scale in a coalescence process, of the order of 10^{-23} s, may prevent the transition from a $\Lambda\Lambda$ state to an H-particle in free space. Here, double Λ-hypernuclei may serve as a catalyst for the H-particle. The long lifetime, of the order of 10^{-10} s, of two Λ hyperons bound together in a nucleus may help to overcome a possible repulsive interaction at short distances. It might be possible to observe its traces since the mass of the H-particle might drop inside a nucleus [89] and due to hyperon mixing [90, 91]. Thus, high resolution spectroscopy of $S = -2$ hypernuclei can give important information on this fascinating object.

2.5.3 Hyperatoms

Finally, hyperatoms created during the capture process of the hyperon will supply new information on fundamental properties of hyperons. Intrinsic properties of hadrons reflect the properties of the mutual interaction between the individual constituents inside the complex particles. The Ω hyperon (sss) is particularly interesting because of its long lifetime of 82 ps and the spin quantum number of 3/2. It is the only elementary baryon with a non-vanishing spectroscopic quadrupole moment, $Q_s \propto 3J_z^2 - J(J+1)$. As a consequence, the quadrupole moment can principally be measured directly without taking recourse to theoretical models [92] by the hyperfine splitting in Ω^- atoms. It is expected that the Ω^- quadrupole moment is mainly determined by the one-gluon exchange contribution to the quark-quark interaction [93]. However, predictions of the Ω quadrupole moment in various models range from 0 to about $3 \cdot 10^{-2}\,\mathrm{e} \cdot \mathrm{fm}^2$ [94]. The measurement will not only provide first information on the shape of a baryon but also represents a unique benchmark for our understanding of the quark-quark interaction. Like in the deuteron, where the long-range tensor potential is tested by the quadrupole moment, the tensor component of the quark-quark interaction determines the quadrupole deformation of the Ω hyperon. In addition, the simplicity of the Ω baryon with 3 identical and rather heavy quarks makes it an ideal test case for theoretical studies on the lattice. As will be sketched in Sec. 9.1.3 the $\overline{\mathrm{p}}\mathrm{p} \to \Omega\overline{\Omega}$ reaction makes it possible to produce a large number of Ω^- atoms and to observe x-ray transition from the exotic atoms. However, a precise measurement of the hyperfine splitting caused by the quadrupole moment of the Ω^- will require additional effort. It is worthwhile to mention that this experiment will particularly benefit from studies of anti-protonic atoms at the low energy antiproton facility FAIR at GSI.

2.6 Further Options

2.6.1 Open charm physics

HESR running with full luminosity (limited by the production rate of $2{\cdot}10^7\,\overline{\mathrm{p}}/\mathrm{s}$) at momenta larger than 6.4 GeV/c would produce large numbers of D meson pairs. Such an installation can be considered as a hadronic factory for tagged open charm, with about 100/ s charmed pairs around $\psi(4040)$. Despite the small ratio ($5{\cdot}10^{-6}$) of charm production to total cross section, the background conditions are expected to be favorable because the hadrons are produced at threshold without phase space for additional hadrons in the same process. The high yield and the well defined production kinematics of D meson pairs allows to investigate e.g. D and D_s and their rich physics spectrum.

2.6.1.1 Open Charm Spectroscopy

The B-Factory experiments have discovered several resonances in the D ($\mathrm{c\overline{d}}$, $\mathrm{c\overline{u}}$ and c.c.) and D_s ($c\overline{s}$ and c.c.) sector where two are extremely narrow, ($D^*_{sJ}(2317)$ [95] and $D_{sJ}(2458)$ [96, 97, 98]). The measurements have triggered intense discussions since they appear at unexpected locations giving rise to speculations about their nature. The large mass shift (compared to theoretical predictions [99]) is discussed in terms of chiral aspects in heavy-light systems [100, 101]. The models would have strong implications on any system with a single light quark. It is important to verify this finding and to settle this question albeit that there is some evidence for the scalar D state [102, 103]. Threshold pair production can be employed for precision measurements of the mass and the width of narrow excited D and D_s states.

2.6.1.2 Rare Decays

The study of rare decays can open a window onto physics beyond the standard model since it probes symmetry violation. Lepton flavor number violat-

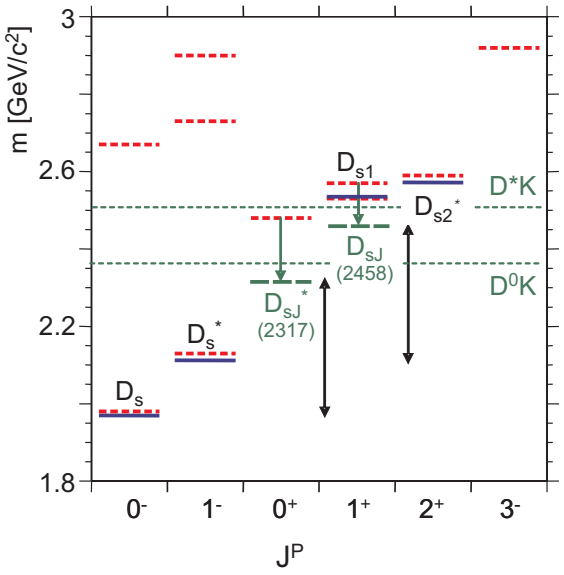

Figure 2.4: Spectrum of D_s mesons. The newly found $D^*_{sJ}(2317)$ and $D_{sJ}(2458)$ may fit into the $q\overline{q}$ spectrum but the masses are more than 140 MeV/c^2 lower than expected from potential models, thus showing strong chiral effects.

ing decays, e.g. $D^0 \to \mu e$ or $D^\pm \to \pi\mu e$, could be searched for. Flavor changing neutral currents like in the decay $D^0 \to \mu^+\mu^-$ can occur in the standard model through box graphs or weak penguin graphs with branching fractions smaller than 10^{-15}. However, the signatures of the decays are clean leaving hope for their observation, if processes exist that boost the decay branch.

2.6.1.3 $\mathcal{CP}$ Violation

$\mathcal{CP}$ violation [104] has been observed in neutral kaon and in neutral B meson decays [105, 106]. In the standard model, $\mathcal{CP}$ violation arises from a single phase entering the Cabbibo-Kobyashi-Maskawa (CKM) matrix. As a result, two elements of this matrix, i.e. V_{ub} and V_{td} have large phases. The elements have small magnitudes and involve the third generation and $\mathcal{CP}$ violation is small in the K^0 system. The violation is predicted to be even smaller in the D^0 system [107]. Thus, a deviation from the small standard model effect indicating "new physics" can be more easily distinguished in experiments in the D meson system.

Working with D mesons produced at the $D\overline{D}$ threshold has advantages arising from the strong correlation of the $D\overline{D}$ pair which is kept in the hadronization process. Formed near threshold, asymmetries are not expected in the production process and the observation of one D meson reveals the quantum numbers of the other one when produced in a charge symmetric environment (flavor tagging). Thus, flavor ($D\overline{D}$) mixing and $\mathcal{CP}$ violation can be searched for in analogy to methods in the B-system produced on the $\Upsilon(4S)$ [108].

The two-body channels $\overline{\mathrm{p}}\mathrm{p} \to \psi(3770) \to D\overline{D}$ and $\overline{\mathrm{p}}\mathrm{p} \to \psi(4040) \to D^*\overline{D^*}$ have been chosen to investigate the open charm reconstruction abilities of the detector.

2.6.2 Crossed-channel Compton Scattering and Related Exclusive Processes

The theoretical framework of Generalized Parton Distributions (GPDs) [109, 110] has recently been developed [111, 112, 113]. The results caused excitement in the field of understanding the structure of the nucleon in terms of QCD. It has recently been shown that exclusive $\overline{\mathrm{p}}\mathrm{p}$ annihilation into two photons at large s and t can be described in terms of GPDs [114, 115, 116]. Using the handbag diagram (Fig. 2.5), the process is separates into a soft part which is parametrised by GPDs and a hard part which describes the annihilation of a quasi-free $q\overline{q}$ pair into two photons. Estimates of the expected count rates based on a simple model predict a few thousand $\gamma\gamma$-events per month for a luminosity of $2 \cdot 10^{32}\,\mathrm{cm}^{-2}\mathrm{s}^{-1}$ at an energy of $\sqrt{s} = 3.2\,\mathrm{GeV}/c^2$ [117]. Other estimates, based on cross section measurements of the inverse process $\gamma\gamma \to \overline{\mathrm{p}}\mathrm{p}$, predict count rates up to a factor 50 [118, 119] above the estimate of [117] but still are consistent with the handbag ansatz. The experiment E760 at Fermilab has measured the process $\overline{\mathrm{p}}\mathrm{p} \to \gamma\gamma$ at various angles. However, the measured count rates were dominated by background from processes like $\overline{\mathrm{p}}\mathrm{p} \to \pi^0\pi^0$ [120].

It is proposed to measure the crossed-channel Compton scattering and the related exclusive annihilation processes with a scalar meson, a vector meson, or a lepton pair in the final state [121]. For the latter case, a new approach has recently been developed using a factorization diagram as shown in Fig. 2.6 [122]. The comparison of the differential cross sections for the various processes and the comparison with GPD based models will allow new insights into the annihilation process in terms of quark models and QCD.

First, rather preliminary simulation results are discussed in Sec. 13.5.5.

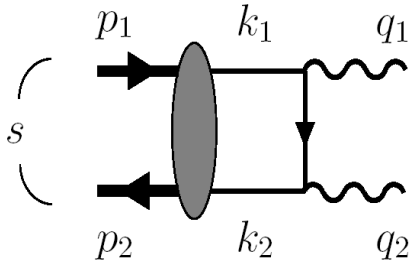

Figure 2.5: Using the handbag diagram, the $\overline{\text{p}}$p annihilation into two photons can be separated into a soft part which is parametrised by GPDs and a hard part which is described by QCD.

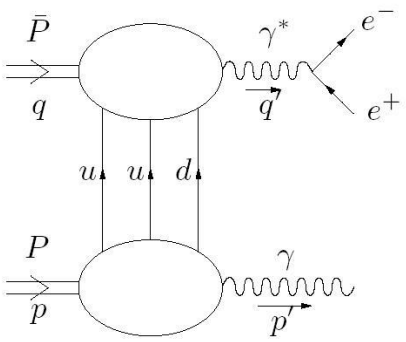

Figure 2.6: The production of a hard virtual photon (upper part) is a hard sub-process that is claimed to factorize from the lower part which can be described by a hadron to photon transition distribution amplitude.

2.6.3 Transverse Quark Distributions and Drell–Yan Processes

At leading twist level, the quark structure of hadrons is described by three distribution functions:

- the unpolarized function $f_1(x)$ representing the probability of finding a quark with a fraction x of the longitudinal momentum of the parent hadron, regardless of its spin orientation
- the longitudinal polarization distribution $g_1(x)$ that measures the net helicity of a quark in a longitudinally polarized hadron
- the transverse polarization $h_1(x)$ which is the number density of quarks with transverse polarization in a transversely polarized hadron

The distributions $f_1(x)$, $g_1(x)$ and $h_1(x)$ would contain all information on the internal dynamics of the nucleon if quarks were perfectly collinear. Instead, the number of distribution functions would increase if a finite quark transverse momentum $\boldsymbol{k}_\perp$ were allowed. In particular, two T-odd functions, the distribution functions of an unpolarized quark inside a transversely polarized parent hadron, $f_{1T}^\perp(x, \boldsymbol{k}_\perp^2)$, and of a transversely polarized quark inside an unpolarized parent hadron, $h_1^\perp(x, \boldsymbol{k}_\perp^2)$, are needed to describe the nucleon structure. The experimental

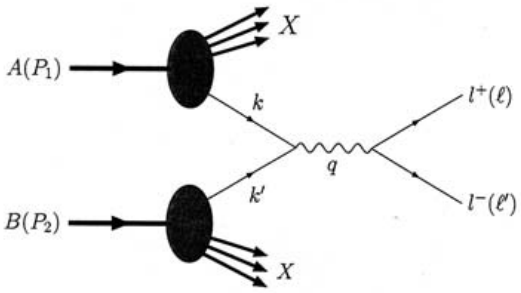

Figure 2.7: Drell–Yan dilepton production.

information on $h_1(x)$ and on $h_1^\perp(x)$ is very poor. The distributions, being chirally odd, are not observable in fully inclusive deep inelastic scattering (DIS), the reaction that provided the largest amount of the existing data on structure functions. Data on transversity are presently collected by COMPASS on semi-inclusive DIS and Hermes.

On the other hand, $h_1(x)$ can only be extracted by unfolding the data with fragmentation functions obtained from other experiments. The study of quark transverse polarization via Drell–Yan lepton pair production in $\overline{\text{p}}$p collisions is more accessible. Fig. 2.7 shows k and k' as the four-momenta of the quark q and antiquark $\bar{q}$ annihilating into a virtual photon (with four-momentum q) that originates the lepton pair with invariant mass M. The Drell–Yan cross section will depend on the cross-section of the elementary $q\bar{q} \rightarrow \gamma^*$ process. The transverse distributions of valence quarks appear at leading twist level and the cross section does not contain unknown quantities besides the transversity distributions themselves. This makes theoretical predictions easier with respect to the other reactions.

The angular distribution of dileptons, for unpolarized p and $\overline{\text{p}}$, is:

$$\frac{1}{\sigma}\frac{d\sigma}{d\Omega} = \frac{3}{4\pi}\frac{1}{\lambda+3} \times (1 + \lambda\cos^2\theta + \mu\sin^2\theta\cos\phi + \frac{\nu}{2}\sin^2\theta\cos 2\phi) \quad (2.2)$$

where θ and ϕ are defined in the rest frame of the lepton pair (see Fig. 2.8). The term ν can be ex-

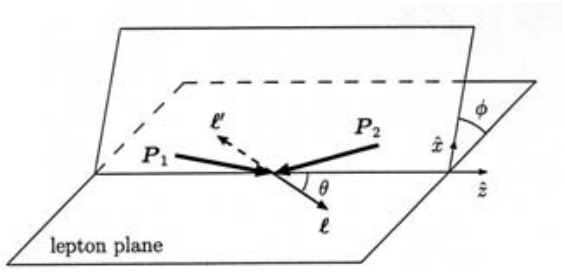

Figure 2.8: The geometry of the Drell–Yan production in the rest frame of the lepton pair.

pressed in terms of structure functions:

$$\nu = \sum_a \left(e_a^2 \mathcal{F}\left[(2\hat{\mathbf{x}}\cdot\mathbf{k}_\perp\cdot\hat{\mathbf{x}}\cdot\mathbf{p}_\perp - \mathbf{p}_\perp\cdot\mathbf{k}_\perp)\right.\right. \times h_1^\perp(x_1,\mathbf{k}_\perp)\bar{h}_1^\perp(x_2,\mathbf{k}_\perp)/(M_1M_2)\left.\right]\Big) / \sum_a e_a^2\mathcal{F} f_1(x_1,\mathbf{k}_\perp)\bar{f}_1(x_2,\mathbf{p}_\perp) \quad (2.3)$$

where the correlation factor

$$\mathcal{F} = \int d^2\mathbf{p}_\perp d^2\mathbf{k}_\perp \delta^2(\mathbf{p}_\perp + \mathbf{k}_\perp - \mathbf{q}_\perp) \times f^a(x_1,\mathbf{k}_\perp)\bar{f}^a(x_2,\mathbf{p}_\perp) \quad (2.4)$$

For p and $\overline{\text{p}}$, $h_1^\perp(x)$ and $\bar{h}_1^\perp(x)$ have the same shape. Therefore, a measurement of ν will provide $h_1^\perp(x)$. Measurements of angular distributions of DY dimuons, performed with pion beams [123], show significant effects with ν as large as 30%. Care has to be taken in the choice of the CM energy $\sqrt{s}$ and the mass range of the di-muons as the simple expression given for ν is valid only for $\sqrt{s} > 10\,\text{GeV}$ and for dimuon masses in the "safe" region. The safe region lies between the $c\bar{c}$ and the $b\bar{b}$ bound states (4–8.6 GeV). For lower values of $\sqrt{s}$ and lower values of dimuon masses, higher twist T-even contributions to the $\cos 2\phi$ of comparable size appear [124, 125].

If the DY interaction $\overline{\text{p}}\text{p} \rightarrow \mu^+\mu^- X$ takes place between a transversely polarized proton and an unpolarized antiproton, the experimental asymmetry ρ depends on the $\sin(\phi + \phi_{S_1})$ term where ϕ_{S_1} is the azimuthal angle of the proton spin ($\boldsymbol{S}_\perp$) in the frame of Fig. 2.8. This term is $\propto h_1(x_2,\boldsymbol{k}_\perp^2)\,\bar{h}_1^\perp(x_1,\boldsymbol{k}_\perp'^2)$, as shown by [126]:

$$\rho = \frac{\sum_a e_a^2\mathcal{F}\left[\hat{\mathbf{x}}\cdot\mathbf{k}_\perp \frac{h_1\bar{h}_1^\perp}{M_2}\right]}{\sum_a e_a^2\mathcal{F}[f_1\bar{f}_1]} \quad (2.5)$$

$h_1(x)$ can be inferred from the measurement of the single spin asymmetry and introducing the values of $h_1^\perp(x)$ (from Eq. 2.3).

For the DY process between a p and a $\overline{\text{p}}$ both transversely polarized, the transverse double spin asymmetry A_{TT} is given by:

$$A_{TT} = \frac{\sin^2\theta\,\cos 2\phi}{1+\cos^2\theta}\,\frac{\sum_a e_a^2 h_1^a(x_1)h_1^{\bar{a}}(x_2)}{\sum_a e_a^2 f_1^a(x_1)f_1^{\bar{a}}(x_2)} \quad (2.6)$$

Here, $h_1(x)$ can be directly obtained from the fit of A_{TT}. The present configuration of the HESR system, with a maximum momentum for the antiproton beam of 15 GeV/c and unpolarized protons and antiproton, only allows for the measurement of ν (see Eq. 2.3). Furthermore, higher twist effects are difficult to disentangle in the limited kinematic region of $\sqrt{s} < 6\,\text{GeV}$.

The option of using the $\overline{\text{P}}$ANDA detector and the HESR in a second stage in an asymmetric collider mode is currently under investigation. It will provide both the necessary CM energy ($\sqrt{s} > 10\,\text{GeV}$), transversely polarized protons and, possibly, antiprotons, opening a new field of investigations.

In addition to the study of the Drell–Yan processes, the determination of spin observables of the reaction $\overline{\text{p}}\text{p} \rightarrow \Lambda\overline{\Lambda}$ can be performed in parallel. Taking advantage of the self-analyzing power of the Λ and $\overline{\Lambda}$, observed trough the weak decay $\Lambda \rightarrow \text{p}\pi^-$ ($\overline{\Lambda} \rightarrow \overline{\text{p}}\pi^+$), the spin correlations between hyperons and the polarized proton (and possibly antiproton) can be studied. This provides a check of the factorization approach and of the hadronization process. The $\Lambda\overline{\Lambda}$ production has been studied in detail for this report (see Sec. 13.5.8).

Recent suggestions of indirect transversity tests via Drell–Yan experiments on nuclear targets with unpolarized antiprotons have been made [127]. The measurement of azimuthal asymmetries should be performed on at least two different nuclear targets with different atomic numbers.

Di-muon simulations originating from $\overline{\text{p}}\text{p}$ annihilation could not be performed for this report due to resource limitations.

2.6.4 Electromagnetic Form Factors of the Proton in the Time-Like Region

The electromagnetic form factor of the proton in the time-like region can be extracted from the cross sections for the process $\overline{\text{p}}\text{p} \rightarrow e^+e^-$. First order

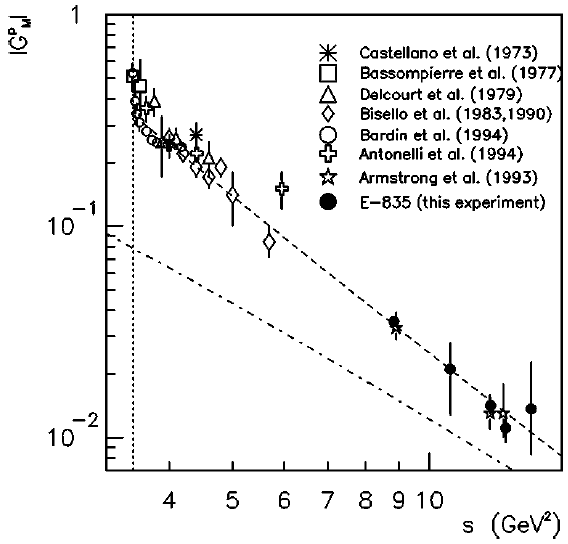

Figure 2.9: Electromagnetic form factor $|G_M|$ measurements for proton.

QED predicts:

$$\frac{d\sigma}{d\cos\theta^*} = \frac{\pi\alpha^2\hbar^2c^2}{2xs}[|G_M|^2(1+\cos^2\theta^*) + \frac{4m_p^2}{s}|G_E|^2(1-\cos^2\theta^*)] \quad (2.7)$$

with G_E and G_M the electric and magnetic form factors, respectively. Data at high Q^2 are crucial to test the Q^2 behavior and the space-like–time-like equality for corresponding Q^2.

The proton time-like form factors have been measured by several experiments in the low Q^2 region down to threshold. At high Q^2 the only measurements have been achieved by E760 and E835 at Fermilab [128, 129] up to $Q^2 \approx 15\,\mathrm{GeV}^2/c^2$ (see also Fig. 2.9). However, due to limited statistics $|G_M|$ and $|G_E|$ have not been measured separately and could only be extracted using the assumption $|G_E| = |G_M|$.

In $\overline{\mathsf{P}}$ANDA, it will be possible to determine the form factors over the widest Q^2 range with a single experiment, from threshold to $20\,\mathrm{GeV}^2/c^4$ and above, depending on the beam time availability. Due to much improved statistics and angular coverage it will be possible to significantly improve the results of E760 and E835 and to measure $|G_M|$ and $|G_E|$ separately.

The real and imaginary parts of the time-like form factors could be determined with a polarized beam and/or target. A modulation of the azimuthal distribution will certainly help disentangling the electric and the magnetic parts and provide information on the relative phase, even if this will be most likely limited by the luminosity to moderate Q^2 values. Most of the anticipated measurements could be run together with other programs. The proximity of resonance peaks should be avoided to reduce systematic uncertainties. Therefore parasitic measurements with almost maximum beam energy could be performed while running for the charmed hybrid.

2.7 Detector Requirements

The rich experimental program described in the previous sections can only be pursued with a universal and hermetic detector capable of detecting charged and neutral particles with nearly 4π solid angle coverage and high resolution. The basic elements are:

- Hidden-charm physics and the search for exotics require the concurrent detection of lepton pairs as well as good kaon identification and high efficiency for open-charm final states. In addition, the detection of low energy photons, either from radiative decays and/or background channels, is extremely important. Thus, muon detection capability and a highly-segmented low-threshold electromagnetic calorimeter are important for the tagging and precise reconstruction of hidden-charm and the reduction of background. Good vertex recognition and particle identification for charged kaons from very low energies up to a few GeV/c is mandatory to reconstruct light hadronic and open charm final states.

- The detector must withstand large radiation dosage from hadrons emitted from the spallation process when using nuclear targets. Spallation products are dominated by neutrons down to thermal energies.

- The specific demands for experiments with a secondary target require good detection of antihyperons and low momentum K^+ in the forward region. A compact high resolution solid state tracker for absorption and tracking of low momentum hyperons at large angles is needed. The geometry of the secondary target is determined by the short mean life time of the Ξ^- of only 0.164 ns. A high resolution and high-efficiency Ge-array for γ-ray detection is envisaged in order to measure radiative transitions.

- Open-charm spectroscopy and electromagnetic reactions have similar demands as are envisaged in the hidden-charm and exotics programs

(see Sec. 2.2 and 2.3). It should be mentioned that the decay of a charmed hadron releases rather high p_t (up to 1.5 GeV/c) as compared to light and even strange meson decays. This leads to large opening angles of particles in the laboratory reference frame.

The detector concept is based on a combination of a solenoid which allows particles above polar angles of 5° to be measured and a dipole magnet for the most forward angles. Complete coverage of the target region is necessary because of the high energies released in the decay of charmed hadrons. Even in reactions induced by $\overline{\mathrm{p}}$ of 10 GeV/c many decay products are emitted under rather large polar angles in the laboratory reference frame whereas others - due to the c.m. velocity - are emitted with high energies under very small angles. The combination of two spectrometers allows full angular coverage and the wide range of energies are taken into account. The setup has sufficient flexibility such that individual components can be exchanged for specific experiments. The requirements on the detector for the specific physical processes are summarized in the following.

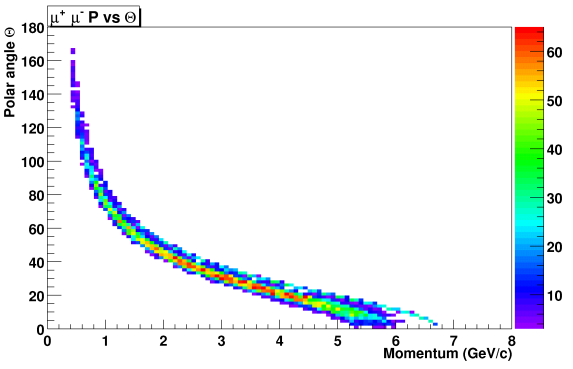

Figure 2.10: Momentum *vs.* polar angle distribution of muons from the formation reaction of the $\psi(3686)$.

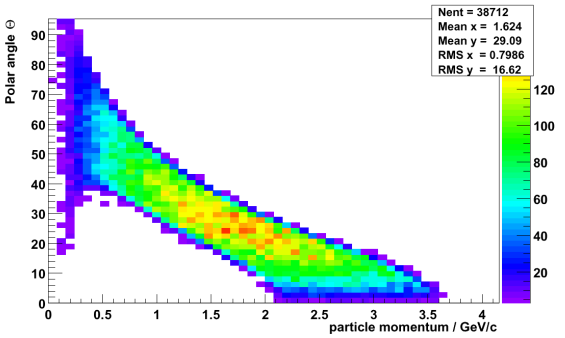

Figure 2.11: Momentum *vs.* polar angle distribution of decay kaons from the reaction $\overline{\mathrm{p}}\mathrm{p} \rightarrow \phi\phi$ at $\sqrt{s} = 3.6$ GeV.

2.7.1 Charmonium Spectroscopy

An important advantage of using antiproton-proton annihilation for charmonium spectroscopy measurements is that charmonium states with any quantum number can be produced in both production and formation experiments. In both cases, the detection strategy is based on either a clean identification of the charged lepton pair or the multiple hadrons in the final state. As an example for typical momenta, the momentum vs. polar angle correlation of the final state muons emitted in a formation experiment of the $\psi(3686)$ is plotted in Fig. 2.10.

In this figure, the sharp line corresponds to the dilepton decay of the ψ. In addition, a broader band results from the cascade $\psi' \rightarrow J/\psi X$ ($J/\psi \rightarrow \mu^+\mu^-$). The equivalent distribution for e^+ and e^- looks similar, except for additional contributions from Dalitz decays of decay hadrons. Muon identification is only possible up to laboratory polar angles Θ of about 60°. Beyond these angles, the muon momentum is too low for muon/hadron discrimination. The momentum versus polar angle distribution for decay hadrons is restricted below the lepton curve due to kinematic constraints. For example, the decay kaons extend up to $\Theta \approx 60°$ and have a maximum yield near $\Theta = 20°$ and $p = 1.5$ GeV/c.

2.7.2 Charmed Hybrids

The studies involve final state particles with a similar angle/momentum distribution as for the hadronic decay of charmonium states. For example, the polar angle versus particle momentum correlation is presented in Fig. 2.11 for the reaction $\overline{\mathrm{p}}\mathrm{p} \rightarrow \phi\phi \rightarrow 4K$ at $\sqrt{s} = 3.6\,\mathrm{GeV}/c^2$. The distribution demonstrates the need for pion-kaon separation up to ~ 3 GeV/c at forward angles. By exploiting the relationship between the ring radius and velocity, a radiator with index of refraction $n = 1.02$ is suitable at forward angles and a higher value of n is required for larger polar angles.

2.7.3 Open Charm Hadrons

Most processes of interest involving D mesons take place at small excess c.m. energies so that the D mesons themselves are mostly produced in the forward direction. The kinematics of the decay particles are therefore mostly determined by the D me-

son decay itself. The decay of a charmed hadron releases a rather high p_t (up to 1.5 GeV/c) as compared to light and even strange meson decays. This leads again to large opening angles of the decay particles in the laboratory reference frame.

As an example the decay, $D^0 \rightarrow K^-\pi^+$ was studied at production threshold ($\sqrt{s} = 3.8\,\mathrm{GeV}$) and at the maximum of the $D\overline{D}$ cross section ($\sqrt{s} = 4.5\,\mathrm{GeV}/c^2$). Due to the large amount of decay phase space, pions can be emitted at backward angles whereas kaons are more forward but still up to 45° or even 60°. Similar distributions are expected for other charmed hadrons.

The unambiguous reconstruction of weakly decaying charmed hadrons necessitates the detection of a secondary vertex separated from the interaction point implying a track impact parameter resolution of about 100 μm. A very good vertex detector is required which must be radiation hard along with low pileup from the high luminosity.

It will be very difficult, if not impossible, to obtain the high resolution at interaction rates of 10^7 /s already on the trigger level. For decays where a K^0_S is produced as a decay particle, the decay can be selected on the first trigger level. In this way, more time is available for the analysis of the primary vertex on a higher trigger level. The selection of a specific decay channel by the trigger does not necessarily hinder the investigation of other decay modes because of the comparatively large probability of D meson pair production in $\overline{\mathrm{p}}$p annihilations at energies close to the threshold. A specific decay mode of one particle can be selected by the trigger without introducing a bias to the measurement of the other.

Good particle identification above particle momenta of 0.5 GeV/c is required at all angles. At momenta above 0.7–1.0 GeV/c π/K, the separation can be provided by Cherenkov counters. Analog readout of the silicon vertex or a time of flight detector could provide limited $\mathrm{d}E/\mathrm{d}x$ information for particles below 0.7 GeV/c.

2.7.4 Charmed Hadrons in Nuclear Matter

Studies of the properties and interactions of hadrons with both hidden and open charm inside nuclei basically require the same detection capabilities as discussed related to the study of the charmonium spectrum and to searches for charmed hybrids or glueballs in the charm region. The final states involve either dilepton or photon detection in the case of hidden charm below the $D\overline{D}$ threshold or the identification of D mesons using the reconstruction of delayed vertices. However, a few peculiarities should be noted.

This part of the physics program involves nuclear targets which can be realized within the pellet or cluster jet target concept by using gases heavier than hydrogen, or by the implementation of solid wire or thin foil targets at the nominal interaction point, as discussed in Sec. 4.5.

Due to the larger total $\overline{\mathrm{p}}$-nucleus cross section and to the increase of single and multiple scattering with increasing nuclear charge of the target, the maximum luminosity will have to be kept smaller in $\overline{\mathrm{p}}A$ collisions than in $\overline{\mathrm{p}}$p collisions. For instance, for $\overline{\mathrm{p}}$Au collisions, the increased interaction cross section has to be compensated by about a factor 25 reduced number density of target atoms per cm^2 in order to keep the interaction rate at a level of $2 \cdot 10^7$/s as defined by the $\overline{\mathrm{p}}$ production rate. However, the increased Coulomb scattering and, thus, shorter lifetime of the circulating $\overline{\mathrm{p}}$ beam, will further reduce the achievable luminosity. How large the further reduction by beam heating will be, depends on the details of the HESR parameters. Further careful studies of this aspect are needed.

In $\overline{\mathrm{p}}A$ collisions, it will generally not be possible to reconstruct the final state completely. This is a loss of kinematic constraints which are used in $\overline{\mathrm{p}}$p collisions to improve the mass resolution of reconstructed particles. In particular, it is not possible to use the precise information on the $\overline{\mathrm{p}}$ beam momentum, in order to determine the mass of a charmonium state in the formation reaction $\overline{\mathrm{p}}\mathrm{p} \rightarrow c\overline{c}$ if the target proton is bound in a nucleus and thus affected by the Fermi momentum. In this case, its mass must be determined by the detector, e.g. in $\mu^+\mu^-$ or $\gamma\gamma$ final states which puts more weight on the effort to achieve best possible values for the detector resolution. On the other hand, similar requirements are posed by experimental studies of glueballs and charmed hybrids with exotic quantum numbers which are only observable in production reactions. A mass resolution of 1–2% is sufficient to distinguish between the established charmonium states, solely based on the information deduced from the detection system.

In $\overline{\mathrm{p}}A$ collisions, part of the final state particles of the $\overline{\mathrm{p}}N$ annihilation process - mostly pions - initiate an intra-nuclear cascade, which may produce secondary knock-on nucleons and thus may leave the residual nucleus in a highly excited state. The excited nucleus will s further emit neutrons and protons in a thermalization-like proces.

Data on neutron and proton emission subsequent to $\overline{\text{p}}N$ annihilation in nuclei are available from studies at LEAR energies [130, 131]. For specific $\overline{\text{p}}$ momenta and target nuclei expected particle yields can only be estimated based on $\overline{\text{p}}A$ event generators such as UrQMD [132, 133]. Recently, nucleon evaporation was implemented, as described in Sec. 12.3.1.3. An UrQMD simulation was carried out for $\overline{\text{p}}$C, $\overline{\text{p}}$Cu, and $\overline{\text{p}}$Au collisions at 4.05 GeV/c $\overline{\text{p}}$ momentum, corresponding to resonant J/ψ formation for vanishing internal momentum of the struck target proton. The pion and nucleon multiplicities per collision are listed in Table 2.4. It shows that the pion multiplicity is expected to be almost independent of the size of the target nucleus whereas the predicted neutron and proton multiplicities, by far dominated by low energy evaporation processes, increase approximately according to $N^{0.9}$ for neutrons with the neutron number N, and according to $Z^{0.5}$ for protons with the proton number Z. Fig. 2.12 shows that the neutron emitting source has essentially no forward boost and that the low energy neutron emission is almost isotropic. A similar emission pattern is predicted for the dominant low energy part of the emitted protons.

Target	N_n	N_p	N_π
^{12}C	2.3	2.6	6.6
^{63}Cu	9.3	7.0	6.4
^{197}Au	33.4	10.0	5.9

Table 2.4: Multiplicities per collision of neutrons N_n, protons N_p and pions N_π obtained in a UrQMD simulation of 10000 events for 4.05 GeV/c $\overline{\text{p}}$ + ^{12}C, ^{63}Cu, and ^{197}Au. Particles from evaporation processes are included.

The yield of evaporation neutrons and protons in $\overline{\text{p}}A$ collisions defines additional constraints on the required radiation hardness of detector components, depending on the achievable luminosity, and on the fraction of beam time spent on nuclear targets. This will be particularly relevant for the Micro Vertex Detector (MVD) but may also be of concern for other sub-detectors, e.g. the Electromagnetic Calorimeter (EMC). A 1 year duration run of $\overline{\text{p}}$Cu at maximum luminosity $L = 1.4 \cdot 10^{31}\,\text{cm}^{-2}\text{s}^{-1}$ (corresponding to 10^7/s interaction rate) and an overall duty cycle corresponding to a net 100 day run at maximum luminosity is considered in order to illustrate the expected order of magnitude in neutron irradiation. From the UrQMD simulation, a total number of $8 \cdot 10^{14}$ neutrons is expected for a 1 year run. Assuming isotropic emission, this corresponds to $3 \cdot 10^{13}$ neutrons per cm^2 at 1.5 cm distance from the interaction point (about the closest distance to the first MVD layer) and $2.5 \cdot 10^{10}$ neutrons per cm^2 at 50 cm distance (about the closest distance to the inner EMC surface). For heavier targets, like Au, the increase of the neutron multiplicity per collision is expected to be compensated by the reduced maximum luminosity which is limited by the shorter $\overline{\text{p}}$ lifetime due to the higher beam heating effect.

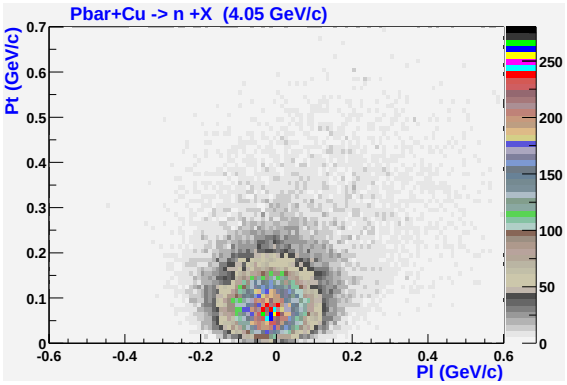

Figure 2.12: Transverse *vs.* longitudinal momentum distribution of neutrons obtained with an UrQMD calculation for 4.05 GeV/c $\overline{\text{p}}$ + Cu, including low energy evaporation processes.

2.7.5 Production of multistrange systems

The simultaneous production and implementation of two Λ particles into a nucleus is not feasible. The conversion of a Ξ^- and a proton into two Λ particles releases – ignoring binding energy effects – only 28 MeV of excitation energy. Accordingly, there is a chance of typically a few percent that both Λ hyperons stick to the same nucleus [134, 135, 136]. Ξ^- hyperons produced in reactions with *stable* hadron beams typically have rather high momenta. Therefore, capture of the Ξ^- in the nucleus is rather unlikely. The capture of Ξ hyperons has to proceed in two (or even three) steps. Using energetic hadron beams, a Ξ^- (together with its associated strange particles) is produced in a primary target. In a second step, the Ξ^- is slowed down in a dense, solid material (e.g. a nuclear emulsion) and forms a Ξ^- atom [137]. After an atomic cascade, the hyperon is finally captured by a secondary target nucleus. It is mandatory to keep the primary momentum of the produced Ξ^- as low as possible in order to reach a high capture probability. If the momentum of the hyperon is too high its stopping time will exceed

the lifetime and hence the Ξ^- will decay prior to the atomic capture with high probability.

Using the (K^+, K^-) double strangeness exchange reaction, Ξ^- hyperons are produced with typical momenta of 500 MeV/c [138, 139]. Most ($\sim$ 80 %) hyperons escape from the target nucleus. However, for a few percent of the reactions the Ξ is captured in the nucleus. The advantage of this production process is that the outgoing K^- can be used as a tag for the reaction. A drawback is the low kaon beam intensity because of the short kaon lifetime and hence the need for thick primary targets.

The $\overline{\Xi}^+$ was discovered in antiproton-proton interactions at 3 GeV/c [140, 141]. Relatively low momentum Ξ^- can be produced in $\overline{\mathrm{p}}\mathrm{p} \rightarrow \Xi^-\overline{\Xi}^+$ or $\overline{\mathrm{p}}\mathrm{n} \rightarrow \Xi^-\overline{\Xi}^\circ$ reactions as will be outlined below. The advantage as compared to the kaon induced reaction is the fact that the antiproton is stable and can be retained in a storage ring. This allows a rather high luminositiy even with very thin primary targets. The associated $\overline{\Xi}$ will undergo scattering or (in most cases) annihilation inside the residual nucleus. Strangeness is conserved in the strong interaction and the annihilation products contain at least two anti-kaons that can be used as a tag for the reaction (see Fig. 2.13).

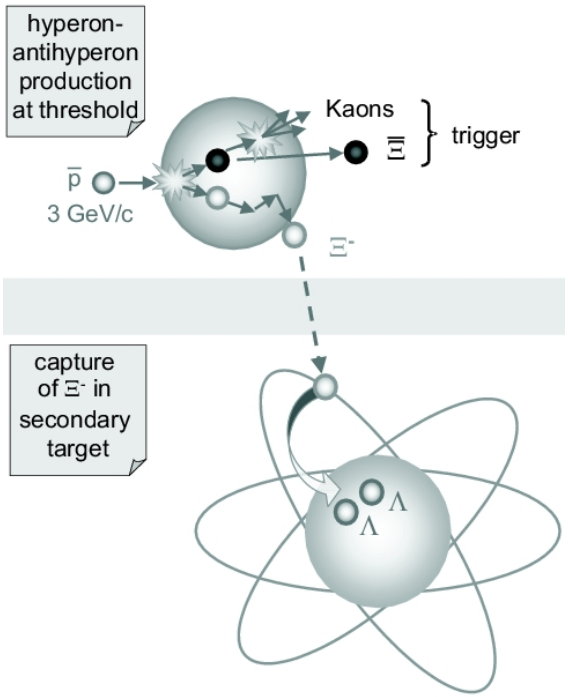

Figure 2.13: Double hypernucleus production.

Because of the two-step process, spectroscopic studies, based on the analysis of two-body reactions like in single hypernuclei reactions, cannot be performed Spectroscopic information on double hypernuclei can only be obtained via their decay. We can distinguish two different steps of the decay process:

1. γ-rays emitted via the sequential decay of an excited double hypernucleus will provide information on the level structure with rather high resolution.

2. Once the ground-state is reached, the weak decay of the hyperon(s) will initiate the emission of several particles. Here, the determination of the ground-state mass requires the knowledge of all masses of the various decay products and their kinetic energies. Hence, unique identification of the final particles and precise determination of their kinetic energies is mandatory. Nuclear emulsions are the only technique which meets all requirements for these measurements of ground-state masses. However, it is impossible to detect neutrons or γ-rays from intermediate, particle-unstable fragments with this method. As a consequence, the determination of the ground-state mass of double hypernuclei is limited to light nuclei which decay exclusively into charged particles.

3. Finally, the kinetic energies of weak decay products are sensitive to the binding energies of the two Λ hyperons.

Because of the need for a fully electronic detection system, the spectroscopic information on double hypernuclei will be obtained via (i) and (iii) at $\overline{\mathrm{P}}$ANDA. Until the end of the last decade, the energy resolution on hypernuclear levels as observed with electronic detectors was limited to typical values of about 1 MeV. Only recently high-efficiency Germanium arrays opened the door to high resolution γ-ray spectroscopy. In combination with the high luminosity at HESR and with a novel solid-state micro-tracker, high resolution γ-ray spectroscopy of double hypernuclei and Ω atoms will become possible for the first time.

For the measurements of double hypernuclei and Ω atoms, the backward part of the calorimetric detector will be removed to place a nuclear target directly in front of the main tracking detectors. In order to minimize the background from associated particles, the production of hypernuclei and hyperatoms will use $\Xi\overline{\Xi}$ and $\Omega\overline{\Omega}$ pair production close to threshold in antiproton nucleus collisions. The trigger will be based on the detection of high momentum antihyperons at small axial angles or – in most cases –

Channel	Energy $\sqrt{s}$[GeV]	$\overline{\text{p}}$ momentum [GeV/c]	final state	related to
$\overline{\text{p}}\text{p} \to \pi^\circ\pi^\circ\eta$	2.98	3.67	6γ	G
$\overline{\text{p}}\text{p} \to \eta_c \to \phi\phi$	2.98	3.67	$K^+K^-K^+K^-$	C^n
$\overline{\text{p}}\text{p} \to \eta_c \to K^\circ_S K^\pm\pi^\mp$	2.98	3.67	$K^\circ_S(\to \pi^+\pi^-)K^\pm\pi^\mp$	C^n, C^h
$\overline{\text{p}}\text{p} \to \eta_c \to \gamma\gamma$	2.98	3.67	2γ	C^n
$\overline{\text{p}}\text{p} \to \gamma\gamma$ (CCCS)	2.98, 4.6, 5.5	3.67, 9.8, 15	2γ	W
$\overline{\text{p}}\text{p} \to D\overline{D}$	3.87	6.56	$2K4\pi$	C^w,D
$\overline{\text{p}}\text{p} \to D^*\overline{D^*}$	4.16	7.7	$2K6\pi$	C^w,D
$\overline{\text{p}}\text{p} \to h_c\eta \to \chi_c\pi^\circ\pi^\circ\eta$	5.5	15.15	$J\!/\!\psi(\to \mu^+\mu^-)7\gamma$	C^h,C^n,C^w
$\overline{\text{p}}\text{p} \to \Lambda\overline{\Lambda}$	3.16, 3.73, 4.16	4, 6, 7.7	$\text{p}\pi^-\overline{\text{p}}\pi^+$	B,S
$\overline{\text{p}}A \to J\!/\!\psi X \to \mu^+\mu^- X$	–	4.05	$J\!/\!\psi(\to \mu^+\mu^-)X$	N,S

Table 2.5: Benchmark channels to be considered for this report. (C^n=related to narrow charmonium, C^w=related to charmonium above open charm threshold, C^h=charmed hybrid related, W=related to cross channel Compton scattering, B=baryon production related, G=related to glueball search, D=related open charm physics, N=charm in nuclei related, S=Spin physics).

of positive kaons produced by the anti-hyperons absorbed in the primary target. The $2K^+$ trigger will provide significantly higher count rates but requires the detection of kaons with a rather low momentum of a few hundred MeV/c. The second element of the experiment is the deceleration and subsequent absorption of the Ξ^- hyperons in a secondary active target. As a third element, an efficient Germanium γ-array is required. This array will be mounted at backward polar angles outside the super-conducting solenoid.

2.7.6 List of Benchmark Channels

In order to optimize the detector design, careful Monte Carlo simulations have been carried out on a number of physics channels, listed in Table 2.5. Hypernuclear physics and the Drell–Yan production have not been investigated in detail by Monte Carlo studies due to resource limitations and time constraints.

References

[1] L. Äystö et al., *An International Accelerator Facility for Beams of Ions and Antiprotons*, GSI, Darmstadt, 2001, Conceptual Design Report.

[2] H. S. Group, Letter of Intent: Construction of a Glue/Charm-Factory at GSI, Darmstadt, 1999, http://www.ep1.ruhr-uni-bochum.de/gsi/part1.ps.gz.

[3] H. S. Group, HESR-Project, Contributions to the Scientific Case, Darmstadt, 1999, http://www.ep1.ruhr-uni-bochum.de/gsi/part2.ps.gz.

[4] K. Seth, in *Proceedings of "Heavy Flavours 8"*, 1999.

[5] S. K. Choi et al., Phys. Rev. Lett. **89**, 102001 (2002), hep-ex/0206002.

[6] D. M. Asner et al., Phys. Rev. Lett. **92**, 142001 (2004), hep-ex/0312058.

[7] B. Aubert et al., Phys. Rev. Lett. **92**, 142002 (2004), hep-ex/0311038.

[8] C. Edwards et al., Phys. Rev. Lett. **48**, 70 (1982).

[9] F. Fang et al., Phys. Rev. Lett. **90**, 071801 (2003).

[10] M. Andreotti et al., Phys. Lett. **B566**, 45 (2003).

[11] B. Mayer, private comm.

[12] T. Armstrong et al., Phys. Rev. Lett. **69**, 2337 (1992).

[13] C. Patrignani, talk presented at "BEACH04", Chicago, U.S.A., June 2004.

[14] A. Tomaradze, talk presented at "QWG04", Beijing, China, October 2004.

[15] T. Armstrong et al., Phys. Rev. **D48**, 3037 (1993).

[16] M. Ambrogiani et al., Phys. Rev. **D62**, 052002 (2000).

[17] T. Barnes, S. Godfrey, and E. Swanson, in prepapration.

[18] S. Eidelman et al., Phys. Lett. **B592**, 1+ (2004), http://pdg.lbl.gov.

[19] J. Bai et al., Phys. Rev. **D57**, 3854 (1998).

[20] L. Antoniazzi et al., Phys. Rev. **D50**, 4258 (1994).

[21] S. K. Choi et al., Phys. Rev. Lett. **91**, 262001 (2003).

[22] D. Acosta et al., Phys. Rev. Lett. **93**, 072001 (2004).

[23] V. Abazov et al., Phys. Rev. Lett. **93**, 162002 (2004), hep-ex/0405004.

[24] B. Aubert et al., subm. to Phys. Rev. Lett. (2004), hep-ex/0406022.

[25] D. Thompson et al., Phys. Rev. Lett. **79**, 1630 (1997).

[26] G. Adams et al., Phys. Rev. Lett. **81**, 5760 (1998).

[27] A. Abele et al., Phys. Lett. **B423**, 175 (1998).

[28] J. Reinnarth, Nucl. Phys. **A692**, 268c (2001).

[29] S. U. Chung et al., Phys. Rev. **D65**, 072001 (2002).

[30] A. Abele et al., Phys. Lett. **B446**, 349 (1999).

[31] P. Salvini et al., Eur. Phys. J. **C35**, 21 (2004).

[32] E. I. Ivanov et al., Phys. Rev. Lett. **86**, 3977 (2001).

[33] S. U. Chung and E. Klempt, Phys. Lett. **B563**, 83 (2003).

[34] J. Kuhn et al., Phys. Lett. **B595**, 109 (2004).

[35] M. Lu et al., hep-ex/0405044.

[36] G. Adams, Talk given at the First GHP Meeting of the APS, Chicago, 2004.

[37] C. Amsler et al., Phys. Lett. **B342**, 433 (1995).

[38] C. Amsler et al., Phys. Lett. **B353**, 571 (1995).

[39] A. Abele et al., Phys. Lett. **B385**, 425 (1996).

[40] A. Abele et al., Eur. Phys. J. **C19**, 667 (2001).

[41] C. Amsler et al., Phys. Lett. **B340**, 259 (1994).

[42] K. Juge, J. Kuti, and C. Morningstar, Phys. Rev. Lett. **90**, 161601 (2003).

[43] C. Bernard et al., Phys. Rev. **D56**, 7039 (1997).

[44] C. Bernard et al., Nucl. Phys. (Proc. Suppl.) **B73**, 264 (1999).

[45] K. Juge, J. Kuti, and C. Morningstar, Phys. Rev. Lett. **82**, 4400 (1999).

[46] Z.-H. Mei and X.-Q. Luo, Int. J. Mod. PHys. **A18**, 5713 (2003), hep-lat/0206012.

[47] T. Manke et al., Nucl. Phys. (Proc. Suppl.) **B82**, 4396 (1999).

[48] P. Chen, X. Liao, and T. Manke, Nucl. Phys. Proc. Suppl. **94**, 342 (2001).

[49] C. Michael, in *Proceedings of "Heavy Flavours 8"*, 1999.

[50] R. Cester, in *Proceedings of the "Super LEAR Workshop"*, pages 91–103, Zürich, 1991.

[51] M. Gaillard, L. Maiani, and R. Petronzio, Phys. Lett. **B110**, 489 (1982).

[52] C. Morningstar and M. Peardon, Phys. Rev. **D60**, 34509 (1999).

[53] J. Sexton, A. Vaccarino, and D. Weingarten, Phys. Rev. Lett. **75**, 4563 (1995).

[54] P. Page, in *Proceedings of the "pbar2000 Workshop"*, edited by D. Kaplan and H. Rubin, pages 55–64, Chicago, 2001.

[55] R. Jones, in *Proceedings of the workshop "Gluonic excitations"*, Jefferson Lab, 2003, in print.

[56] A. Bertin et al., Phys. Lett. **B400**, 187 (1995).

[57] A. Bertin et al., Phys. Lett. **B385**, 493 (1996).

[58] A. Bertin et al., Phys. Lett. **B400**, 226 (1997).

[59] C. Cicalo et al., Phys. Lett. **B462**, 453 (1999).

[60] F. Nichitiu et al., Phys. Lett. **B545**, 261 (2002).

[61] C. Morningstar and M. Peardon, Phys. Rev. **D56**, 4043 (1997).

[62] H. Geissel et al., Phys. Rev. Lett. **88**, 122301 (2002).

[63] H. Geissel et al., Phys. Lett. **B549**, 64 (2002).

[64] H. Geissel et al., Phys. Rev. Lett. **92**, 072302 (2004).

[65] M. Nekipelov et al., Phys. Lett. **B540**, 207 (2002).

[66] Z. Rudy et al., Eur. Phys. J. **A15**, 303 (2002).

[67] Y. Shin et al., Phys. Rev. Lett. **81**, 1576 (1998).

[68] R. Barth et al., Phys. Rev. Lett. **78**, 4007 (1997).

[69] F. Laue et al., Phys. Rev. Lett. **82**, 1640 (1999).

[70] P. Crochet et al., Phys. Lett. **B486**, 6 (2000).

[71] K. Wisniewski et al., Eur. Phys. J. **A9**, 515 (2000).

[72] F. Klingl, N. Kaiser, and W. Weise, Nucl. Phys. **A624**, 527 (1997).

[73] F. Klingl, S. Kim, S. Lee, P. Morath, and W. Weise, Phys. Rev. Lett. **82**, 3396 (1999).

[74] S. Lee and C. Ko, Phys. Rev. **C67**, 038202 (2003).

[75] S. Lee, Proceedings of Int. Workshop 'HADRON 2003', in *Hadron Spectroscopy*, edited by H. K. E. Klempt and H. Orth, Aschaffenburg, 2004.

[76] W. Weise, Proceedings of Int. Workshop 'Structure of Hadrons', Hirschegg, 2001.

[77] A. Hayashigaki, Phys. Lett. **B487**, 96 (2000).

[78] A. Sibirtsev, K. Tsushima, and A. Thomas, Eur. Phys. J. **a6**, 351 (1999).

[79] L. Tolós, J. Schaffner-Bielich, and A. Mishra, hep-ph/0411256.

[80] K. Seth, Proceedings of Int. Workshop 'Structure of Hadrons', Hirschegg, 2001.

[81] W. Cassing, Y. Golubeva, and L. Kondratyuk, Eur. Phys. J. **A7**, 279 (2000).

[82] B. Friman, S. Lee, and T. Song, Phys. Lett. **B548**, 153 (2002).

[83] Y. Golubeva, E. Bratkovskaya, W. Cassing, and L. Kondratyuk, Eur. Phys. J. **A17**, 275 (2003).

[84] M. Danysz and J. Pniewski, Phil. Mag. **44**, 348 (1953).

[85] M. Danysz et al., Nucl. Phys. **49**, 121 (1963).

[86] R. L. Jaffe, Phys. Rev. Lett. **38**, 195 (1977).

[87] R. L. Jaffe, Phys. Rev. Lett. **38**, 617E (1977).

[88] G. R. Farrar and G. Zaharijas, hep-ph/0303047, 2003.

[89] T. Sakai et al., Prog. Theor. Phys. Suppl. **137**, 121 (2000).

[90] T. Yamada and C. Nakamoto, Phys. Rev. **C62**, 034319 (2000).

[91] I. N. Filikhin, A. Gal, and V. M. Suslov, nucl-th/0303028.

[92] R. M. Sternheimer and M. Goldhaber, Phys. Rev. **A8**, 2207 (1973).

[93] A. J. Buchmann, Z. Naturforschung **52**, 877 (1997).

[94] Y. Oh, Mod. Phys. Lett. **A10**, 1027 (1995).

[95] B. Aubert et al., Phys. Rev. Lett. **90**, 242001 (2003).

[96] D. Besson et al., hep-ex/0305100.

[97] B. Krokovny et al., hep-ex/0308019.

[98] Y. Mikami et al., hep-ex/0307052.

[99] N. Isgur, R. Kokoski, and J. Paton, Phys. Rev. Lett. **54**, 869 (1985).

[100] M. Nowak, M. Rho, and I. Zahed, hep-ph/0307102.

[101] W. Bardeen, E. Eichten, and T. Hill, hep-ph/0305049.

[102] K. Abe et al., hep-ex/0307021.

[103] J. M. Link et al., Phys. Lett. **B586**, 11 (2004), hep-ex/0312060.

[104] I. Bigi, Surveys High Energy Phys. **12**, 269 (1998).

[105] B. Aubert et al., Phys. Rev. Lett. **87**, 091801 (2001).

[106] K. Abe et al., Phys. Rev. Lett. **87**, 091802 (2001).

[107] G. Burdman, hep-ph/9407378.

[108] P. Harrison and H. Quinn, editors, *The Babar Physics Book*, SLAC, 1998, SLAC-R-504.

[109] K. Goeke, M. Polyakov, and M. Vanderhaeghen, Prog. Part. Nucl. Phys. **47**, 401 (2001).

[110] M. Diehl, (2003), hep-ph/0307382.

[111] D. Müller et al., Fortschr. Phys. **42**, 101 (1994).

[112] A. Radyushkin, Phys. Lett. **B380**, 417 (1996).

[113] X.-D. Ji, Phys. Rev. Lett. **78**, 610 (1997).

[114] A. Radyushkin, Phys. Rev. D **58**, 114008 (1998).

[115] M. Diehl, Eur. Phys. J. **C8**, 409 (1999).

[116] F. Close and Zhao, Phys. Lett. **B553**, 211 (2003).

[117] A. Freund, A. Radyushkin, A. Schäfer, and C. Weiss, Phys. Rev. Lett. **90**, 092001 (2003).

[118] M. Diehl, P. Kroll, and C. Vogt, Eur. Phys. J. **C26**, 567 (2002).

[119] C. Berger and W. Schweiger, Eur. Phys. J. **C28**, 249 (2003).

[120] T. Armstrong et al., Phys. Rev. **D56**, 2509 (1977).

[121] M. Düren, in *Hadron Spectroscopy, Proceedings of Int. Workshop "HADRON 2003"*, edited by H. K. E. Klempt and H. Orth, Aschaffenburg, 2004.

[122] B. Pire and L. Szymanowski, 2004.

[123] J. Conway, Phys. Rev. **D39**, 22 (1989), and refs. therein.

[124] J. Collins and D. Soper, Phys.Rev **D16**, 2219 (1977).

[125] L. Gamberg, G. Goldstei, and K. Oganessyan, arXiv:hep-ph/0411220.

[126] D. Böer, Phys.Rev. **D60**, 014012 (1999).

[127] A. Bianconi and M. Radici, hep-ph/0501055 (2003).

[128] T. Armstrong et al., Phys. Rev. Lett. **70**, 1212 (1993).

[129] M. Ambrogiani et al., Phys. Rev. **D60**, 032002 (1999).

[130] F. Goldenbaum et al., Phys. Rev. Lett **77**, 1230 (1996).

[131] B. Lott et al., Phys. Rev. C **63**, 034616 (2001).

[132] M. Bleicher et al., J. Phys. **G25**, 1859 (1999).

[133] S. A. Bass et al., Prog. Part. Nucl. Phys. **41**, 225 (1998).

[134] T. Yamada and K. Ikeda, Phys. Rev. **C56**, 3216 (1997).

[135] Y. Hirata, Y. Nara, A. Ohnishi, T. Harada, and J. Randrup, Nucl. Phys. **A639**, 389c (1998).

[136] Y. Hirata, Y. Nara, A. Ohnishi, T. Harada, and J. Randrup, Prog. Theor. Phys. **102**, 89 (1999).

[137] C. J. Batty, E. Friedman, and A. Gal, Phys. Rev. **C59**, 295 (1999).

[138] Y. Nara, A. Ohnishi, T. Harada, and S. Shinmura, in *Proc. of the 25th INS Int. Symp. on Nuclear and Particle Physics with High-Intensity Proton Accelerators, Tokyo, Japan, Dec. 3-6, 1996*, edited by T. K. Komatsubara, T. Shibata, and T. Nomura, page 324, Singapore, 1998, World Scientific.

[139] A. Ohnishi, Y. Hirata, Y. Nara, S. Shinmura, and Y. Akaishi, Nucl. Phys. **A684**, 595 (2001).

[140] H. N. Brown et al., Phys. Rev. Lett. **8**, 255 (1962).

[141] CERN, Phys. Rev. Lett. **8**, 257 (1962).

3 Detector Overview

3.1 Introduction

The physics program, as described in Chap. 2, poses significant challenges for the $\overline{\mathsf{P}}$ANDA detector. The tasks are summarized for the individual detectors:

- full angular coverage and good angular resolution for both charged and neutral particles
- particle identification in a large range of particles (γ-rays, leptons, muons, kaons, *etc.*) and energies
- high resolution in a wide range of energies
- high rate compatibility especially for the close-to-target and forward detectors.

The detector is split up into two spectrometers. A target spectrometer (TS) surrounds the interaction region and a forward spectrometer (FS) with a second magnet provides angular coverage for the most forward angles. The basic concept of the target spectrometer is a shell-like arrangement of various detector systems surrounding the interaction point inside the field of a large solenoid. The forward spectrometer will overcome the gap in acceptance and resolution in the forward region of such a system. The use of a large-gap dipole magnet in combination with tracking detectors and calorimeters is likely to be an optimal solution. However, other concepts, like a toroid, are still under evaluation. Both parts, the target spectrometer (TS) and the forward spectrometer (FS), will allow the detection, identification, and energy/momentum reconstruction for both charged and neutral particles. The combination of two spectrometers takes into account the wide range of energies. Meanwhile, it has sufficient flexibility for individual components to be exchanged or added for specific experiments, e.g. for the experiments with hypernuclei or for the special needs of $\mathcal{CP}$ violation studies.

Conceptual designs of the detector are shown in several views in Fig. 3.1. The anti-proton beam will interact with the target at the cross point with the target pipe which is located inside the solenoid.[1] Particles emitted with laboratory polar angles larger than 10° are measured solely in the target spectrometer. Surrounding the interaction volume will be a silicon micro-vertex detector (MVD) including a barrel of five layers around the interaction region and wheel part in forward. Starting from a radial distance of 15 cm from the beam line up to 42 cm a second tracking detector will be situated. It will either consist of 15 double layers of straw tubes (STT) or a time projection chamber (TPC). Particle identification with a ring-imaging Cherenkov (RICH) counter realized by the detection of internally reflected Cherenkov light (DIRC) detector follows at a radial distance of 45 cm. The forward region will be covered by two sets of mini drift chambers (MDC) and another Cherenkov detector, either an aerogel RICH or a flat DIRC. The inner detectors are surrounded by an electromagnetic calorimeter (EMC) consisting of about 19 000 crystals read out with avalanche photo-diodes. The detectors are contained within the coils of a solenoid providing a homogeneous magnetic field. Outside of the return yoke scintillating bars for muon identification (MUO) will be mounted.

Particles emitted with polar angles below 10° and 5° in the horizontal and vertical direction, respectively, are detected with the forward-spectrometer (FS). The current design includes a 1 m gap dipole and tracking detectors for a momentum analysis of charged particles, i.e. mini drift chambers (MDC) and straw-tube trackers. Photons will be detected by a shashlyk-type calorimeter consisting of lead-scintillator sandwiches (EMC). Other neutrals and charged particles with momenta close to the beam momentum will be detected in the hadron calorimeter, and muon counters (MUO).

It is currently under investigation whether an additional RICH detector, like at Hermes, and time-of-flight measurements will be required for event reconstruction. The latter would include fast start detectors close to the target and time-of-flight stop counters (TOF stop) placed suitably inside the target and forward spectrometer.

The basic principle for the $\overline{\mathsf{P}}$ANDA detector was outlined already in the Conceptual Design Report (CDR) [1] and the Letter of Intent (LoI) [2]. Although only six months have passed since the LoI was accepted, this report presents significant improvements arising from ongoing R&D efforts. However, the continued developments imply the choice has not been finalized yet that for all de-

1. A solid target for the studies on hypernuclei will be located in a more up-stream position together with a modified end cap.

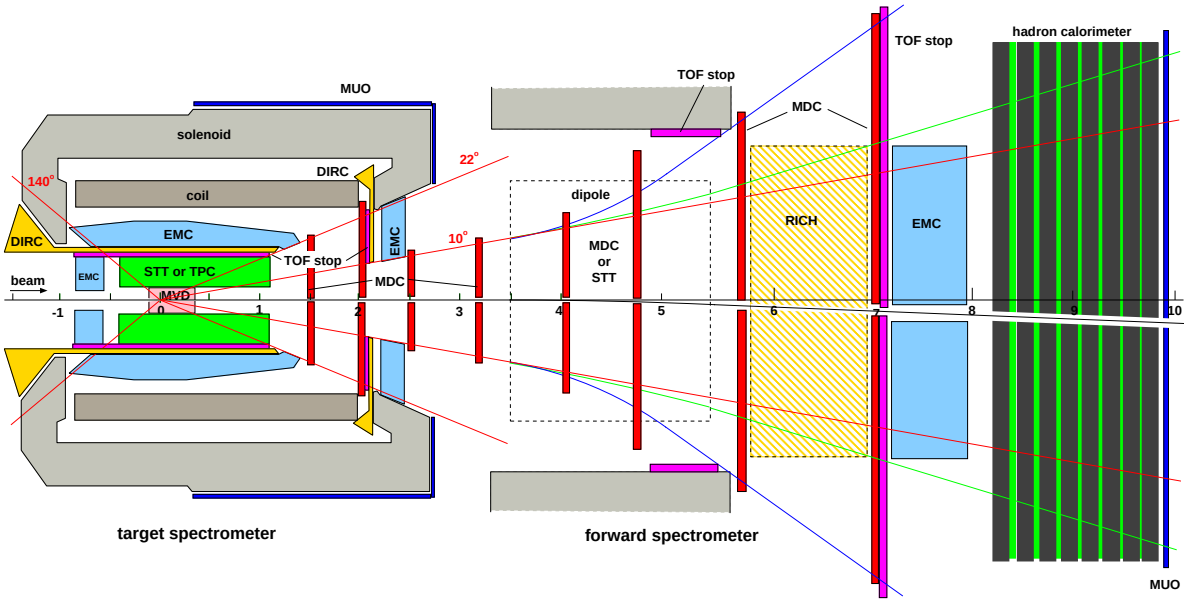

(a) Top view: green and blue lines indicate outermost tracks of charged particles with factors 3 and 15 reduced momenta respectively (compared to the beam – black).

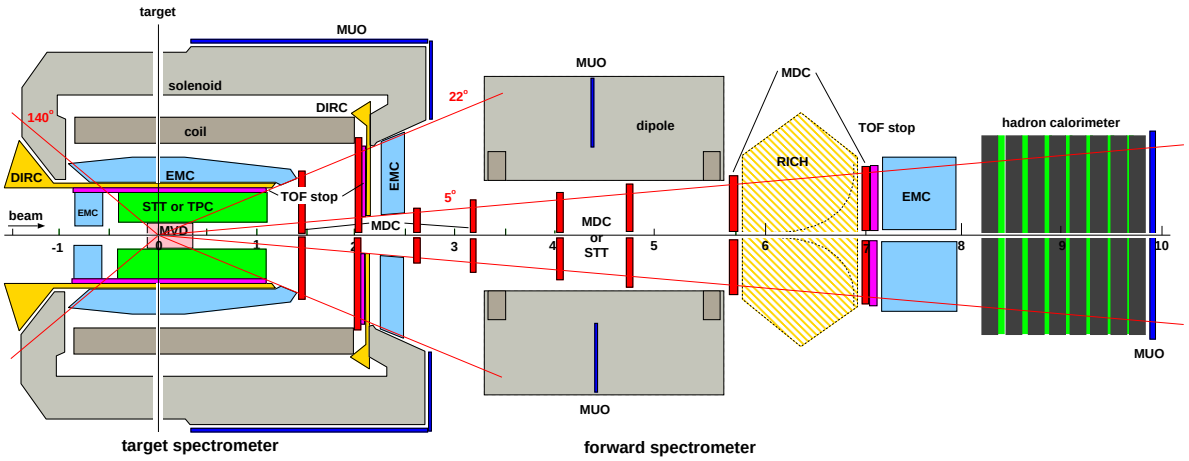

(b) Side view: the HESR beam follows the scale axis.

Figure 3.1: Sketches of the detector viewed from the top and the side in (a) and (b) respectively. The HESR beam enters the detector from the left; it interacts with the target at 0 m on the horizontal scale. The surrounding and forward detectors are indicated: micro-vertex detector (MVD – rosé), straw-tube tracker (STT) or time-projection chamber (TPC) (light green), time-of-flight stop counters (TOF stop – pink), Cherenkov detectors (DIRC and RICH – yellow), electro-magnetic calorimeter (EMC – light blue), mini-drift chambers (MDC – red), hadron calorimeter, and muon counters (MUO – dark blue)

tectors. In these cases, first results for different options are described in the subsequent chapters. In the following, an overview of the general concepts is provided.

3.2 Target Spectrometer

The target spectrometer (TS) contains the azimuthally symmetric system of detectors mostly contained inside the coils of the superconducting

solenoid. This part includes the muon counters on the outside of the magnet return joke and the forward end cap which may be situated just behind the magnet (see Figs. 3.1 and 3D view of the inner part in Fig. 3.2). This part of $\overline{\mathsf{P}}$ANDA will detect all particles emitted with laboratory angles greater than 5° and 10° in vertical and horizontal direction, respectively. For the more forward directed particles tracking and possibly a time-of-flight start signal will be obtained using the MVD and MDCs.

3.2.1 Target System

The compact design of the detector nested inside the solenoid leaves minimal space for a target inside the detector. The operation with hydrogen standard gas or cluster targets has been relying on a small distance of the production to interaction point and large pumping power in this region. In order to reach the design luminosity of $2 \cdot 10^{32}/\mathrm{cm}^2\mathrm{s}$ and assuming 10^{11} stored anti-protons in the HESR ring, a target thickness of about $4 \cdot 10^{15}$ hydrogen atoms per cm^2 is required. These are the conditions posing a challenge for the development of a suitable target.

However, recent years have seen substantial progress in the development of cluster-jet targets and pellet targets consisting of a stream of frozen droplets [3]. The two options are currently under consideration for the $\overline{\mathsf{P}}$ANDA hydrogen target but also heavier gases, like deuterium, nitrogen and argon, can be used. Both approaches have their particular advantages and disadvantages which are currently under R&D within the JRA project on internal targets [4]. In particular, considerable progress has been made over the last year as discussed in detail in Sec. 4. The studies could not yet single out one target system as superior. Continuing studies will have to lead to a decision on which target will be used in the final setup. On the other hand, the geometrical limitations which the target poses on the detectors can be specified for both solutions. Thus, the design of the adjacent detectors can be based on these boundary conditions, especially the MVD design.

The situation is somewhat different for a solid target to be used for hypernuclear studies in conjunction with a modified end cap. This target will be mounted in front of the MVD and housed within the dedicated detector setup.

Cluster-Jet Target To fulfil the demand on target thickness with a cluster-jet target requires a density increase of one order of magnitude compared to what has presently been achieved. In addition, due to detector constraints, the distance between the cluster-jet nozzle and the target has to be increased compared to previous applications. The size of the target region will be mandated by the lateral spread of hydrogen clusters which, when optimized, should stay smaller than 10 mm. The great advantage of cluster targets is the homogeneous density profile and the possibility to focus the antiproton beam at highest phase space density. Hence, the interaction point is defined transversely but has to be reconstructed longitudinally in beam direction. The possibility of adjusting the target density along with the gradual consumption of antiprotons for running at constant luminosity is advantageous. Meanwhile, the badly defined interaction point is problematic for an open-charm measurement. Internal cluster targets can run with other gases as well. Not only hydrogen but also nuclear targets will be provided for by this target technique.

A Pellet Target consists of a stream of frozen hydrogen micro-spheres, called pellets, traversing the anti-proton beam perpendicularly. The design is based on the pellet target placed inside the $4\,\pi$ WASA detector at the CELSIUS storage ring [3, 5, 6]. At the interaction point, typical parameters are a pellet rate of 10–15 kHz, a fall speed $\gtrsim 60$ m/s, and a pellet size of 25 μm which imply a target thickness of a few 10^{15} atoms/cm^2. This corresponds well to the envisaged target thickness at $\overline{\mathsf{P}}$ANDA. However, due to the angular divergence of the pellets of $\sigma = 1.0$ mm, the area, which should be covered by the ion beam, has to be similar in size. Since a single pellet undergoes about 100 interactions during the time it traverses the beam, it will not be difficult to determine the position of individual pellets with the necessary accuracy not only in transverse but also in the longitudinal direction. For $\overline{\mathsf{P}}$ANDA, the present pellet rate and train divergence at the WASA pellet target needs to be improved by factors of 2 or below. The ongoing further development of the target at a dedicated test area at TSL is expected to improve the present performance by this amount at least. In addition to the production of deuterium pellets, which is well established, the use of other gases as target material does not pose problem.

Other Targets are under consideration for the hypernuclear studies where a separate target station upstream will comprise primary and secondary

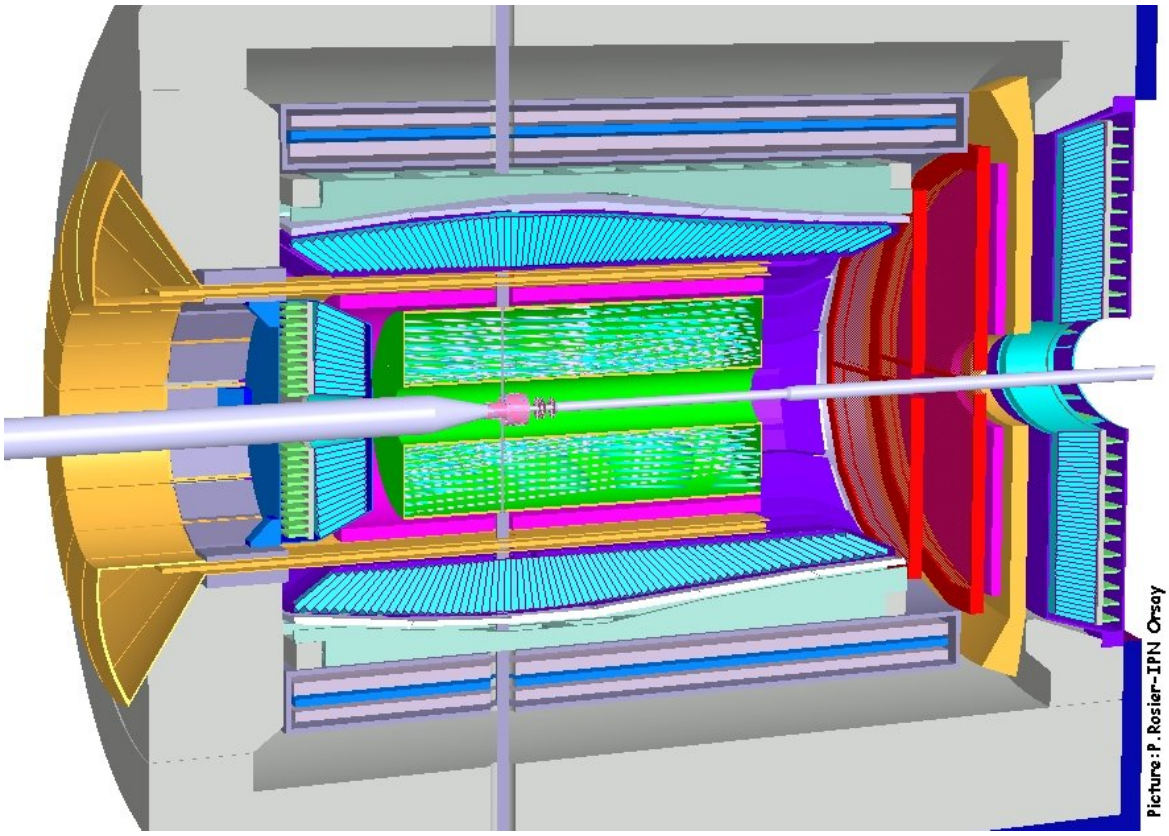

Figure 3.2: View of the detectors inside the target spectrometer

target and detectors. Moreover, current R&D is undertaken for the development of a liquid helium target and a polarized ^{3}He target. A wire target may be employed to study $\overline{\text{p}}$p-nucleon interactions.

3.2.2 Inner Tracking Detectors

The design of the micro-vertex detector (MVD) for the target spectrometer at HESR is optimized for the detection of secondary vertices and maximum acceptance close to the interaction point. It will also strongly improve the transverse momentum resolution. In addition, a layer of diamond or silicon detectors may provide a start signal for time-of-flight detectors.

The concept of the MVD is based on radiation hard silicon pixel detectors with fast individual pixel readout circuits and silicon strip detectors. The layout foresees a five layer barrel detector with an inner radius of $\gtrsim$1 cm and an outer radius of 6 cm. The three innermost layers will most likely consist of pixel detectors while the outer 2 layers are considered to consist of silicon strip detectors.

Five detector wheels arranged perpendicular to the beam will achieve the best acceptance for the forward part of the particle spectrum. Here, at least the two last layers will be striped detectors while the layers closest to the target will consist of pixel detectors.

The present design of the pixel detectors comprises detector wafers which are 200 μm thick (0.25% X_0). The readout via bump-bonded wafers with ASICs as it is used in ATLAS and CMS [7, 8] is foreseen as the default solution. It is highly parallelized and allows zero suppression as well as the transfer of analog information at the same time. The readout wafer has a thickness of 300 μm (0.37% X_0). An alternative readout scheme is presently in development for future high energy experiments and has already been used in X-ray astronomy [9]. Active pixels contain the charged particle sensitive part on one side and implement each pixel readout circuit on the other side of the same silicon wafer. The clear advantage is that only half of the material thickness has to be used for the same detection capability which reduces multiple scattering and secondary interactions.

3.2.3 Outer Tracking Detectors

The charged particle tracking devices must handle the high particle fluxes that are anticipated for a luminosity of up to $2{\cdot}10^{32}\,\mathrm{cm}^{-2}\mathrm{s}^{-1}$. The momentum resolution $\delta p/p$ should typically be on the percent level. The detectors should have good detection efficiency for secondary vertices which can occur outside the inner vertex detector (e.g. K^0_S or Λ). This is achieved by the combination of the silicon vertex detectors close to the interaction point (MVD) with two outer systems. One system is covering a large area and is designed as a barrel around the MVD. This will be either a stack of straw tubes (STT) or a time-projection chamber (TPC). The small angles will be covered using two sets of cylindrical 8 (or 6) layer mini-drift chambers (MDC), similar to those developed for the Hades experiment at SIS18.

The Straw Tube Tracker (STT) consists of self supporting straws arranged in cylindrical layers around the beam pipe at radial distances between 15 cm and 42 cm with an overall length of 150 cm. Currently 11 double layers are foreseen. The first and last double layers are arranged parallel to the beam axis and the remaining double layers are arranged at skew angles ranging from 2° to 3°. The skew angles cause the stereo layers to form a hyperbolical shape and allow to determine the position of the particles along the beam direction to about 1 mm. In order to remove the left-right ambiguity the straws are assembled in double-layers and packed into supports of Al-Be semi-rings. The straws have diameters ranging from 4 mm (innermost) to 8 mm (outermost). The tube wall will have a thickness of about 30 μm (aluminized mylar, or carbon loaded kapton). As sense wires 20 μm thick gold plated tungsten wires are foreseen. The amount of material could be minimized by self-supporting tubes held by a light Al-Be mechanical frame. The gas mixture used will be Argon based with CO_2 as quencher. It is foreseen to have a gas gain no greater than 10^5 in order to warrant long term operation. With these parameters, a resolution in x and y coordinates of about 150 μm is expected.

A Time Projection Chamber (TPC) is a challenging but relevant alternative to a STT. It consists of one (or two) large gas-filled cylindrical volume(s) surrounding the MVD like a barrel. An electric field along the cylinder axis separates positive gas ions from electrons created by ionizing particles traversing the gas volume. At the end cap avalanche amplification typically occurs in multi-wire proportional chambers, yielding information on two coordinates. The third coordinate of the track comes from the measurement of the drift time of each primary electron cluster.

In contrast to previous setups the TPC planned for $\overline{\mathsf{P}}$ANDA has to operate in continuous mode and with a granularity increased by an order of magnitude. A novel method to achieve gas amplification using the Gas Electron Multiplier, recently invented at CERN, provides features which seem to make this kind of improvement feasible.

Multi-wire Drift Chambers (MDC) Particles emitted at angles below 22° which are not covered fully by the Straw Tube Tracker will be tracked with two multi-wire drift chambers (MDC) placed 1.4 m and 2.0 m downstream of the target. The chambers have to sustain a high counting rate of particles peaked at the most forward angles due to the relativistic boost of the reaction products as well as due to the small angle $\overline{\mathrm{p}}\mathrm{p}$ elastic scattering. With the envisaged luminosity, the expected particle flux in the first chamber in the vicinity of the 5 cm diameter beam pipe is about $3{\cdot}10^4\,\mathrm{cm}^{-2}\mathrm{s}^{-1}$. Also, the chambers have to work in the 2 T magnetic field produced by the solenoid. In order to fulfil these requirements, two different options are discussed, which mainly differ by having wires or foils as cathode.

For the first option quadratic drift cells with an area of $1\,\mathrm{cm}^2$ were chosen. Each chamber will contain several pairs of detection planes. The number of pairs and the orientation will depend on whether insulating rings are used for mounting the most central wires at the position of the beam-pipe. The planes in each pair will be staggered by half a cell width in order to resolve the "left-right" ambiguity. The wires will be mounted on frames of octagonal shape.

Also, the possibility of using cathode foils and frames having a form of a closed semi-circle is explored. The detection planes would consist of pairs of frames put together along the common diameter. The frames could be mounted and dismounted without the necessity for removing the beam pipe.

3.2.4 Particle Identification

Particle identification for hadrons and leptons over a large range of solid angle and momenta is an essential requirement for meeting the physics objectives at the HESR. There will be several dedicated sys-

tems which, complementary to the other detectors, will provide means to identify particles. A time-of-flight TOF system will include TOF start detectors in the MVD, a TOF barrel between STT/TPC and DIRC, a part in the forward end cap, and a large TOF stop wall in the forward spectrometer (FS). Detectors of Cherenkov Light will enlarge the capabilities of this system to the high momenta, where flight times are too short for TOF measurements. Moreover, in certain ranges particle identification will be done by using energy losses in the detectors (MVD for slow charged particles, EMC for γ-rays and leptons). Tracking in the magnetic field is a crucial ingredient and in many cases only the combination of information from many detectors can provide a particle identification.

Time-of-Flight (TOF) Stop counters will provide a stop signal to measure the time a particle has used to travel a certain distance, i.e. its velocity. This relies on a fast start counter close to the interaction point and tracking detectors to define the flight path. In conjunction with the momentum, determined by tracking in the magnetic field, masses and particle identification can be defined. This is possible as long as the particles are not too fast compared to the time resolution. Moreover, at the relativistic limit particles cannot be identified by their speed in principle. Nevertheless, the system may be important to fill the gap between particles which can be identified *via* energy losses and the ones distinguishable using Cherenkov detectors.

The R&D is still going on and a project with the goal to produce low mass scintillation counters with high time resolution has been started [10]. It is aimed at masses below $0.5\%X_0$ and timing resolutions of $\sigma \leq 200\,\text{ps}$. The detectors will cover angles between 22° and 140° using a barrel arrangement around the STT/TPC (about 48 cm radial distance). Another flat layer of detectors will cover the angles between 5/10° and 22° in the forward end cap. Simulations will still show, whether they should be located in front or behind the Cherenkov detectors.

Detectors of Cherenkov Light will be used at two different positions within the the target spectrometer. Charged particles in a medium with index of refraction n, propagating with velocity $\beta c < 1/n$, emit radiation at an angle $\Theta_C = \arccos(1/n\beta)$. Thus, the mass of the detected particle can be determined by combining the velocity information determined from Θ_C with the momentum information from the tracking detectors. Due to the strong variation of the typical particle momentum with polar angle, particle identification is achieved using two systems of Cherenkov detectors in the target spectrometer.

At polar angles between 22° and 140°, particle identification will be performed by the detection of internally reflected Cherenkov (DIRC) light as realized in the BaBar detector [11]. It will consists of 1.7 cm thick quartz slabs ($n = 1.544$) surrounding the beam line at a radial distance of 48 cm. The main costs of the BaBar setup arise from the 11 000 photo-multiplier tubes which allow time information to be used to suppress the large background resulting from the electron beam environment. At $\overline{\text{P}}$ANDA, these costs could be reduced by employing by employing new optical readout schemes e.g. with APD arrays or by replacing one of the two space dimensions for the Cherenkov rings by the time information in the previous detector shell (see Sec. 7.2.1 for details).

Another Cherenkov detector will be located in the end cap of the TS between polar angles of 5° and 22° (described in detail in Sec. 7.3.1). Such detectors are especially suited for π-K separation. In the relevant momentum range, the detector can be either a disc DIRC detector with quartz as radiator or a proximity imaging C_6F_{14}/CsI-RICH. The first option offers the best momentum coverage and spectrometer momentum resolution. Thus it is considered as the default solution. A challenge is the placement of the disk with photo-sensors inside the return yoke of the solenoid.

Muon Detection (MUO) is a delicate task due to both the very low cross section of the interesting channels compared to muons from the decay of pions which are abundantly produced in $\overline{\text{p}}$p annihilation.

Behind the iron yoke of the TS, plastic scintillator counters for muon detection will be installed that cover the laboratory polar angular range from 80° down to the opening for the dipole. Coverage to larger polar angles is not needed since the muons will be stopped in the iron yoke. The momentum of those muons is determined by the TS-tracking. The TS-MUD system will consist of about 96 individual bars that are 10 cm wide, 1 cm thick and about 2 m long. In addition, there is an equal number of bars perpendicular to the beam axis, at the front of the TS-solenoid. The bars are read out with photo-multipliers in combination with ADCs and TDCs. The information can be exploited for the determination of the position for matching with the TS-tracking and the time of flight to suppress

random coincidences. The energy information provides redundant position information as well as a value of $\mathrm{d}E/\mathrm{d}x$ to permit further background suppression.

3.2.5 Electromagnetic Calorimeter

Expected high count rates and a geometrically compact design of the target spectrometer require a fast scintillator material with a short radiation length and Molière radius for the construction of the electromagnetic calorimeter (EMC). In recent years, lead tungstate ($PbWO_4$) has been proposed and confirmed as a high density inorganic scintillator with sufficient energy and time resolution for photon, electron, and hadron detection even at intermediate energies [12, 13, 14]. For high energy physics $PbWO_4$ has been chosen by the CMS and ALICE collaborations at CERN [15, 16] and optimized for large scale production. Apart from a short decay time of less than 10 ns good radiation hardness has been achieved [17]. Recent developments indicate a significant increase of light yield due to crystal perfection and appropriate doping to enable photon detection down to 10 MeV with sufficient resolution. Optional cooling down to -25°C can further increase the light yield by a factor 3–4 compared to room temperature operation. There is R&D performed to verify that these parameters can actually be reached. First results with a new crystal type show an energy resolution below 2 % at 2 GeV with photo-multiplier readout and a timing resolution below 2 ns also. Nevertheless, the use of bismuth germanate (BGO) or other crystal materials is also considered and studies are performed in parallel.

It is proposed to use crystals of approximately 20 X_0 in length achieving an energy resolution below 2 % at 1 GeV [12, 13, 14] at a tolerable energy loss due to longitudinal leakage of the shower. The crystals allow π-e discrimination of 10^3 for momenta above 0.5 GeV/c. Therefore, particle identification does not rely on an additional gas Cherenkov detector in favor of a very compact geometry. Tapered prisms with a front size of $2.2 \times 2.2\,\mathrm{cm}^2$ will be mounted with an inner radius of 50 cm. This implies 11360 crystals for the barrel part of the calorimeter. The backward and forward end caps will comprise additional 7680 modules. The readout of the crystals will be accomplished by large area avalanche photo diodes with optimized light collection, a tolerable nuclear counter effect, and a fast timing behavior.

3.2.6 Solenoid Magnet

The target solenoid consists of a superconducting coil with an inner radius of 90 cm and a length of 2.8 m. The maximum magnetic field is 2 T. The field homogeneity is foreseen to be better than a few percent over the volume of the inner and outer tracker. In order to minimize the amount of material in front of the EMC, the latter is placed inside the magnetic coil. The bending power downstream of the target allows a reasonable momentum resolution even at the smallest polar angles (5°/10°) detected only in the solenoid. The minimum angle of the solenoid acceptance is small enough to allow a 1 m gap height for dipole magnet. The cryostat for the coils has two warm bores of 100 mm diameter one on top and the other on bottom of the target position to allow for insertion of internal targets.

3.2.7 Germanium Detectors

The hypernuclei study will make use of the modular structure of $\overline{\mathrm{P}}$ANDA. Removing the upstream part of the calorimeter will allow to add a second nuclear target station and the required additional detectors for γ spectroscopy close to the entrance of $\overline{\mathrm{P}}$ANDA. (For details please refer to Sec. 9.) While the detection of anti-hyperons and low momentum K^+ can be ensured by the universal detector and its TOF system, two additional components are required for the studies:

A Combined Secondary Target and Solid State Tracker is used for absorption and tracking of low momentum hyperons at large angles. The geometry of this secondary target is determined by the short mean life of the Ξ^- of only 0.164 ns. This limits the required thickness of the active secondary target to about 25–30 mm. It will consist out of a compact sandwich structure of micro strip detectors (as used for the MVD) and absorbing material.

A High Resolution and Highly Efficient Germanium Array is employed for γ-ray detection. Here, the large volume germanium-arrays presently under construction at GSI [18] will be used. The main limitation will be the load due to neutral or charged particles traversing the germanium detectors. Therefore, readout schemes and tracking algorithms are presently being developed which will enable high resolution γ-spectroscopy in an environment of high particle flux.

3.3 Forward Spectrometer

The downstream part of the detector, the forward spectrometer (FS), is dedicated to the detection of particles emitted under laboratory angles below 5° and 10° in vertical and horizontal direction. In the current design, charged particles will be analyzed using a 2 Tm dipole magnet. Neutral and fast particles will be detected in the forward calorimeters. The FS is shown schematically in Figs. 3.1 and as a 3D view in Fig. 3.3.

3.3.1 Dipole Magnet

A dipole magnet with a window frame, a 1 m gap, and more than 2 m aperture will be used for the momentum analysis of charged particles in the forward spectrometer (FS). In the current planning, the magnet yoke will occupy the space of about 3.3 m and 5.8 m downstream of the target. Thus, it covers the entire angular acceptance of the TS of ±10° and ±5° in the horizontal and in the vertical direction, respectively. The maximum bending power of the magnet will be 2 Tm and the resulting deflection of the antiproton beam at the maximum momentum of 15 GeV/c will be 2.2°. The design acceptance for charged particles can cover a factor of 10 or 15 in momentum range with the detectors downstream of the magnet. For particles with lower momenta, detectors will be placed inside the iron yoke, which itself can be instrumented with detectors for ionizing particles. This option will be important for maximizing the muon detection efficiency. The beam deflection will be compensated by two or three correcting dipole magnets, placed downstream of the PANDA detection system. However, field calculations for this solution show that the magnetic field turns out to be strongly inhomogeneous between the solenoid and the dipole. Thus, R&D work is currently under way to understand the advantages and disadvantages of a toroid design (see Chap. 10). Nevertheless, the dipole remains the default solution for PANDA.

3.3.2 Tracking Detectors

The deflection of particle trajectories in the field of the dipole magnet will be measured with a set of multi-wire drift chambers (MDC), two placed in front and two behind the dipole magnet. Additionally, two MDCs or STTs will be placed inside the magnet gap. This will allow to track particles with highest momenta as well as very low momentum particles where tracks will curl up inside the magnetic field. The positions and dimensions are shown in red in Figs. 3.1 and 3.3 and listed in Table 6.11. The chambers will contain quadratic or hexagonal drift cells of 1 cm width, as in the TS-chambers. Each chamber will contain three pairs of detection planes, one pair with vertical wires and two pairs with wires inclined by +45° and -45° (or slightly smaller). This configuration will allow to reconstruct tracks in each chamber separately, also in case of multi-track events. The beam pipe will pass through central holes in the chambers. The most central wires will either be eliminated or separately mounted on insulating rings surrounding the pipe. The expected momentum resolution of the system for 3 GeV/c protons is $\delta p/p = 0.2\,\%$ and is limited by the small angle scattering on the chamber wires and gas.

3.3.3 Particle Identification

Time-of-Flight (TOF) Stop Detectors will consist of tiles made of plastic scintillator and read out on both ends by fast phototubes. Such counters will be placed as a wall about 7 m from the target and inside the dipole magnet opening. The time of flight will be measured between the start detector placed in the target region and the stop counters. The wall in front of the EMC will consist of vertical strips varying in width from 5 to 10 cm to account for the differences in count rate. With the expected time resolution of $\sigma = 50$ ps π-K and K/p separation on a $3\,\sigma$ level will be possible up to momenta of 2.8 GeV/c and 4.7 GeV/c, respectively.

A Ring Imaging Cherenkov Counter (RICH) is proposed to enable the π/K and K/p separation also at the very highest momenta. Currently, it is not clear whether this identification could also be possible using other means, like the TOF system. Thus simulation work will focus on these questions, and the forward RICH has to be considered as an option.

The favoured design is an aerogel RICH detector similar to the one used at Hermes [19] but differing in its details. Using thin carbon-fibre based mirrors and a detector plane outside of the acceptance the thickness can be lower than 8% X_0, possibly as low as 6.8% of a radiation length. Details for this solution can be found in Sec. 7.3.1.

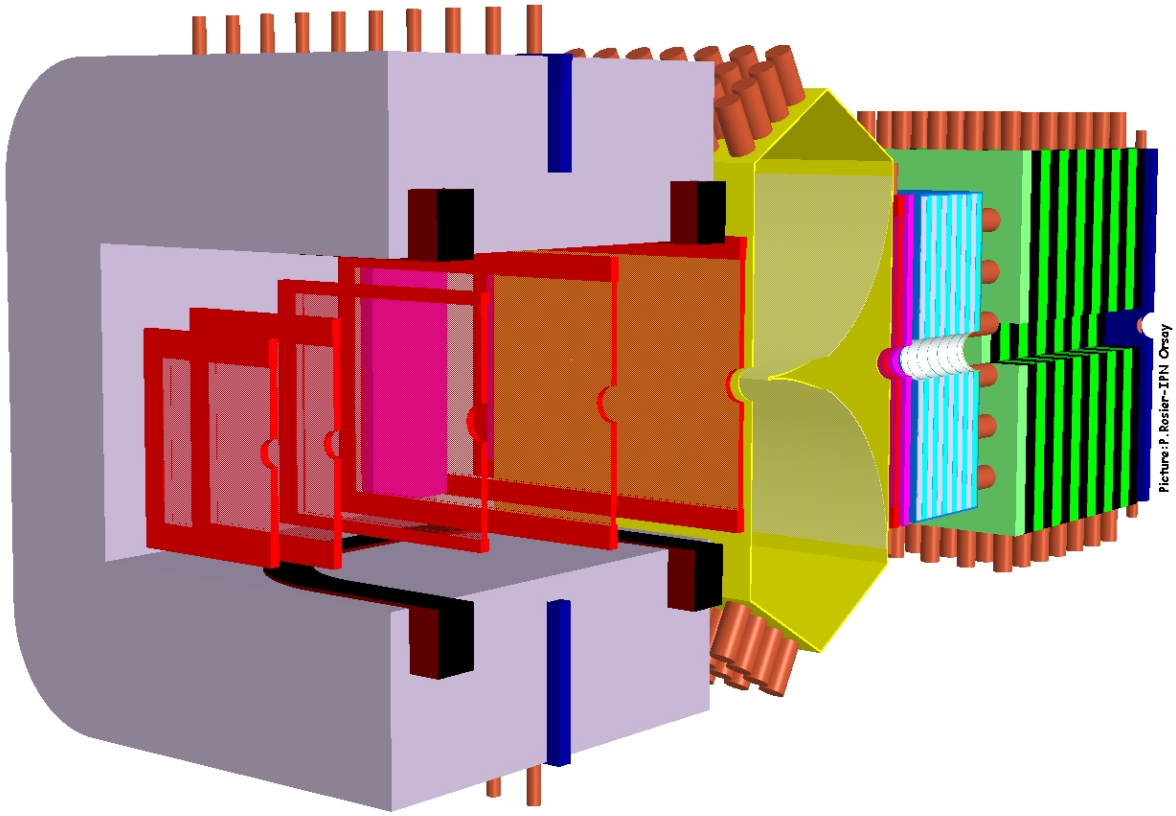

Figure 3.3: View of the forward spectrometer.

3.3.4 Calorimeter and Muon Detection

As a calorimeter for the forward region, a system composed of two parts is considered. The first part will be a Shashlyk-type calorimeter, suited for the detection of photons and electrons with high resolution and efficiency. The detection is based on lead-scintillator sandwiches read out with wavelength shifting fibers passing through the block. The techniques have already been successfully used in the E865 experiment [20]. It has been adopted or is being considered for various other experiments [21, 22, 23, 24, 25, 26]. An energy resolution of $4\%/\sqrt{E}$ [24] has been achieved. To cover the forward acceptance 13 rows and 27 columns will be required, i.e. 351 modules in total, which would be placed at a distance of 7–8 m from the target.

The second calorimeter part is devoted to the energy measurement of neutral hadrons and serves as a fast trigger and active muon filter. In particular, neutrons and anti-neutrons cannot be detected in other parts of $\overline{\text{P}}$ANDA. The second calorimeter is located directly behind the Shashlyk calorimeter and is followed by muon counters. It is considered to refurbish the mid-rapidity calorimeter MIRAC [27] from the WA80 experiment for this purpose. The calorimeter will consist of 40 independent stacks with the dimensions of 22 cm horizontally and 120 cm vertically. A stack consists of a lead-scintillator electromagnetic section $15\,X_0$ long, and a steel-scintillator hadronic section $6\,X_0$ long. The energy resolution for hadronic showers is $(0.034 \oplus 0.34/\sqrt{E/\text{GeV}})\%$, respectively. For $\overline{\text{P}}$ANDA, the MIRAC stacks would be rearranged such that they cover the forward acceptance ($\pm 5°$ and $\pm 10°$ for vertical and horizontal angles, respectively, and up to a factor of 3 below beam momentum). Thus the stacks would occupy an area of 1.8×4.4 m and a length of about 1.4 m between 8 and 10 m from the target.

Finally, behind the second calorimeter, there will be a wall of counters for muon identification similar to the ones surrounding the solenoid. Additional muon counters will be used inside the dipole iron or mounted to the clamping between the solenoid and dipole, to close the gap for angles between 5° and 22°.

3.4 Trigger and Data Acquisition

In many contemporary experiments the trigger and data acquisition (DAC) system is based on a two layer hierarchical approach. A subset of specially instrumented detectors is used to evaluate a first level trigger condition. For the accepted events, the full information of all detectors is then transported to the next higher trigger level or to storage. The available time for the first level decision is usually limited by the buffering capabilities of the front-end electronics. Furthermore, the hard-wired detector connectivity severely constrains both the complexity and the flexibility of the possible trigger schemes.

Here, a data acquisition concept is being developed which is better matched to the high data rates and to the complexity of the next generation of experiments.

In the approach, every sub-detector system is a self-triggering entity. Signals are detected autonomously by the sub-systems and preprocessed. Only the physically relevant information is extracted and transmitted. The data related to a particle hit, with a substantially reduced rate in the preprocessing step, is marked by a precise time stamp and buffered for further processing. The trigger selection finally occurs in computing nodes which access the buffers via a high bandwidth network fabric. The new concept provides a high degree of flexibility in the choice of trigger algorithms. It makes trigger conditions available which are outside the capabilities of the standard approach. One obvious example is displaced vertex triggering.

In addition, sub-detectors can contribute to the trigger decision on the same footing without restrictions due to hard-wired connectivity. Different physics can be accessed either in parallel or via software reconfiguration of the system.

High speed serial (10 Gb/s per link and beyond) and high-density FPGA (field programmable gate arrays) with large numbers of programmable gates and as well as more advanced embedded features are key technologies to be exploited within the DAQ framework. Within the next 3 years, the FutureDAQ project will deal with three major ingredients of the new architecture.

The basic building blocks of the hardware infrastructure which can be combined in a flexible way to cope with varying demands, are the following:

- Intelligent front-end modules capable of autonomous hit detection and data preprocessing (e.g. clustering, hit time reconstruction, and pattern recognition) are needed. A generic sampling ADC module will be developed to be used e.g. for calorimeters and muon chambers.
- A precise time distribution system is mandatory to provide a clock norm from which all time stamps can be derived. Without this, data from subsystems cannot be correlated.
- Buffered data links provide point-to-point communication, typically via optical links, buffering and on-the-fly data manipulation.
- Computing nodes aggregate large amounts of computing power in a specialized architecture rather than through commodity PC hardware. They may employ fast FPGAs (fast programmable gate arrays), DSPs (digital signal processors), or other computing units. The nodes have to deal with feature extraction, association of data fragments to events, and, finally, event selection.

A major component providing the link for all building blocks is the network fabric. Here, special emphasis is put on embedded switches which can be cascaded and reconfigured to reroute traffic for different physics selection topologies.

References

[1] L. Äystö et al., *An International Accelerator Facility for Beams of Ions and Antiprotons*, GSI, Darmstadt, 2001, Conceptual Design Report.

[2] M. Kotulla et al., Strong Interaction Studies with Antiprotons, Darmstadt, 2004, Letter of Intent.

[3] C. Ekstroem et al., Nucl. Instrum. Meth. **A371**, 572 (1996).

[4] JRA7: Internal Target, High Luminosity Internal Targets for Storage Rings, 2003, Proposal to the 6th Framework Programme, European Union.

[5] C. Ekström et al., Phys. Scripta **T99**, 169 (2002).

[6] J. Zabierowski et al., Phys. Scripta **T99**, 159 (2002), http://www5.tsl.uu.se /wasa.

[7] Technical report, ATLAS Technical Design Report 11, CERN/LHCC 98-13.

[8] Technical report, CMS Technical Design Report 5, CERN/LHCC 98-6.

[9] P. Holl et al., IEEE Trans. Nucl. Sc. **47**, 1421 (2000).

[10] P. Achenbach and J. Pochodzalla, private communication.

[11] H. Staengle et al., Nucl. Instrum. Meth. **A397**, 261 (1997).

[12] K. Mengel et al., IEEE Trans. Nucl. Sci. **45**, 681 (1998).

[13] R. Novotny et al., IEEE Trans. Nucl. Sci. **47**, 1499 (2000).

[14] M. Hoek et al., Nucl. Instrum. Meth. **A486**, 136 (2002).

[15] Technical Proposal, CERN/LHC 9.71.

[16] Technical Proposal, 1994, CERN/LHCC 94-38, LHCC/P1.

[17] E.Auffray et al., Moscow, 1999.

[18] http://www-dapnia.cea.fr/ Sphn/ Deformes/ Agata/ index.shtml.

[19] N. Akopov et al., Nucl. Instrum. Meth. **A479**, 511 (2002).

[20] G. S. Atoyan et al., Nucl. Instrum. Meth. **A320**, 144 (1992).

[21] G. David et al., Performance of the PHENIX EM calorimeter, Technical report, PHENIX Tech. Note 236, 1996.

[22] A. Golutvin, (1994), HERA-B Tech. Note 94-073.

[23] LHCb Technical Proposal CERN LHCC 98-4, LHCC/P4, 1998.

[24] I.-H. Chiang et al., (1999), KOPIO Proposal.

[25] H. Morii, (2004), Talk at NP04 Workshop at J-PARC.

[26] G. Atoyan et al., Test beam study of the KOPIO Shashlyk calorimeter prototype, in *Proceedings of "CALOR 2004"*, 2004.

[27] T. C. Awes et al., Nucl. Instrum. Meth. **A279**, 479 (1989).

4 Target and Interaction Region

The experimental requirements for the internal targets are manifold. Ideally, the target should consume only little space around the interaction zone. It should be homogeneous and spatially confined, optimally also providing a primary vertex point independent of the vertex detectors. It should not deteriorate the high vacuum around the storage ring. For many of the experiments a density of up to $4 \times 10^{15}\,\mathrm{atoms/cm^2}$, is required. Furthermore, the use of a variety of target materials is mandatory.

It is obvious that a single system cannot fulfill all those wishes simultaneously. Thus different target techniques have to be pursued. It is planned to operate specific targets for different experiments. There is ongoing R&D on the gaseous targets (pellet, cluster, and ^{3}He targets). New R&D is pursued on the nuclear and wire targets. Among the variety of target techniques shown in the following some may not be followed up, if the continued R&D proves them to be inadequate.

Intimately connected to the target set-up is the design of the interaction region, where sufficient pumping may become a crucial limitation and create boundary conditions for the detectors. In order to comply with the gas load of certain targets effusing into the storage ring vacuum a scheme of distributed pumping, non-evaporable getter and cryogenic adsorption, is being studied.

4.1 Pellet Target

The antiproton-proton experiments, which form the major part of the physics programme of $\overline{\mathsf{P}}$ANDA, require a high density hydrogen target. The approach of using frozen droplets of hydrogen, called pellets, is successfully in operation at the CELSIUS/WASA facility [1, 2]. In fact, the parameters achieved at that installation are already close to the requirements for the experiments at $\overline{\mathsf{P}}$ANDA. The previously unresolved question of the pumping speed necessary to cover the out-gassing of the pellets seems to have been understood. This is due to the vacuum calculations and the experimental cross-check at the pellet test station (PTS), a $\overline{\mathsf{P}}$ANDA-like system recently built up in Uppsala. Thus, the activities in the coming years should concentrate on two topics. Firstly, improvements within factors 2 to 4 have to be achieved on the divergence of the pellet train, as well as the pellet rate. However, this may be achieved with smaller pellets as the required density has already been achieved. Secondly, all procedures must be automated such that dedicated staff is not required for standard operation.

The implementation of the system hardly requires any space within the detector. Thus, a tube of 6 mm diameter through the MVD and straw tracker is proposed. Vacuum calculations show that this is even preferable to a larger-size tube.[1] Thereafter, it may open up slightly depending on the space available. The major part of the setup, the pellet generation and skimmer, will be places on top of the detector together with pumps. Here, 2 m space, magnetic shielding, and a 14 K cryogenic connection should be foreseen. Below, a pellet-beam dump with high pumping speed is required and shielding and some diagnostics are needed. A design proposal for the entire vacuum system based on the current state of vacuum calculations is made.

4.1.1 Requirements

Several major requirements constrain the target:

- To achieve the design luminosity of $2 \cdot 10^{32}\,\mathrm{cm^{-2}s^{-1}}$ an effective target thickness of $3.8 \cdot 10^{15}\,\mathrm{atoms/cm^2}$ is required.
- The detectors are to cover as much solid angle as possible, especially close to the interaction point, i.e. a small target tube and beam pipe are mandatory. The solenoid iron yoke has an outer radius of 1.85 m and very little space is available for an installation closer to the beam pipe.
- For a clean identification of events and secondary vertex reconstruction the background from interactions outside the target point should be small, i.e. the vacuum along the beam pipe should remain high although the pumping speed is quite restricted there.
- A minimum beam disturbance has to be achieved in order to conserve the antiproton beam for maximal use, i.e. the pellet size has to be small enough to avoid large angle scattering

1. The reason is that a conductance change near the interaction region implies the gas flow to increase in the directions of the upper and lower target pumps.

effects on antiprotons which might be impossible to cool. Moreover, the required area for the beam should be minimized by optimizing the spread and rate of pellets in order to get constant count rates.

- The primary vertex needs to be determined to an accuracy better than 100 μm in order to reconstruct short-lived reaction products. Depending on the multiplicity at the vertex it may be difficult or even impossible to obtain the information from the measurement of the reaction products only.

Given the design luminosity of $2 \cdot 10^{32}$ cm^{2}s, a HESR circumference of 574 m, and a number of 10^{11} $\overline{\text{p}}$ stored an effective target thickness of $3.8 \cdot 10^{15}$ hydrogen atoms per cm^2 is required. Geometrically, the target should consume as little space as possible where the detectors are located because it is vitally important for the identification of events to cover a solid angle close to 4π. The Micro-Vertex Detector is planned to extend around the target as close as 1 cm to the center of the $\overline{\text{p}}$ beam pipe. At these distances, a small vertical target tube would be restricting the acceptance. Similarly, for high angular coverage the beam pipe at the interaction point is designed to be only 2 cm in diameter. In the forward region it is planned to slowly open up to 4 cm, and pumps cannot be located any closer than 3 m down-streams. Thus, pumping of a gas load has to be performed from the upstream side (i.e. backward region of $\overline{\text{P}}$ANDA),[2] where the pipe may open up faster. Details on the geometry, compatible with the detector as well as a pellet target, are discussed in Sec. 4.1.7.

The vacuum in the beam pipes around the interaction area is important for two reasons. The decrease of lifetime of the circulating beam due to the interaction with the residual gas is one reason. The effect is mostly independent on the details of the distribution and can be expressed as an area density integrated over the entire length of the beam pipe, see Eq. 4.11. It can be directly compared to the target density and should not affect the operation as long as it stays much smaller than the latter.[3] Furthermore, the background rate arises from the interactions with the rest gas in the detectors. This poses severe constraints and is harmful in several respects. Firstly, the rising count rate, worsening resolution, noise, and radiation damage in the detectors are of concern. Secondly, the identification of events and the reconstruction of secondary vertices, especially from rare or high multiplicity events, becomes difficult and at a certain level impossible. Hence, the gas load at the interaction area is a crucial point for any target.

A pellet target is not a homogeneous sheet and locally rather thick. This has consequences for the antiproton beam. In order to have an optimized duty cycle the beam size should be matched such that at least one pellet is in the beam at any time. At the WASA facility, pellets are produced with a diameter of about 25 μm, corresponding to a local target thickness of $6 \cdot 10^{19}$ atoms/cm^2, with a pellet every 8 mm and a spread of 2.0–2.3 mm. The combination with a beam matched to this size leads to an effective target thickness of $2 \cdot 10^{15}$ atoms/cm^2. Antiprotons experiencing small angle scattering when penetrating a pellet should not be lost to the beam. Thus, it must be ensured that the particles mainly stay within the acceptance of the ring and can be cooled. Monte Carlo calculations were performed for the cooler ring COSY Jülich [3] and earlier for the CELSIUS ring [4]. First dedicated studies involving Monte Carlo simulations have been performed for the HESR ring (see Sec. 4.1.6). The studies do not show a considerable difference in lifetime for the proton or antiproton beam between a WASA-like pellet target and a target assumed to have a homogeneous distribution and the same average density.

Pellets are approximately 25 μm in diameter and the primary interaction vertex can be defined to that order of magnitude. This can be done by either using a pellet tracking system or by using the statistics obtained during the passage of the pellet through the beam. A single pellet will undergo some hundreds of interactions while passing the beam, thus generating sufficient statistics to precisely define its position. Presently, both options are under consideration. Using the latter approach, the trigger may have to process more data than necessary for the physics measurements alone.

4.1.2 WASA Pellet Target

The original idea to use small droplets of frozen hydrogen, so-called pellets, in a narrow stream as an internal target was brought up already in 1984. It is very intriguing as it opens up the possibility to increase the luminosity significantly compared to gas or cluster targets, while reducing gas load and in-

2. There are considerations on the use of NEG coated pipes, which are reviewed in Sec. 4.1.5. These would increase the pumping speed. Investigations on the feasibility are still under way.

3. For the injection, when the beam is larger and the target should be off, stricter limits might apply.

creasing feasible distances to the production area. The latter space can, as a consequence, be used for detectors. A pellet prototype was developed and put in operation in 1993 [5]. Following the build-up and testing of a pellet target system at CELSIUS in 1995 [6, 7], the final system was included in the CELSIUS/WASA set-up in 1999 [2]. Since 2000 the system is in regular operation for regular data-taking within the CELSIUS/WASA project, thus being the first and only hydrogen pellet target in use.

4.1.2.1 Pellet Beam Formation

The process of pellet generation at the WASA pellet target can roughly be divided into three stages. First hydrogen gas is liquefied and cooled down close to its triple point by a two-stage cryogenic cold head. The liquid hydrogen is injected into a low-pressure helium environment in form of a thin jet via a glass nozzle and broken up into uniform droplets by means of acoustic excitations. In the next stage the droplets are injected into vacuum through a narrow capillary while they are cooling further down due to evaporation and freeze to form so-called pellets. (See Fig. 4.1 for the components of this system) Finally a collimated beam of pellets is formed by skimming off the fraction with too high angular deviation. After the interaction with the ion-beam the pellets are collected in a cryogenic dump.

Droplet Generation The cooling power is provided by a commercial, closed-cycle He-gas two-stage cryogenic cold head. The gaseous hydrogen is injected at pressures of 400 mbar to 800 mbar and cooled down to about 50 K in the first stage. In the second stage a heating element is included which is used to regulate the temperature to 14.1 K; the hydrogen is thereby liquefied (at 400 mbar pressure hydrogen liquefies at 17.5 K).

A thin liquid jet is formed by a borosilicate glass nozzle (see Fig. 4.2) with an inner diameter of 12–15 μm at its exit. A stainless steel sintered filter is melted into the entrance of the glass nozzle to remove particles that would block the narrow exit. Acoustical excitations from a piezo-electric transducer attached to the nozzle are transmitted to the hydrogen jet, forcing it to break up into uniformly sized and evenly spaced droplets at the excitation frequency (see Fig. 4.4). Typical values lie in the region of 60–90 kHz. Depending on all these parameters droplets of a 35–40 μm diameter moving at a speed of about 20 m/s are formed.

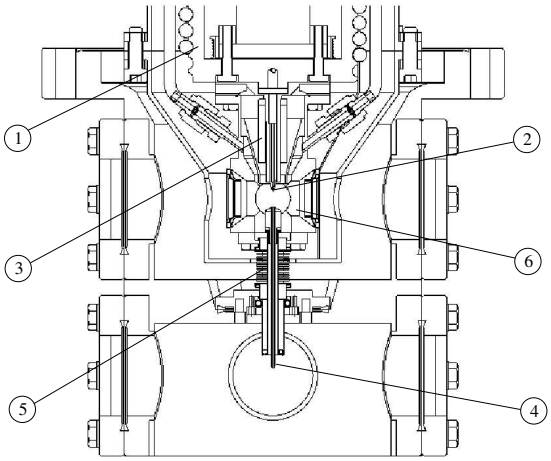

Figure 4.1: Pellet formation unit: The gaseous hydrogen is liquefied in the cryogenic cold head (1). A liquid jet is formed at the borosilicate glass nozzle (2) and broken up into uniform droplets by acoustical excitations from a piezoelectric transducer (3). The micro-spheres are injected into vacuum via a narrow glass capillary (4). A steel bellow (5) allows the alignment of the droplet formation chamber (6) with respect to the vacuum injection capillary.

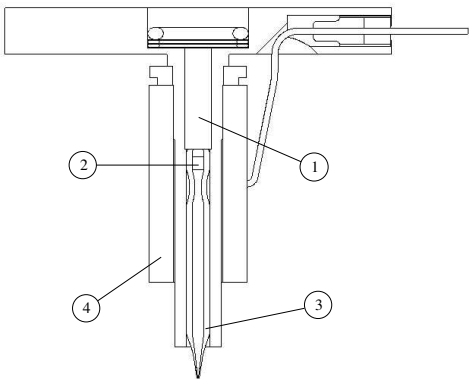

Figure 4.2: Liquid jet nozzle: Liquid hydrogen enters through a copper channel (1) and passes a stainless steel sintered filter (2). A liquid jet is formed by the glass nozzle (3) and broken up into droplets by a piezo-electric transducer (4).

The gas in the droplet formation chamber is a mixture of helium as background gas and hydrogen evaporated by the pellets. The total pressure is regulated to about 22 mbar, resulting in a partial pressure for hydrogen of about 8 mbar, i.e. below its triple point of 72 mbar at 13.96 K [8].

Due to evaporation the temperature of the droplets decreases further causing them to freeze and form pellets. There are a few theoretical models describing the characteristics of this process under the given conditions [9, 10]. Therein it is discussed how far the freezing of the droplets can be delayed due to supercooling. From optical observations of their behavior when hitting solid structures it has been deduced that the micro-spheres are still liquid at the upper end of the vacuum injection capillary while they are clearly frozen when they arrive at the skimmer.

Vacuum Injection The process of injecting the droplets into vacuum is crucial for the angular distribution of the pellets and thus for their effective rate at the interaction point. The task to transfer the droplets from the formation pressure of about 22 mbar to the vacuum (about 10^{-4} mbar) is challenging. On one hand the droplets may experience too strong forces to stay intact. On the other hand any transversal forces, i.e. due to turbulences, will increase the divergence of the pellet train. The properties have been studied extensively, and some results are described in Sec. 4.1.4. Analytical calculations of the gas flow and its interaction with moving droplets are difficult as the gas flow changes from the continuum to the molecular regime. Nevertheless several attempts were performed to study this transition theoretically [11]. Their results were, however, not found reproducible experimentally. Thus tests with a variety of different shaped and sized capillaries was performed. The optimal shape has been found to be a long thin cylinder with a slight contraction at the lower end (see Fig. 4.3). At this stage the speed of the pellets increases from about 20 m/s to 60–90 m/s. Optical measurements, however, also show that the the initially spherical droplets might experience a slight deformation here and their distance is less uniform (see Fig. 4.5). Typically the pellets have a diameter of 25–35 μm and their distance is between 0.5 and 1.5 mm. The capillary currently in use is a glass tube of 70 mm length and an inner diameter of 0.8 mm, ending in a contraction of 0.6 mm. It is mounted at a distance of 7 mm below the liquid jet nozzle.

Beam Alignment After the injection into vacuum the pellet beam shows an angular spread of Gaussian shape (compare Sec. 4.1.4). To obtain a well-defined beam the pellets with too high deviation are removed by a circular skimmer mounted 0.7 m below the vacuum injection capillary. The skimmer can be changed to one of different size in order to vary the pellet beam diameter. Currently in use are skimmers with inner diameters ranging from 0.4 mm–1 mm, corresponding to an angular divergence of 0.6 mrad–1.4 mrad.

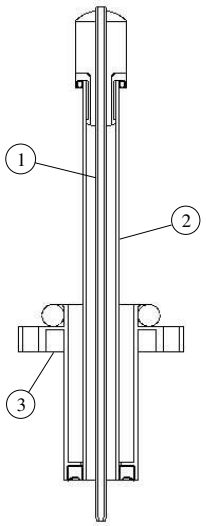

Figure 4.3: Vacuum injection capillary: The capillary (1) is a glass tube of 7 mm length and 0.8 mm inner diameter contracting to 0.6 mm at its lower end. For matters of thermal insulation it is mounted inside another glass tube (2) which itself is attached to a stainless steel support (3).

Through a pipe contracting down to 5 mm inner diameter the pellets reach the interaction point with the ion beam 2.4 m below the vacuum injection capillary. After another 1.2 m flight through a pipe of same size they are collected in a beam dump.

The direction of the pellet beam can be changed via two separate coordinate tables of same design. Each of them has four degrees of freedom: Two that allow $\pm$5 mm movement of the pellet beam in a plane perpendicular to its direction, two to tilt it around the both horizontal axes.

The upper coordinate table carries the liquid jet nozzle, the droplet formation chamber and the cold head and allows to direct the droplet train into the vacuum injection capillary. The capillary, together with the whole system of the upper coordinate table is mounted on the lower table, thus making it possible to move the whole pellet beam and aligning it through the skimmer to the intersection with the ion beam.

4.1.2.2 Diagnostics

Monitoring the droplet- and pellet beam is needed at several points to ensure its correct alignment and to allow the measurement of its properties. This is done optically using lasers, pulsed diodes, strobe lights, and conventional light in conjunction with LCD-cameras or photo-multipliers. The system has in total five observation points, each providing four glass windows into the vacuum system. This allows for the installation of diagnostic instruments on two perpendicular axes at each point.

Droplet Train Imaging The first set of windows is embedded into the droplet formation chamber to observe the droplet train. This is either done with a video camera or a digital photo camera equipped with a macro photo lens allowing to take pictures with magnification ranging from 1 to 5. For photos a flash lamp with flash duration of 100 ns is used. For video observation the droplets are lighted by strobed white light. The strobed light source is made of a standard diode lamp emitting light pulses of about same duration as the photo flash. The pulses are triggered by the jet excitation frequency for "frozen" visual observation, i.e. droplets are at the same spot each time the light is activated.

The images of the video camera are used to align the train of micro-spheres into the vacuum injection capillary, while pictures of the photo camera allow to determine size and velocity of the droplets. The distance between the droplets as well as their size are directly measured from an image with known magnification. It is observed that they are spherical and *equidistant* at the entrance of the capillary. Their velocity can then simply be calculated as distance times excitation frequency. An example of a photo taken at the droplet formation chamber is shown in Fig. 4.4.

Vacuum Injection Imaging As already mentioned the process of vacuum injection is very sensitive to the parameters hydrogen driving pressure, excitation frequency and pressure in the droplet formation chamber. In order to optimize the survival rate and divergence an observation point is situated directly below the vacuum injection capillary. The pellet beam is illuminated by continuous white light and its width and concentration, indicating the amount of pellets and their divergence after the injection, is monitored by a video camera. However, quantitative statements are provided by a pellet counting system described below.

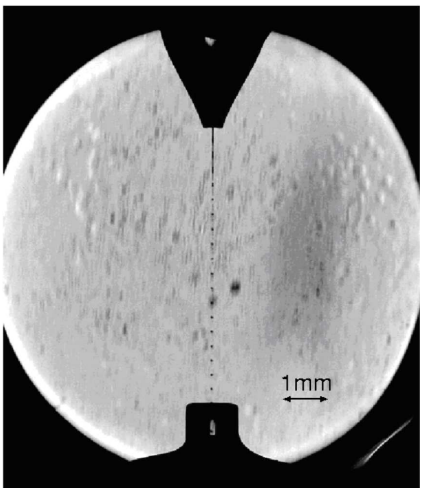

Figure 4.4: Image at the droplet formation chamber: The liquid jet leaving the nozzle (upper dark part) is broken up into a regular train of uniform droplets which enter the vacuum injection capillary (lower dark part).

For detailed studies of single pellets the video camera can be replaced by a digital camera, currently a Fuji Finepix S2 Pro. To achieve the exposure time required by the high speed of the pellets up to 90 m/s a flash light (FX-Xenon from High-Speed Photo System) with flash duration of 100 ns is mounted opposite to the camera. Its light is focused onto the camera by two lenses of 145 mm and 80 mm focal length respectively, allowing to take pictures with discrete pellets. An example for such a picture can be seen in Fig. 4.5. Some micro-spheres have lost their previous uniformity in spacing between one and the next. This effect may vary statistically and thus it is explained by the loss of some of the still not frozen droplets in this high-speed gas flow. This observation is confirmed by studies on pellet rates, discussed in Sec. 4.1.4. Furthermore a deformation of the pellets has been observed using such photographs with a much higher magnification. Both effects and the behaviour of such spheres hitting solid structures show that they are not yet fully frozen at this stage.

Density at the Skimmer Directly above the skimmer, i.e. 0.7 m below the vacuum injection, another set of windows allows the correct alignment of the pellet beam. It is lighted by a diode laser and observed by two video cameras, one at the window opposite to the diode laser and one perpendicular to its direction. The pellet beam can be seen on the image as a light spot, and the lower coordinate table is used to center it onto the skimmer. Here

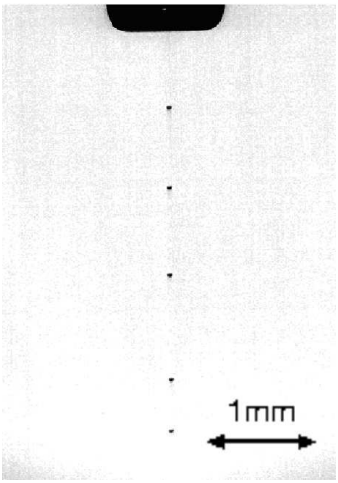

Figure 4.5: Image of the pellet train after vacuum injection: In the upper part of the figure the lower end of the vacuum injection capillary can be seen. Below that individual pellets can be seen following one line but not being *equidistant* anymore.

pellets are observed bouncing back and forth without breaking up, thus they must clearly be solid.

Pellet Counter Below the skimmer a pellet counting system is installed to determine the effective rate of pellets reaching the intersection with the ion beam. Light from a laser diode having a rectangular profile of 5 mm width and 1 mm height is directed onto the pellet beam (see Fig. 4.6). While the laser beam itself is deflected by a mirror, a circular collimator and iris are placed such that light scattered by the pellets into an angle of about 7° is focused by a lens and can either be observed by a camera or directed onto a photo multiplier tube. The latter is continuously used to provide a count rate corresponding to the rate of pellets passing the CELSIUS beam. Typical measured pellet rates for hydrogen lie in the region of 9 000 /s.

4.1.2.3 Vacuum System

As at $\overline{\text{P}}$ANDA the 4π geometry of this detector does not allow for pumps very close to the interaction point. Therefore the generation of pellets is situated about 2.4 m above the beam line. As the detector only extends to about 1.6 m above the beam line, there is enough space there for the pumping systems operating around the production point. The frozen pellets are then directed through a vertical pipe, which reduces in diameter from 150 mm in the outer part to 5 mm for a length of 60 cm above and below

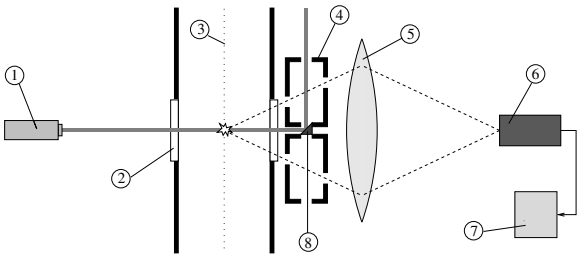

Figure 4.6: Sketch of the pellet counter: Light from a laser (1) enters through a observation window (2) and is scattered by the pellet beam (3). The scattered light passes a collimator (4) and a lens (5) is used to focus it onto a photo-multiplier tube (6) connected to counting electronics (7). The laser beam itself, however, is deflected by a mirror (8).

the target (see Fig. 4.7). Thus at the very central region the detectors can cover a large solid angle.

Due to the restrictions caused by the narrow beam pipe in the WASA-detector the pressure at the intersection of pellet- and ion-beam, a value crucial for the amount of background reactions, can not be measured directly. A pressure gauge in the scattering chamber, situated at a distance of 0.95 m from the interaction point and close to two 1200 l/s turbo-molecular pumps allows to draw only limited conclusions on the actual pressure in the interaction region. Below the WASA detector a cryogenic beam dump is located.

4.1.2.4 Deuterium Pellets

The production of deuterium pellets in the WASA target facility is possible as well and can be performed without major changes in the setup used for hydrogen. The triple point of deuterium at 18.63 K/171 mbar lies considerably higher in both temperature and pressure than that of hydrogen. For operation with deuterium it is thus necessary to increase the temperature of the liquid jet nozzle to a value of about 18.9 K to allow a controlled liquefaction of the gas. The optimal pressure in the droplet formation chamber for obtaining a concentrated pellet beam after vacuum injection lies around 50 mbar. Compared to hydrogen the angular spread of deuterium pellets is significantly reduced (compare Sec. 4.1.4), resulting in pellet rates of typically 16 000 /s.

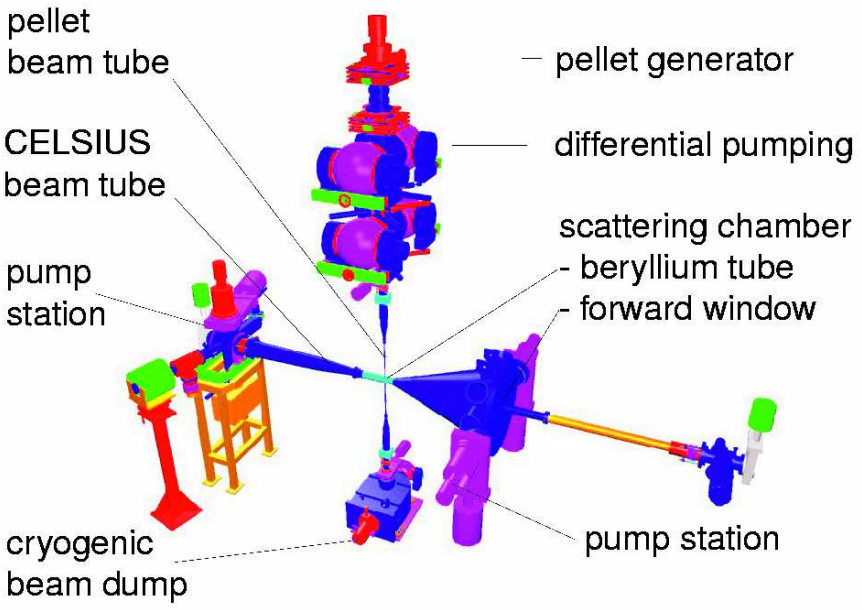

Figure 4.7: Pellet target installation showing the vacuum system at the WASA experiment.

4.1.3 Pellet Test Station (PTS)

A completely new system, which is largely a copy of the previously discussed WASA set-up, has been built-up at The Svedberg Laboratory (TSL). It is designed taking into account the experiences from the WASA system. However, a maximum of compatibility with this system is kept, such that an interchange of nozzles, capillaries, *etc.* is feasible between the systems. The objective is to provide a set-up where tests and modifications are easily possible giving access for the measurement of all variables, like beam diameter, distribution, vacuum, *etc.*. It may, however, be used in large parts for the installation at the future FAIR facility.

The pellet formation system at the PTS is in its principal identical to the one used at WASA. Thus please refer to Sec. 4.1.2.1 for the details of pellet formation. The construction of the cold-head and pellet-generation system (see Fig. 4.8) is slightly different in order to achieve better pumping and less vibrations. Moreover the vacuum can be monitored more reliably, and the system can be heated individually at three stages while controlling these temperatures. The droplet formation chamber is, however, kept similar such that the nozzles and vacuum injection capillaries can be produced for the installation at any system. As mentioned earlier these thin devices do determine to a large fraction the properties of the pellet train. Thus they are under constant development and can now be tested both at WASA as the PTS without modification.

Another improvement compared to the WASA system is the significantly easier access for mounting and dismounting components. In Fig. 4.9 the pellet formation unit with many of the surrounding parts including the coordinate table is shown sitting on rails, which allow the movement to an assembly position. Their easy access from the lower side enables fast exchange of capillary and nozzle. From the shown position it can be lowered in its operational position on the flange on top of the large pumping block.

Below the pumping block (i.e. also below the sustaining floor) a vacuum system has been designed and completed, which simulates on the one hand the situation at $\overline{\text{P}}$ANDA but on the other hand also allows the monitoring of crucial variables like vacuum and beam shape, especially also at the so-called "interaction chamber" (point (6) in Fig. 4.10). This is the point which simulates the beam intersection at $\overline{\text{P}}$ANDA. It is situated 2.16 m below the vacuum injection and hence at a similar distance as in the $\overline{\text{P}}$ANDA design. The chamber is pumped using a turbo-molecular pump with a pumping speed of $S = 150\,\text{l/s}$ but throttled by a (resistive) pipe. The pipe has an inner diameter of 34 mm and a length of 160 mm. The effective pumping speed is thus calculated to be $S_{\text{PTS}} = 56\,\text{l/s}$ from (Eq. 4.8), thus being close to the value which is obtained using the pro-

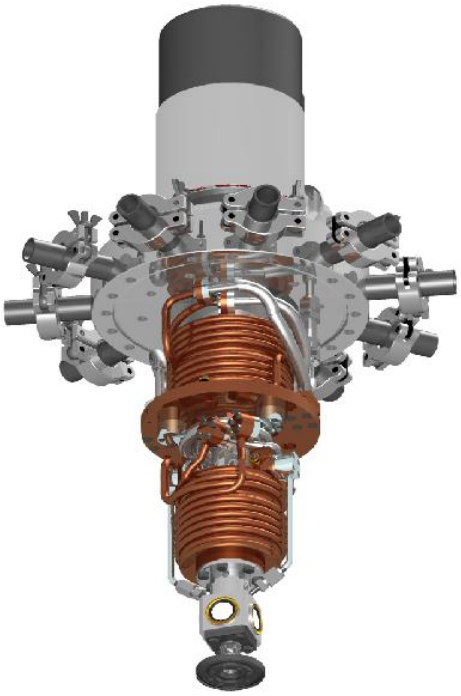

Figure 4.8: Technical drawing of the cold-head and droplet formation chamber of the PTS system. Below the two cooling stages surrounded by copper tubes the droplet-formation chamber is mounted (cubic box with round windows), which is fed with Helium using 2 pipes visible in the figure. Below that the bellow and flange to the vacuum side are shown, whereas the capillary which would sit inside this bellow is omitted as well as all the outer pieces of the construction.

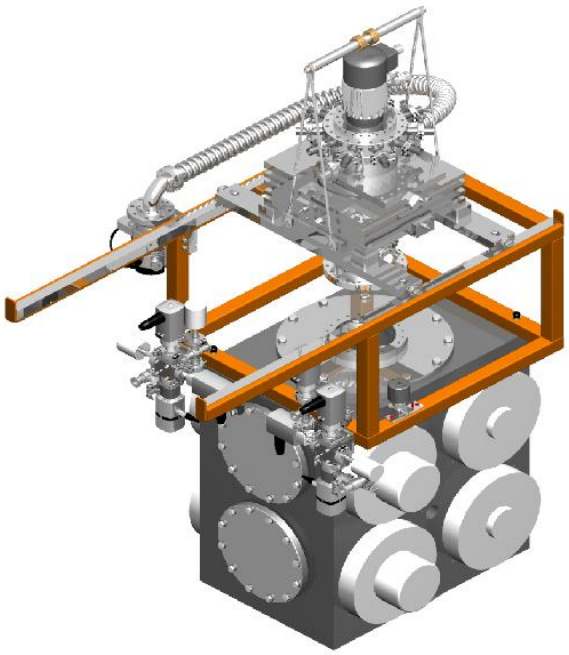

Figure 4.9: Technical drawing of the assembled pellet formation unit with cold-head and coordinate table lifted onto an assembly frame above its operational position on the pumping block. If rolled to the left position an exchange of capillary and nozzle is easily possible, while lowered only the cameras and light-sources have to be mounted to start operation.

posed geometry for the $\overline{\text{P}}$ANDA beam-target interaction point. Nevertheless, we expect to reproduce pumping-wise roughly the situation there. Moreover, the vacuum above and below this point can be measured at several locations (see Fig. 4.10), in order to check for a consistent description of the vacuum situation by the simulation and define possible origins of additional gas load, e.g. due to scattering of pellets and their subsequent evaporation.

Unlike the WASA system, and also the planned design of the $\overline{\text{P}}$ANDA system, the skimmer in the PTS is placed below the large pumps and there is only little pumping (about 25 l/s) in a small chamber just below and before the entrance to the small vertical pipe. This is because access for the observation of the pellet train is necessary just above the skimmer. This is not feasible without major modifications within the existing pumping block. This fact, however, may worsen the vacuum situation, as there is only little pumping and even some scattered pellets at the skimmer may still reach the pipes. Another possible source of additional gas is the beam dump which is, unlike the situation at WASA, not cryogenic but an 16 l/s turbo-molecular pump. Thus it is especially important to have gauges in these sections, as to monitor and, if applicable, include those effects in the calculations. In this part of the system there are in total 5 positions where gauges have been connected. In most cases a combination of Pirani and penning gauges has been used to provide the coverage from atmosphere pressure down to 10^{-7} mbar.

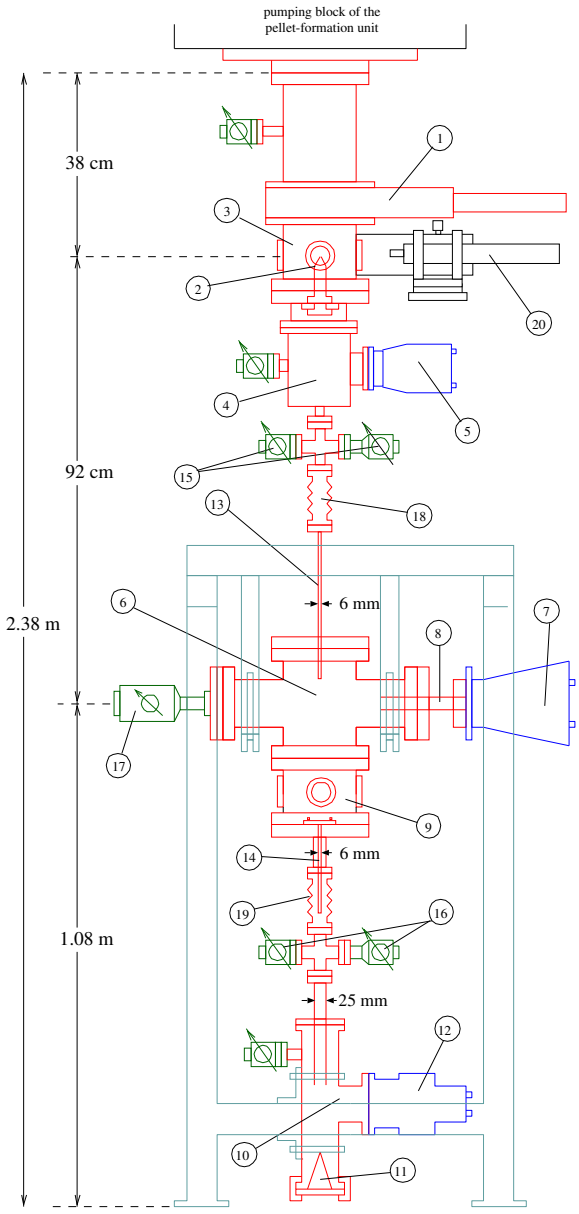

Figure 4.10: Sketch of the vacuum system below the intermediate floor: A valve (1) separates the vacuum system from the pellet formation unit. The skimmer (2) is situated in the upper observation house (3), and a chamber (4) with a small pump (5) is situated directly below. The interaction chamber (6) is connected to a turbo-molecular pump (7) *via* a resistive pipe (8). The lower observation house (9) allows to survey the correct alignment of the pellet train. In the pellet dump (10) the micro-spheres are deflected by a cone (11) and the gas pumped away (12). The parts are connected via pipes contracting to 6 mm inner diameter (13,14) and each equipped with both a pirani and a penning pressure gauge (15,16). A full range pressure gauge (17) is installed at the interaction chamber. Two bellows (18,19) allow the alignment of the system. A laser on a coordinate table (20) may be attached at any window to observe position and dimensions of the pellet train. Cameras, fore-pumps, connection pipes and cables are omitted in this sketch.

The system is designed in a most flexible way. The upper connection pipe (41 cm long) is interchangeable and we worked with inner diameters of 6 mm ($\overline{\text{P}}$ANDA like) and 16 mm for systematic studies. The lower pipe is with 25 mm wider than the ones, which will be used in $\overline{\text{P}}$ANDA in order to be able to simulate different pipe sizes by using inlets into those pipes. Again to simulate panda we used an inlet with 6 mm diameter and a length of 12.5 cm. As there is free access from all sides and it can be separated from the upper part, any modifications can be done easily. Apart from the fast exchange of skimmers and pipes this also enables us to equip it with further diagnostic tools. A first system has been designed and we are waiting for the delivery of the components. This uses scattered light from a laser beam on pellets in a line scan camera with fast readout. We will then be able to measure precisely the pellet train shape and rate. This extensions will enable us to do systematic studies on the these parameters leading to the optimization required for optimal conditions in $\overline{\text{P}}$ANDA.

4.1.4 Pellet-Train Properties

In order to evaluate the properties of the pellet train studies on both the WASA system and the Pellet Test Station (PTS) have been performed. The first offers well-known and stable operation and a large variety of diagnostic tools. Thus the measurements presented in this section have all been done at WASA. These studies are, however, restricted to periods where neither WASA or any other CELSIUS experiment is running. Up to this moment the PTS provides advantages in testing different nozzles and capillaries and studying the vacuum, but it is somewhat restricted in the measurement of concentration, diameter and pellet rate. However, it will be extended such that, quite soon, most of the diagnostic possibilities will be superior to the ones at WASA.

The WASA skimmer, which is 0.59 mm in diameter and situated 0.7 m below the vacuum injection capillary, is restricting the pellet train. A first assumption, that the pellet distribution emerging from the capillary just gets cut off at its edges, was confirmed by several test measurements (one measurement is described in the next paragraph). Moreover, the profile of the initial distribution, i.e. before being influenced by the skimmer, could also be determined to a very high precision by sweeping the pellet train over the skimmer (presented thereafter).

One way to determine the pellet-train size at the interaction area with the beam is to use the geo-

metrical restrictions in that area. The pellet train was tilted while it was ensured that the skimmer is hit centrally and the vacuum was monitored simultaneously in the CELSIUS beam pipes. The vacuum measurement there is sensitive for this quantity as the gauges are located on the horizontal beam pipe, which is, of course, corresponding in level to the interaction point. As soon as pellets hit the walls of the 5 mm wide beam tubes close to the central cross the pressure starts to rise. This can be observed ad the limits of the scans shown in Fig. 4.11. Using just the opening of the tube as input one obtains a pellet beam diameter of (2.1±0.2) mm. This is to be compared with the 2.0 mm calculated from extrapolating geometrically from the skimmer size to the interaction point. Due to this agreement one deduces that the pellets passing the skimmer are in their vast majority not significantly affected by the presence of the skimmer. That signifies that the pellet distribution is merely cut off at the skimmer edges.

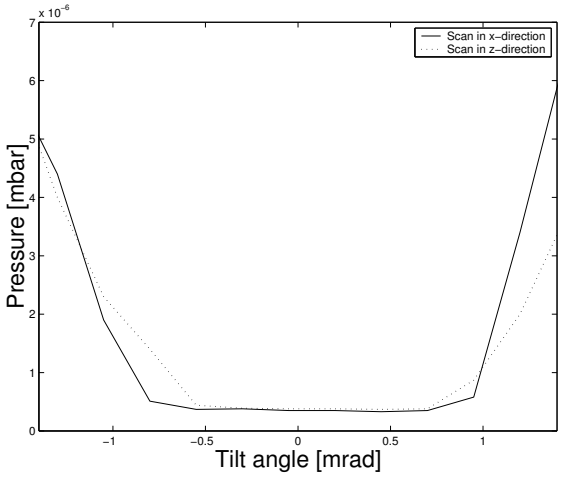

Figure 4.11: Pressure in the scattering chamber while tilting the beam: Scans in x- and z-direction are shown as dotted and solid line respectively. The pressure starts to rise when pellets hit the wall of the beam pipes. The skimmer and pipe had diameters of 0.59 mm and 5 mm respectively.

The profile of the uncollimated pellet beam, i.e. before the skimmer, is taken by sweeping it over the skimmer while measuring the number of pellets reaching the interaction zone below the skimmer. In order to make this number to be a reliable quantity to measure the density distribution at the skimmer, a dedicated automatic procedure has been developed. This ensures the pellet train to stay always on axis, while the coordinate tables are moved such that equidistant steps at the skimmer location in both directions are scanned, and that the pressure is allowed to stabilize the same number of seconds before each parameter log. In parallel the pellet rate and vacuum in the scattering chamber are logged. As an example the measured values are shown for a scan in z_0 with hydrogen pellets in Fig. 4.12. The x and z vectors ie in the plane perpendicular to the pellet train, perpendicular and parallel to the CELSIUS beam respectively. The index "0" labels the system with its origin at the center of the skimmer, whereas x and z have their origin at the nominal position of the pellet train i.e. the mean values for the pellet distribution.

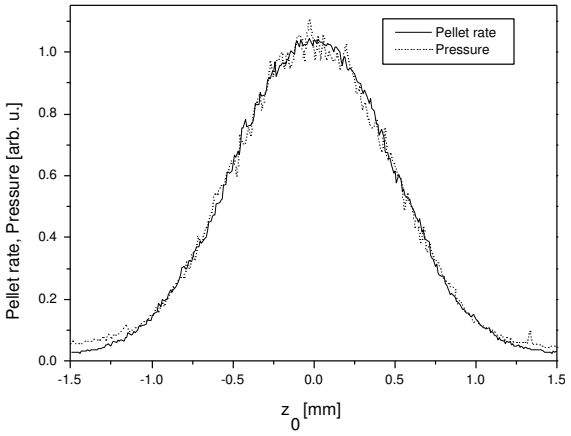

Figure 4.12: Pellet rate and pressure in the scattering chamber normalised at their peak values *vs.* beam position for a scan in z-direction for H_2 pellets. Except for a small background pressure the two curves show a perfect correlation, with fluctuations being lower in the pellet rate. Both curves are scaled to their maximum value on the vertical axis.

The experimental data for the two different parameters agree well within the experimental uncertainties, with only a small offset visible at extreme z_0 values (see limits of Fig. 4.12). This phenomenon is expected due to the finite pressure in the scattering chamber even without any pellets present. Thus the conclusion can be drawn, that the procedure measuring the pellet rate actually works well. Due to the variations, it seems more precise than the vacuum measurement. Hence this parameter is used for the further analysis of the beam profile.

The distribution from Fig. 4.12 can, however, not be taken immediately as the profile of the pellet train. The convolution with the aperture of the skimmer becomes important as it is, in its dimensions, similar in size to the pellet beam. *A priori* the shape of this distribution is unknown. However, by fitting several test-functions to the experimental results (while knowing the skimmer dimensions), it

was found that the a Gaussian shape in both x and z reproduces the measured values best. It will be denoted by $f_g(x, z)$ in the following.

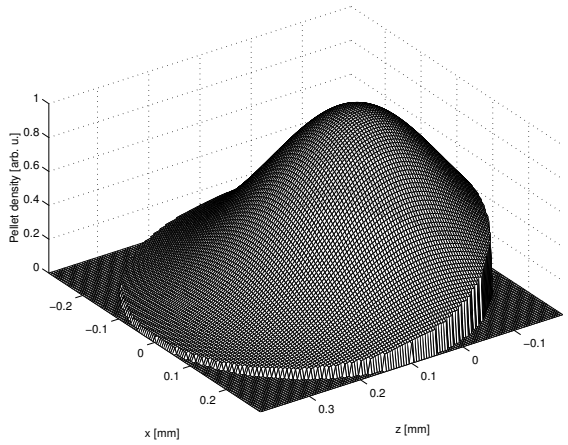

Figure 4.13: Simulated pellet beam density distribution using a two-dimensional Gaussian with $\sigma_x = \sigma_z = 0.15\,\text{mm}$. The distribution is cut by the currently used skimmer with 0.59 mm diameter, where the mean of the pellet train z_0 is off center by 0.1 mm. The pellet rate obtained after the skimmer is proportional to the integral over the density distribution $F(0, -0.1)$ (see Eq. 4.1).

We can now express the average rate of pellets passing the skimmer as a two-dimensional integral

$$F(x_0, z_0) = \iint_{(x-x_0)^2+(z-z_0)^2<R^2} f_g(x, z)\, dx\, dz$$
$$f_g(x, z) = \frac{A}{2\pi\sigma_x\sigma_z}\; e^{\frac{x^2}{2\sigma_x^2}+\frac{y^2}{2\sigma_z^2}} \tag{4.1}$$

over the density distribution at the skimmer $f_g(x, z)$ with its limits set by the skimmer size (radius R). Here A is the total initial pellet rate and σ_x and σ_z are the width of the Gaussians in x and z respectively. For illustration such a distribution is shown for $\sigma_x = \sigma_z = 0.15\,\text{mm}$ in Fig. 4.13.

We can now determine the widths σ_x and σ_z of this Gaussian by fitting the function $F(x_0, z_0)$ to the experimental rate in dependence of the average beam position. It was shown that this can be done independently in x_0 and z_0. Note that only the amplitude and width are free parameters here. Such a fit in z_0 and curves deviating by about 10% to illustrate the sensitivity of this method are shown in Fig. 4.14. The resulting widths of the Gaussian distributions before the skimmer are tabulated for different runs with hydrogen and deuterium in Table 4.1.

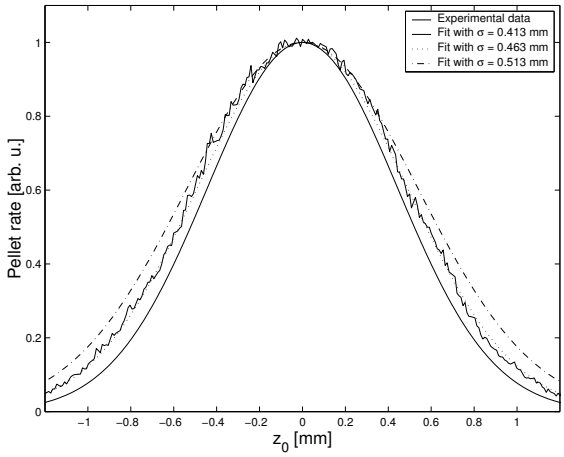

Figure 4.14: Experimental pellet rate (wavy solid line) and calculated distributions for three different widths. A width of the initial Gaussian distribution of $\sigma_z = (0.46 \pm 0.01)\,\text{mm}$ is taken as best fit (dotted line) and curves differing by 0.05 mm are shown for illustration only.

The difference between the runs is relatively small though significant compared to the errors. While this can be explained by varying conditions during the pellet formation, the values seem to be systematically smaller in x than in z direction. Moreover, this effect becomes more significant for the deuterium run, which is about half as wide in terms of beam width.

A possible interpretation of this phenomenon might be that this effect stems from vibrations of the cold head. Video images from the observation point at the skimmer show vibrations of the pellet beam in z- but not in x-direction, suggesting this to be the reason for the different widths. The reduction of those vibrations, caused by the compression cycle of helium in the cryogenic refrigerator, would thus possibly help to decrease the total angular spread of the pellets. An external cryogenic device for liquefying hydrogen, e.g. in connection with the liquid helium cycle used to cool the solenoid magnet, would solve this problem.

Using the mean results for hydrogen (see Table 4.1) and the present skimmer diameter $D = 2R = 0.59\,\text{mm}$ centered at the highest concentration of the pellet train (which is the parameter optimized for running) we can calculate the amount of pellets passing the skimmer as

$$\hat{F}_g(0, 0) = \int_{x^2+z^2<R^2} \hat{f}_g(x, z)\; dxdz = 0.214\, A \tag{4.2}$$

Due to the normalization of $\hat{f}_g(x, z)$ the factor cor-

target material	width at the skimmer σ_x [mm]	σ_z [mm]	angular divergence σ_x [mrad]	σ_z [mrad]
H_2	0.43 ± 0.01	0.46 ± 0.01	0.61 ± 0.01	0.66 ± 0.01
	0.39 ± 0.01	0.44 ± 0.01	0.56 ± 0.01	0.63 ± 0.01
	0.39 ± 0.01	0.45 ± 0.01	0.56 ± 0.01	0.65 ± 0.01
	0.40 ± 0.01	0.45 ± 0.01	0.57 ± 0.02	0.64 ± 0.01
D_2	0.19 ± 0.01	0.24 ± 0.01	0.23 ± 0.01	0.34 ± 0.01

Table 4.1: Pellet beam divergence: Three runs with hydrogen and one with deuterium pellets are compared in both their width at the skimmer as well as the re-calculated angular divergence. Note that, due to the currently used skimmer of 0.59 mm diameter, the angular spread is cut off for any target at 0.42 mrad in half width.

responds directly to the ratio of pellets passing the skimmer. The pellet rate below the skimmer was measured to be typically in the order of 9 000 /s. Using the obtained 21.4% of pellets passing the skimmer this would correspond to a rate of about 42 000 pellets/s above the skimmer. We, however, know the initial production rate of droplets from the transducer frequency of 81 kHz. Hence we may deduce that only about 50% of these droplets reach the skimmer as frozen pellets. The rest seems to be lost at the stage of the vacuum injection. This may also explain the fact that the pellets leave the capillary irregularly though they are perfectly *equidistant* before (see Figs. 4.4 and 4.5). Thus it is clear that the otimization studies will focus on improvements at this stage. There are several ideas which will be pursued. One may e.g. increase the travel distance before the vacuum injection in order to freeze the the droplets beforehand, and study different capillary geometries *etc.*

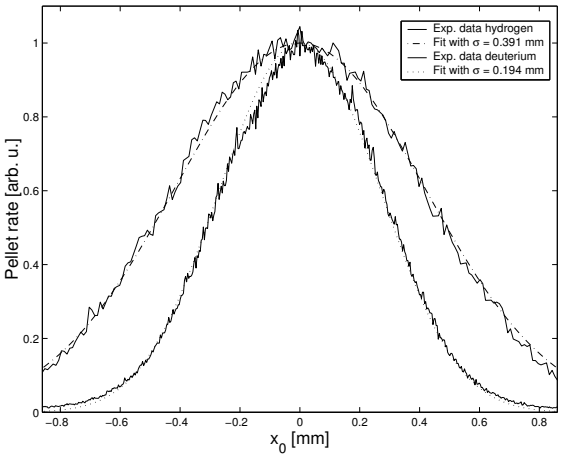

Figure 4.15: Pressure scans as in Fig. 4.14 in x-direction for hydrogen (outer histogram) and deuterium pellets (inner histogram) of the same diameter $D = 30\,\mu$m. The deuterium beam is about half as wide as the one for hydrogen.

Deuterium Pellets The production of deuterium pellets is possible without any changes in the setup of the pellet target. Instead of H_2 gas D_2 gas is used together with palladium purifier at the gas inlet. The settings for the pressures and temperatures at the different stages are, however, differing taking into account the different properties of those gases. Using deuterium the angular spread of the pellets is reduced compared to the operation with hydrogen. This can e.g. be observed sweeping the beam over the skimmer as described previously. In Fig. 4.15 the pressures from two such scans are directly compared, while the results are listed in Table 4.1. Using the same skimmer this, of course, results in a higher density at the ion beam intersection and thus a higher luminosity.

Compared to operation with hydrogen the main change in beam properties for deuterium pellets of same diameter is a significant decrease in width of the pellet density distribution (see Fig. 4.16). The resulting ratios, $\sigma^H/\sigma^D = 2.1$ and 1.9 for x and z direction respectively, lie close to 2.3, the ratio of the densities of solid hydrogen and deuterium. A possible interpretation is that both hydrogen and deuterium pellets experience similar forces at vacuum injection, however, due to their higher moment of inertia, the resulting lateral speed of the deuterium pellets is the corresponding factor lower than that of hydrogen.

The smaller beam width leads to a higher pellet rate after the skimmer. Typical rates are in the order of 16 000 /s. The values of $\sigma_x = 0.19$ mm and $\sigma_z = 0.24$ mm result in a fraction of 61% pellets passing the 0.59 mm diameter skimmer, compared to 21% for hydrogen. Similarly as above we can deduce a micro-sphere survival ratio at vacuum injection of only about 30%.

Though it is clearly welcomed by experimentalists that the pellet rates are almost a factor of two higher, this fact in conjunction with a lower pumping speed than for hydrogen leads to a higher equilibrium pressure in the scattering chamber. Thus more background reactions are observed in WASA, which poses a challenge to both the detector as the reconstruction.[4] In dedicated test runs with the same pellet rates and diameters for hydrogen and deuterium a ratio of equilibrium pressures in the scattering chamber of $P_D/P_H = 1.7 \pm 0.1$ was obtained (see Fig. 4.16).

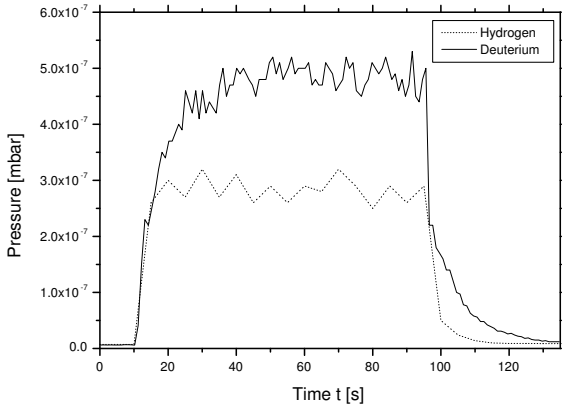

Figure 4.16: Pressure in the scattering chamber for hydrogen and deuterium pellets. In both cases the pellet rate was about 9 000 /s and the pellet diameter 32 μm. The pellet beam is switched on at $t = 10$ s and switched off at $t = 95$ s.

4.1.5 Vacuum Measurements and Calculations

At the PTS described in Sec. 4.1.3 vacuum measurements have been performed which were compared with calculations taking into account out-gassing of pellets, the pumping speeds, and conductances. It could be shown that these calculations can describe the measured data, which in itself are showing a hint on the vacuum situation at $\overline{\text{P}}$ANDA, as the system is very comparable to the $\overline{\text{P}}$ANDA vacuum system. The same calculations are then used to calculate the vacuum in the $\overline{\text{P}}$ANDA system in Sec. 4.1.7.

4.1.5.1 Heating of Pellets by Beam Interaction

The outgassing of pellets in vacuum is dependent on the temperature of the pellets. This temperature might be increased by the interaction with the beam particles. To study this effect we used the proton beam of CELSIUS with $2 \cdot 10^9$ stored protons and an energy of 1450 MeV. By monitoring the vacuum close to the interaction zone with and without beam on target (see Fig. 4.17) we find that, if an effect is existing, it is within the errors of the measurements. Please take into account that the effect of heating is influenced by various parameters like the beam energy. Though the number of particles was much smaller at CELSIUS the effect has to be expected to be compensated partially by a factor of 6 arising from the larger revolution frequency at CELSIUS. Though there has been no effect observed in this first test, we plan to do further studies and do calculations for the experimental conditions at $\overline{\text{P}}$ANDA.

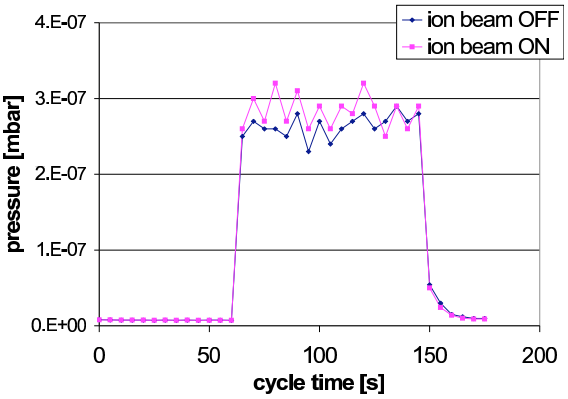

Figure 4.17: Vacuum in the CELSIUS beam pipe measured switching the pellet target on at $t = 70$ s and off at $t = 150$ s. The solid curve shows the behavior without beam whereas the dashed line indicates the values measured with circulating CELSIUS beam. Both distributions were taken at unchanged target conditions.

4.1.5.2 Calculation on Conductances and Pumping Speed

Vacuum calculations are generally difficult and, in order to obtain precise results, Monte-Carlo simulations including the details of the geometry have to be performed. This is very time consuming and can be avoided if we restrict us to certain ranges. In our case we operate in the regime of molecular gas flow. In a pipe of circular cross section of diameter d, hydrogen gas ($T \simeq 298$ K) is in the regime of molecular flow if the pressure P fulfills $\langle Pd \rangle \lesssim 1 \cdot 10^{-3}$ mbar mm. Following Ref. [12] we

4. Note that the the WASA drift tubes and scintillator readout is rather slow.

define the characteristic conductance of an element as

$$C_{\text{char}} = C_{\text{ap}} a \ , \tag{4.3}$$

where

$$C_{\text{aperture}} = 0.347\, d^2\, \text{l/(s mm}^2\text{)} \tag{4.4}$$

and a is the transmission probability. For a given pipe length l, there are two extreme cases. In the limit when $l \ll d$ ("aperture") a equals 1. For the other extreme case, when $l \gg d$ ("long pipe"), the probability is $4d/3l$. Both these limits as well as intermediate cases are well described by the (general-case) probability

$$a_{\text{gen}} = \frac{14 + 4\frac{l}{d}}{14 + 18\frac{l}{d} + 3(\frac{l}{d})^2} \ . \tag{4.5}$$

For the case of a long cone with end diameters d_1 and d_2, where $d_1 < d_2$, the transmission probability in the direction of increasing diameter is

$$a_{\text{cone}} = \left(1 + \frac{d_1 + d_2}{2d_2^2}\right)^{-1} \ . \tag{4.6}$$

The total conductance[5] C_{tot} for a system of several pipes connected in series is obtained from

$$\frac{1}{C_{\text{tot}}} = \frac{1}{C_1} + \frac{1}{C_2} + ... \tag{4.7}$$

but the imposed error is not significant as long as we only use it to add a few pipes.

Using the above equations for the interaction region of the PANDA detector, we can calculate the conductances of the pipes used. For the backward pipe consisting of one pipe ($l = 1700$ mm and $d = 150$ mm) and one cone ($l = 300$ mm, $d_1 = 20$ mm, and $d_2 = 150$ mm) (see also Table 4.3) we get the total conductance to $C_{\text{back}} = 60$ l/s. The dimensions of the forward pipe are discussed in Sec. 4.1.5.6, but we can here simply state that most of the pumping will, by far, be done backward since the forward pipe will be even more conductance limited. Both pipes will, however, be connected to vacuum pumps at their outer ends. A pump with pumping speed S connected to the volume of interest over a pipe of conductance C has the effective pumping speed S^{eff}, given by

$$\frac{1}{S^{\text{eff}}} = \frac{1}{S} + \frac{1}{C} \ . \tag{4.8}$$

Assuming a horizontal pumping speed of $S = 250$ l/s leads to an effective pumping speeds of $S^{\text{eff}}_{\text{back}} = 48$ l/s, which, as mentioned above, will be close to the total effective pumping speed for PANDA, $S^{\text{eff}}_{\text{Panda}}$, since the contribution from $S^{\text{eff}}_{\text{forward}}$ will be of limited importance.

4.1.5.3 Calculation on Outgassing

By using an implicit discretizing scheme, the differential energy transport equation within a hydrogen micro-sphere can numerically be solved [14]. Utilizing an extended version of this program, and a revised version of the classical Hertz–Knudsen evaporation formula [15]

$$\frac{dm_p}{dt} = -1.668A\frac{P_S - P_\infty}{\sqrt{2\pi R_p T}} \ , \tag{4.9}$$

the mass loss and hence the outgassing per individual pellet is calculated. Here, m_p is the pellet mass, A is its surface area, P_S the solid-vapor saturation pressure from Ref. [8], P_∞ the surrounding (vacuum) pressure, and R_p the specific gas constant of the pellet material (hydrogen).

Most of the pellet evaporation will, by far, take place before the equilibrium temperature of about 6 K is reached. The time for this is typically within 1 ms, which corresponds to a travel distance of 6–10 cm. In the vacuum chamber, the distance between the exit of vacuum injection capillary and the skimmer is much greater; 70 cm for WASA and 124 cm for the PTS. Therefore, we can safely state that the mass deposit to take into account will only be the "equilibrium" one, i.e. when the pellet temperature is in equilibrium with the surroundings. The mass loss then converge to an almost constant value. In Table 4.2 these equilibrium values are shown for different pellet sizes. The numbers are to be multiplied with a conversion factor $O(\text{H}_2) = 9.22 \cdot 10^{-6} \frac{\text{Torr L}}{\text{ng}} \frac{dm}{dt}$ and the pellet rate to give the total pellet outgassing.

Initial diameter [μm]	Final mass change [ng/s]
32	−1.7
34	−1.9
36	−2.1

Table 4.2: Pellet mass change in vacuum for different pellet sizes when the equilibrium temperature is reached.

5. The reciprocal formula is valid only if the elements are separated from each other by large volumes. The error can be of the order of some tenths of percent [13]. A limited number of elements is used and the error will not grow too much. The relative error of the forward pipes in Table 4.2 is only 2% if the total transmission probability and its corresponding conductance are considered. In any case, the calculated conductance will be lower than the true one. Thus, the formula is used as a worst-case estimate of the true conductance.

4.1.5.4 Vacuum Calculations for the PTS

The vacuum calculations are performed with VAKLOOP [16], which is an one-dimensional program based on Kirchoff-like rules for non-trivial pipe-systems in the regime of molecular flow. As input parameters are the dimensions and conductances of the pipes, pumping speeds (see Sec. 4.1.5.2), and outgassing (see Sec. 4.1.5.3).

In the measured hydrogen pressure regions the PTS pumps have speeds of 25 l/s, 150 l/s, and 16 l/s, for the skimmer pump, interaction region pump, and dump pump, respectively. Thus, the throttled interaction region pump had a (horizontal) effective pumping speed of 56 l/s from Eq. (4.8), i.e. in the same order as the estimated pumping speed for $\overline{\mathsf{P}}$ANDA.

Since we at the moment lack a pellet counter in the PTS we had to estimate the pellet rate. If we just assume the pellet beam divergence to be the same than the one at the WASA target (see Sec. 4.1.4), we obtain a width of the distribution, which is in good agreement with the optical observation at the skimmer. Then, with a (droplet) transducer frequency of about 88.7 kHz, an estimated pellet survival ratio of $(50 \pm 10)\%$, a skimmer diameter of 1.05 mm, we obtain the rate of pellets to be $8.9^{+0.9}_{-1.4} \times 10^3$ /s, i.e. in the same order as at WASA. This corresponds well again with the optical observation of the concentration at both skimmers.

Other parameters of importance are the pellet size and speed. From measuring the droplet speed and knowing the nozzle diameter of 15 μm, the pellet diameter was derived to 34 μm. The driving pressure for the hydrogen gas of 400 mbar and a pressure of slightly above 20 mbar in the droplet-formation chamber made us deduce the pellet speed to be about 60 m/s. With the value from Table 4.2 the calculations are performed and their results are plotted as lines in Fig. 4.18.

It should be noted that even if the pipe system may look trivial from the drawing, it has to be treated with care. The calculated values result from processing three links; two vertical and one horizontal. The first ones are defined to be above and below the latter, respectively, and are for illustrative reasons put together in Fig. 4.18. The purpose of the horizontal link is to account for the (resistor) pipe and throttled pump. That is, to take into account that the pumping is directed perpendicular to the vertical links and not simply use the effective pumping speed 56 l/s directly. The latter should only be seen as a useful number for comparative reasons to the situation for $\overline{\mathsf{P}}$ANDA.

4.1.5.5 Vacuum Measurements at the PTS

The experimental setup was a $\overline{\mathsf{P}}$ANDA-like system, i.e. pipes with 6 mm inner diameter close to the "interaction region". In our case the upper pipe was 41 cm long and the lower was an insert of 12.5 cm length. In Fig. 4.18 results from measurements at three gauge positions are shown together with the calculated lines. The values are results from a sequence of measurements, whose mean values are plotted together with their uncertainties (1σ). The latter are derived from the specifications of the manufacturer.

To estimate the various contributions to the final uncertainty of the calculation, we take into account the three parameters with major uncertainty: the pellet size $D = (34 \pm 2)\,\mu$m, their speed $v = (60 \pm 12)$ m/s, and the number of pellets N. As the skimmer size and the frequency are precisely known, N depends on the initial divergence $w = (0.60 \pm 0.06)$ mrad and the survival ratio $r = 0.5 \pm 0.1$ only. Furthermore, the uncertainty in size will contribute to the total uncertainty via the mass change, i.e. $\sigma_{\Delta m}$ from Table 4.2. Assuming no correlation between these parameters, the relative uncertainty of the out gassing oxygen becomes

$$\begin{aligned}\frac{\sigma_O}{O} &= \sqrt{\left(\frac{\sigma_w}{w}\right)^2 + \left(\frac{\sigma_r}{r}\right)^2 + \left(\frac{\sigma_{\Delta m}}{\Delta m}\right)^2 + \left(\frac{\sigma_v}{v}\right)^2} \\ &= 32\% \,.\end{aligned} \tag{4.10}$$

which is illustrated in Fig. 4.18 by the blue band.

Considering these error estimates all measured points and the calculation coincide within 2σ. The value of 8.6×10^{-5} mbar at the interaction point lies within the band estimated. Thus we conclude that the assumptions on outgassing of pellets are not too far from reality, and the one-dimensional calculations are indeed capable also to provide dependable predictions for the vacuum.

We, nevertheless, did studies using several other geometries and realized that, if taking vertical pipes of larger inner diameter, the vacuum was getting worse at the interaction point. Partially this effect can be explained by the flow of evaporated gas from the pellets into this region. However, if doing calculations this effect is smaller than the experimentally observed phenomenon. A possible interpretation, which seems consistent with all measurements done, is that an additional flow of gas from both the dump and the skimmer area is responsible for this difference. We can, however, state that we believe to describe quantitatively within factors of 2 the

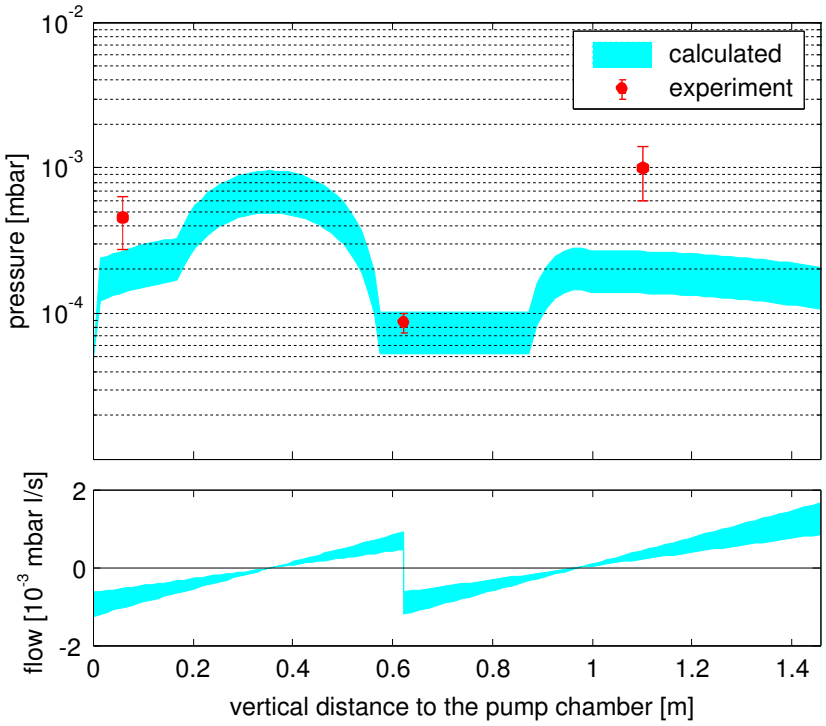

Figure 4.18: Comparison of experimental (red points) and calculated vacuum (light blue band) at the PTS. The errors indicate a 1σ uncertainty (see text). The experimental points lie factors 2 to 4 above the calculated band but agree within 2σ. The lower part shows the calculated gas flow, which is below zero if the gas flows to the left the figure and positive if the flow is to the right, i.e. upwards and downwards respectively at the experiment.

vacuum, using the calculation method and model for out-gassing presented in this section.

4.1.5.6 Vacuum Predictions

Based on the geometry proposed for the beam pipe in Sec. 4.7 but replacing the target pipe with a pipe contracting to 6 mm, which is more appropriate for a pellet target, we have predicted the vacuum distribution along the beam pipe for $\overline{\text{P}}$ANDA (see Fig. 4.21). Used is the discussed way to calculate the vacuum in Sec. 4.1.5.4. These calculations indicate that we may expect a pressure of $1.6 \cdot 10^{-5}$ mbar at the interaction point.

As discussed in Sec. 4.1.5.2, most of the pumping will be done in the backward direction of $\overline{\text{P}}$ANDA. It is, of course, important to get an estimate whether the vacuum is good enough through the whole horizontal $\overline{\text{p}}$ beam pipe. We therefore assume the backward target section to consist of a pump at -2.0 m, followed by the straight pipe and cone (as in Sec. 4.1.5.2) up to the interaction point (0 m). For the forward pipe we use the step-wise increasing diameters in Table 4.3, even though the final geometry will be much smoother. The vertical target pipes are symmetric around the interaction point and are basically consisting of three parts; a 50 cm-long pipe of inner-diameter 6 mm, followed by, in turn, a 50 cm-long 50 mm inner-diameter pipe and 90 cm-long 95 mm inner-diameter pipe. Those lengths sum up to 1.9 m, i.e. outside the iron yoke such that pumping could be placed at the very ends.

The calculated vacuum distribution is shown in Fig. 4.19. We have assumed that the four pump locations all have an effective pumping speed of 250 l/s in the direction of corresponding pipe. Furthermore, the R&D parameters of a pellet rate of 20 000 /s, a pellet diameter of 20 μm, and a pellet speed of 70 m/s are used. Note that with a pellet spread of 1.5 mm this corresponds to an effective target thickness of 2.8×10^{15} atoms/cm^2. The average distance between two successively pellets is then 3.5 mm. Thus, to have one pellet always in the beam, the needed $\overline{\text{p}}$ beam area is 1.5×3.5 mm^2. For this beam size, the corresponding background due to residual gas to signal due to pellet over the

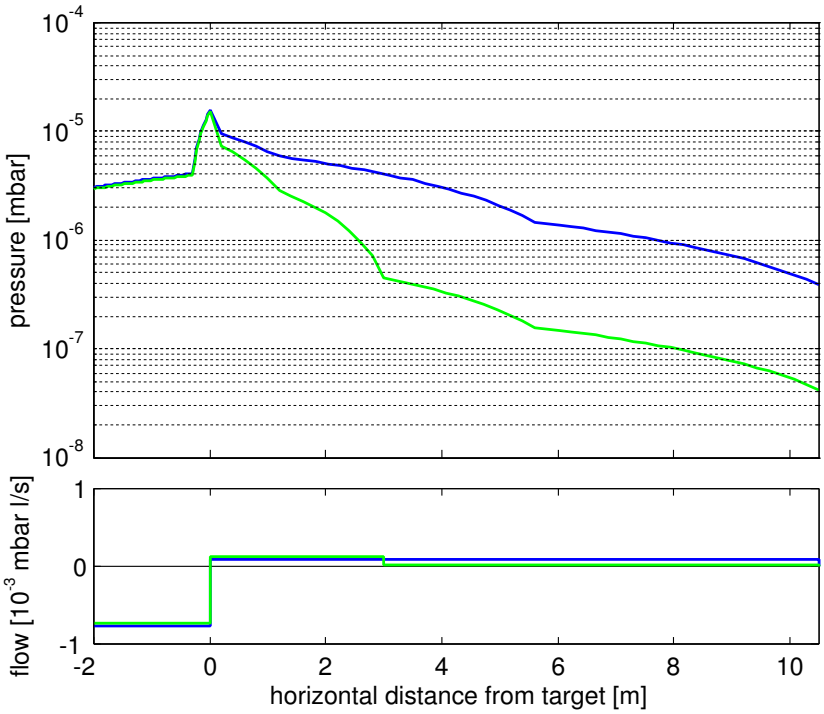

Figure 4.19: Predicted vacuum for the $\overline{\text{P}}$ANDA beam pipe. Locations of target and pumps are listed in Table 4.3. In blue are the results for pumps only before and after the experiment (i.e. 12.5 m apart from each other) and in green additional pumps have been placed between solenoid and dipole.

z coordinate [m]	pipe diameter [mm]
-2	*pump*
-2 to -0.3	150
-0.3 to 0	150 to 20
0	*target*
0 to 0.2	20
0.2 to 1.2	40
1.2 to 5.6	60
5.6 to 10.5	100
10.5	*pump*

Table 4.3: Inner pipe diameters and pump locations at the $\overline{\text{p}}$ beam pipe used for the presented vacuum calculations. The vertical target pipe opens up from 6 mm closest to the target to 95 mm inner diameter thorough the iron of the magnet (see text).

11 m of horizontal pipe between the pumps, is

$$\frac{\text{B}_{\text{gas}}}{\text{S}_{\text{pellet}}} = \frac{\int_{-2.0}^{10.5} \rho_{\text{gas}}(z)\, dz}{\frac{2}{3} D_{\text{pellet}} \rho_{\text{pellet}}} \frac{A_{\text{beam}}}{A_{\text{pellet}}} = 4.8\% \,. \quad (4.11)$$

Here, ρ, D, and A denote density, diameter, and area, respectively.

4.1.5.7 Conclusions

We have performed calculations on the outgassing of pellets and the subsequent vacuum in the beam pipes at $\overline{\text{P}}$ANDA. In order to cross check our calculations experimentally and actually measure the vacuum in such a system we have done vacuum measurements at a system simulating the conditions at the experiment. This especially holds for the pumping speed which was about 50 l/s in both cases and the thinnest pipe diameter of 6 mm. From the comparison of the measurements and calculations we find that, though we slightly underestimate the measurements, we nevertheless can reproduce the values within error bars. Thus we expect these calculations also to provide reasonable predictions for the experiment in HESR.

These calculations show a maximum value of 1.6×10^{-5} mbar at the interaction point, irrespectively of having additional pumping between the solenoid and the dipole (see Figs. 4.19 and 4.21). This would imply background to signal ratio with the beam covering the whole pellet area (full width at half maximum $1.5 \times 3.5\,\text{mm}^2$) of 4.8% and 2.5% without and with intermediate pumping respectively. Thus, in these calculations, the integral is dominated by the

gas close to the interaction point, which can basically not be pumped at all from the beam downstream side. Please keep in mind, that those calculations only consider equilibrium pressures and no outgassing from the walls is included.

Due to the agreement of the calculated and measured values for the PTS, we believe that at $\overline{\text{P}}$ANDA the vacuum for the proposed geometry will stay well below 10^{-4} mbar even at the interaction point.

4.1.6 Pellet-Beam Interactions at HESR

A crucial question for the operation of HESR is the effect of target heating which will, in combination with the stochastic and electron cooling, define the equilibrium beam conditions. This equilibrium is strongly depending on the mechanisms of cooling and is therefore still under study and is discussed the Technical Report for the HESR [17]. For the envisaged luminosity at $\overline{\text{P}}$ANDA the average target thickness is, however, defined to be a few times 10^{15} atoms/cm^2. The question weather the density distribution of the target may also affect the heating has been discussed since the first proposal of a pellet target [11, 6]. This is because in contrast to e.g. a cluster-jet target the target density is not homogeneous, but concentrated in pellets of few tens of micrometer diameter. The local thickness reaches values of a few times 10^{19}atoms/cm^2. Though, as already mentioned, this effect has been investigated for other accelerator and found to be small there [3, 4], we have made dedicated Monte-Carlo simulations for the situation at the HESR which are presented in the following.

The simulations were done using a beam energy of $T_{\overline{\text{p}}} = 800\,\text{MeV}$ and $T_{\overline{\text{p}}} = 14.5\,\text{GeV}$, the lowest and highest energies respectively at which the HESR should operate. The parameters used are tabulated in Table 4.4. They were extracted from the latest MAD files and information from the accelerator group in Uppsala and Jülich [18, 19]. There was no cooling of any kind and no RF included as this is much more model dependent and the exact parameters are not yet fixed. Nevertheless, to first order this would affect both the heating from the homogeneous and inhomogeneous target distributions equally. Thus the results are not meant to reflect the final beam parameters at HESR, but merely illustrate weather differences may be expected between a discrete (pellet-like) and homogeneous target density distribution.

For the target two different scenarios were used.

beam parameters	
$\overline{\text{p}}$ energy	800MeV and 14.5GeV
ϵ_{norm} (v and h)	$\sigma = 2\pi$ mm mrad
$\Delta p/p_{\text{norm}}$	$\sigma = 2 \cdot 10^{-4}$
machine lattice parameters at the target	
$\beta_x = 1.351\,\text{m}$, $\beta_y = 1.592\,\text{m}$	
$\alpha_x = \alpha_y = 0°$, $D_x = D_y = 0\,\text{m}$	

Table 4.4: Initial parameters used for the simulation. The normalised emittance ϵ_{norm}, the normalised momentum spread $\Delta p/p_{\text{norm}}$ and the lattice parameters at the $\overline{\text{P}}$ANDA target position were obtained in close collaboration with the accelerator groups from CELSIUS and COSY, which are working on the HESR design [18, 19].

On one hand a pellet target with pellets of $20\,\mu$m diameter and a divergence, such that a spread of ± 0.75 mm is obtained at the target and the distance of one pellet to the next one to be 3.5 mm. These are values which are believed to be reasonable and achievable with only slight improvements on the current target at WASA. These values would yield an effective target thickness of $2.8 \cdot 10^{15}$ atoms/cm^2 which would, in turn, lead to a luminosity of $1.4 \cdot 10^{32}$/cm^{2}s. This is very close to the design value of $2 \cdot 10^{32}$/cm^{2}s. For comparison a continuous distribution of the same effective thickness was simulated. The results of the Monte-Carlo runs are shown in Fig. 4.20.

It is observed that the growth in emittance is not deviating significantly for both cases. This supports the earlier findings of studies for CELSIUS and COSY [4, 3] that the effect of the strongly inhomogeneous distribution of a pellet target can, what concerns the beam properties, not be distinguished from a homogeneous distribution of the same effective thickness.

4.1.7 Implementation

The geometrical requirements at $\overline{\text{P}}$ANDA (see Sec. 4.1.1) are very similar to those found at WASA [1, 2].

- The outer dimensions are, with 1.63 m and 1.85 m for WASA and $\overline{\text{P}}$ANDA respectively, very similar.

- The target pipe close to the interaction point is 5 mm in diameter at WASA, whereas 6 mm is proposed for $\overline{\text{P}}$ANDA.

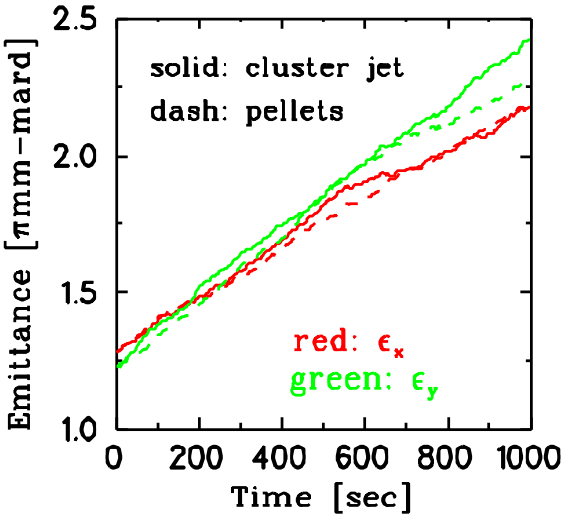

(a) 800 MeV beam energy

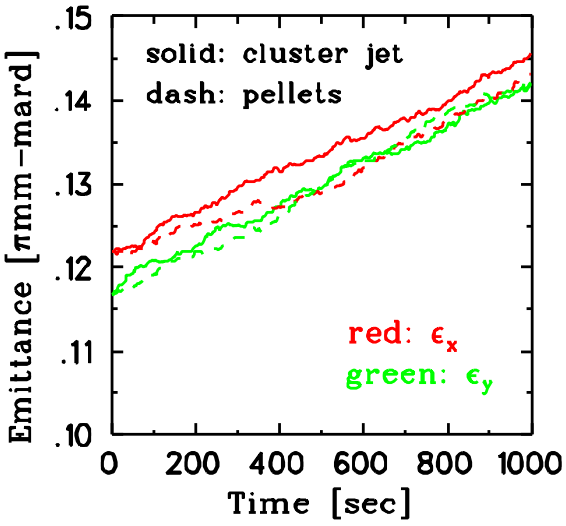

(b) 14.5 GeV beam energy

Figure 4.20: Development of the emittance with time for a homogeneous target distribution (solid lines) and discrete, i.e. pellet-like distribution (dashed lines). Plotted in red and green are the horizontal and vertical emittancies ϵ_x and ϵ_y respectively.

- The target is operating reliably in a solenoid field and with protons stored in the CELSIUS ring. The difference to $\overline{\text{P}}$ANDA is merely the higher energy and anti-protons of HESR.
- Also at WASA the pumping speed close to the interaction zone is quite restricted.

Thus the implementation of the pellet target into the $\overline{\text{P}}$ANDA detector is proposed to be very similar to the one at WASA. Several improvements discussed in Sec. 4.1.3 and 4.1.8 will, of course, be taken into account. These, however, will not affect the design of the detectors and magnets. Thus they will with one exception not be discussed here. The latter topic is the a replacement of the the cold-head by a connection to the cryogenic system of the super-conducting solenoid. This is necessary as to reduce vibrations to an absolute minimum in order to guarantee a stable and low divergence pellet train. This fact has to be foreseen in the planning of the cryogenic system, its positioning, and flow lines.

The system at WASA is mounted vertically as well as the PTS. There is, however, no reason forbidding a horizontal mounting, as the speed of the pellets is too high to be significantly affected by gravity. The only minor change needed in such a case would be the design of modified mounting frames. Thus a decision on the direction of the target may still be taken at a rather late stage of the planning.

The most crucial interplay of the target with the $\overline{\text{P}}$ANDA design becomes the vacuum system. The proposed design (see also Table 4.3) is shown in Fig. 4.21 together the pressure profile obtained from the previously discussed vacuum calculations.

It is recommended to foresee 2 m space above the iron yoke of the magnet for the installation of a pellet target and easy access in case of a vertical mounting. A similar amount of space would be required to one side, if a horizontal mounting is preferred. Currently the system at WASA is exceeding the detector by 1.5 m in height. For the beam dump about 1 m would be sufficient. Easy access is not essential here, but would, of course, be of advantage. In this respect a horizontal system could be preferable.

4.1.8 Timeline

In Fig. 4.22 the timelines for the development of a pellet target for $\overline{\text{P}}$ANDA are listed. The following milestones have already been achieved by now:

- A vacuum system which is pumping-wise comparable with $\overline{\text{P}}$ANDA has been designed, built and is operational for further studies.
- The set-up was completed and prepared for operation.
- Diagnostic elements for the monitoring of the pellet train position and intensity have been set up.
- The pellet production has been started and can now be resumed on short notice.

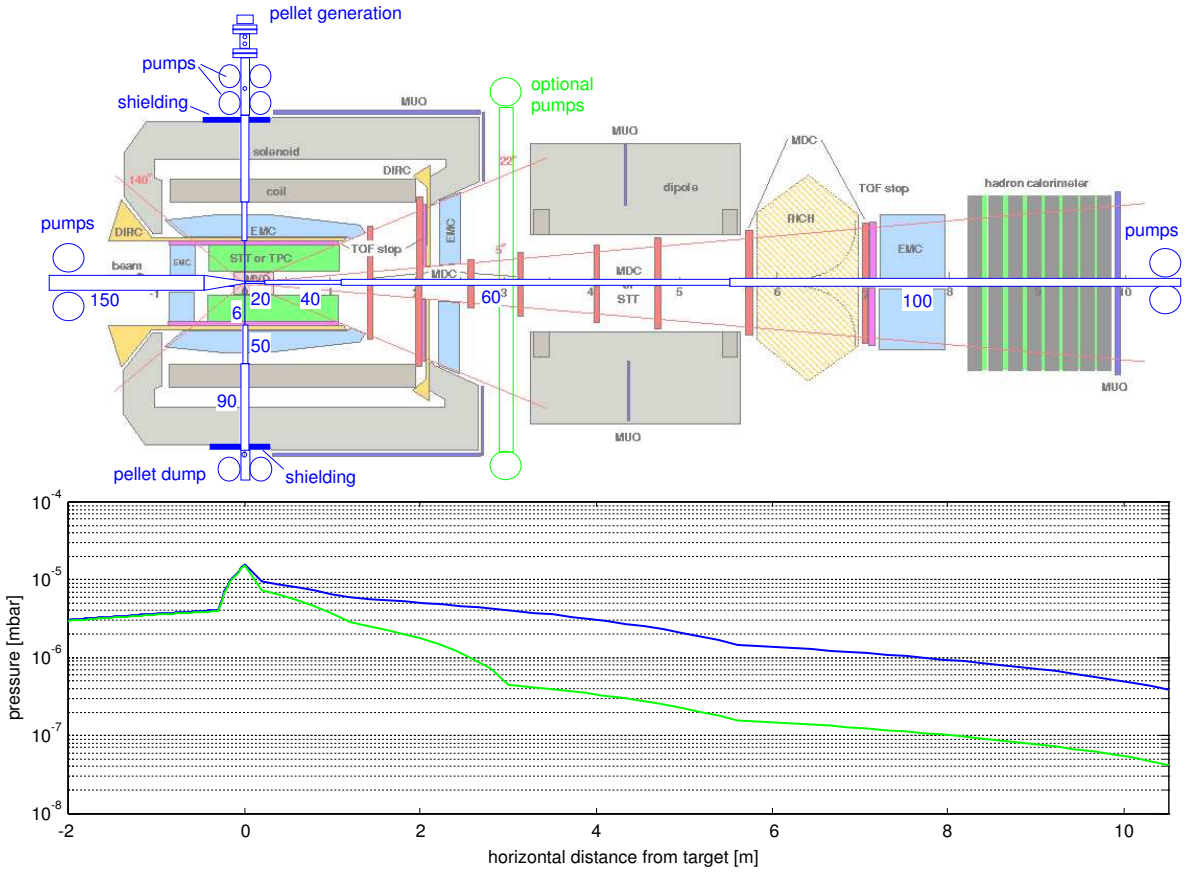

Figure 4.21: Implementation of the pellet target into the $\overline{\text{P}}$ANDA vacuum system.

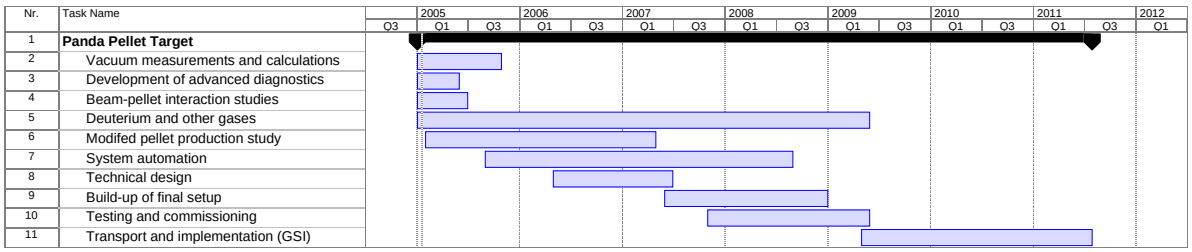

Figure 4.22: Timelines for the development of the pellet target. (See text for details on the topics).

The topics listed below are currently studied but yet not complete:

- First measurements of the vacuum under $\overline{\text{P}}$ANDA-like pumping conditions have been done (see Sec. 4.1.5). However, further studies will be performed during 2005 to reduce systematic uncertainties.
- The development of a newly designed pellet monitoring system, which would provide pellet rates simultaneously to sizes and positions of individual pellets, has just been started. By the middle of 2005 this system should be completed and operational.
- First studies of beam-heating effects due to interaction with pellets show that heating effects are comparable with homogeneous distributions, but the studies have to be continued as the equilibrium emittances with a cooled beam are crucial for the design of both the cooler as the whole HESR.

A number of items still to be addressed remain:

- The feasibility of running with deuterium with even improved parameters compared to hydrogen has already be proven at the WASA set-up. The comparison will, however, also be done at the PTS, where the parameters can be studied easily. Other materials may also be tested, if there is any interest for upcoming experiments.
- A challenging and most important topic for the development is the reduction of the transversal spread of pellets and their distance to each other. This is in direct connection to a reduction in size. Thus extensive studies, which include modification of the pellet production schemes will be performed. As these include a redesign of parts of the system, the studies are not expected to be completed before 2007.
- In parallel the automating of many standard operations should be brought forward. This is required for a long-time operation at $\overline{\text{P}}$ANDA, and may continue till 2008.
- A final technical design for the target at $\overline{\text{P}}$ANDA has to be done and a write-up for the design report is to be written till the beginning of 2007.
- This setup will then be build up, tested and commissioned during the years 2007 and 2008.
- In 2009 the system would then be ready for transportation to Darmstadt, where the implementation into the $\overline{\text{P}}$ANDA detector can be performed.

4.2 Cluster-Jet Target

4.2.1 Overview

An internal gas target for the high-luminosity storage ring experiment $\overline{\text{P}}$ANDA with a 4π-detector geometry has to meet several requirements. Sufficiently high areal densities at the interaction point must be provided. The use of an antiproton beam mandates the gas load on the ring vacuum to be small in order to minimize reactions of the beam with the residual gas. Furthermore, the effective target density has to be stable in time to avoid high instantaneous event rates and to minimize degrading of the stored particle beam. This can be achieved by positioning the target at a minibeta focus of the stored antiproton beam. In addition, the possibility to adjust the target density during the operation is desirable for optimization. One approach is the use of a cluster-jet target.

4.2.2 Test Station

A test station for the cluster-jet target has been set up at the University of Münster in order to perform a realistic study. A basic part of this device in $\overline{\text{P}}$ANDA geometry is the cluster beam source which is shown in Fig. 4.23. The cluster-jet beam is produced in a Laval-nozzle which is mounted on top of a two-stage refrigerator cold head. The corresponding refrigerator system consists of a closed helium circuit driven by a compressor unit allowing for temperatures below 10 K.

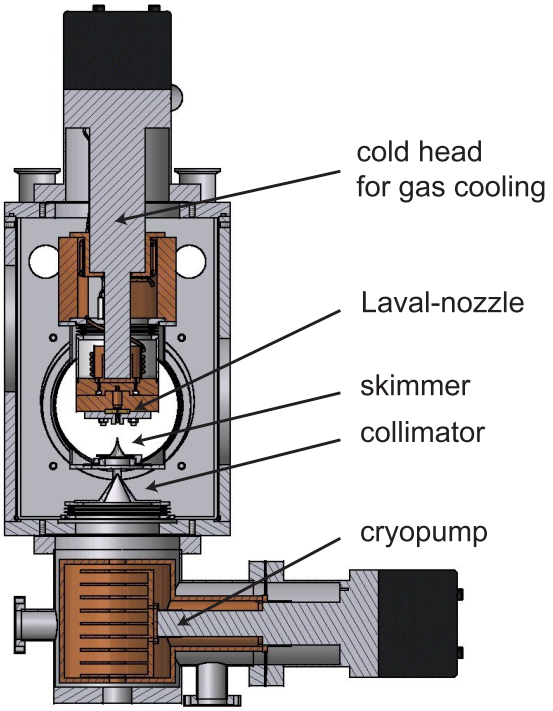

Figure 4.23: A cross section drawing of the cluster-jet source currently in operation at the University of Münster. The cluster-jet beam, produced in the Laval-nozzle (center of the figure), travels through two conical apertures for shape and size preparation and passes a specifically designed cryopump. The external vacuum pumps are not shown.

In the first vacuum stage (skimmer stage) the cluster-jet beam, surrounded by a conventional gas beam, passes through a special shaped aperture (skimmer) for a first preparation of the target beam. After the aperture, the beam enters the second differential pumping stage (collimator stage) which in

turn is separated from the third pumping stage by conical aperture (collimator). This device defines both the final shape and the size of the cluster-jet beam in the following pumping stages. Here, the cluster-jet propagates according to intercept theorems. The last vacuum stage, as shown in Fig. 4.23, is a specially designed cryopump of the Münster type which has been successfully operated in the Münster cluster-jet targets ANKE and COSY-11 at COSY-FZJ).

A photograph of the complete test cluster-jet test station at Münster is shown in Fig. 4.24. The cluster-jet beam travels from the cluster source (right hand side) through a scattering chamber (center of the figure) into the cluster beam dump (left hand side). The three components are connected by long thin vacuum pipes representing a likely situation at the future PANDA setup. The scattering chamber is located at the future antiproton-target interaction point. It contains several devices for monitoring the size, shape, and absolute density of the passing cluster-jet beam as a function of different operational conditions.

4.2.3 Status and Current Results

After setting the test station into operation, first measurements of the planned systematic investigations on the production of high-intensity cluster-jet beams have successfully been performed. A well prepared cluster beam can travel over several meters through a high vacuum system with an angular spread adjustable by the choice of collimators. In Fig. 4.25 corresponding target beam scans in two dimensions perpendicular to the spread direction of the target beam are shown which have been recorded using a computer controlled monitor system. The distributions directly correspond to the areal target density and confirm the homogeneous volume density distribution at the later PANDA interaction point. The absolute size and shape of the target beam in the interaction region can be adjusted by an appropriate choice of apertures in the cluster beam source. Here, a circularly shaped aperture was chosen in order to obtain a cylindrical target beam in the scattering chamber. An important requirement for the latter target for PANDA will be the possibility for a continuous adjustment of the target density in order to adjust the trigger rate or the luminosity. This can easily be done at a cluster-jet target and is routinely used at the COSY-experiments ANKE and COSY-11. In Fig. 4.26 the areal density in the scattering chamber is presented as a function of the nozzle temperature. Obviously, the areal density can be changed continuously over orders of magnitude. This feature is accessible by an electric nozzle heating system. For long term stability, a dedicated temperature control system will be used. This has also been demonstrated over the entire running time of the E835 Experiment at FNAL. Based on the first experience with the test target setup in PANDA geometry at Münster, several improvements have been made at both the gas cooling system and the vacuum system. Furthermore, a new hydrogen palladium gas purifier system is now available allowing for higher gas input pressures at the Laval-nozzle and higher gas flow rates. The improved setup has been put into operation and target densities of $\rho \sim 10^{14}\,\mathrm{atoms/cm^3}$ have been reached in combination with the PANDA geometry. Currently, detailed studies on high-intensity cluster-jet beams are under evaluation. Both the nozzle temperature and the gas input pressure are important parameters for the cluster yield and the cluster beam density ρ at the interaction point. Detailed studies on the functional dependence $\rho(p, T)$ for different nozzle diameters are currently under investigation at Münster. As a recent result, Fig. 4.27 presents the relative volume density of the hydrogen cluster-jet beam in color code. As can be seen from Fig. 4.26, the cluster-beam density at the interaction point can be adjusted over orders of magnitudes by changing the nozzle temperature. Similarly, the target density depends on the gas input pressure at the nozzle. At high temperatures and low gas input pressures only low cluster yields are expected (Fig. 4.27) while the density can be increased drastically by decreasing the nozzle temperature and increasing the pressure. The black line corresponds to the vapor pressure curve for hydrogen which ends at $\sim 33\,\mathrm{K}$. A remarkable result of the studies is that the target can be operated in state below the vapor pressure curve where the gas is expected to be liquid before entering the nozzle. In this region, the gas is in a supersaturated gaseous state which favors the cluster formation inside of the nozzle. Therefore, a focus will be the systematic investigation of this effect in order to achieve highest densities and luminosity.

4.2.4 Integration

According to the current results from the Münster test target facility, it will be possible to shoot a cluster-jet beam through the complete PANDA detection system. Therefore, the main components could be installed outside the 4π-detector except for the vacuum beam pipes. A possible realization of the situation is presented in Fig. 4.28. The clus-

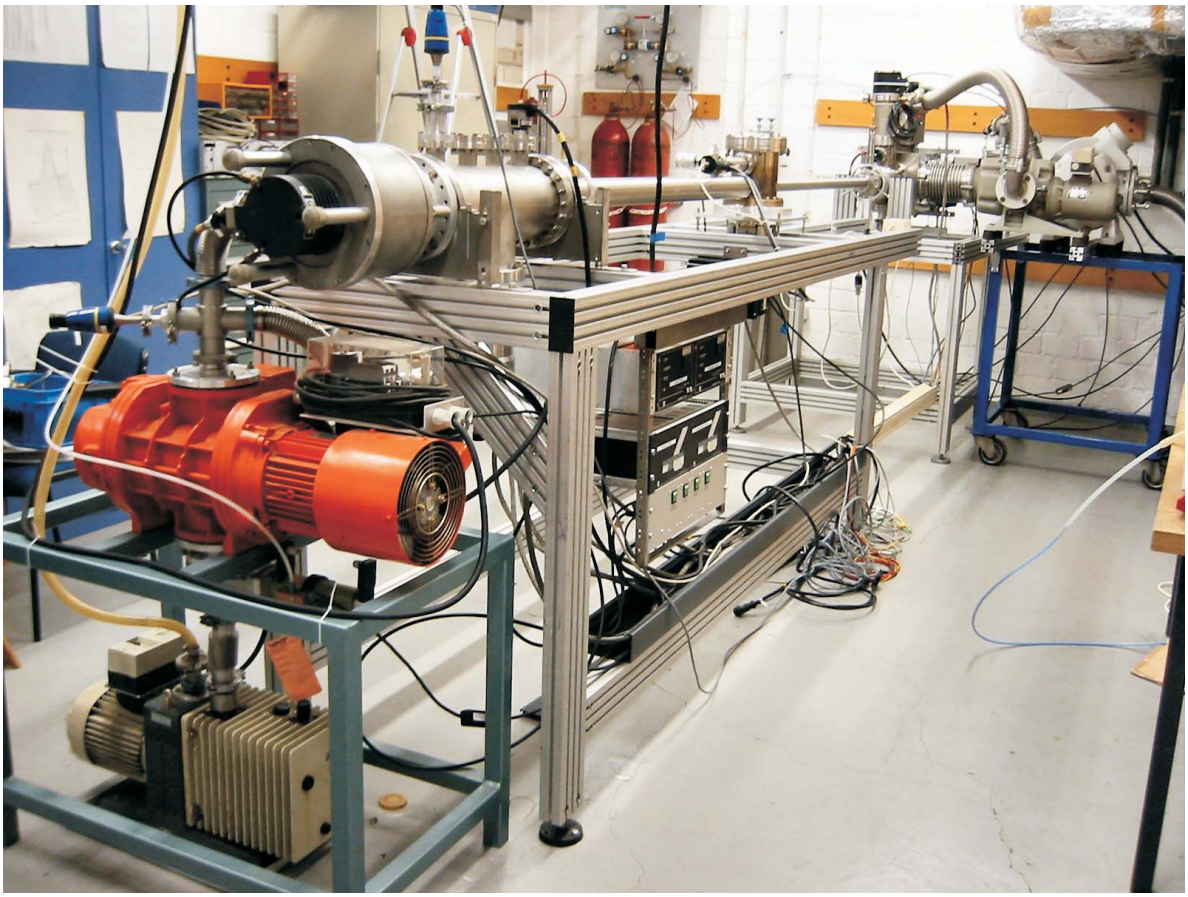

Figure 4.24: Photograph of the cluster-jet test station at the University of Münster. For practical reasons, a horizontal cluster-beam axis is chosen. The cluster source (right hand side) and the cluster beam dump (left hand side) are connected by thin vacuum pipes, reflecting the geometric conditions expected at $\overline{\text{P}}$ANDA.

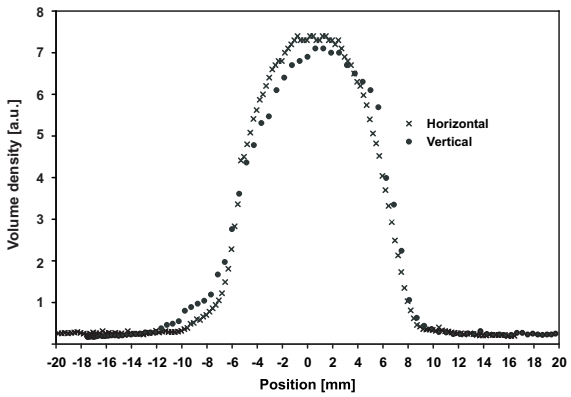

Figure 4.25: Horizontal and vertical density profiles of a cluster-jet recorded with a monitor system located at the virtual $\overline{\text{P}}$ANDA interaction zone. The distributions directly correspond to the areal target density and are in agreement with a homogeneous volume density distribution.

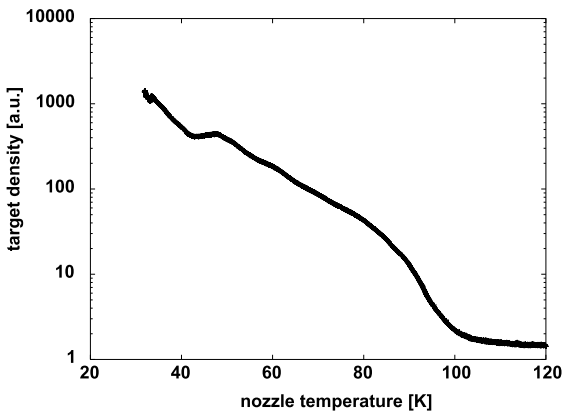

Figure 4.26: Areal density of the cluster-jet beam at the interaction point in the scattering chamber as function of the nozzle temperature. As can be seen, the absolute target density and the luminosity can easily be adjusted over several orders of magnitude.

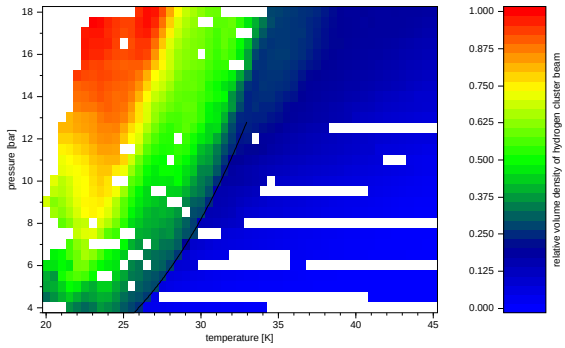

Figure 4.27: Cluster beam density at the interaction zone in arbitrary units as function of the nozzle temperature and the input pressure. The measurement has been obtained using a nozzle with a minimum diameter of 16 μm.

ter beam source and the cluster beam dump will be located outside of the magnet yoke apart from two large cryogenic pumps at the top and the bottom openings of the yoke, respectively. Pumping devices, like forepumps and roots pumps, are not shown in the figure. The vacuum components will be connected to the cluster beam source and cluster beam dump by bellows and will be situated next to the detector. An influence of these components on the detection system can be neglected with sufficient decoupling. In the inner region of the 4π-detector only the vacuum pipes for the target beam will be installed. The pipes have to include special pumping devices (see Sec. 4.7) in order to guarantee the required vacuum conditions in the scattering chamber. Further measurements at the cluster test stations might result in the necessity of additional pumping capacities which have to be mounted in the region near the interaction zone. In Fig. 4.29, the planned vacuum system inside the detection system is presented. The selected diameters meet the requirements for both the cluster-jet solution as well as the use of a pellet target system.

4.2.4.1 Cluster beam source

The main design of the future cluster beam source will be similar to the one of the source at the test cluster-jet target in Münster (for details see Fig. 4.23 and [20, 21]). According to the current results a Laval-type nozzle with an inner diameter of 10–25 μm will be used. Sufficiently high cooling power is required in order to reach high densities. This can be achieved either by liquid helium cooling or by the use of a closed helium refrigerator circuit. Following the very convincing experience over the last years using refrigerator systems with high power cold heads the latter solution will be chosen. The first three differential vacuum stages (skimmer stage, collimator stage, and first cryopump) will be connected by skimmers and collimators defining the shape and size of the cluster-jet beam in the subsequent target stages. Shaped collimators with very thin walls will be used to warrant minimum losses of cluster density at these apertures activated, e.g. by shock waves. Between the apertures, a miniature shutter will be installed allowing to switch the cluster-jet beam in the interaction zone on or off within fractions of a second. Similar devices are successfully in operation at the three running Münster cluster-jet targets.

4.2.4.2 Cryopumps

At the University of Münster, cryopumps of a special design for cluster-jet targets has been developed and are successfully in operation at the two COSY experiments ANKE and COSY-11 as well as at the test target device. The main feature of the pumps is the use of arrays of activated, charcoal-covered cold sheets with a central opening. Maximum pumping speed is reached for removing a surrounding gas load by shooting the cluster-jet beam directly through the cold sheets. The large space available for the cryopumps at both openings of the magnet yoke allows for an array of many large cold sheets. This corresponds to large pumping capacities which in turn allow long regeneration intervals. With an average areal pumping speed for hydrogen [22] of

$$s_{charcoal} = 20 \frac{l/s}{cm^2} \tag{4.12}$$

and mean areal pumping capacities of [22]

$$c_{charcoal} = 0.008 \frac{bar \cdot l_n}{cm^2} \tag{4.13}$$

a total pumping speed of $S = 720000\,\text{l/s}$ and a total capacity of $C = 288\,\text{bar}\cdot\text{l}_n$ are expected for each of the two cryopumps at the magnet yoke. Therefore, the use of the cryopumps allows for high pumping speed which is absolutely necessary. A regeneration interval of 7 weeks results assuming a vacuum pressure of $p = 10^{-7}\,\text{mbar}$ during operation in the cryopumps with the estimated pumping capacity. It should be noted that the data are based on references to literature [22]. Due to the closer packing of activated charcoal on the cold sheets in the case of the cryopumps, total capacities and, thus, regeneration intervals have been measured to be higher by a factor of three.

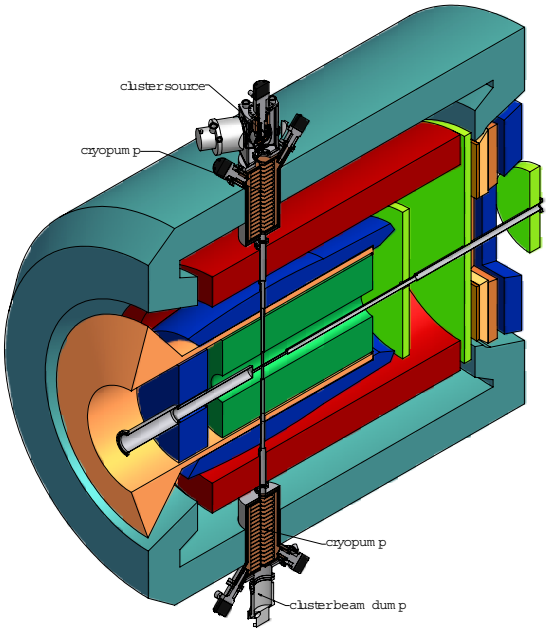

Figure 4.28: Schematic view of a possible integration of a cluster-jet target in the $\overline{\mathsf{P}}$ANDA experiment facility. Specifically designed cryopumps will be integrated in both the cluster source stage (top) and the cluster beam dump stage (bottom) in order to obtain maximum pumping speed and capacity in combination with minimum required space.

4.2.4.3 Cluster Beam Dump

The first stage of the cluster beam dump will again make use of a specifically designed cryopump (see Fig. 4.28) similar to the one of the cluster source. In contrast, the fourth (final) stage of the beam dump will consist of an asymmetric mounted turbo pump which directly pumps on the main flow of the unused cluster-jet beam. The remaining part of the cluster-jet beam which converts at this stage into a diffuse gas load has to be removed as efficiently as possible in order to minimize a contribution to the vacuum condition in the interaction zone. For this reason, the complete cluster beam dump will be divided into four differentially pumped vacuum stages separated by apertures of appropriate diameter. The remaining two vacuum stages, the second and third stage, will also be realized as cryopumps for the reasons mentioned above.

4.2.4.4 Gas Supply System

A schematic drawing of the gas supply system for the cluster-jet target at $\overline{\mathsf{P}}$ANDA is presented in Fig. 4.28. The target device has to be operated with hydrogen gas with as high a purity as possible to avoid blocking of the cryogenic nozzle by impurities like oxygen or nitrogen when operated at temperatures below $30\,K$. For this purpose, hydrogen of standard purity (e.g. 99.999%) will be fed to the gas supply system. The gas is cleaned by a palladium membrane purifier to optimize the purity (i.e. no impurities detectable). For technical reasons, this device has to be operated with nitrogen in parallel. However, nitrogen cannot pass the palladium membrane. For security reasons, both the nitrogen and hydrogen gas bottles have to be placed in a special gas cabinet. The size of this gas cabinet should be sufficiently large to contain at least four hydrogen bottles (50 l, 200 bar) and one nitrogen bottle in parallel. After the purification stage the gas will be led through a gas flow monitor and control system and enters the cluster source unit. At this stage, a micrometer filter is included into the gas feeding system to efficiently remove micro-particles. Finally, the gas passes the cooling stages of the cryogenic cold head and enters the nozzle. A Baratron capacitance manometer is connected to the gas system parallel to the nozzle in order to monitor the gas pressure directly before passing the nozzle. If longer periods with deuterium cluster beams are planned, the gas supply system can be enlarged by a deuterium recuperation system as it is used with the targets at COSY. This system collects the deuterium gas exhausted by the vacuum pumps at the cluster-jet source and supplies it to an

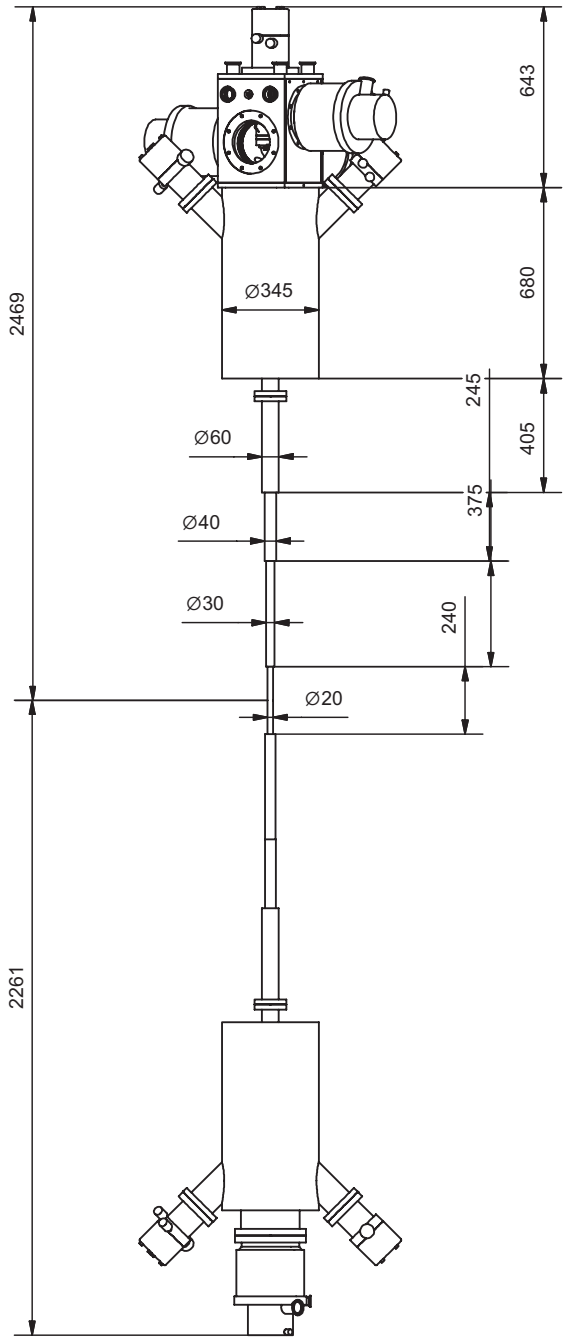

Figure 4.29: A technical drawing of a vacuum system inside the future $\overline{\text{P}}$ANDA detector. The dimensions of the vacuum pipes meet the requirements for a cluster-jet target and as well as a pellet-target solution.

oil-free compressor which finally provides the deuterium gas with a pressure of 20 bar. For a further reduction of the operational cost, a deuterium generator can be used which generates deuterium gas from liquid D_2O with a sufficient quality to feed the palladium purifier of the target installation. Such a system is currently being tested at the experiment ANKE at COSY.

4.2.4.5 Slow Control System

Among the advantages of a cluster-jet target are the comparatively moderate requirements concerning the slow control system. The target parameters do not have to be changed over long periods of time once a stable target beam is produced. Therefore, the major part of the slow control system typically merely concerns the monitoring of the operational parameters. In Fig. 4.31 a schematic of the slow control system is presented. Directly at the experimental setup as well outside of the anti-proton ring two switch boards will be placed allowing to operate devices like vacuum pumps, valves, refrigerators and vacuum meters. Status LEDs will allow for a quick monitoring of the status. In parallel, all of the devices will be controllable by a computer aided system via I/O cards, ADCs and DACs. The platform of this computer control system can either be a commercial system or a LINUX based computer system with a DAQ card as it is used at the COSY targets. Once a regeneration procedure for the cryopumps is needed, the required operational steps can be performed automatically.

4.2.4.6 Electrical Equipment

In Table 4.5, an estimate of the power consumption for pumps and compressors is provided. Due to the large gas flows expected for both the cluster beam source and the final beam dump stage, vacuum pumps with sufficient pumping capacities are required which in turn results in larger electrical power consumption (∼70 kW, 400 V). Furthermore, the cryogenic components will need ∼25 kW (400 V) for the gas cooling and cryogenic pumping devices. In comparison, the required electrical power for the residual target components including slow control is of minor relevance. In total, for the cluster target installation an electrical power of minimum 100 kW (400 V) will be needed.

The exhaust heat from the electrical power consumption has to be handled. However, while the turbo molecular pumps as well as the forepumps and cryogenic compressors must be cooled with water, the applied rotary pumps will be operated using air cooling. Therefore, the power of the water cooling system for the cluster-jet target installation should be in the order of 75 kW. The water pressure has to be in the range of 2–8 bar and in a temperature range of 5–25 °C.

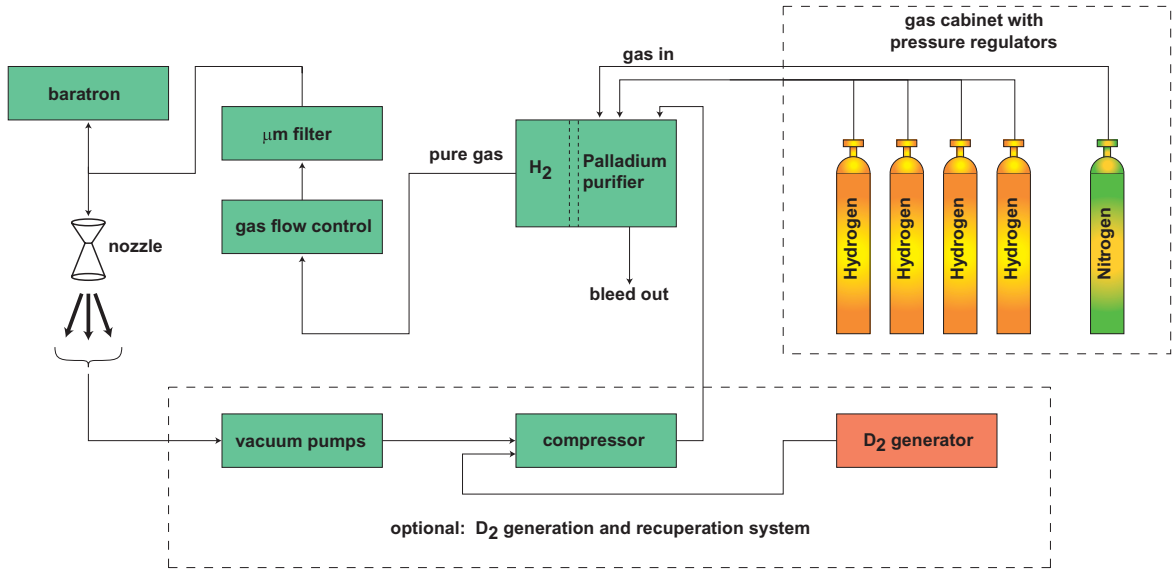

Figure 4.30: Schematic drawing of the gas supply system for the cluster-jet target.

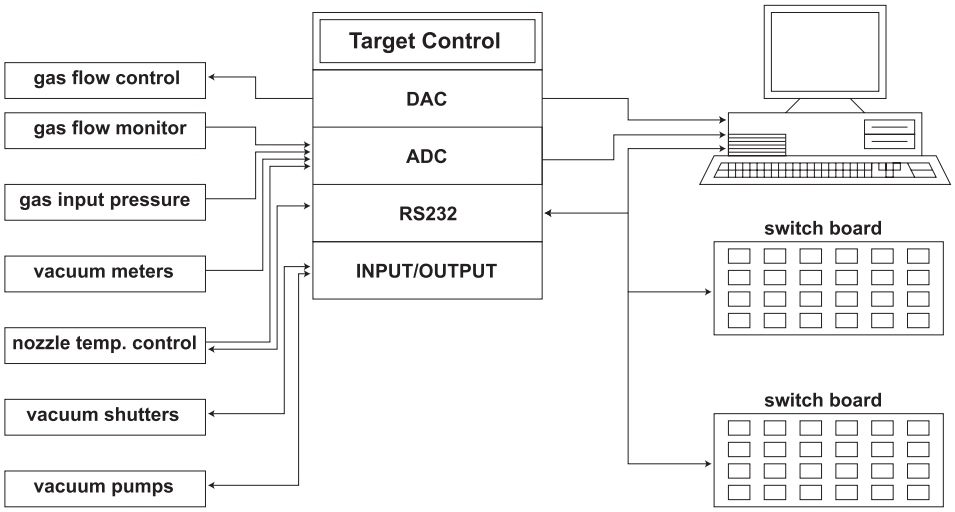

Figure 4.31: Schematic drawing of the slow control system for a future cluster-jet target.

quantity	item	power consumption [kW]	total [kW]
4	Turbo molecular pump	0.4	1.6
2	Roots- and Forepump combination 2 000 m^3/h	22.5	45
1	Roots- and Forepump combination 3 800 m^3/h	23.5	23.5
3	Compressor unit for cryopump	5.3	15.9
1	Compressor unit for gas cooling	8	8
total amount of electrical power consumption			94

Table 4.5: Estimated amount of electrical power consumed by the cluster target.

4.2.4.7 Vacuum System

The vacuum system has to fulfill several requirements. First of all, the vacuum system has to warrant the optimal operation of all vacuum stages of the structural components. Secondly, the gas flow originating from the target installation to the vacuum stages of the accelerator beam line must not exceed a certain limit. This limit itself depends on the pumping speed at the target and at the beam line close to the interaction region, the conductance of vacuum pipes connecting these pumps with the vacuum system as well as on the target thickness itself. Furthermore, regeneration intervals as well as sensitivity to magnetic fields have to be taken into account.

In Fig. 4.32, a realization of the cluster-jet target for the $\overline{\text{P}}$ANDA experiment is presented. The highest gas load ($\sim 4\,\text{l}_n/\text{min}$) pressure is present in the skimmer stage of the cluster source where the nozzle is located and the cluster-jet beam is produced. In this stage, a roots vacuum pump in combination with a sliding vane vacuum pump is necessary in order to guarantee pressures in the order of 10^{-1} mbar. The nozzle itself is mounted on top of a cryogenic cold head. To avoid losses with respect to cooling power, the main part of the surface of this cold head is located in a separate vacuum stage which in turn is pumped by both a turbo-molecular pump and a sliding vane vacuum pump. The cluster-jet beam passes the skimmer stage and enters the next vacuum stage which is connected by a conical aperture with a diameter of $700\,\mu$m. This collimator stage is pumped by two turbo-molecular pumps which are pumped on by a system of a roots and a sliding vane vacuum pump. Finally, the cluster-jet passes the last vacuum stage of the cluster source which is separated from the previous chamber by a conical aperture ($700\,\mu$m). An approved method to evacuate this stage is to use a special designed cryopump (Fig. 4.23). This pump combines pump and vacuum stage in one unit and allows for maximum pumping capacities for the reduction of residual gas (see section Sec. 4.2.4.2).

Important for a minimized flow of residual gas to the interaction point is an optimized design of the cluster beam dump. Due to the presence of high vacuum conditions in these vacuum stages again the use of special designed cryopumps is highly advantageous. An exception here is the last vacuum stage where a turbomolecular pump will be used in order to remove completely a large fraction of the arriving cluster-jet beam. Similar to the situation at the cluster beam source this pump is evacuated by a combination of a roots and a sliding vane vacuum pump. To minimize a gas flow back to the interaction region the differential pumping stages are separated by apertures of appropriate diameters.

Due to the small diameters of the apertures in the cluster source the cryopump will be connected to the collimator stage by a vacuum pipe and a valve for regeneration. This type of connection can be omitted at the larger apertures in the cluster beam dump.

4.2.5 Timeline

In Fig. 4.33 the timeline for the upcoming steps is displayed. At the different target test stations, performance studies are currently in progress and are scheduled to be continued until end of 2008. The experimental phase overlaps intentionally with the construction of the final target installation in order to obtain as much information as possible for an optimized operation. It is planned to finalize studies on the enhancement of pumping capacities until the end of 2007. Studies on the cluster beam diagnostics will start in 2005 and are scheduled up to fall 2007. The Laval-nozzle employed will be essential for the quality of the cluster-jet beam. Here, detailed studies on the development of new nozzles with different shapes and diameters are desirable. Therefore, corresponding studies have already been initiated and are planned to continue up to summer 2008. The technical design report will be prepared starting 2007 until begin of 2008 and will be followed by the construction of the target components. Before the end of 2009, the construction phase is scheduled to be finished. Finally, the installation and the commissioning of the complete target device are planned to start end of 2009 and in summer 2010, respectively.

4.3 Polarized ^{3}He Target

The operation of a polarized hydrogen or deuterium target in the $\overline{\text{P}}$ANDA solenoid is not feasible as both ^{1}H and ^{2}H are highly sensitive to depolarizing resonances in the strong magnetic solenoidal field. In addition, the production of polarized ^{1}H and ^{2}H requires an atomic beam source which has to be located close to the target region. This cannot be accommodated considering the hermetic setup of the $\overline{\text{P}}$ANDA detector.

The situation for a polarized ^{3}He target is easier as ^{3}He is insensitive to depolarization by external magnetic fields and by wall collisions due to the spin-0 configuration of its atomic shell. For this reason, it

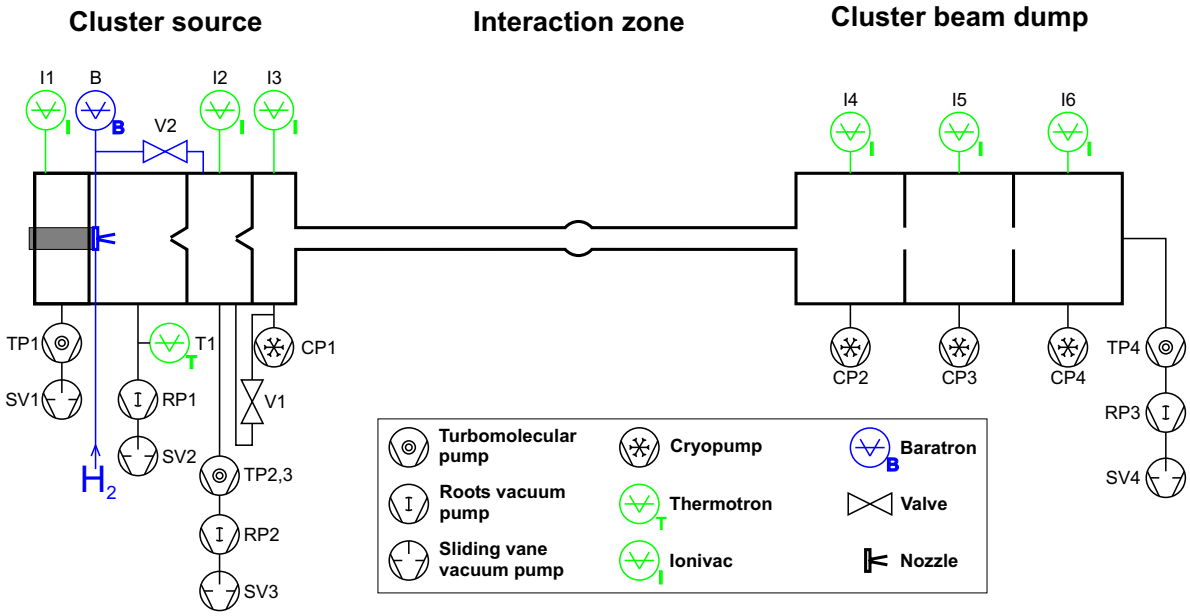

Figure 4.32: Schematic drawing of the vacuum system for the cluster-jet target.

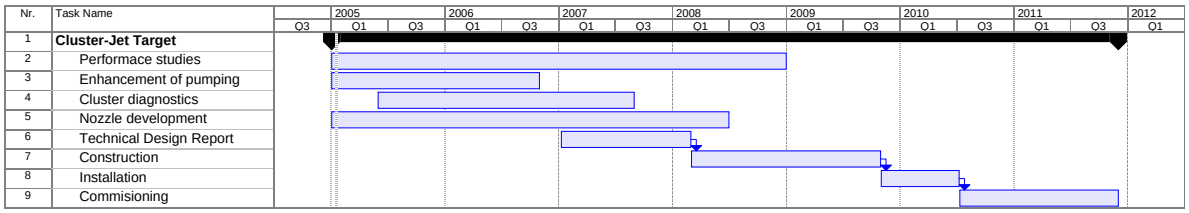

Figure 4.33: Timeline for the Cluster Target.

is possible to polarize ^{3}He gas outside of the interaction region and transport it over a long distance to a storage cell inside the solenoidal magnet. The ^{3}He gas serves as a neutron target where the orientation of the spins of the neutrons will be parallel or anti-parallel to the magnetic field at the target area. A similar technique has been applied e.g. at the Hermes experiment in 1995 [23]. The polarization direction at $\overline{\text{P}}$ANDA would naturally be longitudinal. A transverse target polarization requires local shielding of the strong solenoidal field.

The ^{3}He gas will be polarized in an optical pump cell by polarized laser light, placed outside of the $\overline{\text{P}}$ANDA detector. A polarization of 75% at a flux of 30 bar·l/day can be achieved by a 25 W fibre laser [24]. The gas is transported by a small pipe into a storage cell as shown in Fig. 4.34. It is known from medical applications of polarized ^{3}He gas in NMR tomography that polarization survives the injection into the inhomogeneous regions of large solenoids of several Tesla magnetic field strength [24]. For a luminosity of $\sim 10^{32-33}$N/cm^{2}s about $4\cdot10^{17}$ atoms/s and a storage cell of 10 cm length and 8 mm cross section would be required. The feasibility of such a target at $\overline{\text{P}}$ANDA still has to be studied in detail. In particular, it has to be clarified how an efficient differential pumping system can be integrated into the vertex area in order to obtain a good vacuum in the beam pipe downstream the storage cell.

4.4 Single Filament Superfluid ^{4}He Target

Micron-sized droplets produced via Reyleigh breakup (sound waves) of a single filament of liquid material injected into a high-vacuum region appears to be the most suited candidate as internal target for the future $\overline{\text{P}}$ANDA experiment. To date, considerable experimental efforts have been put into the production of hydrogen droplets, specifically at TSL (Uppsala). To avoid freezing of the jet prior to breakup liquid hydrogen is discharged

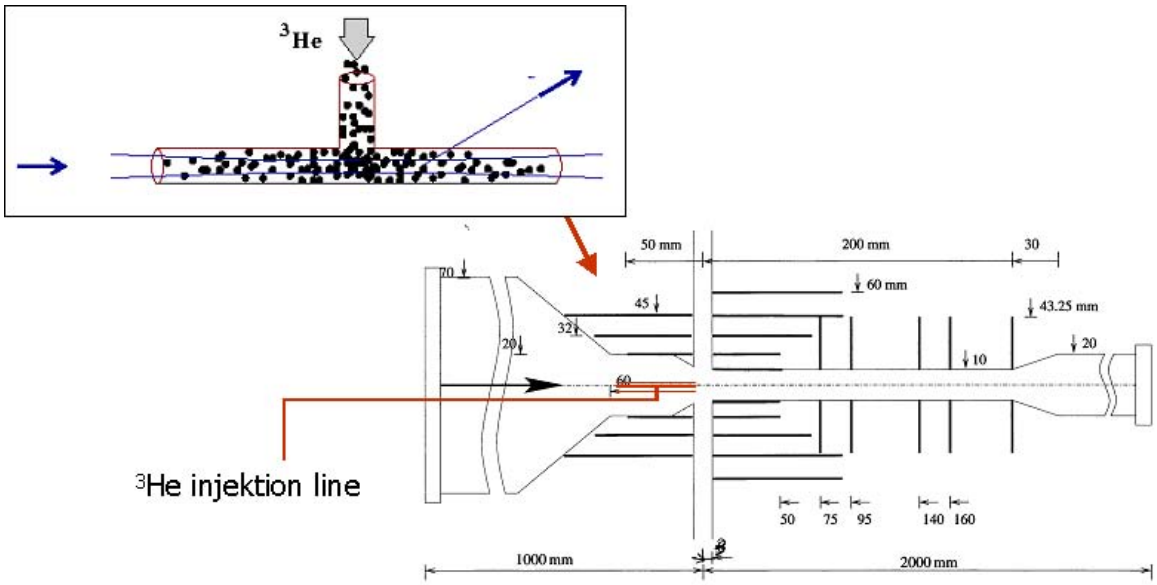

Figure 4.34: Polarized ^{3}He gas feeds a storage cell (similarly used in the the Hermes experiment) allowing to measure the annihilation of antiprotons off polarized neutrons. The storage cell is located upstream of the interaction region of the pellet and cluster target of $\overline{\text{P}}$ANDA.

first into a low-pressure inert gas (helium) region. Successively the droplets are injected into vacuum by use of a long, narrow capillary [5]. Due to the turbulent flow regime inside the capillary this complex injection system partially affects the beam flight direction, with a corresponding broadening of the final droplet angular distribution. This is unfortunate, since the larger the lateral spread the smaller the target density. In addition, large nozzle diameters ($d > 10\,\mu$m) are used to avoid clogging of the orifice under normal operation conditions. Whereas a thick target provides a high luminosity, the lifetime of the projectile beam decreases with increasingly larger target size due to heating. At the institute for nuclear physics in Frankfurt we aim to test a novel internal target produced by discharging superfluid helium at very low temperatures ($T < 2.1\,$K) into vacuum. Motivations for these studies are preliminary results obtained at the Max-Planck-Institut für Strömungsforschung in Göttingen [25]. These indicated a significantly smaller angular divergence associated to a single filament superfluid jet than in the normal liquid case. The droplet beam divergence was found to be $< 500\,\mu$rad without the use of any additional collimating slits. The observed angular divergence corresponds to a lateral spread of less than 2 mm at about 2 m downstream from the nozzle. Owing to the unique high-purity properties of superfluid helium, one major advantage of our injection source is the possibility to use much smaller nozzle diameters, down to $d = 1\,\mu$m, which, while still providing a high luminosity, they would increase the beam lifetime. In addition, since helium is the only substance that remains liquid (superfluid) even at $T = 0\,$K, the use of complex injection source is avoided. The Frankfurt internal target test facility is presently under construction.

4.5 Nuclear Targets

It is foreseen to employ nuclear targets for the exploitation of $\overline{\text{p}}$-nucleus reactions. Here, an important aspect is the search for modifications of meson properties in the nuclear medium. In the present experimental program, particular emphasis is placed on mesons with open and hidden-charm extending ongoing studies to the heavy quark sector (see Sec. 2.4) and J/ψ production.

Fig. 4.35 shows the respective luminosity for different effective target thickness and (proton) beam particles at COSY [26]. Cluster jet or pellet targets can be used for reactions with nuclei [27]. However, a higher luminosity and a better definition of the interaction point are provided by using wire or strip targets, as discussed below.

A feasible scheme for a solid target is a thin fiber that partly overlaps with the beam. Assuming a

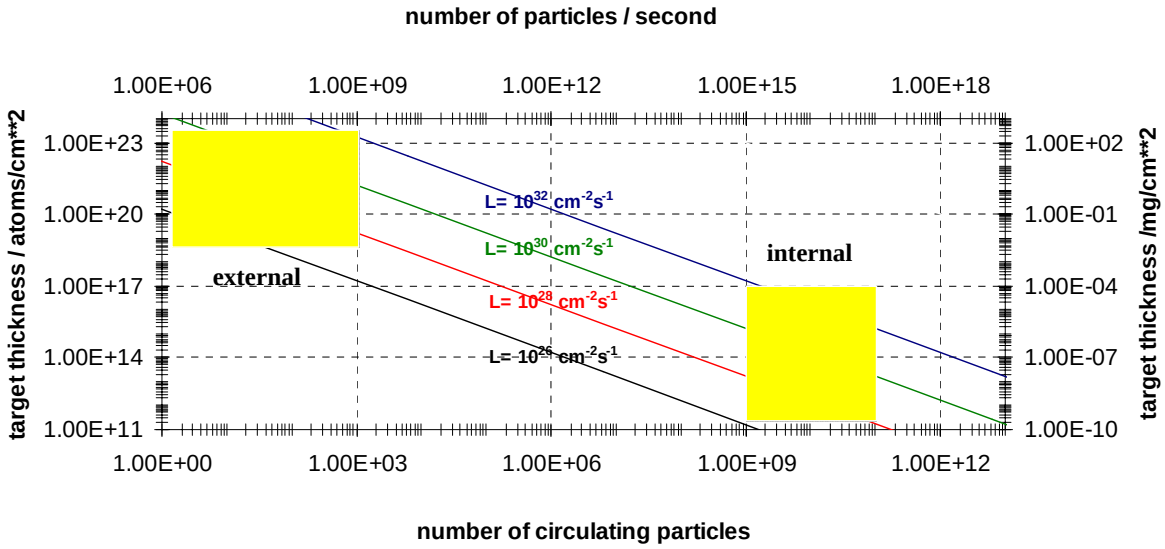

Figure 4.35: Peak luminosity of internal (area indicated right) experiments for different effective target thickness from [26]. The number of circulating particles refers to proton beams at COSY.

horizontal fiber and a Gaussian beam profile in the vertical direction, the effective luminosity is

$$L = \frac{N f \rho_T A}{\sqrt{2\pi}\sigma_y} \exp - \frac{(y - y_0)^2}{2\sigma_y^2}. \qquad (4.14)$$

Here, N is the number of antiprotons stored in the ring, f the revolution frequency, ρ_T the number density of target nuclei, A the cross section area of the fiber, σ_y the standard deviation of the vertical beam profile at the target location, y the vertical position of the fiber and y_0 the beam center. A commercially available carbon fiber with $5\,\mu$m diameter, $A = 20\,\mu\text{m}^2$, $\rho = 9.0 \cdot 10^{22}\,cm^3$ carbon atoms, $\sigma_y = 0.3\,$mm, $y = y_0$, $N = 1 \cdot 10^{10}$ and $f = 0.5 \cdot 10^5\ \text{s}^{-1}$ yields for instance $L = 3.6 \cdot 10^{32}\text{cm}^{-2}\text{s}^{-1}$. CH_2 targets can be prepared using a microtome to cut for instance $4\,\mu$m fibers from a polypropylene (CH_2) foil of $5\,\mu$m thickness. The surface must be made electrically conducting to prevent the buildup of charge due to ionization by the circulating beam. This can be achieved by evaporating a thin ($20\,\mu\text{g/cm}^2$) aluminum coating such that the target is grounded through the supporting aluminum fork. The current from secondary electrons due to the beam-target interaction can be used as a luminosity monitor. This current from ground to target (several ten pA) can be measured using a fast pico-amperemeter.

Using a fast, magnet-driven linear motor the target can be moved with a high speed to the beam center. A fast and accurate measurement of the beam profile can be performed by measuring the secondary electron current as a function of the y-position. The target should be mechanically integrated in the pellet and/or jet target arrangement. Such targets have been used as internal targets at the IUCF Cooler [28] and at COSY [29].

Fig. 4.36 shows an example of mounting a wire target on a fork structure, as done at COSY.

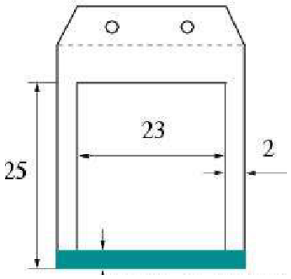

Figure 4.36: Mounting a wire target on a fork structure, as done at COSY, from [30]. Dimensions are in mm.

The realization of a fiber target with linear motor along with a ultra-high vacuum parts would take 1 year.

4.6 Target for Spectroscopy of Hypernuclei

4.6.1 Introduction

For the measurements of double hypernuclei and Ω-atoms the backward part of the calorimetric detector will be removed to place a nuclear target directly in front of the main tracking detectors. At this position, only minor distortions of the beam transport system are expected. Furthermore, the central and forward detector system of can be used for particle tracking in the forward region. The vertex detector and the associated beam pipe will be replaced by a dedicated beam line in order to avoid damage to the main vertex detector by forward scattered particles. Neither a pellet target nor a cluster target will be used and the pumps at the entrance of the $\overline{\text{P}}$ANDA detector can be moved further upstream.

4.6.2 Primary target

The task of the primary (production) target is the production of $\Xi\overline{\Xi}$ pairs and the rescattering of the Ξ hyperon towards larger laboratory angles and smaller momenta. Target nuclei with higher mass numbers are more efficient for rescattering of the produced primary particles and hence for the emission of low momentum Ξ^- hyperons. However, heavier targets increase the neutron and x-ray background in the Germanium detectors.

Taking into account existing elastic scattering data [31, 32, 33], the combined $\overline{\Xi}^+\Xi^-$ escape probability with the required signature is estimated to be about 0.02 %. Calculations with an UrQMD model taking multiple scattering effects into account resulted in even larger probabilities of about 0.2 % for this process [34]. In order to allow a more systematic study of the role of the primary target mass number and the geometry of the secondary target microscopic simulations within the framework of an Intra Nuclear Cascade model [35] were performed. Starting point of the simulations was the two-body reaction $\overline{\text{p}}\text{p} \rightarrow \Xi\overline{\Xi}$. The hyperon pairs were produced with a cross section of 2 μb at a $\overline{\text{p}}$ momentum of about 3 GeV/c [36]. No information was available for the $\Xi^-\overline{\Xi}^+$ production. For the production in nuclei, the $\overline{\text{p}} + \text{n} \rightarrow \Xi^-\overline{\Xi}^0$ reaction was also included while assuming a $A^{2/3}$ dependence where A denotes the target mass number.

The relevant quantity for the optimization of the target system is the rate of the stopped Ξ^- over the produced Ξ^-, in the following called Ξ^- production factor. This factor depends on several parameters: production rate, distance between the production and the hypernuclear targets, beam pipe diameter, materials of the targets and their sizes and shapes.

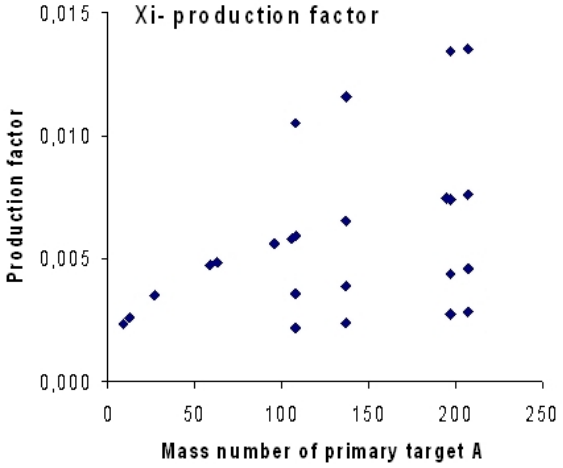

Figure 4.37: Ξ^- Production factor as a function of the mass number of the primary target and various diameters of the beam pipe (10, 20, 30 and 40 mm from top to bottom).

To explore the role of the primary target independently, the secondary target was modelled for simplicity by a solid carbon block with a cylindrical hole of variable diameter representing the beam pipe. Fig. 4.37 shows the dependence of the Ξ^- production factor on the mass number of the primary target. The four different data points for a given mass number correspond to calculations with a beam pipe diameter of 10, 20, 30 and 40 mm (from top to bottom). As expected, the production factor rises with A. Going from carbon to gold one gains a factor of about 3.5.

Considering only the Ξ^- production factor, a heavy target would be preferable. However, another point which needs to be taken into account is the neutron background at backward angles, where the Germanium detectors are located. For lighter targets the neutrons are more forward focused in the laboratory frame, thus reducing significantly the number of neutron hits in the Germanium detectors. As will be outlined in Sec. 9.1.1.2 the use of a target in the Nickel mass region ($Z \approx 30$) allows a stable operation over a sufficiently long measuring period. An additional argument in favor of a light target is the background from atomic x-rays which is in the range of 100 keV in the case of heavy elements. However, a major fraction of the x-rays will be absorbed in the beam pipe or in the neutron moderator (see below). It is preferable to avoid this diffi-

culty by using a target with atomic number below $Z \approx 30$.

The thickness of the primary target is constrained by small angular scattering causing beam heating as well as the possible interaction rate ($10^7\,\mathrm{s}^{-1}$). However, a precise determination of the primary interaction point is not required and the interaction rate can be adjusted by the quality of the beam focus and by steering an appropriate fraction of the beam onto the target. For a hydrogen target a thickness of 50 μm seems acceptable, heavy targets require significantly lower areal densities. Presently, two scenarios are being explored: self-supporting wires of thickness in the order of 10 μm are readily available. However, such a thickness is only acceptable for light elements like e.g. Beryllium. For heavier elements thin metal sheets – as being used at the internal target of the ANKE experiment at COSY – with a thickness of the order of $< 1\,\mu$m can be used. For example, self-supporting filaments attached to a frame could be produced by etching techniques as being used in the production of micro wire detectors.

4.6.3 Secondary Target

The main purpose of the secondary, or hypernuclear, target is the stopping and absorption of the produced Ξ hyperon and the identification of the secondary reaction vertex by tracking of the incident Ξ and charged decay products from the weak decay of the $\Lambda\Lambda$ hypernuclei. Even with a moderate spatial resolution, this information will help to reduce the background in the offline analysis significantly.

The energy release of about 28 MeV during the conversion of the Ξ into two Λ hyperons may give rise to the emission of particles from the secondary target nucleus. As a consequence, a variety of double, single or twin hypernuclei as well as ordinary nuclei may be produced in excited states. In order to simplify the assignment of the various transitions to a specific nucleus four separated sections with up to four different main target materials are foreseen. The initial experiment will concentrate on light target materials like ^{9}Be, ^{10}B, ^{12}C and ^{13}C. In addition, the interactions in the material of the silicon detector can be studied. At the same time, the light elements help minimizing the absorption of γ-rays emitted by the excited hypernuclei.

The geometry of the solid-state micro tracker is mainly determined by the mean life time of the Ξ^- of only 0.164 ns. If the separation between the primary target and the secondary absorber is too big,low momentum Ξ^- will decay prior to stopping. On the other hand, energetic Ξ^- with momenta beyond approximately 500 MeV/c cannot be stopped prior to their decay. This limits the thickness of the active secondary target to a few cm (see Fig. 4.38 and Fig. 4.39).

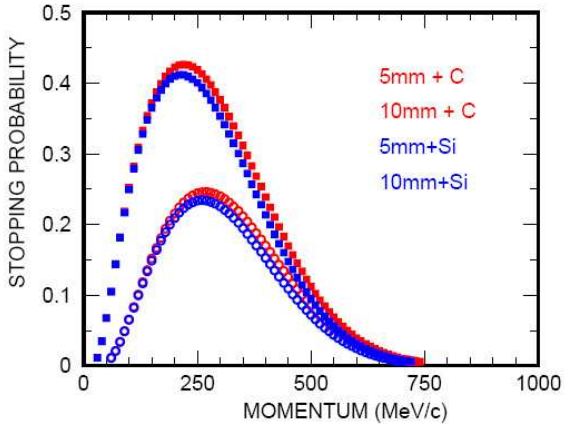

Figure 4.38: Stopping probability of Ξ^- hyperons in carbon and silicon as a function of the momentum. The upper and lower curves correspond to a gap between the primary target and the secondary absorber of 5 and 10 mm, respectively.

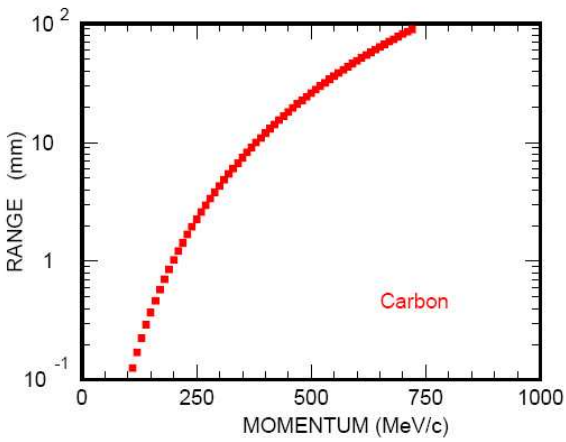

Figure 4.39: Range of Ξ^- hyperons in carbon as a function of the momentum.

In order to determine the required sensitive region of the secondary target we investigated the distribution of the stopping points of the Ξ^- entering the secondary target. While the distance between the primary and secondary target should be minimal, the number of stopped Ξ^- is not very sensitive to this gap. For a safe operation of HESR we therefore foresee a beam pipe with a diameter of 15 mm. In order to track the Ξ^- (and the charged fragments

resulting from the decay of the produced hypernuclei), it is planned to sandwich the secondary absorber with layers of silicon detectors. Outside of the beam pipe we projected in a first design a multilayered structure of 1.5 mm thick carbon absorbers surrounded by 300 μm thick silicon layers. Fig. 4.40 shows the stopping points of Ξ^- hyperons, where the horizontal axis represents the beam direction and the vertical axis is the radial distance from the beam axis. The origin marks the primary target point. Consistent with the schematic calculations shown in Fig. 4.38 and Fig. 4.39 the stopping points are concentrated in an angular range from 40° to 90° and a radial thickness of about 20 mm. The free angular range between 0° and 40° is sufficiently large for the detection of the associated kaons emitted mainly in the forward region (see Sec. 9.1.1.4).

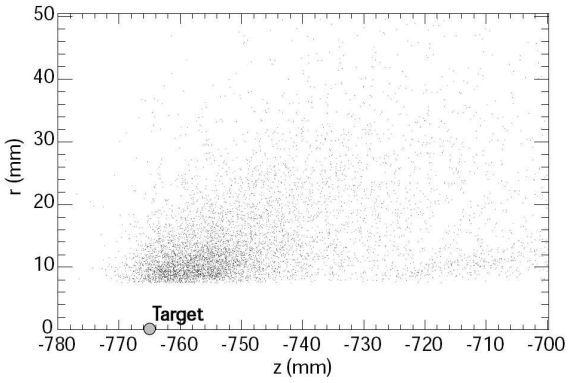

Figure 4.40: Stopping points of Ξ^- hyperons produced in $\overline{\text{p}} + X$ interactions at 3 GeV/c within an INC calculation [35]. The circle marks the position of the primary target.

The number of silicon detectors and the thickness of the absorber is a compromise between the necessary number of readout channels and the corresponding costs on one hand and a large stopping probability on the other hand. Furthermore, in order to keep the γ-ray absorption low, the overall thickness should be kept as low as possible. The γ-rays emitted from the hypernuclei will traverse a typical distance of 2 cm in the secondary target. Therefore, γ-rays with energies of 0.1, 1 and 10 MeV will reach the Germanium detectors with 60, 80 and 93 % probability, respectively. Front-end electronics and upstream cable connections may cause additional losses in the order of 10 %.

For the choice of the silicon detectors we are now exploring two possible options:

(i) A pixel detector based e.g. on the ATLAS pixel chip. This solution would guarantee broad compatibility with the main vertex detector. However, major disadvantages are the small size of the present ATLAS chips and the space needed for the supporting structure onto which the chips are glued. The small size of the chips does not allow a geometry where the readout cables are concentrated in the upstream region. The additional support structures would result in major empty or inactive regions between the main secondary absorber material, thus reducing the stopping and capture probability.

(ii) A silicon strip detector. For a possible readout scheme we plan to follow the developments for the SCT barrel module of ATLAS. A thickness of the readout board of less than 1.5 mm has been achieved by the ATLAS collaboration for e.g. the ABCD chip. Thus, a dense sandwich structure with about 1.5 mm absorber material enclosed by detector layers is feasible. Since in the region of the silicon sensors no additional components are located, this well known technology leads to the required compact configuration of the secondary target.

An optimal coverage of the region between 40° and 90° would require silicon sensors of different sizes (see lower part of Fig. 4.41). The size of the detector closest to the beam is about $15 \times 9\,\text{mm}^2$, the largest of the order of $55 \times 33\,\text{mm}^2$. While such a solution is not impractical we are now exploring also different geometries with sensors allowing identical front-end electronics. One example is shown in the upper part of Fig. 4.41.

In order to estimate the background load from charged and neutral particles microscopic UrQMD calculations were performed. These calculations predict a mean charged particle multiplicity per reaction in the range from 40° to 90° between 3 and 6. At an average interaction rate of $5 \cdot 10^6\,\text{s}^{-1}$ and for a target with atomic numbers $Z \approx 30$ we expect a rate of about $6 \cdot 10^6$ charged particles per second in each silicon layer. Even in case of the smallest conceivable sensor ($15 \times 9\,\text{mm}^2$) and assuming a pitch of 20 μm the rate per strip is less than 10 kHz. For comparison, at COMPASS a shaping time of 300 ns is at present employed, so that the rate limit will be in the range of a few hundred kHz. The outer strip detectors can have a larger pitch (50 μm). Assuming 15 planes in each of the four sectors and a pitch of 50 μm, both geometrical solutions shown in Fig. 4.37 will require about 45 000 readout channels. Since the main vertex detector will be dismounted during the hypernuclei experiments, we plan to share part of the electronics with the main vertex detector.

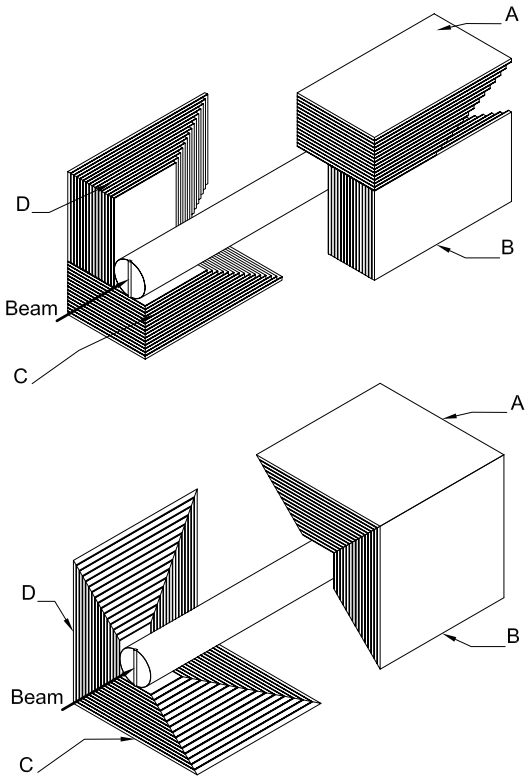

Figure 4.41: Possible geometries of the secondary target showing the four sectors. For the geometry shown on the bottom, front-end boards of different sizes are needed, the geometry on top allows the usage of equally sized front-end electronics. Two sections are displaced for clarity.

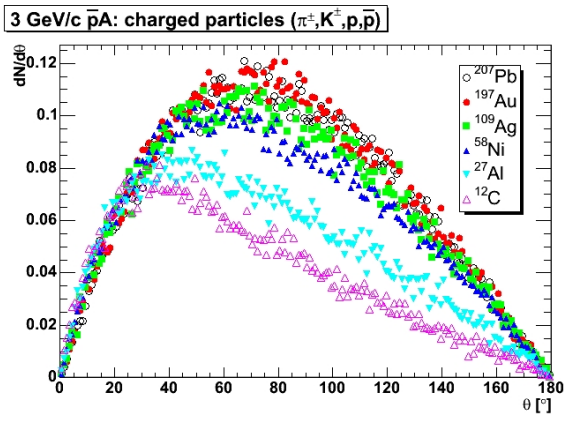

Figure 4.42: UrQMD predictions for the differential multiplicity of charged particles per interacting antiproton for various target nuclei at 3 GeV/c incident momentum.

4.7 Interaction zone

4.7.1 Pumping Scheme

An internal target system necessitates a sufficient pumping system as close to the interaction zone as affordable, to keep the beam vacuum below 10^{-7} mbar.

Conventional pumping systems, such as turbo molecular pumps and ion getter pumps, cannot be installed due to stringent requirements to the available space around the interaction zone. The space is occupied by the necessary detector systems, as is clearly seen in Fig. 4.43. Therefore, it is proposed

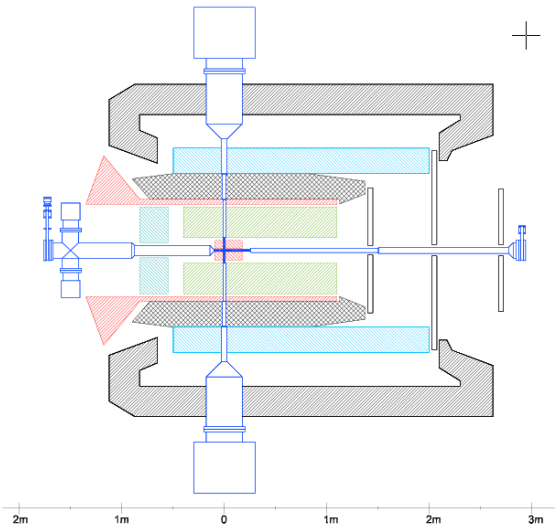

Figure 4.43: $\overline{\text{P}}$ANDA detector system, with the layout of the internal target antiproton beam interaction zone.

to use the walls of the beam pipe inside the detector as well as the internal target vacuum pipe itself as a high-vacuum pump. This can be achieved by coating the surface with a non-evaporable getter (NEG) material as will be used at CERN for the LHC.

Additional pumping is necessary as sketched in Fig. 4.44. Two turbo-molecular pumps, each with a pumping speed of 1 000 l/s, will be installed in front of the $\overline{\text{P}}$ANDA magnet. A specially designed cryo-sorption pump (with an additional pumping speed of 5 000 l/s) will be used. Two additional turbo-molecular pumps (each 1 000 l/s) will be located further away from the beam pipe, in-between the $\overline{\text{P}}$ANDA magnet and the forward spectrometer. Another turbo-molecular pump (1 000 l/s) and an ion getter pump (1 000 l/s) at the end of the forward spectrometer will complete the beam line pumping system (see Fig. 4.44). A detailed study of gas

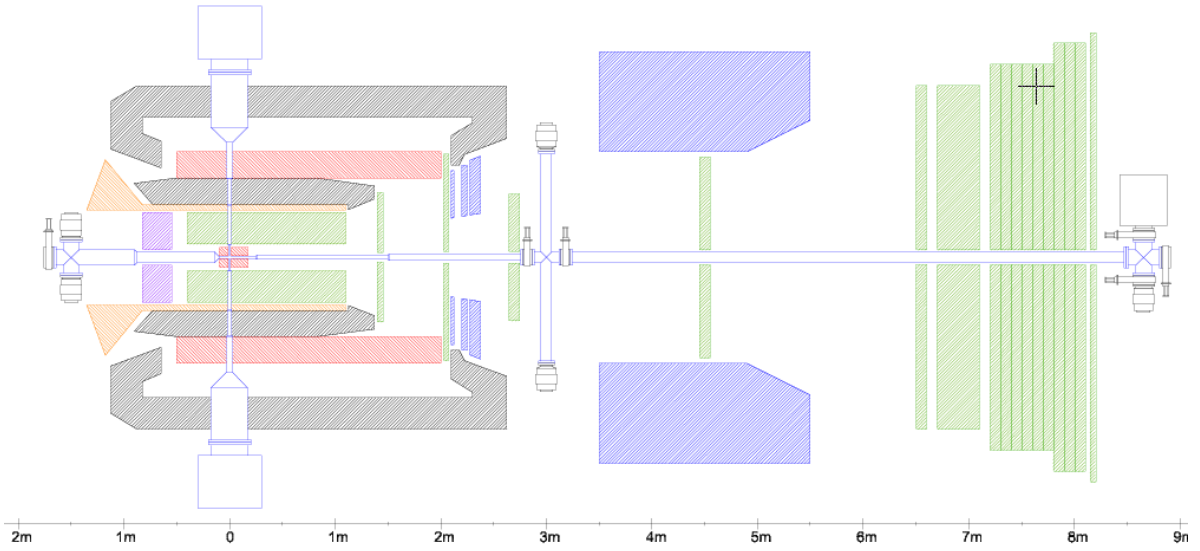

Figure 4.44: $\overline{\text{P}}$ANDA beam line pumping scheme

losses in the interaction region for cluster-jet and pellet targets is under evaluation. A prototype vacuum chamber was designed and is under construction using NEG coated walls. It will be set up with the foreseen effective pumping speed as it would be available with the pumping equipment and dimensions of the beam pipes as shown in Figs. 4.44–4.45.

Different gas loads (hydrogen gas lost in the interaction zone either coming from the cluster-jet or pellet beam) will be measured and compared with the theoretical calculations.

4.7.2 Non-Evaporable Getter (NEG)

Non-evaporable getters remain in the solid state instead of being evaporated and condensed on a surface. This family of getters is usually made of an alloy of zirconium, such as Zr-Al, Zr-V-Fe or Zr-V-Ti. Although they can exist in any solid form, they are most often found as either chunks or pellets or thin films bonded to metallic substrates. NEGs are known for their high pumping speed and capacity for hydrogen. Further advantages are the relatively small size and little weight.

The activation process is required for NEGs. When the getter material is exposed to air for handling or loading into a system or device, the material's surface will "skin over" with reacted gases. This means that the NEG will be entirely enclosed in an envelope of oxides or nitrides. Additionally, the bulk of the material will be saturated with dissolved H_2. Under these conditions, the getter material is essentially inert and will not provide an active getter-pumping surface. Activation prepares the getter surface for pumping and is performed by heating under vacuum after installation. During heating, the reacted "skin" layer will diffuse into the NEG's bulk in an attempt to achieve equilibrium throughout the bulk. The H_2 will be driven out of solid solution into the chamber and pumped away by an appropriate high-vacuum pump. The time and temperature required for activation will vary with the specific getter alloy. The vacuum level required will depend upon the actual application, but a pressure of at least 10^{-6} mbar is usually required. The pumping time must be sufficiently long to ensure that the released H_2 is pumped away. Any remaining H_2 will be reabsorbed by the getter and this will limit the amount of H_2 subsequently pumped by the getter.

After activation, gases will be removed from the vessel by reaction on the NEGs surface until enough gas is reacted to put a gas layer over the surface again ("skin over"). At this point, pumping action for active gases ceases and the reacted "skin" becomes a barrier for further dissolution of H_2. The time required for this to happen is a function of the gas load to be pumped. In ultrahigh-vacuum applications, it can be in the order of years. However, in an environment with high gas loads the time could be reduced to hours or minutes. Gas loads that result in an unacceptably short period of sur-

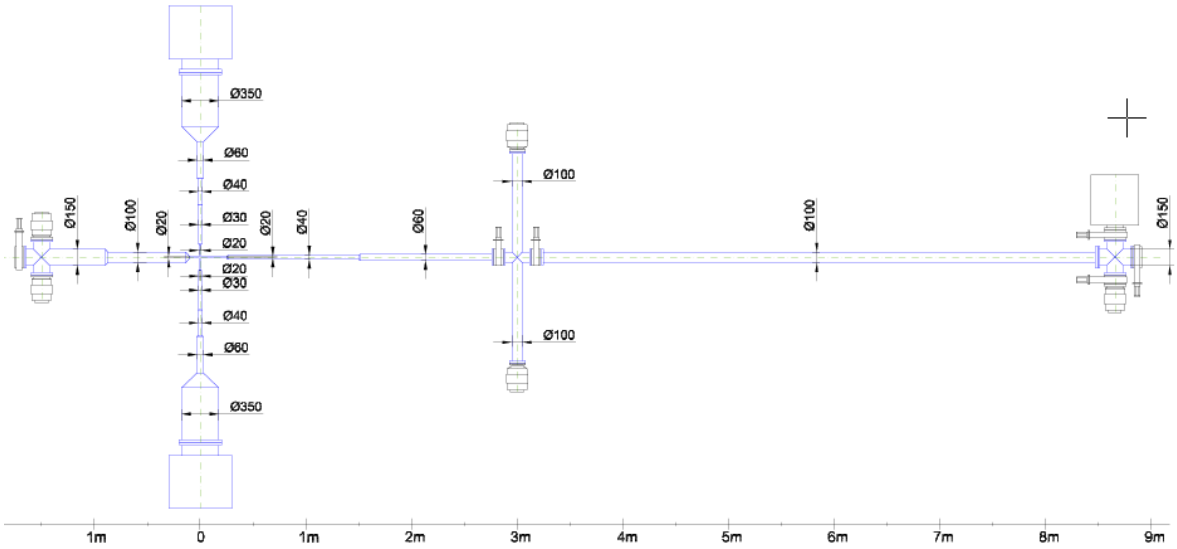

Figure 4.45: $\overline{\text{P}}$ANDA beam line pumping scheme including diameters [mm]

face saturation are usually dealt with by raising the temperature of the NEG to a about 80 to 100°C. . The higher temperature will result in pumping and diffusion into the bulk taking place at the same time.

Systems which are cycled repeatedly to atmospheric pressure require careful consideration. Each time the NEG material is in contact with air or any other active gas, such as N_2, re-activation is required. In a cycled system, the chamber can be released to argon instead of an active gas or the getter can be isolated from the chamber by appropriate valves.

Getters and getter pumps can provide economical and compact pumping in many applications if they are used properly.

Vacuum pumping via non-evaporable getter thin film deposited directly onto the interior of a vacuum chamber is a novel way to produce high vacuum.

4.7.3 Thin film NEG-prototype

The performance of a NEG is characterized by activation temperature, sticking probability, surface capacity and total pumping capacity. For the study of a thin film NEG coated vacuum chamber, having similar dimensions as it will be used at the interaction zone (see Fig. 4.44), a prototype will be set up to measure

- gas load,
- pumping speed
- recycling time

for a realistic assumption of hydrogen gas losses using an internal target device.

4.8 Luminosity Monitor

The research program is based on annihilation of antiprotons in a circulating beam with protons on a target which can be regarded as being at rest. Most of the spectroscopic studies are to be based on the formation of the hadrons of interest, by making accurate measurements of their excitation function as the momentum of the antiproton beam is varied by small steps. Measurements at each antiproton momentum must be normalized to the luminosity making precision measurements of the luminosity mandatory. The measured yield in the excitation function contains not only the resonance yield but generally a several times larger yield from the underlying continuum. (See, for example, E835 measurements of two photon decays of η_c, χ_{c0}, χ_{c2}, and the $\pi^0\pi^0$ decay of χ_{c0}). The identification of the resonance signal requires luminosity measurements with an absolute precision of at least $\pm 2\%$. This is a formidable task.

In e^+e^- annihilation experiments where similar precision measurement of the luminosity is required,

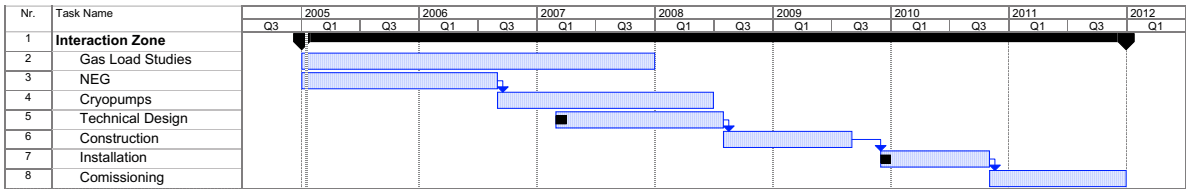

Figure 4.46: Timeline for the interaction zone.

the theoretically precisely known Bhabha scattering is available for normalization. In contrast, the absolute elastic scattering cross sections for $\overline{\text{p}}$p are not known and the experimentally challenging job of making precision measurements of elastic scattering in the extreme forward direction must be tackled where Coulomb scattering dominates over nuclear processes and absolute Coulomb normalization can be used. At momentum transfers squared of the order of $t = 0.0002\,\text{GeV}^2/c^4$, the Coulomb cross section is $\sim 98\%$ of the total at 15 GeV/c and $\sim 95\%$ of the total at 3 GeV/c. This means that precision measurements of differential elastic scattering cross sections need to be made at theta = 0.94 mrad for 15 GeV/c, and at $\theta = 4.7$ mrad for 3 GeV/c. This is a formidable task considering the direct beam. In the E760/E835 experiments this difficulty was avoided by measuring not the forward scattering of antiprotons at small angles but by measuring recoil protons at angles near 90°. The recoil protons had energies less than 25 MeV and could be conveniently detected with solid-state detectors with an overall precision of the order of $\pm 2\%$ (For details see [37]). This technique was only possible because the E760/E835 detector did not have a magnetic field and the recoil particles had a straight-line trajectory to the detector. The technique is not possible with the $\overline{\text{P}}$ANDA detector and its magnetic field. Here, the forward elastic scattering itself must be measured. Detectors which are designed for this purpose are called Roman Pots.

Roman Pot detectors consist of retractable detectors in the beam pipe which can be moved close to the beam for forward scattering measurements, and withdrawn during beam injection and diagnostics. In order to make measurements at small angles, these detectors have to be located at large distances from the interaction point while still in the straight section of the accelerator ring. Apart from making extreme demands on the position resolution in the roman pot detectors, these requirements impose stringent demands on the beam quality as well as the ring structure.

A measurement at the scattering angle of 0.94 mrad is the most demanding. Since the Coulomb cross section falls off rapidly with t^{-2}, no more than 10% acceptance in t is desirable. Therefore, the detector must be capable of an angular resolution of ≈ 0.05 mrad. The detector for $\overline{\text{P}}$ANDA has to be able to subtend angles from ≈ 0.5 mrad to ≈ 5 mrad at the interaction point and have an angular resolution of ≈ 0.05 mrad. If located at a distance of 10 m, this corresponds to a detector covering the radial distance of $\approx 500 - -5000\,\mu$m microns from the beam center and a position resolution of $\approx 50\,\mu$m.

Roman pot detectors, originated at ISR by Amaldi [38], are now regular fixtures in many experiments for measuring forward scattering. Various designs, albeit optimized for measurements at hundreds of GeV-TeV energies, exist in the literature. The performance will need to be critically evaluated and the concept modified for the use with $\overline{\text{P}}$ANDA. It is necessary to position the detectors in the beam vacuum and to provide for the desired beam emittance in the region. It should be mentioned that Roman Pots are extremely useful for optimizing the beam intensity and position during commissioning.

References

[1] C. Ekström et al., Phys. Scripta **T99**, 169 (2002).

[2] J. Zabierowski et al., Phys. Scripta **T99**, 159 (2002), http://www5.tsl.uu.se /wasa.

[3] R. Koch, private communication, 2004.

[4] Y.-N. Rao and D. Reistad, Monte carlo simulations of Thin Internal Target Scattering in Ceslius, in *Internal Note*, The Svedberg Laboratory, Uppsala University, 2001, TSL Note 2001-07-25.

[5] B. Trostell, Nucl. Instrum. Meth. **A362**, 41 (1995).

[6] C. Ekstroem et al., Nucl. Instrum. Meth. **A371**, 572 (1996).

[7] C. Ekström, Internal targets, in *16th RCNP Osaka International Symposium on Multi GeV High Performance Accelerators*, Osaka, Japan, 1997.

[8] P. C. Souers, *Hydrogen Properties for Fusion Energy*, University of California Press, Ltd., 1986.

[9] O. Nordhage and G. Norman, Evaporation-cooled Hydrogen Droplets inside a Pellet Target, Internal note, TSL Uppsala, 2003.

[10] Z. Li, Simulations on Hydrogen Pellets in Vacuum, Internal note, TSL Uppsala, 2004.

[11] H. Tinoco, Vacuum Injection System for Hydrogen Micro-Spheres in the CELSIUS Storage Ring, in *Internal Note*, The Svedberg Laboratory, Uppsala University, 1990, WASA report 1/90.

[12] K. Jousten, editor, *Wutz Handbuch Vakuumtechnik*, Friedr. Vieweg & Sohn Verlag, GWV Fachverlage GmbH, Wiesbaden, 2004.

[13] J. F. O'Hanlon, *User's Guide to Vacuum Technology*, John Wiley & Sons, Inc., 3 edition, 2003.

[14] B. Trostell, The thermodynamics of hydrogen micro-spheres as internal targets in ion storage rings, in *Proc. 1st Europ. Particle Accelerator Conf.*, edited by S. Tarrazi, 1988.

[15] T. Ytrehus and S. Østmo, Int. J. Multiphase Flow **22**, 133 (1996).

[16] V. Ziemann, Vacuum tracking, SLAC-PUB-5962, 1993.

[17] Technical Report for the HESR, Technical report, 2005, HESR Consortium, Technical Report for the HESR.

[18] D. Reistad and B. Galander, private communication, 2004.

[19] K. Bongardt, talk on the 5th HESR Consortium Meeting, FZ-Jüelich, Germany, 2004.

[20] Meeting: Targets and Magnets for PANDA, Genova, July 29 -30, 2004, http://www.oeaw.ac.at/ imep/ Panda2.htm.

[21] T. Rausmann, *Diploma thesis*, PhD thesis, University Münster, 2004.

[22] M. Wutz, H. Adam, and W. Walcher, Vieweg-Verlag, 1988.

[23] D. D. Schepper et al., Nucl. Inst. Meth. **A419**, 16 (1998).

[24] W. Heil, Univ. Mainz, private communication.

[25] R. E. Grisenti and J. P. Toennies, Phys. Rev. Lett. **90**, 234501 (2003).

[26] A. Lehrach et al., Proceedings EPAC 2004, Luzerne, CH .

[27] M. Büscher et al., COSY Annual Report 2003 .

[28] P. Schwandt and H. O. Meyer, editors, New York, USA, 1985, AIP conference proceedings 128.

[29] D. Albers et al., Eur. Phys. J. **A22**, 125 (2004).

[30] F. Goldenbaum, priv. comm. .

[31] G. R. Charlton et al., Phys. Lett. **32B**, 720, 1970.

[32] R. A. Muller, Phys. Lett. **39B**, 671, 1972.

[33] J. M. Hauptman, J. A. Kadyk, and G. H. Trilling, Nucl. Phys. **B125**, 29, 1977.

[34] S. Soff, private communication.

[35] M. Agnello, F. Ferro, and F. Iazzi, hep-ex/0405061, 2004.

[36] Kaidalov and Volkovitsky, Agenda of the Second Meeting of the Working Group: Physics with Secondary Beams, GSI, 1996.

[37] Nucl. Inst. Meth **A355**, 308 (1995).

[38] U. Amaldi, M. Jacob, and G. Matthiae, Ann. Rev. Nucl. Sci. **26**, 385 (1976).

5 Micro Vertex Detector

5.1 Introduction

The Micro Vertex Detector (MVD) of the $\overline{\text{P}}$ANDA installation at the HESR storage ring for antiprotons will be of central importance for a number of the physics goals defined in Chap. 2. Experiments aiming at the identification of open charm and strangeness depend on the identification of secondary decays of particles in displaced vertices. Some examples of decays which hold the potential to be identified by purely geometrical means are listed in Table 5.1.

Decays of charged particles are often accompanied by neutral particles in the final state and cannot be reconstructed from the observed charged decay products. The presence of a significant kink may be used to enhance the detection probability, such as the Σ^+, Σ^- and other baryons. However, this will not work for kinks that come very close to the primary vertex as in case of the charged D meson. Here, exclusive detection of the decay particle tracks will be needed for the reconstruction of displaced vertices. As a minimum requirement, two charged tracks intersecting at a space point displaced from the primary vertex could be used for an identification of delayed decays early in the data acquisition chain.

The table exhibits two classes of decays. Strange hadrons have decay lengths on the order of cm while charmed mesons and baryons decay within several tens to a few hundred μm. The vertex detector and the adjoining tracking device will have to be suited for both. While $\overline{\text{P}}$ANDA will focus on charm production, the identification of kaons will greatly enhance the efficiency for D mesons with large branchings into channels accompanied by kaons. Thus, a design that can handle both length scales will greatly improve the efficiency of $\overline{\text{P}}$ANDA.

All experiments currently employing or planning to employ silicon pixel detectors work at rather high particle energies. The charged particles usually are minimum ionizing. $\overline{\text{P}}$ANDA will have to handle significantly slower particles as well. This offers the opportunity to contribute to the particle identification with energy loss measurements. However, the detector thickness will be a crucial parameter for the detector design compared to other applications. Experiments, such as BaBar [1, 2], have chosen to construct the vertex detector from silicon strip detectors which allow smaller material budgets for the same angular coverage. However, the concept compromises on the number of hits per unit area and time that can be handled. With the interaction rates foreseen for the $\overline{\text{P}}$ANDA experiment, expected in experiments using heavy targets, the innermost detector layers will be exposed to high particle densities. A pixel design is favored at least for the innermost layers. The structure may be augmented by additional layers of strip detectors for the longer decay lengths. $\overline{\text{P}}$ANDA plans for five track points in the vertex detector which will provide information for the lower trigger stages even if one of the detectors is missing in a track. Fig. 5.1 shows that the energy deposit in silicon changes rapidly in the momentum range encountered in $\overline{\text{P}}$ANDA experiments (partly due to the fixed-target nature of the setup). Below 700 MeV/c, the energy loss may be used to discriminate between particle species.

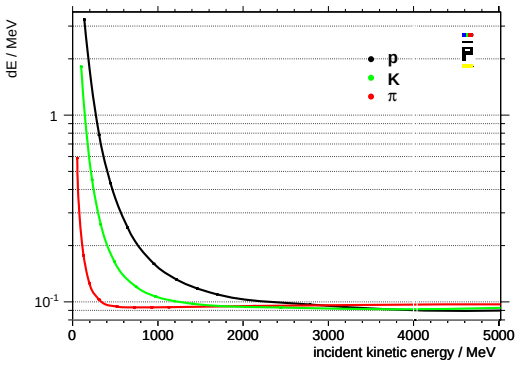

Figure 5.1: Energy loss of the indicated particle species in 400 μm of silicon as a function of momentum.

The high interaction rates stress the issue of radiation hardness of the sensors and readout electronics. The expected neutron flux will be considerable and push the limits of present-day technology for radiation-hard electronics albeit not beyond the estimates for collisions of nuclei at high energies like in the ALICE experiment. Our estimate lies about an order of magnitude below a reasonable limit for typical detector lifetimes of the order of ten years. Therefore, while the issue still cannot be neglected completely, it is not a limiting factor for the layout and does not warrant extensive research and development on radiation-hard electronics.

The physics of several key experiments for PANDA has been discussed in greater detail in Chap. 2. Some of the channels of interest put a high demand on the vertex detector performance. The issues thus raised have been used as benchmark tests for the Monte Carlo simulation studies of the vertex detector performance. They are discussed in the subsections on 'Physics with the MVD' and 'Monte-Carlo simulations for the MVD'. The results obtained in the studies have given rise to a newly developed and improved layout of the micro-vertex detector as detailed in the chapter on 'General MVD layout'. Details on the choice of sensors, the readout options, and additional options that may become available during the R&D phase for the PANDA vertex detector. The results are worthwhile pursuing because of the special features presented in the chapter 'Technical options for the MVD design. The use of state-of-the-art pixel sensors developed for the LHC experiments such as ATLAS [3], CMS [4] and ALICE [5] and similar readout schemes still requires R&D as described in the chapter on 'R&D for the MVD. In addition, a solution based on a custom design for the PANDA vertex detector is developed which, while being somewhat more expensive, would allow to circumvent the problematic adoption of present-day technology. In particular, a custom design will allow a selection of pixel sizes better suited for the needs of PANDA. For the front-end of the readout, a change in chip manufacturing techniques from present 0.25 μm to 0.13 μm feature size can be anticipated. Following the change in technology, a custom design for PANDA may prove to be advantageous both for physics as well as for practical reasons. Presently, this choice cannot be made. We therefore intend to study both options as well as the possible advantages that may be gained from novel detector materials such as GaAs:Cr or SiC. The R&D period is two take three years and will provide a selection of one technology for the MVD. The summary chapter provides more detail on timelines and schedules for the PANDA MVD.

5.2 Physics with the MVD

The key experiments are discussed in detail in Sec. 2. Some of them can only be performed with a vertex detector of high quality that features resolutions suitable for the task of charm identification. Tracks of charged mesons have to be reconstructed with a spatial resolution on the order of the typical decay lengths of $\sim 100\,\mu$m. This is the case for experiments as listed in Table 5.2 which require the vertex detector for quite different reasons. The most stringent requirements are imposed by reaction channels where the D decay will be used to select certain event patterns from the data stream during data acquisition, as indicated in the last column of the table.

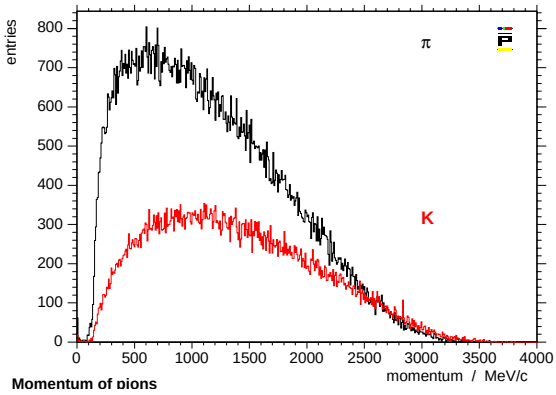

Figure 5.2: Momentum spectra of K and π from the reaction $\bar{p}p \rightarrow D\overline{D}$ at a beam momentum of 6.7 GeV/c. The detected charged particles are produced in the decay of the D mesons via $D^{\pm} \rightarrow K^{\mp}\pi^{+}\pi^{-}$.

For charmonium spectroscopy, slightly above the $D\overline{D}$ threshold, the momenta of the outgoing particles are confined by the center-of-mass motion which is conserved in the D's direction and velocity. As the combined mass of the particles in the D decay is much lower than the D's mass, particles acquire additional momentum still somewhat correlated with detection angle. This is shown in Figs. 5.2, 5.3, and 5.4 for the K's and π's from the reaction $\bar{p}p \rightarrow D\overline{D}$. The covered momentum range is large. The particles are emitted with appreciable transverse momentum components (Fig. 5.3, showing the transverse as a function of the longitudinal momentum component). Emission into the forward hemisphere in the laboratory system is nevertheless favored due to the high Lorentz boost. This is demonstrated in Fig. 5.4 where momentum is plotted as a function of detection angle. The physics requirements call for a very high granularity and optimum resolution for the forward region while coverage up to 90° may be sufficient in many cases.

The energy loss of slower protons, kaons and pions in the silicon detectors may be used while particle identification above 700 MeV/c will be facilitated by the DIRC, Sec. 7. It can also be inferred from the figure that scattering in the Si layers is a major concern since small-angle scattering drastically increases with decreasing particle energy, as seen in Fig. 5.5 for protons. Fig. 5.6 shows the average scattering angle for protons, kaons, and pi-

particle	lifetime	decay length $c\tau$	decay channel (fraction)
K_S^0	895.3(6) ps	2.6842 cm	$\pi^+\pi^-$ $((68.95 \pm 0.14)\%)$
$D^\pm$	1.040(7) ps	311.8 μm	e^+anything + *c.c.* $((17.2 \pm 1.9)\%)$
			K^-anything + *c.c.* $((27.5 \pm 2.4)\%)$
			K^+anything + *c.c.* $((5.5 \pm 1.6)\%)$
			$\overline{K}^0$anything + K^0anything $((61 \pm 8)\%)$
			e.g. $K^-\pi^+\pi^+$ + *c.c.* $((9.2 \pm 0.6)\%)$
			$\overline{K}^0\pi^+\pi^+\pi^-$ + *c.c.* $((7.1 \pm 1.0)\%)$
D^0	410.3(15) fs	123.0 μm	e^+anything + *c.c.* $((6.87 \pm 0.28)\%)$
			μ^+anything + *c.c.* $((6.5 \pm 0.8)\%)$
			K^-anything + *c.c.* $((53 \pm 4)\%)$
			K^+anything + *c.c.* $((3.4 \pm 0.4)\%)$
			$\overline{K}^0$anything + K^0anything $((53 \pm 4)\%)$
			e.g. $\overline{K}^0K^+K^-$ $((1.03 \pm 0.10)\%)$
			$K^-\pi^+\pi^+\pi^-$ + *c.c.* $((7.46 \pm 0.31)\%)$
			$\overline{K}^0\pi^+\pi^-\pi^0$ + *c.c.* $((10.9 \pm 1.3)\%)$
$D_s^\pm$	490(9) fs	147.0 μm	e^+anything/*c.c.* ($\approx 8\%$)
			K^-anything + *c.c.* ($\approx 13\%$)
			K^+anything + *c.c.* ($\approx 20\%$)
			$\overline{K}^0$anything + K^0anything ($\approx 39\%$)
			e.g. $K^+K^-\pi^+$ + *c.c.* $(4.4 \pm 1.2)\%$
Λ	26.32(20) ps	7.69 cm	$p\pi^-$ $((63.9 \pm 0.5)\%)$
Σ^+	80.18(26) ps	2.404 cm	$p\pi^0$ $((51.57 \pm 0.30)\%)$
			$n\pi^+$ $((48.31 \pm 0.30)\%)$
Σ^-	147.9(11) ps	4.434 cm	$n\pi^-$ $((99.848 \pm 0.005)\%)$
Ξ^-	163.9(15) ps	4.91 cm	$\Lambda\pi^-$ $((99.887 \pm 0.035)\%)$
Ω^-	82.1(11) ps	2.461 cm	ΛK^- $((67.8 \pm 0.7)\%)$
			$\Xi^0\pi^-$ $((23.6 \pm 0.7)\%)$
			$\Xi^-\pi^0$ $((8.6 \pm 0.4)\%)$
Λ_c^+	200(6) fs	59.9 μm	$p\overline{K}^0$ $((2.3 \pm 0.6\%)$
			$pK^-\pi^+$ $((5.0 \pm 1.3\%)$
			$\Lambda\pi^+\pi^+\pi^-$ $((3.3 \pm 1.0\%)$
			$\Sigma^0 + \pi^+\pi^-$ $((3.6 \pm 1.0\%)$
Ξ_c^0	112(13) fs	33.6 μm	$\Xi^-\pi^+(unknown)$

Table 5.1: Strange and charmed candidates for identification by means of their delayed decay, as listed in [6].

reaction channel	detected particle	tracking used for ...
$\overline{\mathrm{p}}\mathrm{p} \rightarrow \phi\phi$	$2K^+\ 2K^-$	momentum measurement (PID)
$\overline{\mathrm{p}}\mathrm{p} \rightarrow \eta_c$	$K^\pm\ \pi^\mp\ K_S^0$	momentum measurement (PID)
$\overline{\mathrm{p}}\mathrm{p} \rightarrow \psi(3770)$	$D\overline{D}$	charm detection online
	$\rightarrow K$'s and π's	momentum measurement (PID)
$\overline{\mathrm{p}}A \rightarrow D\overline{D}\ X$	D	inclusive charm ID online

Table 5.2: Benchmark experiments that require optimum performance of the vertex tracking. The most serious challenge will be D identification due to the very short decay lengths of these mesons.

ons as a function of the particle momentum. The increase at small momenta is clearly visible and demonstrates that $\overline{\mathsf{P}}$ANDA needs optimization in view of the material budget in the tracking detector section. In addition, the experimental program at $\overline{\mathsf{P}}$ANDA puts emphasis on the high-resolution spec-

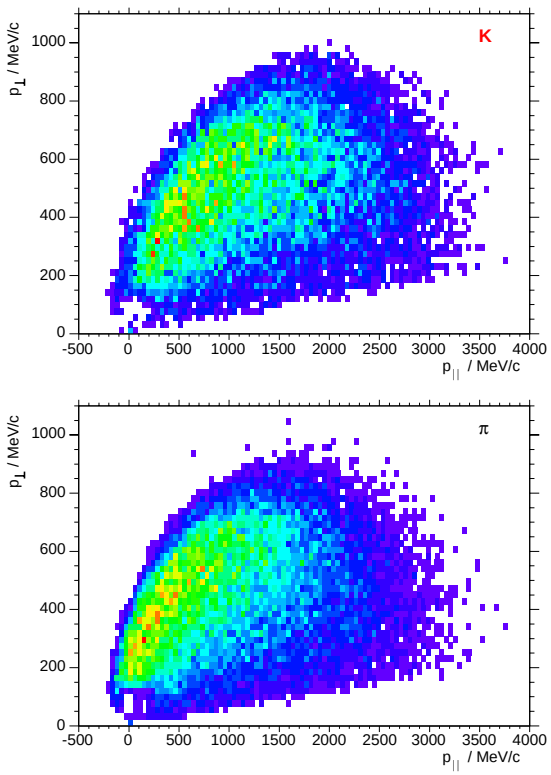

Figure 5.3: Transverse *vs.* longitudinal momentum of K and π from the reaction $\overline{\text{p}}\text{p} \rightarrow D\overline{D}$ at a beam momentum of 6.7 GeV/*c*. The detected charged particles are produced in the decay of the D mesons via $D^{\pm} \rightarrow K^{\mp}\pi^{+}\pi^{-}$.

troscopy of electrons as well as photons. Photons can be used to reconstruct the neutral part of the hadronic spectrum from the particle decay chains, in particular the π^0 and η meson momentum vectors. They may also be of interest as electromagnetic probes for certain reactions. Electrons are excellent tags for D meson spectroscopy (Table 5.1). They carry information on the flavor of the decaying charm. e^+e^- can also be used to reconstruct mesonic properties inside the nuclear medium when heavy targets are studied. Therefore, any material, especially high-Z material near the primary target may cause background due to bremsstrahlung and pair production. Vertex reconstruction may help to discern primary e^+e^- from pairs generated in secondary interactions. However, background restricts the use of electrons for the event recognition during data acquisition. Therefore, further minimization of the material load close to the interaction region while maintaining the spatial resolution of the detector will be advantageous.

In summary, the main issues for the R&D phase of the $\overline{\text{P}}$ANDA MVD are:

The thickness of the material used for the MVD construction is of major concern since $\overline{\text{P}}$ANDA will have to cope with low-energy particles which stands in contrast to the high-energy experiments considered as model detectors for the layout. In addition, energy loss measurements would be advantageous as they could be used in the particle identification at low energy.

Layout for a fixed-target experiment While the forward-focussing of all particles reduces the quality requirements for the backward hemisphere of the barrel structure, the fixed-target layout of the experiment requires good coverage of very forward angles with very good spatial resolution. As angles below about 20° cannot be reasonably covered with barrel structures, additional layers have to be added in forward direction with a more disk-like structure oriented perpendicular to the beam.

Applicability to a variety of physics cases and experimental setups of the target region At present, the options for the $\overline{\text{P}}$ANDA target include hydrogen pellet targets as well as hydrogen gas jets Sec. 4. In addition, heavy targets will be used as wires or foils. The options introduce quite different interaction geometries and will have to be handled equally well with the same vertex detector.

5.3 Monte-Carlo Simulations for the MVD

Monte-Carlo studies of the detector performance are being pursued in a number of participating institutes. The studies start from the original vertex detector layout sketched in the Conceptual Design Report [7] and shown in Fig. 5.7. Further simulations have guided the modelling of increasingly more realistic setups, the study of their interaction with the other detector elements, and the applicability to the physics issues which $\overline{\text{P}}$ANDA will address. The early version of the detector was used to verify the basic parameters of the detector. It features a barrel section with five layers of pixels which were taken to be $50 \times 300\,\mu\text{m}^2$ in size and five forward disk structures with pixel sizes of $100 \times 150\,\mu\text{m}^2$. Each silicon sensor layer was assumed to be $200\,\mu$m thick (corresponding to 0.25% X_0). The position resolution of

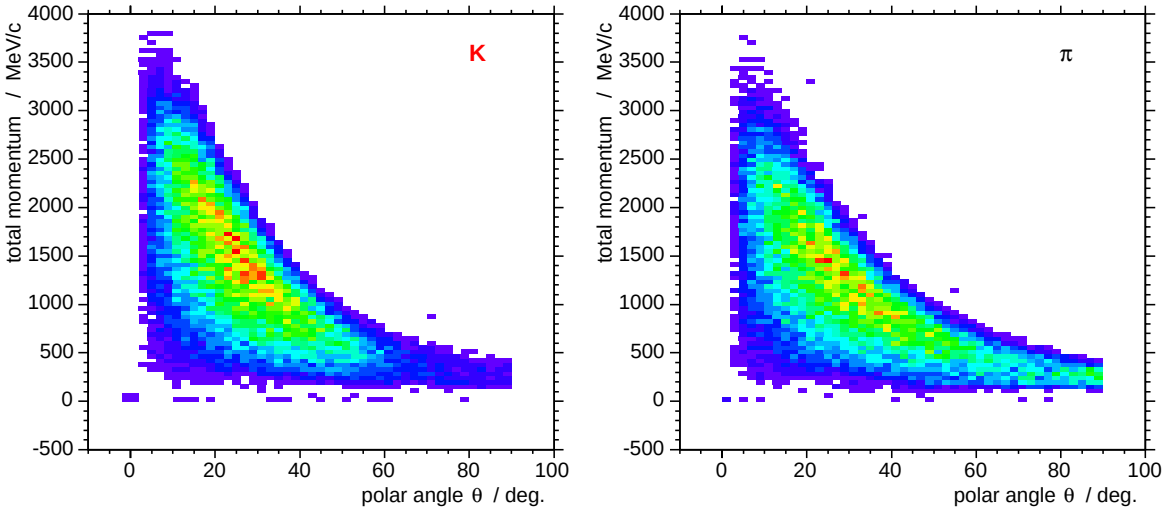

Figure 5.4: Momentum of K and π from the reaction $\overline{\mathrm{p}}\mathrm{p} \rightarrow D\overline{D}$ at a beam momentum of 6.7 GeV/c as a function of the laboratory angle. The detected charged particles are produced in the decay of the D mesons via $D^{\pm} \rightarrow K^{\mp}\pi^{+}\pi^{-}$.

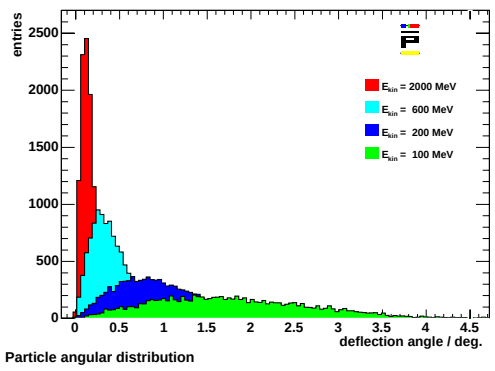

Figure 5.5: Small-angle scattering spectrum of protons in 400 μm of Si for various proton energies.

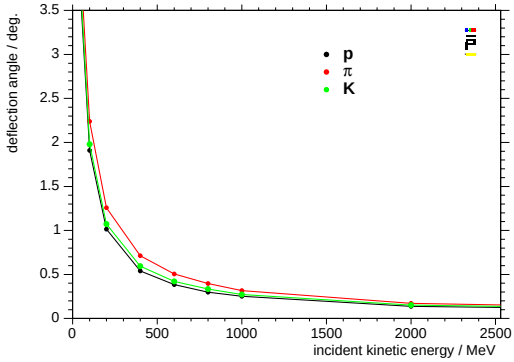

Figure 5.6: Average deflection due to small-angle scattering as a function of incident energy for protons, kaons, and pions in 400 μm of Si.

the arrangement was approximated by a standard deviation of $\sigma = d/\sqrt{12}$ where d is the pixel size in either direction independently. In reality, charge sharing among a number of neighboring cells will likely result in a somewhat better resolution than assumed by geometry alone. The beam pipe was assumed to consist of BeAl alloy with a thickness of only 500 μm. The barrel structure has about 7.2 million pixels while the forward wheels add another 2 million. It was shown that the nominal resolution of $\sigma_\phi = 25\,\mu$m and $\sigma_z = 100\,\mu$m for the first three barrel layers, $\sigma_\phi = 100\,\mu$m and $\sigma_z = 25\,\mu$m for the outer two barrel layers (chip readout turned by 90°) and $\sigma_\phi = \sigma_z = 50\,\mu$m for the disks is sufficient to allow spatial single-track resolution of $\sigma_D = 50\,\mu$m in transverse and $\sigma_z = 85\,\mu$m in longitudinal directions. These values are within the design values requested for the D meson tagging and additional scattering will contribute to the resolution. This issue needs further consideration incorporating more realistic designs, geometries, and knowledge about the detector. For example, the 200 μm sensors have not yet been equipped with readout chips. This is mandatory in a scenario where present-day detector layouts are used where a readout chip of about the same thickness is bump-bonded to each sensor. The detector support structure, cabling, and cooling fur-

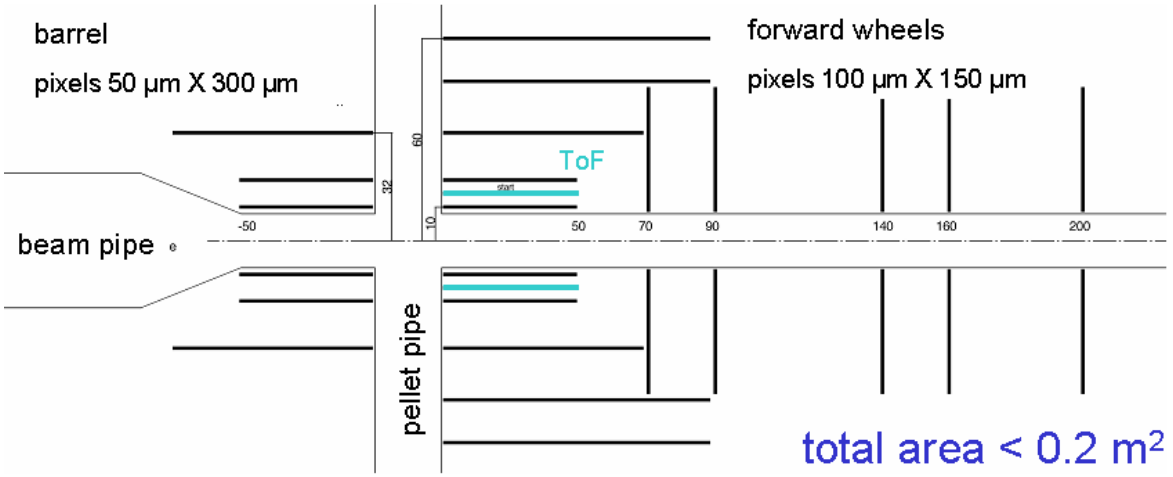

Figure 5.7: Sketch of the detector layout as used in the conceptual design of PANDA.

ther add to the material budget. The combined effects have been successively incorporated into the Monte Carlo treatment of the detector setup and their influence has been systematically investigated.

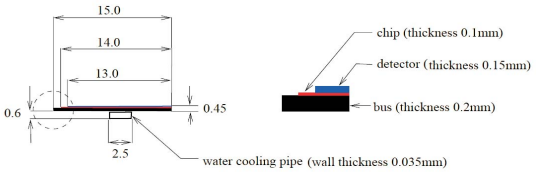

Figure 5.8: Sketch of the detector layout as used in a later stage of the PANDA simulation. The figure shows the cross section of one of the detector staves. The staves are used in the arrangement of the barrel part. The forward disks as shown in Fig. 5.9.

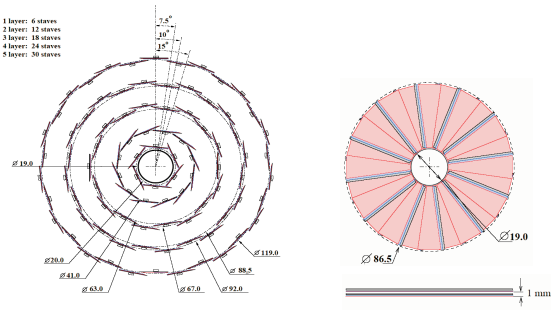

Figure 5.9: Sketch of the detector layout as used in a later stage of the PANDA simulation. 90 of the staves (as shown in Fig. 5.8) are used in the arrangement of the barrel part. The same type of staves arranged into wedge-shaped structures are used in the design of the forward disks, as shown on the right side.

Fig. 5.8 shows a schematic drawing of the cross section of a vertex detector stave as incorporated into the next generation of simulations. The thickness of the sensor and the readout chip have been chosen to match the values of the ALICE detector design and are smaller than previously used. The Monte Carlo representation of the detector now contains support structures and cooling as well as a bus structure as an equivalent for the readout and detector utilities. The total material budget which a traversing particle meets is not homogeneously distributed and ranges between 0.96% and 3.6% radiation lengths. A cross section through the barrel structure is shown in Fig. 5.9. The right hand side shows a disk structure made from similar sensor staves in wedge shape. Fig. 5.10 is an view of the full detector.

Results from the analysis of a simulation using the arrangement shown in Fig. 5.10, without the target pipe, are summarized in Fig. 5.11. The pixel sizes used are $(400 \times 50)\,\mu\text{m}^2$ and $(150 \times 100)\,\mu\text{m}^2$ in the forward direction. Here, the data describe muons originating from the decay of a of $\psi(3770)$ resonance produced in $\bar{\text{p}}\text{p}$ annihilation. The variation in the resolution as a function of polar angle both for the transverse (D_0) as well as the longitudinal (Z_0) resolution is obvious. The effect stems from the rather large variation of massive material that has to be penetrated by the particles depending on their emission angle. This is one of the shortcomings of the depicted design independent of version and orientation of the individual pixel lay-

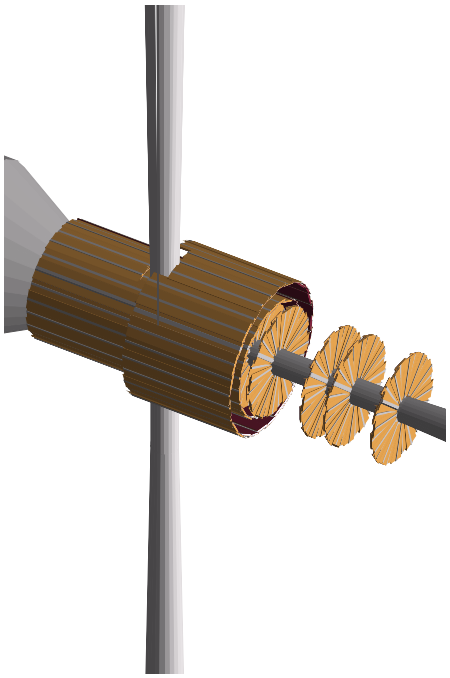

Figure 5.10: View of the detector structure as outlined in the text.

ers. Further improvements in the layouts are described below. The considerable error bars in the very backward region are due to the lack of statistics for the reaction. Here, muons carry a large longitudinal momentum component from the center-of-mass motion. The calculation does not yet include the pipes for the target in- and outlet which will add further material at angles around 90° and result in smaller efficiencies for particle tracking in the MVD. For particles penetrating the five detector layers perpendicular to the sensor orientation, resolutions better than 20 μm can be achieved.

5.4 Basic Requirements

The basic requirements for the vertex detector can be deduced from the physics goals of $\overline{\mathsf{P}}$ANDA, the simulation results, and the overall layout of the experiment. These include:

Spatial Resolution The vertex detector should have a spatial resolution better than 100 μm. One of the most demanding tasks is the recognition of $D\overline{D}$ events in standalone mode as decay products of $c\bar{c}$ resonances not much heavier than the meson pair. Therefore, excellent resolution is required along the beam (z) direction. The resolution in r/ϕ direction should not be significantly inferior to the z-direction.

Material Budget A five-layer pixel structure would add too much material and the fifth layer would does not contribute to the track resolution. In addition, conversion in the layers would generate an excessive amount of photon conversion into e^+e^- pairs which must be considered to be background for the observation of reactions such as Dalitz decays, leptonic decays of charmed mesons and e^+e^- decays of vector mesons, for example in nuclear matter. Therefore, the inner three layers are planned to be constructed from pixel sensors, the outer two from double-sided strip detectors.

Minimized Photon Conversion The conversion is in principle connected to the material budget and further influenced by the charge number of the material used in the construction. High-Z materials, like lead or gold, will contribute more to the photon-to-e^+e^- showers than low-Z material like carbon fiber.

In view of the last two arguments, the contribution of the vertex detector to the total material budget, in units of radiation length, should be kept below $X/X_0 = 4\%$.

Geometry of the Barrel and the Disks The minimum radius of the innermost layer of the vertex detector is determined by the beam pipe for which 1 cm was defined. The outer radius of 14 cm defines the maximum, limited by the straw detector inner holding structure. Also, the minimal radius is defined by the beam pipe which must allow sufficient pumping power to generate a gas gradient from the target to the downstream exit where pumps can be positioned. With $\overline{\mathsf{P}}$ANDA being a fixed-target experiment, the beam momentum will cause an excess of particles in the forward hemisphere. The region around the beam pipe is important for the complete reconstruction of final states.

Readout Speed The readout has to be different from other experiments in order to allow continuous data collection from the detector without triggering. Multiplicities are expected to be small with a maximum of 16 charged particles as estimated in Sec. 11.2. The more serious aspect of data extraction from the vertex detector is the high interaction rates, in excess of 10^7 annihilations per second. Several elements have to be considered as possible bot-

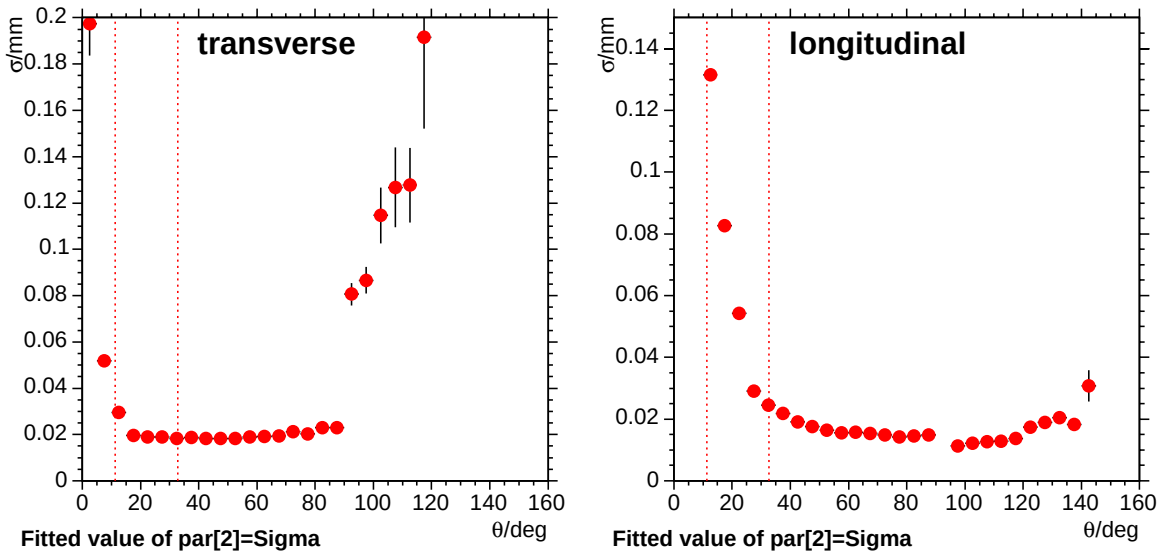

Figure 5.11: Resolution of the transverse and longitudinal coordinates, respectively, as simulated for the reaction $\bar{p}p \rightarrow \psi(3770) \rightarrow \mu^+\mu^-$. The vertex detector setup used in the simulation is from the previous figure, but without a target pipe. See text for details.

tlenecks in the readout process:
Each pixel has an analog deadtime determined by the deposited charge of a traversing particle and the feedback current of the preamplifier. The latter defines the settling time necessary to return to the baseline following a signal and to be selected within certain limits. Typical values are around $1\,\mu s$ for minimum-ionizing particles. This also determines the double-pulse resolution of a pixel.
The readout deadtime depends on the number of hits in a column. In the ATLAS design, each hit needs two clock cycles to be scanned by a common readout device. Data from two neighboring columns are read by one scanner. A pixel that contains a hit is busy and blocked until it has been read out. Therefore, the length of a column must be matched to the clock cycle (40 MHz at ATLAS, for example) and the number of hits in the column per time unit. The events of a double-column have to be stored in buffers for readout. Buffer overflow must be avoided. The same holds for the readout of a full chip and the readout of each control module collecting the data of all readout chips of a sensor.

5.5 Technological Options and Research

The layout of the PANDA MVD have been described in the previous chapters. The choice of technology and the layout of the parts are a matter of ongoing discussion and research. The basic options are summarized in Fig. 5.12. Fully evolved off-the-shelf options have been proven functional in high-energy physics experiments or are presently being mounted at the LHC. First, a choice will have to be made between monolithic and hybrid technology. The MAPS and DEPFET sensors offer the advantage of much smaller material budget which is of particular interest for PANDA, as discussed before. However, radiation hardness and readout speed are not yet competitive. Therefore, the default choice is the hybrid technology. Here, LHC type sensors and front-end chips are available and will be tested in view of their applicability in the PANDA environment. In parallel, a PANDA-specific custom solution will be studied for the front-end on account of specific differences from the LHC requirements concerning readout. Furthermore, research efforts will be put into novel materials for the pixel sensors which offer the prospect of superior performance in view of radiation hardness and signal properties.

The options will be discussed in the following chapters. The currently available pixel detectors and those under construction will be scrutinized. In addition, the present state of monolithic active pixel sensor technologies will be evaluated. Strip detectors as the primary choice for the outer layers will be described. After that, plans and strategies for R&D will be discussed in detail.

At the time of this report, a final decision on the vertex detector design appears premature in view of the rapid developments in the field of microelectronics. This is reflected in the chapters on R&D issues.

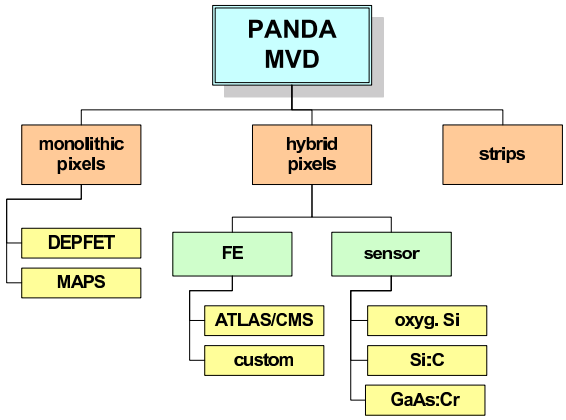

Figure 5.12: Chart of vertex detector options considered in the PANDA MVD project.

Some requirements are imposed by the physics goals and the data acquisition architecture such as the triggerless readout, spatial resolution, and need for minimized material budgets. Other requirements are suggested by projected changes in the Si chip manufacturing procedures. At present, Si chips require larger investments. This may well change with time as indicated below. Other, still more challenging options for novel sensor materials with improved properties are also given room because they show promising features that may prove superior in the future and shall be followed up to the final choice of technology.

The default option for the MVD at present is an adoption of hybrid active pixel technology developed for the LHC experiments as discussed in Sec. 5.5.1. This includes standard silicon sensors as well as front-end electronics. The outer layers will be covered using silicon strip detectors. Even though adopting standard technology, this option still needs R&D for the special case of PANDA as outlined in Sec. 5.5.4.4. R&D is under way for a custom option of the MVD sensors and readout in PANDA, as outlined in Sec. 5.5.1.2. The option builds on technology changes which are presently being introduced to the commercial chip manufacturing processes and which will allow the development of more specialized and superior features for pixel readout. The part of this report devoted to future materials for pixel sensors, Sec. 5.5.2, outlines R&D on GaAs:Cr and SiC. Both materials exhibit promising properties for the manufacturing of sensors with favorable performance characteristics and may replace the Si-based pixel matrices in the future.

5.5.1 Hybrid Active Pixel Detectors

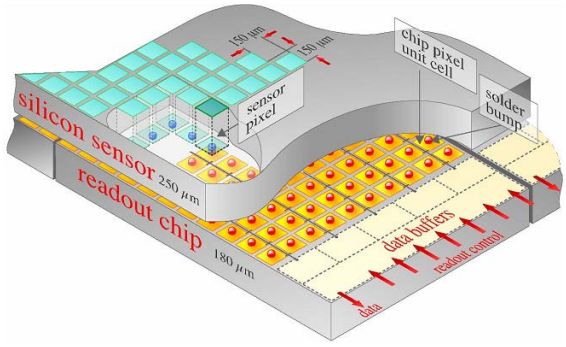

Figure 5.13: Schematic view of a hybrid pixel detector, from [8].

Hybrid pixel detectors have been widely used as micro vertex detectors in a variety of medium or high energy physics projects. The basic component is a pixel module usually consisting of a large sensor, a number of front-end ASICs, one or more controller chips, and a high density interconnection for the signal and power traces between the chips and the external readout system (Fig. 5.13). Both the sensor and the readout electronics can be developed independently from each other within certain margins.

Two different strategies are possible. Either, one of the existing pixel detector systems is adopted to the needs of the experiment or the front end electronics, the sensor, or both are completely redesigned.

5.5.1.1 Adoption of an LHC Pixel Detector Concept

The development of hybrid pixel detectors is mainly driven by three large LHC experiments, ALICE [5], ATLAS [3] and CMS [4] which independently developed the micro vertex detector systems. Common to the experiments is the use of silicon as basic sensor material. Several techniques, like the oxygenation of silicon [9] or the use of n^+-on-n sensors [10, 11], were developed in order to improve the radiation tolerance of silicon sensors up to the maximum radiation dose of $1 \cdot 10^{15}\, n_{eq}/\mathrm{cm}^2$, sufficient both for the LHC experiments and for PANDA.

The three pixel modules have a longitudinal shape with sensor dimensions from $(12.8 \times 70)\,\mathrm{mm}^2$ up to $(20 \times 60)\,\mathrm{mm}^2$ with a thickness between $200\,\mu$m and $250\,\mu$m. The pixel cells have dimensions of approx. $(50 \times 400)\,\mu\mathrm{m}^2$ for ALICE and ATLAS and $(100 \times 150)\,\mu\mathrm{m}^2$ for CMS (see Table 5.3).

exp.	sensor size [mm^3]	pixel size [μm^2]	type
ALICE	12.8×70×0.2	50×425	p-in-n
ATLAS	18.6×63×0.25	50×400	n-in-n
CMS	18.6×66×0.28	100×150	n-in-n

Table 5.3: Overview of the different silicon sensors of the LHC experiments [3, 4, 5].

Apart from the development of a radiation-tolerant sensor, the design of new front-end electronics was one of the main R&D aspects of the LHC experiments. The front-end chip has to allow for a good spatial resolution, mainly determined by the pixel geometry, a time resolution on the order of 40 MHz, a medium power consumption to reduce the cooling load, and a medium radiation tolerance. In addition, a minimum in charge resolution is desirable for particle identification of low momentum particles and an improvement of the spatial resolution for double hits.

The radiation tolerance of the three different front-end types is determined by the use of a 0.25 μm process technology which proved to be radiation tolerant if special design rules are observed [12, 13, 14, 15]. A summary of the other $\overline{\text{P}}$ANDA-relevant features of the front-end chips is listed in Table 5.4.

The ALICE1LHCB chip has the largest pixel cell, the highest power consumption, and the lowest operation speed. Therefore, it is not the best choice for the $\overline{\text{P}}$ANDA experiment.

The two other front-end chips have comparable power consumption and ability to measure charge either via time over threshold (ToT) or directly via an analogue signal. The main difference between the CMS and ATLAS pixel detectors is the geometry. The ATLAS pixel detector is optimized to measure the tracks of the particles with the highest resolution in the r/ϕ direction and with a broader resolution in the z direction. The orientation had to be changed to provide the best resolution in z for the $\overline{\text{P}}$ANDA experiment. The CMS pixel detector gives nearly the same spatial resolution in both directions. Therefore, a modification of the orientation would not be necessary but the resolution is worse than the resolution of the ATLAS module in the small pixel direction.

The material budget of the pixel layers can be estimated from the values found for ALICE:

- Silicon sensor (200 μm thick): 0.21% X_0
- Front-end chip (150 μm thick): 0.16% X_0
- Multilayer kapton bus with Al (300 μm thick): 0.30% X_0
- CF support structure (200 μm thick): 0.1% X_0
- Cooling: 0.17% X_0

This leads to a total amount of 0.94% X_0 per layer [5]. Reducing the front-end chip thickness (100 μm) and the silicon sensor thickness (150 μm) a total 0.84% X_0 value could be obtained. In principle, the thinning of the front-end chip is easier because the active volume is limited to a tiny fraction (a few microns) of the wafer. The thinning of the sensor is more delicate since a smaller sensor thickness determines a reduction of the signal amplitude and worsens the signal-to-noise ratio. Additionally, thinner components are more difficult to handle and the yield of bump-bonding should also be assessed. The thickness used in ALICE serves as a reference solution while thinner materials may be explored for a further improvement of the performance of the pixel system.

To adopt an existing design like ATLAS or CMS has the advantage that the systems are tested. A new development of new front-end electronics for $\overline{\text{P}}$ANDA is not necessary. The solution has the disadvantage that the front-end chips are not optimized for the requirements of the micro-vertex detector. There are two major differences between $\overline{\text{P}}$ANDA and the LHC experiments:

- The triggerless readout of the hits

  Both front-end chips from ATLAS and CMS offer the possibility to work in a self triggered mode which enables the chips to be used in an triggerless experiment. This feature is widely used in the ATLAS chip to perform source scans with γ-sources. For the CMS chip the feature still has to be tested. Unfortunately, the module controller chip used by ATLAS is not able to run in a completely triggerless mode. Therefore, a redesign of this chip is necessary.

- The need to reduce the material budget

  Due to the high number of low momentum particles, the requirements for the radiation length of the detector are more strict than for the LHC experiments. Therefore, steps have to be taken to reduce the material budget. It is necessary to thin down the electronics and the sensor as far as possible and still achieve an acceptable bump-bonding yield. In addition the geometry of the MVD has to be optimized to reduce the number of particles traversing the modules at

front-end chip	chip size [mm^2]	pixels	readout	freq. [MHz]	power [W/cm^2]	status
ALICE1LHCB (ALICE)	15.6×13.7	8 192	binary	10	0.51	in production
front-end -I 3(ATLAS)	11×7.3	2 880	ToT	40	0.33	in production
PSI 46 (CMS)	9.8×7.9	4 160	analog	40	< 0.3	end of prototyping

Table 5.4: Overview of the different front-end electronics of the LHC experiments [3, 4, 5] The PSI46/CMS is not yet the final version.

a small angle. New sensor sizes are necessary with only ten or even eight front-end chips for data taking.

5.5.1.2 Custom Readout Electronics

The reuse of sensors and front-end electronics developed for other applications would prevent the full customization of the MVD detector, thereby leading to sub-optimal performance. The size of the ATLAS pixels, for instance, determines an asymmetric spatial resolution (see also Sec. 5.5.1) complicating the layout of the barrel modules. In addition, the adoption of an off-the-shelf solution may require the use of two different pixel cells. As discussed in Sec. 5.3, to obtain the nominal resolution in $\overline{\text{P}}$ANDA, two kinds of pixels with different geometry have been used in the simulations: $(50 \times 400)\,\mu\text{m}^2$ (ATLAS-like) along the beam axis for the barrel, and $(100 \times 150)\,\mu\text{m}^2$ (CMS-like) in radial arrangement for the disks. In practice, such an approach would require to incorporate two systems with different readout architectures. Additionally, the analog readout of existing systems is optimized for a high-energy physics applications where basically all particles are minimum ionizing. Hence, the dynamic range of the front-end may not be suitable where a large number of low-momentum particles is expected. Finally, the capability of time-tagged events with a resolution as high as possible would be beneficial in a triggerless environment. The development of a custom solution for the sensor and the front-end electronics is considered to be a very promising alternative.

In a hybrid approach, the size of the pixel cell is usually a trade-off between two conflicting requirements. Maximum spatial resolution calls for small pixel dimensions. However, the front-end electronics must fit into the same area as the sensing element. Therefore, sufficient space has to accommodate the required signal processing. In addition, with a bigger pixel less power density is necessary for functionalities in the front-end electronics. A possible drawback of bigger pixels is that they have a higher leakage current. However, the impact of the currents on the noise can be kept under control by choosing an adequate shaping time. In contrast, reducing the surface of the pixel increases the perimeter-to-area ratio and the input capacitance which is dominated by the inter-cell capacitance. As a consequence, increasing the granularity of the sensor beyond the necessity may deteriorate the system performance. On the basis of the above arguments, it is proposed to investigate a solution based on a unique type of sensor where the individual pixels have a maximum area of $(100 \times 100)\,\mu\text{m}^2$. This choice represents an acceptable compromise between the dimensions of the two simulated geometries, CMS and ATLAS, and should lead to a sensor which is well suited for the barrel and the forward disks. The small cell size may be accomplished using a smaller feature size on the readout chip, as described in the following.

Front-end architecture

In the scenario of a custom development, a new front-end chip has to be developed in conjunction with the sensor. As in any hybrid pixel system, this Application Specific Integrated Circuit (ASIC) will have a matrix of readout elements that will match the sensor matrix. The front-end chip has to provide two basic functions:

- Identifying the hits, associating them with a timestamp
- Measuring the hit charge, in order to allow particle identification via $\text{d}E/\text{d}x$ measurement.

As explained in Table 5.4, pixel chips with analog readout have been designed for the ATLAS and CMS experiment at the LHC and for the BTeV experiment at the Tevatron at Fermilab. In the ATLAS approach, the analog information is preserved through a time-over-threshold (ToT) measurement, while in the BTeV design a 3-bit flash ADC has been introduced after the shaper. In both circuits, the digitization occurs at the pixel level. In the

CMS chip, the analog value is sampled and held locally and then digitized outside the pixel cell. In case of PANDA, a 7-bit digitization would probably be sufficient to provide an adequate $\mathrm{d}E/\mathrm{d}x$ measurement. With a pixel size of $100 \times 100\,\mu\mathrm{m}^2$ and a power budget of $0.5\,W/cm^2$ (which is the same as in the ATLAS chip), a power of about $50\,\mu\mathrm{W}/pixel$ results. In these conditions it is very difficult to integrate a fast ADC at the pixel level, and two options are left:

- Performing locally a slow digitization
- Sampling locally and digitizing outside the cell with a faster ADC.

The high granularity of the system leads to an estimated event rate of the order of 10 kHz per pixel. Assuming a reference clock of 50 MHz, a 7-bit digitization using, for instance, a ToT approach would require 2.56 μs. As a baseline solution, we chose to perform the digitization locally via ToT. This approach also has the advantage that it does not require the transmission of analog information outside the pixel, and this can increase the robustness of the system. In the triggerless environment of PANDA, only the master clock is distributed to the pixel chip. The ASIC must therefore provide timestamp information, in order to allow the reconstruction of the event. A first concept of a possible architecture is depicted in Fig. 5.14.

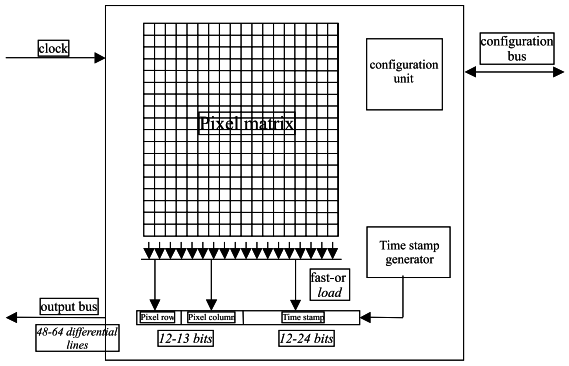

Figure 5.14: A possible architecture of the pixel front-end chip.

In this approach, a global timestamp generator provides the timing information. When a hit is detected, this information is latched in registers located at the end of each column and an End of Column (EoC) logic takes care for associating the pixel address to the correct timestamp. It must be noted that for each event a considerable amount of information must be sent out of the chip. Given the limited space available for the output connections, at most only one event can be send per clock cycle and a clever zero-suppression and buffering scheme must be implemented on board. A careful optimization of the chip architecture at the system level will clearly be the focus of the first R&D stage.

Technology choice

In recent years, deep-submicron CMOS processes have become the standard solution for the implementation of radiation-tolerant custom integrated circuits for High Energy Physics experiments. It is therefore natural that a main-stream CMOS technology is chosen for the production of the front-end chip of our application. At the time of writing two options can be considered for the PANDA MVD ASIC: 0.25 μm and 0.13 μm CMOS. The 0.25 μm process is based on heavily doped wafers, having a bulk resistivity of about 10 mΩ/cm and a high resistivity epitaxial layer on top of it. The circuits fabricated in this technology achieve a very good resistance to ionizing radiation, provided that Enclosed Layout Transistors (ELTs) are systematically employed in the design. The use of ELTs unfortunately leads to some area penalty. It can in fact be estimated that a circuit implemented using ELTs is about four times bigger than its counterpart realized with standard geometry devices. In addition, the need of ELTs prevents the use of commercial digital libraries. A key advantage of the 0.25 μm generation is that this process is well known and relatively cheap (the cost of a set of masks is about 150 k€). However, being a mature technology, there is the risk that it may phase out before PANDA reaches the production and installation stage. The 0.13 μm technology is based on lightly doped wafers with a high resistivity (about 10 Ω/cm). The main advantage of this process for our application is that it allows a higher component density and reduced power consumption. It is estimated that the same circuit block implemented in the 0.13 μm process occupies one fourth of the area required by its 0.25 μm equivalent. In addition, technological considerations suggest that the intrinsic radiation tolerance of a 0.13 μm process could be good enough so that ELT transistors would not be necessary any more. If this will be confirmed experimentally, the improvement with respect to a 0.25 μm process would be impressive. In this case, a circuit implemented in 0.13 μm with linear transistor would be sixteen times smaller than its 0.25 μm counterpart designed with ELTs [15]. It can be expected that for the same functionality a digital core in 0.13 μm would dissipate one fourth of the power. The 0.13 μm process is therefore our baseline choice,

since a pixel chip implemented in this technology would be far superior in performance compared to its 0.25 μm counterpart. Presently, the main disadvantage of the 0.13 μm technology is the cost that can be up to 600 k€ for a single set of masks. A detailed cost review is presented in Sec. 5.5.1.2.

Ancillary electronics
In the system, a number of functions are required besides the main signal processing chain. These include, to name just a few, monitoring of the vital parameters of the system, power regulation and power management, transmission of data to the outside world. In the pixel systems designed up to now, these tasks are carried out by additional electronics which is located close to the modules. Being inside the sensitive volume, these components need to be radiation tolerant and are usually implemented in the same technology as the main front-end IC. With the use of a 0.13 μm CMOS technology, some of these blocks could be incorporated directly into the front-end chip. Adding extra-functionality on the front-end, however, means to increase the dead area of the chip, so there is a limit to the amount of extra electronics that can be put on the main ASIC. On the other hand, these functions are more standard, so it is easier to re-use components developed for other experiments. Our strategy here would be to limit custom developments to a minimum. We expect that power management, detector control chips and optical transmission system can be re-used from other applications (e.g. the LHC experiments and their possible upgrades). On the basis of the experience of existing projects we may expect that besides the front-end chip a dedicated digital supervisor chip would be necessary to control the functionality of the modules.

Material budget and cooling
The material budget of the sensor layers is discussed in Sec. 5.5.1. Values as given by the thinnest solution of the LHC experiments, the ALICE pixel detector, are of the order of 1% X_0 per layer [5].

Since more processing and speed are requested in the front-end electronics compared to the standard solution at LHC, digital activity on the chip will be greater, increasing the power dissipation. Supposing that the charge analysis requires only ToT information, that no particular time resolution is necessary and that the occupancy of pixel cells is small so that the average readout time for occupied cells is within 10 μs, then the electronic power dissipation turns out to be in the same order as that of LHC experiments. Otherwise, the new digital activity required by the management of a 50 MHz master clock could increase the power request, but according to the properties of the new 0.13 μm technology quoted in the previous paragraphs, a realistic power dissipation provision could be of a few hundreds of mW/cm^2. Additionally, the use of a new structural composite material with high thermal conductivity could be an improvement to obtain an efficient cooling system, as the application of a micro-channel cooling [16, 17].

R&D activity The starting point of the R&D program will be to optimize the architecture of the front-end chip. A final choice of the pixel size must be made as soon as possible on the basis of realistic simulations. Once a particular pixel geometry has been selected, it will be possible to evaluate how much signal-processing can be put at the pixel level and how much has to be hosted at the periphery. Particular care has to be applied in this phase to system level modelling and simulation. The first stage of the work will allow the identification of critical building blocks that will be prototyped in a first submission through a multi-project wafer (MPW) run.

The second phase of the activity will concentrate on the design and production of a reduced-scale prototype. This chip will embed already the whole architectural functionality, but will have a reduced number of pixel cells in order to keep the cost at a manageable level.

The third stage foresees the fabrication of the final chip through a dedicated engineering run. Although we plan to re-use as much as possible of the ancillary components, a development of a digital supervisor chip seems unavoidable. The development of this chip will be performed in parallel with the one of the front-end ASIC. A sensor of the same type as those used in the LHC experiments is well suited for $\overline{\text{P}}$ANDA. The design of the sensor does not entail particular issues and can be done in a relatively short time scale. Since the development of the front-end chip will be a lengthy and critical process, it is very important that it is decoupled as much as possible from the development of the rest of the system. Preliminary studies on mechanics, cooling and bump–bonding on very thin sensors can be in fact carried out using dummy components.

The duration of the R&D studies (INFN Torino) and tests is planned for three years, with a time schedule which is very parallel to that of the baseline MVD option.

5.5.2 Future Materials for Pixel Sensors

In this chapter, specific options for the micro-vertex detector of PANDA which are not off-the-shelf but may be better suited to meet certain of the discussed selection criteria better than the hybrid design will be discussed. The proposed materials are very interesting as they do not suffer from radiation defects as much as silicon does. This holds for both SiC and GaAs:Cr sensors proposed here. Both materials require more R&D until they may reach applicability.

5.5.2.1 MVD with GaAs Sensor Matrix

Introduction
Semi-insulating Gallium Arsenide (SI GaAs) is known as a good alternative to Silicon (Si) and Germanium (Ge) in the production of semiconductor detectors. GaAs permits room temperature operation. The nuclear charge Z of GaAs is close to that of Ge, thus demonstrating the advantages of Ge detectors, namely high detection efficiency and robustness and avoiding the disadvantage of the low-temperature cooling.

The general characteristic features of GaAs in comparison with Si are presented in Table 5.5.

The detectors which are widely studied are p-i-n structures made on Liquid Encapsulated Czrochalski (LEC) grown semi-insulating Gallium Arsenide, SI GaAs:EL2, with EL2 centres as doping admixtures. LEC SI GaAs detectors have been shown to be radiation-hard to non-ionizing radiation up to 10^{15} particles/cm^2.

Another Gallium Arsenide material doped by diffusion Chromium, GaAs:Cr, has been developed in SIPT, Siberian Institute of Physics and Technology, in Tomsk (see references [18],[19],[20],[21], [22],[23],[24]). GaAs:Cr differs from SI GaAs by some features caused by its resistive structure, in particular by higher radiation hardness (see below). It also operates at room temperature like SI GaAs.

This is why GaAs:Cr has been proposed for producing the sensor matrix of the micro-vertex detector in PANDA. In this sub-section we discuss the comparison of GaAs:Cr and Si sensors for the MVD.

Sensor response
The response signal of a detector is determined by an amplitude of induced currents which, in turn, is determined by two factors: the ionization energy loss and the average drift velocity of carriers. Both

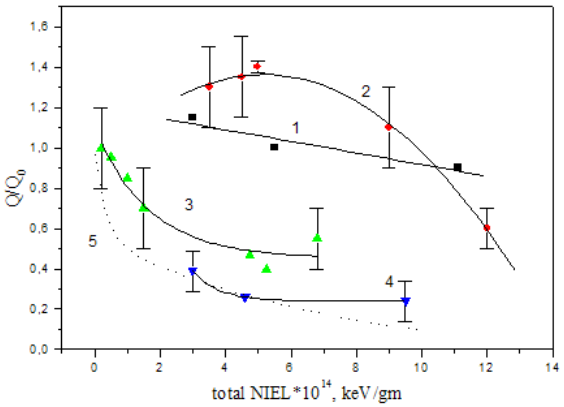

Figure 5.15: Percent change of the charge amplitude in GaAs:Cr *vs.* non-ionizing energy losses of particles: 1) 20 MeV neutrons; 2) 1 MeV neutrons; 3) 1 GeV protons; 4) 330 MeV π-mesons; 5) dependence for SI GaAs taken from [25].

factors are larger for GaAs (they can be found in Table 5.5), giving a signal response gain factor 5 for p-i-n GaAs structures and a gain factor 7 for the resistive structure of GaAs:Cr at a given thickness of the detector.

Cooling
For the silicon sensors, the exponential temperature dependence of leakage currents requires a refrigeration at temperatures well below 0°C. Just the contrary, Gallium Arsenide sensor performance is quite tolerant to the temperature deviations, and GaAs sensors operate at room temperature. A thermostabilization system is still necessary for evacuating heat from front-end electronics (a few W per module).

Radiation hardness
In comparison with pure silicon, Gallium Arsenide is much more ($\sim 10^2$) radiation resistant because the mean lifetime of the electron-hole pairs, t_0, in GaAs is quite tolerant to the radiation up to fluences of $\sim 10^{14}$ particles/cm^2, and then t_0 decreases slowly.

In pure silicon, t_0 undergoes catastrophic decrease as early as at $\sim 10^{12}$ particles/cm^2. However, a technology of oxygenated silicon has been found allowing to produce silicon which is rather radiation hard (see the ATLAS Notes on radiation hardness of silicon enriched by oxygen in ref. [26] and ref. [27]).

SI GaAs detectors have been shown to be radiation resistant to neutron irradiation for fluences up to

10^{15} n/cm^2 and to charge particle doses of a few Mrad (see [28, 29, 26, 30]).

The GaAs:Cr radiation hardness was studied in refs. [18, 20, 21, 22] and it appears to be even more radiation resistant than SI GaAs. GaAs:Cr keeps 50% CCE (Charge Collection Efficiency) at neutron fluences of (a few units)$\cdot 10^{15}$ neutrons/cm^2, at charge particle doses of a few Mrad and more than 90% CCE at gamma doses ≥ 50 Mrad.

In Fig. 5.15, the response amplitudes caused by non-ionizing energy loss (NIEL) are shown. They are presented for GaAs:Cr (solid curves 1,2,3,4) and for SI GaAs (dotted curve 5 taken from ref. [25]. As is seen, the radiation hardness of GaAs:Cr is in general higher than that of SI GaAs. This GaAs:Cr feature was indicated as early as in 1997 [31].

GaAs:Cr tolerance in gamma irradiation was tested up to the dose of 51 Mrad [32].

Table 5.6 taken from [18] represents particle fluences at which GaAs:Cr detectors still keep the 50%-level of the response signal. The dose rates which are very high are also indicated.

Multiple scattering
GaAs has a larger value of Z than Si, so the direct replacement of the silicon sensor by the GaAs sensor of the same thickness will cause an enlargement of the coordinate uncertainty in accordance with the dependence $\Delta\theta_z \sim \sqrt{z/X_0}$, where θ_z, z and X_0 are the multiple scattering angle, thickness along z-axis and radiation length of the medium, respectively. In the baseline option of MVD, the thickness of the silicon detector is 450 μm (250 μm Si sensor and 200 μm Si readout). The position inaccuracy on one detector plane of the MVD caused by multiple scattering is about 4 μm.

Replacing the 250 μm Si sensor by a 100 μm GaAs sensor, we can keep the same position inaccuracy on one plane of $\sim$ 4 μm and still have the advantage of the larger response from the sensor.

GaAs:Cr option of MVD
The idea of exploring gallium arsenide sensors with existing silicon FE electronics is not new. The GaAs matrix was successfully used in conjunction with the Medipix I chip with 64×64 channels; see, for example, ref. [33] where SI GaAs was used for the purpose of mammography. The choice of GaAs with respect to silicon (largely used in other applications and with a more established technique) was made because of the much better detection efficiency and a very good charge collection efficiency.

New development will be made with the Medipix II chip (256×256 channels) [34].

In the $\overline{\mathsf{P}}$ANDA MVD, the baseline option follows a design adapted from the LHC solutions, and it includes a silicon sensor matrix of about 250 μm in thickness, in which pixels have dimensions 50 μm × 400 μm and a 200 μm thick front-end readout part. Some amount of the material budget comes from a control chip.

In the GaAs option, the 250 μm thick silicon sensor matrix is replaced by a 100 μm thick matrix made of GaAs:Cr, Gallium Arsenide doped by Chromium, and the front-end electronics will be, generally, the same as in the baseline option. The conjunction of the GaAs:Cr matrix and the front-end part will be made in the technique of bump-bonding either with solder bumps or Indium bumps. The general layout will be very similar to the one shown in Fig. 5.13 for a conventional hybrid pixel detector. The front-end electronics is assumed to be of the same type as in the baseline option of MVD.

Such a design has a number of advantages which are discussed above and summarized below in Table 5.7.

R&D work
The first stage of the R&D studies of the hybrid pixel detector according to the formula (GaAs sensor⊕Si front-end) is planned for two years and it includes six basic directions:

1) selecting an appropriate front-end chip;
2) production and testing a number of 100 μm thick GaAs:Cr pixel matrices corresponding to the selected chip;
3) a study of making GaAs:Cr sensor matrices thinner down to 50 μm (SIPT, IHEP);
4) pixel-to-pixel bump bonding the GaAs:Cr matrix to the front-end chips (vendor);
5) tests of integrated modules (IHEP, Dresden TU, FZ Jülich);
6) simulations (Dresden TU, FZ Jülich, IHEP).

The duration of the first stage of the R&D studies is 24 months.

5.5.2.2 SiC as a New Detector Material

Currently the vertex detectors used in different particle and nuclear physics experiments are based on chips made from silicon as main material. As it is well known, these devices exhibit a deterioration in their performances due to the damage induced by the exposure to strong radiation rates. The research on radiation-harder devices is, therefore, of

Parameters	GaAs:Cr	Si
Energy ionization loss per MIP, MeV/cm	7.44	3.6
Ionization density, $\mathrm{d}N/\mathrm{d}x$ (pairs/μm)	177	90
Charge drift velocity, (cm/s)	$1{\cdot}10^7$	$3{\cdot}10^6$
Response (amplitude of induced current per MIP), μA	3	0.4
Energy threshold for electron-hole pair, eV	4.2	3.6
Charge carriers mobility, $\mathrm{cm}^2/\mathrm{Vs}$:		
electrons	8 500	1 500
holes	400	100
Specific weight, $\mathrm{g/cm}^3$	5.36	2.33
Atomic number	Ga 31, As 33	14

Table 5.5: Comparison of semi-conductor materials GaAs:Cr and Si.

Beam type	Accelerator	Irradiation rate (particles/cm^2 per hour	Final fluence at 50% signal degradation, $Q/Q^0 = 0.5$
20 MeV neutrons	Protvino I-100	$(4\text{-}5){\cdot}10^{12}$	$1.2{\cdot}10^{15}$
1 MeV neutrons	RAL ISIS	$(1.5\text{–}3){\cdot}10^{12}$	$1.0{\cdot}10^{15}$
1 GeV protons	Protvino booster	$5{\cdot}10^{13}$	$1.5{\cdot}10^{14}$
(0.8-1)GeV protons	Protvino booster	$5{\cdot}10^{14}$	$1.1{\cdot}10^{13}$
Mixed secondary beam	CERN SPS neutrino facility	$(2\text{–}4){\cdot}10^{12}$	$1.3{\cdot}10^{15}$

Table 5.6: The fluences and dose rates at which GaAs:Cr detectors keep the 50%-level of the response signal. Q^0 and Q are charge amplitudes before and after irradiation, respectively [18].

Item	**Default option** (250 μm Si sensor)$\oplus$ (200 μm front-end)	**GaAs:Cr option** ($\leq$ 100μm GaAs:Cr sensor)$\oplus$ (300 μm front-end)
Pixel size and module dimensions	$(50 \times 400)\,\mu\mathrm{m}^2$ $(18.6 \times 63.0)\,\mathrm{mm}^2$	$(50 \times 400)\,\mu\mathrm{m}^2$ $(18.6 \times 63.0)\mathrm{mm}^2$
Pixels/front-end chip	2 880	2 880
Pixels/module	46 080	46 080
Sensor matrix Operation temperature	(0–10)°C	room temperature
Radiation hardness	as described in TPR (presumably high level)	high level of tolerance for the sensor matrix
Effect of multiple scattering	$\Delta z \sim 4$ mm on one plane	$\Delta z \sim$ 4mm on one plane
Sensor response amplitude (arbitrary units)	1 (at 250 μm)	1.5–2.5 (at 100 μm)
Material budget	as described in TPR	reduction might be expected
Front-end electronics	as described in TPR	as described in TPR
Power consumption	$\sim$4 W per front-end module	$\sim$4 W per front-end module
Performance	development is expected for Panda requirements	R&D and prototyping needed for sensors and integration

Table 5.7: A summary of basic features of the baseline and GaAs:Cr options of MVD.

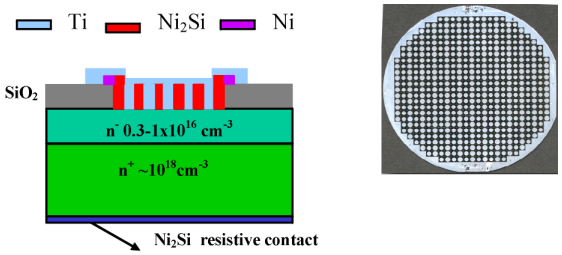

Figure 5.16: SiC 2" wafer, with Schottky diodes as in part b). Radii of single diodes are 0.5 and 0.25 *mum*.

big interest also for other branches of research and industry as for example aeronautics and space research. Among the materials recently considered also for industrial production of microelectronics components, Silicon-Carbide (SiC) has raised large interest. SiC is a semiconductor of big gap (3.0 eV) whose properties make it interesting for application involving high temperatures, powers and frequencies and for radiation detectors.

In all these applications this material is superior to other traditional semiconductor radiation detectors as Si and GaAs. The advantages of devices made of such material have not been totally exploited because of the lack of epitaxial substrates with a low defect density and reproducible electrical characteristics. In the last years, however, the research on growing and processing of SiC has undergone a notable development [35, 36, 37].

In particular the fabrication technique of Schottky diodes and of low defect epitaxial substrates has been developed. Moreover fundamental processes like the realization of resistive contacts, Schottky barriers, board structures and some specific processes for SiC have been studied and produced and are compared to the properties of other semiconductors in Table 5.8. The formation of the barrier in Schottky diodes is obtained through the growing of metals (Ti and Ni) on SiC for various temperatures and processes environments. This allows a better control of the height of the barrier.

SiC diodes allow to use high electrical voltages (up to 1 kV) generating uniform electric fields which, in the case of minimum ionising particles, should allow a better space and time resolution of the detector, compared to the silicon ones. Moreover these devices present very low leakage current even at very high reverse bias values and therefore they should have an optimum signal to noise ratio.

In addition SiC has a radiation hardness which is about two orders of magnitude bigger than silicon, in particular concerning the production of point-defects (interstitial and vacancy), which are responsible for the deterioration in the signal-to-noise ratio of the devices. Therefore it would be extremely interesting to compare experimentally the radiation hardness of SiC devices with standard Si, SiO and GaAs ones as well as their properties as radiation detectors.

5.5.3 Monolithic Active Pixel Sensors

In the last years new monolithic active pixel detectors were developed which have the unique feature that they combine the first preamplifier stage of the front-end electronic with the silicon sensor material on one substrate. This has the advantage that the noise of the system is vastly reduced which allows thin sensors with small signals. In addition very small pixel sizes with $(25 \times 25)\,\mu\mathrm{m}^2$ are possible and a low power consumption of these devices can be achieved.

In principle there are two approaches to combine sensor and electronics. The first starts with an electronic sensor and uses an epitaxial layer of silicon as active detection material like it is done by the IReS-LEPSI collaboration for the development of MAPS detectors [38]. Fig. 5.17 shows the operation principle of these type of detectors. An ionising particle generates electron hole pairs in the epitaxial layer. Without an electric field they recombine or move by thermal diffusion to the potential minimum of the n-well implantations. There the charge is collected and amplified by a series of n-mos transistors shielded by a p-well implantation from the epitaxial layer.

The second detector concept, DEPFET [40, 41], is based on a special silicon sensor with an additional FET structure on top for the amplification (Fig. 5.18). The full detector is sidewards depleted and a deep n-implantation creates a potential minimum underneath the FET (internal gate). The electrons generated by an ionizing particle drift to the potential minimum and accumulate there which causes a change in the current through the FET transistor like a change of the gate voltage. The collected charge is periodically removed out of the internal gate by a special clear contact at the side of the transistor. A differential current measurement before and after the clearance of the internal gate gives the information of the collected charge in the sensor.

Both solutions are compatible in means of power

	Si	GaAs	6H-SiC	4H-SiC	3C-SiC
Bandgap [eV]	1.1	1.42	3.0	3.2	2.3
Breakdown field $\times 10^{17}\,\mathrm{cm}^{-3}$ [MV/cm]	0.6	0.6	3.2	3	>1.5
Electron mobility $\times 10^{16}\,\mathrm{cm}^{-3}$ [cm^2/Vs]	1 100	6 000	370	800	750
Saturated electron drift velocity [cm/s]	10^7	10^7	2×10^7	2×10^7	2.5×10^7
Thermal conductivity [W/cm$K$]	1.5	0.5	4.9	4.9	5.0
Hole mobility $\times 10^{16}\,\mathrm{cm}^{-3}$ [cm^2/Vs]	420	320	90	115	40
Commercial wafers	12”	6”	1.375”	1.375”	none

Table 5.8: Comparison of the properties of various semiconductor materials.

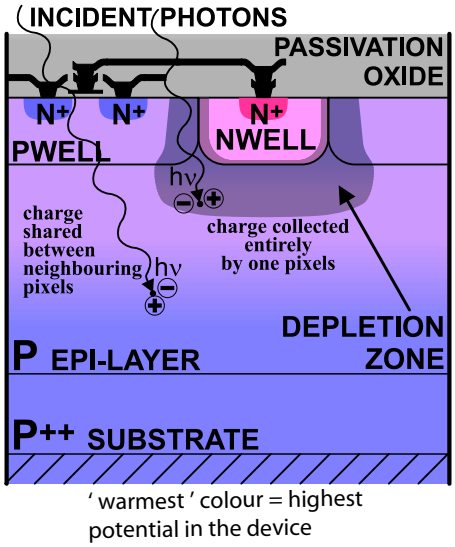

Figure 5.17: Schematic of a MAPS pixel cell, from [39].

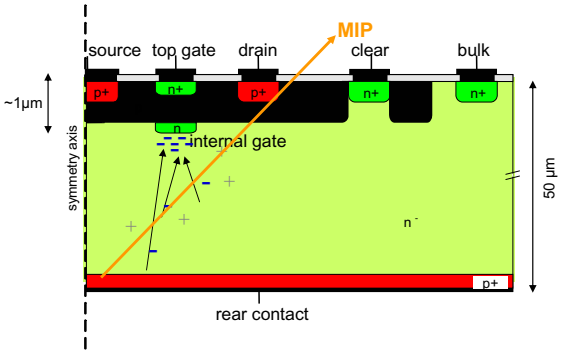

Figure 5.18: Schematic of a DEPFET pixel cell, from [41].

consumption, material thickness, spatial and charge resolution. The main difference between the two is the production process. The MAPS chips are produced in a commercially available standard CMOS process. This offers the advantage of a low price but the epitaxial layer which is used as active sensor material is not of a high importance for the vendor and therefore may be changed without notice. In contrast the DEPFET matrices are produced only by the HLL Munich who constantly optimize the production steps for the needs of the DEPFET project.

The drawback of both technologies is that the time resolution is not sufficient for the use in PANDA at the moment but several groups are working on these issues and some progress can be expected in the next few years. MAPS in addition have up to now little radiation hardness.

5.5.4 Double-sided Strip Sensors

The material budget in particular close to the interaction region is of major concern for many aspects of the PANDA physics program. Silicon strip detectors present an advantage in terms of material load per layer of the inner vertex device compared to silicon pixel detectors. They are comparably fast in readout and radiation tolerant.

5.5.4.1 Strip Detectors for Particle Tracking

Silicon strip detectors are widely used for particle tracking in nuclear and particle physics. Strip detectors are made from a layer of p type silicon

which carries an implemented strip structure made from of differently doped silicon, usually of n+ type. This yields the typical geometrical segmentation as sketched in Fig. 5.19. The strip pitch defines the geometrical resolution in one direction only. Typical values vary from 50 to 200 microns for state of the art modules. This leads to a geometrical resolution down to $\sigma \approx 16\,\mu$m. For $\overline{\text{P}}$ANDA it would be desirable to reach a resolution of $\approx 20\,\mu$m in z, as well as in the r/ϕ dimension.

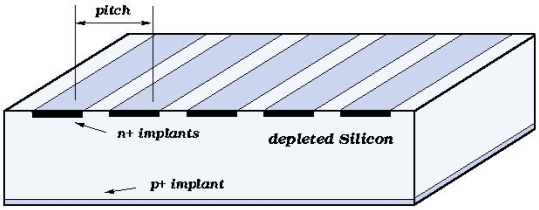

Figure 5.19: The segmentation of the sensor layer defines the geometrical resolution in one direction.

Microstrip detectors are often realized as double-sided devices. It is either possible to implement strip structures both on the n- and the p-side or to mount two single-sided devices back to back. The latter solution, however, doubles the material budget of a detector for a given spatial resolution and is therefore not acceptable in the present scope. Compared to a pixel detector, the double-sided device allows the hit point reconstruction with about half of the material load. The different charge carriers produced by the traversing particle drift towards the opposite surfaces along the field lines.

Microstrip detectors also provide the opportunity of energy loss measurement which can very helpful to distinguish in particular between pions and kaons below the detection threshold of the Cherenkov counters. For example, the vertexing device of BaBar [42] provides a stand-alone tracking for particles with low perpendicular momentum components ($p_\perp < 120\,MeV/c$). To have a sufficient signal it is necessary to combine a minimum number of hits belonging to a particle trajectory and correct the flight path through the sensor material. The $\mathrm{d}E/\mathrm{d}x$ measurement in an individual sensor is usually done via time-over-threshold digitization and can be a very important feature for $\overline{\text{P}}$ANDA.

5.5.4.2 State-of-the-Art Strip Devices

There is a large variety of silicon microstrip detectors for many different experiments. One of the advantages of strip detectors is the relatively easy adaptation of the basic parameters such as sensor thickness and strip pitch produced in standard technologies. Table 5.9 (see Refs. [43, 44, 45, 46] for details) lists the main features of strip sensors which have been used in other experiments so far.

The sensors can be shaped to match the needs of the application. Often, rectangular sensors are used e.g. in cylindrical layers surrounding the beam pipe. Then, neighbouring strip modules can be daisy-chained together to physically elongate the strips along the cylinder. In such a case the readout chip can be positioned at the very outside of the layer. There it can be used for a number of sensors. This will reduce the number of readout channels but it must be scrutinized in occupancy studies.

$\overline{\text{P}}$ANDA has a fixed target and most of the particles from various reactions are emitted in forward direction. The acceptance towards small polar angles cannot be covered efficiently by cylindrical layers surrounding the beam pipe. In addition, end cap-like structures are needed to minimize the scattering and conversion probabilities of traversing particles.

In order to cover the solid angle in an end cap structure it is possible to use trapezoidal sensors to avoid large overlapping regions of neighbouring modules. This can be done by lowering the pitch dimension e.g. as is planed for the CMS mini microstrip end caps [4]. The strip pitch reduces by 20% with a mean pitch width of $60\,\mu$m for the innermost module of the mini end cap. The inner width of this module is $w_i = 40.4\,$mm. The module widens over the module height of $h = 78.2\,$cm to an outer width of $w_i = 54.3\,$mm. The module is optimized to be placed at a radius of 218 mm from the beam-pipe. However, in $\overline{\text{P}}$ANDA we have to cover forward regions down to $r_i = (1-2)\,$cm inner radius with a microstrip end cap. This is not possible with available sensors developed by other experiments if minimal overlap between neighbouring sensor elements has to be achieved. To avoid large overlapping regions, the readout pitch has to decrease stronger toward the beam pipe. This induces a non-uniformity in resolution in r/ϕ depending on the radius which is unacceptable. Therefore a sensor layout adopted to $\overline{\text{P}}$ANDA will have to be developed.

exp.	sensor thickness/μm	pitch/μm	device (stereo angle)
CMS	320/500	80 − 130	single/double (6°)
BABAR	300 ± 30	50 − 210	double (90°)
Belle	300	75 (r/ϕ), 50 (z)	double
BTeV	300	100	single

Table 5.9: Strip detector standard parameters used by various experiments. Note that CMS uses two single-sided sensors mounted back-to-back.

5.5.4.3 Integration in MVD Layout

It is foreseen to replace the silicon pixel modules of the two outermost layers of the MVD barrel, as it has originally been conceived, with microstrip modules. The same holds for the forward end caps. The two disks mounted most forward shall also consist out of microstrip sensors. Since large overlapping regions of neighbouring detector modules in the forward wheels must be avoided, rectangular-shaped arrays of microstrip detectors may be used. Tracking can be done as in a typical forward spectrometer [46]. Small inactive regions in a specific layer will be adequately covered by the other layers in front or behind since the distance to the primary vertex is larger.

5.5.4.4 R&D for the Strip Detectors

For the microstrip component of the micro vertex detector, various restricting parameters have to be considered. Since $\overline{\text{P}}$ANDA will use a continuous beam, this puts higher demands on the readout architecture in order to reduce event mixing and dead time and requires changes in the readout scheme compared to many other experiments which are using microstrip detectors in a triggered readout mode.

- Radiation tolerance

  Strip detectors are produced in standard radiation-resistant technology. Therefore no problems are expected in withstanding the radiation background at least for the outer barrel layers, though more detailed studies in radiation loads are still necessary. Strip modules located near the beam pipe in the microstrip end cap have to deal with higher doses.

- Material budget

  It is of interest to reduce the sensor thickness as much as possible. In principle, there is no strong technological constraint which may rule out thinning down the sensor below 150 μm or even less. However, due to the readout of the strip along its longest dimension, the strip noise accumulation has to be considered. The design goal is to reach a signal-to-noise ratio of more than $S/N \geq 10$ even after some years of operation in the $\overline{\text{P}}$ANDA environment. This effect becomes more important if modules are daisy-chained together in the barrel part in order to have the readout chip at the end of the readout chain.

- Readout architecture

  The readout of the microstrip modules has to be as fast as possible and has to be done in an untriggered way. This is very much the same requirement as compared to the readout of the silicon pixel detector and requires an adaptation of commonly used readout architectures for strip devices.

5.5.5 Detector Support Structure

Light-weight detector support structures have been developed for a large number of vertex detector setups referred to in the present report. However, the mere adoption of a standard layout based on carbon fiber structures will be difficult due to the forward-backward asymmetry of a fixed-target experiment and the need for target inlet and outlet pipes. Quite possibly, mounting and support structures as well as cooling, detector infrastructure and readout can be optimized for the special requirements in $\overline{\text{P}}$ANDA and adopted to the overall detector layout. Novel materials as the ones mentioned before for cooling purposes [16, 17] will be taken into account. For this optimization procedure, support has been gained from the EU funds in the 6^{th} framework. A total of some 300 k€ has been granted to the partners from Catania, Jülich and Dresden for the engineering task.

5.6 Organisatorial Issues

The Fig. 5.20 presents an estimate for the timeline of the $\overline{\mathsf{P}}$ANDA MVD.

5.7 Summary

The present report demonstrates the current status of the MVD project for the $\overline{\mathsf{P}}$ANDA detector. The collection of ideas and options for the micro-tracking is grouped into three parts. While the available manpower suggests the adoption of proven state-of-the-art technology developed for the much bigger LHC experiments with a minimum of adoption to the special needs of the $\overline{\mathsf{P}}$ANDA environment, a second solution is presented that is even better suited to the task, but will require a somewhat higher budget. This solution, while still based on present-day technology, tries to take future developments in Si chip technology into account in the construction of a custom $\overline{\mathsf{P}}$ANDA vertex device. Presently, the monolithic active detector solutions that do not require a readout chip exhibit features that prohibit their use in vertex devices, which require high readout speeds and are subjected to high radiation levels. This may change within the next years because of ongoing R&D efforts which have been discussed. Several alternatives for sensor materials, which presently are under development at various institutions, part of which are members of $\overline{\mathsf{P}}$ANDA, are demonstrated. The timeline for the $\overline{\mathsf{P}}$ANDA project still leaves about three years for parallel R&D and careful observation of possibly promising developments, before a final scrutinizing summary has to lead to a selection of the technology for the $\overline{\mathsf{P}}$ANDA vertex detector.

References

[1] BaBar Technical Design Report, Technical report, SLAC, 1995.

[2] S. Aubert et al., Nucl. Inst. Meth. **A479**, 1 (2002).

[3] ATLAS Technical design report, Technical report.

[4] CMS Technical design report, Technical report.

[5] ALICE Technical Design Report, Technical report, 1999, CERN LHCC 99-12.

[6] S. Eidelman et al., Phys. Lett. **B592**, 1+ (2004), http://pdg.lbl.gov.

[7] $\overline{\mathsf{P}}$ANDA Conceptual Design Report, Technical report.

[8] T. Rohe, News from the CMS-Pixel Detector, 2003.

[9] G. Lindstrom et al., Nucl. Instrum. Meth. **A466**, 308 (2001).

[10] A. Dorokhov et al., Nucl. Instrum. Meth. **A530**, 71 (2004).

[11] I. Gorelov et al., Nucl. Instrum. Meth. **A489**, 202 (2002).

[12] N. Shiono et al., Japanese Journal of Applied Physics **22**, 1430 (1983).

[13] N. Saks et al., IEEE - Trans. on Nucl. Science **31**, 1249 (1984).

[14] W. Snoeys et al., Nucl. Instrum. Meth. **A439**, 349 (2000).

[15] G. Anelli et al., IEEE Trans. Nucl. Sci. **46**, 1690 (1999).

[16] J. Ha and G. Peterson, ASME Journal of heat transfer **120** (1998).

[17] L. Jiang, M. Wong, and Y. Zohar, Journal of Microelectromec. Syst. **8**, 35 (1999).

[18] V. B. Chmill et al., Nucl. Instrum. Meth. **A395**, 65 (1997).

[19] S. S. Khludkov et al., Nucl. Instrum. Meth. **A410**, 36 (1998).

[20] V. B. Chmil et al., Nucl. Instrum. Meth. **A410**, 54 (1998).

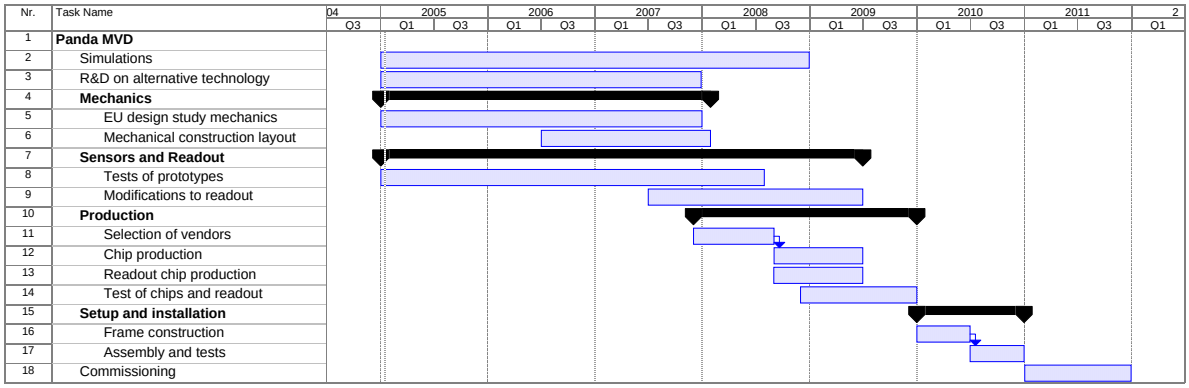

Figure 5.20: Projected time schedule for the $\overline{\text{P}}$ANDA vertex detector project including milestones.

[21] V. B. Chmil et al., Nucl. Instrum. Meth. **A409**, 247 (1998).

[22] A. I. Ayzenshtadt et al., Nucl. Instrum. Meth. **A448**, 188 (2000).

[23] A. I. Ayzenshtat et al., Nucl. Instrum. Meth. **A466**, 25 (2001).

[24] A. I. Ayzenshtat et al., Nucl. Instrum. Meth. **A494**, 120 (2002).

[25] A. Chilingarov, J. Meyer, and T. Sloan, Nucl. Instrum. Meth. **A395**, 35 (1997).

[26] See refs. therein, weblib.cern.ch/Home/ATLAS_Collection/ ATLAS.

[27] M. Alam et al., Nucl. Instrum. Meth. **A456**, 217 (2001).

[28] ATLAS Technical Proposal, Technical report, 1994, CERN/LHCC/94-43.

[29] M. Rogalla et al., Nucl. Instrum. Meth. **A395**, 45 (1997).

[30] S. P. Beaumont et al., Nucl. Instrum. Meth. **A321**, 172 (1992).

[31] R. Bates et al., Nucl. Instrum. Meth. **A392**, 269 (1997).

[32] Y. Arestov, GaAs:Cr sensor matrix for MVD, Talk at the PANDA Collab. Meeting, GSI, Darmstadt, June 2004.

[33] S. Amendolia et al., Nucl. Instrum. Meth. **A422**, 201 (1999).

[34] see http://medipix.web.cern.ch.

[35] F. Via et al., Microelectronic Engineering **60**, 269 (2002).

[36] F. Roccaforte et al., Appl. Phys. A **77**, 827 (2003).

[37] F. Roccaforte et al., Appl. Phys. Lett. **83**, 4181 (2003).

[38] G. Claus et al., Nucl. Instrum. Meth. **A465**, 120 (2000).

[39] G. Deptuch, W. Dulinski, Y. Gornushkin, C. Hu-Guo, and I. Valin, Nucl. Instrum. Meth. **A512**, 299 (2003).

[40] J. Kemmer and G. Lutz, Nucl. Instrum. Meth. **A253**, 365 (1987).

[41] R. H. Richter et al., Nucl. Instrum. Meth. **A511**, 250 (2003).

[42] C. Bozzi et al., Nucl. Instrum. Meth. **A473**, 7 (2001).

[43] J.-L. Agram et al., Nucl. Instrum. Meth. **A517**, 77 (2004).

[44] C. Bozzi et al., Nucl. Instrum. Meth. **A461**, 162 (2001).

[45] G. Alimonti et al., Nucl. Instrum. Meth. **A453**, 71 (2000).

[46] S. Kwan, Nucl. Instrum. Meth. **A511**, 48 (2003).

6 Tracking Detectors

This section describes technical solutions for detector elements fulfilling the outer tracking requirements in $\overline{\text{P}}$ANDA. Both, the cylindrical tracking devices for the central spectrometer and the planar tracking devices for the forward spectrometer are addressed. The inner (silicon) tracker is subject of a separate chapter.

6.1 Introduction

The tracking system has to provide efficient reconstruction of charged particle tracks by meeting the following requirements:

- almost full solid angle coverage around the interaction area;
- resolving complex pattern of multiple tracks;
- high spatial resolution for secondary vertices, $\sigma_{r\varphi} \sim 150\,\mu$m, $\sigma_z \sim 1$ mm;
- high momentum resolution of reconstructed trajectories, $\delta p/p \sim 1\%$;
- minimal detector material, $X_0 \sim 1\%$ for low multiple scattering and energy loss of passing tracks and suppression of secondary background production by interactions with the detector material;
- high rate capability of the detector and especially of its components in the forward region reaching values of $3 \cdot 10^4\,\text{cm}^{-2}\text{s}^{-1}$, fast electronic readout;
- resistance against ageing effects with the expected accumulated charge density on the level of 0.1–1 C/cm/year;
- operation in non-uniform magnetic field of the $\overline{\text{P}}$ANDA dipole magnet varying by up to 0.3 T along the wires of the forward tracking detectors.

This will be achieved by surrounding the vertex detector with a cylindrical low-mass device, and placing two sets of Multiwire Drift Chambers (MDCs) in the forward direction. Another set of 4 similar chambers will be placed downstream of the TS: 2 chambers will be located in front of and 2 after the dipole magnet.

For the cylindrical device inside the TS, two solutions could be chosen: a Straw Tube (STT) array, or a high-rate Time Projection Chamber (TPC). Owing to the beam characteristics of the HESR, the chamber should be operated in continuous mode, i.e. without gating. Therefore, with respect to the STT option the second solution poses a challenge both from the scientific and the technological point of view. On the other hand, this more complex detector would provide undeniable advantages: a low material TPC is the ideal device for tracking particles in 3-dimensional space since the material budget may be reduced. Furthermore, it could provide $\text{d}E/\text{d}x$ measurements which are extremely useful for particle identification. At present, the collaboration did not yet make a final decision. In the following sections, both options are described.

The challenge in constructing the forward drift chambers is the high count rate of particles peaked at the most forward angles due to the relativistic boost of the reaction products as well as due to small angle $\overline{\text{p}}$p elastic scattering. With the envisaged luminosity, the expected particle flux in the TS chambers in the vicinity of the 5 cm diameter beam pipe is about $2 \cdot 10^4\,\text{cm}^{-2}\text{s}^{-1}$. As a basis for the development of high rate tracking detectors, the chambers with quadratic cells are considered which were used in the "μTRV" experiment at PSI [1]. Here, the chambers worked stably in fluxes of positrons of $5 \cdot 10^4\,\text{cm}^{-2}\text{s}^{-1}$. A drawback of PSI chambers are relatively massive frames, needed to support the cathode wires. Therefore, as an alternative solution, drift chambers proposed by the Dubna group containing aluminized Mylar foils are considered instead of cathode wires. This option is especially important for the TS chambers due to the lack of space. An additional advantage of the Dubna chambers is the special shape of frames having the form of a closed semi-circle. The detection planes would consist of pairs of such frames put together along the common diameter. The frames could be mounted and dismounted without having to remove the beam-pipe.

6.2 Physics benchmarks

There are several decay channels, which impose increased demands to the tracker. They can be used as benchmark for PANDA tracking system.

One of them decays of D^0 and $D^{\pm}$ mesons, which can be produced via the reaction chains - $\overline{p}p \rightarrow \psi(3770) \rightarrow D\overline{D}$ or $\overline{\mathrm{p}}\mathrm{p} \rightarrow \psi(4040) \rightarrow D^{*+}D^{*-} \rightarrow D^0\pi^+\overline{D^0}\pi^-$. These mesons can be identified using only the charged final state particles, e.g. $D^0 \rightarrow K^{\mp}\pi^{\pm}$ or $D^{\pm} \rightarrow K^{\mp}\pi^{\pm}\pi^{\pm}$. As long as each of this reaction chains contain at least six charged particles in the final state, it is necessary to identify all of them in order to reconstruct invariant mass of $D\overline{D}$ pair. That requires the good single track efficiency and momentum resolution.

Some reaction, like $\overline{\mathrm{p}}\mathrm{p} \rightarrow \eta_c \rightarrow \phi\phi \rightarrow 4K$, requires the very good kaon identification, which could be provided by $\mathrm{d}E/\mathrm{d}x$ information from the tracker.

These benchmark reaction will be discussed in great details in the Chap. 13.

6.3 Central Tracker

The main tracking element of the PANDA spectrometer is the Central Tracker (CT). It will occupy a region inside the superconducting solenoid starting at a radial distance of 15 cm from the beam line, up to 42 cm. Along z this region extends $\approx$ 50 cm upstream and $\approx$ 100 cm downstream of the target. The actual dimensions will depend on the specific implementation. The magnetic field will have a strength of 2 T with a homogeneity of about 1% inside the tracking volume. The CT will provide measurements of track coordinates, in both x and y directions, with a resolution of about 150 μm, and along z of about 1 mm. The expected rate of events is 10^7 per second, with a multiplicity of 4–6 tracks per event. Therefore, drift-chamber devices with small cell sizes should be used.

In the following sections, two alternatives consisting of an straw tube tracker Sec. 6.4.1 or a time projection chamber with GEM readout will be considered.

6.4 Straw Tube Tracker

6.4.1 Overview

The Straw Tube Tracker (STT) will consist of a set of double-layers of 150 cm long drift tubes (straws) placed to fill the CT region. The first and the last double-layers will be aligned parallel to the beam axis, while the remaining layers will be arranged at skewed angles ranging from 2° to 3°, allowing z-coordinate reconstruction. In the region closer to the beam pipe the occupancy will be higher, due to curling low-momentum tracks. Therefore, the straw diameters will vary from 4 mm for the innermost tubes, to 6 mm for the central ones, and to 8 mm for the outmost layers. The final number of layers is not yet established. Monte Carlo simulations have been performed varying not only the cathode thickness but also the number of layers in order to find the setup that warrants the best momentum resolution at minimal material budget. Figure 6.1 shows a possibility with 11 double layers.

The momentum bite of the PANDA spectrometer ranges from a few hundred MeV/c, in the backward region, to some GeV/c in the forward region. This implies a compromise in the choice of technical solutions. According to the experience of other experiments, on the basis of software simulations, a detector with straw tube wall thickness of about 30 μm, anode wire diameter of 20 μm, and Argon

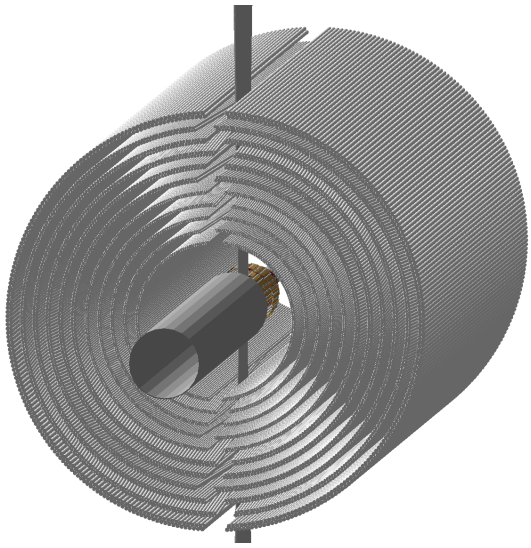

Figure 6.1: View of STT with 11 double layers.

based gas mixture is proposed. Software simulations have shown that the use of Helium based gas mixtures does not significantly reduce the density of the detector while considerably worsening the detector performance (see Fig. 6.2). In the following, possibilities fulfilling the physics requirements are described.

6.4.2 Straw Tubes

Straw tubes are gas-filled cylindrical tubes with a conductive inner layer as cathode containing a stretched sense wire along the cylinder axis. A high electric field between the wire and the outer conductor separates electrons and positive ions produced by a charged particle along its trajectory through the gas volume. Usually, the wire is on positive voltage of a few kV and collects the electrons while the ions drift toward the cathode. By choosing thin wires, with a diameter of few tens of μm, the electric field strength near the wire is high enough to start further gas ionization by electron collisions. Depending on the high voltage and the gas characteristics, an amplification of 10^4–10^5 of the primary charge signal is possible and sufficient for readout.

Information about the minimum particle track distance from the wire is obtained by measuring the drift time of the electrons arriving earliest. The relation between drift time and radial track-wire distance is given by the electron drift velocity which depends on specific gas parameters, electric, and magnetic field. Therefore, this fundamental relation has to be calibrated using reference tracks with known space and drift time information.

To obtain the track coordinate along the wire, several straw layers with crossing (skewed) tube orientations could be used like in the WASA or FINUDA detectors [2, 3]. Another method to obtain the z-coordinate is to use the length-dependent wire resistivity and comparing the charge amplitude readout at both straw ends (charge division method).

Straw tubes are made of thin metalized plastic foils by wrapping two long, thin strips (e.g. 12 μm thick, 16 mm wide mylar film) around a rotating mandrel and gluing the two half-overlapping strips together. Then, the cylindrical film tube can be stripped off. Nowadays, mass products of up to some hundred thousands of tubes of different film materials, thickness, diameters and lengths are available [4], and straws are widely used to build up large detector arrays (see Table 6.1).

High momentum resolution tracking requires minimal scattering and energy loss of passing tracks. In addition, the high particle rate up to 10^8 per second needs a high suppression of secondary background by interactions with the detector material. Table 6.2 lists the thickness (X) in radiation lengths (X_0) of the different components of a straw tube. The main contribution comes from the film thickness (d) with $X/X_0 \propto d$. If thinnest ($d \sim 30\,\mu$m) film tubes are used, a total detector thickness of $X/X_0 \simeq 1.3\%$ is feasible.

A straw tracker has several advantages compared to larger, conventional drift chambers due to the highly symmetric, cylindrical shape of a drift tube:

- robust electrostatic configuration. The shielding tube around each high voltage wire suppresses signal cross-talk and protects neighboring straws in case of a broken wire;
- robust mechanical stability if the straws are arranged in close-packed multi-layers;
- high tracking efficiency due to minimal dead zones ($\sim 1\%$) at tube ends and between neighboring straws if close-packed;
- high spatial resolution, $\sigma_{r\varphi} < 150\,\mu$m, depending on tube diameter and gas characteristics. Simple calibration of space-drift time relation due to the highly symmetric, cylindrical, isochronous shape;
- small radiation length, $X/X_0 \sim 0.05\%$ per tube, if straws with thinnest (30 μm) film tubes are used;

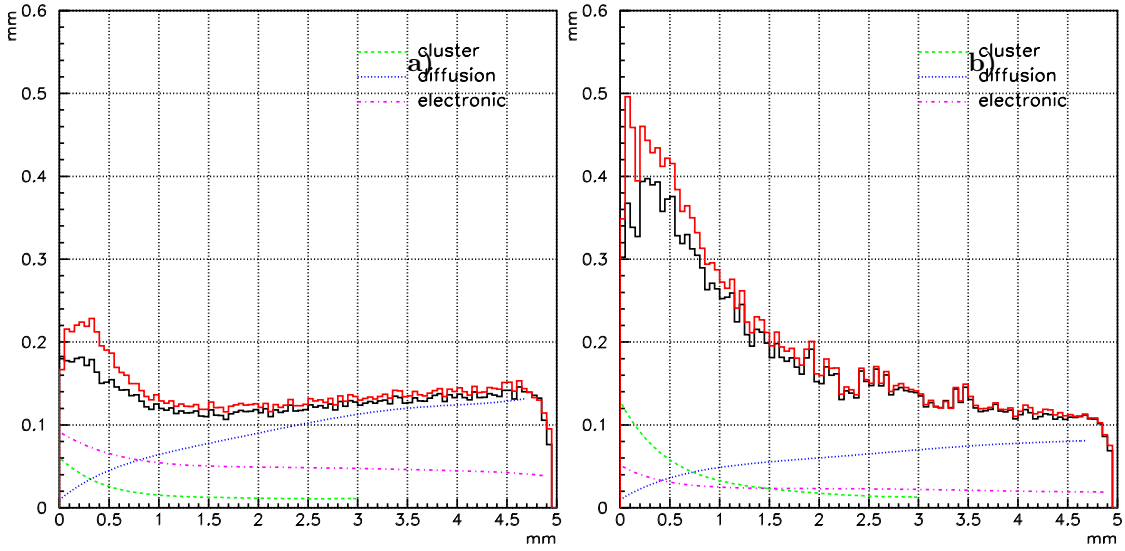

Figure 6.2: Space resolution of STT with different gas mixtures: a) Ar 90% CO_2 10%. b) He 90% i-C_4H_{10} 10%. The main contributions to the resolution are shown in different colors.

Experiment	Operation Start	Straw Properties			
		No	$L \times D \times d$ [mm^3]	Material	Resolution [μm]
WASA [2]	1998	1 738	$424 \times 4,6,8 \times 0.025$	Mylar	200($\sigma_{x,y}$) 500 (σ_z)
LHCb [5]	2008–09	60 000	2 500×5 × 0.1	Kapton	
BTeV [6]	2008–09	78 132	800×4 × 0.05	Kapton	
FINUDA [3]	1997	2 424	2 500×15 × 0.03	Mylar	150($\sigma_{x,y}$) 500 (σ_z)
COSY-TOF [7]	2005–06	3 100	1 050×10 × 0.03	Mylar	150($\sigma_{x,y,z}$)
COMPASS [8]	2002		3 000×6, 10 × 0.06	Kapton	200($\sigma_{x,y}$)

Table 6.1: Recent experiments using straw chambers. Straw dimensions include tube length (L), diameter (D) and tube wall thickness (d).

Element	Material/Thickness	X [mm]	X_0 [cm]	$\frac{X}{X_0}$
Film Tube	Mylar, 30μm	0.1	28.7	$3.5{\cdot}10^{-4}$
Film Tube	Kapton, 30μm	0.1	28.6	$3.5{\cdot}10^{-4}$
Coating	Al, 0.1 μm	$3{\times}10^{-4}$	8.9	$3.5{\cdot}10^{-6}$
Gas	Ar/CO_2 (80/20%, NTP)	7.85	11 933	$6.6{\cdot}10^{-5}$
Wire	W/Re, 20μm	$3{\cdot}10^{-5}$	0.35	$8.6{\times}10^{-6}$
			$\sum_{straw}$	$4.3{\cdot}10^{-4}$
			$\sum_{(11 double-layers)}$	0.009

Table 6.2: Mean thickness (in radiation lengths) of the different straw tube components for orthogonal incident tracks. The last number is the sum for 11 double layers which is one of the option discussed for a PANDA straw tracker.

- high rate capability can be improved by reducing the occupancy using smaller tube diameter and/or choosing a fast drift gas.

6.4.3 Measurement of z-coordinate

There are different methods to reconstruct the track coordinate (z) along the wire. For instance, several straw layers with crossing (skewed) tube orientation could be used like with the WASA or FINUDA detectors [2, 3]. The advantage of this method is that simple, relatively cheap electronics can be

used. Unfortunately, there are several serious drawbacks of this scheme. First of all, the geometry of skewed layers is rather complicated. It has a varying diameter along the tracker length and gaps between the tube ends which leads to geometrical inefficiencies. Secondly, due to the gaps, tubes cannot be glued together. Therefore, the tracker cannot be self-supporting and needs a massive side support. Thirdly, the reconstruction of the z-coordinate is complicated posing a difficulty for online triggering.

An alternative option to obtain the z-coordinate makes use of the charge division technique [9]. This method uses two-point charge splitting to identify the position of an ionizing event along the tube (see Fig. 6.3). In this case, two amplifiers at the two ends of a straw, are needed. Each preamplifier receives a fraction of the total charge. The relative position x of the event along the straw can be calculated as:

$$x = l\frac{Q_r}{Q_r + Q_l}$$

where l is the total length of the straw, Q_r is the charge collected at the right end and Q_l is the charge collected at the left end of the straw. The spatial resolution achievable with this method is typically 0.5–1% of the sensitive wire length [10]. For the $\overline{\mathsf{P}}$ANDA STT one can expect a spatial resolution of 7–15 mm. This is about 2–3 times worse than can be achieved using the geometry with skewed tubes. Another disadvantages of this scheme is it requires twice the number of electronics channels which need to register the amplitude of the signal.

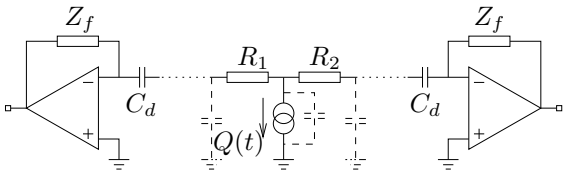

Figure 6.3: A scheme of a straw tube with charge amplifiers at both ends. The resistances R_1 and R_2 are proportional to the distances to both ends of the anode wire. C_d are decoupling capacitances. The current signal delivered by the detector is $Q(t)$. Impedances Z_f terminate the straw tube at both ends relative to the virtual ground through decoupling capacitors.

Nevertheless, the charge division method has advantages. First of all, it can provide the fast information about the track position which is very important for the online triggering. Secondly, the simpler detector geometry makes it possible to avoid a heavy mechanical frame. Finally, the number of electronics channels can be reduced by connecting the straws in pairs and by reading them only at one end albeit that this will worsen the spatial resolution by a factor of two.

A final decision on the method to be used will be taken after further R&D. Studies of the applicability of the charge division method are under way at Jülich.

	Mylar	Kapton
Young's modulus [N/mm^2]	4.500	2.400
Tensile strength [N/mm^2]	196	165
Moisture absorption	0.8%	4%

Table 6.3: Compilation of Mylar and Kapton properties.

6.4.4 Straw Cathode Material

Particle densities foreseen at $\overline{\mathsf{P}}$ANDA are similar to those of other experiments like LHCb and BTeV. Therefore, the tracking detector will adopt similar technical solutions. Straw tubes are normally made from thin plastic foils (polyester Mylar [11], polyimide Kapton [12]) coated with conducting layers (aluminum, copper. etc.). Copper coating has a very low resistivity ($\approx 0.1\,\Omega/\square$) and the unavoidable oxide that forms on the surface is conductive. Therefore, they show very good performance but are scarcely used due to the high cost. The aluminum conductivity is in principle similar to that of copper, but Al_2O_3 oxide has a high resistivity reducing the conductivity of the pure metal by a factor 10^8. Nevertheless, aluminum coating is less expensive and widely used.

Mylar has better mechanical properties than Kapton (see Table 6.3) and has a lower permeability. On the other hand, Kapton can be loaded with carbon resulting in a slightly conductive material (Kapton XC by DuPont). This is extremely useful for building robust straw tubes avoiding the risk of damaging the conductive coating. When the tubes are operated inside high radiation environments, discharges may evaporate any kind of coating. This is not the case with Kapton XC: the conducting property proceeds via the bulk material and cannot be easily damaged. Kapton XC is produced by DuPont in two types: Kapton 160XC, with a thickness of 40 μm and a resistivity of 200 $\Omega/\square$ and Kapton 100XC with a thickness of 25 μm and a resistivity of $5 \cdot 10^6\,\Omega/\square$. The high resistivity is not sufficient for a good signal transmission, and produce cross-talk among the tubes. In order to avoid this inconvenience, Kapton XC can be metalized

with very thin metallic layer, of the order of 1 000 Å, or can be laminated with a 12 μm thick layer of conductive material to have better electrical properties. Aluminum/copper coated tubes could be $\approx 60\,\mu$m thick (including adhesive) whilst laminated tubes would be $\approx 85\,\mu$m thick. At present, the different materials are investigated as solutions for the straw cathodes. Material samples from BTeV, LHCb and Pamela straw tubes are being tested to evaluate the characteristics of each one (see Table 6.4).

The setup installed at LNF, together with the BTeV local group, consist of a thermally insulated stainless steel box. The gas mixture, the temperature and the pressure can be varied and monitored constantly. Two load cells with online readout are located inside the box. Each cell holds a single strip at a typical straw tube mechanical tension of ≈ 200 g. It was verified that the strip tension varies with the percentage of CO_2 present in an Argon based gas mixture. Different tests with 0%, 22.2%, 50% and 100% CO_2 were carried out. Each measurement takes five hours which is necessary to stabilize the system. By increasing the CO_2 percentage all strips tend to relax (tension decreases). This effect is recoverable when the CO_2 percentage decreases. Tension variations of about 3 g corresponding to a displacement of 1 μm are noticeable. The pure Argon tension value has been set as the reference value. The percentage variation of the load can then be converted into percentage elongation: Fig. 6.4 summarizes the results of the performed tests.

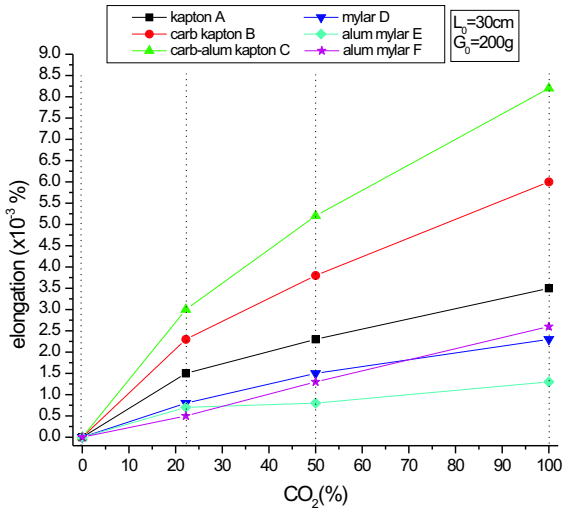

Figure 6.4: Strip elongation *vs.* CO_2 percentage into the gas atmosphere of the test setup. The data have been obtained without assuming effects on the elastic modulus.

6.4.5 Straw Resolution

For a constant gas mixture and density and a given electric field the spatial information of a track inside a straw tube is smeared by the statistical spread of the primary ionization charges along the track, the diffusion of the electron cloud drifting to the anode wire and the gas amplification process. Finally, the electronic readout resolution of the amplified and shaped charge signal is limited by the pulse rise time and noise smearing at the discriminator threshold level. Fig. 6.2 shows a simulation of the different contributions to the spatial resolution for two different gas mixtures.

The detection efficiency of a tube is mainly limited by the minimum number of primary ionizations needed to produce a sufficient charge signal being discriminated by the readout electronics. Therefore, minimal track length through the gas layer, sufficient gas amplification near the wire, good electronic pulse amplification and shaping, and a low discriminator threshold above the noise level are important. Table 6.4 lists the properties of some commonly used gas components and mixtures. Since the detector density given in radiation lengths (X_0) is dominated by the film tube thickness (see Table 6.2), an Ar based gas mixture is preferred compared to a He mixture. Adding a $\sim$ 10% fraction of CO_2 as the quencher component, this Ar/CO_2 mixture has a much higher number (N_p) of primary ionizations per track length for a better efficiency and spatial resolution near the wire.

Fig. 6.5 shows a measured [13] distribution of the spatial detection efficiency of a single straw tube with a diameter of 10 mm and filled with an Ar/CO_2 gas mixture. The efficiency is better than 99% over most of the diameter and drops down to $\sim$ 75% near the tube wall, where the length of the track is too short to produce a sufficient number of ionization charges to be electronically discriminated. The arrangement of a staggered (by half a tube diameter), close-packed double layer of straws helps in this respect. Here, a track crossing the first layer near the tube wall (with lower efficiency) often passes the tube in the next, second layer near the wire, where the efficiency is highest.

6.4.6 Wire Tension

Both efficiency and resolution of a straw are best for a perfect cylindrical shape of the film tube and the wire being exactly located along the cylinder

Material	Identification letter	Thickness [μm]	Width [cm]	Length [cm]
Kapton	A	25 ± 2	1	30
Kapton XC	B	25 ± 2	1	30
alum Kapton XC	C	25 ± 2	1	30
Mylar	D	12 ± 1	1	30
alum Mylar	E	12 ± 1	1	30
alum Mylar with glue	F	12 ± 1	1	30

Table 6.4: Main characteristics of cathode material strips (see text for more detail).

Gas or gas mixture	Z	A	E_x [eV]	E_i [eV]	W_i [eV]	$(\mathrm{d}E/\mathrm{d}x)_{\mathrm{mip}}$ [keV/cm]	N_p [cm^{-1}]	N_t [cm^{-1}]	X_0 [m]
He	2	4	19.8	24.5	41	0.32	4.2	8	5 299
Ar	18	40	11.6	15.7	26	2.44	23	94	110
CO_2	22	44	5.2	13.7	33	3.01	35.5	91	183
i-C_4H_{10}	34	58	6.5	10.6	23	5.93	84	195	169
Ar-10%CO_2	-	-	-	-	26.7	2.5	24.6	93	117
He-10%i-C_4H_{10}	-	-	-	-	39.2	0.88	12.7	26.7	1 313
He-20%i-C_4H_{10}	-	-	-	-	37.4	1.44	20.6	45.4	749

Table 6.5: Properties of different gas mixtures for straw detectors.

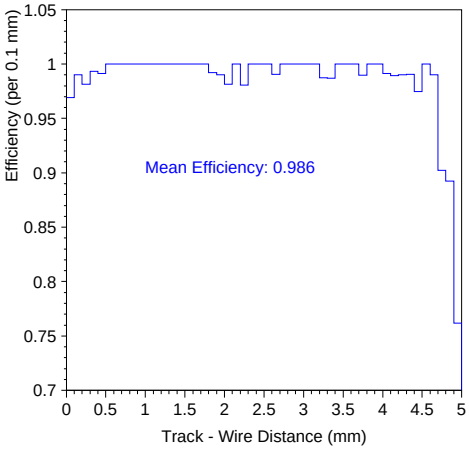

Figure 6.5: Efficiency distribution of a single straw tube with 10 mm diameter.

axis. With a wire tension[1] of about 50 g inside a 1.5 m long, horizontal straw tube the maximum sag due to gravitation in the tube center is less than 40 μm [2]. For 10 000 straws this would add up to a tension equivalent to about 500 kg which must be maintained. Usually, this is done by fixing the straw tubes inside a strong and massive surrounding frame or by adding reinforcement structures like CF-strips along the tubes to keep them straight. All methods inevitably increase the detector thickness given in radiation length by this additional materials.

Therefore, a new technique based on self-supporting straw layers with intrinsic wire tension has been developed to reduce the overall detector weight to an absolute minimum [13]. This straw tracker will upgrade the COSY-TOF experiment [7] and consists of 15 planar double-layers of close-packed straw tubes bond together at few points. Different azimuthal directions of the double-layers allow accurate 3-dimensional track reconstruction with a resolution of about 150 μm ($\sigma_{x,y,z}$). At a gas overpressure inside the straws of 1.2 bar all tubes become straight and the wires adopt the nominal tension of 40 g. For more than 1500 produced straws the measured tension spread is only 0.6 g (σ) and mainly influenced by small temperature variations ($\sim 1\,K$) between straw production and measurement. The temperature coefficient of mylar film elongation, $\Delta L/\Delta T \simeq 50\,\mu$m/K, yields a change in tension of $\Delta m/\Delta T \simeq 0.5$ g/K. Nevertheless, seeing such effects on the level of $\Delta L/L \simeq 0.005\%$ shows the reliability of the wire stretching method by intrinsic gas over-pressure.

1. Usually given as the mass weight used to stretch the wire.

2. The electric field acting on an eccentric wire will induce an additional bending of roughly the same magnitude, but depending on the actual voltage applied to the wire.

The limit of this method for the used thin film tubes was studied in more detail. Fig. 6.6 shows the measured tension with decreasing gas pressure. A well-defined tension (constant slope of about 10 g/1 bar) is seen, even down to zero over-pressure where only the stiffness of the mylar film tube maintains a wire tension of 28 g.

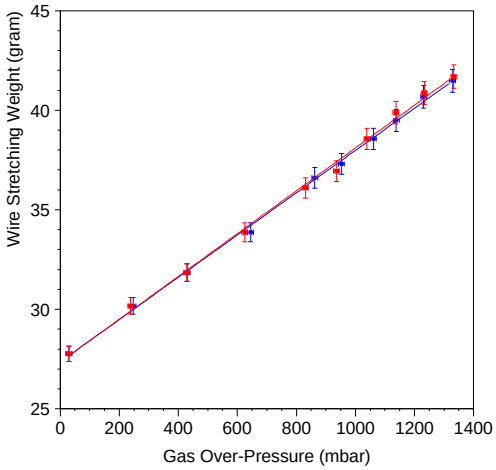

Figure 6.6: Measured wire tensions (weight equivalent) at different gas over-pressures inside two straws. The nominal tension is 40 g at 1.2 bar over-pressure.

6.4.7 Straw Chamber Design

The PANDA STT will consist of up to 10 000 straw tubes, each 150 cm long and parallel to the beam axis, packed in a set of cylindrically-bent double-layers with increasing radius from 15 cm to 42 cm, around the beam pipe. Each cylinder-set will be split into 2 halves to provide mounting around the beam pipe. Also, a few cm space for the vertical target pipe must be left, by taking shorter straws in this area. The the half cylinders will fixed at the up- and downstream ends using reference rings. All electronic readout, gas and high-voltage supply will be located at the upstream end of the detector. The detector density should be as low as possible for a clean and background-free tracking in a high particle rate environment. This also concerns mechanical support structures, necessary to pickup the detector weight and align the tubes over their full length. Necessarily, these structures will add material at both ends of the detector barrel. In particular, at the downstream end the support structures will interfere with the tracking through the following detectors. In this respect, self-supporting straw layers which maintain the necessary wire and film tube tension by the applied intrinsic gas over-pressure are very interesting. This technique has been successfully developed at IKP-FZJ institute to build a planar tracker consisting of close-packed double-layers of straw tubes with 100 cm length. Here, only light-weight frames based on a foam core ($\rho = 0.05\,\mathrm{g/cm^3}$) reinforced by thin ($0.3\,mm$) Carbon-fiber strips are used to support the detector weight. The more complicated, barrel-like geometry at PANDA and the longer straw tubes require additional, dedicated prototype studies. As a test, straw tubes are glued together building planar modules. Studies to produce cylindrical modules of glued straws are under way at Frascati INFN laboratories (LNF).

At the moment we will focus on two different design options. A more standard design uses layers, skewed with respect to each other by a small ($\sim 2{-}4\,^o$) angle to obtain the track coordinate along the wire by the crossing tube position. Such straw trackers are installed in the WASA [2] and FINUDA [3] detectors. The advantage of a relatively high z-resolution ($\sigma_z \sim$ mm) is accompanied by several disadvantages, including reduced geometrical symmetry and acceptance (open gaps), and smaller mechanical stability due to the hyperbolic layer shape. The latter also requires additional support structures to align the tubes over the full length. The second, more symmetric and mechanically robust tracker layout would consist of close-packed, cylindrical layers of straw tubes, exactly parallel to the beam and magnet axis. Here, the layers can be made highly self-supporting, avoiding additional reinforcement structures. To obtain the track coordinate along the wires, the charge division method is used (see section 6.4.3). Nevertheless, the method needs dedicated studies and optimization of wire materials (resistivity) and electronic charge amplitude readout. The first 150 cm long straw tubes with different anode wire resistivity have been assembled at IKP-FZJ (Fig. 6.7) to start the prototype studies.

6.4.8 Gas System

The STT gas system will be an open-flow circuit providing a two-component gas mixture. The two gases presently considered are Argon and CO_2. The system will include a mixing section, a distribution section and a control system.

- The gas mixing section will combine the two components, supplied by high pressure bottles,

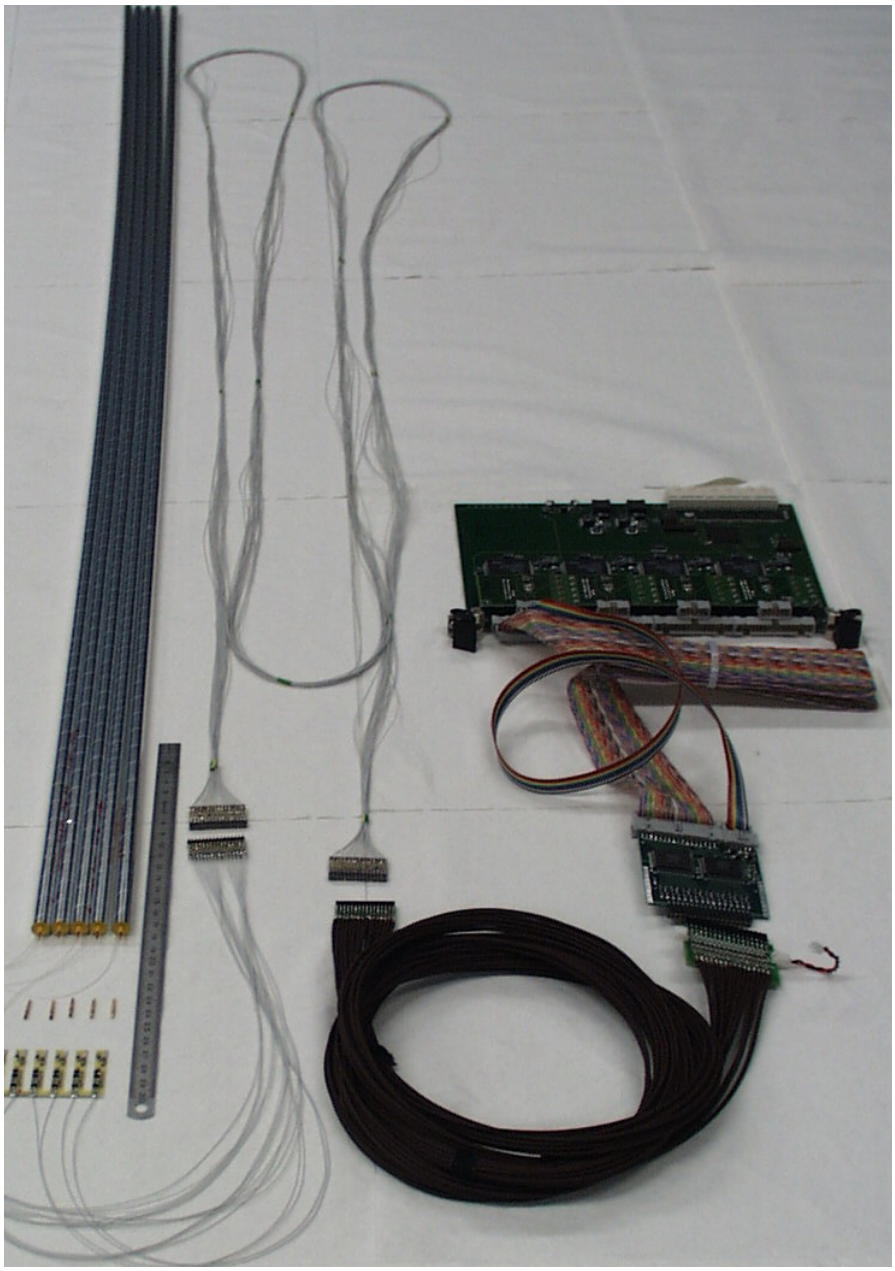

Figure 6.7: Prototype straws for the charge-division tests.

in appropriate proportions using mass flow controllers. Mixture pressure and temperature will be controlled electronically. The gases, before entering the mixer, will pass trough a filtering rack to remove oxygen and moisture.

- Since the detector will have a large number of elements ($\sim 9\,000$) the gas distribution system need to have a high level of parallelization. The output of the mixing rack will feed 11 parallel lines (one per layer). Controllers will be placed on each branch to check electronically the gas flow, the temperature and the pressure. Calibrated impedances will be mounted at the inlet and outlet of each tube in order to maintain the same operating conditions inside each tube. The use of impedances will help in maintaining the correct flux in the tubes even in case of leakages in a single or in a small group of straws. The impedances could be stainless steel capillaries (length few mm, diameter hundred μm) obtained by cutting with electric erosion a long pipe. The use of electric erosion technology is needed to preserve the small diameter of

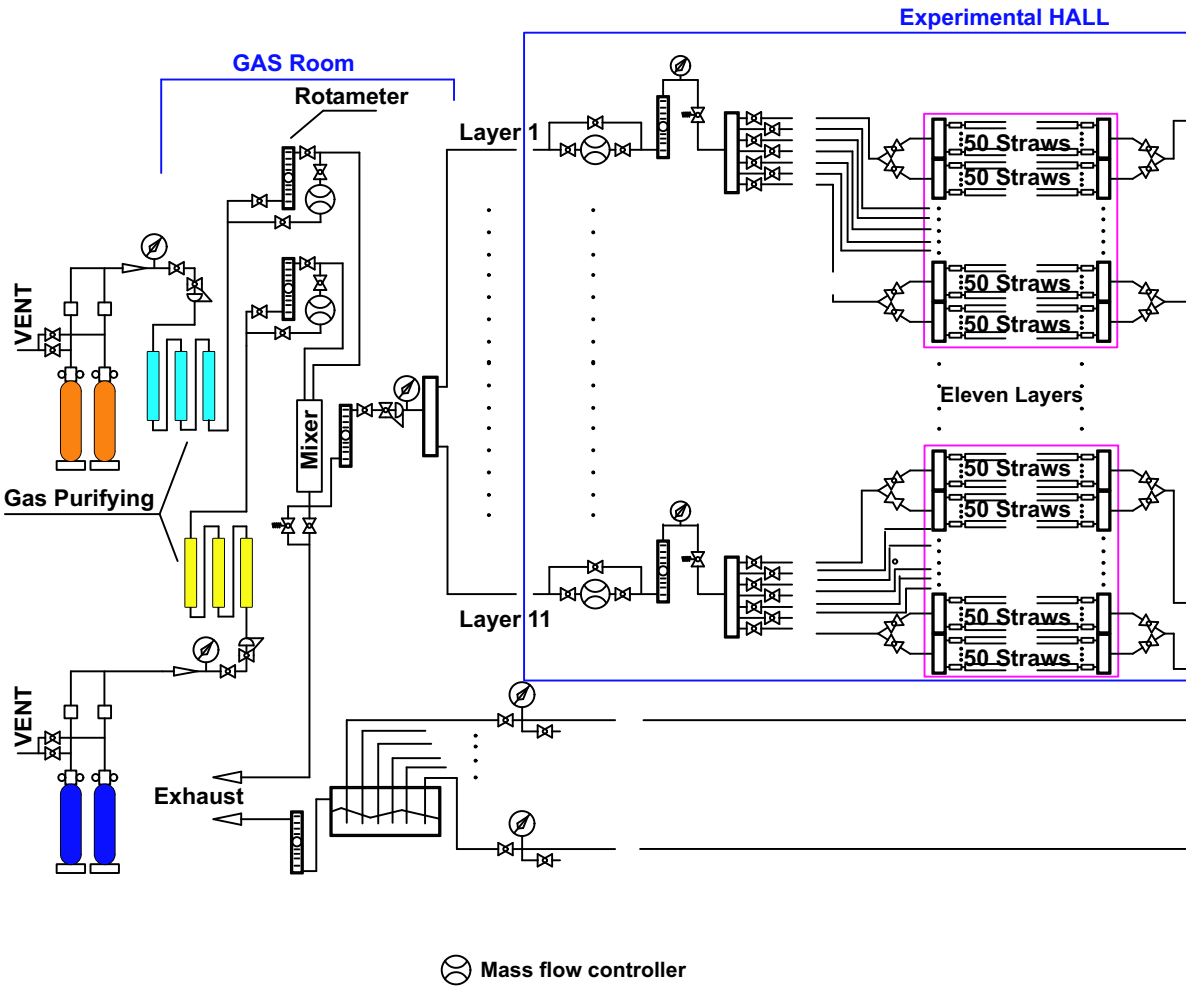

Figure 6.8: Layout of the straw tube gas system.

the pipe. The precise size of the impedances will be determined experimentally in order to have the gas flux inside the straw tube insensitive to small variations of the inlet pressure (±10 mbar). Each layer distributor will feed many lines at the same time in order to provide gas mixture to groups of 50 straws. The outgoing fluxes, from the 11 layers, will be collected with a scheme similar to that of the inlet, and feed to the exhaust line. Here, other mass flow controllers will measure the output flux of each layer.

- A dedicated slow control system will read and set all the transducer parameters (temperature, pressure and gas flow). Hardware and software safety protections will be provided to avoid that the gas pressure inside the straws exceed the specified level. A hardware security valve will be located both at gas inlet and outlet. The valves will be set to open if the overpressure becomes too high.

An external measurement of temperature and pressure will be added to this setup. A schematic view of the system layout is shown in Fig. 6.8. The high level of parallelization will give advantages for finding gas losses and for isolating faulty straws. Fig. 6.9 shows the logic of the control system.

6.4.9 Readout Electronics

The PANDA straw tubes will be operated with a gas mixture of moderate gain ($\sim 10^4$–10^5). Therefore, a relatively high gain preamplifier will be necessary to treat the straw tube signals. In the present scheme for the detector front-end electronics the electronics boards, housing a transimpedance pre-amplifier and a HV filter, are placed directly on one side of the straw tube. VME boards, housing a sampling FADC, FPGA for auto-triggering logic, and a TDC,

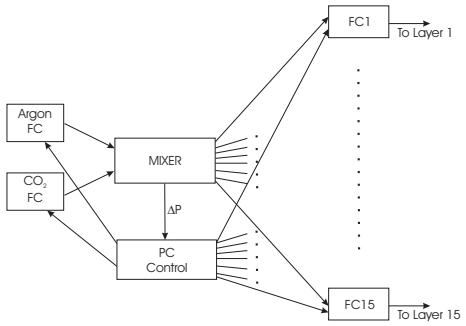

Figure 6.9: Layout of the gas control system

would be placed outside the solenoid, together with the HV distribution system. A schematic layout of the proposed electronics is shown in Figs. 6.10 and 6.11.

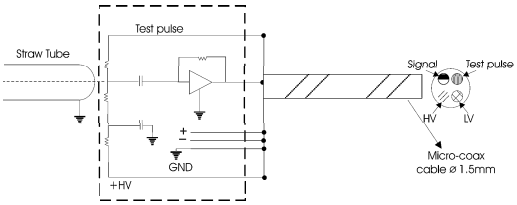

Figure 6.10: Layout of the straw tube front-end electronics cards.

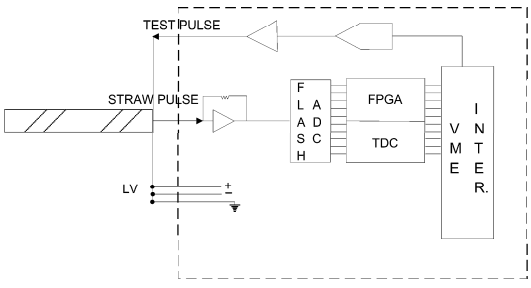

Figure 6.11: Scheme of the straw tube VME electronics card.

6.4.10 Timeline

The timeline of the straw tube detector project is shown in Fig. 6.12.

6.5 Time Projection Chamber

6.5.1 Introduction

A time projection chamber (TPC) [14] with its low material budget constitutes an ideal device for tracking charged particles in 3-dimensional space, fulfilling all the requirements on $\overline{\text{P}}$ANDA tracking discussed in Sec. 6.1. Such a device has been successfully employed in many experiments such as PEP-4, ALEPH [15], DELPHI [16], NA49 [17, 18], STAR [19, 20]. It consists of a large gas-filled cylindrical volume inside a solenoid magnetic field, surrounding the interaction point, and covering the full 4π solid angle [21]. Fig. 6.13 shows a schematic view of a TPC.

An electric field along the cylinder axis separates positive gas ions from electrons created by ionizing particles traversing the gas volume. The primary electrons then drift towards the readout anode end cap of the cylinder, the transverse diffusion being reduced by the strong magnetic field parallel to the drift direction. At the end cap avalanche amplification occurs typically in Multi Wire Proportional Chambers (MWPCs), the induced signals being detected by an arrangement of pad electrodes measuring the projection of the track onto the end plane. The third coordinate of the track comes from a measurement of the drift time of each primary electron cluster, requiring a precise knowledge of the electric drift field in the chamber. Distortions of the electric field in the drift volume due to the accumulation of space charge from primary ions or avalanche ions drifting back into the drift volume deteriorate the resolution and have to be kept a minimum. To this end all TPCs up to now have been operated in a pulsed mode, where an electrostatic gate to the readout region is opened only when an interaction in the target has occurred, and is closed immediately thereafter, preventing avalanche ions from penetrating the drift volume.

Owing to the beam properties at the High Energy Storage Ring (HESR), with its high luminosity of $10^{32}\,\text{cm}^2 s^{-1}$ and 10^7 $\overline{\text{p}}$ annihilations per second, the TPC in $\overline{\text{P}}$ANDA, on the contrary, has to operate continuously, i. e. the technique of gating cannot be applied.

Apart from the obvious problem of ions feeding back into the drift volume, continuous tracking calls for about an order of magnitude higher granularity in all three spatial coordinates than in previous TPCs in order to disentangle hits belonging to different tracks.

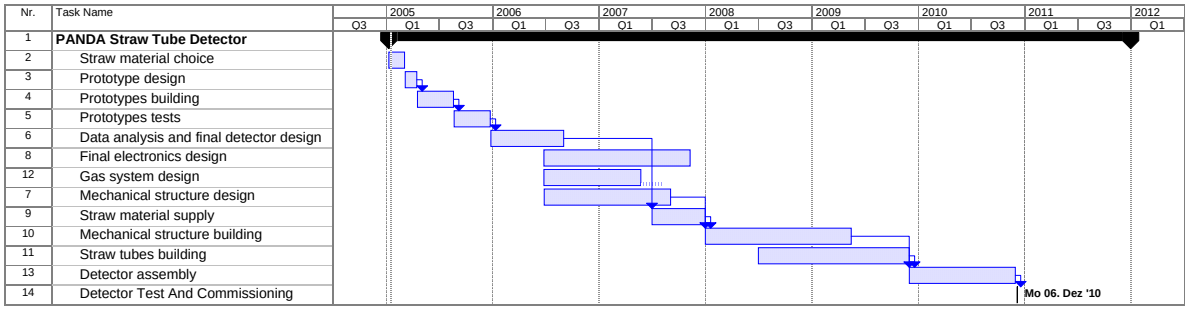

Figure 6.12: Timeline of the straw tube detector activity.

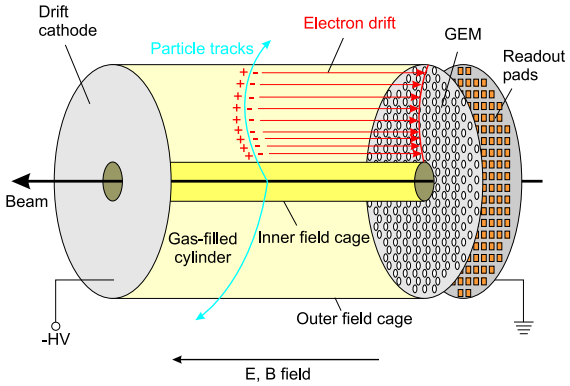

Figure 6.13: Schematic view of a GEM-based TPC.

These limitations of MWPCs may be overcome using the Gas Electron Multiplier (GEM) [22] as charge amplifier, a novel micropattern gas detector recently invented at CERN and successfully employed [23] at the COMPASS experiment [24]. Its main features, rendering possible a continuous readout TPC, are:

- high granularity and corresponding high rate capability,
- intrinsic suppression of ion feedback due to peculiar field geometry,
- no preferred direction (as for wires), therefore isotropic $\boldsymbol{E} \times \boldsymbol{B}$ effects.

The GEM readout scheme is also envisaged for the TPC of the TESLA [25] linear collider detector at DESY, and combined efforts are currently concentrating on further developing this technique. The increased granularity of such a detector necessarily leads to larger event sizes and requires substantial data reduction already at the level of front-end electronics.

In conclusion, a TPC read out by the Gas Electron Multiplier (GEM) is an interesting alternative to the Straw Tube Tracker for PANDA. The development of such a detector constitutes a challenge both scientifically and technologically, but would buy a number of advantages, such as very low material budget, particle identification at low momenta, and very good tracking performance.

6.5.2 Conceptual Design

6.5.2.1 Geometry

A cross section of the overall layout of the TPC proposed for PANDA is shown in Fig. 6.14. The

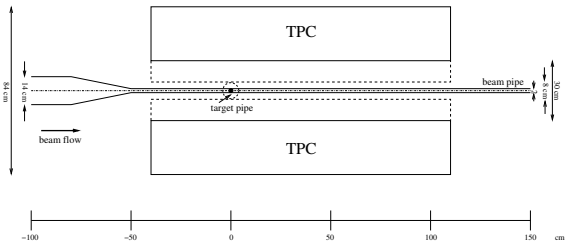

Figure 6.14: Horizontal cross section of the PANDA TPC.

main mechanical parameters are listed in Table 6.6.

Parameter	Value
Mechanical inner radius	15 cm
Mechanical outer radius	42 cm
Mechanical length	150 cm
Gas volume	700 l

Table 6.6: Main mechanical parameters of the TPC.

In order to leave space for the vertical pipe of the pellet target, which intersects the beam pipe perpendicularly, the cylindrical gas volume is cut in two half cylinders along the beam direction, as can be seen from Fig. 6.15. This results in a reduction of

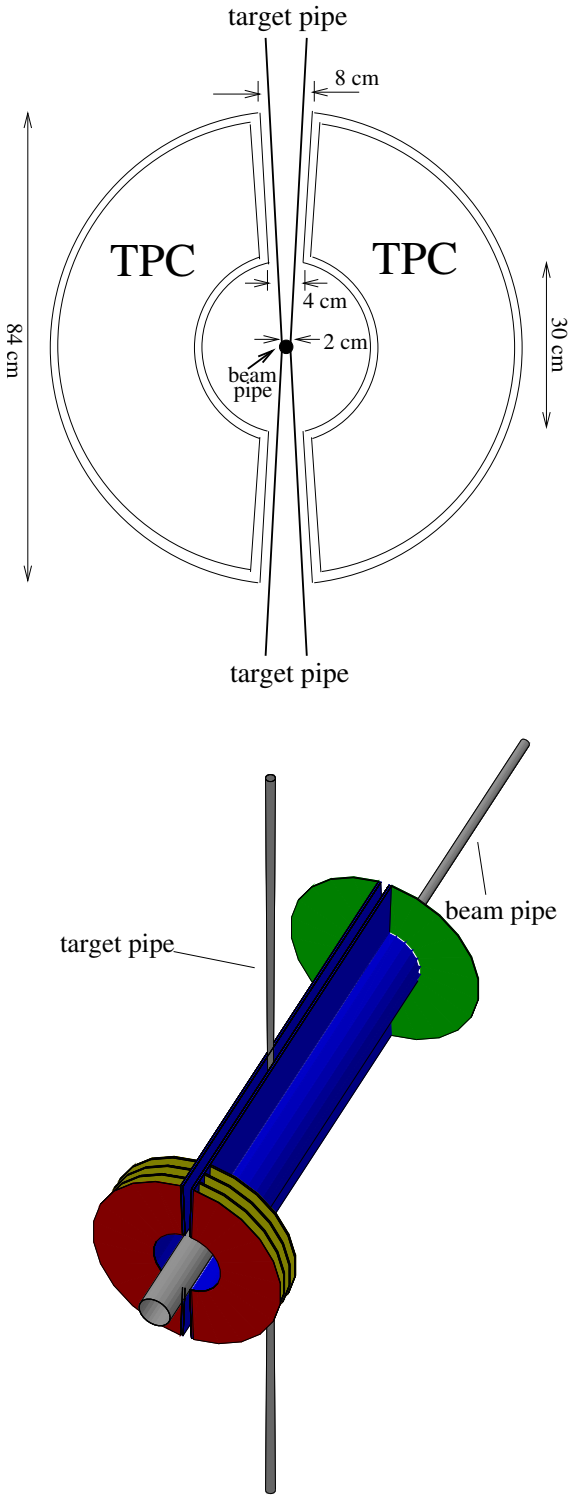

Figure 6.15: Cross section perpendicular to the beam axis and 3D view of the two halves of the TPC, together with the beam and target pipes.

acceptance by 10% compared to the full barrel acceptance of 3.8π. Due to the fixed target-like kinematics the interaction point is not in the center of the TPC, but shifted upstream, so that the TPC extends 40 cm in upstream, and 110 cm in downstream direction.

6.5.2.2 Operation

A negative high voltage (HV) of several tens of kV is applied to the downstream end plane of the cylinder, causing electrons to drift in the upstream direction towards the anode plane. At the end of the drift section the electrons enter the amplification section, consisting of a stack of cascaded GEM foils, operating at a gas gain of several 1 000. The charge cloud emerging from the last GEM is collected on a pad plane on ground potential. The signals on each pad are sampled at a frequency of several tens of MHz, providing spatial and time information. The front-end electronics is mounted close to the upstream plane of the TPC, thus minimizing the material crossed by particles emitted in forward direction.

6.5.2.3 Detector Gas

The choice of detector gas is crucial to the design of the TPC [26]. It not only influences the performance of the detector, but has impact on the design and electrical properties of the field cage, the amplification region, and the readout electronics. The requirements to the gas mixture for a TPC are manifold, and partly contradictory:

- high electron drift velocity for fast clearing of the gas volume,
- saturated drift velocity: variations with electric field, temperature, pressure small,
- low electron diffusion: spatial resolution,
- constant gain: variations of T, p, material,
- low electron attachment,
- high ion mobility: accumulation of space charge controllable,
- specific ionization: $\mathrm{d}E/\mathrm{d}x$ vs. space charge,
- low density, high radiation X_0: multiple scattering,
- no aging.

Experiment	Gas mixture	Proportion
ALEPH	Ar/CH_4	91/9
NA49 VTPC	Ne/CO_2	90/10
NA49 MTPC	$Ar/CO_2/CH_4$	90/5/5
STAR	Ar/CH_4 (P10)	90/10
ALICE	Ne/CO_2	90/10
TESLA	$Ar/CO_2/CH_4$	93/2/5

Table 6.7: Gas mixtures used in TPCs already operating or under construction.

Operating TPCs have been filled with a variety of gas mixtures, some of which are summarized in Table 6.7. Fig. 6.16 shows the drift velocity, Fig. 6.17 the transverse and longitudinal diffusion constant of several popular gas mixtures as a function of the electric drift field.

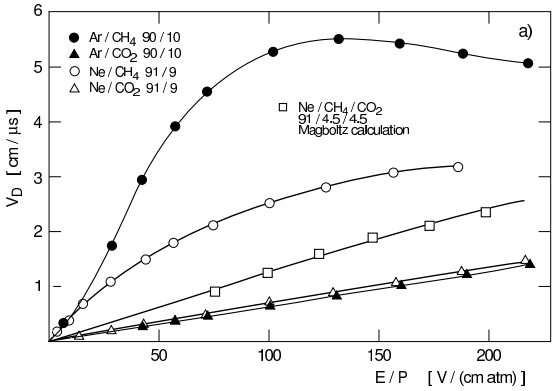

Figure 6.16: Drift velocity as a function of the electric drift field for a number of gas mixtures.

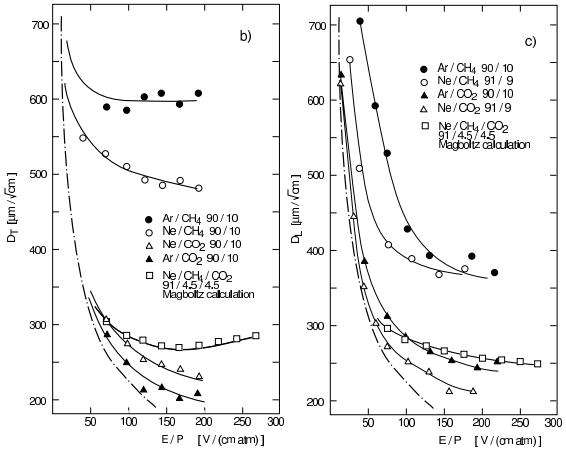

Figure 6.17: Diffusion constants as a function of the electric drift field for a number mixtures.

Only the noble gases Argon and Neon qualify as the main component. Helium is difficult to contain and hence has a high leak rate, Krypton and Xenon are rare and hence not affordable in larger quantities. In addition, their high density leads to significant multiple scattering. Due to its lower abundance, Neon is about a factor of 8 more expensive than Argon, making a closed gas system indispensable. Table 6.8 summarizes the important parameters of some noble gases and common admixtures.

Gas	ρ [g/l]	X_0 [g/cm^2]	X_0 [m]	n_{mp} [1/cm]
He	0.1785	94.32	5280	2.7
Ne	0.89990	28.94	322	16
Ar	1.784	19.55	110	38
Kr	3.733	11.34	30.4	63
Xe	5.887	8.48	14.4	115
CH_4	0.717	46.22	645	30
CO_2	1.977	36.2	183	50
C_2H_6	1.356	45.47	335	59
CF_4	3.93	36	90	97

Table 6.8: Properties of gases commonly used in TPCs.

The radiation length is about a factor of 3 larger for Ne than for Ar, leading to reduced photon conversion and multiple scattering in Ne. The primary ionization rate is about a factor of two smaller for Ne ($n_{\mathrm{mp}} = 16$) than for Ar ($n_{\mathrm{mp}} = 38$), requiring a higher gain in the case of Ne. On the other hand, space charge effects will be significantly lower for Ne than for Ar, supplemented by mobility of Ne ions which is a factor of 2-3 larger than that for Ar ($\mu_{\mathrm{Ne}} \sim 4\,\mathrm{cm}^2/\mathrm{Vs}$ for $E < 10^4\,\mathrm{V/cm}$). Following these arguments, the preferred main gas component for the PANDA TPC would be Ne.

As quenchers, either organic gases such as Methane (CH_4), Ethane (C_2H_6), Isobutane (iC_4H_{10}), freons such as CF_4, or CO_2 are most widely used. CH_4, used in e.g. P10 (Ar/CH_4 90/10) is a very convenient quencher, since it has a maximum drift velocity of $5\,\mathrm{cm}/\mu\mathrm{s}$ at an electric field of only $125\,\mathrm{V/cm}$, greatly simplifying the design of the field cage. A strong longitudinal magnetic field is necessary, however, in order to reduce transverse diffusion. The drawback of organic mixtures is that they may cause aging by forming polymeric deposits on the electrodes of the chamber when the accumulated charge is large. CF_4 is in principle interesting as quencher, since it provides a high drift velocity at low electric fields in mixtures with Ar or Ne. In addition, it is sometimes used in attempts to etch polymer deposits from electrodes. Its high reactivity, however, makes its use very dangerous to other components of the gas system, like glass joints, or

Aluminum parts. In addition, fluorine is electronegative and attaches electrons. CO_2 remains as an uncritical quencher, with the advantage of low diffusion, and the disadvantage of lower drift velocities. Hence, CO_2 is the preferred quencher for the $\overline{\text{P}}$ANDA TPC, possibly augmented by small admixture of CH_4 in order to increase the drift velocity.

Fig. 6.18 shows the drift velocity, Fig. 6.19 the transverse and longitudinal diffusion constant of several Ne/CO_2 gas mixtures as a function of the electric drift field, calculated with MAGBOLTZ [27, 28].

6.5.3 Mechanical Structure

The mechanical structure of each half cylinder of the TPC will be composed of a vessel containing the field cage and the detector gas, and two end flanges housing the HV plane on the downstream end, and the readout detectors and front-end electronics on the upstream end. While providing sufficient mechanical stiffness to guarantee the stability of the detector, it should introduce as little material as possible to the detector.

6.5.3.1 Vessel

To this end, the vessel consists of a self-supporting sandwich structure made of two skins of fiber glass composite material (e.g. Vetronit) and a core of Aramid fiber honeycomb (e.g. NOMEX), as shown in Fig. 6.20. Thin layers of Tedlar foil provide gas tightness of the vessel.

6.5.3.2 Field Cage

The electric field in the drift volume is provided by the HV plane at the downstream end made of copper-clad Kapton foil, and precision concentric cylindrical field cage rings along the barrel part, stepwise degrading the HV to ground potential at the anode. For improved homogeneity, the cylindrical field cage consists of two sets of copper strips on both sides of an insulating Kapton foil, where the outer strips cover the gaps between the inner strips. The potential on each ring is defined by a precision resistor chain located outside the gas volume. Possibly a thin layer of CO_2 gas will be necessary in order to provide sufficient electrical strength to hold up to 100 kV between the field cage and the vessel, which has to remain on ground potential. In Table 6.9 the thickness of the various components we intend to use for the TPC vessel and the field cage is given.

6.5.3.3 Temperature Stabilization

Depending on the gas mixture actually used, the drift velocity will vary with temperature. In order to achieve the desired resolution in the z coordinate, the temperature over the whole gas volume will have to be stabilized with a precision better than 1 K. In ALICE, e. g. it is foreseen to operate the TPC at a working temperature of 25 °C, well above the ambient temperature, in order to achieve a temperature stabilization of about 0.1 K over a much larger volume than in $\overline{\text{P}}$ANDA [29]. The heat dissipated in the readout modules as well as in the voltage divider (several tens of W) will have to be disposed of by water cooling circuits.

6.5.4 Gas System

6.5.4.1 Operational Requirements

One of the main requirements on the gas system, including the detector itself, is the limitation of oxygen and water vapor concentration. In the case of Ne/CO_2 mixtures for example the electron attachment is 1% per ppm oxygen and meter of drift. One severe consequence is a degradation of the particle identification power since the dE/dx-measurement (see Sec. 6.5.7) gets worse. The contamination is mainly due to bad sealing joints and scales roughly with the total surface of the detector. For the proposed design of the $\overline{\text{P}}$ANDA TPC the volume-to-surface ratio is only about 0.1 m, which is small compared to other existing or planned TPCs, e.g. DELPHI (0.34 m) or ALICE (0.70 m). These chambers reached or aim for an oxygen contamination lower than 5 ppm. In addition to the gas purity, the accuracy and stability of the Ne/CO_2 gas mixture is crucial. As can be seen from Fig. 6.18 and Fig. 6.19, important parameters like the drift velocity or diffusion within the gas depend strongly on the Ne/CO_2 ratio. This topic is also closely related to the pressure regulation of the detector.

6.5.4.2 Principal Design

The large detector volume of about 0.7 m^3 as well as the usage of a high-cost gas mixture leads to a closed circulation gas system as the natural choice. Fig. 6.21 presents a possible basic layout of such a system, similar to the one which will be used for the ALICE TPC. It is built up by functional modules (highlighted in blue) which should be placed at different locations (highlighted in red) depending on the required access possibilities. For simplicity the

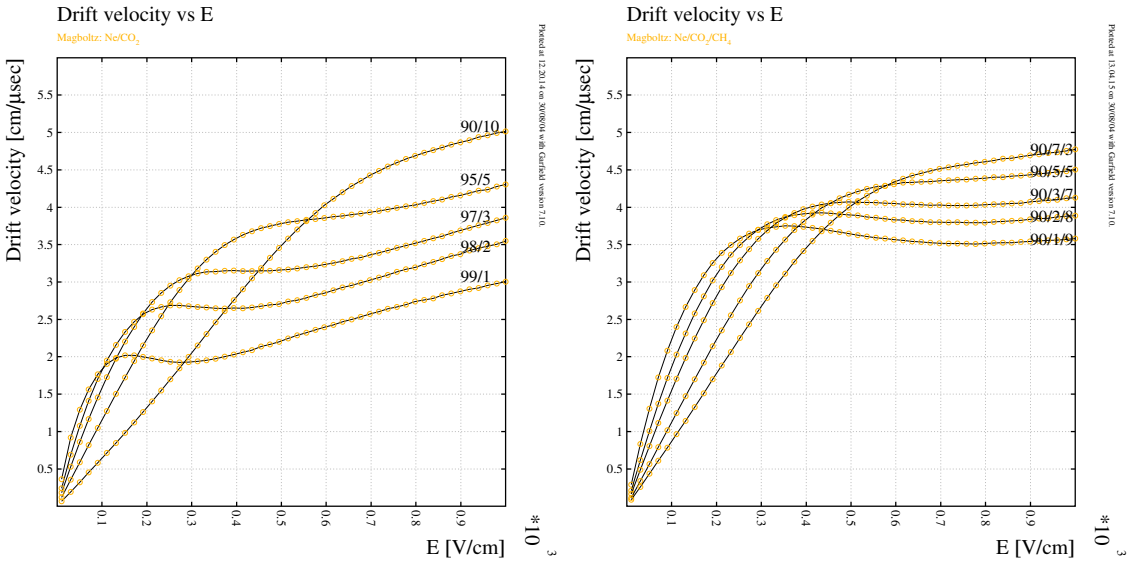

Figure 6.18: Drift velocity as a function of the electric drift field for a number of Ne/CO_2 (left) and $Ne/CO_2/CH_4$ (right) gas mixtures.

Element	Material	Thickness [mm]	X_0 [mm]	X/X_0 [%]
Strips	Cu	0.018	14.3	0.126
Carrier	Kapton	0.1	286	0.035
Gas Seal	Tedlar	0.05	301	0.017
Laminate	Vetronit G11	0.5	194	0.258
Honeycomb	Nomex	5	17833	0.028
Laminate	Vetronit G11	0.5	194	0.258
Gas Seal	Tedlar	0.05	301	0.017
Ground	Al	0.05	89	0.056
Σ				0.795
Total(2 Walls)				**1.6**
Drift gas	Ne/CO_2 (90/10)	300	308100	0.097
Drift gas	Ar/CO_2 (90/10)	300	117300	0.256

Table 6.9: Thickness of various components of the mechanical structure of the TPC.

TPC is drawn as one gas volume instead of two (see Fig. 6.15). While full lines mark the gas pipelines, the dashed lines correspond to control connections.

For normal running most of the gas should be recycled through a purifier and go back to the main loop with a moderate fresh gas injection of only a few percent. Therefore the return gas from the detector has to be compressed and pumped back to the gas supply building. This building should host the fresh gas supply bottles, the mixing system (see Fig. 6.22) and the purifier, which is supplemented by an O_2 and H_2O analysis unit.

The detector is planned to be operated constantly at 1 mbar over atmospheric pressure. This is achieved by an independent control loop consisting of a pressure transducer, a stand-alone control unit and an adjustable valve, which is installed in parallel to the compressor. The transducer measures the pressure directly in the TPC volume, submits the value to the control unit which then regulates the valve. In order to check the resulting pressure, it is measured permanently at three different positions by transducers. In addition, the total gas flow is watched by a flowmeter and can be adjusted manually by an adjustable valve. A main TPC gas monitor system collects all this information and also checks the gas quality at different points within the circulation system. Like the stand-alone pressure control system, it should be easily accessible inside a general control area close to the experiment.

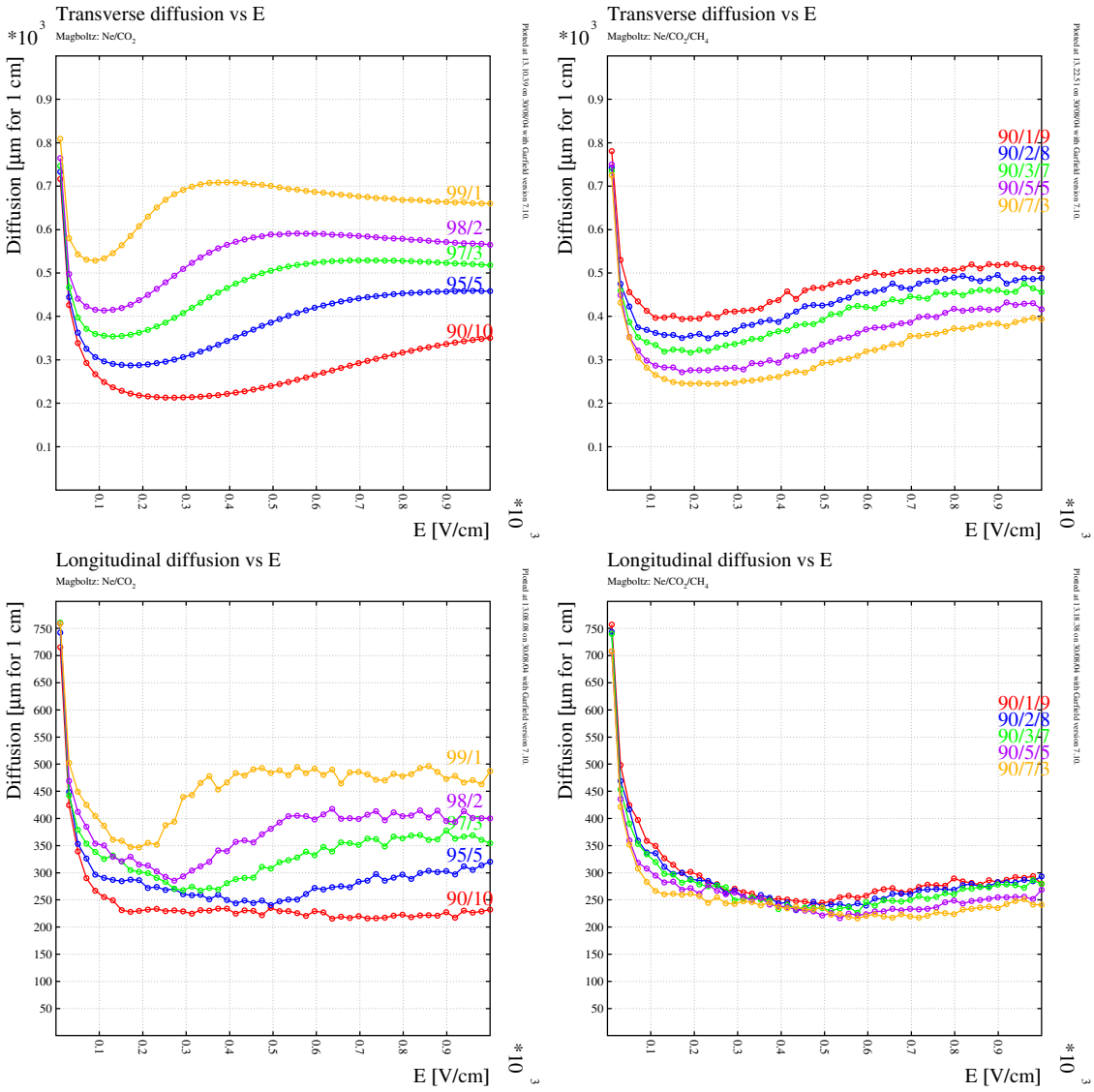

Figure 6.19: Transverse (top) and longitudinal (bottom) drift velocity as a function of the electric drift field for a number of Ne/CO_2 (left) and $Ne/CO_2/CH_4$ (right) gas mixtures.

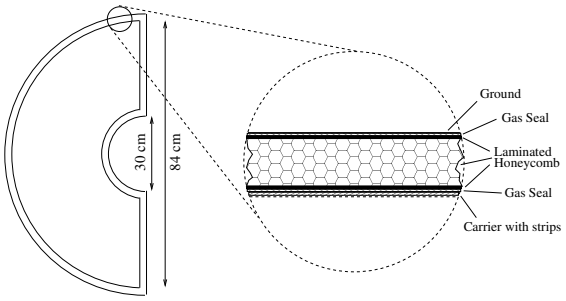

Figure 6.20: Shape and detailed design of the TPC vessel and field cage.

6.5.4.3 Emergency System

Very close to the TPC an emergency system has to be installed. If for any reason the main system stops working (e. g. because of a power cut), this backup system keeps the pressure inside the TPC constant. In case of over pressure gas is relieved through a security bubbler which is adjusted to 1 mbar over atmospheric pressure. In case of under pressure premixed Ne/CO_2 is injected from a bottle.

6.5.4.4 Filling, Purging and Calibration

Filling of the detector with operating gas will be done without recirculation and with a at least

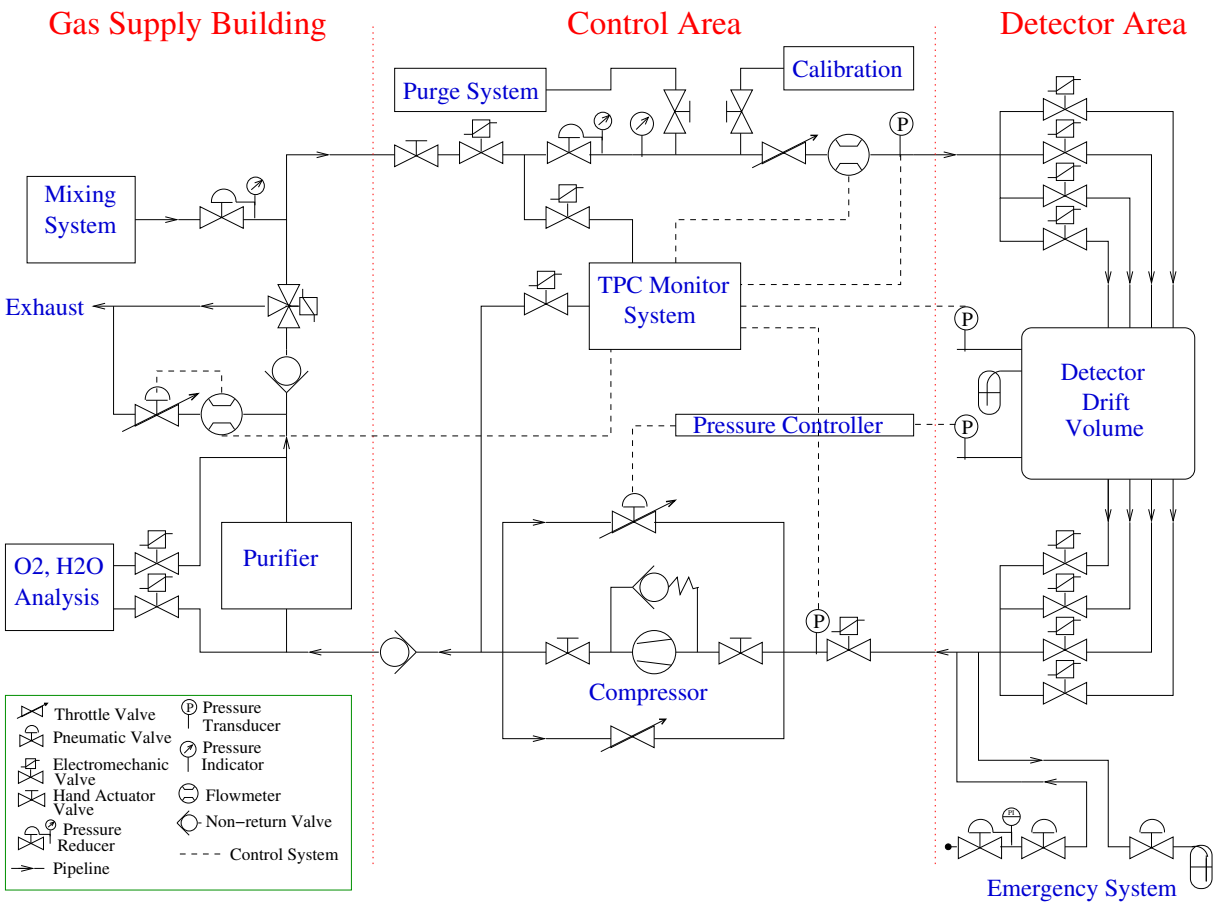

Figure 6.21: Basic layout of the TPC gas circulation system.

ten times higher inlet gas flow, compared to normal running conditions, from the mixing unit (see Fig. 6.22). For this a three way valve at a position close before the fresh gas input can be set to "exhaust". At the same time a second set of flowmeters within the mixing unit is used to increase the flux. By this a gas exchange of at least one whole TPC volume should be possible in one day.

For purging the TPC, a separate input gas line could be connected. From there for example CO_2 is injected into the gas system, flushed through the detector and exhausted through a bubbler. In case of a longer shutdown one can fill the two TPC chambers with CO_2 and then use the backup system to keep them at a constant pressure. For gain calibrations of the TPC and its readout channels a radioactive noble gas isotope could be admixed to the operating gas. Again a separate gas input line or also a bypass could serve to implement this.

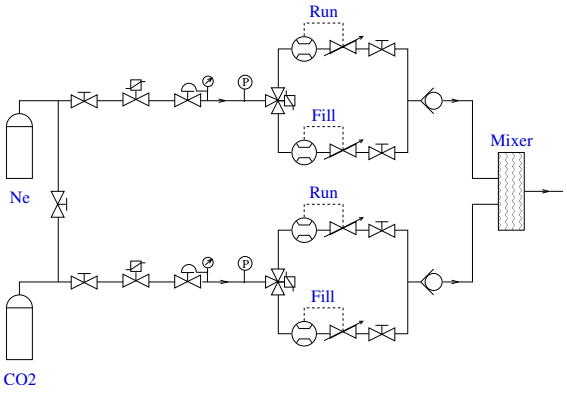

Figure 6.22: Schematic drawing of the mixing unit, based on the standard LHC design.

6.5.5 GEM Detectors

6.5.5.1 Gas Electron Multiplier

The Gas Electron Multiplier (GEM) [22], shown in Fig. 6.23, consists of a thin polymer foil

(typ. 50 μm Kapton), metal-clad (typ. 5 μm Cu) on both sides. It is perforated by a large number of holes (10^4/cm^2), arranged in a regular pattern. The so-called standard GEM has holes of a double-conical cross section, as can be seen from Fig. 6.23, with an inner diameter of 50 μm and an outer diameter of 70 μm at a hole pitch of 140 μm.

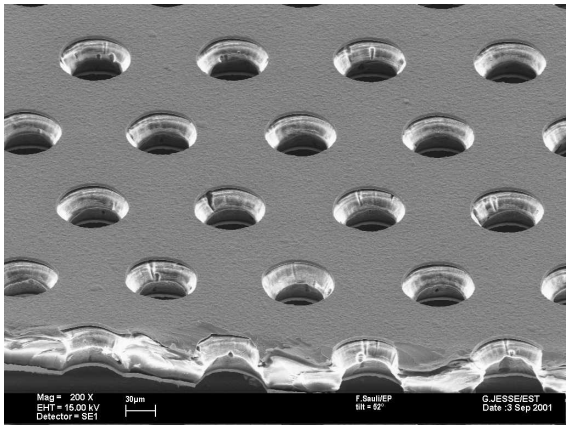

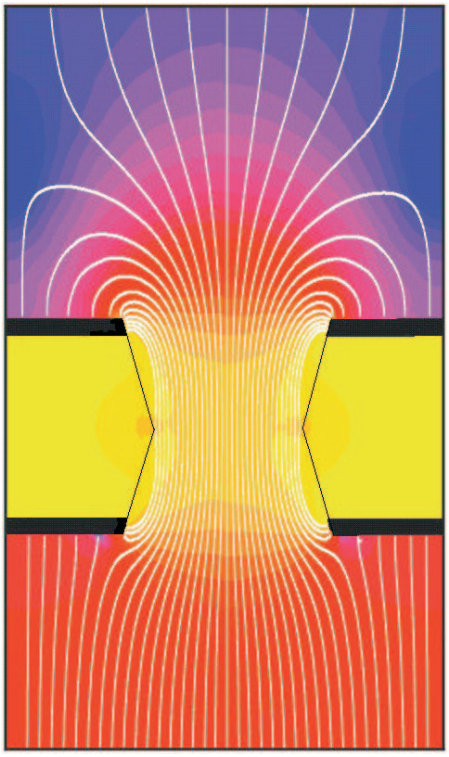

Figure 6.23: Electron microscope photograph of a GEM foil (top) and illustration of electric field lines in a GEM hole (bottom).

Inserted between a pair of parallel plane electrodes, and upon application of a suitable potential difference ($\sim$ 400 V) between the two Cu layers of the foil, an electric field configuration similar to the one shown in Fig. 6.23 (right) is achieved. Primary electrons are efficiently collected inside the holes, where they undergo avalanche multiplication due to electric fields of the order of 50 kV/cm. The resulting charge cloud is then extracted on the other side of the foil, ready to be collected on a readout anode, or to undergo additional amplification in subsequent GEM foils.

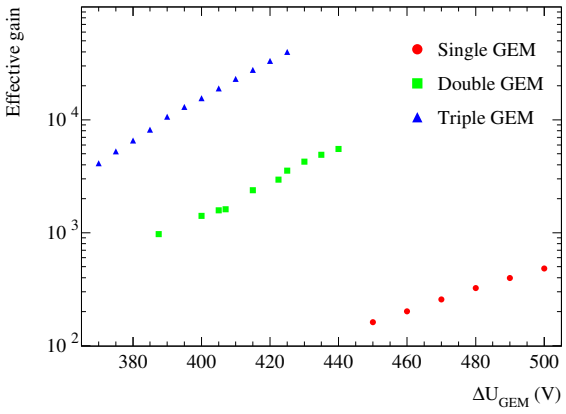

Figure 6.24: Effective gain as a function of potential difference applied to each GEM foil for single, double and triple GEM detectors.

By cascading several GEM foils high gains of the order of several $\cdot 10^4$ can be achieved at a relatively low amplification of a single foil. Fig. 6.24 shows the effective gain, defined by the ratio of charge collected by the readout electrode and primary charge produced by ionizing radiation, for single, double and triple GEM devices, operated in Ar/CO_2 (70/30), as a function of the potential difference between the two GEM electrodes.

The fact that, for a given gain, the triple GEM can be operated at much lower voltages over each GEM foil was found to reduce the probability of a gas discharge in presence of heavily ionizing radiation by more than one order of magnitude compared to a double GEM device [30, 31, 32]. Further optimization steps to completely prevent gas discharges include an asymmetric sharing of the total gain between the three foils, gradually decreasing by $\sim$ 10% at each amplification step, and segmentation of the GEM foils on one side, decreasing the energy stored in each sector [33].

6.5.5.2 Triple GEM Detectors in COMPASS

COMPASS at CERN is the first high-luminosity particle physics experiment to rely on a set of 22 triple

GEM detectors for tracking in the near-beam area [34]. As shown in Fig. 6.25, the COMPASS GEM detectors consist of three $31 \times 31\,\mathrm{cm}^2$ large GEM foils, stacked on top of each other and separated by thin spacer grids [34]. The signals are read out

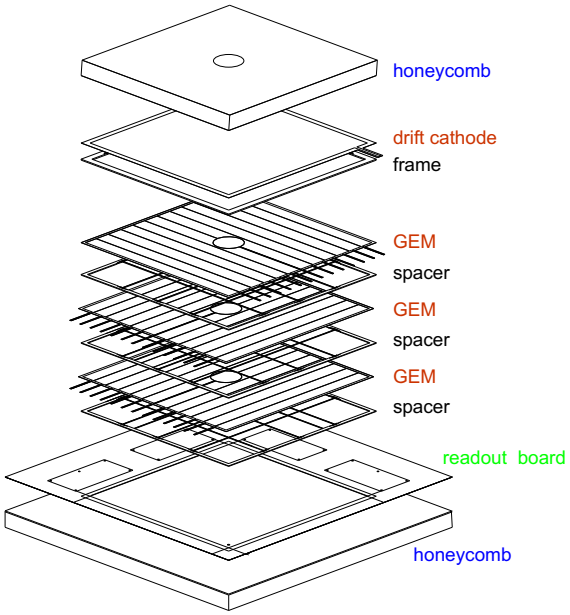

Figure 6.25: Exploded view of a COMPASS triple GEM detector.

by two sets of strips, at 90° to each other, yielding two projections of the particle trajectory per chamber. Strong correlations of the signal amplitudes measured on these two projections help to resolve ambiguities in multi-hit events [35]. All detectors in COMPASS are operating stably at an average single plane efficiency $> 97\%$ [23]. Fig. 6.26 shows the distribution of residuals, i.e. the difference along one coordinate of expected track and measured hit position, plotted for all hits seen by one of the GEM detectors. The spatial resolution determined from these residuals by deconvoluting the error from track reconstruction for all 40 planes are found to be very uniformly distributed around an average value of 69.6 μm for track angles $\leq 0.2°$.

6.5.5.3 Aging

In COMPASS, the GEM detectors are exposed to extremely high particle fluxes of charged particles (up to $500\,\mathrm{kHz/mm^2/s}$ close to the beam axis), imposing considerable requirements to the radiation tolerance of their performance. No degradation of performance was observed in the three years of operation up to now, both with μ and hadron beams.

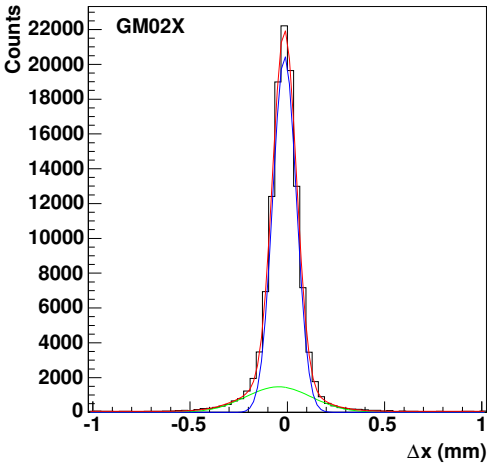

Figure 6.26: Difference between expected track and measured hit coordinate (residuals) for one COMPASS GEM plane.

In laboratory aging tests, more than $7\,\mathrm{mC/mm^2}$ of charge were collected on the readout strips using an intensive beam of X-rays without loss of gain or energy resolution [36]. This corresponds to the total charge collected in more than 7 years of operation in COMPASS. Owing to the facts that the antiproton beam does not cross the GEM detectors in PANDA, and that the detectors are located in the backward hemisphere of the TPC, the operating conditions for the GEM detectors in PANDA are expected to be less harsh.

6.5.5.4 Signal Readout

The width of the electronic signal, both in time and laterally, determines the two-track resolution in space, and depends mainly on

- diffusion constant,
- drift velocity,
- distance between last GEM and pad plane,
- shaping time.

Contrary to wire chambers, the signal in a GEM detector is produced entirely by the motion and collection of electrons, which are created in the last foil before the readout anode. The slow ions do not contribute to the signal, which is therefore intrinsically fast. Consequently, the sampling rate in time (or, equivalently, in z coordinate) will have to be considerably higher than the $\sim 10\,\mathrm{MHz}$ normally used in TPCs with wire chamber readout.

The effect of the GEM amplification on the lateral size of the signal cluster can be inferred from the COMPASS triple GEM detectors, where the distance between the last GEM and the readout anode is 2 mm, and the corresponding field is 3.75 kV/cm. There, an average cluster size above threshold of about 1.2 mm was found, as can be seen in Fig. 6.27. Other measurements with similar field configurations but distances of 1 mm between the last GEM foil and the readout gave cluster sizes of the order of 0.7 mm. For a TPC, this number has to

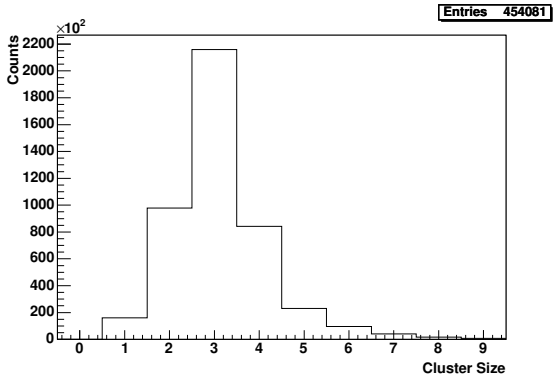

Figure 6.27: Cluster size distribution for a COMPASS triple GEM detector in units of strips, where one strip corresponds to 0.4 mm. Here, cluster size means number of strips/channels above threshold.

be convoluted with the spread of the primary electrons due to diffusion inside the long drift volume. Here, the expected contribution to the cluster width is $\sigma < 2$ mm for a drift length of 100 cm in a Ne/CO_2 (90/10) mixture, as can be seen from Fig. 6.19. Therefore, a pad size of not smaller than $2 \times 2\,mm^2$ seems reasonable, taking into account the large number (several hundred) of pads which contribute to a track. This topic has to be studied in more detail and measurements with prototypes as well as Monte Carlo simulations have to clarify the final pad design.

6.5.5.5 Ion Feedback

By applying a higher electric field on the extraction side of a GEM foil than on the collection side, as in Fig. 6.23 (right), ions created in the amplification region are preferentially collected at the upper layer of the GEM foil while electrons are efficiently extracted on the bottom side of the foil. In case the ion feedback, i.e. the number of ions reaching the cathode divided by the number of electrons collected at the anode in the same time interval, can be suppressed to a level of $1/G_{\mathrm{eff}}$, where G_{eff} denotes the effective gain, i.e. the number of electrons collected at the anode divided by the number of primary electrons per unit time interval, this feature can be exploited to avoid the need of a gating grid.

Extensive research is currently performed on optimizing the field configuration of a multi GEM structure in terms of ion feedback. For a triple GEM detector with standard foil geometry, as for COMPASS, it was found that minimal ion feedback can be achieved by alternating the electric field strengths between the various electrodes [37],

- $E_{\mathrm{drift}} = 200\,\mathrm{V/cm}$ (fixed),
- $E_{\mathrm{trans1}} = 8\,\mathrm{kV/cm}$,
- $E_{\mathrm{trans2}} = 60\,\mathrm{V/cm}$,
- $E_{\mathrm{ind}} = 8\,\mathrm{kV/cm}$,

and by producing most of the total avalanche charge in the last GEM foil (see Fig. 6.28 for an explanation of symbols). With these settings, the ion feedback

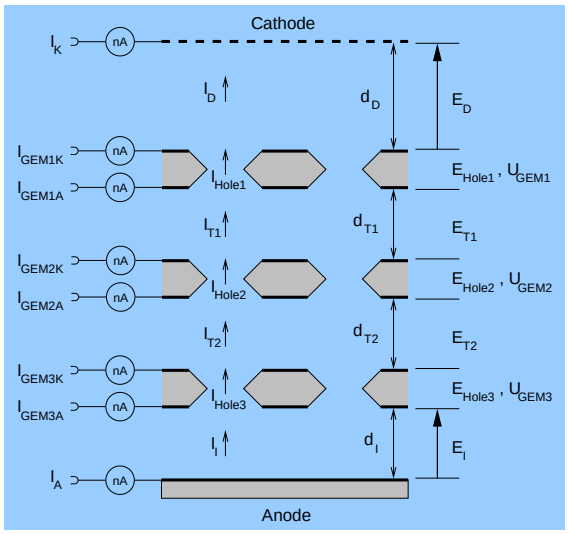

Figure 6.28: Definition of fields and currents in a triple GEM detector.

of a triple GEM detector was then measured as a function of the longitudinal magnetic field, shown in Fig. 6.29. At a field of 2 T, as envisaged for the PANDA solenoid, an ion feedback of $\sim 0.35\%$ was measured with a gas mixture of $Ar/CH_4/CO_2$ (93/5/2). Considering the fact that the applied field settings are in contrast to the optimum found in terms of discharge probability (low E_{ind}, largest amplification in first GEM), it remains to be shown that a chamber can indeed operate at such extreme values of electric fields.

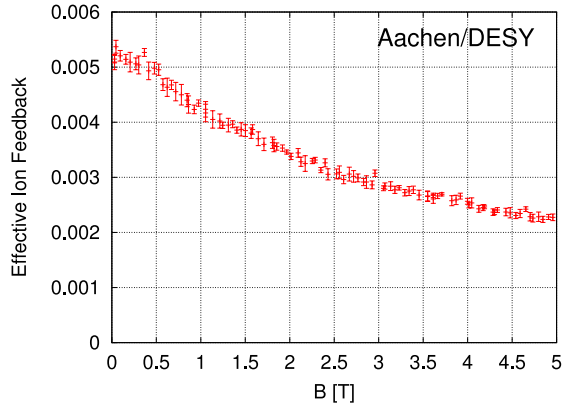

Figure 6.29: Ion feedback as a function of the magnetic field, measured at optimized field configuration for a triple GEM detector.

A possibility to further decrease the ion feedback is to add a GEM foil with unit gain on top of a triple GEM stack. In this case, it is essential for good $\mathrm{d}E/\mathrm{d}x$ resolution that no primary electrons are lost in the first foil, i.e. the transparency of the GEM should be close to unity. Here, the geometry of the GEM foil, like its thickness, hole size, pitch and shape (conical, double conical, *etc.*) was found to play a key role [38, 39]. This can be seen from Fig. 6.30, where the transparency of a single GEM for electrons is plotted as a function of the potential difference across the GEM for different geometries. Note that no charge amplification takes place at po-

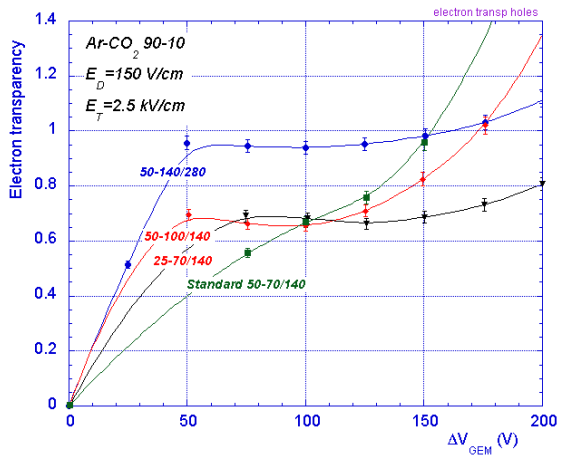

Figure 6.30: Electron transparency of a single GEM foil as a function of the potential difference across the foil, for different foil geometries. The notation is thickness - diameter / pitch in units of μm.

tential differences smaller than $\sim$ 150 V. Obviously, the fraction of electrons entering the hole, which is actually extracted from the hole, increases when the hole diameter and the pitch are doubled simultaneously with respect to the standard foil, leaving the aspect ratio constant.

In summary, the use of GEMs (and of other micropattern gas detectors like MicroMeGas or MHSP) in a TPC is a very active field of research world wide, partly triggered by the proposal to use a TPC as the central tracking device for an electron linear collider, which has similar requirements than the device envisaged for PANDA.

6.5.6 Electronics and Data Reduction

6.5.6.1 Requirements

In a TPC, the position perpendicular to the z (drift) direction of a charged particle interaction in the gas volume is simply given by the location of pads on which a signal is induced by the primary electrons. The position in the z direction is determined by measuring the drift time of the primary electrons to the readout anode.

The granularity of the front-end electronics both in space and time should be sufficiently small in order not to deteriorate the resolution. The arrival time of the charge cloud at the pads is normally determined by sampling the signal shape. Considering the fast signal from the GEM, and in order to guarantee that the two track resolution in z is limited by the longitudinal diffusion rather than by the sampling speed of the ADC, a sampling frequency of the order of 100 MHz is required. With a pad size of $2 \times 2\,\mathrm{mm}^2$, as suggested in Sec. 6.5.5, the TPC will have about 100 000 electronic channels, less than other TPCs currently under construction (ALICE) or proposed (TESLA) will have.

The high sampling rate and the high density of channels, however, require the design of highly integrated and inexpensive front-end electronics with low power consumption of a few mW per channel, which clearly constitutes a challenge. Massive data reduction by zero suppression and online extraction of features such as pulse charge and hit time, followed by pattern recognition and intelligent compression into track segments is necessary in order for the DAQ network to be able to digest the data.

In the standard operation of a TPC, the start signal for the drift time measurement is either given by an external trigger defining an event, or by predefined bunch crossings in a collider. In PANDA, the continuous nature of the beam does not allow the association of hits arriving at the TPC readout

plane with an absolute timestamp relative to the corresponding interaction. Instead, tracks from up to 1 000 events will be superimposed and mixed in time in one TPC "picture", depending on the gas mixture. In order to fix the absolute z coordinate of tracklets in the TPC, intelligent algorithms have to be developed, making use of special event topologies and the information from other detectors.

6.5.6.2 Front-end Electronics

We foresee to use an analogue method to fulfill the tasks of time and amplitude measurement. The signal on each TPC pad will be amplified by a fast, high-bandwidth amplifier and sampled at a rate up to 100 MHz by an 8-bit FADC. Fig. 6.31 shows the basic architecture of one front-end channel.

Zero suppression will then be performed on the basis of the digitized data; signals above individual thresholds for each channel will be stored in a large FIFO for further processing by FPGAs and/or DSP. The total integral over the pulse shape determines the energy loss $\mathrm{d}E/\mathrm{d}x$ in this particular bin. The arrival time of the charge cloud at the anode pads will be determined from the analysis of the digitized signal shape. In addition, clustering and pile-up handling will be performed already at the front-end level.

6.5.6.3 Pattern Recognition

The raw hit rate of the TPC represents a serious challenge for the readout system: at up to 20 MHz interaction rate, 5 charged tracks per interaction and about 1 000 hits per track 10^{11} hits have to be read per second. It is out of question to feed this data rate into an ordinary networked processing farm let alone put it to mass storage. There are only three viable options to tackle this problem:

- One buffers the raw data of the TPC for a very long time (seconds) until the final event building step takes place. There are two main disadvantages in this scenario: due to the large drift window in the TPC a big pileup of tracks of several hundred interactions has to be dealt with, in the worst case stored multiple times. Secondly the very late reading makes it impossible to use the signature of decaying particles in an earlier trigger selection level.

- The second possibility is to reconstruct already at the front-end level *tracklets* from the TPC hits. A tracklet as such represents a much smaller amount of data and is parametrized by two coordinates, two slopes, the curvature and the energy loss. In further processing levels it still has to be matched in time with other detectors to an interaction, but it can be used to search for decay signatures.

- Assuming that full online track reconstruction is too challenging and too risky in terms of recalibration and re-fitting of hits, a third option is to perform a compression of data based on a maximum of physical input. Here a similar scheme as for the online reconstruction is used for pattern recognition, but here as a preliminary grouping of hits to *hit trains*, which are then treated and compressed together.

Since we believe that the second option, although being technically challenging, is the most desirable solution, R&D should evaluate its feasibility. The third option is however a safe fallback and shares much of the infrastructure and algorithms needed for the second option. Here we outline the basic concept which could be a realizable implementation of an online TPC track finding.

It is assumed that in the initial part of the readout clusterisation, time reconstruction and amplitude determination took place. Each valid hit consists of a 3D address (x, y and t within a 50 μs window) and packed data for cluster centroid, time and amplitude. The first step after readout is now to store the cluster and clock it through the buffer at a rate equivalent to a reasonable fraction of the time resolution (e.g. 20–40 MHz). The buffer length has to be big enough to allow the processing units to safely find all good track segments.

The tracking algorithm to be realized in hardware is inspired by the Game of Life and Pacman. For that reason the basic processing unit is called *track eater*: each track eater eats its way along the hits of a track accumulating and fitting on the way all tracking parameters (slopes, energy loss, curvature).

To be more precise and speak in more technical terms: the track reconstruction hardware consists of the buffer described above, a set of processing units and a routing hardware transmitting at high rates hit data from the buffer to the track eaters. To have a reasonable safety margin about 5 000 track eaters should be available for an occupancy of 2 500 tracks per full drift window. The processing steps proceed as follows:

- When a valid hit, which is not yet assigned to a processing unit, appears in the active timeslice a track eater is called to start the track following. It marks in the routing table a region of

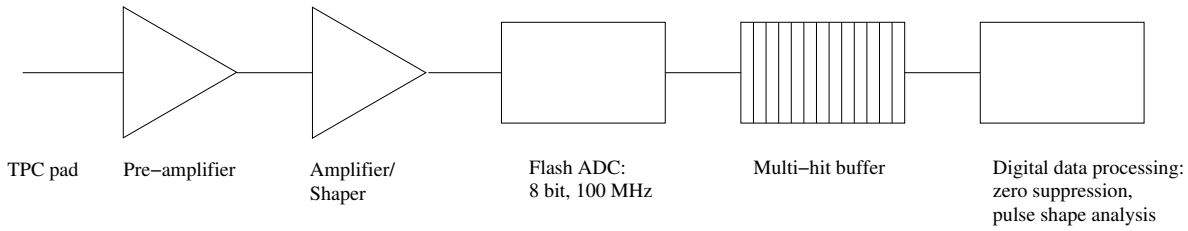

Figure 6.31: Basic architecture of one front-end channel of the TPC.

interest around the pad where the hit appeared to be read in the next cycle.

- The raw data network provides the track eater with all cells marked by it for hit search. The track eater checks all cells and if it finds a compatible next hit it updates the track parameters. It then selects the next region of interesting cells.

- The step above is repeated as along as hits can be appended to the tracklet or hit train. The track eater "dies" if no further hits are found for a certain number of cycles. If the found tracklet is too short, no information is retained, since the hits were most likely noise. A valid tracklet or hit train is put into the output data stream. If the track eater on the other hand finds more than one valid cluster or observes a significant track kink for some cycles it aborts as well and calls for the assignment of new track eaters after storing the output track segment marking a possible forking.

The basic difference between the second and third option in this scheme is the data output: in case of hit trains, a compressed hit information grouped by the pattern recognition is transfered resulting in a larger total event size. The advantage is that at pre-processing level possible physical signatures (kinks, decays, *etc.*) still can be detected and track reconstruction takes much shorter as long as it can use hit trains. Without the track fit, however, calculating invariant masses is not yet possible.

In the described setup one processing unit is not necessarily equal to one processor. Several units may be implemented in parallel in high performance FPGAs operating independently but on the same chip.

Although the total raw data rate of the TPC is of the order of 1 TB/s splitting it over 5 000–10 000 processing units means that a bandwidth of 1–2 Gb/s per unit is already sufficient for the processing. Given that for today's top-of-the-line FPGAs this is not an exceptional figure the feasibility of this design within the next 10 years is at hand.

The crucial point lies therefore rather in the speed and reliability of the pattern recognition algorithm. In this context it also has to be evaluated how one reacts to bad calibration constants which are effectively degrading the recorded data and how serious the fact of never having the raw hits stored is. See also the comments on online calibration in Sec. 11.3.1. In any case the deployment scenario would be to start with the third option and verify pattern recognition with hit trains before moving on to real online track reconstruction.

6.5.6.4 Event Deconvolution

TPCs are usually considered slow detectors, due to the long drift times. In a Neon-based gas mixture, the drift velocity for electrons at a drift field of 400 V/cm is approx. 2.7 cm/μs. This gives a maximum drift time for an electron in the TPC of 56 μs. At full luminosity, 560 events will be superimposed in this time window, corresponding to about 3 000 tracks. The relative time of arrival of hits will allow the reconstruction of tracklets or hit trains inside the TPC only, without fixing their absolute time (or z coordinate). There are several strategies and pieces of information which can be exploited to achieve this:

- Identify tracks coming directly from the well-defined interaction point.

- Identify secondary vertices with 4-vectors adding up to the interaction point.

- Match tracklets in the TPC with tracks from the MVD.

- Match tracklets in the TPC with hits in detectors outside the TPC, e.g. a position sensitive TOF system or the EMC. Due to the low density of tracks at the outer radius of the TPC, a moderate position resolution will be sufficient.

- The penetration point through the TPC end caps fixes z and t for forward and backward going tracks.

Algorithms for event deconvolution are being developed and will be tested in a realistic environment using Monte-Carlo simulations of the full $\overline{\mathrm{P}}$ANDA detector. The feasibility of a TPC in $\overline{\mathrm{P}}$ANDA depends strongly on the performance of these algorithms.

6.5.7 Performance

In this section simulation results for the $\overline{\mathrm{P}}$ANDA TPC are presented. The focus is on important performance characteristics like momentum resolution and particle identification. In addition the problem of space charge accumulation is discussed.

6.5.7.1 Momentum Resolution

It is important to test whether the TPC, in combination with the magnetic field of 2 T foreseen for the target spectrometer of $\overline{\mathrm{P}}$ANDA, covers the whole kinematical region of the physics channels. For example the muons from charmonium decays have momenta up to 6 GeV/c in the angular region covered by the TPC. Kaons from the $\eta_c \rightarrow 4K$ decay instead have momenta between 0.2 and 2 GeV/c, overlaped by background pions (see Fig. 6.34). For these pions Fig. 6.32 shows the relative momentum resolution as obtained from the simulation with the TPC. The plot shows results for three scattering

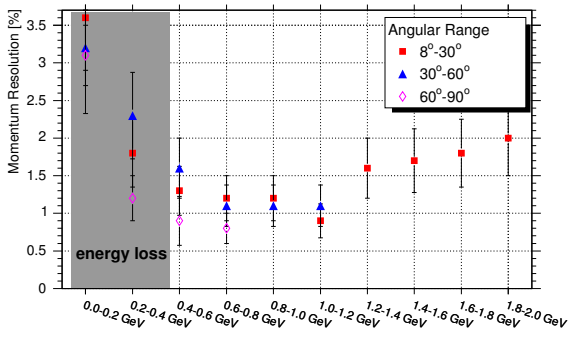

Figure 6.32: Relative momentum resolution for background pions, shown for three scattering angle ranges (arcsin(p_t/p)) and for ten momentum ranges; TPC acceptance starts at $\sim$ 8°; energy loss of low momentum particles not taken into account in the track reconstruction.

angle ranges. For each angular range ten momentum ranges from 0.2 to 2 GeV/c are plotted. As expected, the resolution is best for large angle tracks. The worse performance for particles with momenta less than 500 MeV/c arises from the fact that these particles already lose a considerable amount of energy in the detector which is not taken into account in the track reconstruction so far. Apart from small angle and low momentum tracks the obtained relative momentum resolution is $\sim$ 1 %, as required.

In order to investigate the TPC performance at higher momenta, a particle gun was used which shoots particles with momenta between 2 and 8 GeV/c isotropically through the TPC. The results are presented in Fig. 6.33. Again ten momentum

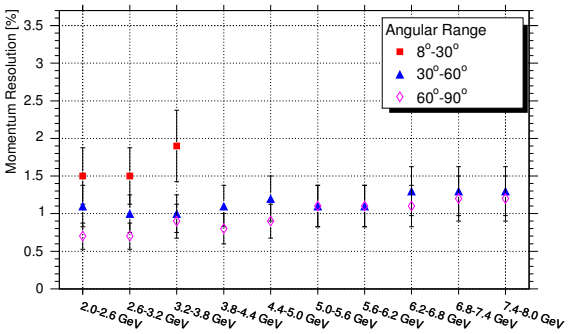

Figure 6.33: Relative momentum resolution for particles with momenta between 2 and 8 GeV/c, isotropically shot through the TPC, shown for three scattering angle ranges (arcsin(p_t/p)) and for ten momentum ranges; TPC acceptance starts at $\sim$ 8°.

bins are chosen, this time in steps of 0.6 GeV/c, and the same three angular ranges. It is clearly visible that the resolution gets better for higher scattering angles. For the large angle tracks it is again $\sim$ 1 % and, up to the maximum tested momentum of 8 GeV/c, very uniform.

It should be emphasized that the results shown here are very preliminary. First of all no cuts on the track quality have been performed. It was just checked whether the global fit of the track reconstruction went well and whether the TPC was hit by this track and participated in the reconstruction. The fit applied to the obtained residual distributions was a gaussian plus a constant background. Especially in low statistics bins this was not always perfectly adapted to the actual distribution. The error on the shown resolutions has therefore been estimated to a rather large value of 25 %. It is also important to keep in mind that the present status of the $\overline{\mathrm{P}}$ANDA simulation does not include a completely realistic track reconstruction, especially regarding track finding and fitting.

6.5.7.2 Particle Identification (PID)

Motivation:
Fig. 6.34 illustrates the usefulness of additional PID below 1 GeV/c. It shows the momentum distribution of the kaons resulting from the η_c decay. Within the same figure, the momentum distribution for background pions is also presented, generated just at the η_c resonance. About half of the kaons have momenta below 1 GeV/c, while the background pions are also prominent in this region. PID with Cherenkov detectors can not be used at such low velocities (see section 7). The TPC can contribute valuable PID information here, thus recovering a considerable amount of statistics at low momenta.

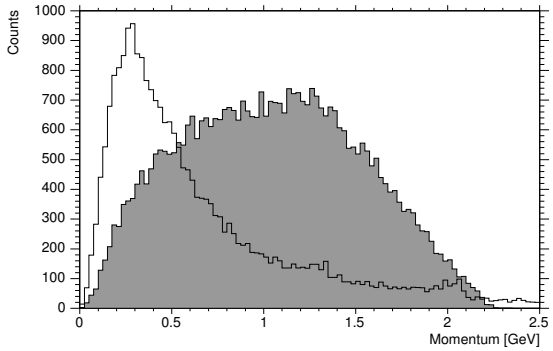

Figure 6.34: Momentum distribution of kaons from $\eta_c \rightarrow 4K$ decay (dark plot) and background pions (transparent).

PID with gas detectors:
The mean energy loss per track length in noble gases is a function of the velocity of the traversing charged particle. It is described by the well-known Bethe-Bloch-formula [21]:

$$\frac{\mathrm{d}E}{\mathrm{d}x} = \frac{4\pi N e^4}{mc^2}\frac{1}{\beta^2} z^2 \left(\ln \frac{2mc^2}{I}\beta^2\gamma^2 - \beta^2 - \frac{\delta(\beta)}{2} \right).$$

A measurement of this quantity in addition to the obligatory momentum measurement allows in principle for particle identification with any gas detector. This is referred to as the $\mathrm{d}E/\mathrm{d}x$-method which will be discussed in the following. A TPC is in particular qualified for this kind of PID since it provides a large number of energy loss measurements, basically the number of pads belonging to a track, within one detector volume.

PID with the PANDA TPC:
Fig. 6.35 shows the results of the application of this method in the PANDA simulation with the TPC as central tracker. The data were generated based on an event generator which shoots p, K, π, μ, e and the corresponding antiparticles through the whole detector. All tracks come from the interaction point (IP), with momenta between 0.2 and 3 GeV/c. As chamber gas Ne/CO_2 [90/10] has been used. The effects of primary ionization of the gas, drift and diffusion as well as the pad response have been taken into account. Loss of charge through electron attachment by gas impurities has been neglected here. Also with the perfect track finder (compare Sec. 12.3.3.2) we do not consider the loss of hits because of pattern recognition inefficiencies. These issues will be investigated in the near future.

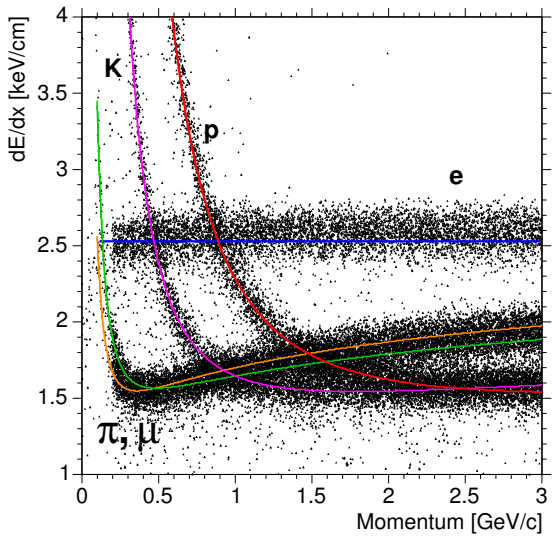

Figure 6.35: Energy loss over track length vs. momentum for p, K, π, μ, e; lines are fits of a parameterization.

To get rid of the long Landau tails in the distribution of the ionization strength a truncated mean algorithm [21] has been used in the reconstruction. To get the ionization strength of one particle the deposited charge in track-pieces of 6 mm length along the reconstructed trajectory is measured. The result of this is a distribution of about 100 $\frac{\Delta E}{\Delta x}$ measurements, which has a Landau-like shape. The upper 40% of these values are discarded. From the rest of the distribution the mean is calculated and taken as the $\mathrm{d}E/\mathrm{d}x$ of this particle. The graphs in Fig. 6.35 are fits of a parameterisation [21] to the data. They clearly reproduce the characteristic Bethe-Bloch curves for the different particle species. For the fits the curves have been separated using the Monte Carlo truth. In the real experiment these data have to be measured and the separation has to be done based on kinematic reasoning.

The $\mathrm{d}E/\mathrm{d}x$ resolution for one particle species is defined as the width of the associated $\frac{\Delta E}{\Delta x}$ distribution at a given momentum. Fig. 6.36 shows the performance which can be achieved by the TPC. The res-

olution is better than 5% for all particle species over the whole momentum range.

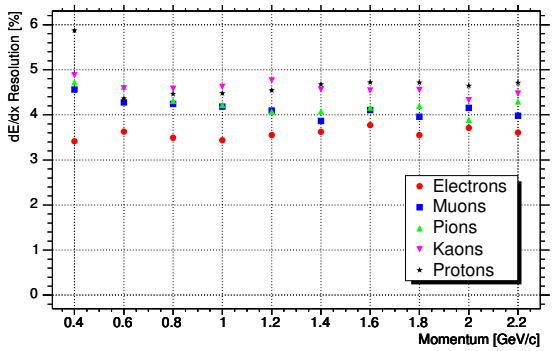

Figure 6.36: $\mathrm{d}E/\mathrm{d}x$ resolution of the TPC.

To demonstrate the momentum range in which the TPC can be used for PID Fig. 6.37 shows the achievable separation power of the TPC in a momentum range up to 4 GeV/c. The separation power between two particle species is defined as [21]:

$$D_{1,2} = \frac{2|I_1 - I_2|}{(\delta I_1/I_1 + \delta I_2/I_2)} \quad .$$

Here, I stands for the $\mathrm{d}E/\mathrm{d}x$ of the respective particle. For the calculations a constant resolution of 5% has been used.

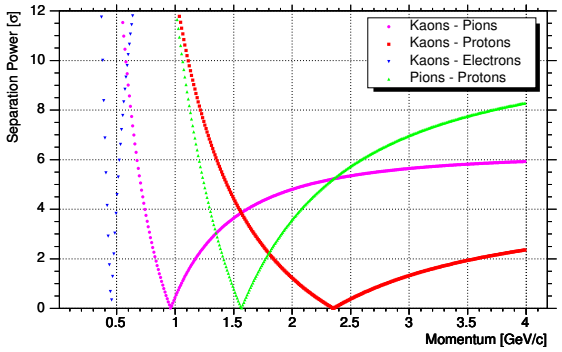

Figure 6.37: Separation power of the TPC for different combinations of particles ($\mathrm{d}E/\mathrm{d}x$ resolution is 5%).

The most important information the TPC can add to the overall PID, is to provide a good separation of kaons from pions. This is obviously possible for K-momenta below approximately 800 MeV/c. Between 800 MeV/c and 1.2 GeV/c the Bethe-Bloch curves of kaons and pions overlap and the separation power drops to values that do not allow a separation. Nevertheless the different shapes of the relativistic rise regions again allow a separation at even higher momenta on the 5σ level.

Fig. 6.38 shows an example how this information can be used to improve the particle identification efficiency in the analysis. The plot shows a stacked histogram of the momentum spectrum of reconstructed kaon candidates from the charmonium decay $\eta_c \rightarrow \phi\phi \rightarrow K^+K^-K^+K^-$ (see Sec. 13.5.2).

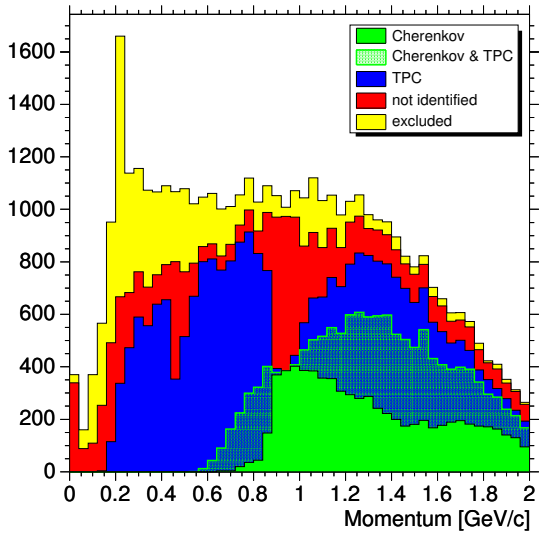

Figure 6.38: Stacked histogram: momentum distribution of kaon candidates from $\eta_c \rightarrow \phi\phi \rightarrow K^+K^-K^+K^-$ (including secondaries); blue: kaons which are identified by the TPC; green: DIRC and RICH contribution; yellow: excluded from the kaon hypothesis.

The colors denote the contributions of different PID subsystems to the identification of the kaons. The likelihood cut for the kaon hypothesis was set to 0.5 in this case. The yellow fraction is composed of particles which are clearly excluded from being kaons - indeed they are mostly delta electrons and other secondary particles. This is emphasized by the fact that the rest of the histogram (red, blue, and green fractions) nicely follows the kaon momentum distribution (compare Fig. 6.34). The red area corresponds to particles for which no clear decision could by made, while the blue and green fractions belong to particles clearly identified as kaons by the TPC and the Cherenkov detectors respectively. In the blue-green area a good identification with the TPC as well as the Cherenkov detectors was possible. For the TPC (blue fractions) the excellent efficiency at low momenta is prominent. The two steep valleys at 0.5 GeV/c and at 0.9 GeV/c correspond to those points in the Bethe-Bloch plot (see Fig. 6.35) where the kaon curve crosses the electron curve and the pion/muon curve respectively.

We conclude that the TPC is able to supplement the PID information of the DIRC and the RICH in

a region, where these detectors are not sensitive any more and can even contribute to the identification of charged particles at high momenta.

6.5.7.3 Estimates of Space Charge

The charged particles which are traversing the TPC create a trace of ionised gas atoms and electrons. While the electrons are removed comparatively quickly by the drift field, the positively charged ions remain in the detector volume for a longer time, because their drift velocity is slower by a factor of approximately 1 000 compared to the electrons. The resulting space charge distribution which will distort the drift field in the TPC is an inherent feature and cannot be avoided.

The readout chambers of the TPC are another possible source of ions. To keep the ion feedback low GEM detectors will be used in the PANDA TPC. Due to their special geometrical design these devices provide an intrinsic suppression of the ion backdrift (see section 6.5.5.5). Still some ions may reach the drift volume and contribute to the accumulating space charge there. The distribution of the developing space charge in the detector volume is investigated under the assumption of an unmodulated beam.

Fig. 6.39 shows the density distribution of positively charged ions after 155 ms at a rate of 10^7 events per second in a Ne/CO_2 standard mixture. We assume the ideal case of an ion feedback suppression which is equal to $1/G_{eff}$. That means that for every electron reaching the GEMs one ion is liberated into the drift volume.

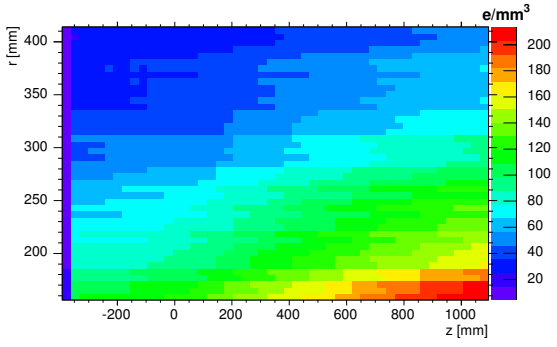

Figure 6.39: Spatial distribution of charge density in the drift volume after 155 ms at 10^7 events/s.

To simulate the development of the charge density the TPC volume is divided into concentric cylindrical sheets of different radii and into slices at different z. The resulting volumes are ring-segments which cover regions of 3 cm in z-direction and 6 mm in r. In the simulation a very simple transportation algorithm is used. Time steps are chosen to be the time the ions need to drift through one volume element. Drifting ions and charge from primary ionization which comes from events, that happen in the respective time step are added and passed to the next volume element. Feedback ions are simply added to the first bin and propagated through the TPC.

The density map clearly shows the decrease of charge density with increasing radius. In forward direction the accumulated charge density is higher, due to the fact, that most particles are boosted into the forward direction.

Interesting for any attempt of an offline correction of the effect, that this space charge will have on the track reconstruction is the stability of the distribution in time.

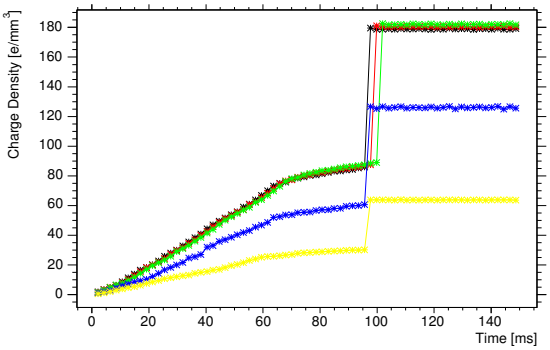

Figure 6.40: Development of space charge in time. The black, red and green graphs correspond to volumes in the TPC which are at the same radius (r = 174 mm)but are displaced by a few cm in z each. The blue and green graphs are at the same z as the black one (95 cm downstream of target), but reflect the charge density at different radial distances.

In Fig. 6.40 the time development of the charge density in five different bins of the map (Fig. 6.39) is shown. There are several features to observe:

- As one would expect the charge density drops with the radial distance (from black to yellow).
- The sharp step at $\sim$ 95 ms marks the moment when the front of feedback ions from the readout plane reaches this point in the TPC. Consequently this time is slightly different for those bins which are at different z.
- After these ions have reached a certain point the space charge is saturated there.

- The kink in graphs (between 55 and 65 ms) can be understood when one looks at the distribution of the primary ionization in the detector volume (Fig. 6.41).

To understand this picture consider one volume element in the TPC. Since the time between two events is much smaller than one drift step, the drift (neglecting the feedback ions for the moment) basically integrates the deposited primary ionization over those bins in z that are upstream of the volume under consideration. With proceeding time the ions from bins which are further and further away reach this point. So in time the integration range is growing. This is why the space charge density is rising with time. This also explains, why the saturation is reached at the same time as the feedback ions arrive, because the feedback ions are produced at the very end of the TPC.

The kink is easily explained by the structure of the primary ionization which is deposited in the detector volume. Fig. 6.41 shows a map of the primary space charge. There is a sudden drop in the density at angles larger than $\sim$ 75°. The reduced flux of charge from these regions leads to a smaller rise in the curves. The angle of $\sim$ 75° (dotted line) also explains the different times at which this becomes visible in Fig. 6.40.

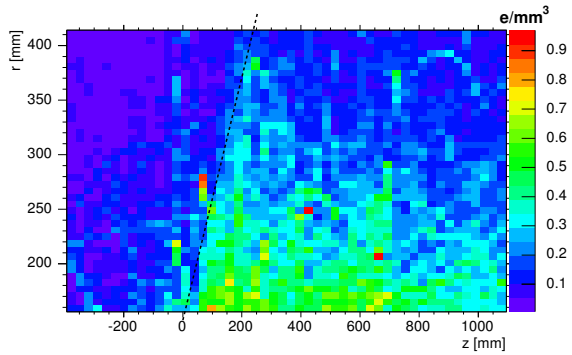

Figure 6.41: Charge density from primary ionization (2 000 events).

The time scale on which the chamber reaches equilibrium between produced and off-drifting charge is one ion drift time ($\sim$ 100 ms), depending on the drift field and the gas mixture.

Once the whole chamber has reached an equilibrium, the charge density stays very stable because of the very short period between two events compared to the ion drift time. This should allow us to correct the distortions of the drifting electrons at the reconstruction stage. For the STAR TPC such a space charge correction has already been applied successfully [40].

6.5.8 Prototypes

This section describes the ongoing work on the prototype development for the $\overline{\text{P}}$ANDA TPC. Two small GEM-based TPC prototypes are currently under construction, one with 8 cm and one with 24 cm drift length. Both have a diameter of 20 cm and are, apart from the different drift length, designed in exactly the same way.

The short prototype has been designed to fit into a dipole magnet which is available at TU Munich. This dipole can provide homogeneous magnetic fields up to 1 T for an area of about $(5\times5)\,\text{cm}^2$. With this setup we plan to study the performance of a GEM-based TPC in a magnetic field. An X-ray gun will be used to create space charges inside the TPC gas volume. With the longer prototype we intend to study in more detail the effect of the drift distance on the detector performance, e.g. concerning electron attachment.

The layout has to guarantee easy replacement and modification of gas amplification stage, readout-PCB and front-end electronics. A robust design, a sufficient number of irradiation windows for X-rays and low-energy β-rays as well as a pad-readout at ground potential facilitate the handling and manipulation during measurements. All mechanical support structures like flanges or the cathode end cap are made out of Ferrozell Vetronit G11.

In addition to the TPC prototype development a $(10 \times 10)\,\text{cm}^2$ triple GEM detector has been constructed and commissioned. It has been designed to allow easy changing of the GEM foils, the goal being to further study ion feedback, e.g. with different hole geometries.

6.5.8.1 Fieldcage and Support Vessel

The design of the mechanical parts of the TPC prototype has been adapted from a similar detector built and successfully operated with GEMs at Karlsruhe for the TESLA TPC [41]. The fieldcage consists of a 125 μm thick Kapton foil which has a set of 18 μm thick copper strips on each side. The strips are 3 mm wide and are arranged with a pitch of 4 mm. The strips on one side overlap with the strips on the other side in a way that the 1 mm gap is completely covered.

From inside out, the fieldcage is surrounded by a 125 μm Kapton foil for electric insulation, a 4 mm honeycomb support structure which is laminated on

both sides by 200 μm Ferrozell Vetronit G11 and a 50 μm copper foil connected to ground to define the ground potential and to shield the detector. Several windows for irradiation are foreseen by sparing out the honeycomb structure and the copper foil at certain positions. Fig. 6.5.8.1 shows pictures of an example fieldcage very similar to the one currently under construction. The inner copper strips are visible as well as the irradiation windows, the resistor chain and the HV feedthroughs which define the potential of the first and the last strip.

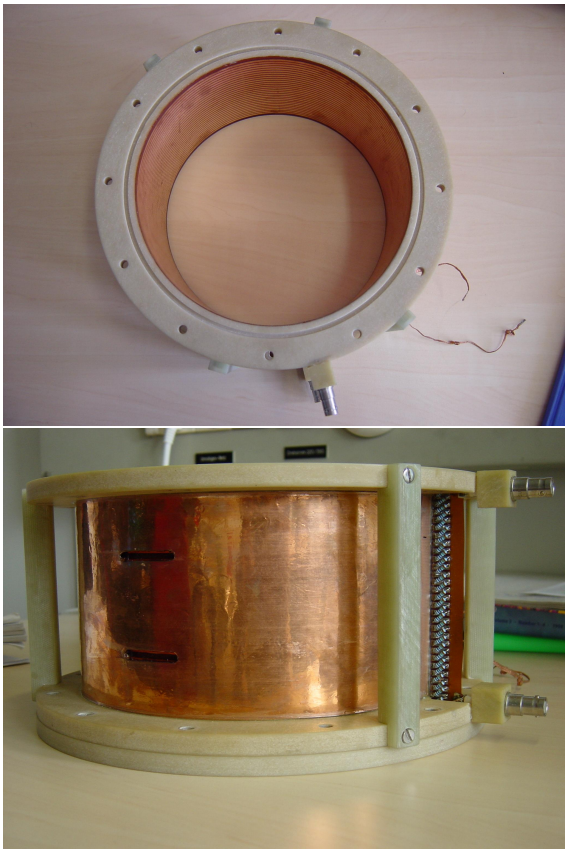

Figure 6.42: Photograph of the prototype fieldcage; top: inner copper strips; bottom: irradiation windows, resistor chain and HV feedthroughs.

6.5.8.2 Readout Plane and GEM foil stack

The readout plane is designed in a way that it is easily exchangeable , using a flange system (see Fig. 6.5.8.1). Gas tightness is assured by an O-ring. The readout plane itself is a 2.4 mm thick multilayer PCB (G10) which contains the pads. The pads have an area of $0.8 \times 6\,\text{mm}^2$ and a pitch of 1 mm and 6.2 mm respectively. The analogue signal from each pad is transferred to a 64-pin SMD connector soldered on the backside of the PCB using contact vias which are displaced in the different layers of the PCB to ensure gas tightness. The readout plane also hosts the high voltage feedthroughs for the GEM foils and a gas inlet. Also the GEM stack is mounted on the readout PCB, fixed by four plastic rods. In total an active area of $(10 \times 10)\,\text{cm}^2$ is covered by the GEM foils and the readout pads.

6.5.8.3 High Voltage System

The fieldcage foil is folded and brought out of the gas volume at one side of the support vessel (see Fig. 6.5.8.1). By this it is possible to connect the copper strips through a resistive voltage divider chain without heating up the counting gas and without distorting the field inside the detector. 10 MΩ resistors of 1% tolerance are used for the resistor chain. The potential of the first and the last strip is defined with the help of two high voltage feedthroughs, also visible in Fig. 6.5.8.1.

On the side opposite of the readout plane, the cathode is realized as copper-clad Kapton foil glued on a 10 mm Vetronit G11 plane. Here another high voltage feedthrough exists to define the cathode potential. On the anode side, a copper plate shields the part not covered by the GEM foils to avoid field distortions of the drift field outside the square GEMs. All potentials, starting from the cathode plane, including the fieldcage strips, the GEM foils and the correction plate, have to be adjusted in a way, that the voltage drop to the pads on ground potential is uniform. In order to get an electric field of the order of 400 V/cm, a high voltage of about 10 kV is necessary for the 24 cm prototype.

6.5.8.4 Gas System

At the moment only an open gas system is designed for the first prototype operation but for the future also a closed system is foreseen. For the open system the setup is rather simple, basically it is possible to mix three gases with the help of three flowmeters. These flowmeters are adjusted and calibrated for different gases and flows providing the possibility to use Ar or Ne as main counting gas, CH_4 or CO_2 as quencher and for example CF_4 as third admixture. They are all linked through a control unit which regulates the flow of each gas and thereby sets the mixture ratio. With this setup we plan to test the GEM-based TPC prototypes with different mixtures of the mentioned gases.

6.5.8.5 Front-end Electronics

For the front-end electronics we will use at least for the beginning the system which was developed for the ALICE TPC. One front-end card contains the complete readout chain for amplifying, shaping, digitizing, processing and buffering of the TPC signals. In particular each readout channel is comprised of four basic units: a charge sensitive preamplifier/shaper (PASA), a 10-bit 10 MHz low-power ADC, an ASIC which performs baseline subtraction and zero-suppression (the ALTRO chip) and a multiple-event buffer. The PASA chip can handle 16 channels while the ALTRO chip is designed for 8 channels. One whole card can process 128 channels. Since the ALICE TPC is wire-based detector the signal polarization is opposite compared to a GEM-based detector. Therefore a converter card has been developed at CERN which makes it possible to use the ALICE front-end cards also for GEM-based TPCs.

6.5.8.6 Triple GEM Detector for Ion Feedback Studies

As mentioned above a $(10 \times 10)\,\mathrm{cm}^2$ triple GEM detector has been designed and commissioned. It has a single projection microstrip readout with strips of 200 μm pitch and its design allows for a very flexible handling and operation of the GEM foils. Each electrode has its own high voltage channel including a current meter with a resolution of the order of nA. By this it is possible to set the voltages of all foils independently and measure the corresponding currents at the same time. Also the separation of GEM foils with respect to each other and the readout strips is changeable. Similar to the TPC prototypes windows for X-ray irradiation are integrated. Their position has been designed in order to have the X-rays parallel to the foils and also below the first foils. Fig. 6.43 shows a photograph of this detector.

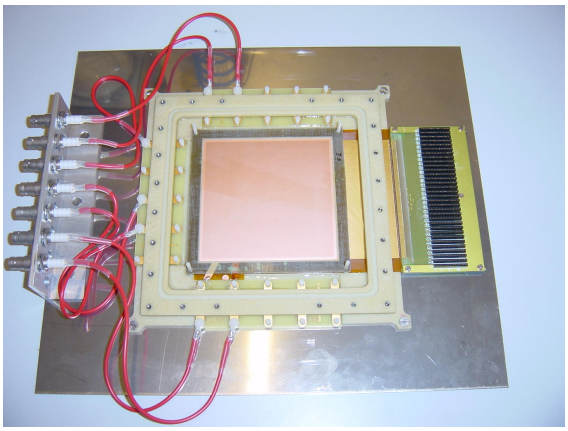

Figure 6.43: Photograph of a triple GEM detector for laboratory studies of ion feedback. The top cover of the gas vessel has been removed to open the view to the GEM foil. The HV feedthroughs are visible as well as the wire-bonded readout card.

6.5.9 Quality Control and Calibration

6.5.9.1 GEM Detectors

COMPASS was the first large-scale experiment to use GEM-based detectors. A lot of experience has been gained during the construction of these detectors. Quality assurance procedures for all detector components have been established in order to guarantee a uniform and stable operation of the chambers [34]. These will be adopted to a large extent for the $\overline{\text{P}}$ANDA TPC.

The production and handling of GEM foils and the construction of GEM detectors will be done under cleanroom conditions (class 10 000 or better). The foils and all mechanical parts on contact with high voltage (HV) will be tested for HV stability before being mounted, and after each mounting step. For use in a TPC, a good uniformity of gain over all GEM foils is essential in order to achieve the desired $\mathrm{d}E/\mathrm{d}x$ resolution. This will be tested using optical methods to verify uniform transparency, and will be measured on control samples in a dedicated test setup.

The final detectors will be subjected to extensive tests using X-rays and radioactive sources, before they are mounted to the TPC. Since the active detector surface required for the $\overline{\text{P}}$ANDA TPC is only about a quarter of the total active area of GEM detectors in COMPASS, the construction and testing of the GEM detectors can be done in a relatively small laboratory, without having to rely on external companies.

6.5.9.2 Mechanics and Gas

Due to its complexity and the requirements on stability and uniformity, the mechanical components of the $\overline{\text{P}}$ANDA TPC (field cage, end plates, cooling system, gas system) are expected to be manufactured by specialized companies. Detailed sets of specifications will be given to the manufacturers. Tests of dimensions, temperature stability, *etc.* will

be performed both before and after delivery, and during assembly. In addition to adherence to mechanical tolerances, the choice of materials and fabrication procedures for components in contact with the detector gas have to guarantee that the detector operates at the desired performance and within the envisaged costs. Here, a lot of work has been and is currently being done for the LHC gas detectors, on which we can rely without having to reinvent the wheel. Final certification of a set of materials in connection with the final gas mixture, however, remains mandatory.

6.5.9.3 Calibration

Operating a TPC poses the challenging task of having about 100 000 channels, each with its own amplifier, shaper, ADC, responding in precisely the same manner to a given number of electrons created by the primary ionizing track. To this end, gas purity, gas amplification, and signal induction have to be well under control. In addition, the response of each channel to a well-defined signal has to calibrated, and the results of this calibration have to be available online for data processing. Several methods have been developed for this purpose in the past. For PANDA, we consider several options for pulse height calibration, among them the so-called Krypton method, where trace amounts of radioactive Krypton are introduced into the detector gas during dedicated calibration runs, and the use of laser tracks for online monitoring.

6.5.10 Timeline

Fig. 6.44 shows the timelines for the development and the construction of the PANDA TPC.

6.6 Forward Tracker

Particles emitted at polar angles below 22° which are not fully covered by the Central Tracker will be traced in two planar drift chambers – DC1 and DC2, placed 1.4 m and 2.0 m downstream of the target, inside the TS magnet. The diameters of the active areas of the chambers will be 1.2 m and 1.6 m, respectively. Two pairs of planar drift chambers, DC3-DC4 and DC7-DC8, will be installed before and after the magnet for measurements of the deflection of particle trajectories in the Forward Spectrometer (FS) dipole magnet. Additionally, for tracing of low energy particles being bent inside the dipole magnet gap towards the magnet yoke, a drift chamber pair DC5-DC6 will be installed inside the gap. The chambers DC3,..,8 have rectangular active areas with dimensions specified in Table 6.10. The extensions of the active areas for the DC3 and DC4 chambers correspond to the angular acceptance of the Forward Spectrometer, i.e. ±10° horizontally and ±5° vertically. The horizontal extensions of the DC5,..,DC8 chambers are bigger than the dimensions resulting from the horizontal acceptance of the FS, allowing to trace the particles deflected in the vertical magnetic field of the dipole magnet beond the FS angular range. The requirements for

Chamber	Distance	Active area
DC1	1.4 m	Ø=1.2 m
DC2	2.0 m	Ø=1.6 m
DC3	2.6 m	1.0 m × 0.45 m
DC4	3.2 m	1.2 m × 0.56 m
DC5	4.0 m	1.7 m × 0.70 m
DC6	4.7 m	2.8 m × 0.82 m
DC7	5.65 m	3.5 m × 0.99 m
DC8	6.95 m	5.4 m × 1.22 m

Table 6.10: Distance from target and dimensions of active areas of the forward drift chambers.

PANDA tracking are given in Sec. 6.1.

For the forward tracking, the use of drift chambers with square drift cells is planned, with sense and cathodes wires mounted on massive self-supporting frames. However, for DC1 and DC2 the alternative solution of drift chambers with cathode foils is considered, based on light frames. Therefore, the chambers would easier fit in the limited inner space of the PANDA solenoid. In the next chapter, the drift chambers with cathode wires as well as the chambers with cathode foils are described. The final choice between will be made after constructing prototypes and testing them in a high rate environment.

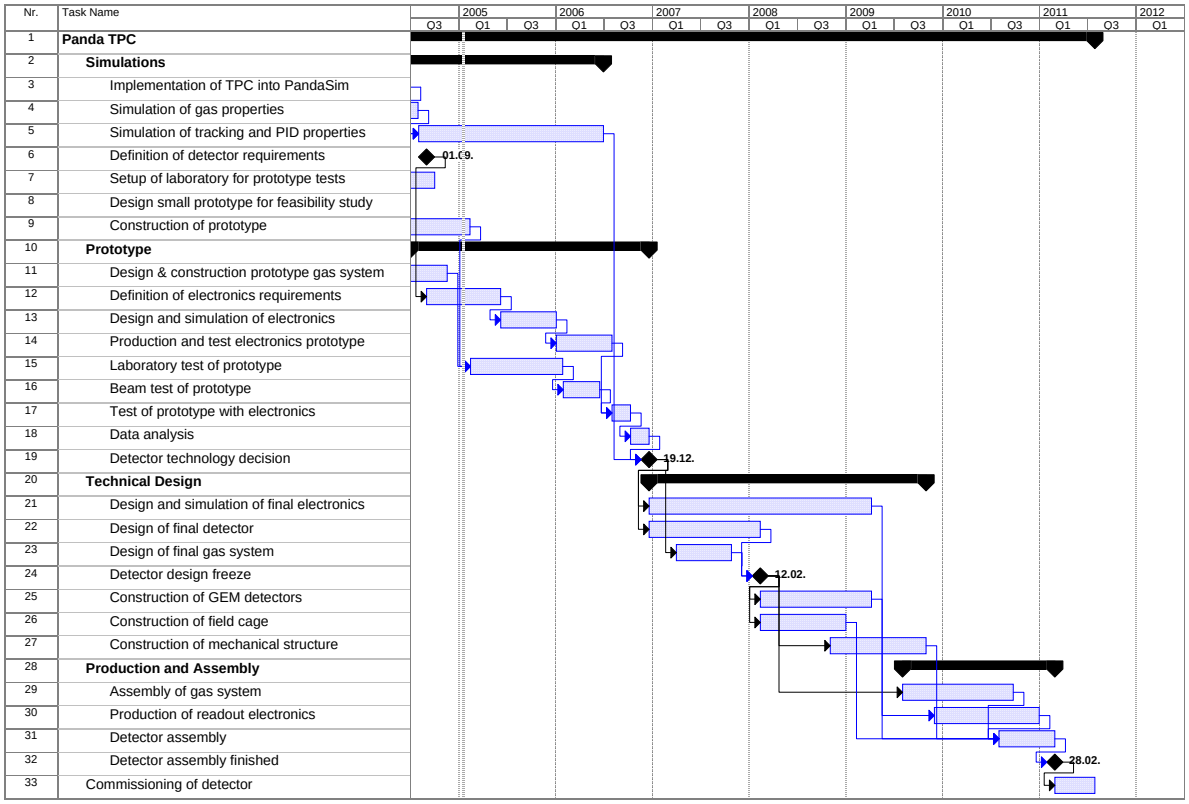

Figure 6.44: Timelines for the TPC development and construction

6.6.1 Cathode Wire Type

6.6.1.1 Layout

The chambers contain $(1 \times 1)\,\mathrm{cm}^2$ square drift cells (see Fig. 6.45) identical with the structure used in the drift detectors for the μTRV experiment at PSI [1]. Here, the electric field has approximately cylindrical symmetry, and the distance-drift time relation depends only weakly on the particle angle of incidence. In the PSI detectors, the sense wires were made of 20 μm thick gold-plated tungsten, whereas for the 50 μm field and cathode wires a Cu(98%)-Be(2%) alloy was used. The cathode as well as the field wires were grounded and the sense wires were set at a positive potential. With the gas mixture of 90% Ar + 10% ethane with addition of ethanol vapor saturated at 5°C the chambers were operated at relatively low working voltage of +1 550 V [1]. In the FS chambers, instead of argon-ethane it is intended to use Ar/CO_2 mixture. According to the recent studies on high rate detectors for LHC, this mixture allows large accumulated charges of the order of 1 C/cm as expected in the central region of the forward drift chambers at $\overline{\mathrm{P}}$ANDA (see Sec. 6.6.7.3). Furthermore, it is planned to use thicker cathode and field wires with a diameter of $\varnothing = 110\,\mu$m in order to keep the field at the surface below 20 kV/cm to minimize conditions causing cathode deposits. Also, it is planned to use aluminum instead of a Cu(98%)-Be(2%) alloy for the field and cathode wires in order to reduce the multiple scattering. Gold plated aluminum 5056 alloy from the California Fine Wire Company is one choice. For the sense wires it is intended to use 20 μm thick gold-plated tungsten offered by the Luma Sweden Company, as has been used for the PSI detectors. The detection planes are grouped in pairs in the same orientation of the wires, staggered by a half cell width in order to resolve the left-right ambiguity of the track position with respect to the sense wire (see Fig. 6.46). In the DC1,2 chambers, the wires are stretched on frames of octagonal shape, while for the DC3–DC8 chambers rectangular frames are used. The beam-pipe will pass through central holes in the chambers and the most central wires will either be eliminated or mounted on additional insulating rings surrounding the pipe. In the first case, the chambers DC1 and DC2 contain four pairs of detection planes with wires oriented at 0°, 90°, +45°, -45° with respect to the vertical direction (see Fig. 6.47). The configuration allows to compensate the inefficiency caused by a lack of central wires and makes it possible to

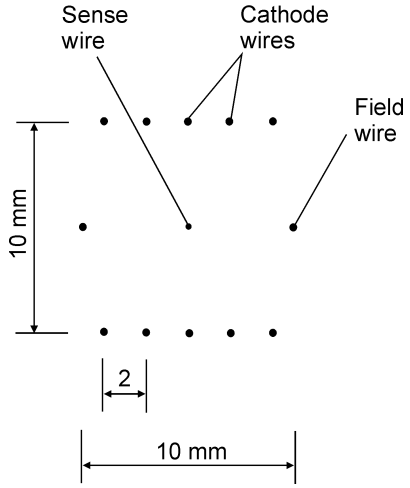

Figure 6.45: Scheme of quadratic drift cell.

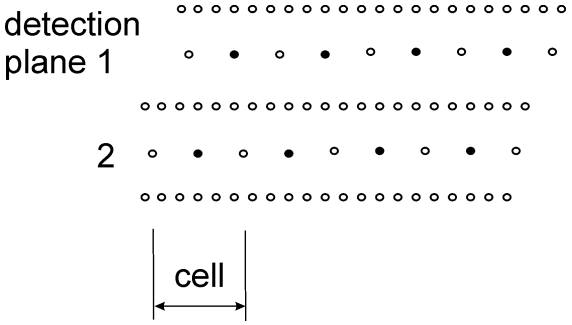

Figure 6.46: Double layer of drift cells.

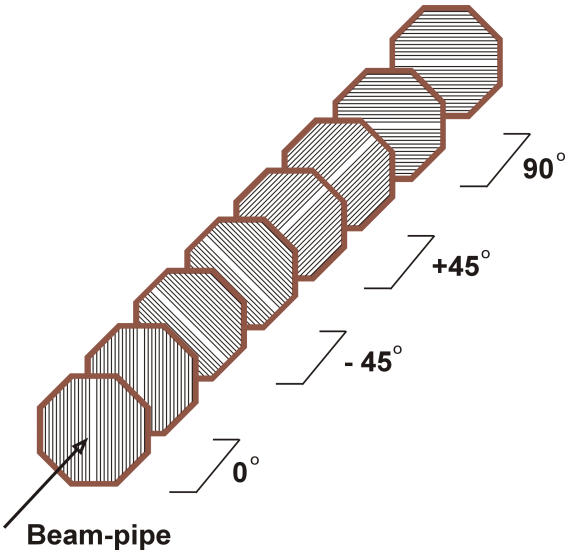

Figure 6.47: Pack of eight detection planes grouped in four double layers. The most central wires are skipped leaving place for the beam pipe.

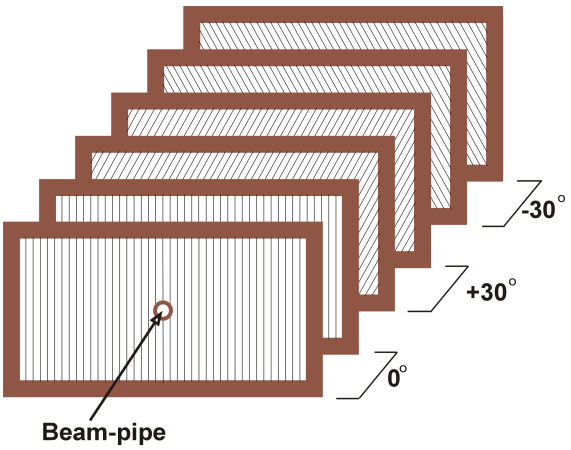

Figure 6.48: Pack of six detection planes grouped in three double layers. The most central wires are mounted on insulating rings.

perform three-dimensional reconstruction of tracks in the entire active area of the chambers. For the DC3–DC8 detectors, the orientation of wires in subsequent pairs of detection planes will be 0°, +30°, -30°, +60° or similar. The smaller inclinations of wires as compared to the DC1 and DC2 case are dictated by the vertical orientation of the magnetic field in the FS dipole magnet and, consequently, the crucial role of the reconstruction of tracks in the horizontal plane for the momentum determination. The solution of mounting the central wires on insulating rings was used for the proportional chambers built for internal experiments at the IUCF-ring [42]. The main advantage of this solution is that, due to the higher overall detection efficiency, the number of pairs of detection planes can be reduced to three. In this case, one can choose wire inclinations of 0°, +45°, -45° for DC1,2 and of 0°, +30°, -30° for DC3–DC8 (see Fig. 6.48). The mechanical and electrostatic properties of the insulating rings shown schematically in Fig. 6.49 have still to be optimized and tested. In particular, the question of the minimal width of the rings and the extension of dead areas introduced by them has to be answered. The geometrical parameters of the chambers are collected in Table 6.11.

6.6.1.2 Mechanical Construction

The chamber frames are made of 5 mm thick Stesalit 4411W, a disordered epoxy-fiberglass composite commonly used in construction of wire detectors. Each detection plane consists of three frames with glued printing boards for soldering the wires

Chamber	Distance from target	Dimensions of windows	Number of layers	Inclination of wires	Number of cells
DC1	1.4 m	Ø=1.2 m	8	0°, 90°, +45°, -45°	$8 \times 112 = 896$
DC2	2.0 m	Ø=1.6 m	8	0°, 90°, +45°, -45°	$8 \times 152 = 1216$
DC3	2.6 m	1.1 m × 0.5 m	6	0°, +30°, -30°	$2 \times 108 + 4 \times 118 = 688$
DC4	3.2 m	1.3 m × 0.6 m	6	0°, +30°, -30°	$2 \times 128 + 4 \times 140 = 816$
DC5	4.0 m	1.8 m × 0.9 m	6	0°, +30°, -30°	$2 \times 178 + 4 \times 188 = 1108$
DC6	4.7 m	2.9 m × 0.9 m	6	0°, +30°, -30°	$2 \times 288 + 4 \times 294 = 1752$
DC7	5.65 m	3.6 m × 1.1 m	6	0°, +30°, -30°	$2 \times 358 + 4 \times 364 = 2172$
DC8	6.95 m	5.5 m × 1.4 m	6	0°, +30°, -30°	$2 \times 448 + 4 \times 544 = 3072$

Table 6.11: Basic dimensions of the forward drift chambers. Number of wires in the chambers DC1,2 was calculated under the assumption that the central wires are omitted and, consequently, the number of layers is equal to 8 in each chamber. The chambers DC3–DC8 contain 6 detection planes each, and the central wires are mounted on insulating rings.

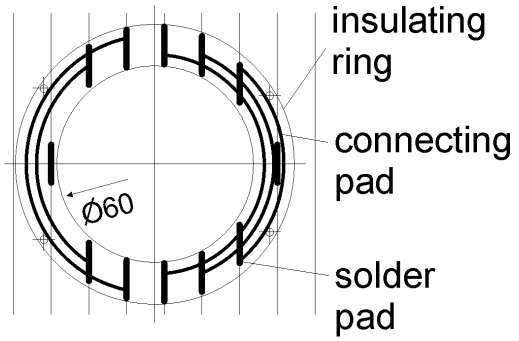

Figure 6.49: Ring for mounting wires in the central part of the chambers.

(see Fig. 6.50). One frame contains the alternating sense and field wires with a 5 mm spacing. On either side of it there are two frames with the cathode wires spaced by 2 mm. The field wires will be wound up with a winding machine on auxiliary frames equipped with combs for fixing the relative distance of the wires. Then the auxiliary frames will be placed on the fibreglass frames and the wires will be soldered on the printing boards. The sense and the field wires will be stretched individually. The wire positions are defined by Ø = 2 mm plastic pins which are fixed at the printing boards near the soldering pads. The openings for these pins will be drilled with a CNC jig boring machine assuring a positioning accuracy better than ±0.02 mm. Each wire touches two pins which guarantees a high accuracy in the positioning. Fig. 6.51 shows printing board designed for soldering the sense and field wires. Openings for inserting the plastic pins used for positioning the wires are also indicated. The high voltage is connected to sense wires through 1 MΩ resistors and the signals are read out through 1 nF coupling capacitors. Each pair of planes is screwed to an auxiliary frame made of 10 mm thick aluminum (see Fig. 6.52). With a mechanical tension of 30 g for the sense wires and of 100 g for the 110 μm aluminum cathode wires, the total load coming from wires in one double-layer of DC2, the largest chamber inside the $\overline{\text{P}}$ANDA solenoid, is about 268 kg. This force is partly overtaken by the aluminum frame. The alignment of the epoxy-fiberglass frames and the aluminum frame in one pair of detection planes is achieved by means of Ø = 18 mm brass pins penetrating the frames. Pairs of detection planes mounted on the aluminum support frames form independent mechanical units. These units are positioned in the $\overline{\text{P}}$ANDA setup by means of linear bearings which are fixed to the TS magnet in the case of DC1,2 and to the support of the dipole magnet for DC3,..,8. The linear bearings make it possible to displace the chambers along the beam-pipe and thus they allow to push in and out the chambers from the required position e.g. inside the dipole magnet. A schematic drawing showing a side view of the DC5–DC6 pair mounted on common linear bearings is shown in Fig. 6.53. The chambers will be aligned using conventional optical techniques. It will be checked and refined by means of tracing particle tracks with the field of the $\overline{\text{P}}$ANDA dipole magnet turned off. The packs of detection planes forming separate chambers are closed from both sides with 20 μm Kapton windows glued to the aluminum support frames. The gas tightness is guaranteed by Ø=2 mm O-rings placed in grooves machined in the frames. A system of gas inlets and outlets allows for thorough flushing of the chamber volumes with the gas mixture at a slight overpressure with respect to the atmospheric pressure. In the neighborhood of the beam pipe, the chamber volume is limited by a cylinder made of Kapton foil (see Fig. 6.54).

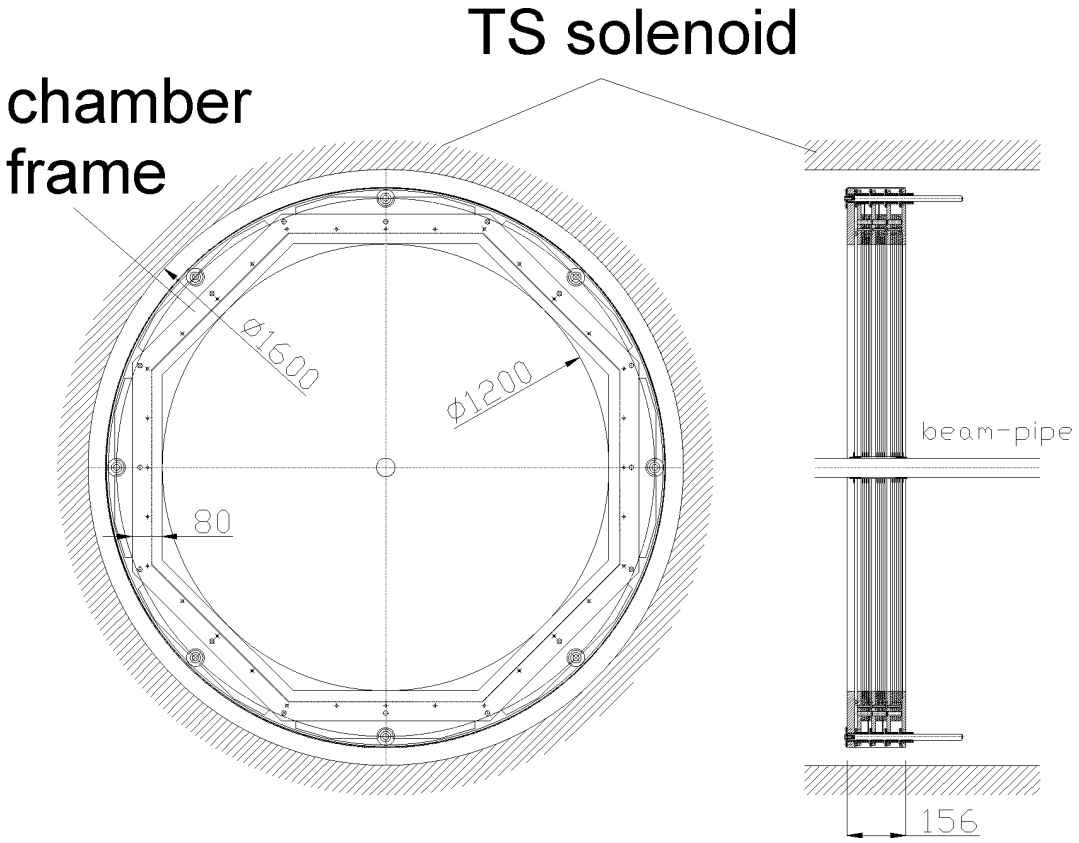

Figure 6.50: Front and side view of the DC1 chamber.

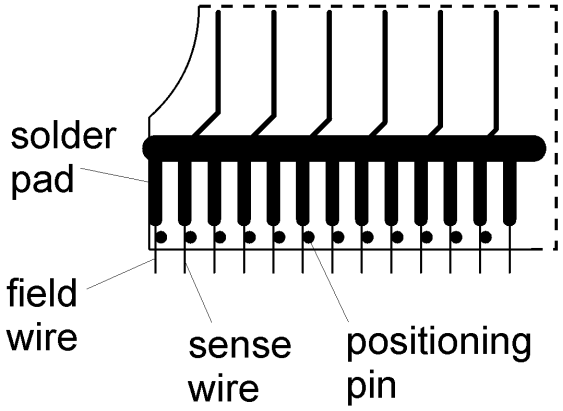

Figure 6.51: Printing board for mounting the sense and field wires.

6.6.2 Cathode Foil Type

6.6.2.1 Proposed MDC Design

In order to detect tracks of charged secondary particles emitted in the forward direction inside the PANDA solenoid, two mini-drift chambers (MDCs) with cathode foils are proposed as the DC1 and DC2 chambers. They are considered as an alternative solution for the drift chambers with cathode wires presented in the previous section. An overview of these chambers without gas containers is shown in Fig. 6.55.

Each MDC will consist of two boxes located left and right of the beam pipe. Each box is designed with six drift cell layers in the coordinate doublets (xx', uu', vv') (see Fig. 6.56). Each MDC contains 6 mm wide cells width and 6 mm gap (see Fig. 6.57). The radius of the active areas is $R = 600$ mm and $R = 800$ mm for DC1 and DC2, respectively. Each layer of drift cells consists of a plane of alternating anode and potential wires between a pair of cathode foils. The potential wires and cathode foils are at negative high voltage and the anode wires are at the ground potential. The wires are vertical for the x-planes and at an angle of $\pm 30° - 35°$ to the vertical direction for the u and v planes. The x',u' and v' planes are shifted with respect to their partners by half of cell size in order to resolve the left-right ambiguities. Each sense plane consists of a fiberglass-epoxy (G-10) frame laminated to a printed circuit

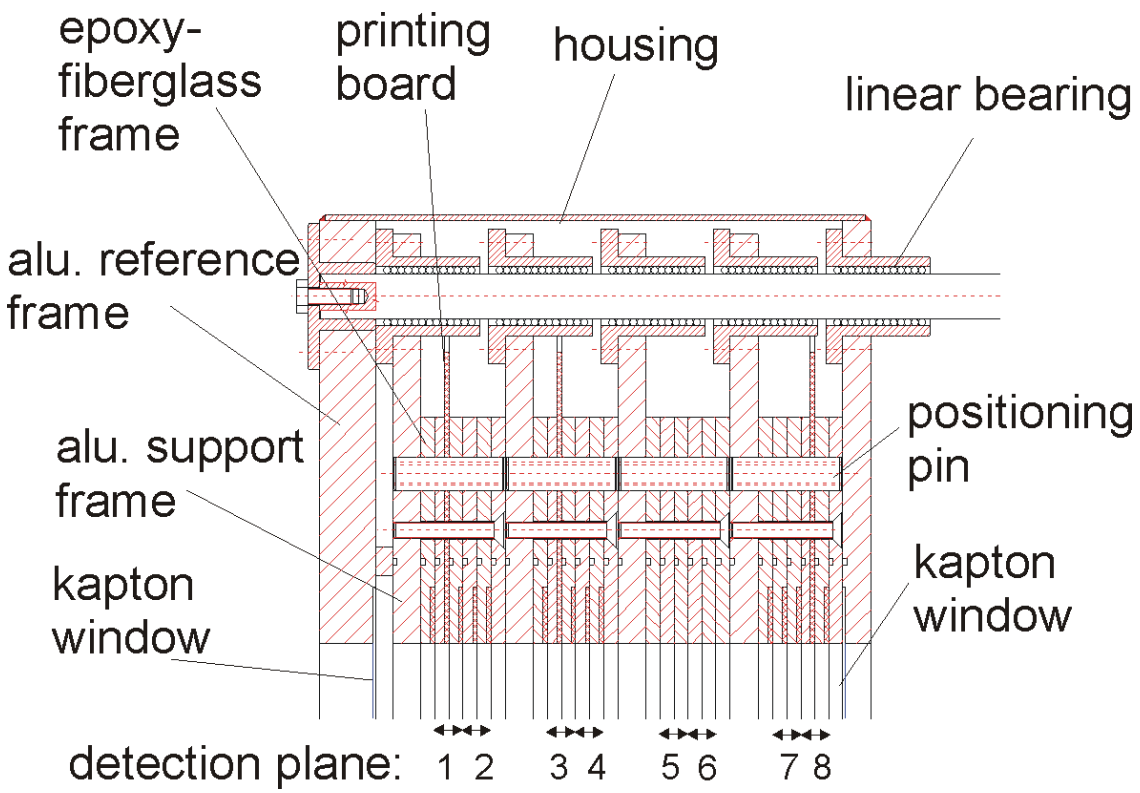

Figure 6.52: Cross section of the drift chamber frames.

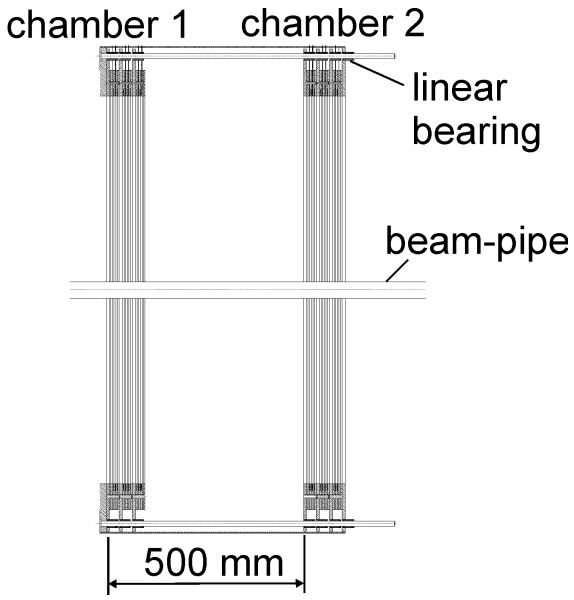

Figure 6.53: Setup of two chambers – DC5–DC6 mounted on linear bearings.

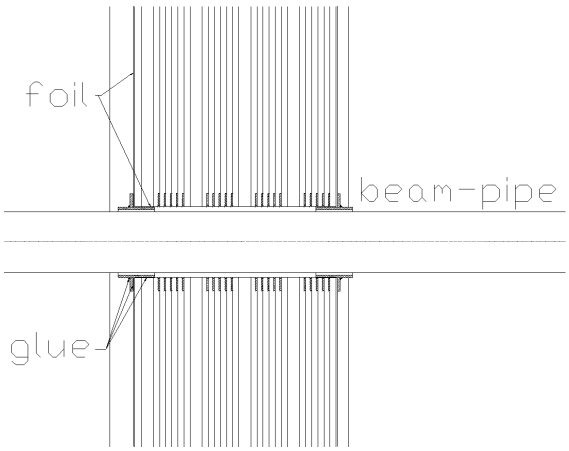

Figure 6.54: Crossover of the chamber with the beam pipe.

board that has solder pads for the wires. Length of wires will be different in the present design for all planes of the MDCs. A general view of MDC is shown in Fig. 6.58. An example of a similar design are the rectangular Drift Vertex Chambers (DVCs), which were developed and produced in JINR for the Hermes spectrometer [43].

Each chamber box corresponds to a single gas enclosure; all planes within a box have individual internal precise alignment. This layout is chosen in order

Figure 6.55: MDCs inside of the PANDA solenoid.

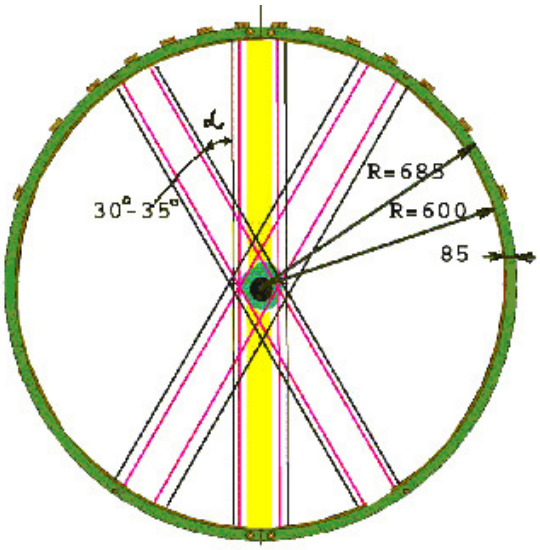

Figure 6.56: The signal wire arrangement of MDCs.

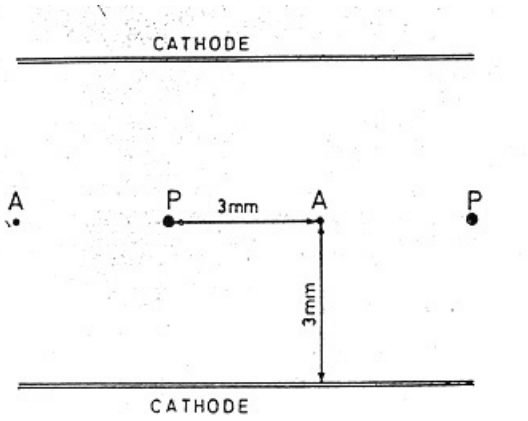

Figure 6.57: Drift cell of an MDC. A-anode wire Ø=30 μm,P-potential wire Ø=50 μm.

to have efficient areas of the planes as close to the beam pipe as possible. Each of the six wire planes in a box has its own pair of cathode foil planes (see Fig. 6.59).

The planes can be installed together in the box while they are connected via a signal feedthrough. Thereafter, the planes are precisely aligned by two pins (6) (Fig. 6.59) equipped with gas seals, inserted through the box and the planes. The ends of these pins provide external reference marks for alignment purposes. A gas injector is inserted through the box wall into each sensitive plane (3) after its installation in the box. The mechanical design of both the signal feedthroughs and the gas injectors aims at avoiding constraints when the planes are aligned with respect to the box.

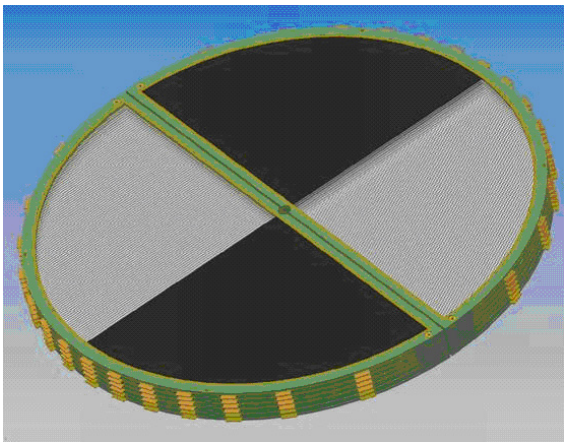

Figure 6.58: Overview of the MDC without the gas container.

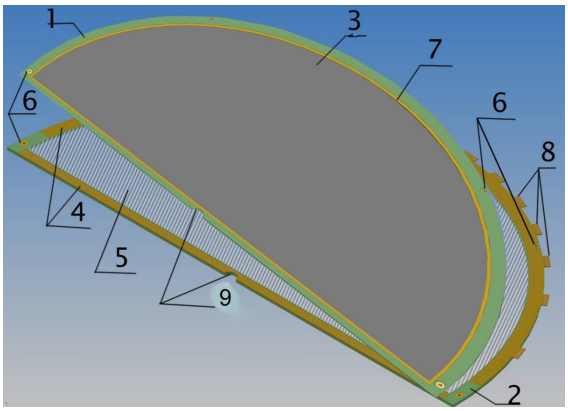

Figure 6.59: One of the DC1, 2 planes. (1), (2) the frames a fiberglass-epoxy (G-10), (3) HV foils with carbon covering, (4) the frame with signal wires, (5) the signal wires, (6) the precisions elements for alignment (pins), (7) the foil frame, (8) the connector pads for signal wires, (9) - the cut to pass the beam pipe.

6.6.2.2 Container Design

Each of the half-planes of the DC1, 2 (Fig. 6.60) chambers are placed in individual containers (BOX left and BOX right), which are connected by pins placed very accurately with respect to the wires and fixed by bolts. The forward and back walls (1) of the BOX are made of an Al-Mg alloy and have a thickness of 12–15 mm. The entrance windows (2) of each BOX are made from 30-50 μm thick mylar foil with vacuum copper covering. The foil is glued on the fiberglass frame (3); a rubber ring provides the hermetic sealing of the gas volume of each BOX; the copper layer serves as an electromagnetic shielding of the sensitive planes inside the BOX. A semi-circular "cover" (4) with an O-ring provides a hermetic sealing of the BOX, and serves as a support element for the front-end electronics. The contacts of a transitive socket from the PCB of the sensitive planes pass through the "cover" via special grooves . O-rings are placed between the case for a transitive socket and the "cover" to provide hermetic sealing.

The brass copper-covered panels are placed on the "cover". The front-end guides are mounted on panels. The front-end is protected by the electromagnetic screen (9), which acts also as an element of the cooling system. The BOX "Bottom" (5) is made from mylar of 30–50 μm thickness with vacuum copper covering.

The "cut" (6) for the beam pipe is made at the "Bottom" center. The details (7) are made from fiberglass. Thus the design presented here provides the smallest possible amount of material near the beam pipe zone.

The holes (8) in the walls of the container will be drilled with high precision both in diameter and in position. They match the holes in cartridges on the frames of the sensitive planes. The specially designed bolts pass through the holes in the BOX walls and through cartridges of the sensitive planes, providing communication between internal and external alignment. The control alignment tools can be mounted in relation to holes on the BOX walls.

A similar BOX design was developed and realized for the Hermes setup [43] and has been used during the data taking runs since 1997.

The "left" and "right" BOXes are connected together by bolts. The alignment of these BOXes relative to each other is done by special pins, the holes for which are drilled with high precision both in the diameter and in the location relative to the holes (8).

The "input - output" of the gas mixture and connection of the high voltage to sensitive planes is carried out through the BOXes "cover".

The MDC adjusting system will be done using the classical "three-dot" circuit.

All the elements of the MDC design will be done from diamagnetic materials (alloys of aluminum, fiberglass, brass, titanium) exclusively.

6.6.3 Quality Assurance Procedures

Because of the strong requirements on radiation resistance great care must be taken in the choice of materials and to ensure maximal cleanliness dur-

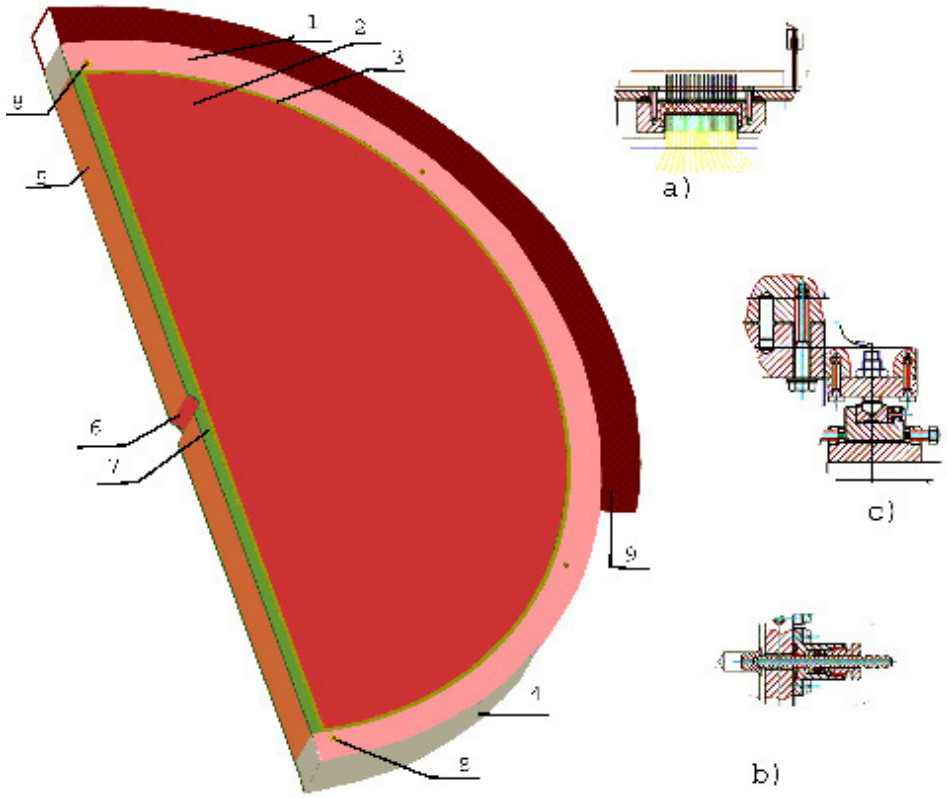

Figure 6.60: General view of the MDC container.

ing all assembly work. Therefore, all construction will be carried out in clean rooms and the chamber components like frames or printing boards will be cleaned with detergents and alcohol prior to assembly. A strict quality control during the chamber construction has to be developed and continuously exercised. In particular, the following steps of the quality control are planned:

- measurement of isolation of the high voltage pads on the printing boards,
- measurement of wire position and tension,
- measurement of gas leakage rate in the chambers,
- control of any anomalous activity such as dark currents.

6.6.4 Choice of Gas Mixture

For the chambers we plan to use an Ar (90%)+ CO_2(10%) mixture because of its very high radiation resistance [44]. An additional advantage of this mixture is its non-flammability and a wide operating voltage plateau of several hundred volts. However, as pointed out in Ref. [44], the ageing performance of Ar-CO_2 is very sensitive to hydrocarbon contaminations and even to minor traces of silicon pollutants. Therefore, we consider adding some properly optimized amount of CF_4 to decrease the risk of Si polymerization and polymerization of hydrocarbons.

6.6.5 Gas System and High Voltage Supply

Sense wires in individual detection planes will be grouped in a few consecutive sections and the high voltage will be supplied for each section separately. In case of problems with overcurrent drawn by some wires in a given section, only high voltage for this section and not for the whole detection plane will be reduced or turned off. The high voltage system should have the option of a temporary reduction of the voltage to a certain safe level, which might be needed during the beam injection phase.

The total volume of the chambers is about 2 m^2 and

in order to exchange the gas mixture once per hour, a relatively large gas flow of 33.3 l/min is needed. Therefore, we intend to build a gas system with a recirculation line similar to the one used for the CLAS drift chambers [45]. This gas system contains mass-flow controllers for precise mixing, large buffer tanks for the gas mixture and a system of filters allowing to remove various contaminations like oil, water or oxygen from the mixture. The gas will be delivered to each chamber individually and the pressure in the chambers will be stabilized at a level of about 1 mbar above the atmospheric pressure. A slow control system will be used to monitor and archive various parameters including flow, oxygen content, pressure and temperature as well as gas amplification and drift velocity measured with proportional counters installed on the input and output lines from the chambers.

6.6.6 Readout Electronics

A front-end card for drift chambers should contain analog signal shaping circuit, digital processing with zero suppression and cluster recognition capabilities. This functionality could be achieved by the following components:

- a fast amplification stage with large gain to allow to run chambers with a small gas amplification (few times 10^4) and a fast pulse discrimination. There are several chips available on the market with similar specifications: ASDBLR and ASDQ are used in ATLAS for straw tubes, CARIOCA is used in the CMS muon arm and the NINO chip has been prepared for the ALICE RPC.
- Drift time measurement system: either based on a free-running digital TDC chip (i.e HPTDC from CERN) or fast sampling Flash ADC (FADC). 10 MHz fast-sampling ADC, as discussed for other $\overline{\text{P}}$ANDA detectors, should be able to provide 2 ns resolution equivalent to a space resolution of 100 μm. In this case an additional circuit converting the time difference between a free running clock and the discriminator output into amplitude would be necessary. The clock is distributed by the common distribution system.
- Autonomous zero suppression and a cluster recognition algorithm based on fast memories and parallel processing in FPGAs; determination of the cluster time stamp; fast data output with connection to wide-band network (i.e. Gigabit Ethernet) to a computer node.
- Computer node for data collection, transport and event processing including correlations with other detectors and event determination.

The raw rates of the data flow from the chambers were estimated taking into account the expected track multiplicity (about 2 in the chambers DC1,2 and 1 in the chambers DC3–DC8). Since for the forward chambers the track incidence angles are close to 90° and, consequently, the number of firing wires in one detection plane is equal in average to the number of passing tracks, then the hit multiplicity is equal to the track multiplicity multiplied by the number of detection planes. Each hit from a single sense wire is represented by 32 bits carrying the following information:

- chamber number (8 bits),
- detection plane number (4 bits),
- wire number (8 bits),
- drift time (12 bits).

Table 6.12 shows the number of electronic channels and an estimate of the expected $\overline{\text{P}}$ANDA average data flow rate from individual chambers for an interaction rate of $2 \cdot 10^7\,\text{s}^{-1}$. The readout system for the drift chambers including the data collection, cluster recognition and data transport is schematically presented in Fig. 6.61. Signals are amplified and converted in front-end cards, including time digitization and channel number generation. Hits from one chamber are moved into an input derandomizing buffer. In the input buffer two types of data are stored: A, containing only wire and plane numbers (12 bits) necessary for fast local feature extraction and B, containing corresponding drift time values (12 bits) needed only for the further more precise data processing. Data are addressed by time stamps generated by the common clock distribution system. The feature extraction for each MDC is based only on information stored in buffer A. It makes use of cluster search for wires from all 8 wire planes, however it can be performed in parallel for pairs of planes (i.e. two 0° planes, or two 45°, *etc.*). Processing is performed in fast logic boards based on FPGA technology and search for groups of wires forming clusters corresponding to tracks originating from the target region. Data from wires which contribute to clusters are transferred to the output buffer and the cluster coordinates (C_x, C_y), wire numbers, common time stamps and corresponding TDC values from one chamber are collected. Other hits are discarded. In this way all hits from secondary particles produced outside the target will

Chamber	Number of channels	Average track multiplicity	Average hit Multiplicity	Data rate [MB/s]
DC1	896	2	16	1280
DC2	1216	2	16	1280
DC3	688	1	6	480
DC4	816	1	6	480
DC5	1108	1	6	480
DC6	1752	1	6	480
DC7	2172	1	6	480
DC8	3072	1	6	480

Table 6.12: Number of electronic channels (equal to the number of drift cells), track multiplicity, hit multiplicity and data flow rate from the forward drift chambers.

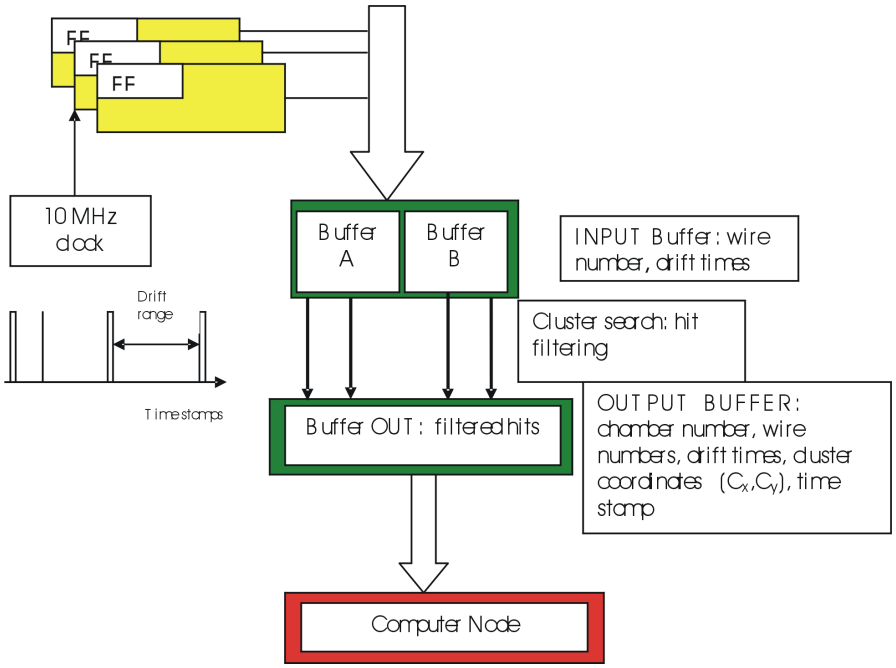

Figure 6.61: Readout system for the drift chambers.

not be transferred to further processing. In the next step track segment parameters such as polar and azimuthal angles are calculated. Track parameters can be extracted from the cluster coordinates of the DC1,..,DC4 chambers, assuming emission from the target region. After extraction of track segment parameters from the DC1,..,DC4 chambers, correlation with clusters found in the DC5,.., DC8 chambers can be used to provide a rough extraction of the track momentum using mapping between deflection angle and momenta.

Additional information from other detectors, for example TOF wall, RICH detector, can be incorporated on the stage of computer nodes to allow for particle identification. This operation should be performed in the computer node of the LVL2 level.

6.6.7 Expected Performance

6.6.7.1 Operation in non-uniform Magnetic Field

The influence of a magnetic field on performance of drift chambers was investigated in a number of works (see for example Refs. [46, 47, 48, 49]). The presence of a uniform magnetic field can be taken into account by a suitable correction of the distance-drift time relation. However, the chambers DC4 and DC7 will work in the fringe field of the $\overline{\text{P}}$ANDA dipole magnet. The non-uniform magnetic field results in a variation of the distance to drift-time relation along individual wires and, thus, it can lead to deterioration of the precision of the track recon-

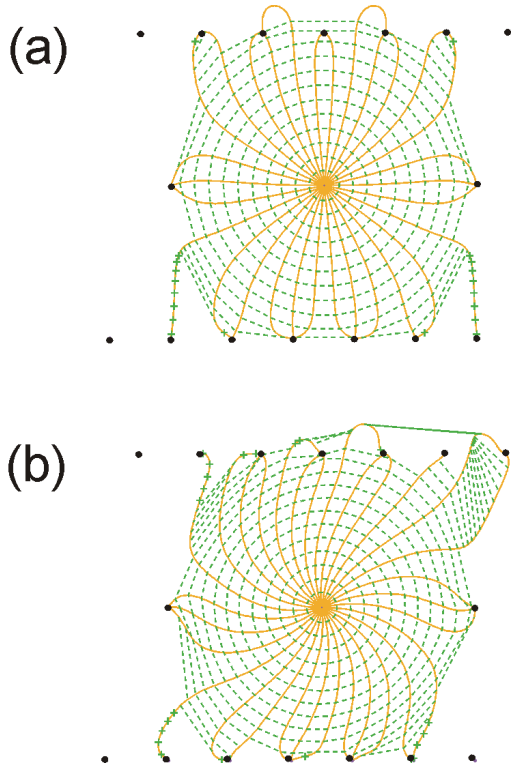

Figure 6.62: Drift paths and isochrones calculated in 20 ns steps of the electron drift in a gas mixture of 90% Ar + 10% CO_2 at sense wire voltage of 2 kV without magnetic field (a) and with magnetic field of 1 T parallel to the wires (b).

struction if not taken properly into account. We studied this effect with the help of the GARFIELD code [50]. Fig. 6.62 shows the deformation of the drift paths and of the isochrones caused by the presence of a 1 T field parallel to the wires. A vertical component of 0.3 T expected in the center of DC4 leads to a deviation of the distance-drift time relation of less than 100 μm for distances from the sense wire smaller than 5 mm and for track inclination angles smaller than 20°. This deviation is comparable with the expected position resolution and can be neglected in the track reconstruction.

6.6.7.2 Momentum Reconstruction

The precision in the particle momentum determination in a magnetic field is limited by the effect of multiple scattering on tracking detectors and by the finite position resolution of the detectors. The thickness of the drift chambers containing six detection planes with cathode wires is equal to 0.17% of radiation length. The main contribution to the thickness comes from the gas mixture (0.106% X_0) (see Table 6.13). The angle θ_{mult} quantifying the multiple scattering on the chambers and calculated using a Gaussian approximation to the theory of Moliere, changes from 0.58 mrad at 1 GeV/c to 0.042 mrad at 10 GeV/c (see Table 6.14). The uncertainty in track angle resulting from the limited position resolution of the chambers is equal to 0.24 mrad and it was estimated assuming that this angle is measured with two chambers spaced by 60 cm, as is the case for the DC3-DC4 pair, and that the position measured with a single chamber has an accuracy of 100 μm, which is typical for drift detectors. The uncertainty in track angle $\Delta\theta_{defl}$ was obtained by adding in quadrature θ_{mult} and θ_{det}. The relative uncertainty in the momentum determination $\delta p/p$ was calculated as the ratio $\sqrt{2}\Delta\theta_{defl}/\theta_{defl}$, where the factor $\sqrt{2}$ in the numerator takes into account the fact that the particle trajectories are measured before and after the dipole magnet with two pairs of position sensitive detectors (DC3-DC4, DC6-DC7) and θ_{defl} is the angle of deflection of the particle trajectory in the 2 Tm field of the $\overline{\text{P}}$ANDA dipole magnet. The uncertainty $\delta p/p$ changes from 0.15% at 1 GeV/c to 0.57% at 10 GeV/c (see Table 6.14). At lower momenta it is dominated by the multiple scattering in the detectors and at higher momenta it is limited by the finite position resolution of the detectors.

6.6.7.3 Rate Effects and Ageing

Drift chambers with cells identical to the ones shown in Fig. 6.55 were tested with high intensity beams at the IHEP booster. The tests have shown that the chamber performance does not change up to counting rates of $3 \cdot 10^5\,\text{cm}^{-2}\text{s}^{-1}$ [51]. In the $\overline{\text{P}}$ANDA forward drift chambers the highest counting rate is expected in the central part of the chambers close to the beam pipe and it is of about $3 \cdot 10^4\,\text{cm}^{-2}\text{s}^{-1}$ (see Fig. 6.63). This radiation level can still create serious problems due to ageing effects. The resulting rate of ageing processes was estimated assuming that the gas amplification is equal to $5 \cdot 10^4$. With 100 primary electrons per track we expect an accumulated charge density of about 0.75 C/cm in one year, which lies in a region above 0.1 C/cm in which serious ageing-related problems are likely to occur. Only a suitable choice of materials for chamber construction and a careful optimization of the working conditions (including the gas mixture) will make it possible to extend the lifetime of the chambers over the period of many years foreseen for the running of $\overline{\text{P}}$ANDA.

Material	X_0 [cm]	Thickness X [cm]	X/X_0
Sense wires: W Ø20 μm	0.35	0.000006	0.00002
Cathode wires: Al Ø110 μm	8.9	0.0048	0.00054
Gas mixture: Ar/CO_2 (90/10)	11 730	12.5	0.00106
Windows: $2 \times 20\,\mu$m Kapton	28.6	0.004	0.00014

Table 6.13: Material budget in the drift chambers with six detection planes.

Momentum [GeV/c]	θ_{mult} [mrad]	θ_{det} [mrad]	$\Delta\theta_{defl}$ [mrad]	θ_{defl} [mrad]	$\delta p/p$
1	0.58	0.24	0.63	600	0.15%
3	0.15	0.24	0.28	200	0.20%
5	0.086	0.24	0.25	120	0.29%
10	0.042	0.24	0.24	60	0.57%

Table 6.14: Estimate of the momentum resolution for 1, 3, 5 and 10 GeV/c protons measured with the FS.

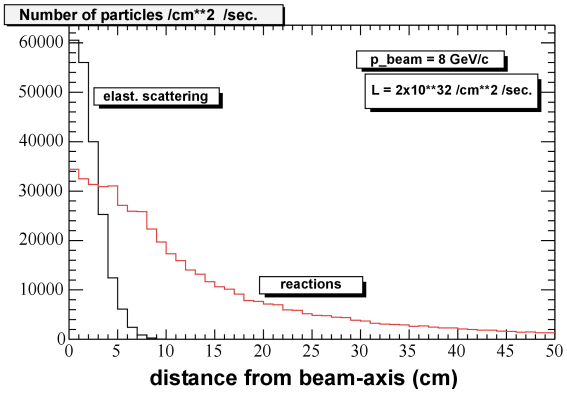

Figure 6.63: Counting rate at the position of the chamber DC1 as a function of the distance from the beam axis.

6.6.8 Prototypes

In the years 2005, 2006 we plan to build and test real scale prototypes of the DC1 chamber with cathode wires and with cathode foils. The prototype of the chambers with cathode wires will consist of eight detection planes. Four planes will contain the plastic rings surrounding the beam-pipe for mounting the most central wires and in the remaining four planes the central wires will be skipped. Construction of the prototypes will allow us to test various technical solutions including:

- the system of transferring the frames with wires from the mounting table to the aluminium support frames,
- the mechanical stability of the chamber frames,
- the precision in the positioning of wires,
- the application of insulating rings for mounting the central wires.

The prototypes will be tested with radioactive sources as well as using accelerator beams. In particular, we plan tests with scattering of a few GeV proton beam on a hydrogen target which is close to the $\bar{p}p$ scattering at PANDA as far as the counting rate at forward angles is concerned. In these studies we want to study:

1. the input parameters of preamplifiers allowing for possibly low gas amplification, which is required because of the expected high counting rate and for minimizing the ageing effects,
2. the optimal working conditions for the chambers allowing to reach the highest possible counting rate with efficiency close to 100%, and
3. the rate of ageing processes.

6.6.9 Timeline

The timeline for the drift chambers with cathode wires is shown in Fig. 6.64.

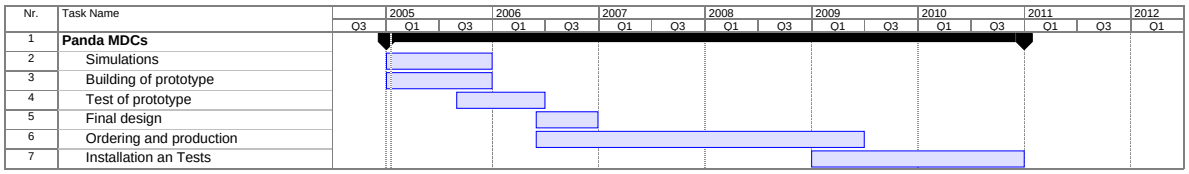

Figure 6.64: Timeline for the Cathode Wire DCs

References

[1] I. C. Barnett et al., Nucl. Instrum. Meth. **A455**, 329 (2000).

[2] R. Bilger et al., Nucl. Phys. **A663&664**, 1073c (2000).

[3] L. Benussi et al., Nucl. Phys. **A419**, 648 (1998).

[4] LAMINA Dielectrics Ltd, Billingshurt, Sussex RH 149SG, England.

[5] CERN/LHCC-98-004, 1998.

[6] http://www-btev.fnal.gov/ DocDB/ 0000/ 000032/ 002/ ptdr.html, 1999.

[7] M. Abdel-Bary et al., Phys. Lett **B595**, 127 (2004).

[8] V. N. Bychkov et al., Part. and Nucl. Lett. **2**, 111 (2002).

[9] A. Pullia et al., IEEE Trans. Nucl. Sci. **49**, 3269 (2002).

[10] D. Chernyak et al., Nucl. Instrum. Meth. **A419**, 370 (1998).

[11] Mylar, poliester film, registered trademark of DuPont, www.dupont.com.

[12] Kapton, polyimide film, registered trademark of DuPont, www.dupont.com.

[13] P. Wintz et al., in *AIP conf. Proc.*, volume 698, page 789, 2004.

[14] D. Nygren and J. Marx, Phys. Today **31**, 46 (1978).

[15] P. Marrocchesi et al., Nucl. Instrum. Meth. **A283**, 573 (1989).

[16] C. Brand et al., Nucl. Instr. Meth. **A283**, 567 (1989).

[17] S. Wenig, Nucl. Instrum. Meth. **A409**, 100 (1998).

[18] S. Afanasev et al., Nucl. Instrum. Meth. **A430**, 210 (1999).

[19] K. H. Ackermann et al., Nucl. Phys. **A661**, 681 (1999).

[20] K. H. Ackermann et al., Nucl. Instrum. Meth. **A499**, 713 (2003).

[21] W. Blum and L. Rolandi, *Particle Detection with Drift Chambers*, Springer-Verlag, Berlin, 1 edition, 1994.

[22] F. Sauli, Nucl. Instr. Meth. **A386**, 531 (1997).

[23] B. Ketzer, Q. Weitzel, S. Paul, F. Sauli, and L. Ropelewski, Nucl. Instr. Meth. **A535**, 314 (2004).

[24] G. Baum et al., COMPASS: A proposal for a COmmon Muon and Proton Apparatus for Structure and Spectroscopy, CERN/SPSLC 96-14, SPSC/P 297, 1996.

[25] The TESLA Collaboration, TESLA: Technical Design Report, DESY 2001-011, 2001, http://tesla.desy.de/ new_pages/ TDR_CD/ start.html.

[26] R. Veenhof, Choosing a gas mixture for the ALICE TPC, ALICE-INT-2003-29, 2003.

[27] S. Biagi, Nucl. Instr. Meth. **A283**, 716 (1989).

[28] S. Biagi, Nucl. Instr. Meth. **A421**, 234 (1999).

[29] The ALICE Collaboration, ALICE: Technical Proposal for A Large Ion Collider Experiment at the CERN LHC, CERN/LHCC/95-71, 1995.

[30] S. Bachmann et al., Nucl. Instr. Meth. **A470**, 548 (2001), CERN-EP-2000-116.

[31] S. Bachmann et al., Nucl. Instr. Meth. **A479**, 294 (2002), CERN-EP-2000-151.

[32] B. Ketzer et al., IEEE Trans. Nucl. Sci. **48**, 1065 (2001).

[33] B. Ketzer et al., IEEE Trans. Nucl. Sci. **49**, 2403 (2002), CERN-OPEN-2002-004.

[34] C. Altunbas et al., Nucl. Instr. Meth. **A490**, 177 (2002).

[35] B. Ketzer, Nucl. Instr. Meth. **A494**, 142 (2002).

[36] M. Altunbas et al., Nucl. Instr. Meth. **A470**, 249 (2003).

[37] M. Killenberg et al., Nucl. Instr. Meth. **A530**, 251 (2004).

[38] J. Kaminski et al., Charge carrier transfer in the gas electron multiplier at low gas gains, in *Proceedings of the International Workshop on Linear Colliders, Jeju Island (Korea)*, 2002.

[39] F. Sauli, S. Kappler, and L. Ropelewski, IEEE Trans. Nucl. Sci. **50**, 803 (2003).

[40] J. Dunlop and J. Thomas, Space Charge Distortions in the STAR TPC, 2002, http://www-library.lbl.gov/ docs/ LBNL/ 499/ 57/ abstracts/ RNC_abstracts.html.

[41] J. Kaminski et al., Nucl. Instr. Meth. **A535**, 201 (2004).

[42] K. Solberg et al., Nucl. Instrum. Meth. **A281**, 283 (1989).

[43] K. Ackerstaff et al., Nucl. Instrum. Meth. **A417**, 230 (1998).

[44] M. Titov, Radiation damage and long-term aging in gas detectors, physics/0403055.

[45] M. D. Mestayer et al., Nucl. Instrum. Meth. **A449**, 81 (2000).

[46] Nucl. Instrum. Meth. **124**, 349 (1975).

[47] Nucl. Instrum. Meth. **111**, 467 (1973).

[48] S. Eismann et al., Nucl. Instrum. Meth. **217**, 140 (1983).

[49] Preprint CERN/EP80-99, 1980.

[50] R. Veenhof, GARFIELD, Simulation of gaseous detectors, Version 7.04, CERN Program Library Writeup W5050, CERN, Geneva, Switzerland, 2001.

[51] I. E. Chirikov-Zorin et al., Nucl. Instrum. Meth. **260**, 142 (1987).

7 Charged Particle Identification

7.1 Introduction

Particle identification (PID) for hadrons and leptons over a large range of solid angle and momenta is an essential requirement for meeting the physics objectives at the $\overline{\text{P}}$ANDA detector. Different behaviour of charged particles traversing active and passive detector material can be used to identify (on a probabilistic level) the nature of a charged particle. The following effects provide the basis for the PID detectors used in $\overline{\text{P}}$ANDA:

Specific Energy Loss. Charged particles lose energy while traversing dense materials. For particles other than electrons the main processes are ionization and atomic excitation. The mean energy loss per unit length, usually referred to as $\mathrm{d}E/\mathrm{d}x$, is described by the Bethe-Bloch equation which depends on the velocity rather than momentum of the charged particle. This energy loss can in principle be measured by tracking detectors, if the signal amplitude is recorded in addition to the space points. Due to fluctuations of the actual energy loss per unit length, especially prominent in gaseous detectors, however, a large number of measurements per track is usually necessary in order to apply truncation methods. A Time Projection Chamber (TPC) is a very powerful tool exploiting this possibility, and is discussed in detail in Chap. 6.5.

Cherenkov Effect. Charged particles in a medium with refractive index n propagating with velocity $\beta > 1/n$ emit radiation at an angle $\Theta_C = \arccos(1/n\beta)$. Thus, the mass of the detected particle can be determined by combining the velocity information determined from Θ_C with momentum information from the tracking detectors.

Time-of-flight. Particles with the same momentum, but different masses travel with different velocities, thus reaching a time-of-flight counter at different times relative to a common start.

Absorption. A thick layer of passive material absorb most particles due to electromagnetic (e^+e^-, γ) or hadronic interactions (all charged and neutral hadrons). After a certain amount of material only muons and neutrinos survive. The muons can then be detected easily with any kind of charged particle detector, depending on the desired speed and resolution.

The techniques considered in the $\overline{\text{P}}$ANDA setup (some in the target as well as in the forward region) are discussed in the sequent sections. Due to the very different momentum ranges and the desired resolution different implementations are under investigation.

7.2 Target spectrometer

7.2.1 DIRC

7.2.1.1 Overview

Motivation In the barrel section of the target spectrometer, the particle identification of reaction products of momenta up to several GeV/c can be performed by the Detection of Internally Reflected Cherenkov (DIRC) light as realized in the BaBar detector [1, 2, 3]. Particles are in this angular range of 22°–140° relatively slow, so that one can use materials with high refraction index favoring the internal reflection of photons. The lower momentum threshold of kaons which produce Cherenkov light is for an refractive index of $n = 1.47$ as low as $p = 460\,\mathrm{MeV}/c$. The polar angles and energies of kaons from the decay of J/ψ mesons are shown in Fig. 7.1.

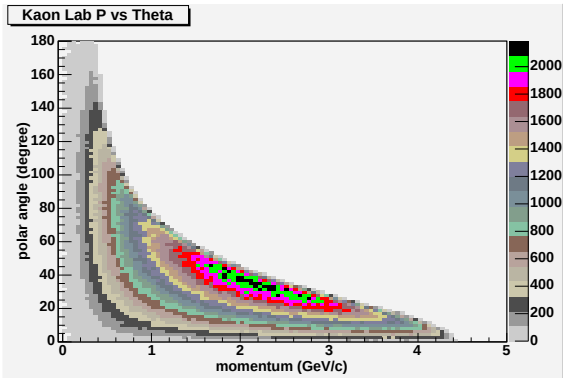

Figure 7.1: Radiative decays of resonances in formation experiments like $J/\psi \to K^+K^-\gamma$ for the search of glue-balls [4]. The figure shows the polar angle *vs.* momentum distribution of the kaons.

Basic Technique The DIRC utilizes totally internally reflecting Cherenkov photons in the visible and near UV range [5]. The geometry of the DIRC

is shown schematically in Fig. 7.2. It uses long, thin, flat quartz radiator bars with a rectangular cross section. The quartz bar is surrounded by a material with a small refractive index $n_3 \sim 1$ (nitrogen in the case of BaBar). As it traverses the quartz bar, a particle of will radiate Cherenkov photons in a cone of half opening angle Θ_C around the particle trajectory. Since the refractive index of the radiator bar n_1 is large, some of the Cherenkov photons will be totally internally reflected, regardless of the incidence angle of the tracks, and propagate along the length of the bar. To avoid having to instrument both bar ends with photon detectors, a mirror is placed at one end, perpendicular to the bar axis. This mirror returns most of the incident photons to the other (instrumented) bar end. Since the bar has a rectangular cross section and is made to optical precision, the direction of the photons remains unchanged and the Cherenkov angle conserved during the transport, except for left- right/up-down ambiguities due to the reflection at the radiator bar surfaces. The photons are then proximity focused by expanding through a stand-off region filled with purified water (index $n_2 \sim 1.34$) onto an array of densely packed photo-multiplier tubes placed at a distance of about 1.2 m from the bar end, where the Cherenkov angle is measured from the radius of the Cherenkov ring, determining the particle velocity. Combined with the momentum information from the drift chamber, the mass of the particle is identified.

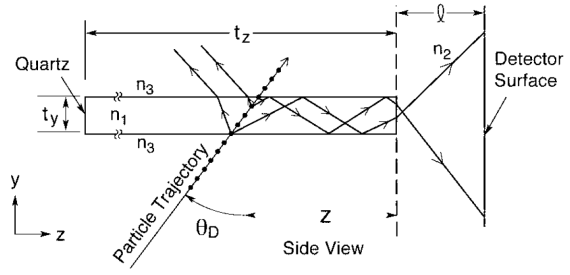

Figure 7.2: Imaging principle of the DIRC. A particle traverses the quartz bar and emits Cherenkov light. The light is reflected internally until it exits the quartz bar where the light is detected.

New Technique The main costs of the BaBar setup arises from the 11 000 PMTs, which allow timing information to be used to suppress the large background resulting from the electron beam environment. To reduce the costs of the photon detector one has to replace the two dimensional photon detector by a one dimensional readout where one of the dimension is replaced by the timing information of the detector. This is already proposed by the TOP1-project of the Belle-collaboration at KEK [6]. This option will be subject of detailed R&D. The presently envisaged DIRC detector has a photon readout with 7 000 PMTs, reflecting the smaller diameter of the radiator barrel compared to BaBar.

The DIRC provides a positive kaon identification. It serves also for the distinction of gammas and relativistic charged particles entering the TS-EMC behind and is, therefore, part of the trigger.

7.2.1.2 Radiator

The choice of the material for the radiator is artificially fused quartz. It has a sufficient high refractive index of $n = 1.47$ and a reasonable low dispersion. Its radiation hardness for gammas was investigated by the BaBar collaboration [7] and shown to be sufficient. The radiation for the $\overline{\text{P}}$ANDA detector will be slow neutrons, especially when nuclear targets are used. Therefore, radiation studies of radiator materials from different companies [8, 9] have to be performed with thermal neutrons. MC-simulations have to provide the needed quality of the bulk, surfaces and edges of the quartz slabs. They have a cross section of $(17 \times 30)\,\text{mm}^2$ and the photons which are internally reflected approach the edges often. Therefore, care has to be taken to produce sufficient perfect edges and to protect them handling the slabs. This requires also a quality control procedure with the mechanic shops specialized for grinding and lapping. The R&D for using the timing information (TOP1-project) uses quartz slabs which are $(17 \times 240)\,\text{mm}^2$ in cross section, here the edges are hit less often and the use of acrylic glass instead of artificially fused silica should be investigated. The optical properties are similar, however the transmission not as good as artificially fused silica. The surface of acrylic glass is determined by the mold.

7.2.1.3 Photon Readout

The photon readout is done by 7 000 PMTs and ultra-purified H_2O as coupling between radiator end and PMTs. The large distance between radiator end and PMTs serve as a pin hole focus. There are two other options which should be subject of R&D: firstly, the measure of the lateral position of photons directly at the exit of flat radiators together with their arrival time. Here, a time reference from a timing barrel with a timing resolution

in the order of 100 ps is needed. Secondly, each radiator is read out by a small mirror at its end an a APD array working in the Geiger mode [10]. The arrays are still under development and need R&D in doping issues in order to have self quenching to stop the Geiger mode. For the method replacing one spatial coordinate by the time of arrival information for the photon the detector number reduces drastically by a factor of 60 from 7 000 to about 120 PMTs. The fact, that the tubes are connected directly to the radiator slabs implies that the tubes have to work in a magnetic field of 2 T. There are channel plate photo-multipliers (CP-PMT) currently produced which fulfill this condition. The PLANACON 85001 channel plate photo-multiplier from Burle [11] was already tested in the field of the ALADIN magnet at GSI. The results in response to a LED are shown in the Fig. 7.3.

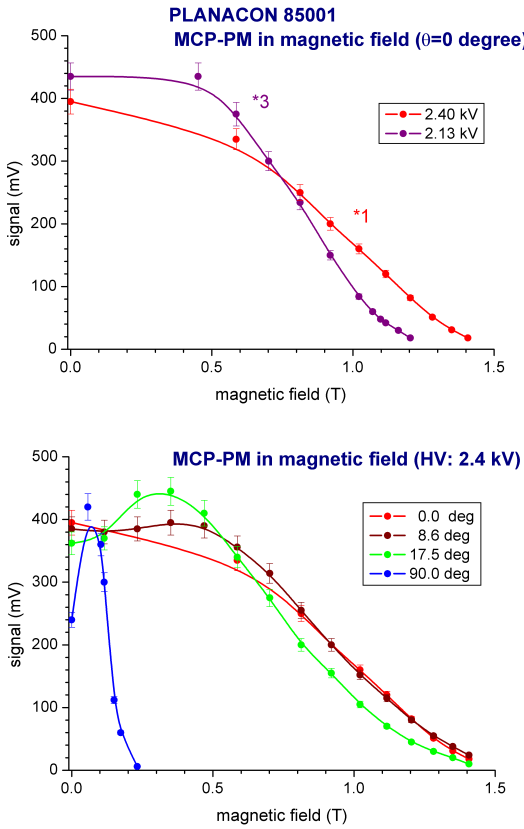

Figure 7.3: Top panel: response of the PLANACON 85001 channel plate photo-multiplier to the light of an LED as function of the magnetic field perpendicular to the photo-cathode surface. The curves are for two different values for the high Voltage. Bottom panel: response as function of the angle of the magnetic field. 0° is here a magnetic field perpendicular to the photo-cathode.

The diameter of the channels of 25 μm allow a reasonable operation up to a magnetic field of 1 T. For the test of the timing resolution we generated Cherenkov photons in the quartz window of the photo-multiplier with electrons from a ^{207}Bi source. No substantial change in the rise time of the signal from the photo-multiplier was observed. The signals observed with an oscilloscope with and without magnetic field of $B = 1.2$ T are shown in Fig. 7.4. In contrast to the amplitude, no significant change

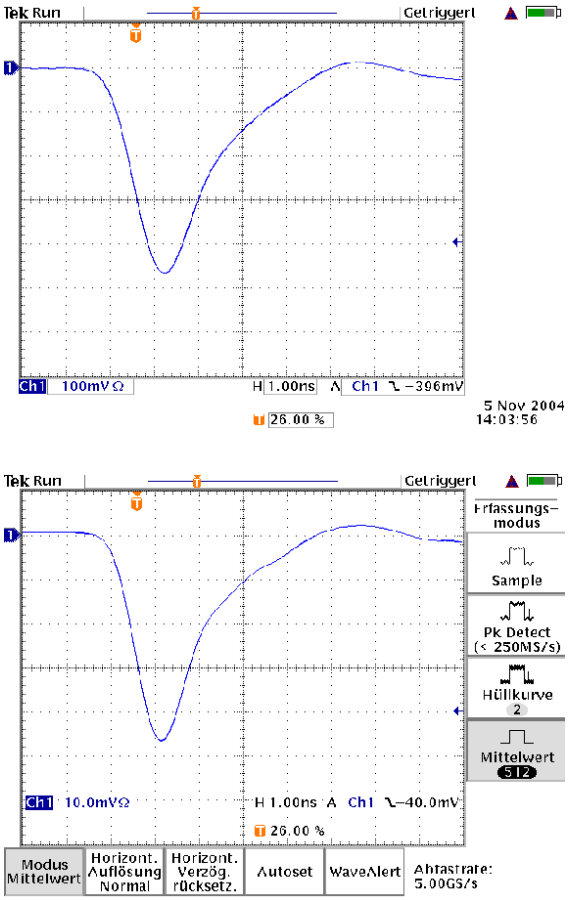

Figure 7.4: Top panel: response of the PLANACON 85001 channel plate photo-multiplier to Cherenkov light of electrons from a source irradiating the quartz window in front of the photo-cathode surface. The curve was taken without magnetic field. Bottom panel: the same curve for a magnetic field of $B = 1.2$ T.

of the shape of the signal (timing resolution) was observed up to highest measured magnetic field of $B = 1.5$ T. The smaller the tube radius of the micro channel the better is the performance in the magnetic field. Blue light wit an energy of 3 eV has in an magnetic field of $B = 1$ T an Larmor-radius of $R = 6\mu$m. CP-PMTs with channel diameter of 7 μm are produced in Novosibirsk [12]. They oper-

ate in a magnetic field of up to 2.2 T and will be tested in 2005.

The use of "cheap" gas detectors with multi anode readout is limited to the ultraviolet photon spectrum due to the photon-electron converters. At those wavelengths ($\lambda < 200\,\mu$m) the dispersion of the radiators is too large. If one can measure the 2-dim photon direction and the arrival time, the wavelength and dispersion corrections are accessible. This cannot be achieved with gas detectors because the time resolution of $t < 100$ ps is necessary.

7.2.1.4 Electronics

The readout electronics has to match the photo-multiplier solution and has to enable a trigger scheme, based on pipeline techniques. The design should orient itself on existing schemes like the Hades RICH electronics. For the readout a possible solution could be the modular concept of the TAQUILA front-end-electronics [13] which allows to process the timing and analog information of the photon detector. The costs of the high voltage power supply for the 7 000 PMTs can be reduced by using an high voltage divider with a low bleeder current of $I = 0.5\,A$. This allows to operate 5 PMTs at one high voltage channel. Alternatively, Cockroft-Walton voltage multiplier can be used. [14].

7.2.1.5 Mechanical construction

The mechanical construction orientates itself to that of the BaBar DIRC. The whole device, the radiator barrel and the photon detector, is hold by a gosset which is shown in Fig. 7.5. This gosset is screwed to the upstream side of the iron yoke of the target spectrometer. Within the barrel an iron ring at the position of the iron yoke reduces the magnetic field for the photo-multipliers. More details can be seen in Fig. 7.6 which is a blow up of Fig. 7.5. The barrel consists of radiator slabs (light red) and possibly of a scintillator layer for time of flight measurements (red). The radiator and scintillator layer is supported by a light weight honeycomb structure made out of carbon fiber. In addition the barrel is surrounded by an aluminum sheet. How the bars can be arranged to slabs is illustrated in Fig. 7.7.

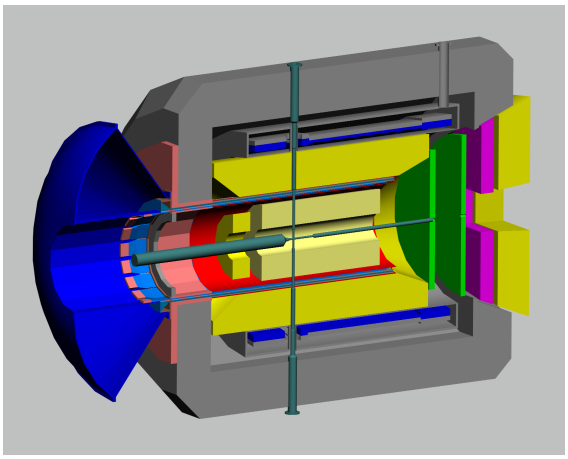

Figure 7.5: Position of the DIRC radiator barrel and the photon detector within the target spectrometer.

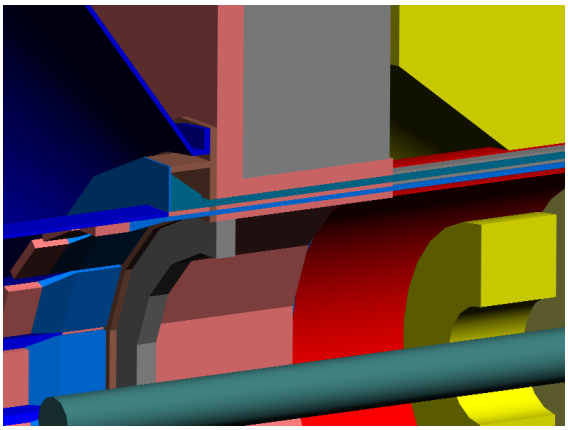

Figure 7.6: Blow up of Fig. 7.5.

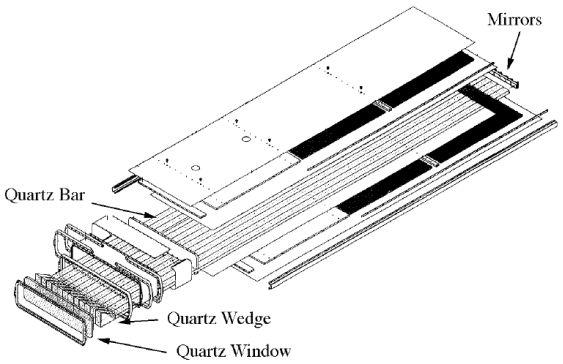

Figure 7.7: Sketch of the container structure (slab) for the quartz bars used by BaBar.

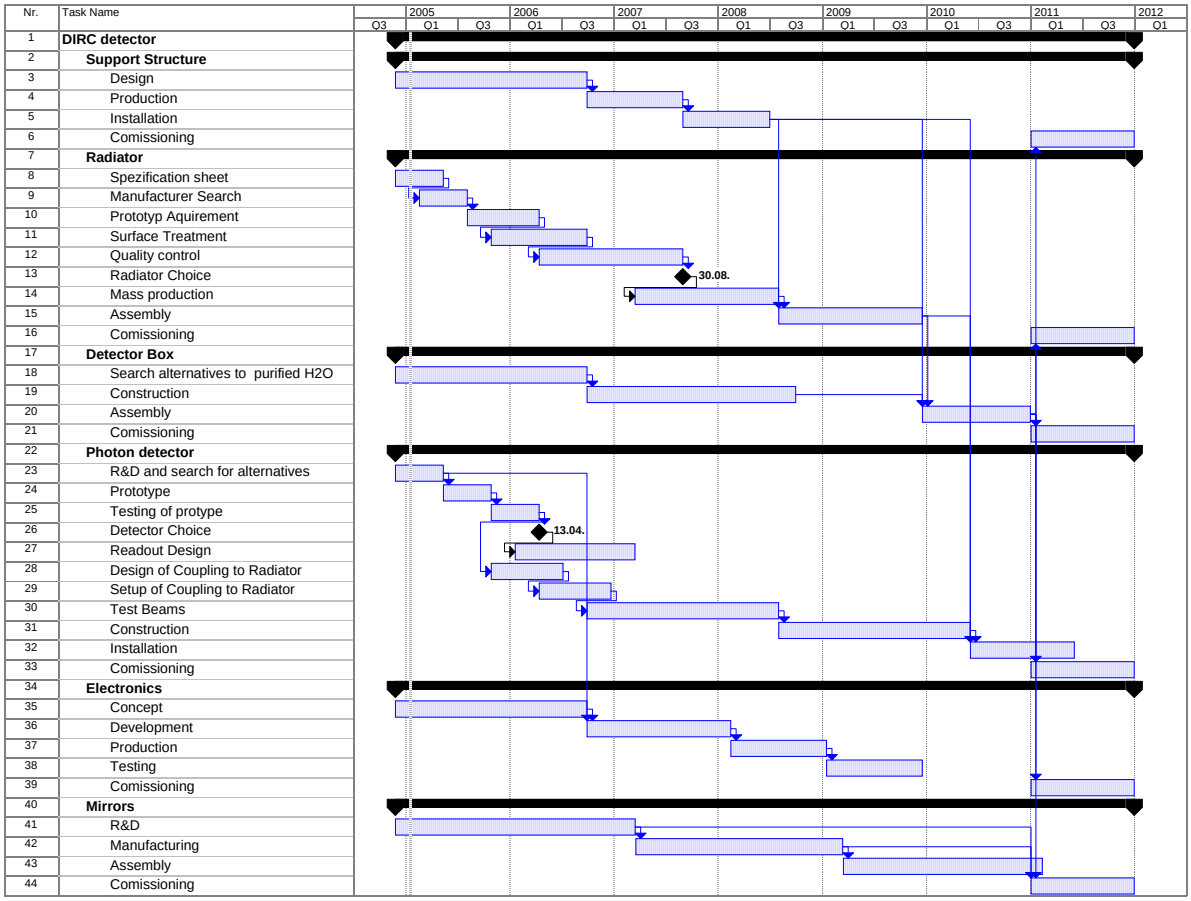

Figure 7.8: Timeline for the DIRC detector.

7.2.2 Time Projection Chamber

A very powerful tool for particle identification at momenta below 800 MeV/c, and also at momenta above 2 GeV/c, is the measurement of the fractional energy loss $\mathrm{d}E/\mathrm{d}x$ per unit track length in a gaseous tracking detector like a TPC. This detector option is described in detail in Sec. 6.5. The enhancements for particle identification are reported in Sec. 6.5.7, as well as in Sec. 13.5.2.

7.2.3 Cylindrical Time-of-Flight Counter

In reactions with multi particle final states, at low beam energies, and for backward emitted particles at high beam energies, the released energies per particle are low. For the particle identification of slow charged particles, for one option of the DIRC detector, and for track deconvolution of the TP-Chamber it becomes more and more obvious, that a time of flight barrel in the target spectrometer is desirable. It also increases redundancy for other sub-detector systems. Examples of such time-of-flight barrels are implemented at STAR and PHOBOS at the RHIC accelerator complex.

In order to achieve a low energy threshold, the barrel is located in front of the radiator barrel of the DIRC and could also become mechanical combined with the latter. For an assumed time resolution of $\sigma = 100$ ps, one expects a three standard deviation π/K separation up to 430 MeV/c at 90° and up to 760 MeV/c at a polar angle of 22°. For the hyper-

nuclei physics program, where the secondary target is displaced by 70 cm upstream, these momentum thresholds raise up to 1 GeV/c, respectively.

For the DIRC subsystem, the TS-TOF barrel could serve as a time reference, which is needed, when one coordinate of the Cherenkov images is replaced by the photon arrival time at the radiator end 7.2.1.3. This would reduce the needed amount of 7 000 to about 120 photo-multipliers and drastically reduce the costs of the DIRC photon detector system.

The optional time-projection chamber will also gain performance with the fast timing information and a rough position information. It helps to deconvolute the tracks, which are "stored" within the TPC volume Sec. 6.5.6 due to the long drift time of the electron clouds. An only rough position measurement by reading out the scintillator strips from both ends is sufficient, since the track density at the outside of the TPC is low.

The setup consists of 96 strips of a fast scintillator like BC404, made by the Bicron Corporation. It has good timing characteristics (a 1.8 ns decay constant) and a moderate attenuation length (1.6 m). Its wavelength of maximum emission (408 nm) is close to the wavelength at which the response of most fast photo-multiplier tubes peak (420 nm). The thickness of only 0.5 cm allows to mount it mechanically together with the DIRC radiator slabs. For the photo-multipliers we envisage channel-plate photo-multipliers, which can operate in magnetic fields up to 2.2 T [12] and which are fast enough. It is foreseen to read out the strips from both sides. The mechanical setup is shown in Fig. 7.6.

7.3 Forward spectrometer

7.3.1 Forward Cherenkov Detectors

7.3.1.1 Requirements

There are a series of basic requirements that must be considered for the particle identification with Cherenkov imaging detectors in the forward spectrometer:

- momentum range for hadron identification about 0.5–8 GeV/c,
- minimum material budget to avoid a degradation of the momentum resolution of the forward spectrometer,
- readout in large, inhomogeneous magnetic fields,
- radiation hardness,
- possibility to extend the momentum range to higher momenta, anticipating a later upgrade of HESR to 22 GeV.

7.3.1.2 Detector Design Options

For Cherenkov-based particle identification in the relevant momentum range there are three different radiators that can be considered: aerogel, perfluorhexane (C_6F_{14}) and quartz. Table 7.1 shows estimates for the momentum ranges for the three different radiators. The minimum momentum is determined by the kaon threshold, but should be set at least 0.2 GeV/c higher for a signal that exceeds a noise threshold. The maximum momentum is set by the maximum momentum for π/K-separation, estimated by using

$$\begin{aligned} p_{max} &= \sqrt{\frac{m_2^2 - m_1^2}{2k_f n_\sigma}} \\ k_f &= \tan\theta \frac{\sigma_\theta}{\sqrt{N}} \\ \frac{d^2N}{dEdx} &\approx 370 \quad \sin^2\theta. \end{aligned} \tag{7.1}$$

For this estimate the single photon resolution is assumed to be $\sigma_\theta = 4$ mrad, n_σ is set to 4.652, corresponding to 1% contamination and the number of photoelectrons N is assumed to be 10 for aerogel [15]. The first p_{max} value for aerogel corresponds to the combination of third-generation aerogel and GaAsP-cathode HPDs (see below), the second value (in brackets) corresponds to the materials used in the Hermes RICH.

radiator	n	$p_t(K)$	p_{min}	p_{max}
radiator	n	[GeV/c]	[GeV/c]	[GeV/c]
aerogel	1.05	1.54	1.8	9.6 (8.1)
C_6F_{14}	1.30	0.59	0.80	7.5
quartz	1.46	0.46	0.70	7.0

Table 7.1: Comparison of different radiators.

The three radiators can be combined with different imaging and readout options, some of which are known to work because they are used in other experiments. Some key properties of the different assemblies are listed in Table 7.2.

Perfluorhexane can be combined with CsI multiwire proportional chambers (MWPCs). This is the design of the ALICE HMPID [16, 17, 18]; a test module is currently working successfully within the STAR experiment. A further advantage of this design is the fact that it could be located inside the solenoid together with the electromagnetic calorimeter, leading to the smallest costs of the calorimeter. A disadvantage is the high material budget. With 17% of a radiation length it is prohibitively large to be located in front of the forward spectrometer, the momentum resolution of the spectrometer would be significantly degraded. Therefore this design could only be used to cover angles above 5°.

Aerogel can be used in a proximity imaging or a mirror imaging setup. Unfortunately, it cannot be combined with a CsI based readout, because aerogel is only transparent above 200 nm, while CsI detectors only register photons below 200 nm. A possible alternative readout for a proximity imaging aerogel RICH detector could be provided by flat-panel PMTs. The material budget in this case would be considerable (14%), so that also this detector could only be used above 5°. In addition, flat panel PMTs are not very tolerant of magnetic fields, so that this design could not be used inside the solenoid.

The alternative design, using mirror imaging, is being used at Hermes since 1998 and is planned for LHCb. Using thin carbon-fibre based mirrors and a detector plane outside of the acceptance the thickness can be lower than 8% X_0, possibly as low as 6.8% of a radiation length. This is therefore the only detector design that could be located in front of the forward spectrometer while covering all angles. A further advantage is the possibility to extend the momentum range up to 18 GeV/c by filling the volume of the detector with C_4F_{10}, turning the detector into a Hermes-style dual radiator RICH. The comparatively high kaon threshold at 1.54 GeV/c is perhaps the main drawback of using aerogel as radiator, while the size required by the mirror imaging is a disadvantage of this detector design.

A quartz radiator can be used by exploiting the DIRC principle, similar to the barrel DIRC described above. The geometry in this case could be a disc, ideally consisting of a single piece of fused quartz, read out around the circumference of the disc, perhaps using an expansion volume like the BaBar DIRC. While this detector design is in principle proven, no disc DIRC has been built up to now. Using a 1.2 cm thick disc the material budget would be 10% X_0. The low kaon threshold at 0.46 GeV/c allows the best coverage of low momentum particles of all detector designs. It may be necessary to locate this detector outside of the solenoid, leading to a modest increase in size and therefore costs for the electromagnetic calorimeter. However, it will be investigated if this detector could also be located inside the solenoid, in which case no additional indirect cost would be caused. There is a variety of readout options, including flat panel PMTs, multianode PMTs and avalanche photodiodes (APDs).

7.3.1.3 Possible Spectrometer Configurations

With the possible exception of an aerogel RICH detector all detector designs have too much material to cover the acceptance of the dipole magnet at the angles below 5°. The logical solution is to combine two detectors, one for angles between 5° and 22°, located in front of the dipole, and a second one behind the dipole for angles below 5°. At these small angles the particle momenta are typically higher and comparatively high kaon threshold of aerogel is no disadvantage. At the same time the possibility to upgrade an aerogel to a dual radiator RICH becomes a clear advantage. Therefore the second detector should be an aerogel RICH, while the first detector can be either a disc DIRC detector or a proximity imaging C_6F_{14}/CsI-RICH.

The only possible single detector solution involves a large aerogel RICH detector in front of the magnet. However, if at least part of the detector should be located inside the solenoid, simple geometry shows that the detector will have to be large and rather complicated. A single photon detector plane at the inside of the magnet yoke would not be sufficient and a more complex geometry with multiple focusing mirrors and two photon detector planes would be necessary. The dipole magnet would have to be moved about 0.5 m downstream and size and cost of the electromagnetic calorimeter in front of the di-

radiator	imaging	readout	material [% X_0]	readout in mag.field	examples
C_6F_{14}	proximity	CsI MWPCs	17	yes	ALICE, STAR
aerogel	proximity	flat panel PMTs	14	no	n/a
aerogel	mirror	HPDs, MA-PMTs	8	yes	Hermes, LHCb
quartz	DIRC	MA-PMTs, APDs flat panel PMTs	10	yes	BaBar

Table 7.2: Read-out for different radiators.

pole would roughly double. Fig. 7.9 illustrates the three different forward spectrometer configurations.

Version 1, the combination of quartz disc DIRC and aerogel RICH, offers the best momentum coverage and spectrometer momentum resolution. These two detectors will therefore be described in more detail in the following subsections. Version 2, C_6F_{14}/CsI-RICH and aerogel RICH, may be less expensive due to a smaller calorimeter, but it introduces together with the barrel DIRC three different Cerenkov imaging technologies into the experiment. Version 3, the single large aerogel RICH, would on balance be the worst option. The complicated mirrors would be difficult to construct with sufficient quality and the design would require a large number of readout channels and therefore be expensive.

7.3.1.4 Quartz Disc DIRC

Cherenkov light emitted by charged particles inside a circular transparent disc with parallel surfaces and transported by one-dimensional total internal reflection has its angle preserved. In the suggested design (Fig. 7.10) one of the prisms at the rim then extracts the light from the plate into an expansion volume where the angle information converts into position information. Then the photons are recorded by detector pixels.

A parallel light beam of finite width due to finite plate thickness can be focussed with a cylinder lense placed on the prism exit face, the wavelength-dependent Cherenkov angle can largely be corrected in using a prism material with a chromatic dispersion different to that of the radiator disc.

For feasibility checks and performance calculations the following rounded values were used. The sensitive disc area is limited by the inner edge of the solenoid return yoke (red line in Fig. 7.10) at 1000 mm radius. The fused silica disc 10 mm thick continues to the outer edge of the return yoke at 1500 mm radius, followed beyond the prisms by a gaseous expansion volume and finally the photon detectors at 2000 mm radius.

With the disc radius being larger than the sensitive area the light paths are closer to normal incidence on the prism exit face, thus improving performance. Positioning the detection plane upstream of the disc places the photon detectors in a shielded location and a weak magnetic field of less than 10 mT, an advantage in case photocathode-based photon detectors are used.

Assuming 20% quantum efficiency in the wavelength range $\lambda = 300 - 600\,\text{nm}$ one arrives at a figure of merit $N_0 = 1\,520\,\text{mm}^{-1}$. For particles with normal incidence and $\beta = 1$ combining $N = N_0 \cdot L \cdot \sin^2\vartheta_C = 82$ detectable photons with the geometrical transmission efficiency $\epsilon_{tr} = 0.61$ one arrives at an average of 50 detected photons. With proper focussing and chromaticity correction and the hypothetical use of arbitrarily small pixel sizes one is able to separate pions and kaons at the 3.5σ level well beyond a momentum of $p = 25\,\text{GeV}/c$.

The onset of total internal reflection determines the lower momentum threshold for positive particle identification. The bottom line in Fig. 7.11 shows the kaon threshold. Starting at 1.2 GeV/c for normal incidence ($\vartheta = 0°$) it falls rapidly with increasing angle, for instance to 0.7 GeV/c at $\vartheta = 10°$.

For 32×72 pixels $10\,\text{mm}(z) \times 5°(\varphi)$ plus an area of larger pixels, 24×36 pixels $10\,\text{mm} \times 10°$ in size, one achieves the 3.5σ limit curve shown in black in Fig. 7.11 which in starting above 10 GeV/c at $\vartheta = 0°$ and decreasing to 5 GeV/c at $\vartheta = 25°$ closely follows the shape of kinematical momentum-angle correlations. The lines starting at $\vartheta = 5°$ show the effect of an elliptical hole for particles traversing the disc along the minor axis.

The photon propagation time in a dispersive medium is determined by the group velocity (and not the phase velocity) [5] which shows a 7% variation in the range $\lambda = 300 - 600\,\text{nm}$. While in the case of the barrel DIRC it may nevertheless be possible to determine the Cherenkov angle by measuring the photon time-of-flight (TOP project), the higher momenta found at more forward angle

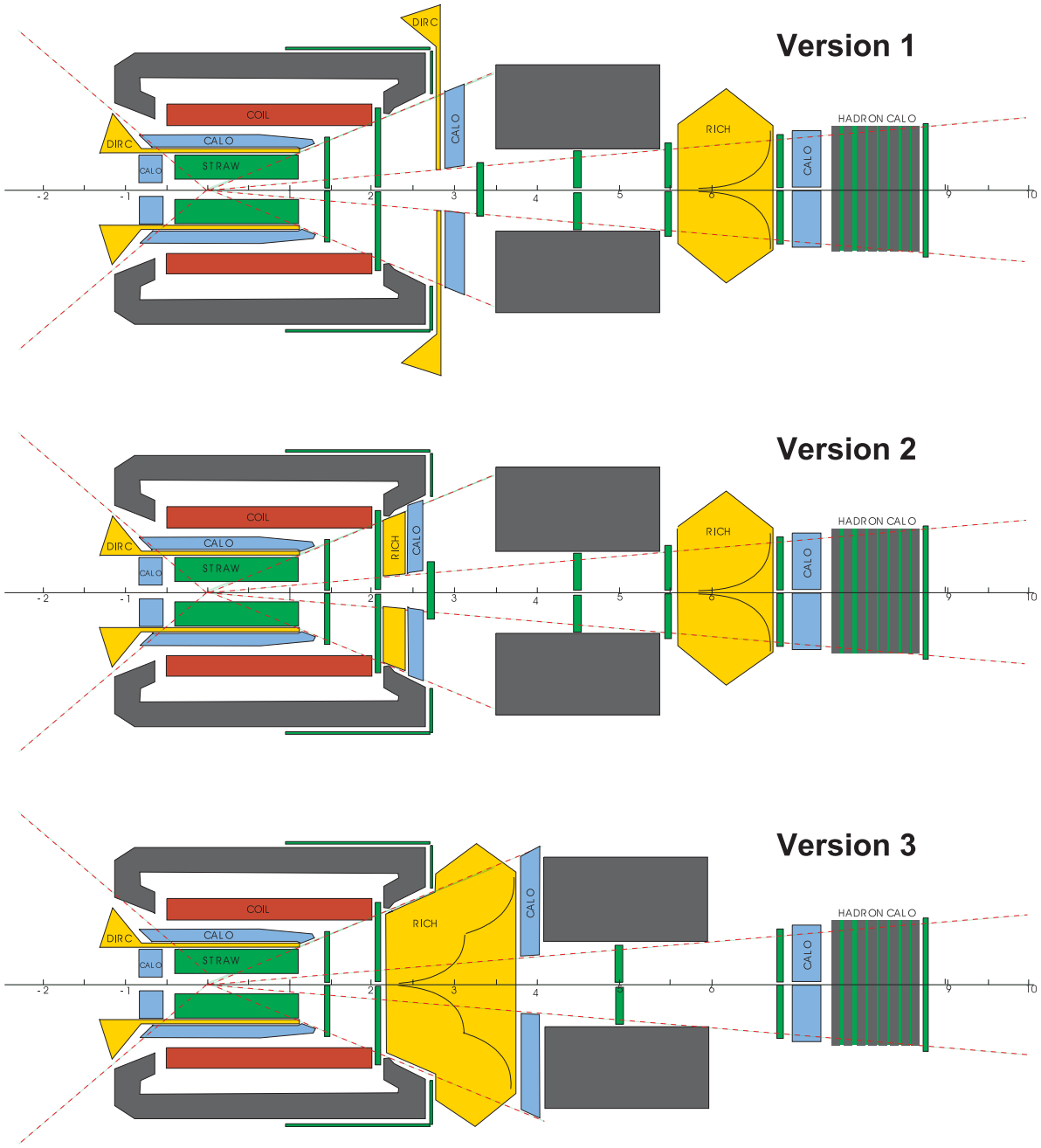

Figure 7.9: Three possible configurations of the forward spectrometer. Version 1: Disc DIRC and aerogel RICH detector with mirror imaging, Version 2: Proximity imaging C_6F_{14}/CsI-RICH and aerogel RICH detector with mirror imaging, Version 3: large aerogel RICH detector with multiple focusing mirrors.

make this no longer possible, even if one counterintuitively reduces the accepted wavelength range.

One has looked into placing the fused silica disc inside the solenoid return yoke at position 1 in Fig. 7.14. Access to the detector components for maintenance may be provided via a detachable rear return yoke part, but the currently foreseen geometry for solenoid and return yoke leaves very little space for focussing optics and photon detectors.

As an example of a more detailed design study [19] Fig. 7.12 shows how the photon focussing at the quartz disc perimeter onto a detection plane may be technically realised. This design in particular aims at a very compact photon detection unit for a situation where space availability is at a premium.

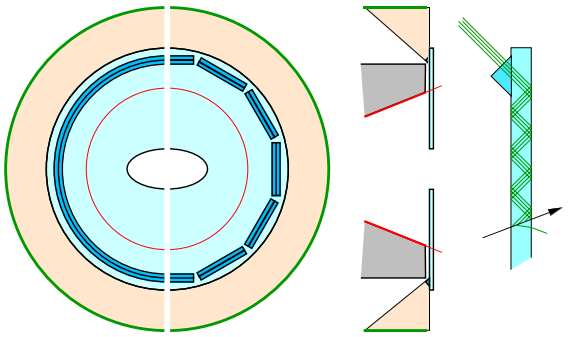

Figure 7.10: Schematic front and side views of a DIRC detector with total internal reflections in only one dimension. Inside a fused silica disc the Cherenkov light travelling towards the edge is extracted via a prism ring from the disc into an expansion volume and then impinges on a cylindrical photon detection plane (green ring). The performance difference between the prism ring (ideal situation, left half) and the polygon of linear prisms (righ half) is minimal.

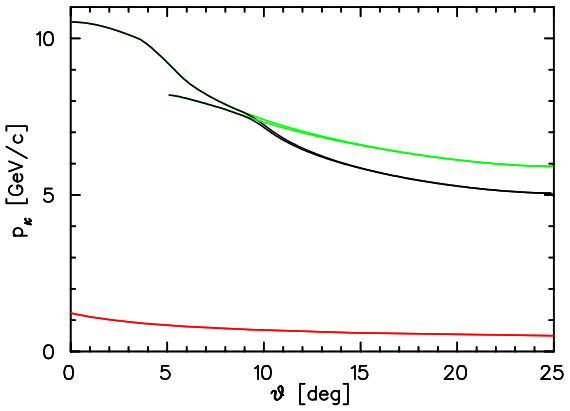

Figure 7.11: Momentum range for pion-kaon-separation with lower limit and upper limit values shown. The red line at the bottom shows the momentum threshold of the total reflection transmission for kaons ($n = 1.47$). The upper lines show the 3.5σ-limit for pion-kaon-separation, the green line for small detector pixels only, the white line for two areas of different granularity.

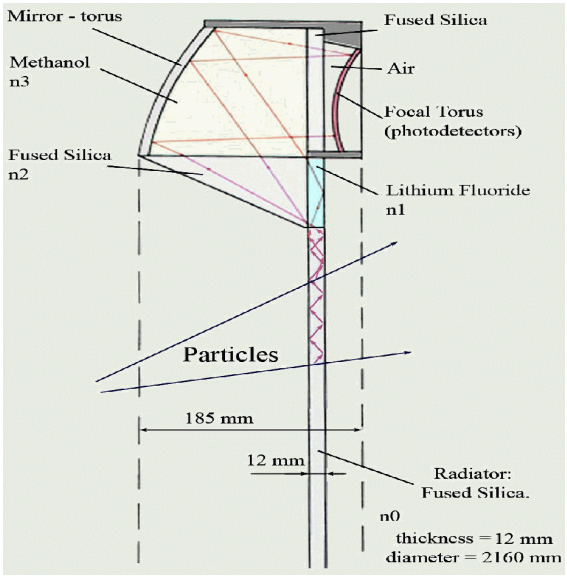

Figure 7.12: Design study for the optical readout of a quartz disc.

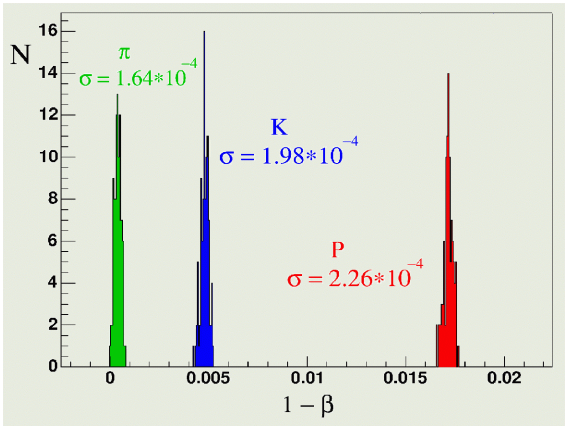

Figure 7.13: Distributions of reconstructed velocities (β) for pions, kaons and protons with a momentum of 5 GeV/c and a polar angle of $\vartheta = 6°$.

Reconstructed particle velocities shown in Fig. 7.13 from a simulation implementing this specific detector geometry illustrate the widths and separation of different particle distributions for pions, kaons and protons emitted with momentum 5 GeV/c under $\vartheta = 6°$ at the target vertex.

The disc at position 1 in Fig. 7.14 would yield negative indirect costs relative to the reference of a RICH detector at position 2. While keeping position 1 for the disc only one might use lightguides along the inner yoke surface and an expansion volume just downstream of the yoke. For a given number of photon detection pixels it would somewhat reduce the upper momentum limit and the use of light guides would result in a blind area of $\Delta\vartheta = 1°$ at $\vartheta = 22°$.

For the photon detection a large choice of different detector designs is available in principle, like standard photomultipliers, multianode phototubes, HPDs, APDs. There are, however, large uncertainties in future designs and prices, and the detailed discussion of this point in the following section on an aerogel based RICH detector holds for this DIRC design, too.

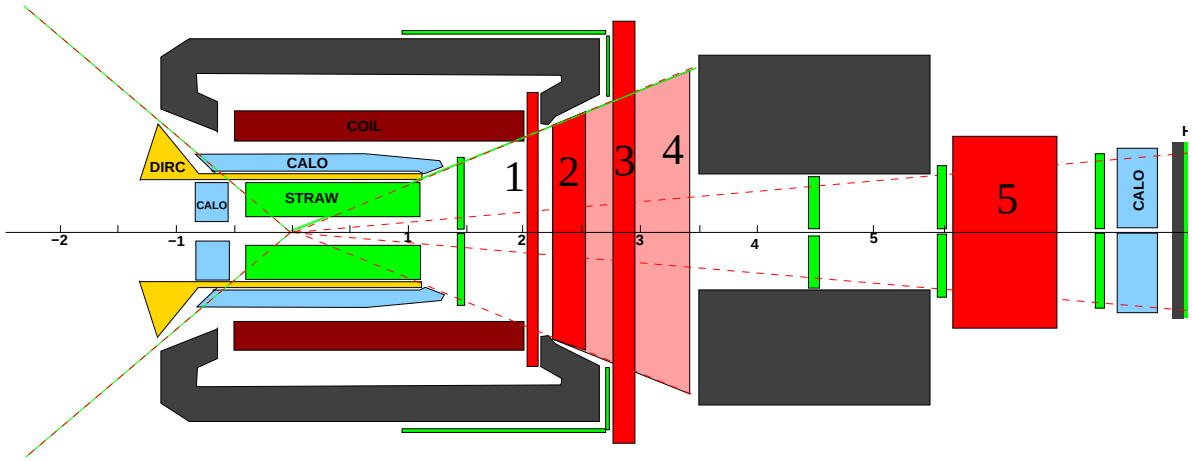

Figure 7.14: Possible locations for quartz or aerogel PID detectors.

Timeline. The timeline for the forward quartz disc DIRC is given in Fig. 7.15.

7.3.1.5 Aerogel RICH

As of this summer a new third generation aerogel produced by Matsushita has become available for tests [20]. The material is hydrophobic, the transmittance is $> 80\%$ at 400 nm (cf. Fig. 7.16) and in contrast to the aerogel used at Hermes the tile surfaces will be flat, i.e. without a "meniscus" caused be surface tension during the production.

Hamamatsu has recently presented test results with a new type of multi-pixel hybrid photodetector, consisting of a photocathode and a multi-pixel avalanche diode [21]. This detector has 64 pixels of $(2 \times 2)\,\mathrm{mm}^2$ size, a timing resolution of better than 100 ps and it has been shown to operate in a magnetic field of 1.5 T. Equipped with a GaAsP-photocathode quantum-efficiencies of up to 60% have been reached (cf. Fig. 7.17), the sensitivity covers exactly the desired range of 300–700 nm and it has an excellent single-photon resolution. This detector, especially with the GaAsP-photocathode, is an ideal match for an aerogel radiator: It has an extremely high quantum efficiency in the visible light region and a built-in cut-off at 300 nm, automatically blocking out most of the Rayleigh-scattering background.

The combination of these newly available technologies allows the construction of an aerogel RICH detector that will have more than twice the number of photoelectrons as the Hermes RICH.

Timeline. The timeline for the forward aerogel Rich is given in Fig. 7.18.

7.3.2 Forward Time-of-Flight Wall

7.3.2.1 Introduction

Identification of forward going particles detected by FS with momenta below 4–5 GeV/c is performed with the help of TOF technique. As simulation shows a good separation of pions, kaons and protons will be possible with time resolution of $\sigma = 50$ ps. This is offline resolution obtained taking into account the hit position in a scintillation bar which is found with the help of FS tracking chambers. Momentum resolution of the dipole spectrometer is assumed to be about FWHM = 1%.

7.3.2.2 Requirements

At $\bar{\mathrm{p}}$ beam intensity $5 \cdot 10^{10}$ incident on pellet target, luminosity of $2 \cdot 10^{32}\,\mathrm{cm}^{-2}\mathrm{s}^{-1}$ is expected. This corresponds to about $2 \cdot 10^{7}\,\mathrm{cm}^{-2}\mathrm{s}^{-1}$ interactions in the target. Proceeding from that one may expect very roughly some $(2\text{–}4) \cdot 10^{7}\,\mathrm{cm}^{-2}\mathrm{s}^{-1}$ forward going hadrons. Assuming that a scintillation counter may sustain a good TOF resolution at admitable counting rate of $\sim 5 \cdot 10^{5}\,\mathrm{s}^{-1}$ one obtains that average granularity (number of individual TOF channels) must be of about 40–80.

7.3.2.3 Overview

In order to meet the requirement of a good pions, kaons and protons TOF separation a scintillation

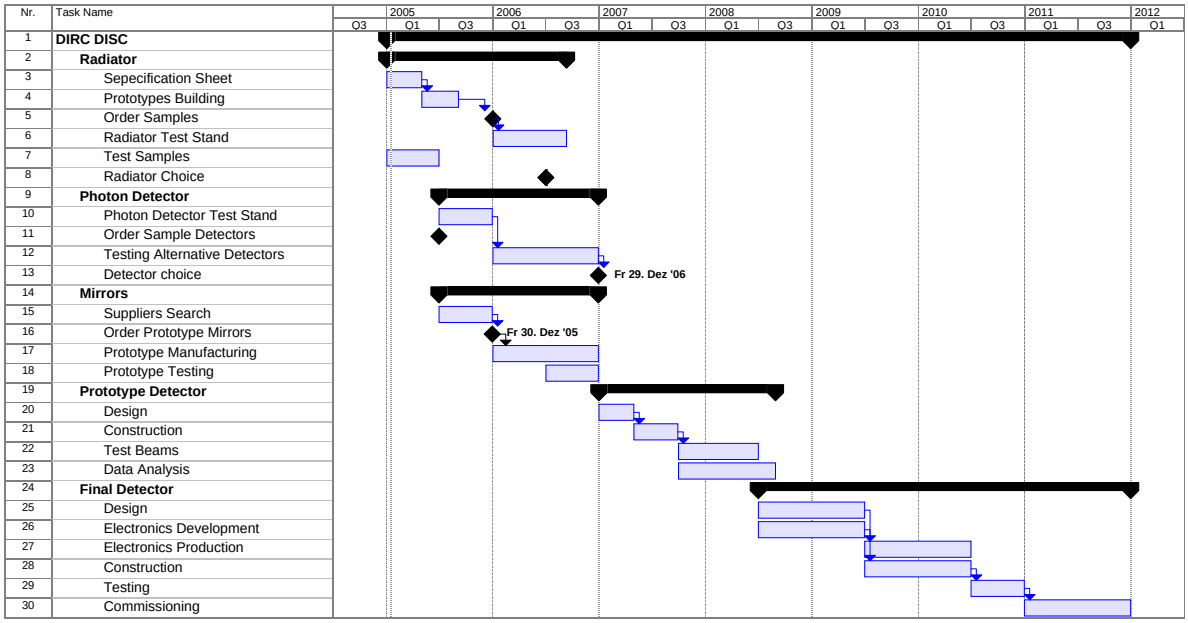

Figure 7.15: Timeline for the quartz disc dirc.

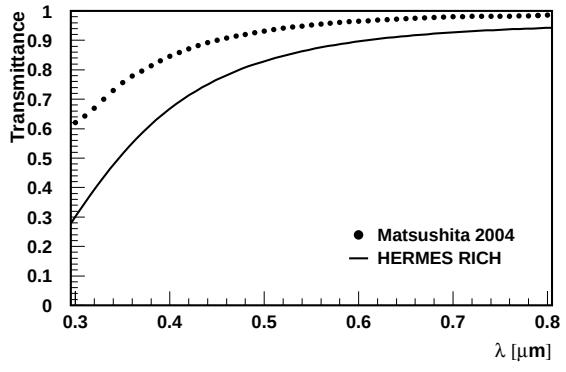

Figure 7.16: Transmittance for new third-generation Matsushita aerogel in comparison to the aerogel used in the Hermes RICH.

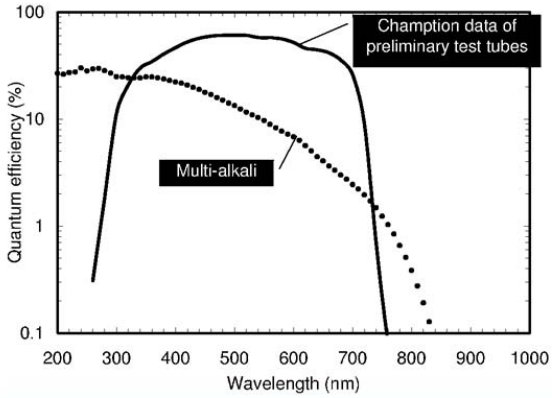

Figure 7.17: Quantum efficiency for Hamamatsu HPDs with conventional multi-alkali cathode and new GaAsP cathode.

wall has to be built at a certain distance from the start detector placed in the target region.

One should note that besides PID function, the signal from a scintillation wall counter in coincidence with a start signal might be used for a first level trigger to start up readout of the FS tracking devices.

The TOF scintillation wall is suggested to be placed downstream of the dipole magnet at the distance of 7 m from the interaction point. Proceeding from the FS acceptance ($\pm 5°$) and expected horizontal deflection of the low momentum particles by the dipole the dimensions of the wall are taken to be: height = 1.4 m, width = 5.6 m. The wall consists of vertical strips. In the central part, close to the beam and ,respectively, with higher counting rate, 20 strips of 5 cm width each will be located. This part corresponds to a horizontal acceptance of $\pm 3.8°$. The peripheral left and right part of the wall consists of 24 and 22 strips, respectively, each of 10 cm width. The total number of strips is 66. In addition to the main TOF wall, two side walls will be installed inside the dipole magnet gap, near the left and right wall of the magnet yoke, in order to register low momentum charged particles being bent in the dipole field towards the yoke. Each of the side hodoscopes will consist of five vertical scintillator strips, each of 10 cm width and 100 cm

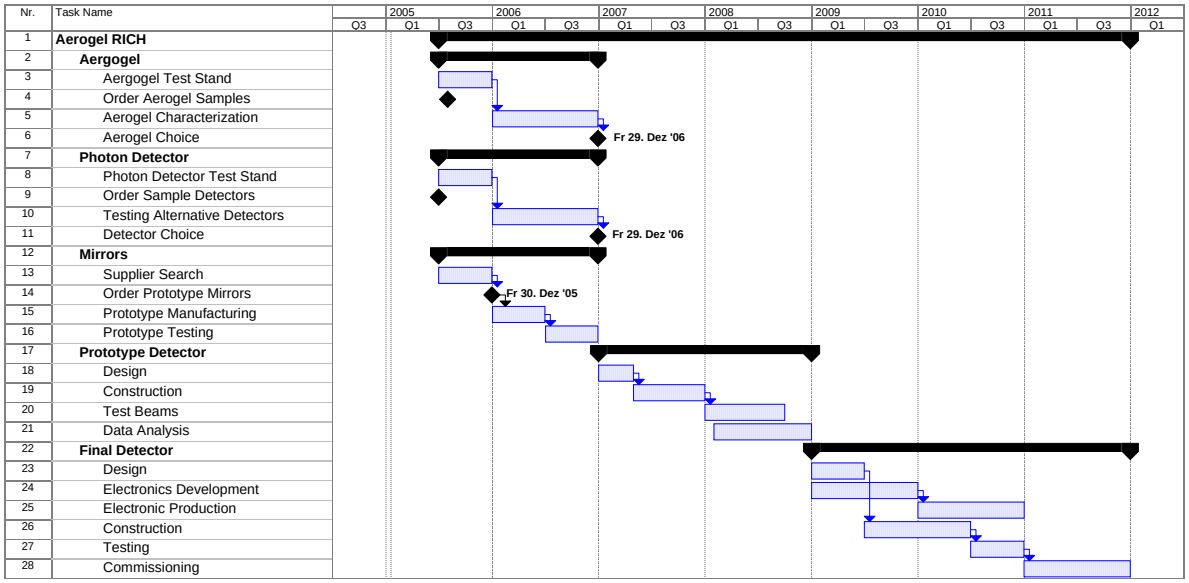

Figure 7.18: Timeline for the aerogel rich.

height.

7.3.2.4 Single Module Parameters

A single scintillation strip is made of plastic scintillator BC408 (BICRON catalogue) coupled at each end via lightguides to PMT R4998 Hamamatsu ,1" diameter for TOF measurements, read out by a fast front-end electronics. Mu-metal shielding against influence of the dipole magnetic field is foreseen. For the side walls, the optical coupling between the scintillators and the PMTs placed outside the magnetic field in the dipole gap will be accomplished by means of fiber light guides.

7.3.2.5 Mechanical Setup

The main scintillation wall is shown schematically in Fig. 7.19 and a side wall is shown in Fig. 7.20. The beam vacuum pipe crosses the main scintillation wall. A possible design of the scintillation counters upper and below the beam vacuum pipe is shown in Fig. 7.21. The light produced in the scintillator is detected with two PMT's. One is coupled to the scintillator, another accepts the light reflected with the help of the prism.

It is assumed that all the scintillators in the wall together with PMT's and cabling will be assembled on a rigid mechanical structure allowing easy access to the cables, PMT's and light guides. The mechanical structure must be supplied with necessary mechanical arrangements for the 3D alignment of the wall with the accuracy of $\sim$0.3mm. It is assumed that the alignment of the wall will be done in the process of overall (laser/optical) alignment of FS components using special fiducial reference marks firmly connected to the device.

7.3.2.6 Simulation

The simulations have been done using the $\overline{\mathsf{P}}$ANDA DPM generator for $\overline{\mathrm{p}}$p events at the primary beam momenta 2, 5 and 15 GeV/c. The input parameters used in the simulations are listed below:

- TOF length $L = 7\,\mathrm{m}$,
- Forward Spectrometer momentum resolution $\sigma_p = 0.005$ (FWHM $\approx 1\%$),
- overall TOF offline resolution $\sigma_{TOF} = 0.05\,\mathrm{ns}$,
- Selected particles are π^+, π^-, K^+, K^-, p, $\overline{\mathrm{p}}$. In our analysis we have not distinguished between the particle charges.

With above parameters the TOF separation has been studied for three momentum ranges of the secondary particles: 0.9–1.9 GeV/c, 1.9–3 GeV/c, 3–3.49 GeV/c. Reconstruction of the particle mass has been simulated by applying Gaussian smearing generators to the generated value of the particle momentum and to the calculated (unsmeared) TOF value. The results are strongly dependent on TOF smearing (TOF resolution) and much less sensitive

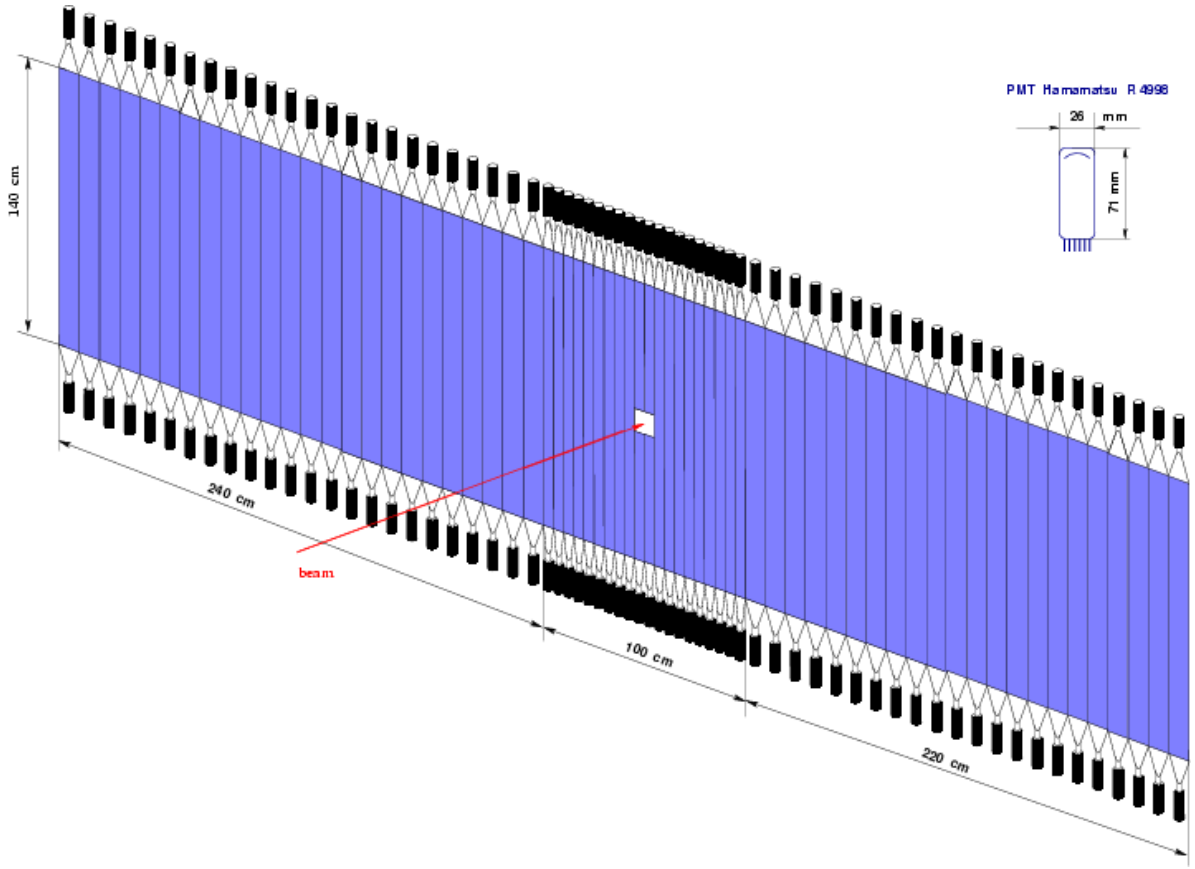

Figure 7.19: Isometric view of the scintillation wall.

to the momentum smearing. The momentum resolution might be taken twice worse without visible effect on mass separation. Results of simulation for the antiproton beam momentum of 5 GeV/c are shown in Fig. 7.22. The reconstructed mass spectra obtained for the simulation are shown in Figs. 7.23-7.25.

7.3.2.7 Prototypes

The prototype module will be designed and produced in PNPI together with front-end electronics.

7.3.2.8 Realization

Responsibilities. PNPI takes resposibility for

- design and test of the prototype module;
- procurements of the scintillation materials and PM's;
- design and fabrication of the mechanical structure;
- assembly and tests of the wall in place;
- incorporation of the TOF information in the $\overline{\text{P}}$ANDA DAQ
- alignment within general $\overline{\text{P}}$ANDA alignment concept

Timeline. The timeline for the forward time-of-flight wall is given in Fig. 7.26.

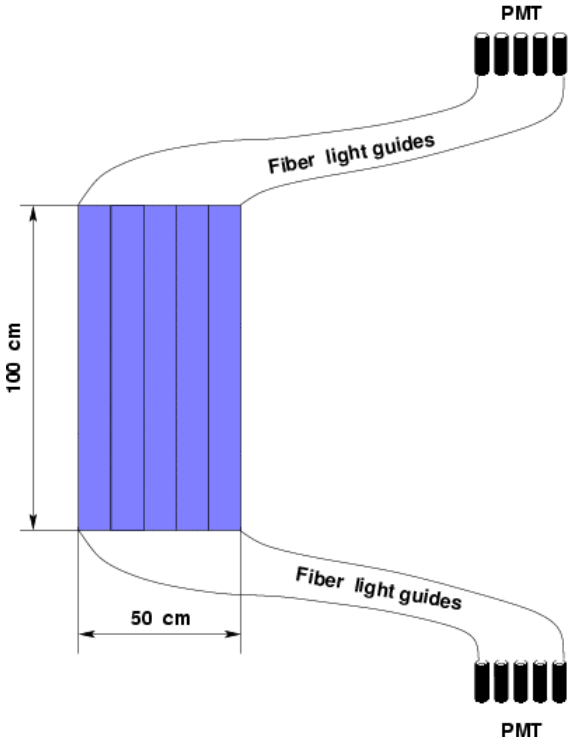

Figure 7.20: Scheme of a side wall for TOF measurements.

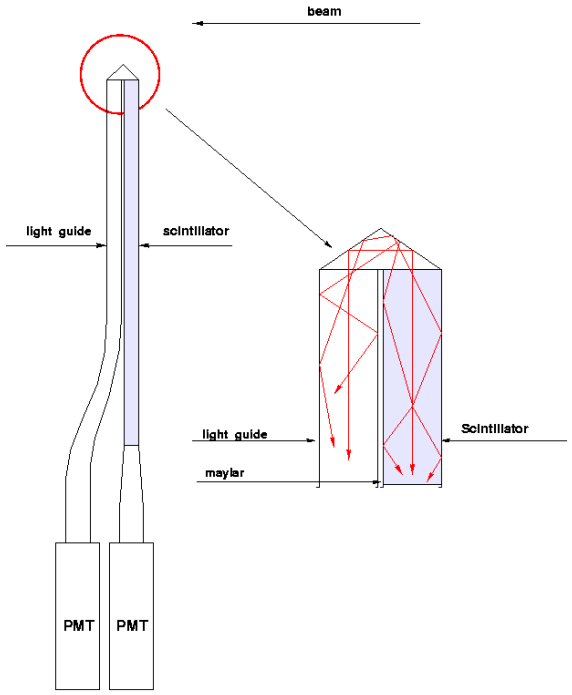

Figure 7.21: Side view of the scintillation counter upper and lower the beam vacuum pipe.

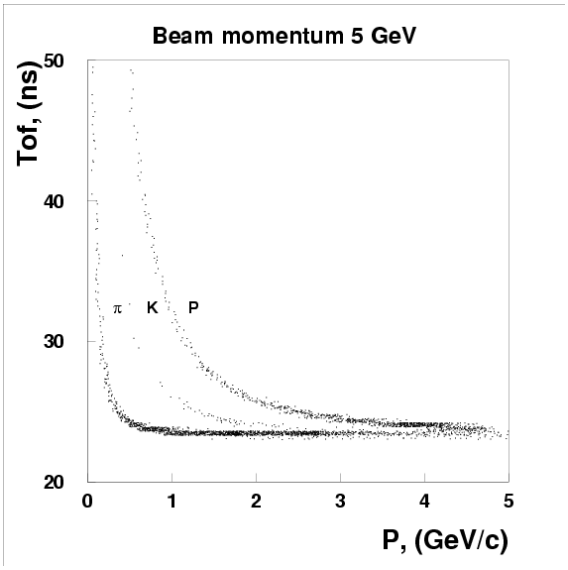

Figure 7.22: Time-of-flight *vs.* particle momentum at primary beam energy of 5 GeV.

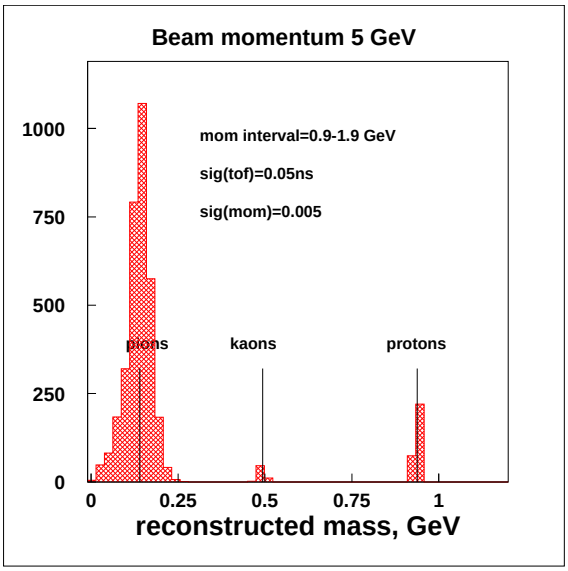

Figure 7.23: Invariant mass spectra for particle momentum interval 0.9–1.9 GeV/*c*.

7.4 Muon Detectors

7.4.1 Physics requirements

The need to measure muons in $\overline{\mathrm{P}}$ANDA with relatively small momenta (J/ψ, charmonium, Drell–Yan, *etc.*) requires good muon identification. For example, if one takes DY muon pairs as a benchmark process to evaluate the performance of $\overline{\mathrm{P}}$ANDA detector the following features matter - av-

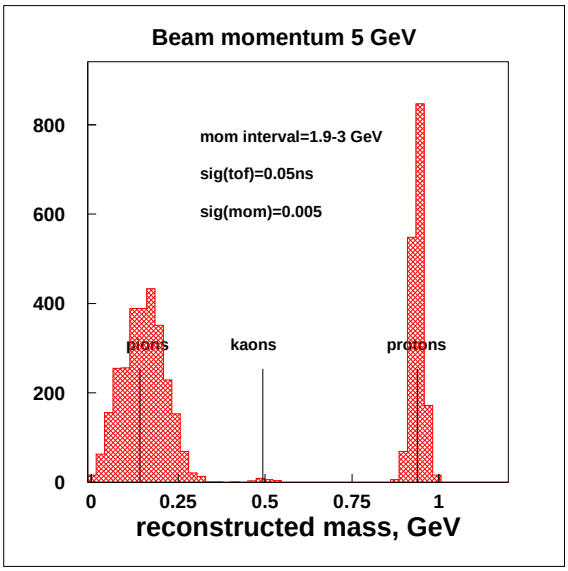

Figure 7.24: Invariant mass spectra for particle momentum interval 1.9–3 GeV/c.

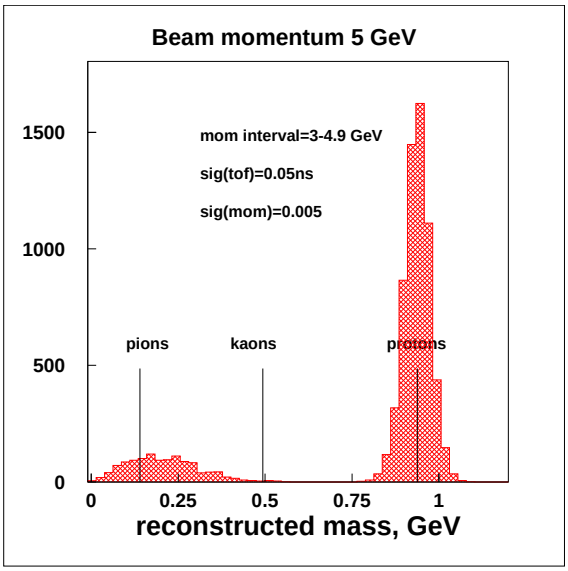

Figure 7.25: Invariant mass spectra for particle momentum interval 3–4.9 GeV/c.

erage energy about few GeV and maximum reachable around 10 GeV as well as polar angle of muons approaching 150 degrees (in lab system, for the 15 GeV/c beam momentum).

Generally saying the processes of interest having muons in final states have small cross sections compared with background. This supposes very good muon identification to maximize signal to background ratio. Muon identification may be done by three different detector systems and methods:

- scintillator counters (time-of-flight measurement);
- calorimetry, both electromagnetic and hadronic (dE/dx energy deposition of MIP);
- muon tracker (good clear track sample visibility even in presence of showers).

The last system may be regarded as the main one for reliable muon identification, two others as important but complimentary. Correlating the signals from all three independent systems should provide desirable level of signal purity for muons. These correlations become more important with the lower beam energy.

As usual, the main task of muon system is pattern recognition (for muon identification) and matching to the track segment inside the magnets. The precise muon momentum measurement is being performed by inner trackers of the magnetic spectrometers.

7.4.2 Scintillator counters

Behind the iron yoke of the TS, plastic scintillator counters for muon detection (MUD) will be installed that cover the laboratory polar angular range from 60° down to the opening for the dipole. Coverage to larger polar angles is not needed since the muons will be stopped in the iron yoke. The momentum of the muons is determined by the TS-tracking. The TS-MUD system will consist of about 96 individual strips that are 10 cm wide, 1 cm thick and about 2 m long. In addition there is an equal number of strip perpendicular to the beam axis, at the front of the TS-solenoid. The strips are read out on both ends with photomultipliers fed to ADCs and TDCs. This information can be used to determine the position for matching with the TS-tracking, and the time-of-flight, to suppress random coincidences. The energy information provides not only a redundant position information, but also a value of dE/dx to permit further background suppression. The use of photomultipliers also enable the MUD to be included into the first level trigger.

The price for the scintillation counter is about 500 k€, where half of the cost is for the scintillator and half for the PMTs.

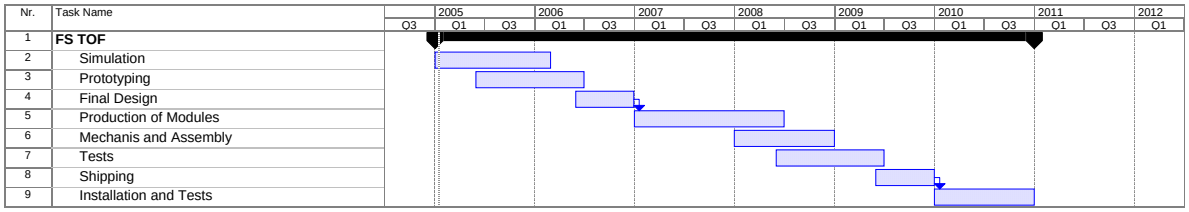

Figure 7.26: Timeline for forward TOF wall.

7.4.3 Muon tracking: MDT option

7.4.3.1 System overview

The joint Dubna–Torino team regards the MDT detectors as the possible choice for the $\overline{\text{P}}$ANDA muon system. The motivation includes:

- features of detector comprising good spatial and time resolution, simplicity and flexibility of design permitting to cover big and complicated surfaces, robustness and reliability, high longetivity (small ageing);
- performance of MDTs in muon systems which is proven in the big experiments like DØ at FNAL [22] (6 300 detectors, 50 000 readout channels) and COMPASS at CERN (1 000 detectors, 8 000 readout channels);
- team of experts in JINR/Dubna capable to design, produce, assemble and maintainance the MDT based muon system as well as availability of the big workshop with productivity adequate to the $\overline{\text{P}}$ANDA construction schedule.

The Mini-Drift Tube detector is the development of Iarocci tubes (streamer tubes) [23] which has the same basic geometry (proved to be very practical and flexible) but uses proportional mode of operation instead of streamer and replaces the plastic cathode by the metallic one; the last two points serve for much higher longetivity of MDTs in high rate background conditions.

The MDT detector (see Fig. 7.27) comprises the following parts: metallic cathode - aluminum extruded comb-like profile (2) and stainless steel cover (1), anode wire (4) and plastic envelope (3) for gas tightness and high voltage protection. Typical wall thickness of the profile may be selected in the range above 0.45 mm (with tolerances about $\pm 0,05$ mm). Smaller wall thickness should be selected for the muon stations having small number, say four, of detector layers to increase slightly the geometrical efficiency. The plastic may be chosen (PVC, ABS,

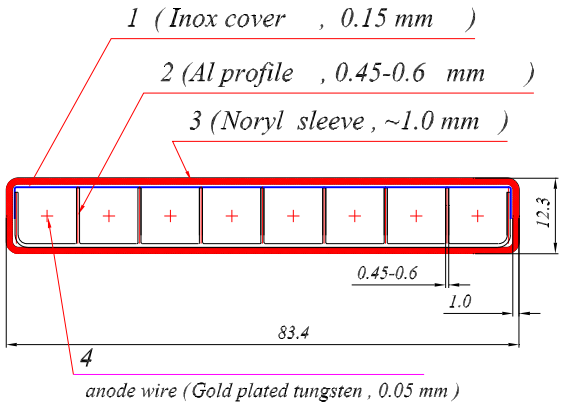

Figure 7.27: Mini-Drift Tube (MDT) cross section.

Noryl) depending on the safety environmental requirements in the Lab. The signal wires pitch is 10 mm.

The relevant features of the MDT detectors like efficiency plateau, time resolution, coordinate accuracy, ageing etc were thoroughly investigated [24, 25] and proven by large scale experiments. The experience with MDT detectors has also shown their high reliability and robustness. The Table below shows the summary of the main MDT parameters. Presently the MDTs are used either as drift chambers (DØ/FNAL) or proportional (COMPASS/CERN, Yes/No readout of the wires), but in both cases as the one-coordinate detector only. The MDT design permits also to use it as two-coordinate detector by readout of induced signal on external sample of electrodes (strips or pads). For that the stainless steel cover (Fig. 7.27, position (1)) should not be installed during the assembly of detector. This point requires R&D studies to optimize the readout of the second coordinate.

7.4.3.2 Detector geometry

The conceptual layout of the $\overline{\text{P}}$ANDA muon tracker is presented in Figs. 7.28 and 7.29. Here and everywhere only most relevant for muons elements of the

Gas mixture	coord. acc. (rms)	time res.	ageing	eff. plateau
CF_4:CH_4 = 90:10	$0.7 - 0.8$ mm	$50 - 100$ ns $(*)$	> 2 C/cm	400 V
Ar/CO_2 = 70:30	$0.4 - 0.5$ mm	$150 - 300$ ns $(*)$	> 1 C/cm	200 V

$(*)$ angle range $0° - 30°$.

Table 7.3: Summary of MDT parameters.

$\overline{\text{P}}$ANDA setup are shown, like magnetic system and hadron calorimeter. The muon system covers practically full azimuthal angle and polar angle up to about 60°. It consists of muon stations having either 4 or 6 detector layers each. These stations are organized in such a way which gives an opportunity to trace the muons penetrating through massive material like iron yokes and electromagnetic and hadron calorimeters. Position of the stations also permits to measure/estimate the magnetic bending of the muon track thus providing for better match with the inner track of known momentum. The muon stations inserted in the hadron calorimeter allow to intercept even those low momenta muons which would be otherwise overlooked due to the $\mathrm{d}E/\mathrm{d}x$ losses. These stations also may help in search for a muon even in the presence of hadronic shower.

The example of design of the muon stations consisting of both 4 and 6 detector layers is given on Fig. 7.30 for the target spectrometer. The basic constructional element of the muon stations is a "biplane" composed of the aluminum frame (about few cm thick) carrying 2 layers of MDTs on both sides. This design has proved itself as simple and reliable, permitting to cover complicated surfaces with typical mechanical acuracy well below 1 mm r.m.s. In practice the achievable coordinate accuracy for such a design when measuring the drift time of MDTs varies within 0.5–0.8 mm r.m.s.

Muon stations in the target spectrometer follow its octogonal shape (see Fig. 7.31). Those two stations surrounding the yoke have 8 chambers each (A-A cross section). The chambers have rectangular shape and wires stretched along z-axis (beam direction) to measure the magnetic bending of the tracks. The vertical station (view B) has 8 chambers (6 detector layers each) of trapezoidal shape. The direction of MDTs is seen on the picture. This vertical station also helps to fix the angle of a muon entering the dipole magnet yoke. The forward spectrometer has muon stations surrounding the dipole magnet as well as those inserted into the hadron calorimeter (Fig. 7.32, see also Figs. 7.28 and 7.29). There are 8 chambers around the magnet each having 6 MDT layers. Four of them have rectangular (Figs. 7.28 and 7.29) and four - trapezoidal shape (Fig. 7.32, view C). The wires of all chambers are stretched along x and y-axes to measure the magnetic bending of the muons.

The muon stations of the hadron calorimeter are relatively numerous for to recognize the muon track even in the presense of hadronic shower. Two inner stations have 4 MDT layers each ($2x$-$2y$ orientations, see Fig. 7.28 and Fig. 7.32,view D) and outer station has 6 MDT layers ($3x$-$3y$ orientation).

As it was mentioned before the muons in $\overline{\text{P}}$ANDA have relatively low momenta. This may lead to some losses of them, mainly in the irone yoke of the dipole magnet having depth around 2 m along the Z-axis. Due to ionization losses this imposes the cutoff in the muon's momentum below 2 GeV. To avoid this instrumental effect it is worth regarding an extended $\overline{\text{P}}$ANDA option with cut dipole magnet (Fig. 7.33). Two muon stations inserted in the magnet' slots have 4 MDT layers each and rectangular shape, they look like those pictured on Fig. 7.32 (view C). It is also worth mentioning the possibility to extend muon system around the whole target spectrometer thus having full hermiticity for the muons.

7.4.3.3 Readout electronics

The type of readout and the number of channels should be finally decided only after detailed Monte Carlo studies of the $\overline{\text{P}}$ANDA muon system response for the different processes. Presently we regard the combined readout which includes three modes: simple y/n readout of the MDT's wires, drift time measurement and strips/pads readout of induced charge. The Dubna – Torino group will rely on experience gained during the design and production of detectors and electronics for the COMPASS experiment at CERN (see for example [26]).

It is supposed that due to the multiple scattering limitations the target spectrometer and muon stations around the dipole magnet should be equipped with y/n readout of the wires and strips.

The muon stations of the hadron calorimeter should be equipped with a drift time readout of the wires and analog readout of strips and pads (for the first station only). Such composition of the readout

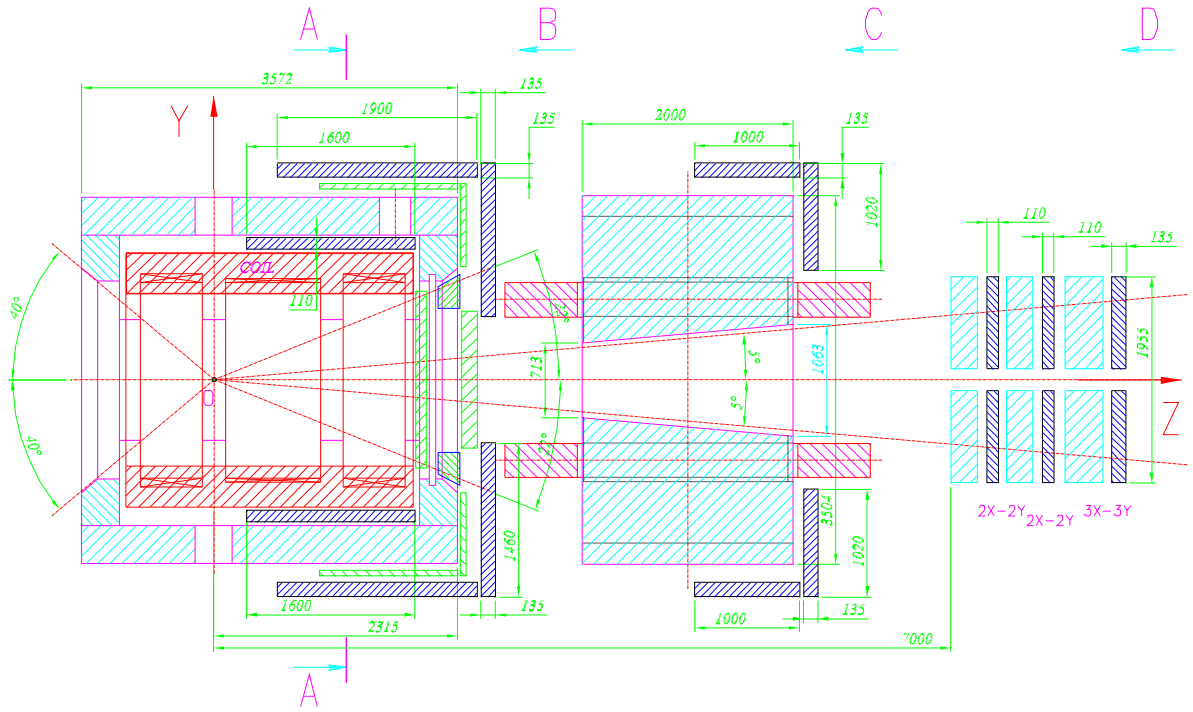

Figure 7.28: The conceptual layout of the $\overline{\text{P}}$ANDA muon system; muon stations are indicated by deep blue dashed lines.

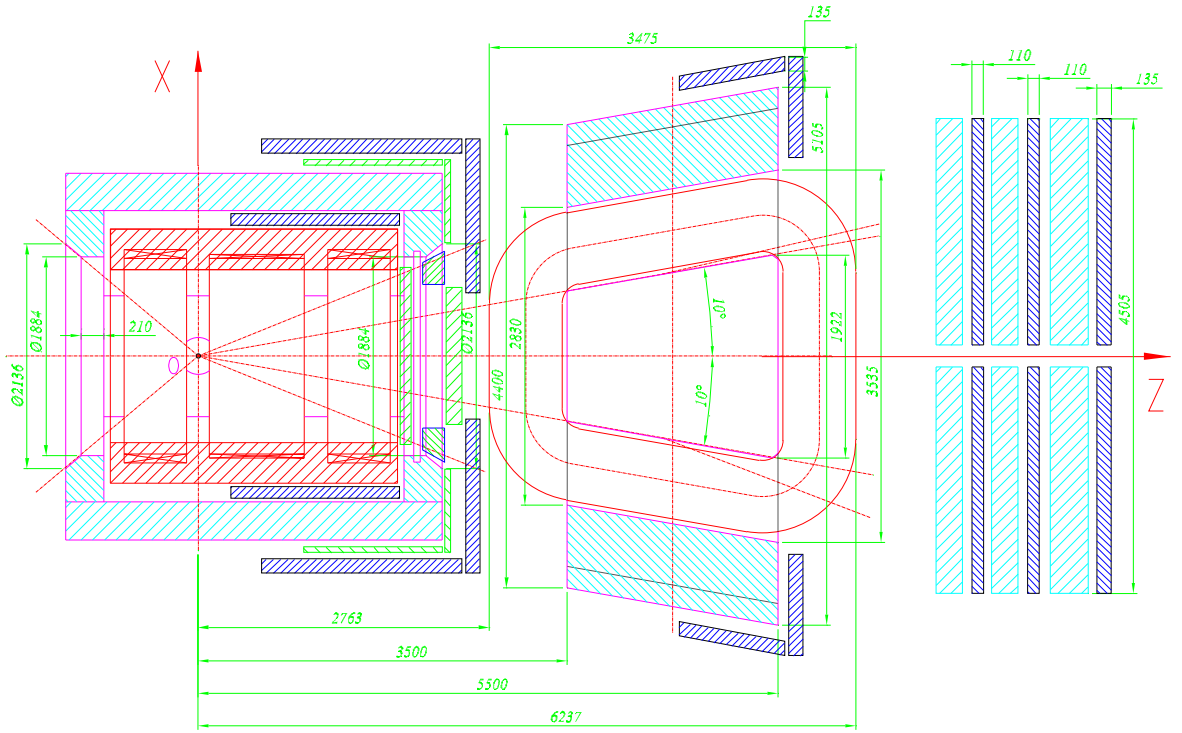

Figure 7.29: The $\overline{\text{P}}$ANDA conceptual muon system; top view.

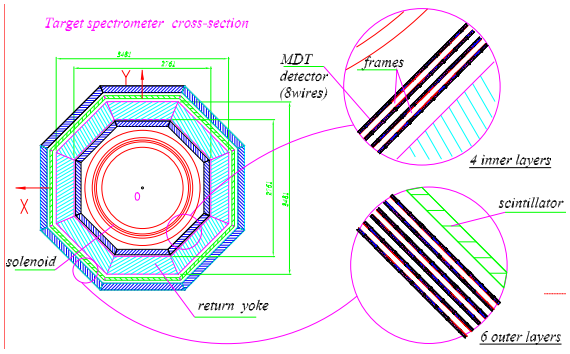

Figure 7.30: Example of the muon stations consisting of 4 and 6 MDT detector layers.

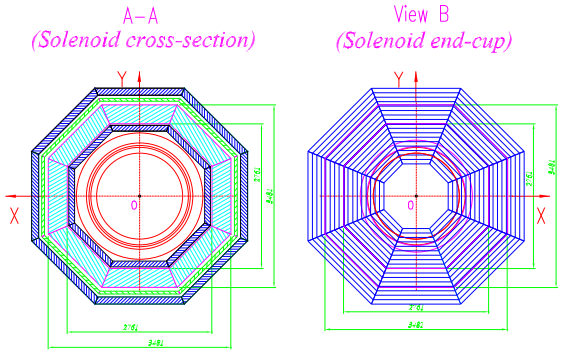

Figure 7.31: Muon stations of the target spectrometer.

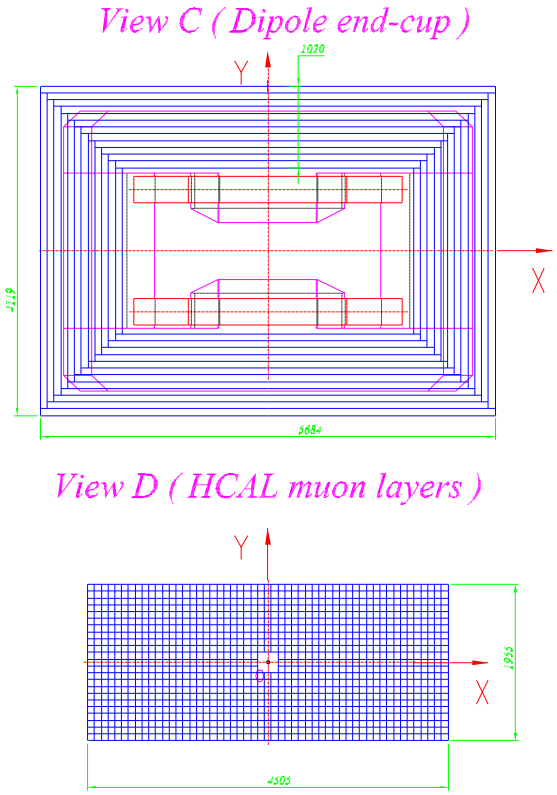

Figure 7.32: Muon stations of the forward spectrometer.

schemes permits for a good two-coordinate spatial accuracy (about 1 mm r.m.s.) in the forward region where higher muon momenta may be registered. The system of pads readout serves for a good muon pattern recognition in presence of hadronic showers.

7.4.4 Muon tracking: CMS DT option

7.4.4.1 Introduction

Muons are an unmistakable signature of a wide class of the processes we are going to study with the PANDA spectrometer (Drell-Yan physics, J/ψ production, *etc.*). The ability to trigger and to reconstruct muons is the very important item to the PANDA detector concept, thus the modern detector techniques must be used. This is why considering different options for the PANDA muon detector we paid a special attention to the possibility to gain of the "state of the art" knowledge accumulated in the LHC projects, like Compact Muon Solenoid (CMS) for example, in spite even of rather different energy scale.

Apart of that, obviously, it is very important to get the best possible performance/cost ratio, what was not least reason to take into account during different options discussion.

Thus, we propose to use CMS like Drift Tube Chambers [27, 28, 29] as a possible solution for the PANDA muon detector. This solution looks rather attractive because of the possibility to use the INFN-Torino production line already installed and successfully exploited for the CMS muon detectors construction. Important, that this option does not exclude the usage of other muon detectors types (like Mini Drift Tubes for example), so the combined muon system might be considered.

7.4.4.2 System overview

The choice of a drift chambers as a muon tracking detectors in both PANDA Forward Spectrometer (FS) and Target Spectrometer (TS) was dictated by not extremely high particles rates and by almost absent magnetic field in the region of muon detec-

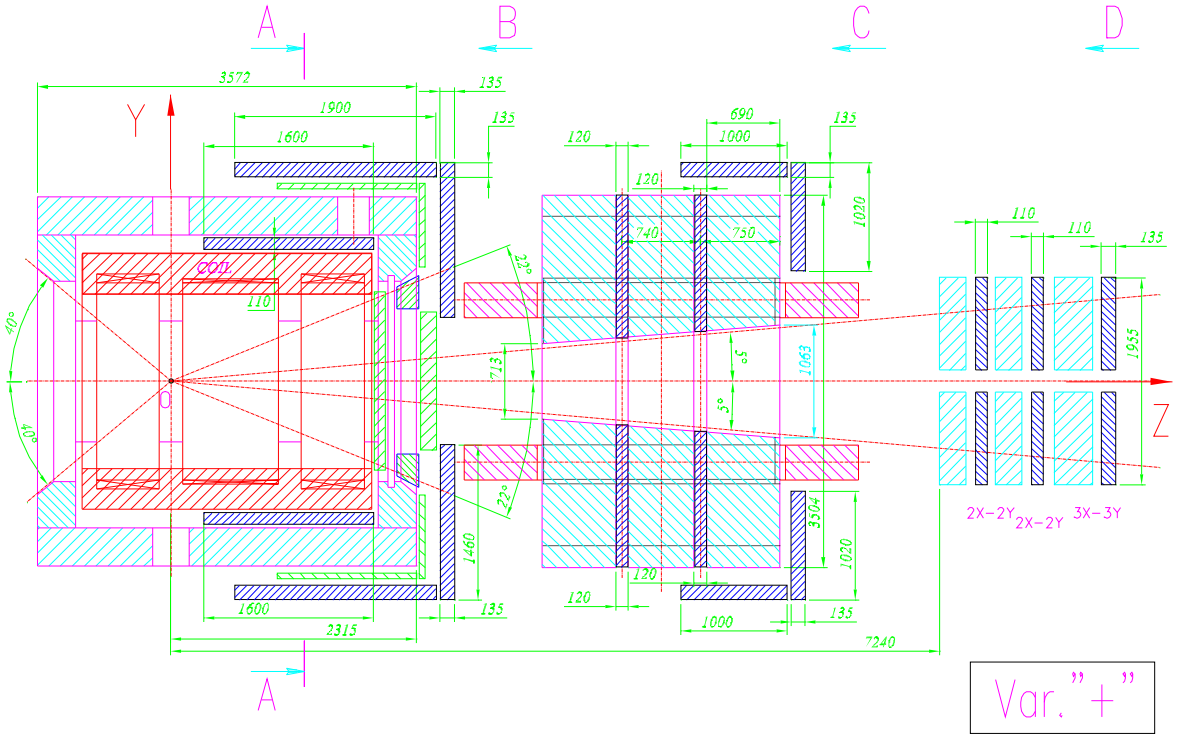

Figure 7.33: Extended $\overline{\text{P}}$ANDA muon system with cut dipole magnet.

Type of muon system:	conventional	extended
Number of MDTs:	3880	4328
Total detector length:	9.6 km	11 km
Digital readout channels:	16 000, y/n wires	17 850, y/n wires
	15 000, y/n strips	17 000, y/n strips
Analog readout channels:	15 000 drift/wires	15 000 drift/wires
	10 000 FADC	10 000 FADC

Table 7.4: Readout electronics for the muon detectors.

tors. A tube as a basic unit was preferred in order to have natural protection against damage from the broken wire and to partially decouple the contiguous cells. The simple solution is to assemble together four drift layers to form the super-layers, and then two super-layers to form the drift chamber - a single easy to manipulate rigid structure. It was shown that even a simple gas mixture based on Ar/CO2 and dedicated super-layer structure can provide rather good space resolution ($\approx$ 250 μm per layer) and sufficient time resolution (order of several nanoseconds). That provides a possibility to use such a detector as an adequate instrument for the muon identification taking advantage of the modern $\overline{\text{P}}$ANDA triggerless DAQ system.

7.4.4.3 Drift cell geometry

The baseline drift cell design, shown in Fig. 7.34, has a pitch of 40 mm by 13 mm. At the center is the anode wire, made out of 50 μm diameter stainless steel. The cathods defining the cell width are alu-

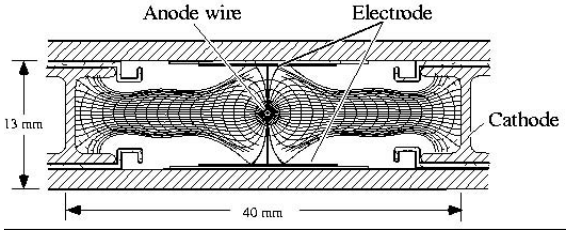

Figure 7.34: Transverse view of the CMS Drift Tubes drift cell.

minum I-beams 1.2 mm thick and 9.6 mm high. A plastic profile, made of 0.5 mm thick extruded policarbonat plastic (Lexan), is glued n the upper and lower parts of the I-beams to provide cathodes electrical insulation from the aluminum plates. These plates, which are kept at ground potential, forms the two remaining sides of the cell.

A pair of positively-biased strips is placed at the center of the cell and has an effect of "squeezing" the drift lines, improving the linearity of the space/time relationship ($R(t)$) and the resolution of the drift cell. These electrodes are custom-made stripes of 0.1 mm thick and 20 mm wide mylar tape on which a 14 mm wide and 700 μm thick copper stripe is glued. The 3mm of mylar on each side of the copper stripe prevents sparking from the copper to the Al plates. The electric field obtained with this geometry and with the HV settings: $V_{wire} = +3.6\,\text{kV}$, $V_{cathode} = -1.2\,\text{kV}$ and $V_{strip} = +1.8\,\text{kV}$ is also shown in Fig. 7.34.

The wire length varies from 2–4 m, no intermediate wire supports are used. The wires are pulled at a tension equal to 2.9 N, which corresponds to 90 % of the elastic limit. The resulting wire sags are 35 μm and 135 μm for 2 m and 4 m long wires respectively. The wire positioning defined by means of plastic end-plugs that glue to the aluminum plates at the end of each cell. Between two adjacent end-plugs, the wire holding piece is inserted which holds the crimping block Fig. 7.35. The wire can be crimped

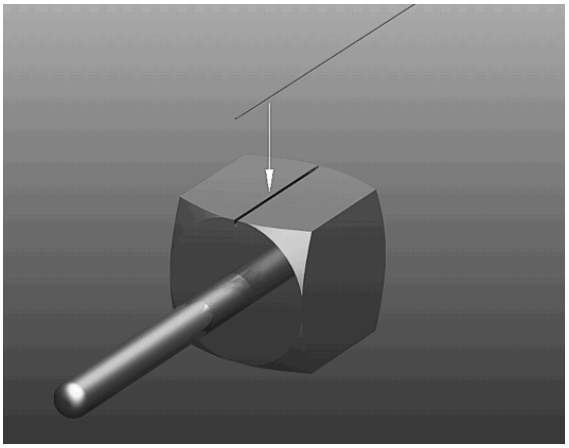

Figure 7.35: 3D view of the crimping block.

in advance and stored then in appropriate place, such that they are easily available for rapid assembly.

The plastic end-plugs also house the necessary HV contacts for the wires, stripes and cathodes.

7.4.4.4 Layer, Super Layer and chamber geometry

The geometry of one layer is very simple, it is just a series of the drift cells confined between two aluminum plates. There are several possibilities to assemble a single layer, but normally it contain 50 to 60 drift cells. 3D computer simulates image of the single plane(layer) on can see in Fig. 7.36. We

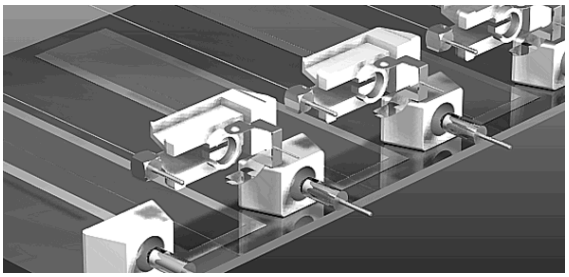

Figure 7.36: 3D computer simulated view of the drift layer.

propose to made a drift tube chamber of two Super Layers (SL) to form the rigid self-supporting object with 8 drift layers in total ($4x \times 4y$, or $4\varphi \times 4\theta$ depend of the spectrometer part we are going to install them) and the total sensitive area $(2.5 \times 4)\,\text{m}^2$. The wires in two SLs oriented perpendicularly with respect to each other $\Theta_{SL1-SL2} = 90°$. To reinforce the chamber rigidity one can consider the possibility to glue both SLs on an aluminum intermediate honeycomb structure, as it was done in the CMS Fig. 7.37. Each SL is made of five aluminum sheets,

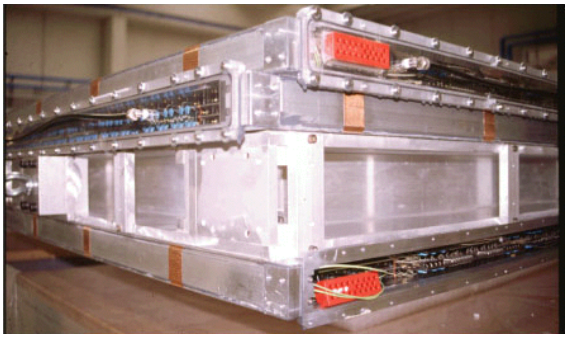

Figure 7.37: The photo of the full size prototype of the CMS DT chamber.

2 mm thick, separated by insulated, 9.6 mm high 1.2 mm aluminum thick I-beam. The cell pitch is 40 mm, while the layer pitch is 13 mm. The layers are staggered by a half pitch in the chess order to resolve left/right ambiguity and to improve the geometrical acceptance. The HV connectors to the cell and front-end electronics are located at opposite ends of the wire.

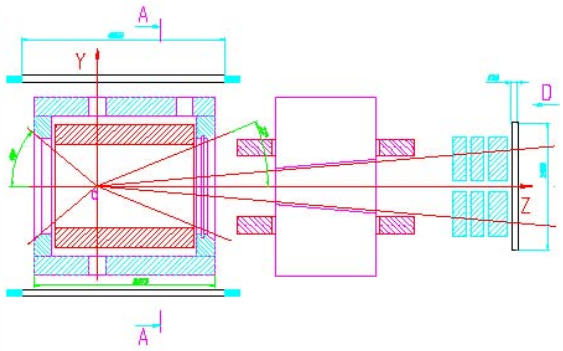

Figure 7.38: Schematic side view of the $\overline{\text{P}}$ANDA muon spectrometer.

We suppose that in $\overline{\text{P}}$ANDA we do not need to have three Super Layers joint in the single chamber, as it is done in the CMS Fig. 7.37, two would be enough.

7.4.4.5 Detector geometry

We propose to use the SMC like muon detectors in both spectrometers of the $\overline{\text{P}}$ANDA apparatus, i.e. in the Target Spectrometer and in the Forward Spectrometer. The side view of the panda one can see in Fig. 7.38. The active area size of one DTs chamber allows us to cover completely the whole acceptance of the FS, as it is shown in the Fig. 7.38. To strength the tracking efficiency together with pattern recognition one can consider the possibility to use two DTs chambers (8 layers each) separated by approximately 50cm of the iron made hadron absorber. To cover the acceptance of the $\overline{\text{P}}$ANDA barrel detector one can arrange the DT chambers as it is shown in Fig. 7.39. Still to be discussed in more details how the access to the cryostat of the superconducting $\overline{\text{P}}$ANDA magnet. In any case the important axial (top/bottom) symmetry might be easily provided. The DT chambers arrangement in the way designed in Fig. 7.39 provide us a rapid access to the f/e electronics if necessary.

7.4.4.6 Readout electronics

The read/out electronics scheme in $\overline{\text{P}}$ANDA in not yet completely fixed, it depends very much on the DAQ scheme, at least what concerns the digital part of electronics. For the analog part (amplifier/discriminator) we have very well studied solution based on the MAD4 preamplifier chip, designed especially for the CMS muon chambers [30]. Apart of that the same MAD4 chip was used to read out several detectors of the Compass spectrometer and Torino group has an adequate experience to be able to adopt the earlier designed inside the group solutions [31, 26] for the readout of the $\overline{\text{P}}$ANDA muon detectors.

7.4.4.7 Detector performance

The detailed report about the performance of the CMS muon DT chambers on can find in ref. [32]. The final muon chamber was tested at the CERN Gamma Irradiation Facility (GIF). The performance of the detector was studied for several operating conditions and for gamma rates similar to the ones expected at LHC.

The muon chamber was installed inside the GIF experimental zone. In addition to a set of scintillating counters providing the trigger, three delay chambers were used to track the incident muons. The beam covered a chamber area of about $(10 \times 10)\,\text{cm}^2$, its angular spread was $\approx$2 mrad. Background was produced by ^{137}Cs γ source, which was located 4 m upstream of the chamber.

Here we would not like to discuss in details the results of the test, but we will just recall the basic features of the CMS muon chamber, i.e. the time resolution, space resolution and efficiency.

To obtain the time resolution the timing spectra from the chamber was analyzed. Before that, the relative pedestal time T_0's correction was performed during the special pulser runs. The pulser signals were produced by a pulse generator, split by a split box and injected then at the electronics front-end. The relative channel-to-channel correction was not exceed 6 ns. In Fig. 7.40 one can see the derivative of the time-jitter distribution in the leading edge region. The Gaussian fit of the derivative distribution was performed in this region. A sigma of (2.68 ± 0.05) ns is obtained. To estimate the space resolution of the chamber so called self-tracking

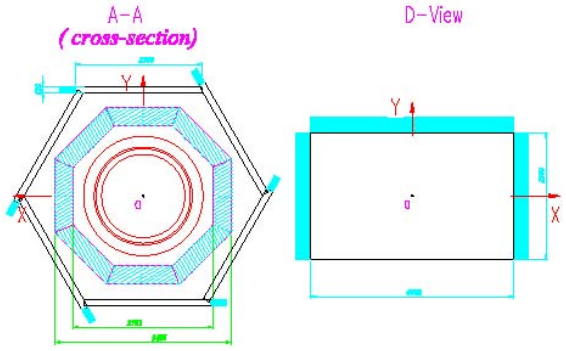

Figure 7.39: Schematic front view of the $\overline{\text{P}}$ANDA muon spectrometer.

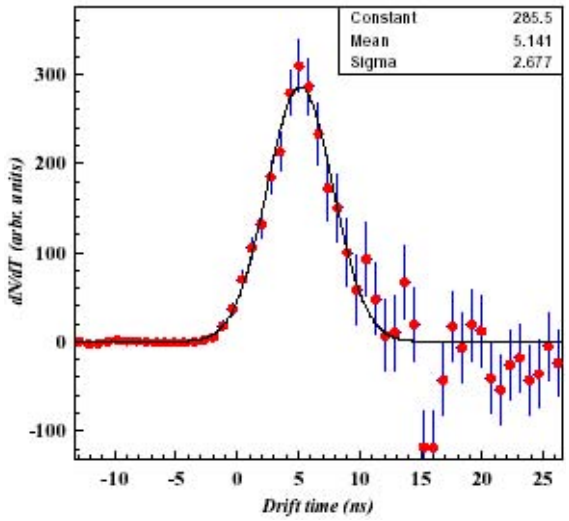

Figure 7.40: The time-jitter derivative distribution in the leading edge region. The parameters of the Gaussian fit are given.

method was used. Hits in every super-layer were fitted to a straight segment by minimizing the χ^2. All possible fits with at least three hits were studied. For the same number of hits, the fit with the best χ^2 was chosen for the further analysis. In Fig. 7.41 one can see the residual distributions for all four layers belonging to one super-layer.

To obtain these residual distributions, first, the T_0 and drift velocity calibration was performed. The drift velocity turned out to be equal to 18 ns/mm. Then the fit was performed as it was mentioned above and the $\chi^2 \leq 0.3\,\mathrm{mm}^2$ was applied. One need to note that it was not the standard χ^2 definition applied (the sum of the squared residuals divided by the resolution squared), because the resolution squared is the result of the analysis itself. Thus we call here as χ^2 only the numerator of the standard distribution. As one can see the single plane space resolution obtained is better then 200 μm, what might be considered as an excellent result. The average efficiency was found equal to (99.9±0.01)%.

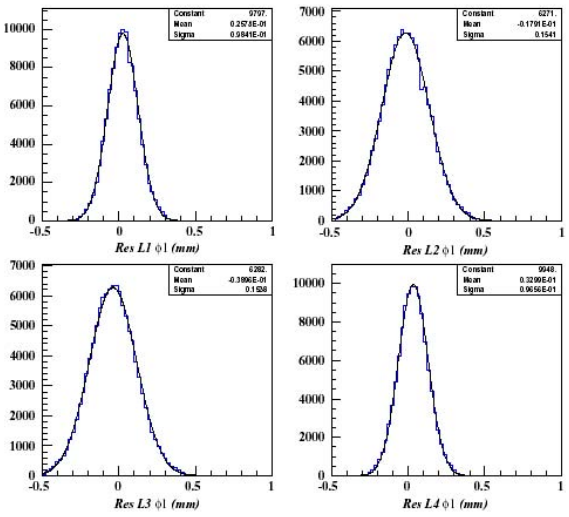

Figure 7.41: Space residual distributions layer by layer.

7.4.4.8 Timeline

The timeline for development, construction and assembly of the muon detector is shown in Table 7.42.

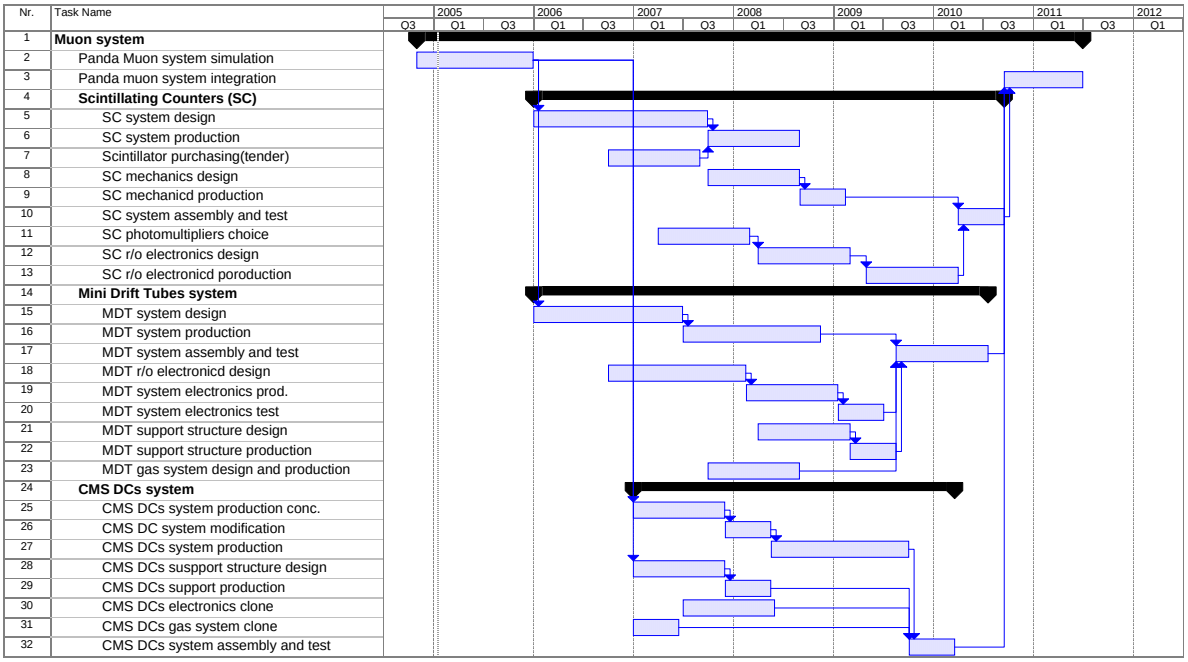

Figure 7.42: Timeline for the muon detectors

References

[1] R. Aleksan et al., Nucl. Inst. Meth. **A397**, 261 (1997).

[2] I. Adam et al., SLAC-PUB-10516.

[3] G. Vasileiadis, Nucl. Instrum. Meth. **A384**, 175 (1996).

[4] M. S. Chanowity and S. R. Scharpe, Phys. Lett. **B**, 413 (1983).

[5] B. Ratcliff, Nucl. Inst. Meth. **A502**, 211 (2003).

[6] Y. Enari et al., Nucl. Inst. Meth. **A494**, 430 (2002).

[7] J. Cohen-Tanugi et al., Nucl. Inst. Meth. **A515**, 680 (2005).

[8] http://www.schott.com/ lithotec/.

[9] http://www.quartz.saint-gobain.com/.

[10] R. Wilson, Nucl. Inst. Meth. **A433**, 487 (1999).

[11] http://www.burle.com/.

[12] V. V. Anashin et al., Nucl. Inst. Meth. **A357**, 103 (1995).

[13] A. Schüttauf, Nucl. Inst. Meth. **A533**, 65 (2004).

[14] http://www.hvsys.dubna.ru/.

[15] N. Akopov et al., **A479**, 511 (2002).

[16] F. Piuz et al., Nucl. Inst. Meth. **A433**, 178 (1999).

[17] A. DiMauro et al., Nucl. Inst. Meth. **A433**, 190 (1999).

[18] F. Piuz et al., Nucl. Inst. Meth. **A433**, 222 (1999).

[19] B. Morosov et al., Forward Ring Image Cherenkov Detector (RICH) with achromatic and short focusing optics for PANDA setup., private comm., 2004.

[20] Matshushita Electric Works Ltd., priv. comm.

[21] Hamamatsu Photonics UK Ltd., priv. comm.

[22] V. Abramov et al., Nucl.Inst. Meth. **A419**, 660 (2004).

[23] E. Iarocci, Nucl. Inst. Meth. **217**, 30 (1983).

[24] G. Alexeev et al., Test of MDT Prototype for the D0 Forward Muon System, Technical report, Fermilab, 2001.

[25] G. Alexeev et al., Mini-Drift Tubes Ageing Test with D0 Gas System, Technical report, Fermilab, 2002.

[26] O. Denisov, A. Maggiora, and G. Alexeev, RICH Wall detector of the COMPASS spectrometer, Technical report, CERN, 2002.

[27] CMS, The muon project. Technical Design Report, Technical report, CERN, 1997, CERN/LHCC/97-32.

[28] F. Gasparini et al., Nucl. Inst. Meth. **A336**, 91 (1993).

[29] G. Barichello et al., Nucl. Inst. Meth. **A360**, 507 (1993).

[30] F. Gonella and M. Pegoraro, A prototype front-end asic for the read-out of the drift tubes of CMS barrel muon chambers, Technical report, CERN, 1998.

[31] A. Maggiora et al., Fast front-end electronics for Compass MWPCs.

[32] C. Albajar et al., Nucl. Inst. Meth. **A525**, 465 (2004).

8 Calorimeters

8.1 System Overview

8.1.1 Physics Objectives

The envisaged physics program relies heavily on the capability to measure photons with high energy, position and timing resolution over a wide dynamic range starting at a few tens of MeV up to several GeV energy. The reconstruction of the electromagnetic shower has to deliver the energy as well as the point of impact of the photon with high precision in a completely closed geometry. In particular the identification of single photons as well as the coincident detection of the decay photons from multimeson exit channels relies on a high and homogeneous efficiency. The invariant mass reconstruction requires in addition the precise determination of the opening angle between the decay photons, which can be achieved only by a highly granular calorimeter. Choosing a compact scintillator material with a short Molière radius, such as lead tungstate $PbWO_4$ or bismuth germanate $Bi_4Ge_3O_{12}$, provides in addition a minimum occupancy of the detector modules. This is true even in case of high charged and neutral particle multiplicities considering heavy targets up to the highest beam luminosities.

8.1.2 Design Considerations

The expected high count rate, a geometrically compact design and severe constraints on good energy and position resolution for the detection of high energy photons require a homogeneous electromagnetic calorimeter based on inorganic scintillator crystals. To minimize the low energy threshold as well as the overall size, the calorimeter has to be placed inside the coil of the superconducting solenoid. That implies the readout of the scintillation light in a strong magnetic field $< 2\,\mathrm{T}$ and thus excludes the use of standard photomultiplier tubes.

Based on the physics objectives and the geometrical layout aiming for a compact target spectrometer a fast scintillator material with short radiation length and Moliére radius becomes mandatory.

The material of first choice is lead tungstate, $PbWO_4$ (PWO), a very compact and radiation hard material. About ten years ago PWO has been reinvented primarily for high energy applications and was chosen consequently by the CMS [1] and ALICE [2] collaborations at CERN. The manufacturing process has been optimized for large scale production. Timing on the level of $\approx 1\,\mathrm{ns}$ can be achieved using an appropriate readout with Avalanche Photo Diodes (APDs). Due to expected annihilation rates of up to a few times $10^7/\mathrm{s}$, the possibility for fast timing matches well with the requirement of a high count rate. Therefore, besides the reconstruction of the electromagnetic shower it can deliver input for fast trigger decisions, timing correlations between different detector components and a very sensitive capability of background reduction.

Since the $\overline{\mathrm{P}}$ANDA detector aims for the detection of photons well below 20 MeV energy, the present quality of the luminescence yield has to be improved by at least a factor of five, which can partly be achieved by operation at low temperatures $< -20°\mathrm{C}$. The required improvement factor has been extrapolated from response functions measured in the past for large size crystals of similar dimensions but readout with photomultiplier tubes at temperatures only slightly below room temperature [3]. It has been confirmed that, even at medium energies, photon, electron, and hadron detection can be achieved with good energy and excellent time resolution relying on photomultiplier readout [4],[5]. As a limiting factor, the readout of the scintillation light via one or two large size APDs will never cover the end face of the crystal completely. However, part of the missing sensitivity due to the limited active area can be compensated by the higher quantum efficiency of the sensor.

Bismuth germanate, $Bi_4Ge_3O_{12}$ (BGO), with a light yield larger by a factor of > 10, represents an alternative and backup solution. The electromagnetic section of the former L3 detector at CERN used for the first time pure and doped crystals of $22\,X_0$ overall length [6] assembling a large fully closed calorimeter. Nowadays BGO is primarily used for technical and medical applications, since it delivers sufficient scintillation light even for low energy radioactive sources. However, there are also disadvantages. Timing and count-rate capabilities can never reach the level of PWO due to its rise- and decay-times. These are longer at least by an order of magnitude compared to PWO. It remains unclear if this has any implication on the operation in $\overline{\mathrm{P}}$ANDA. It is one of the R&D projects for BGO. Moreover, R&D will become necessary to verify homogeneity, radiation hardness and the technology

for mass production of large size crystals. Also the question of a reliable supply remains open, as currently there is only one supplier offering reasonable priced crystals.

Long term operation of the detector in an environment of a high integral dose due to electromagnetic probes as well as charged and neutral hadrons will have to cope with possible radiation damage of the scintillator material and of the photo sensor, i.e. the APD. The present considerations are guided by the large experience and technological development within the CMS collaboration. However, in case of $\overline{\text{P}}$ANDA significantly lower dose rates and integral doses can be expected in spite of the much lower energy regime and interaction rates. A final estimate based on realistic simulation can not be presented now.

8.2 Requirements

8.2.1 Geometrical Coverage and Dynamical Energy Range

As outlined in the previous section the geometrical coverage of the calorimeter section has to be as close as possible to 4π. This is to provide a significant efficiency for multi-photon exit channels and a sufficient reduction of the background due to missing photons from meson decays to make the identification of single photons possible. The central area will be covered by the target spectrometer consisting of a scintillator barrel closed by two annular end caps. In backward direction an opening will be left for the incoming beam. A larger window at forward angles will be covered by the forward calorimeter located behind the dipole magnet (see Sec. 8.11).

From the simulations of selected key reaction channels, which are discussed in detail in Chap. 12, the acceptance range in energy can be deduced. The upper limit of approximately 10 GeV photon energy is set by the projectile energy range. The envisaged lower limit of a few tens of MeV has to be made reachable by the detector quality. However, the final energy cut will depend on the integral absorption of the material sandwich placed in front of the calorimeter, caused by detector material, support structures and additional layers for cooling and thermal shielding.

Details on the tolerable amount on dead material are not yet knwon and will strongly depend on the final construction of all detector components. Conversion directly in front of the active calorimeter volume will have the least impact.

8.2.2 Energy, Position and Time Resolution

The energy resolution of the electromagnetic calorimeter is determined by the statistics of photo electrons collected in the photosensor and the statistical fluctuations of the leakage or containment of the electromagnetic shower within the detector. Therefore, the detector material has to provide sufficient luminescence yield per deposited energy unit. The containment of the shower energy has to be guaranteed by sufficient depth, which ranges between 18 and 20 X_0 for the maximum energies, and a minimized dead space and material in between adjacent elements. The individual crystal element has to allow minimum energy thresholds in the order of 0.1-1 % of the typical photon energy. Beside the contribution of statistics and electronics noise to the overall resolution, given as

$$\frac{\sigma_E}{E} = \frac{a}{\sqrt{E}} \oplus \frac{b}{E} \oplus c \quad , \tag{8.1}$$

the constant term c reflects the accuracy of intercalibration but also time-instabilities and inhomogeneities. In particular, the strong temperature dependence of the scintillation process and the response of the APD photosensor cause a great technological challenge.

The achievable energy resolution will depend on the size of the active volume, which is composed of the direct or even next neighbours of the directly hit calorimeter component. The acceptable cluster size will depend on the multiplicity of reaction products and the occupancy of the modules. However, the geometrical arrangement should foresee that the electromagnetic probes are always impinging aligned to the crystal axis. In addition, the experimental cluster size can be used to discriminate electromagnetic showers and the narrow track of charged particles as long as they do not initiate an electromagnetic shower.

The position resolution is primarily determined by the granularity and the dimension of the crystal diameter with respect to the Moliére radius R_M. The proposed diameter close to R_M will allow a position resolution better than 10 % of the crystal diameter, which will be < 2 mm.

The compact design of the target calorimeter can not provide sufficient resolution for particle/photon discrimination via time-of-flight. However, the envisaged and in case of PWO achievable time resolution of ≈ 1 ns for relevant photon energies can have significant advantages, which have not been considered in the basic Monte Carlo simulations.

Presently operating calorimeters such as the Crystal Barrel composed of CsI(Tl) [7] and the NaI(Tl) Crystal Ball [8] rely heavily on fast triggering additional detector components due to their slow read-out and slow scintillation response. Besides a fast trigger input, the reachable time resolution provides strong selectivity to correlate additional detectors or reduce background. The consequences on the read-out circuits have not been investigated yet.

8.2.3 Count-Rate and Occupancy Limits

The count-rate limit is primarily determined by the luminescence properties of the chosen scintillator. In that respect $PbWO_4$ represents the optimum material due to its extremely short decay kinetics, which is dominated by the prominent component of $\tau = 6.5\,\text{ns}$ (97 %). Even an operation foreseen at lower temperatures will guarantee the complete light collection within a gate width of $< 100\,\text{ns}$. Therefore, even an event rate of 10^7 annihilations per second will not lead to pile-up effects in the scintillator. The read-out via APDs or vacuum triodes, both in combination with charge sensitive preamplifiers and subsequent shaping, might reduce the count rate capabilities. A sufficiently long shaping time might become necessary to optimize the signal-to-noise ratio in particular for low energy signals. Experimental results are presently not yet available.

The foreseen segmentation of the target calorimeter in elements with a diameter comparable to the Moliére radius will not impose a limit on the acceptable occupancy for antiproton induced reactions on hydrogen or helium. The expected values for heavy targets have to be still simulated.

8.2.4 Radiation Hardness

The long year development for the electromagnetic calorimeter ECAL of CMS provides detailed experimental data for the radiation hardness with respect to high radiation dose rates as well as a high integral dose extrapolated for a typical 10 year operation. A rough estimate based on the expected luminosity of the HESR delivers a significantly lower radiation yield, but detailed calculations are not net present due to the large complexity and several unknown facts.

The investigation of the sensitivity of $PbWO_4$ to the damage due to electromagnetic and hadronic probes shows, that the degradation is primarily caused by a reduction of the optical transmission of the crystal due to color center formation. No permanent damage due to structure defects have been identified. The moderate recovery time leads to a saturation of the transmission loss to a level of typically 95 to 97 % for the radiation dose of LHC operation. Since the HESR luminosity is lower by orders of magnitude, only a long term deterioration of the crystal performance has to be taken into account, which can be monitored during off-line data analysis. CMS studies of the radiation damage due to neutrons or protons have shown very contrary results, probably due to crystal samples of not identical quality. Performed first irradiation measurements impinging with 90 MeV protons, see Sec. 8.3.1.6 for details, confirm sufficient radiation hardness.

The development of radiation hard APDs has been a major task for CMS, which has been successfully performed in case of small size APDs of $(5 \times 5)\,\text{mm}^2$ active area. In particular the manufacturing process of the surface structures was essential to stabilize the functionality. Based on that experience further R&D are necessary to establish similar quality for large size sensors, which are mandatory for $\overline{\text{P}}$ANDA. The tuning process for CMS requires a pre-irradiation of the sensors to sort out weak components and to guarantee the long term operation. As a negative consequence, a significant increase of the dark current has to be accepted, which might cause limitations for the measurement of photons in the MeV range due to a large noise level. The expected significantly lower dose rates for $\overline{\text{P}}$ANDA will hopefully make such treatments obsolete. Nevertheless, detailed studies of the damage due to highly ionizing low energy protons, generated for example via (n,p)-reactions in the crystal, have to be performed and have been started already (see Sec. 8.4.1). Additional complication might arise when operation at lower temperature might block or delay annealing processes in the silicon.

8.3 Scintillator Crystals

8.3.1 Lead Tungstate (PWO)

8.3.1.1 General Considerations

Lead tungstate, $PbWO_4$ (PWO) scintillation crystals meet in general the requirements to be an extremely fast, compact, and radiation hard scintillator. However, a significant improvement of the light output is mandatory for the application in $\overline{\text{P}}$ANDA as has been explained already in Sec. 8.1.2. Some of the relevant parameters of PWO are given in Table 8.1.

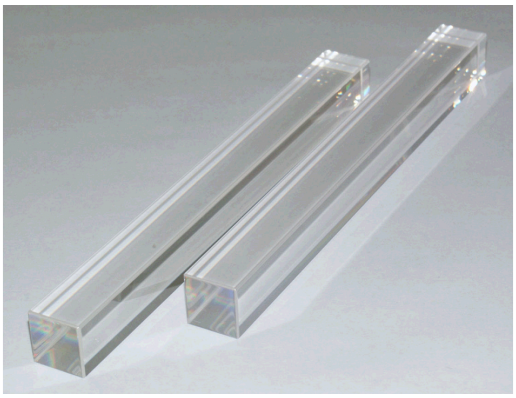

Figure 8.1: Lead tungstate crystals for $\overline{\text{P}}$ANDA/EMC prototyping. The size of the elements amounts to $20 \times 20 \times 200\,\text{mm}^3$.

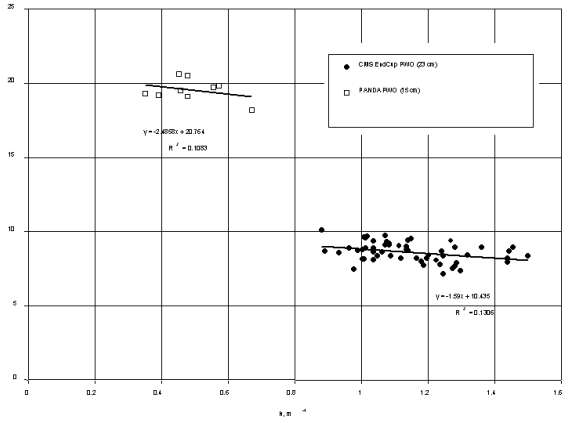

Figure 8.2: Light yield of optically polished PWO crystals with dimensions $28 \times 28 \times 230\,\text{mm}^3$ used for the CMS end cap construction (points on the right) compared to PWO-II prototypes with dimensions of $20 \times 20 \times 150\,\text{mm}^3$ produced for $\overline{\text{P}}$ANDA (left).

Parameter	PWO	
ρ	8.28	g/cm^3
MP	1123	°C
X_0	0.89	cm
R_M	2.0	cm
dE/dx	13.0	MeV/cm
λ_I	18	cm
τ_{decay}	6	ns
λ_{max}	420	nm
n	2.2	at λ_{max}
Relative output	1.2	% (LY NaI)
Property	not hygroscopic	
d(LY)/dT	-1.9	%/°C

Table 8.1: The relevant properties of $PbWO_4$ (PWO).

The specifications, which were developed and obtained aiming for the application in experiments at LHC at CERN [9] are stated as reference for the envisaged and achieved optimisation of lead tungstate crystals. Radiation hardness, fast scintillation kinetics, and large-scale production had been the most crucial parameters. Initiated by the CMS/ECAL Collaboration, the scintillator material for the electromagnetic calorimeter has reached a luminescence yield of the fast component only, of at least 20 photoelectrons (phe) per MeV deposited energy observed in small samples (several cm^3). Full size crystals of 24 cm length ($28\,X_0$) still reach a value of 9–11 phe/MeV.

In the first stage of R&D, performed in 1998–2002, it has been shown that the overall PWO light output can be improved by additional doping [10, 11, 12]. Among the investigated possibilities of appropriate ions the co-doping of the PWO crystal with molybdenum (Mo) and lanthanum (La) at concentrations < 100 ppm has provided best results. However, such crystals show in addition to the fast component also a strong slow scintillation component ($\tau_g = 1 - 4\,\mu$s). This is limiting their application at high counting rates. Two additional R&D concepts could lead to a further improvement:

1. increasing of the structural perfection of the crystal, and
2. activation of the crystal with luminescent impurity centres. These have a large cross section to capture electrons from the conduction band, combined with a sufficiently short delay of radiative recombination.

Beside crystal activation with impurity centres, authors of Ref. [13] investigated the possibility to redistribute the electronic density of states near the bottom of the conduction band by the change of ligands contained in the crystal. However, similar to Mo doped crystals slow components in the scintillation kinetics appear at room temperature.

One obvious possibility to reduce the concentration of point structure defects, is doping the with yttrium (Y), lanthanum (La), or lutetium (Lu) ions, which can suppress oxygen and cation vacancies in the crystal matrix. An activator concentration at a level of 100 ppm is needed. This concept has been followed up successfully by the CMS collaboration, and led to mass production technologies of radiation hard crystals at the Bogoroditsk Technical Chemical Plant [9].

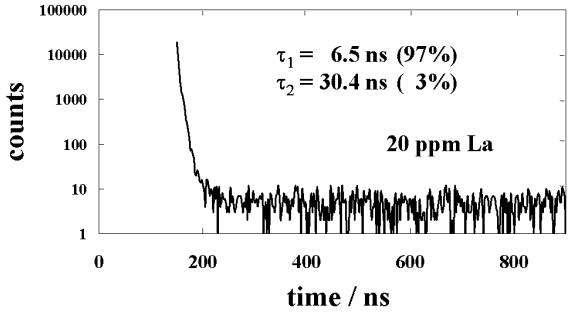

Figure 8.3: Scintillation kinetics of a crystal grown from corrected melt with a La/Y-concentration of 20 ppm measured at a temperature of $T = 300$ K.

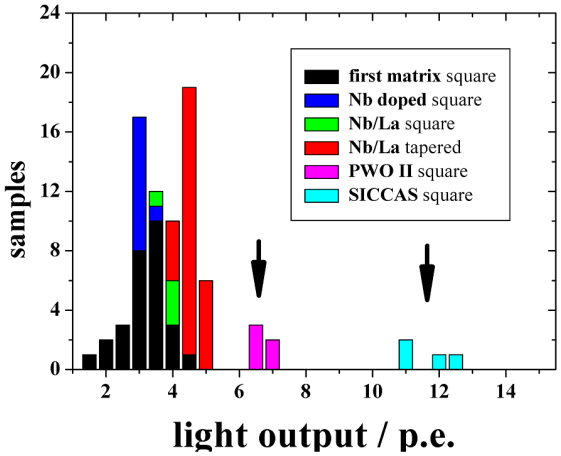

Figure 8.4: Mean number of photoelectrons detected for γ-rays of a ^{60}Co source using a high-resolution hybrid photomultiplier. Compared are different PWO samples of 15 cm length and identical cross section of $2 \times 2\,\mathrm{cm}^2$.

A further increase of the scintillation yield by 30–50 % can be achieved by a reduction of the La-concentration to $\sim$ 40 ppm or less, which is then not sufficient for a complete compensation of vacancies. Combined with a structural perfection of the crystal remaining point defects can be suppressed. That has been realized by combining an improved control of the stoichiometric composition of the melt, from which the crystal is grown, and by activating it with impurities of the mentioned elements at concentrations $<$ 40 ppm. Then both systematic and statistical origins of vacancies in the crystal will remain at a significantly lower level.

8.3.1.2 Properties of PWO

The Bogoroditsk Technical Chemical Plant (BTCP) carries out the mass production of 25 X_0 length crystals for the CMS/ECAL exploiting the Czochralski method. Currently, more than one thousand of certified scintillation elements are produced per month. Smaller quantities are produced by North Crystal (Russia) for the PHOS detector of ALICE at CERN. The Shanghai Institute of Ceramics and the Beijing Glass Research Institute are using a modified Bridgeman method [14]. The Furukava Company (Japan) [15], the Institute of Single Crystals in Kharkov (Ukraine) [16], and several smaller research groups [17] are additional manufacturers. Lead tungstate in crystalline form nowadays is a mass produced material, and is easily available on the market.

At BTCP in Russia lead tungstate crystals are produced with high yield by the Czochralski method, using standard "Crystal 3M" or "Lazurit" equipment. Crystals are grown from raw material high purity of close to 6N specification. However, additional pre-crystallization is required. Ingots of 250 mm length with a cross section close to an ellipse of a large axis ranging from 36 to 84 mm are available. Crystals up to 100 mm diameter may also be produced using different industrial ovens for crystal growth [18]. Crystals can be pulled with nearly the same quality in directions close to the a- or c-axis of the crystal. Nevertheless, the direction along a-axis seems to be superior to produce long scintillating crystals of high quality. The pulling process is carried out in an isolated nitrogen-filled chamber. Pulling rate and rotation speed for the crystal growth can be varied over a wide range depending on the required ingot diameter. Crystal ingots are annealed in air in industrial temperature gradient-free ovens to minimize the radial and axial stresses before mechanical treatment. $\overline{\mathrm{P}}$ANDA prototype scintillation elements with dimensions $20 \times 20 \times 200\,\mathrm{mm}^3$ are shown in Fig. 8.1.

PWO as crystalline material is transparent in the visible spectrum, colourless, and bi-refringent. The density of the synthetic crystal can vary by a few per cent depending on the technological conditions. The refractive index and many other properties are well known [19, 20].

Lead tungstate crystals occur in nature as tetragonal stolzite [21], scheelite type and monoclinic raspite [22]. The synthetic lead tungstate crystal has been determined by X-ray diffraction as a scheelite-type crystal of tetragonal symmetry with a space group of $I4_1/a$ and unit-cell parameters $a = b = 5.456(2)$, $c = 12.020(2)$ Å. Systematic deficiency of the lead in the crystal introduces additional peculiarity to the crystal structure. A super-

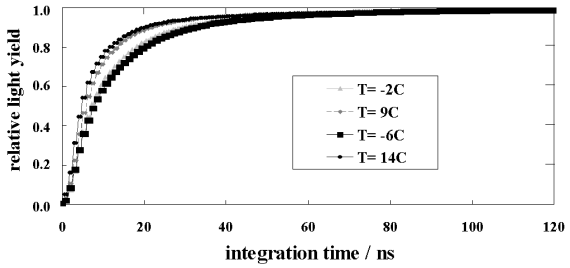

Figure 8.5: Yield of the scintillation light as a function of the integration time measured at various temperatures for a PWO-II sample.

structure created by cation vacancies is identified by combined X-ray and neutron diffraction measurements [23]. In fact, the ordering of the vacancies is compensated by a distortion of the tungstate anionic polyhedron. The electronic structure of conduction and valence bands of pure and defective lead tungstate crystals is described in detail in Ref. [24].

8.3.1.3 Scintillation Mechanisms in PWO

The luminescence appears in PWO crystals because of charge-transfer transitions in anionic tungstate molecular complexes. Both regular WO_4^{2-} and irregular WO_3 tungstate groups serve as luminescence centres. Because the WO_4^{2-} complex has a T_d point crystalline field symmetry, final configurations of the energy terms is found to be $^3T_1$,$^3T_2$ and $^1T_1$, $^1T_2$ with the $^1A_1$ ground state. The spin and parity forbidden radiative transition $^1T_1$, $^1T_2 \rightarrow {}^1A_1$ is the origin of the intrinsic blue luminescence. When an anion vacancy appears in a WO_4^{2-} anionic complex, the local symmetry of the new WO_3 complex is reduced to C_{3v}. An additional low-symmetry component of the crystalline field splits triplet terms in (A+E) components, giving some shift of the excited energy terms. A transition similar to the previous one causes a green luminescence in an irregular WO_3 centre in the crystal.

One can also attribute to the characteristic luminescence centres a molybdenum (Mo) based one. It is related to a MoO_4^{2-} anion complex impurity, which turns out to be a stable electron trap. Since a Mo-ion is chemically very close to a tungsten ion, it is rather hard to separate Mo in the raw material. Thus it is usually present in all crystals at the level of < 1 ppm. The properties of a (MoO_4^{3-}) centre and its influence on PWO scintillation parameters are described in Refs. [25, 26, 27, 28]. All the luminescence centres mentioned above contribute to the scintillation mechanism. Note however that, at room temperature, the blue luminescence dominates, which is related to the regular anionic complex.

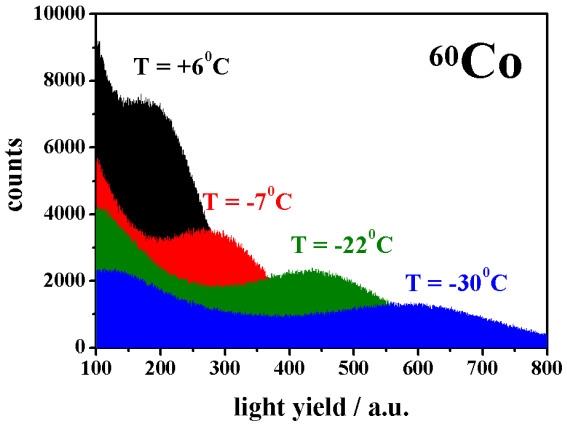

Figure 8.6: Light yield of a PWO-II crystal at several operating temperatures measured using the γ-line from a ^{60}Co source.

PWO is very sensitive to the conditions of the growing process. Applying the Czochralski method from stoichiometric raw material, a dominant leakage of lead from the melt takes place, leading to the creation of cation vacancies V_c on the lead site in the host. This effect is confirmed also for the crystals obtained by the modified Bridgeman method [29]. After X-ray irradiation and subsequent filling of traps only three characteristic electron centres can be observed in lead tungstate by the method of Electron Paramagnetic Resonance (EPR). It is not only much more sensitive, but by far more conclusive than optical absorption, which is mainly used to detect radiation induced defects in scintillator materials.

The shallowest of them occurs in all crystals since it is an intrinsic defect: An additional electron autolocalized at an anionic WO_4^{2-} complex via a Jahn-Teller distortion creates a WO_4^{3-} polaronic centre [30, 31, 32]. This trap releases trapped charges near a temperature of 50 K with an activation energy of 50 meV. The released electrons recombine partly via radiative processes or are partly caught by deeper traps.

The second one is a Pb^{1+}-V_0 centre, which is stable in the crystal up to 175 K [33, 34]. It is not excluded that instead of a Pb ion another ion may create such a centre near an anion vacancy. But in any case as a consequence the electron is trapped by a heterovalent cation in the vicinity of an oxygen vacancy. This has been clearly confirmed by a

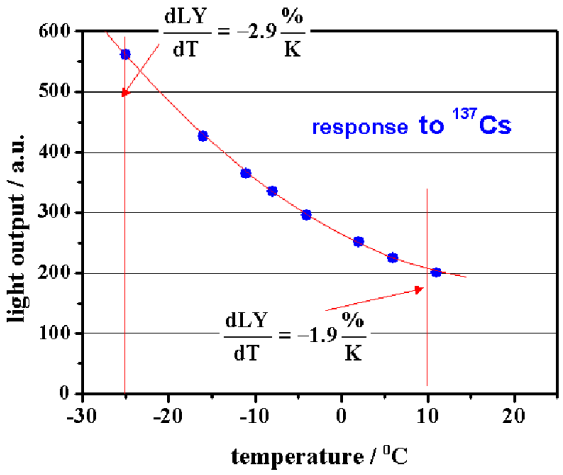

Figure 8.7: Shift of the photopeak position E_γ = 662 keV of a ^{137}Cs source as a function of temperature measured with a PWO-II crystal. The temperature gradient of the light yield is indicated in the figure.

relatively large deviation of the g factor, for all such magnetically non-equivalent species, from g_e. This centre is photo-ionised by infrared light (IR) with a threshold of 0.9 eV.

The third one is a WO_4^{3-} electron centre, which is created on a base of a regular tungstate anionic complex disturbed by a nearby rare earth (RE) trivalent impurity ion like La, Lu or Y [31]. It decays near 97 K and has an activation energy of $\sim$ 200 mev. Careful partial annealing experiments showed that the rate of decrease of the EPR intensity of WO_4^{3-}-La coincides with the thermostimulated luminescence (TSL) emission in this temperature region [33]. In addition, the doping of the crystal with stable trivalent rare earth ions such as La, Lu, Gd and Y with concentrations of some tens of ppm redistributes electron-trapping centres, reducing the number of deep ones [35, 36]. Such ions localized at Pb-sites introduce in the crystal an extra positive uncompensated charge and will thus compete with the creation of V_0 vacancies. In addition, the doping ions introduced in the crystal above the stoichiometric ratio occupy empty lead sites in the lattice and suppress thus the superstructure fraction with its distorted tetrahedron in the crystal. Another way to compensate for cation vacancies is the creation of the 2RE-V_c centres during the doping. However, the probability of creating such associations is rather small. This is due to a small concentration of cation vacancies and compensating centres and their statistical distribution in the melt and the resulting crystal.

Another trap centre with an activation energy of 130 meV appears in the crystal with rare earth (RE) doping. This centre is not paramagnetic and probably is a RE-$(WO_4)^{4-}$ centre. This is in agreement with the fact that RE-doped PWO crystals show a larger TSL intensity near 100 K. An electron release from 130 meV traps causes the simultaneous production of the lowest electron centres by re-trapping, as well as through the creation of RE-$(WO_4)^{3-}$ causing an increase of the TSL intensity in that region.

The deepest electron trap centre is a Frenkel type defect, which occurs in the crystal at the displacement of the oxygen ion into the interstitial position. This causes an optical absorption band at 360 nm which is converted using ionising radiation into the characteristical absorption band with a maximum near 410 nm.

8.3.1.4 Fast Scintillation Increase (PWO-II)

Based on the R&D for large-scale production at Bogoroditsk the highest light yield has been obtained in crystals doped with La and Y simultaneously and grown from the pre-synthesized stoichiometric high purity raw material. Double doping is required to compensate smoothly point structure defects along the crystal growth axis. Due to a distribution coefficient > 1 the La doping is localized in the seed part of the crystal. In contrast, yttrium with a distribution coefficient < 1 is concentrated in the bottom part. To prevent correlated implantation of the doping ions they have been introduced into the crystal at different stages of the raw material preparation and crystal growth. The EPR study has confirmed that only single RE-$(WO_4)^{3-}$ (RE=La,Y) electronic centres are formed if the doping concentration remains < 20 ppm for each ion. Samples of several cm^3 volume cut from crystals grown with La, Y total concentration of about 40 ppm show a light yield of $\sim$ 41 phe/MeV at room temperature. This result is based on a measurement done with a photomultiplier with bialkali photocathode. Full size crystals of 15 cm length, cut from the same crystal have a light yield of about still 20 phe/MeV at 18°C. Fig. 8.2 shows the light yield of 15 cm long prototype crystals for $\overline{\text{P}}$ANDA in comparison to CMS crystals prepared for the end cap. Both samples of crystals have a similar ratio of transversal to longitudinal dimension between 0.12–0.13, to exclude the influence of the geometrical factors in light collection. However, a larger volume also implies a larger amount of light scattering defects, which may reduce the total light yield. The comparison is

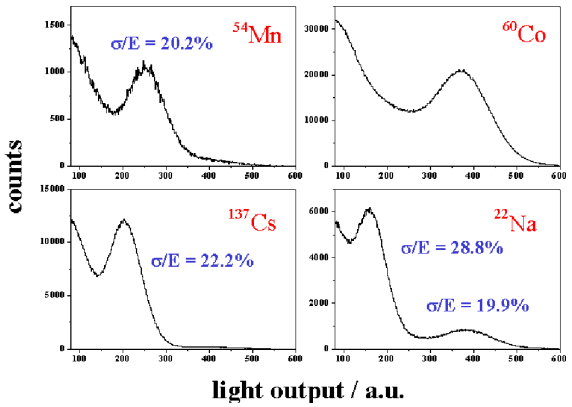

Figure 8.8: Light yield and energy resolution of a PWO-II crystal to γ-rays of different low energy sources.

not distort scintillation kinetics down to a temperature of 250 K. Decreasing further the temperature the quenching process becomes less intensive leading to slow components. Thus an optimum should be reached at about 250 K. In first tests with a sample of only $2 \times 2 \times 2\,\mathrm{cm}^3$ we obtained a light yield dependence shown in Table 8.2.

Sample temperature [K]	Light yield [phe/MeV]
318	33
296	41
278	53
258	66

Table 8.2: Change of the light yield of a small PWO-II crystal with temperature.

shown as a correlation between light yield and the optical absorption at a wavelength of 360 nm, which is sensitive to the concentration of Frenkel type defects. As a result of the improvement, the double doped PANDA crystals contain two times less Frenkel type defects and provide a scintillation light yield increased by 80 % to the previous type. We will name them PWO-II in the following. Fig. 8.3 shows the scintillation kinetics of a PWO-II sample measured at room temperature and documents the dominance of the fast decay components to 97 %. Centres on the basis of irregular WO_3 groups, which can cause components with $\tau_{sci} \approx 30$ ns, stay below 3 %.

Improvements of the luminescence are illustrated in Fig. 8.4, which shows the mean value of the light output measured for γ-rays ($E_\gamma \approx 1.2$ MeV) of a ^{60}Co source. The results given in photoelectrons are measured using a hybrid photodiode with a bialkali photocathode. Shown are different PWO samples produced at different development phases in the past and compared to PWO-II quality. All samples have an overall length of 15 cm and a 2x2 cm^2 quadratic cross section. Some samples of the same production line but marked as tapered show a slightly improved light yield due to the focusing of the tapered geometry. Recently manufactured crystals from SICCAS, Shanghai are listed in comparison. These test samples will be described below. A series 25 prototype crystals of $2 \times 2\,\mathrm{cm}^2$ crosssection and 20 cm length, which have been recently delivered, shows an average light yield of 18.5 phe/MeV.

Due to the thermal quenching of the luminescence process at room temperature, cooling of the crystals can significantly increase the light yield. The concentration of the deep traps is so low that they do

Due to suppression of irregular centres in the crystal the scintillation kinetics stays constant, even after a temperature decrease. Fig. 8.5 shows the total light yield collected within increasing time gates measured at temperatures between -6°C and +14°C. Only a slight slowing down of the scintillation kinetics within the first 50 ns becomes visible. No strong slow component appears, which could limit the applicability at high counting rates due to signal pile-up.

The improvement of the light yield as well as of the achievable energy resolution have been measured for larger crystal samples of $16 \times 16 \times 30\,\mathrm{mm}^3$. Fig. 8.6 shows the change of the response function to low energy gamma rays from a ^{60}Co source for different temperatures. The shift of the photopeak at 662 keV for γ-rays from a ^{137}Cs-source is shown in Fig. 8.7. This allows us to deduce the temperature gradient of the light yield LY, which varies from $\mathrm{d}(LY)/\mathrm{d}T = -1.9\,\%/\mathrm{K}$ down to -2.9 %/K at 10°C and -25°C respectively. Fig. 8.8 illustrates the achieved resolution using several γ-sources obtained at a temperature of -20°C. The red points in Fig. 8.31 show the energy resolution *versus* their temperature for such crystals with PMT readout. Note that the electronics was not optimised in this experiment, therefore a further improvement is expected.

8.3.1.5 High Quality Crystals from SICCAS

Based on long time collaboration with the Shanghai Institute of Ceramics (SICCAS) at Shanghai, China, during different scintillator developments, state of the art test crystals of various sizes have been received now. A full matrix comprising 25

modules of 200 mm total length with identical cross section of $20 \times 20\,\mathrm{mm}^2$ is scheduled for delivery in January 2005. It will allow a direct comparison of the PWO-II and PWO-III crystals developed in close collaboration of RINP, Minsk, Belarus [37] and the Bogoroditsk Techno Chemical Plant (BTCP), in Tula, Russia, the main manufacturer for CMS.

The crystals are grown along the *c*-axis by a modified Bridgeman method [39] in contrast to the BTCP crystals, which are grown along the *a*-axis by the Czochralski technique. As a consequence both crystal types differ in the longitudinal and transverse optical transmittance. Fig. 8.9 shows a comparison of measured transverse and longitudinal transmission. The measurements performed for a sample from both manufacturers are compared to theoretical limits assuming no internal absorption [40, 38]. The crystal from BTCP corresponds to CMS quality. The three different calculations are using the refractive index of ordinary light, which propagates along the *c*-axis and has a polarization perpendicular to the *c*-axis. Extraordinary light propagates perpendicular to the *c*-axis and has a polarization along the *c*-axis. Finally, un-polarized light is assumed to propagate perpendicular to the *c*-axis. Because of the birefringence, the theoretical limit of the extraordinary light is about 3 % higher than that of the ordinary light. Since the Chinese crystals are grown along the *c*-axis, the experimental longitudinal transmission should be compared to the theoretical limit for propagation along the *c*-axis independent of polarization. Consistent with the theoretical calculations, the samples from BTCP show a better longitudinal transmission. However, the measurement of the absolute yield of the detected scintillation light is superior for the Chinese products, which are doped exclusively with yttrium ions. Compared to CMS standards, these crystals show approximately 50 % more light.

The crystal samples, which were tested so far at room and lower temperatures, confirm the excellent photon statistics. Fig. 8.10 shows the achieved resolution for low energy γ-rays at two different temperatures for a test sample of $16 \times 16 \times 30\,\mathrm{mm}^3$ volume read out with a photomultiplier. An excellent resolution of $\frac{\sigma_E}{E} = 14.5\,\%$ has been obtained at an operating temperature of -26°C. Fig. 8.11 documents that the scintillation mechanism remains fast at low temperatures, since there is no significant improvement of the response function, when the width of integration gate is more than doubled.

First full size crystals of 200 mm length deliver a light yield of 18.0 photoelectrons per MeV deposited energy, and are comparable to the recent PWO-II crystals produced at BTCP. However, further detailed investigations concerning defects and radiation hardness have to be performed. The studies have been started in collaboration with SICCAS. They will provide small test samples from all those ingots, the crystals to be delivered are cut from. First differences in paramagnetic centers in PWO have been identified as discussed below.

Since SICCAS has signed a contract to deliver also a major part of the CMS calorimeter, we might profit from the further development of their mass-production technology.

8.3.1.6 Radiation Induced Absorption in PWO-II

Stability of scintillation material parameters in the radiation environment is often considered as non-crucial. If, however, building a precise electromagnetic calorimeter, it is one of the important properties required. PWO represents a very promising material in that respect. The scintillation mechanism is not damaged in crystals grown in optimized conditions. The damage due to irradiation affects only the optical transmission caused by colour centres with absorption bands in the visible spectral region. The induced absorption spectrum evolves with time, depending on the origin of the participating colour centres and on the mechanism of their annihilation. Double doped PWO crystals with lower concentration of Frenkel type defects show good radiation hardness to ionizing radiation. Fig. 8.14 shows the induced absorption measured at room temperature applying a low and high (saturating) absorbed dose, respectively. Two 1 cm thick PWO samples cut from the top and bottom parts of a 20 cm long crystal have been irradiated with a dose rate up to 100 krad/hour from a ^{60}Co source.

The comparison of the induced absorption spectra measured show only a slight non-uniformity of the radiation damage along the crystal growth axis indicating good suppression of the point structure defects over the whole crystal ingot.

In a first test at the KVI (Kernfysisch Versneller Instituut), Groningen (The Netherlands) a small $1.6 \times 1.6 \times 3.0\,\mathrm{cm}^3$ crystal made of PWO-II, integrated into a complete detector with a photomultiplier readout, has been irradiated with a total yield of 1×10^{12} protons (5×10^9protons/mm^2) of 90 MeV energy, which are completely stopped within the first half of the crystal length. Special installations allow a homogeneous illumination under an absolutely known integral dose. The repeated measurements of elastic proton scattering on a CH_2-

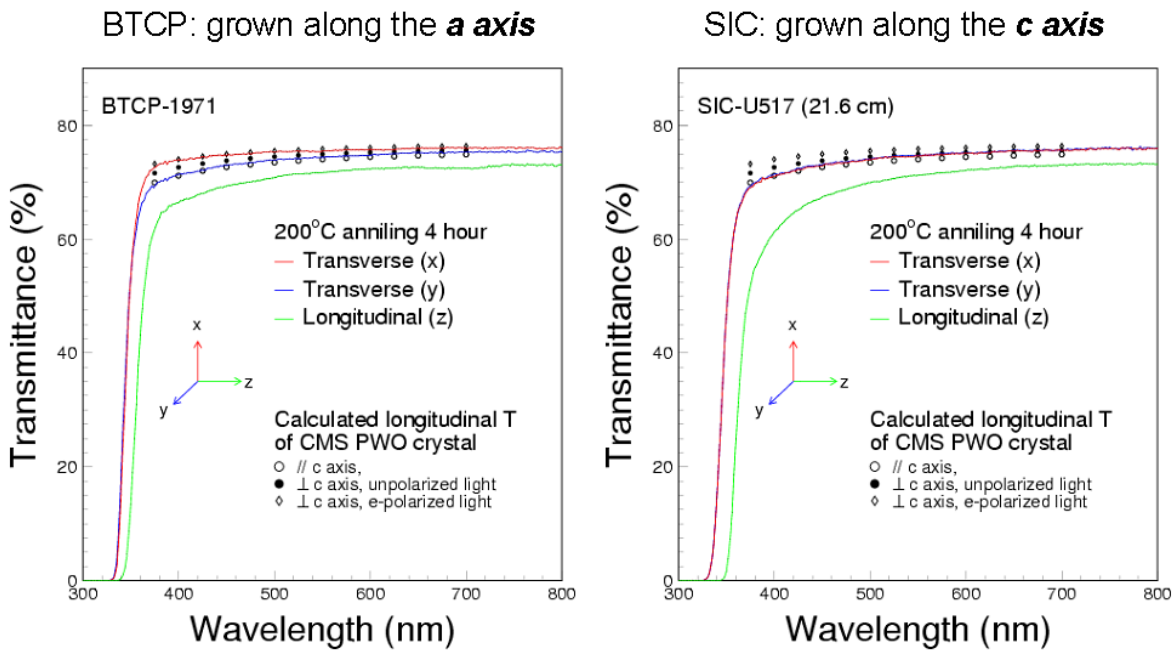

Figure 8.9: Comparison of the optical transmission of two crystal samples from the manufacturers BTCP and SICCAS, respectively. The experimental data are compared to theoretical calculations described in the text. The figures are taken from Ref. [38].

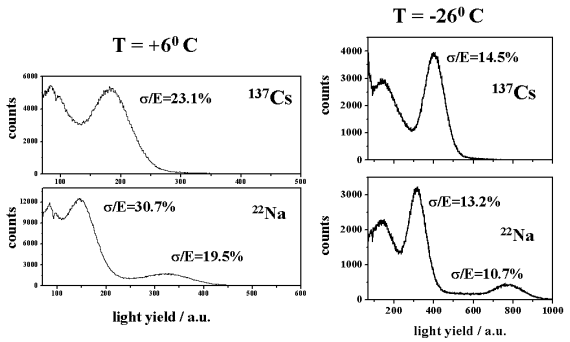

Figure 8.10: Response to low energy γ-rays for a test crystal manufactured by SICCAS. The measurements have been performed at two operating temperatures using photomultiplier readout.

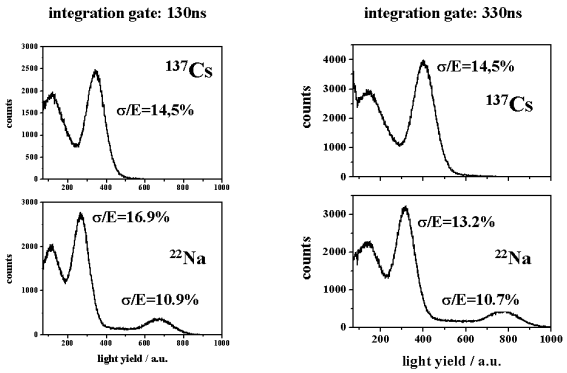

Figure 8.11: Response to low energy γ-rays for a test crystal manufactured by SICCAS. The spectra are obtained at a temperature of -26°C using two different integration gates for the photomultiplier output.

target after the irradiation indicate a reduction of the signal amplitude of $< 20\,\%$. Fig. 8.15 illustrates the optical transmission after irradiation measured perpendicular to the crystal long axis. The structures above 450 nm are caused by the spectrometer and do not reflect any absorptive center.

8.3.1.7 Fast PWO:La,Mo scintillator

As previously shown [27], Mo doping increases the light yield primarily by introducing slow components. Co-doping of the crystal with La at the level of several tens of ppm can also improve the performance. However, such a crystal shows simultaneously contributions with 200–300 ns decay time at a level of 50 % or more. We have found that the fraction of the slow component in the μs

range can be significantly decreased, if the crystal is heavily doped with Mo but with a very low La-concentration at a level of tens of ppm. A comparison of the radio-luminescence spectra of PWO:La,Mo, called PWO-III, with a typical mass produced crystal is shown in Fig. 8.16. The emission spectrum is caused by luminescence of Mo based oxyanionic complexes and has a maximum in the green wavelength range and remains fast. In Fig. 8.17 the scintillation kinetics of PWO-III is compared with that of a standard crystal. The dominant component in PWO-III has 30 ns decay time. The obtained crystal emits more than 95 % of the light within a 200 ns wide gate.

The emission spectrum of PWO:La,Mo is centered in the long wave region as seen in Fig. 8.16 and far away from the optical absorption edge as indicated in the transmission spectrum shown in Fig. 8.18. The shift is caused by heavy doping of the crystal with Mo [26]. Note that, the radiation-induced spectrum stays practically the same as measured for a typical radiation hard crystal produced for CMS. The induced absorption at a dose rate of 100 krad per hour and a total accumulated dose of 5 krad is presented in Fig. 8.19. It indicates that even in case of heavy doping with Mo a lead tungstate crystal can show high perfection of the host matrix. We will continue the investigation of PWO:La,Mo crystals to determine their potential for PANDA detector with APD readout. This readout provides an even larger enhanced quantum efficiency for a scintillator emitting green light.

Paramagnetic centers in $PbWO_4$

	at cation site	at anion site
Tetragonal centers	Mn^{2+}, Eu^{2+}, Gd^{3+} Nd^{3+}, Ce^{3+}, Er^{3+}	$(WO_4)^{3-}$ $(MoO_4)^{3-}$ $(CrO_4)^{3-}$
Low symmetry centers	Pb^{+} - V_O Pt^{+} Cu^{2+} (I) Cu^{2+} (II) (X^{+} - V_O) ?	$(WO_4)^{3-}$ -Lu^{3+} $(WO_4)^{3-}$ - Y^{3+} $(WO_4)^{3-}$ - La^{3+} WO_3^{-} F^{+}

After irradiation; metastable
Influenced by annealing processes

Figure 8.12: List of the most common paramagnetic centres in $PbWO_4$ and some of their properties.

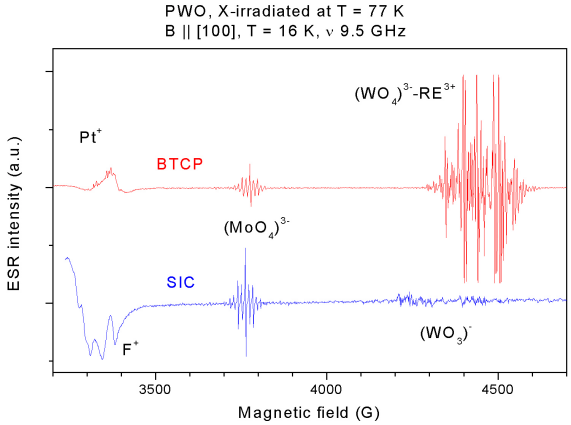

Figure 8.13: Identification of luminescence centres in crystal samples produced at Bogoroditsk Technical Chemical Plant, Russia (BTCP) and SICCAS, China by the electron spin resonance technique.

8.3.1.8 Luminescence Centres and Defects

Research and development with respect to new applications of PWO beyond CMS concentrate mainly on the increase of light yield, whereas stability against radiation damage plays a less important role. The latter, however, will be crucial for the use of PWO as scintillator material for PANDA, too. A lot of the newly developed crystals provided by different suppliers were systematically checked with help of the EPR method. Fig. 8.12 shows a table of the most prominent paramagnetic centres in $PbWO_4$, which are generated due to irradiation, remain metastable and can be influenced by different annealing processes.

Due to extensive research work of several groups — including our own — accompanying the development of PWO scintillator crystals for LHC a lot of impurities and radiation induced defects in this material as well as their dependencies on various treatments (radiation type and condition, annealing procedures *etc.*) are well characterized. Most important, with respect to scintillation, are a polaronic tungstate centre, its slightly modified variant coupled to a three-valent rare earth (RE) ion and, as a harmful concurrent, the corresponding molybdate centre. The worst effect with respect to radiation damage influencing the optical properties, have oxygen vacancies and defects coupled to them.

Within the PANDA collaboration we started our work with the investigation of PWO crystals irradiated with 90 MeV protons at the KVI in Groningen. In order not to miss short-living radiation defects the experiments were conducted in parallel, one sample being stored in liquid nitrogen immediately after irradiation and kept cold until investigation by EPR in the group of den Hartog and Vainshtein at Groningen university, the other kept at room temperature and investigated in Gießen. Both crystals showed slowly decaying radioactivity after the treatment which caused some delay for the

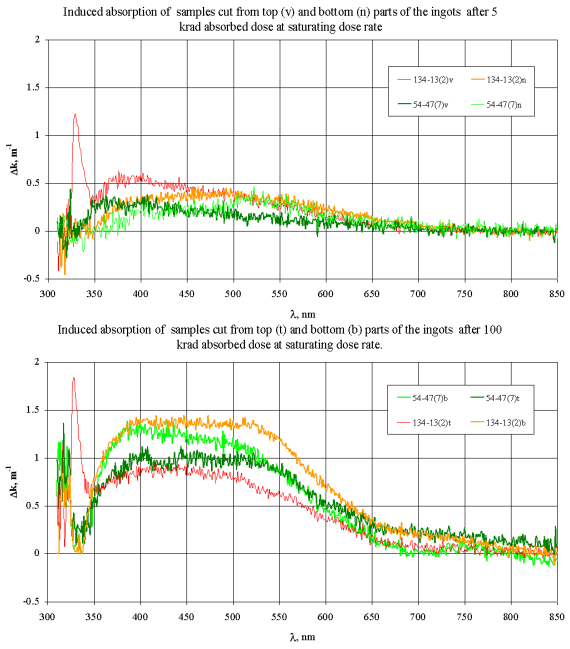

Figure 8.14: Induced absorption spectra measured at room temperature for PWO:La,Y (20,20 ppm) crystal samples cut from the top and bottom parts of a 20 cm long ingot obtained at low (top) and high (bottom) absorbed doses delivered from a ^{60}Co source.

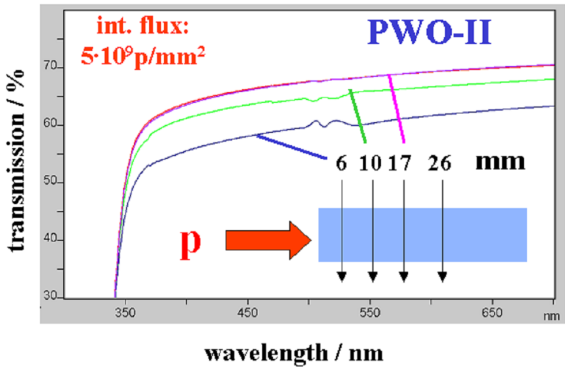

Figure 8.15: Optical transmission of a PWO-II crystal measured after irradiation with 10^{12} protons of 90 MeV energy. The transmission is measured at different positions perpendicular to the crystal long axis.

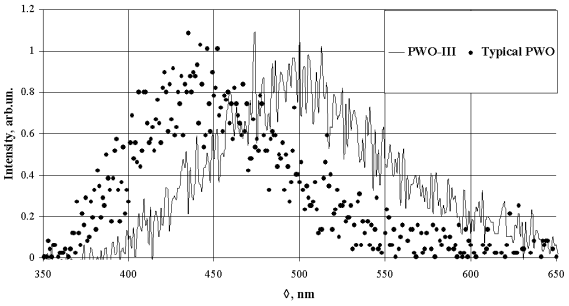

Figure 8.16: Radioluminescence emission spectra of PWO:Mo,La (PWO-III) compared to a mass produced PWO:La,Y (PWO) sample after excitation by a ^{57}Co source at room temperature.

EPR measurements, but in both cases no additional radiation induced defects could be detected. This is in agreement with measurements of optical absorption which, after this irradiation, also did not reveal an additional coloration, expressed by discrete absorption bands. Only an overall reduction of the transmission has been observed, as can be seen in Fig. 8.15.

Further experiments were done to accompany the development of crystals optimized for PANDA at BCTP and SICCAS. These two suppliers differ not only in the method of crystal growth (Czochralski at BCTP, Bridgman at SICCAS), but also follow different concepts, as to the intentional modification of PWO. BTCP tries to increase light the yield by co-doping with two rare earth ions (e.g. La and Y) since this reduces the amount of oxygen vacancies and by that increases radiation hardness and at the same time increases the radiative recombination by disturbing the tungstate complexes responsible for the scintillation. Such a co-doping always faces the problem of segregation coefficients and related to this uniform distribution of both ions over large crystal volumes. Our EPR analysis of several samples fortunately showed that this problem is under control at the growth conditions used. Radiation damage is also no severe problem for those crystals.

The PWO from SICCAS seems to behave in a slightly different way. Because of delays in delivery we could investigate only a few samples by now. They contain, as expected, at least on a level of several ppm no rare earth ions. Therefore the modified variant of the polaronic tungstate centre coupled to a three-valent rare earth ion does not show up either. Instead after irradiation two paramagnetic centres show up which are clearly related to oxygen vacancies. The identified centres are indicated in the resonance spectrum shown in Fig. 8.13. How much these centres contribute to radiation damage relevant for the use at PANDA will be further investigated as soon as new crystals from China arrive.

8.3.1.9 Quality Control and Crystal Characterization

The development of PWO crystals at Bogoroditsk has been supervised by the collaborators at

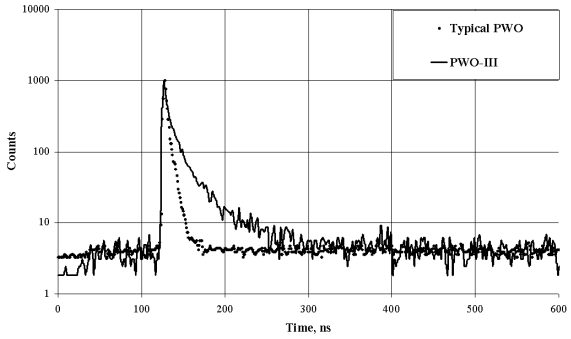

Figure 8.17: Scintillation kinetics of PWO:Mo,La (PWO-III) in comparison to a standard PWO sample measured at room temperature.

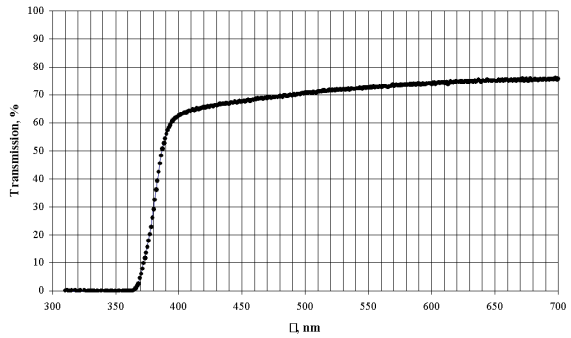

Figure 8.18: Longitudinal optical transmission of a $20 \times 20 \times 200\,\mathrm{mm}^3$ PWO-III crystal measured at room temperature.

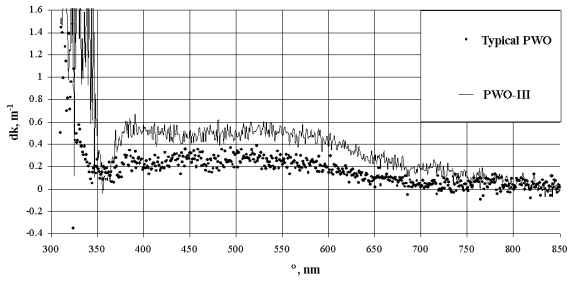

Figure 8.19: Comparison of radiation induced absorption spectra of PWO:Mo,La (PWO-III) and mass produced PWO measured under the same conditions at room temperature.

Minsk [37], who have investigated the samples and prototype crystals in a first prestudy to transmit the necessary response immediately back to the manufacturer.

To perform the R&D, to characterize full size elements for prototyping, and to prepare crystal quality control for final mass production for the $\overline{\mathrm{P}}$ANDA calorimeter some appropriate equipment has been designed, developed and manufactured already. Quality control and characterization of crystal properties consist of two parts:

- visual inspection and
- measurements of the scintillation performance.

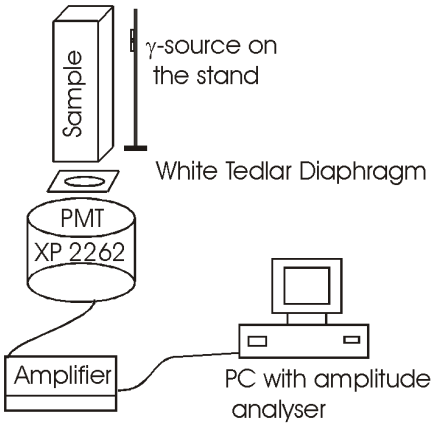

Figure 8.20: Schematic layout of a device to measure the light yield and its non-uniformity along the crystal axis.

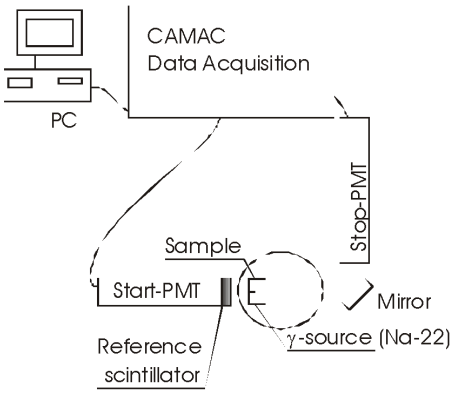

Figure 8.21: Scheme of a setup to measure the kinetics of the scintillation process.

Visual inspection includes control of macro-defects in the entire volume and local defects on the polished surfaces and chamfers. In this process possible defects are specified and passed to the production facilities. These can then be used for accounting at the internal rejection of the crystals at the production site.

The light yield is measured with customized laboratory equipment. Identical equipment is already employed at the producer facilities to make on-site

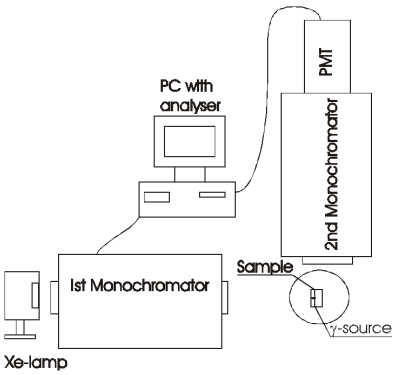

Figure 8.22: Schematic arrangement of the equipment to obtain luminescence and radio-luminescence spectra.

characterization of the crystal parameters by the measurement of the light yield of samples cut from top part of the ingot. The scheme for the device for the measurements of the light yield (LY) and the non-uniformity of the light yield (NUF LY) is shown in Fig. 8.20.

The measurements of LY and longitudinal NUF LY of full-size PWO crystals up to 23 cm length can be performed with the present equipment. The crystal sample is placed on the photo multiplier tube (PMT) with optical glue. A sheet of white TEDLAR can be placed between the sample and PMT to simulate different sizes of the active area of the photo sensor. A γ-source (^{60}Co, $E_\gamma \approx 1.2\,\mathrm{MeV}$) can be moved along the lateral side of the sample in arbitrary steps. The amplified PMT signals are digitized and stored in a PC.

The scintillation kinetics can be controlled by a customized spectrometer. The schematic layout is shown in Fig. 8.21. An identical device has been installed at the production facility for on site control. The spectrometer allows carrying on measurements in a temperature range between 250 and 350 K respectively. It is based on the start-stop method with a ^{22}Na γ-source emitting anti-collinear two coincident annihilation photons of $E_\gamma = 0.511\,\mathrm{MeV}$. Signals from the detectors are processed by a data acquisition system based on CAMAC.

Optical absorption spectra of the samples and full size crystals are controlled by a Varian Carry1E spectrophotometer operating in air at room temperature. The radiation induced absorption spectra can be measured 20 minutes after irradiation by γ-rays at the nearby located irradiation facility. Luminescence spectra after photo- and γ-quanta excitation can be obtained with the equipment shown in Fig. 8.22. The sample to be investigated is placed in the holder. Light from a Xe-lamp propagates through the first monochromator. The luminescence light is detected in a PMT after passing through the second monochromator. To measure radio luminescence, the γ-source is placed in front of the sample. The present characterization facilities allow performing complete measurements of 20 full size scintillation elements per day.

First results on the reproducibility of mass produced crystals have been obtained for a batch of 25 prototype crystals. The shape of the crystals corresponds to straight bars of $20 \times 20 \times 200\,\mathrm{mm}^3$ volume. This enables us to compare the results to investigations in the past and to exclude any focusing effects of tapered shapes. Such crystals of similar length yield 2-3 phe/MeV more but with a larger non-uniformity of the light collection along the crystal axis.

The tested crystals have been produced under identical technological conditions with the goal to investigate the reproducibility and dependence of the crystal scintillation properties on the crystallization number. Fig. 8.23 shows the change of the crystal light yield with increasing crystallization cycles indicating that the quality remains stable until the 9th or 10th crystal growth cycle. A similar behavior has been observed for barrel type crystals of the CMS calorimeter.

The reproducibility of the light yield is shown in Fig. 8.24 leading to a mean value of 16±2 phe/MeV. Since the crystals were polished manually, the quality of crystal surface might have contributed to the variations as well.

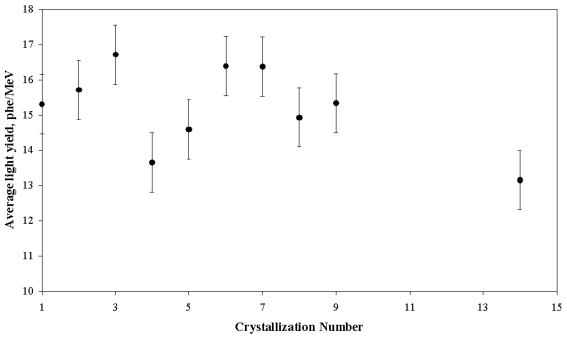

Figure 8.23: The achieved average light yield of 200 mm long PWO-II crystals is shown as a function of the crystallization number.

The typical scintillation kinetics measured for one of the 200 mm long crystals is shown in Fig. 8.25. The kinetics of a PWO crystal of CMS barrel type is given for comparison. One can state that the

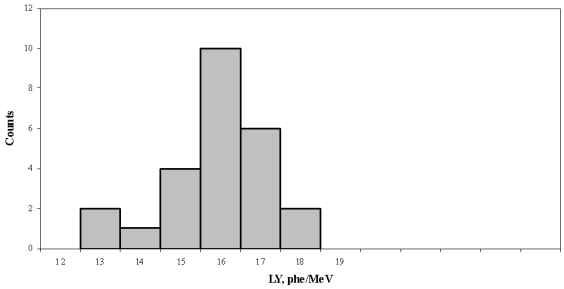

Figure 8.24: Distribution of the light yield for 25 PWO-II crystals.

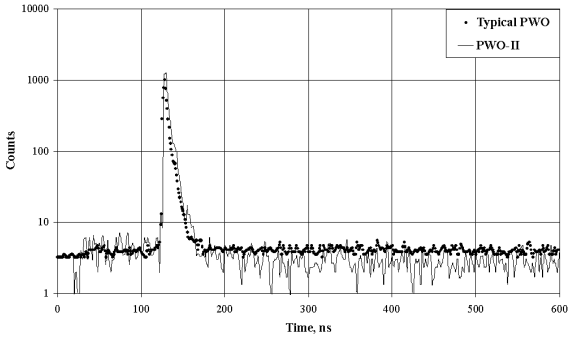

Figure 8.25: Scintillation kinetics of a PWO-II crystal compared to a crystal of CMS Barrel type measured at room temperature.

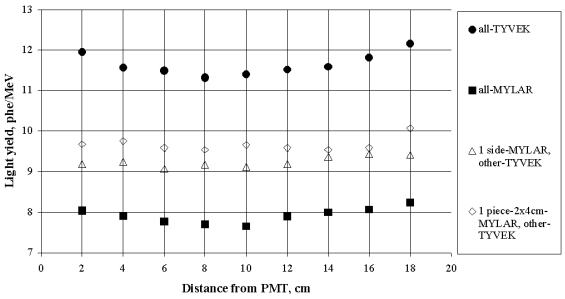

Figure 8.26: Measurement of the non-uniformity of a 200 mm long PWO crystal covered with different wrappings.

scintillation kinetics at the presently achieved level of technology does not depend on technological factors. Moreover, due to high perfection of the PWO-II crystals a lower level of background can be observed, which indicates the negligible level of afterglow in such crystals.

As a first test of the overall uniformity, the light yield of 200 mm long crystals with different wrappings was measured and is illustrated in Fig. 8.26. A 200 mm long crystal with a diaphragm from white

Wrapping	RNUF % X_0	FNUF % X_0
all-TYVEK	-0.99	0.78
all-MYLAR	-0.86	0.84
1 side-MYLAR, other-TYVEK	-0.15	0.41
1 piece-2 × 4 cm=MYLAR, other-TYVEK	-0.36	0.41

Table 8.3: Front and rear non-uniformity of the light yield for the investigated techniques of wrapping.

TEDLAR on the output side is placed onto a PMT. A γ-source (^{60}Co, $E_\gamma \approx 1.2$ MeV) has been moved across the lateral side of the crystal in 2 cm steps. Four series of measurements with different wrapping were carried out:

- 4 lateral and 1 top side were wrapped in two layers of TYVEK;
- All sides were wrapped in aluminized MYLAR;
- 1 lateral side was covered by aluminized MYLAR, all others by TYVEK;
- A piece (2×4 cm) of MYLAR was placed on the top part of the one lateral side and the remaining surface of the crystal was wrapped in TYVEK.

Front (FNUF) and rear non-uniformity (RNUF) are defined as a slope of the linear approximation of the non-uniformity curve within two regions: from 0 to 8 cm and from 8 to 20 cm — rear part, i.e. nearest to the PMT and front part respectively. For all examples the front and rear non-uniformity were fitted by linear regression and the slope coefficients are given in units of [%/X_0], normalized to the value of light yield measured at the distance $x = 8$ cm. The extracted data is listed in Table 8.3.

8.3.2 Bismuth Germanate (BGO)

Bismuth Germanate ($Bi_4Ge_3O_{12}$, BGO) is a well known scintillator material since many decades [41]. Several experiments, like L3 at CERN or GRAAL at Grenoble, have build well performing electromagnetic calorimeters using this material [42, 43, 44]. BGO is also widely used in medical applications as Positron-Electron-Tomography (PET) scanners [45].

The properties of BGO, listed in Table 8.4, allow for the design of a very compact and also fast calorimeter. The light yield is, with 9 % of the light yield of

Parameter	BGO	
ρ	7.13	g/cm^3
MP	1050	°C
X_0	1.12	cm
R_M	2.3	cm
dE/dx	9.0	MeV/cm
λ_I	21.8	cm
τ_{decay}	300	ns
λ_{max}	480	nm
n	2.15	@λ_{max}
Relative output	9	% (LY NaI)
Property	not hygroscopic	
d(LY)/dT	-1.6	% /°C

Table 8.4: Properties of BGO [46].

sodium iodide (NaI), about an order of magnitude higher than of PWO. Combined with modern readout devices, which are discussed in the next section (8.4), makes BGO an excellent detector material for spectroscopy with low energy thresholds.

8.3.2.1 Light Yield

Readout with PMT Fig. 8.27 shows the spectrum of a ^{60}Co source acquired with a small ($1 \times 1 \times 1\,\mathrm{cm}^3$) BGO crystal mounted to a Hamamatsu PMT R2059.

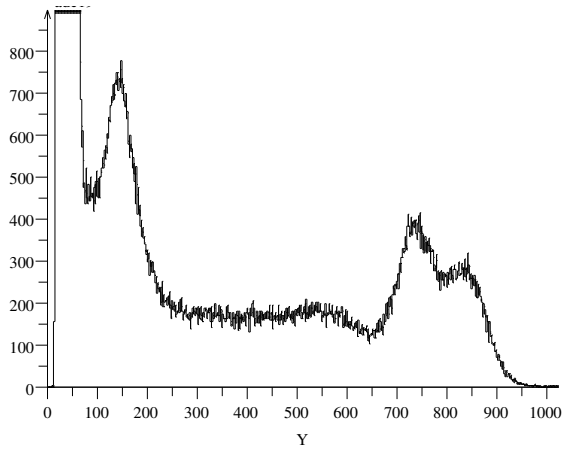

Figure 8.27: Spectrum of a ^{60}Co source, acquired with a small BGO crystal mounted to a Hamamatsu PMT R2059 (integration time 100 ns).

Readout with APD Fig. 8.28 shows the spectra of ^{60}Co, ^{22}Na and ^{137}Cs sources acquired with a small ($1 \times 1 \times 1\,\mathrm{cm}^3$) BGO crystal mounted to a Hamamatsu LAAPD (active area $10 \times 10\,\mathrm{mm}^2$).

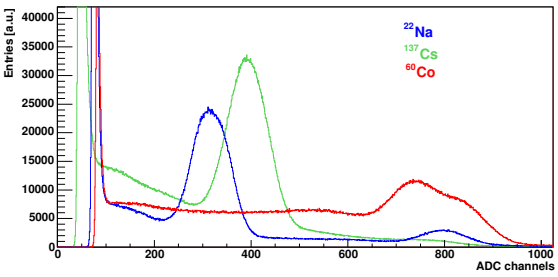

Figure 8.28: Spectra of ^{60}Co, ^{22}Na and ^{137}Cs, acquired with a small BGO crystal, read out by a LAAPD connected to a BaBar preamplifier (shaping time 250 ns).

First tests of long BGO crystals ($3 \times 3 \times 20\,\mathrm{cm}^3$) were done at the In-Beam-Polarimeter at the KVI Gronigen. One crystal was mounted to a Hamamatsu PMT R2059, another one was equipped with a CMS-type APD (active area $5 \times 5\,\mathrm{mm}^2$). The crystals were mounted to the In-Beam Polarimeter and the spectra of 90 MeV protons scattered off carbon and CH_2 targets were measured at two different angles ($\theta = 18°, 28°$) to the beam direction. A typical spectrum using APD readout is shown in Fig. 8.29. The APD was connected to a spectroscopic preamplifier (Tennelec TC106) and a shaping amplifier (Tennelec TC205A) with 500 ns shaping time.

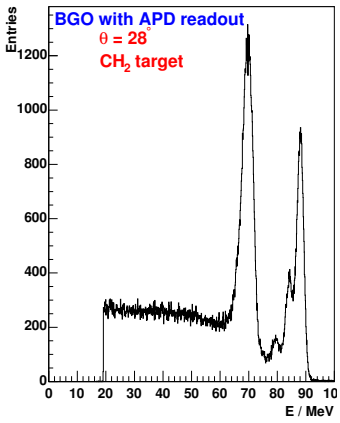

Figure 8.29: Spectrum of 90 MeV protons scattered off a CH_2 target into 28°, detected using a BGO crystal with CMS type APD readout. The left peak corresponds to scattering off the proton, the right peaks correspond to scattering off the carbon, including the first and second excited states (right to left).

Temperature Dependence The temperature dependence of the light yield was also investigated during the experiment at the In-Beam Polarimeter at the KVI Groningen. In order to do that, the BGO crystals were mounted in an aluminum block, which was cooled to the specified temperature. Fig. 8.30 shows the mean values of the proton peak and the carbon peak (ground state) at five different temperatures. From these results, the temperature dependence of the light yield was determined to be $-0.8\ \%/°\mathrm{C}$. To exclude any temperature variation effects of the APD readout at this point, only the data taken with PMT readout were used. Although the light yield of BGO changes with temperature, the energy resolution was within errors constant, at a level of $\sigma_E/E = 1\,\%$ (see blue points in Fig. 8.31).

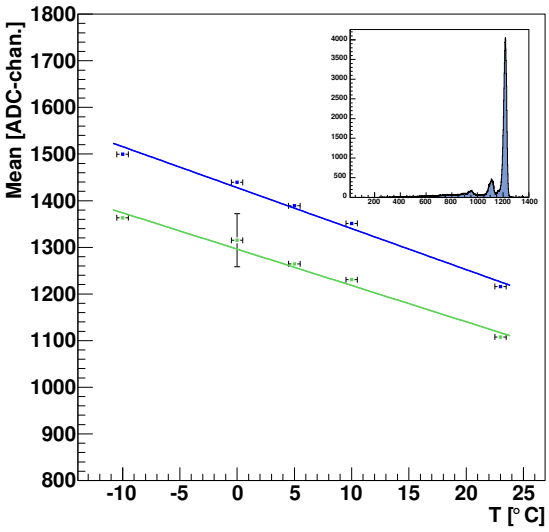

Figure 8.30: Proton (green) and carbon (blue) ground state positions *vs.* crystal temperature using PMT readout. The scattering was measured at a polar angle of $\theta = 18°$.

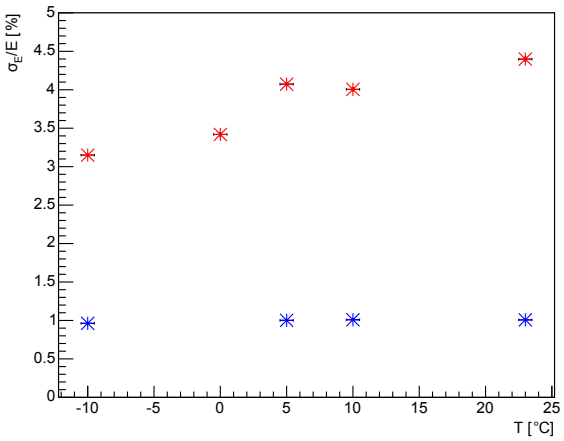

Figure 8.31: Energy resolution *vs.* temperature for PWO (red) and BGO (blue) crystals measured with PMT readout. The data were acquired during the run at KVI Groningen.

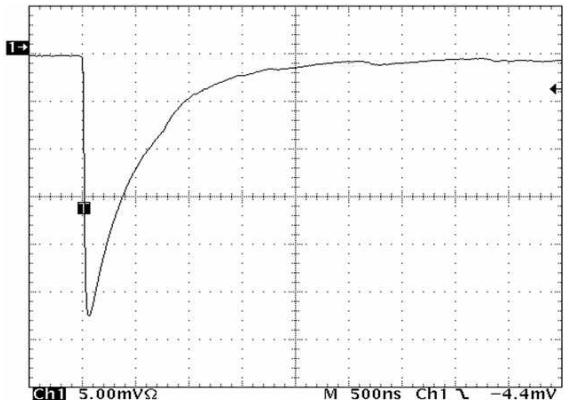

Figure 8.32: Signal shape of a BGO crystal with PMT readout.

8.3.2.2 Timing Performance

The high light yield of BGO has a trade-off in the decay time with $\tau_{decay} = 300\,\mathrm{ns}$. A typical signal shape, acquired with a PMT, is shown in Fig. 8.32. The necessary high rate capability for the interaction rate of 10^7 /s of $\overline{\mathrm{P}}$ANDA requires in first order a time resolution of 10 ns to assure a precise timestamp for the correct event building.

Readout with APD The readout of scintillation light with an APD requires the use of a preamplifier. To improve the performance of the readout system in terms of noise, the shaping stage should be placed as close as possible to the preamplifier stage. Therefore, the best solution is to integrate the preamplifier and shaping stages within a single unit. First studies for the APD readout of a BGO scintillator with electronics close to principle design were done with a BaBar preamplifier. This device was developed at SLAC for the readout of thallium doped caesium iodide crystals, CsI(Tl), with photodiodes. The decay constant of CsI(Tl) is almost four times larger than that of BGO, but to prevent pile-up, the shaping time of the BaBar preamplifier was chosen to 250 ns, which is suitable for BGO. A typical signal of this preamplifier for a ^{137}Cs source, detected with a small BGO crystal and a LAAPD is shown in Fig. 8.33.

A sample of cosmics rays, detected with a large BGO crystal and a CMS type APD (active area

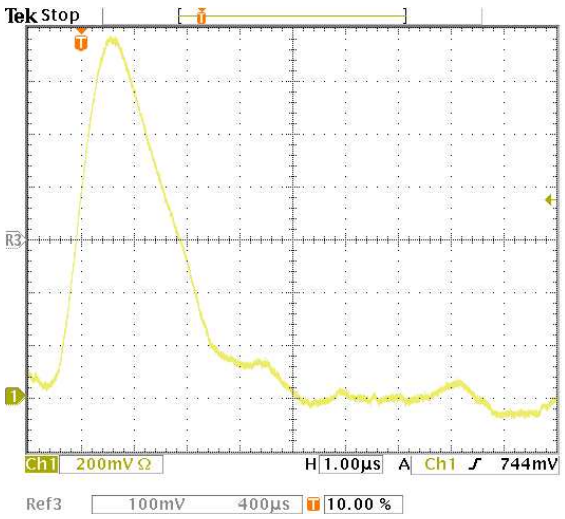

Figure 8.33: BaBar preamplifier signal for a ^{137}Cs source, detected with a small BGO crystal and a LAAPD.

$5 \times 5\,\mathrm{mm}^2$) and a BaBar preamplifier was used as input for initial simulation studies of the timing performance. The line shape was described using a Landau function. To get the time information, the leading edge of the pulse was fitted with a linear function and the value at half-maximum taken as the timestamp (see Fig. 8.34). The typical noise to signal ratio in the input sample was at the order of $N/S = 0.5\,\%$. Different noise environments were simulated by varying this ratio. The signal processing was simulated as flash-ADC (FADC) readout with different sampling rates.

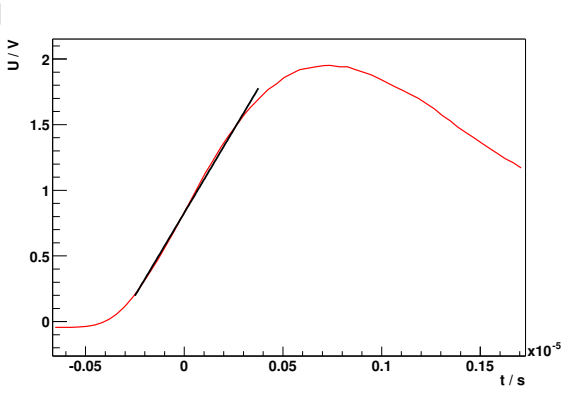

Figure 8.34: Timestamp definition for leading edge.

The simulation results for 5, 10 and 20 MHz FADCs are listed in Table 8.5. The required time resolution in first order (10 ns) can be achieved with all sampling rates, in most cases even for noise environments worse than the one seen in the initial samples.

σ_V [V]	N/S [%]	ΔT [ns]	σ_T [ns]
0.01	0.5	100	2.5
0.02	1.0	100	5.5
0.03	2.0	100	10.2
0.04	5.0	100	39.8
0.01	0.5	200	2.8
0.02	1.0	200	6.2
0.03	2.0	200	12.3
0.04	5.0	200	46.5
0.01	0.5	50	2.4
0.02	1.0	50	4.6
0.03	2.0	50	9.7
0.04	5.0	50	41.9

Table 8.5: Simulation results for timestamp precision.

These simulation results have to be verified with experiments in different, controlled noise environments, especially at a facility with tagged photons.

Further studies are required for the dynamic range of the readout electronics. Sophisticated algorithms for the signal processing allow to disentangle signal pile-up, as long as the signal peaks are separable and the amplification electronics is below saturation conditions.

8.3.2.3 Radiation Hardness

Scintillator materials as BGO are damaged when exposed to intense radiation, resulting in decrease of the light yield. Affected can be the scintillation process itself as well as the transmittance of the crystals.

In the literature controversial result can be found for BGO. Some authors report a recovery within days or similar effects by exposure to intense short wave light from fluorescent lamps [47, 48, 49, 50].

Since many of these studies are rather old, it is advisable to perform new studies with actually available material. The crystal production techniques are continuously improving, especially for BGO, because it is one of the standard materials for medical applications as Positron-Electron-Tomography (PET) Scanners.

Initial Studies First studies of the radiation damage of BGO due to intense radiation were done at the KVI Groningen. A long crystal ($3\times3\times10\,\mathrm{cm}^3$) was irradiated at the radio-biology facility at the KVI. The crystal was irradiated up to an integrated

fluence of $5 \cdot 10^9$ protons/mm^2 with a 90 MeV proton beam posessing a homogeneous intensity profile.

Before the irradiation the transmittance of the crystal perpendicular to the long axis was measured at several points. This crystal was also used in the experiments mentioned in Sec. 8.3.2.1.

The measurements of transmittance and of the proton spectra at the polarimeter were both repeated after the irradiation. Fig. 8.35 shows the spectra taken with a CH_2 target before and after the irradiation. The observed reduction in light yield is in the order of 18 %. Fig. 8.36 shows the relative transmittance of the crystal vs. the wavelength. The transmittance in the blue green region is reduced by 6–7 % in the area close to the front face, where protons with an energy of 90 MeV are mostly stopped. The transmittance in the area far away from the front face is almost unchanged.

Similar experiments have to be repeated with a larger number of samples and also on a longer time scale to investigate rate dependencies of the damage as well as self-recovery effects.

The radiation hardness of BGO might be improved by specific doping. The Shanghai Institute for Ceramics (SICCAS) offered the option of doping BGO crystals with Europium (Eu).

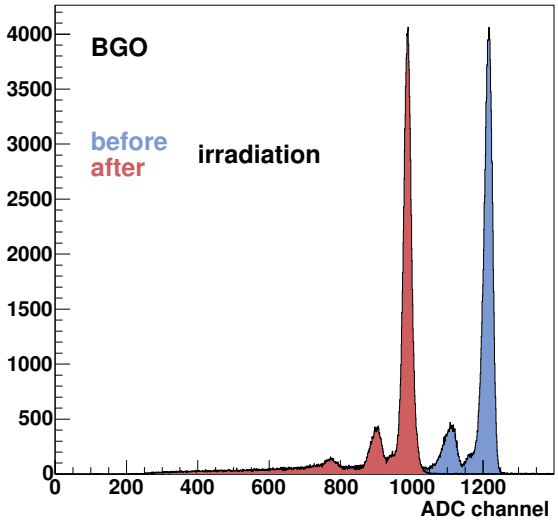

Figure 8.35: Spectrum of 90 MeV protons scattered off a CH_2 target into 18°, detected using a BGO crystal with PMT readout before (blue) and after (brown) irradiation with $5 \cdot 10^9$ protons/mm^2.

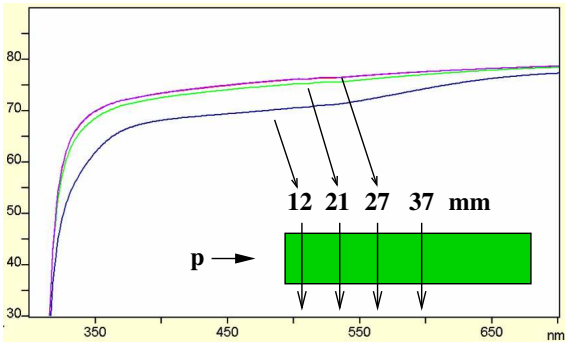

Figure 8.36: Change of optical transmittance of a BGO crystal after irradiation with 90 MeV protons.

8.3.2.4 Crystal Mass Production

Manufacturers Initial tests of actually available crystals have started with samples purchased from Crismatec (Saint-Gobain Crystals & Detectors) and SICCAS (Shanghai Institute of Ceramics Chinese Academy of Sciences).

Availability Both contacted crystal manufacturers stated their ability to handle the mass production for the $\overline{\text{P}}$ANDA electromagnetic calorimeter. First evaluations during a visit of the SICCAS production facility have shown that the crystal delivery rate from there would be limited by the on-site crystal quality assurance (QA). The crystal production itself has a maximum of 5 tons each month. The first QA step for these crystals should be done on-site at Shanghai either by the personnel from $\overline{\text{P}}$ANDA or the trained on-site personnel. Here the mass production will have the limit of approximately 1 000 crystals per month.

Costs The currently stated price from SICCAS for BGO is below 6\$/ cm^3, almost independent of the crystal geometry, without overhead and guaranteed for the complete delivery.

8.3.3 Alternative Scintillator Materials

The present design places the target calorimeter inside the superconducting coil of the solenoid. Therefore, the scintillator material has to be compact to minimize the radial thickness of the calorimeter barrel. Besides PWO and BGO there are no materials presently available, which are developed for mass production of large crystals at a considerable prize.

Parameter		CeF_3	LSO(Ce)
ρ	g/cm^3	6.16	7.40
X_0	cm	1.77	1.14
R_M	cm	2.6	2.3
τ_{decay}	ns	30	40
λ_{max}	nm	330	420
n		1.63	1.82
relative LY	% (LY NaI)	10	75
hygroscopic		no	no
$d(LY)/dT$	% /°C	0.1	-0.3

Table 8.6: Properties of CeF_3 and LSO(Ce).

Among alternative scintillators, which are available or presently developed, two candidates are under investigation:

- CeF_3 and
- LYSO.

CeF_3 has been invented already in 1989 by D. F. Anderson [51] and identified as a fast scintillator with maximum emission wavelength between 310 and 340 nm. The luminescence process is dominated by radiative transitions of Ce^{3+} ions, which explains the fast decay time of ≈ 30 ns and the insensitivity to temperature changes. The luminescence yield is comparable or even higher than the fast component of BaF_2, corresponding to approximately 10 % of NaI(Tl) as a reference. Since the crystal matrix is extremely radiation hard, it was considered for the CMS calorimeter during a long period of R&D, supported by the short radiation length and Moliére radius, respectively. However, homogeneous crystal samples beyond $10\,X_0$ length, grown by the Bridgeman method, have never been produced with adequate quality.

Detailed studies of the response function [52] to low energy protons and high energy photons have documented excellent time and energy resolutions, which are limited only in case of the reconstruction of the electromagnetic shower energy by the inhomogeneity of the available crystals. The way to improvement is by optimization of the manufacturing process.

At the present stage of the proposed PANDA design, the implementation of CeF_3 is not considered since it would double the radial thickness of the calorimeter shell.

In the last decade cerium doped silicate based heavy crystal scintillators have been developed for medical applications, which requires high light output for low energy γ-ray detection. Mass production of small crystals Gd_2SiO_5 (GSO), Lu_2SiO_5 (LSO) and $Lu_{2(1-X)}Y_{2X}SiO_5$ (LYSO) has been established in the meantime. Because of the high stopping power and fast and bright luminescence, these crystals have also attracted interest in calorimetry. However, the need for large homogeneous samples and the presently high costs, partly justified by the high melting point, are retarding the R&D.

LYSO, which has similar physical and scintillation properties as LSO and shows identical emission, excitation and optical transmittance spectra, has been recently produced in samples up to 20 cm length [53]. The light output is about 4 times of BGO but with a decay time shorter by one order of magnitude. It is intended to test an array of prototype LYSO crystals in 2005.

8.4 Photo Detectors

8.4.1 Avalanche Photodiodes

8.4.1.1 Introduction

The possible leakage of ionization radiation at the rear of the crystals and the magnetic field of 1.5 T preclude the use of conventional photomultipliers. On the other hand is the signal generated by ionization in a PIN photodiode by a traversing charged particle too large for our applications. To solve these problems a photosensor insensitiv to magnetic fields and posessing a small response to ionizing radiation has to be used. In case of lead tungstate, which has a relatively low light yield, an internal gain of the photosensor is required in addition.

These requirements can be satisfied by silicon avalanche photodiodes (APDs). Avalanche photodiodes are reverse biased diodes with an internal electric field used for avalanche multiplication of charge carriers. The CMS collaboration has developed APDs in collaboration with Hamamatsu Photonics optimized to detect the scintillation light from lead tungstate crystals. Those APDs have several advantages: compactness with an overall thickness of $\approx 200\,\mu$m (Fig. 8.37), high quantum efficiency of 70–80 % at the wavelength of maximum emission intensity of lead tungstate, insensitivity to magnetic fields and low cost in mass production. A disadvantage of this photosensor is its relatively small active area of $5 \times 5\,mm^2$ compared to the area of the crystal end faces. Therefore we started the R&D of large area APDs (LAAPDs) with an active area of $(10 \times 10)\,mm^2$ in collaboration with Hama-

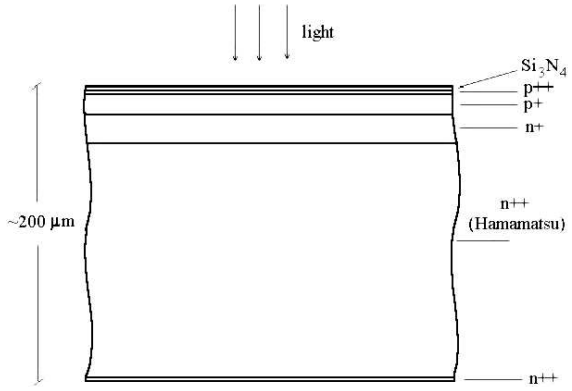

Figure 8.37: Schematic view of an APD with reverse structure [54].

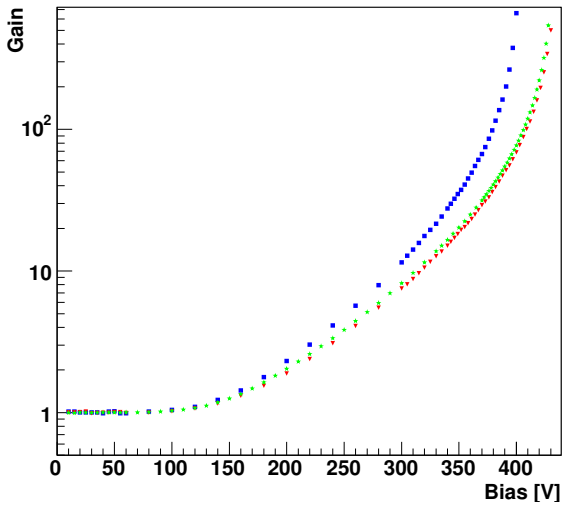

Figure 8.38: Gain dependence of bias voltage for different APD types: CMS (blue), S8664-55SPL (red) and the LAAPD S8664-1010SPL (green).

matsu Photonics. Two LAAPDs will be used to detect the scintillation light of one crystal. Our R&D of LAAPDs is based on the same internal structure as has already been tested by the CMS collaboration (see Fig. 8.37): Light enters the APD via the p^{++} layer and is absorbed in the following p^{+} layer, where electron-hole pairs are generated. The electrons drift in the electric field towards the p-n junction where they are amplified by impact ionization, yielding avalanche gain, and drift through the n-material to the n^{++} electrode where the charge collection takes place. In front of the p^{++} layer a passivation layer made of silicon nitride Si_3N_4 is used which reduces the decrease of quantum efficiency caused by reflection losses from the surface of the Si wafer.

8.4.1.2 Temperature and Voltage Dependence of Gain

Due to interactions of charge carriers with phonons the gain of an APD decreases with increasing temperature. The degree of sensitivity to temperature changes can be determined by the proximity of the applied bias voltage to the value of breakdown voltage and by the device characteristics as a result of internal structure:
A decrease of capacitance of the APD results in an increasing sensitivity to temperature changes. The temperature dependence of gain has a value of -2.2 %/°C at an internal gain of $M = 50$ in case of a CMS-APD [55].
The voltage dependence of gain is strongly influenced by the proximity of the applied bias voltage to the value of breakdown voltage. Different types of APDs were tested to evaluate their voltage dependence of gain: CMS-APDs (active area: $(5 \times 5)\,\mathrm{mm}^2$), first prototypes of LAAPDs (type: S8664-1010SPL, active area: $(10 \times 10)\,\mathrm{mm}^2$) and, for direct comparison with the results of CMS, prototypes with the same internal structure as the LAAPDs, but with smaller active area (type: S8664-55SPL, active area: $(5 \times 5)\,\mathrm{mm}^2$). The internal gain M of the APDs has been evaluated from the ratio of photo currents measured for high and low bias voltages (equivalent $M = 1$) at a fixed wavelength of $\lambda = 440\,\mathrm{nm}$. The results of these measurements are shown in Fig. 8.38. From these measurements the gain variations (caused by bias voltage variations) can be calculated for different values of internal gain. The results of these calculations are shown in Fig. 8.39 for the three tested APD types. As it can be seen the two APD types S8664-55SPL and S8664-1010SPL show the same gain variations as the CMS-APDs. At gain $M = 50$ a value of $1/M \cdot dM/dV \approx 3\,\%/\mathrm{V}$ has been evaluated which is in good agreement with the value given for CMS-APDs in [55].

8.4.1.3 Excess Noise Factor

The APD internal charge carrier multiplication via avalanche is a statistical process. A characterization of these statistical fluctuations is given by the excess noise factor F. Its r.m.s. broadening of a signal from n photoelectrons is given by $\sqrt{F/n}$. The value of the excess noise factor is determined by the internal structure of the APD and is related to the amplification of electrons and holes at a given value

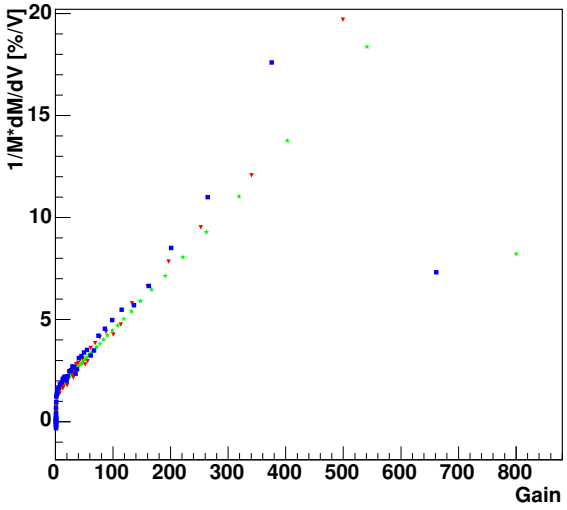

Figure 8.39: Calculated gain variations depending on internal APD gain for different APD types: CMS (blue), S8664-55SPL (red) and the LAAPD S8664-1010SPL (green).

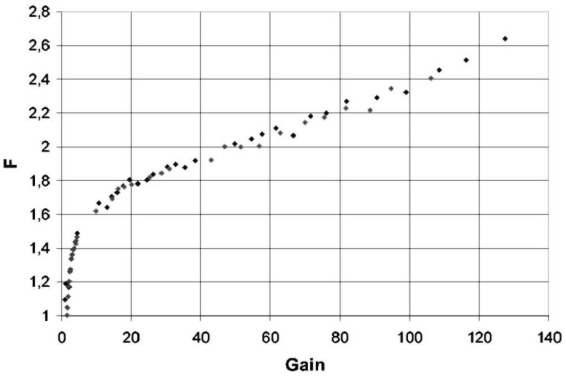

Figure 8.40: Measured excess noise factor F as a function of the internal gain of a CMS APD [56].

of the internal gain M:

$$F \approx k \times M + \left(2 - \frac{1}{M}\right) \times (1 - k), \qquad (8.2)$$

with k defined as the ratio of the ionization coefficients for electrons to holes. Its value is determined by the shape of the electric field near the p-n junction. The value of the excess noise factor at an internal gain of $M = 50$ of the CMS-APDs is $F = 2.0$ (Fig. 8.40), at gain $M = 100$ F is increasing to $F = 2.33$. The excess noise factor of the first LAAPD prototype S8664-1010SPL was measured at the APD laboratory of the CMS collaboration at CERN in April 2004. The result of this measurement is shown in Fig. 8.41. At an internal gain of $M = 50$ the excess noise factor of these LAAPDs

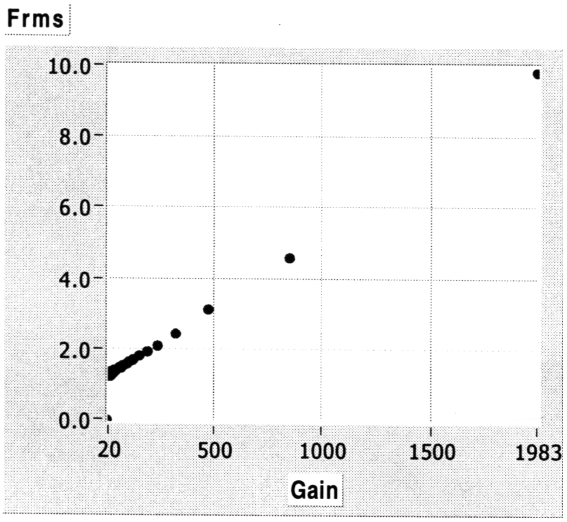

Figure 8.41: Measured excess noise factor F as a function of the internal gain of the first prototype of the LAAPD S8664-1010SPL manufactured by Hamamatsu.

has a value of $F = 1.38$, at gain $M = 100$ its value is $F = 1.57$.

8.4.1.4 Electrical and Optical Properties of the tested APD Types

The optical and electrical properties of available APDs mentioned above are summarized in Table 8.7. The properties of the two tested prototypes (S8664-55SPL and S8664-1010SPL) are in good agreement with the properties of the APDs developed by the CMS group in collaboration with Hamamatsu Photonics. Due to the four times larger active area of the LAAPD prototype its capacitance is much larger than those of the two tested $(5 \times 5)\,\mathrm{mm}^2$ APD types.

8.4.1.5 Radiation Damage due to Proton Irradiation

Irradiation of an APD with protons causes two different kinds of radiation damage:

- ionization effects at the surface reflected in the surface dark current I_s, and
- atom displacements inside the silicon bulk causing the bulk dark current I_b.

Thus the irradiation with protons was chosen to get an upper limit of the APD dark current expected after 10 years of operation of PANDA.
The irradiation was done at PSI (Villigen) with

Property	Condition	S8664-55SPL	CMS APD	S8664-1010SPL
Active area [mm^2]		5×5	5×5	10×10
Quantum efficiency QE [%]	$M = 1, \lambda = 420\,\mathrm{nm}$	65	70	65
Breakdown voltage U_{br} $[V]$	$I_d = 100\,\mu A$	400	400	400
Dark current I_d $[nA]$	$M = 50$	3	5	10
Terminal capacitance Ct $[pF]$	$M = 50$	80	80	270
Excess noise factor F	$M = 50$	not measured	2.0	1.38
Excess noise factor F	$M = 100$	not measured	2.33	1.57

Table 8.7: Electrical and optical properties of the tested APD types.

$E_p = 70\,\mathrm{MeV}$ for all three APD types listed in Table 8.7. During irradiation the increase of dark current was monitored. Fig. 8.42 shows the increase of the measured current of four tested CMS APDs during proton irradiation up to an integrated fluence of $10^{14}\,\mathrm{p/cm^2}$. The irradiation of the pre-series APDs was done the same way. Two of the four tested APDs type S8664-55SPL were irradiated up to a value of fluence of $10^{13}\,\mathrm{p/cm^2}$, the other two were unmounted after a fluence of $10^{12}\,\mathrm{p/cm^2}$ was reached. The increase of the measured APD current during proton irradiation is shown in Fig. 8.43. It can be seen in Fig. 8.43 that a saturation of the dark current during the irradiation of the $5 \times 5\,\mathrm{mm^2}$ APD prototypes is conceivable.
Fig. 8.44 shows the increase of the dark current of the LAAPD S8446-1010SPL prototype during proton irradiation. After an irradiation with $5 \cdot 10^{12}\,\mathrm{p/cm^2}$ the value of the dark current was twice as high as the dark current measured with the smaller area prototypes after an irradiation with $10^{13}\,\mathrm{p/cm^2}$ (see Fig. 8.43). Thus the one tested S8664-1010SPL prototype shows a behavior which indicates that these LAAPDs are not radiation hard according to CMS standards.

Due to the excellent optical and electrical properties of the LAAPD prototypes measured before irradiation the influence of proton irradiation on these properties was tested. Therefore the measurements of the LAAPD characteristics were repeated at PSI 18 days after initial irradiation.
It turned out that the radiation damage caused by protons only results in an increase of dark current (see Fig. 8.45) and has no impact on the other LAAPD parameters, e.g. the Gain-Bias characteristic of the irradiated prototype (see Fig. 8.46).

One main difference between the internal structure of the CMS APDs and the prototypes which have been tested is a groove inside the CMS APD structure to reduce the surface current of these APDs. Therefore the next step in the R&D of Large Area APDs was the implementation of such a groove into the LAAPD S8664-1010SPL internal structure.

First prototypes of LAAPDs with groove (type S8664-1010) from Hamamatsu Photonics were delivered in September 2004.
First irradiation tests with protons were done in November 2004 at the KVI in Groningen using 90 MeV protons. Similar to the measurements done at PSI the current of these APDs was measured during irradiation. Its increase is shown in Fig. 8.47. After reaching a fluence value of $10^{12}\,\mathrm{p/cm^2}$ the beam current was increased by a factor of 10 to start an additional irradiation with $10^{13}\,\mathrm{p/cm^2}$.
After an irradiation with $1.1 \cdot 10^{13}\,\mathrm{p/cm^2}$ a maximum current of $\approx 55\,\mu A$ was measured which is a factor of 4 smaller than the current of the LAAPD prototype S8664-1010SPL (see Fig. 8.44) measured after an irradiation with $5 \cdot 10^{12}\,\mathrm{p/cm^2}$.
Another difference to the measurements done with the first prototypes is the fact that the increase of the S8664-1010 current shows linear behavior for the two different values of used beam current.
Concerning the radiation hardness of the LAAPDs due to proton irradiation the behaviour of the dark current shows that the LAAPDs type S8664-1010 are radiation hard up to an integrated fluence of $10^{13}\,\mathrm{p/cm^2}$.

8.4.1.6 Delivery Conditions and Costs

The readout of the electromagnetic calorimeter will involve the use of nearly 22 000 APDs. Hamamatsu Photonics assured a delivery of 1 000 LAAPDs per month. The price of each APD, for a delivery of 22 000 pieces, will be 114 €.

8.4.2 Alternative Photo Sensors

The large dynamic energy range of the calorimeters down to a few tens of MeV photon energy relies

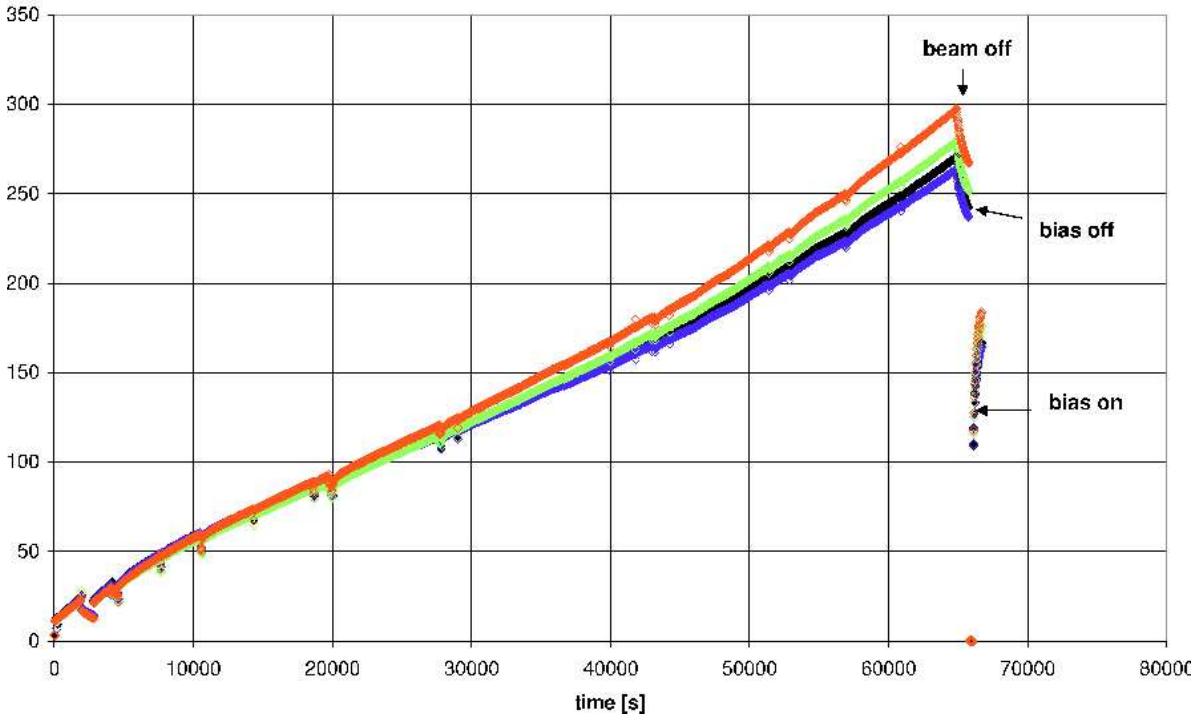

Figure 8.42: Current of four CMS APDs measured during proton irradiation up to a fluence of 10^{14} p/cm^2.

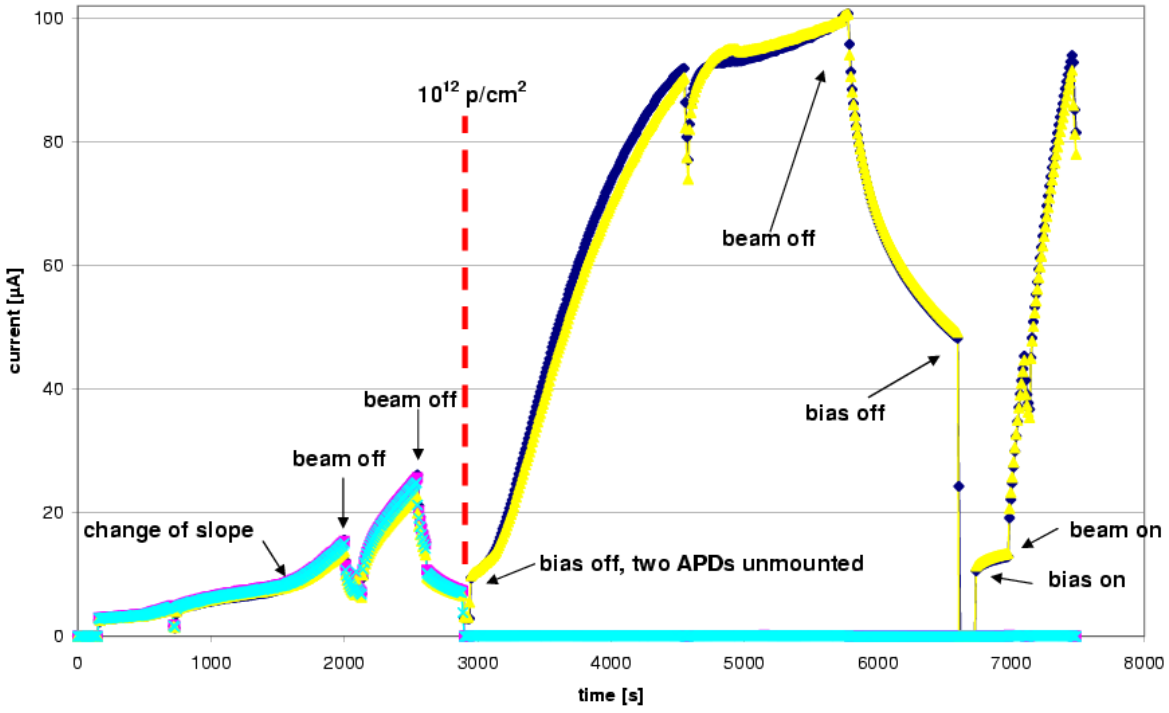

Figure 8.43: Current of the four $5 \times 5\,\text{mm}^2$ APD prototypes. Two of them were irradiated up to a fluence of 10^{13} p/cm^2, the remaining two were dismounted after the fluence of 10^{12} p/cm^2 was reached.

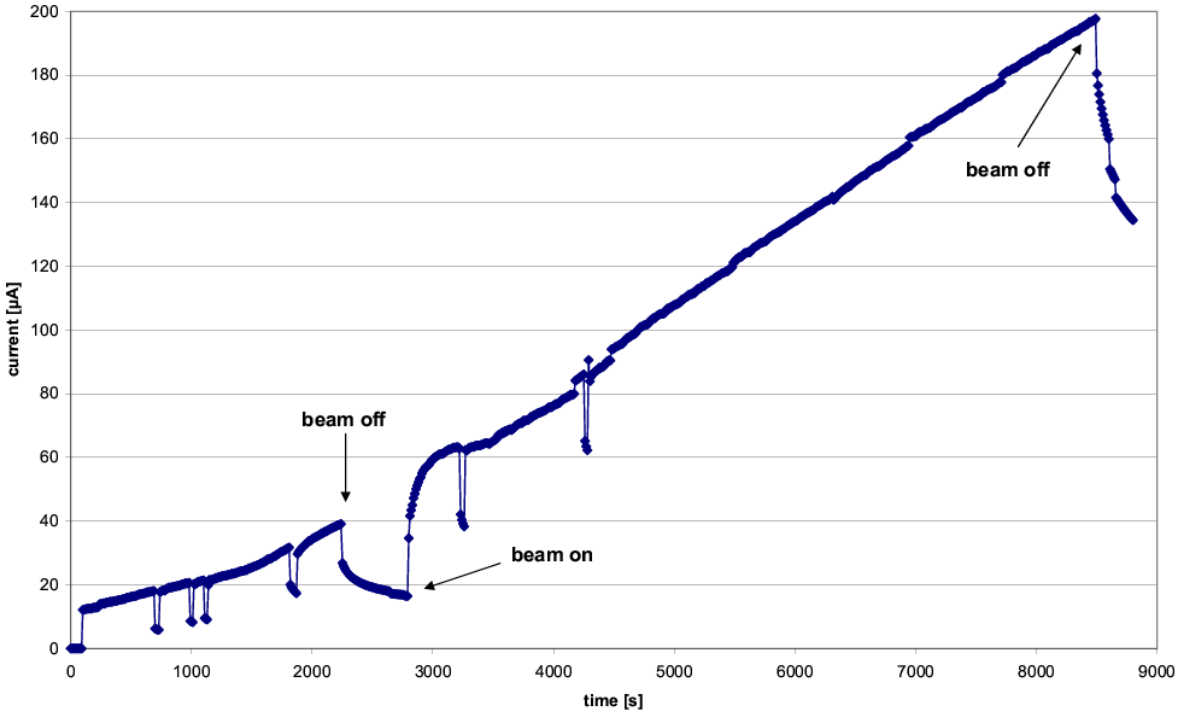

Figure 8.44: Current of one LAAPD S8664-1010SPL prototype measured during proton irradiation up to a fluence of $5 \cdot 10^{12}$ p/cm^2.

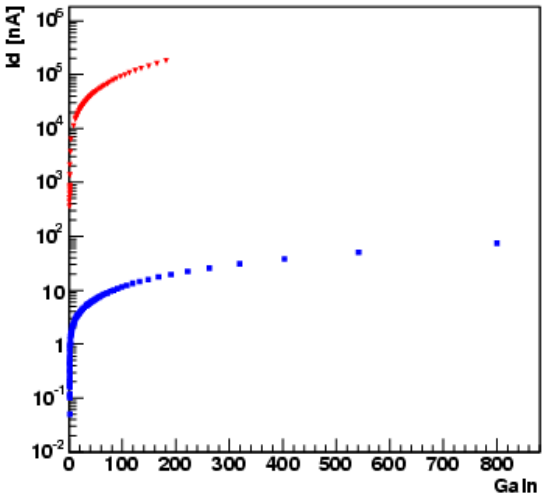

Figure 8.45: Current-Gain dependence of LAAPD S8664-1010SPL before (blue) and after (red) irradiation with $5 \cdot 10^{12}$ p/cm^2.

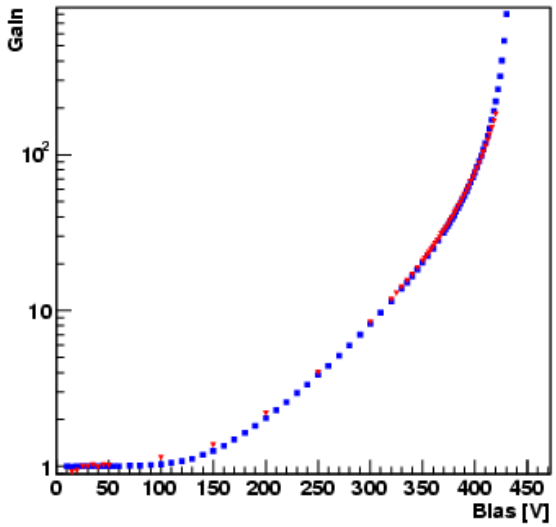

Figure 8.46: Gain-Bias characteristics of LAAPD S8664-1010SPL before (blue) and after (red) irradiation with $5 \cdot 10^{12}$ p/cm^2.

on an efficient collection and conversion of the scintillation light, in particular of PWO. Therefore, a full success for the development of large size APDs is mandatory for the readout concept. In parallel, investigations of two alternative photo sensors for operation in strong magnetic fields have been started:

- Hybrid photomultiplier with channel plate am-

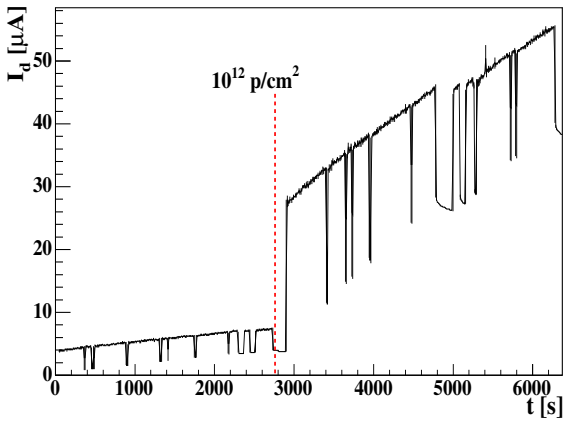

Figure 8.47: Current of LAAPD type S8664-1010 (10×10) mm^2, with groove) measured during proton irradiation up to a fluence of $1.1 \cdot 10^{13}$ p/cm^2.

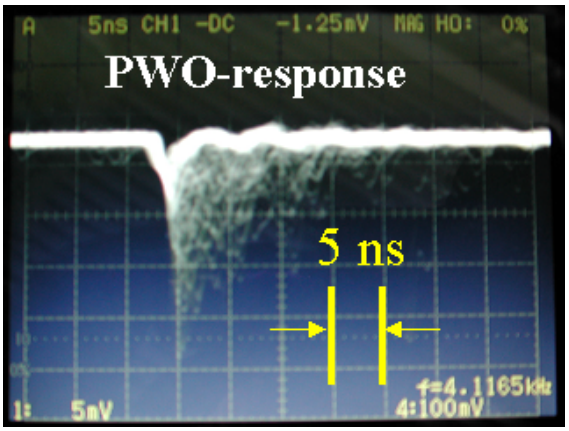

Figure 8.49: Anode signal of one PLANACON S85001-501 pixel showing the response of a PWO crystal to low energy γ-rays measured at room temperature.

plification

- Vacuum phototriodes

8.4.2.1 Study of the PLANACON hybrid photomultiplier

The PLANACON^{TM} S85001-501 photomultiplier (see Fig. 8.48), fabricated recently by the company BURLE [57], combines low sensitivity to a magnetic field with extreme fast response time (< 2 ns). The hybrid vacuum photo sensor achieves via a stack of two channel plates a gain up to $5 \cdot 10^5$ at maximum bias voltage of ≈ 2400 V with nanosecond rise time as illustrated in Fig. 8.49 for a typical PWO signal generated by low energy γ-rays. The quadratic 5.0×5.0 cm^2 photocathode has 4-fold segmentation with a common bias voltage but individual pixel readout.

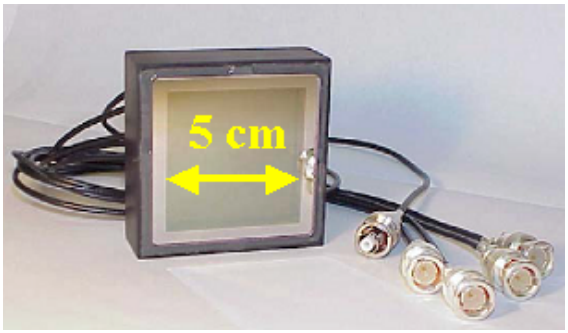

Figure 8.48: The new PLANACON^{TM} S85001-501 hybrid photomultiplier.

In a first test, a 2×2 PWO matrix of 12 cm long crystals of CMS quality has been coupled to one PLANACON tube. The coincidence between two vertically adjacent crystals has been required to identify cosmic muons and to record the energy deposition of minimum ionizing particles. Fig. 8.50 shows a typical pulse height spectrum representing the distribution of the lengths of the trajectories of muons across the crystal. The peak position corresponds to the most probable value of $\sim$ 3.2 cm length, close to the crystal diagonal, and is equivalent to an energy deposition of $\sim$ 40 MeV. The result is typical for photomultiplier readout.

The same setup allows deducing the individual time resolution from the relative time measurement of the responding segments in coincidence (see Fig. 8.51). A value of $\sigma = 420$ ps has been achieved using commercial electronics.

First measurements of the intrinsic amplification as a function of the direction and strength of an external magnetic field show a reduction of the anode signal by 50 % at a field strength above 0.8 T directed perpendicular to the surface of the photo cathode [58].

8.4.2.2 Study of Vacuum Phototriodes

The study of vacuum phototriodes has been started using small size samples from Hamamatsu. The version R2148MOD-2 provides a typical gain of 10 at 800 V bias voltage. The diameter of the tube matches the end surface of the presently used PWO crystals. Fig. 8.52 illustrates the fast response time of the anode signal inspected directly and after a fast amplification stage, respectively, initiated by a fast light emitting pulser. Presently an appropriate charge sensitive preamplifier is under development.

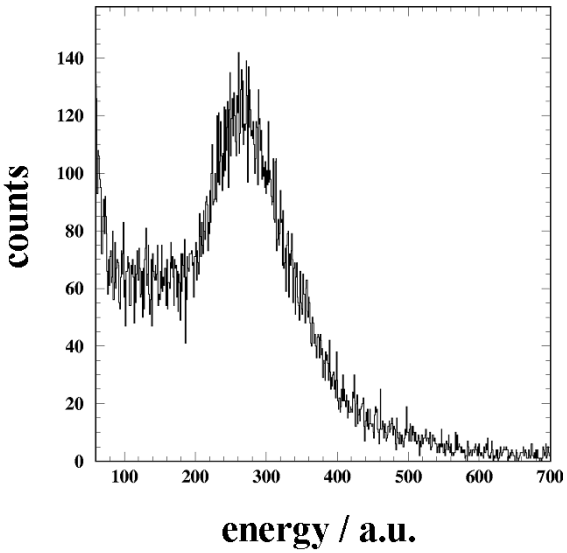

Figure 8.50: Response of a large PWO crystal ($3.2 \times 3.2 \times 12.0$) cm^3 to cosmic muons measured with a PLANACON hybrid photomultiplier at room temperature.

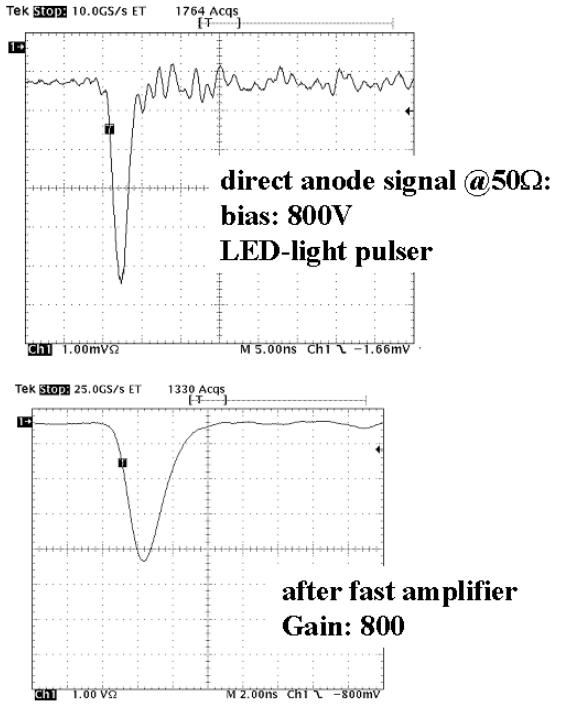

Figure 8.52: Response of a R2148MOD-2 vacuum phototriode to a light emitting pulser inspected before and after additional amplification.

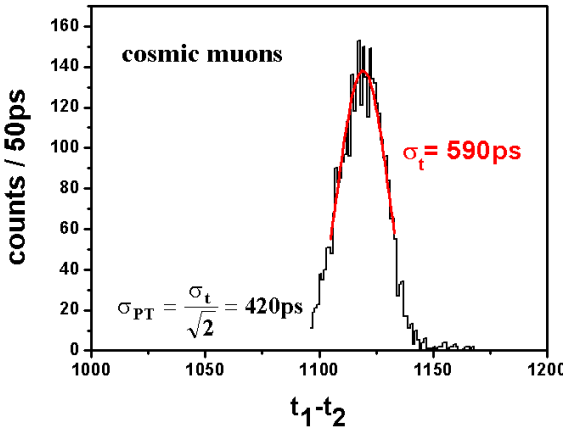

Figure 8.51: Spectrum of the time difference between two PWO crystals measured with two adjacent pixels of the PLANACON photomultiplier in coincidence to deduce the time resolution.

8.5 Front End Electronics

8.5.1 Readout Chain and System Layout

The readout of the electromagnetic calorimeter, based on the digitization of the response of APD photosensors to the light output of PWO or BGO crystals, will consist of extremely low noise front end electronics and a digitization stage. Both have to be located as close as possible near the detector modules within the calorimeter volume for optimum performance and minimum space requirements for signal transfer via cables or optical fibers.

At the present stage of the design there has been started no development yet started on the electronics with the exception of charge sensitive preamplifiers for tests of APDs and response functions of the test crystals. In particular the readout of small and compact subarrays required very small preamplifier geometries. In addition, experimenting has been started with signal processing using VME-based flash ADCs to study the general applicability and develop and to test analysis algorithms.

A more concrete description of the envisaged electronics chain can not be presented due to the uncertainties of final crystal and APD qualities, the definition of the dynamic range, acceptable energy limits, the parallel generation of a fast timing signal, the optimum signal shaping and the required sampling rate of a FADC, which depends strongly on the detector materials with significantly different rise and decay times.

The present design of low noise preamplifiers is achieved with discrete components to establish and define finally the performance parameters. To minimize space and power consumption a development

of an ASIC for charge collection and shaping appears almost mandatory but has to be postponed to a much later stage of R&D.

8.5.2 Preamplifier for APD-Readout

In order to perform tests for the APD-readout of PWO prototype detectors it was necessary to select a commercially available or to develop a low noise preamplifier, in particular to adapt it to the parameters of the presently available APDs with (5×5) and $(10 \times 10)\,\text{mm}^2$ active area, manufactured by Hamamatsu. In particular the geometrical dimensions had to be adjusted for the aimed readout of closely packed matrices of 3×3 up to 5×5 crystals of $(2 \times 2)\,\text{cm}^2$ cross section to measure the response function to high energy photons.

8.5.2.1 Specifications

After reviewing presently available preamplifiers the collaboration has decided to design a Low Noise / Low Power Charge Preamplifier (LNP-Preamp). The LNP-Preamp is a relatively simple and low cost combination of a J-FET with a fast integrated amplifier. The circuit diagram of the LNP-Preamp is shown in Fig. 8.53.

As the name implies, the LNP-Preamp is a low noise charge preamplifier combined with low power consumption. It has a charge sensitivity of 0.5 V/pC if terminated with 50 Ω. The maximum input charge of 6 pC corresponds to a positive output pulse with a peak voltage of 3 V at 50 Ω. Due to the relatively small feedback time constant of 25 μs, the LNP-Preamp is able to cope with high energy, high rate signals up to several 10 000 events/second without pile-up problems. The LNP-Preamp handles detector capacitances in a range from 50 pF to 300 pF and therefore is applicable for different types of APDs including the $(10 \times 10)\,\text{mm}^2$ Large Area APDs (LAAPD) with a detector capacitance of about 270 pF. The short rise time of 6 ns with a detector capacitance of 82 pF and 12 ns with 270 pF allows also precise timing measurements. The LNP-Preamp holds also the low-pass (LP) filtering network for the APD bias voltage (up to +500 V) and it is still small-sized ($L \times W \times H = 60 \times 17.8 \times 14\text{mm}^3$). It can be directly plugged onto the APD attached to a scintillation-crystal with a face side of $(20 \times 20)\,\text{mm}^2$.

The $PbWO_4$ scintillation-crystals have to be cooled to -25°C to increase the light-yield; the APDs as well as the preamplifiers stay at the same low temperature. To minimize the cooling power of the complete EMC, the power dissipation of the preamplifier has to be small; the stand-by power consumption of the LNP-Preamp is just 50 mW. By cooling only the LNP-Preamp to -25°C the noise is decreased by 15–20 % with respect to room temperature (+25°C). A much bigger noise improvement comes from the cooled APD due to its smaller dark current at lower temperatures. The APD dark current drops at -25°C, with respect to room temperature, by about a factor of ten. So the APD noise is reduced by a factor of 3–4 depending on the selected internal APD-gain which is strongly dependent on the applied APD bias voltage.

All the equal noise charge (ENC) numbers given below, are derived by using a shaping amplifier (ORTEC 450 Research Amplifier) with an integration time of 250 ns and differentiation time of 2 μs; these time constants correspond to a standard (FWHM/2.35) shaping time of 750 ns. For an input capacitance of 82 pF (corresponding to the $(5 \times 5)\,\text{mm}^2$ CMS-type APD) the LNP-Preamp shows at room temperature a typical ENC of 780 e_{RMS} and for a capacitance of 270 pF (corresponding to the $(10 \times 10)\,\text{mm}^2$ LAAPD) an ENC of 2 000 e_{RMS}. At a temperature of -25°C these numbers drop to 645 e_{RMS} at 82 F respective 1600 e_{RMS} at 270 pF.

Measured ENCs at -25°C with an APD connected to the LNP-Preamp are slightly higher due to the small but noisy dark current flowing through the APD: 700 e_{RMS} for the CMS-type APD (5 x 5 mm^2, $\sim$ 82 pF) and 1900 e_{RMS} for the LAAPD ($(10 \times 10)\,\text{mm}^2$, $\sim$ 270 pF). Using the LNP-Preamp followed by the shaper described above, the $(10 \times 10)\,\text{mm}^2$ LAAPD (factor of four larger area) leads to signal to noise ratio improvement of about 45 % with respect to the $(5 \times 5)\,\text{mm}^2$ CMS-type APD. Simulations show that an optimal shaping time for the LAAPD would be around 4 μs which would increase the signal to noise ratio by nearly a factor of two.

8.5.2.2 Circuit Description

The circuit diagram of the LNP-Preamp is shown in fig. 1. The AC-coupled input stage consists of a low noise J-FET of the type IFN152 from the US company InterFET; it is a successor of the obsolete low noise J-FET type 2SK152 from the Japanese company Sony. The IFN152 has a typical input voltage noise of $0.8\,\text{nV}/\sqrt{(f/\text{Hz})}$ at 10 kHz and at room temperature. The J-FET input capacitance is about 15 pF and the forward transductance is typically 15 mS. Combined with the 470 Ω AC-dominant

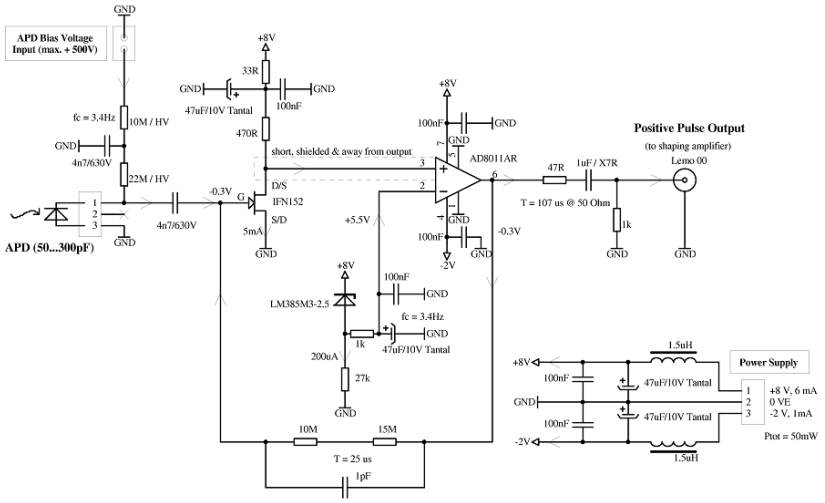

Figure 8.53: The complete circuit diagram of the LNP-preamplifier. To prevent noise pick-up via the power supply lines, the input supply voltages are first LC low-pass filtered before they are distributed to the circuit.

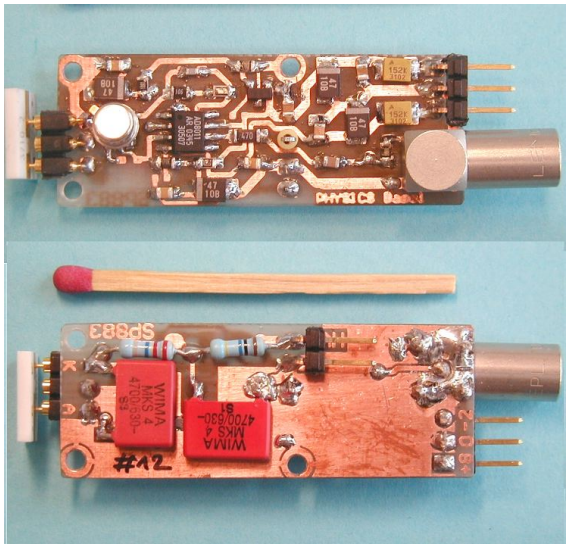

Figure 8.54: The top and the bottom sides of the LNP-preamplifier. The PCB carries SMD components as well as 'through the holes' components. For mechanical installation of the PCB three holes with a diameter of 2.2 mm are provided.

drain resistor this transductance results in a transient voltage gain of seven for the J-FET input stage.

The input stage is followed by a broadband (300 MHz), fast (2 000 V/μs) and low power ($\pm$1 mA) current feedback amplifier of the type AD8011 from the US company Analog Devices. With a typical input voltage noise of only 2 nV/$\sqrt{(f/\mathrm{Hz})}$ at 10 kHz this amplifier is compatible with the low noise design. The output of this amplifier is DC-coupled via the feedback network (1 pF + 25 MΩ) to gate of the J-FET and in parallel it is AC-coupled via a 47 Ω series resistor to the LEMO 00 coaxial output of the LNP-Preamp. Therefore the output voltage is divided by a factor of two if terminated with 50 Ω.

The supply voltages are asymmetric +8 V and -2 V resulting in a higher positive output swing which is compatible with the positive pulse output of this preamplifier. The LNP-Preamp draws a typical quiescent current of 6 mA from the +8 V supply and 1 mA from the -2 V supply; this leads to a total power consumption of only 50 mW.

The negative supply voltage of -2 V is only needed to adjust the 5 mA operating-point drain-source current through the J-FET by the DC output voltage of the operational amplifier. A typical voltage in a range of -0.2 V to -0.8 V, depending on the DC characteristics of the individual J-FET, is fed back via the 25 MΩ resistor to the gate input. The operating-point is set by the well filtered DC-voltage applied to the inverting input of the operational amplifier. This set-point voltage is obtained by subtracting 2.5 V from the positive supply voltage (+8 V) by using a 2.5 V Zener diode. So the same voltage drop of 2.5 V must be present over the total drain resistor of 503 Ω (470 Ω + 33 Ω); this results in a stabilized DC-drain current of about 5 mA.

On the LNP-Preamp printed circuit board (PCB) the APD bias voltage is first LP filtered by a 10 MΩ resistor and a 4.7 nF high voltage (HV) capacitor

which gives a cut-off frequency of 3.4 Hz. After this filter the bias voltage is fed via a 22 MΩ resistor to the cathode of the APD; the anode of the APD is grounded. The gate input of the J-FET is also decoupled via a 4.7 nF HV capacitor. A maximum bias voltage of +500 V can be applied and the total leakage current under dry conditions at room temperature is below 2 nA.

Fig. 8.54 shows the top and the bottom sides of the LNP-Preamp. On the left top side one can see the plugged in $(5 \times 5)\,\text{mm}^2$ CMS-type APD (ceramic housing) and on the right top side the Lemo 00 output connector as well as the power supply connector. The connector for the APD bias voltage as well as the LP filter are located on the bottom side of the PCB.

8.6 Mechanical Design

8.6.1 Design Considerations

The electromagnetic calorimeter of $\overline{\text{P}}$ANDA comprises two main parts: the central target calorimeter covers in cylindrical geometry almost completely the target area. A second planar arrangement located further downstream behind the dipole magnet serves the most forward range up to an azimuthal angle of 5° with respect to the beam axis. This forward calorimeter will be described in the separate Sec. 8.11.

The target calorimeter is illustrated in Fig. 8.55 and comprises three major parts:

- the barrel: 2.5 m length and 0.54 m radius, composed of 11360 crystals
- the upstream end cap: radius 0.34 m, 816 crystals
- the downstream end cap: radius ≈1 m, 6864 crystals

The present design concept is based on a homogeneous electromagnetic calorimeter composed of fast and compact scintillator crystals as active absorber material to be operated within the magnetic field of the solenoidal magnet. Large size avalanche photodiodes (APDs) are considered as photosensors in the barrel part. To achieve the envisaged large dynamic range in energy reaching from 10 GeV down to a few tens of MeV, the proposed scintillator $PbWO_4$ (PWO) has to be operated at low temperatures of -25°C to guarantee the sufficient luminescence yield. The limited size of the photosensor and the consequently moderate coverage of the crystal endface have to be compensated by the significantly higher quantum efficiency of the sensor compared to standard bialkali photo converters and an improved scintillator performance.

The operation conditions impose additional, but feasible to fulfil, requirements on the mechanical construction, insulation and temperature stability (±0.1°C), to keep the strong temperature dependence of the luminescence mechanism as well as of the APD gain at a tolerable level. In contrast, the use of BGO would allow the operation at room temperature but requires similar temperature stability of the APD readout.

This report presents the principles of the calorimeter design in a first iteration focusing on the definition of crystal geometry, the mechanical housing and support structure and the thermal aspects with respect to cooling (-25°C) and its fine regulation (±0.1°C).

The calculations are based on PWO as detector material. To maintain the proposed crystal depth of $22\,X_0$ requires a scaling factor of 1.2 for the longitudinal dimensions of BGO due to its larger radiation length (see Table 8.4). The overall granularity of the calorimeter is related to the Moliére radius to achieve the reconstruction of the electromagnetic shower with an adequate energy and position resolution and to limit the occupancy even for the highest event rates and multiplicities.

The presented concept is based on experience within the collaboration and on similar calorimeter concepts for BaBar [59], CMS [1], ALICE [60] or CLAS-DVCS [61]. A further improved design will rely on the design and construction of prototypes primarily to study the technology of extremely light crystal containers as well as the cooling and temperature control.

8.6.1.1 Individual Crystal

The basic crystal shape, a tapered parallelepiped, shown in Fig. 8.56, is kept fixed for all calorimeter elements. It is based on the "flat-pack" configuration used in the CMS calorimeter. Right angle corners are introduced in order to simplify the CAD design and the mechanical manufacturing process to reduce machining costs. Different dimensions of crystals are necessary. They are illustrated in the respective figures for the barrel (Fig. 8.57, Fig. 8.58) or both end caps (Fig. 8.63, Fig. 8.64), respectively.

In case of the barrel, two different geometries are presented to show the options. Both arrangements

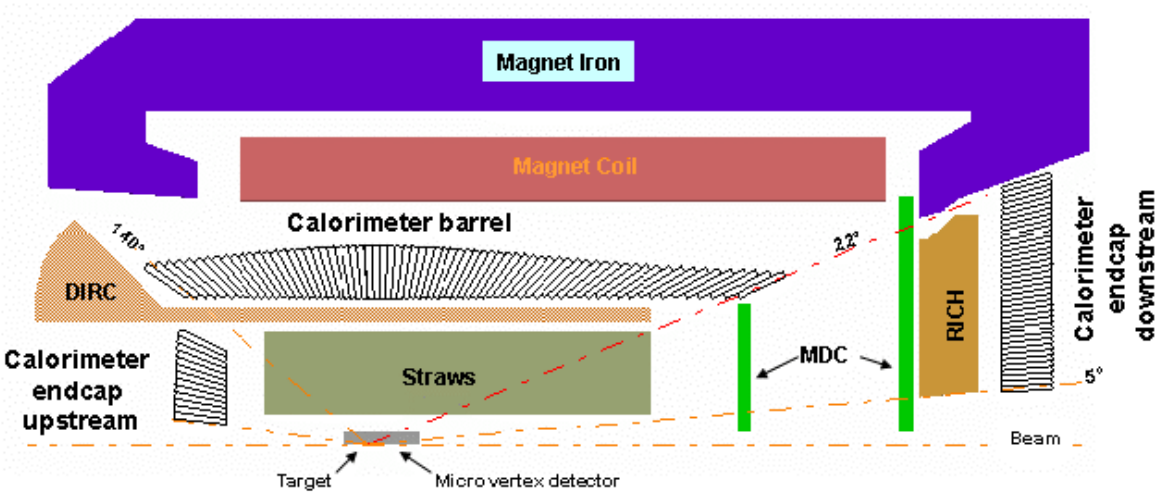

Figure 8.55: Overall view of the integration of the electromagnetic calorimeter into $\overline{\text{P}}$ANDA.

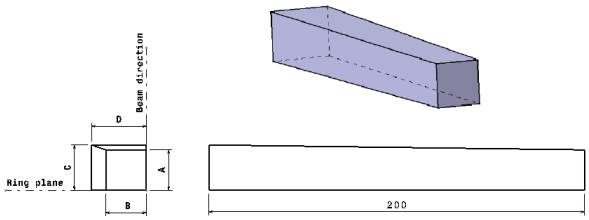

Figure 8.56: The shape of the scintillator crystal and the definition of geometrical parameters.

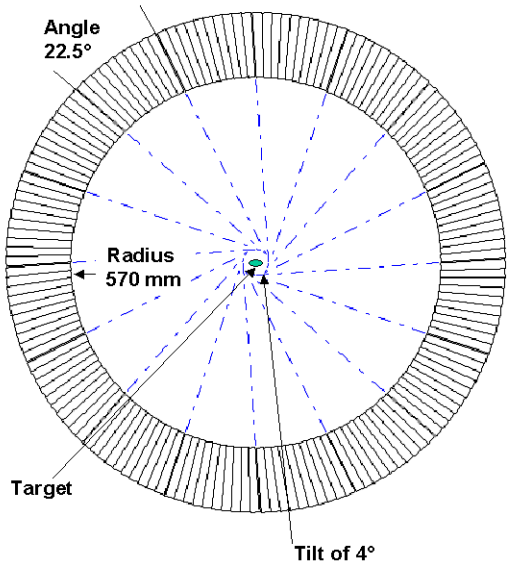

Figure 8.57: The segmentation of the calorimeter along the circumference of the barrel part. The 160 crystals are grouped into 16 subunits named slices.

foresee that the crystals are not pointing towards the target location. The tilt angle of $\approx 4°$ corresponds to a shift of the focus by $\approx$ 4 cm downstream. The symmetrical version reduces the number of different crystal shapes from 18 down to 11. The average mass of one crystal is close to 1 kg (from 1.025 to 1.060 kg). All given dimensions are nominal and the tolerances of the crystals are 0/-100 μm (the achievable tolerance is based on the present delivery for CMS from the Bogoroditsk Plant as well a for the DVCS calorimeter at JLAB).

The crystals are wrapped with a reflective material in order to optimise light collection as well as to reduce cross talk. Considered materials are TEFLON, TYVEK or Radiant Mirror Film VM2000 from 3M accounting for a thickness $<$ 70 μm. To compensate the longitudinal dependence of light collection, the structure of the crystal surface (optically polished, roughed, lapped) or the selection of an inhomogeneous reflector need further investigation. First tests have been performed (see Sec. 8.3.1.9).

8.6.1.2 Carbon Alveoles

In the present design the crystals will be contained in carbon alveoles of expected wall thickness $<$ 180 μm. For cost and time manufacturing reasons, it is proposed to group crystals by packs of 4 tightened together strongly to prevent from any

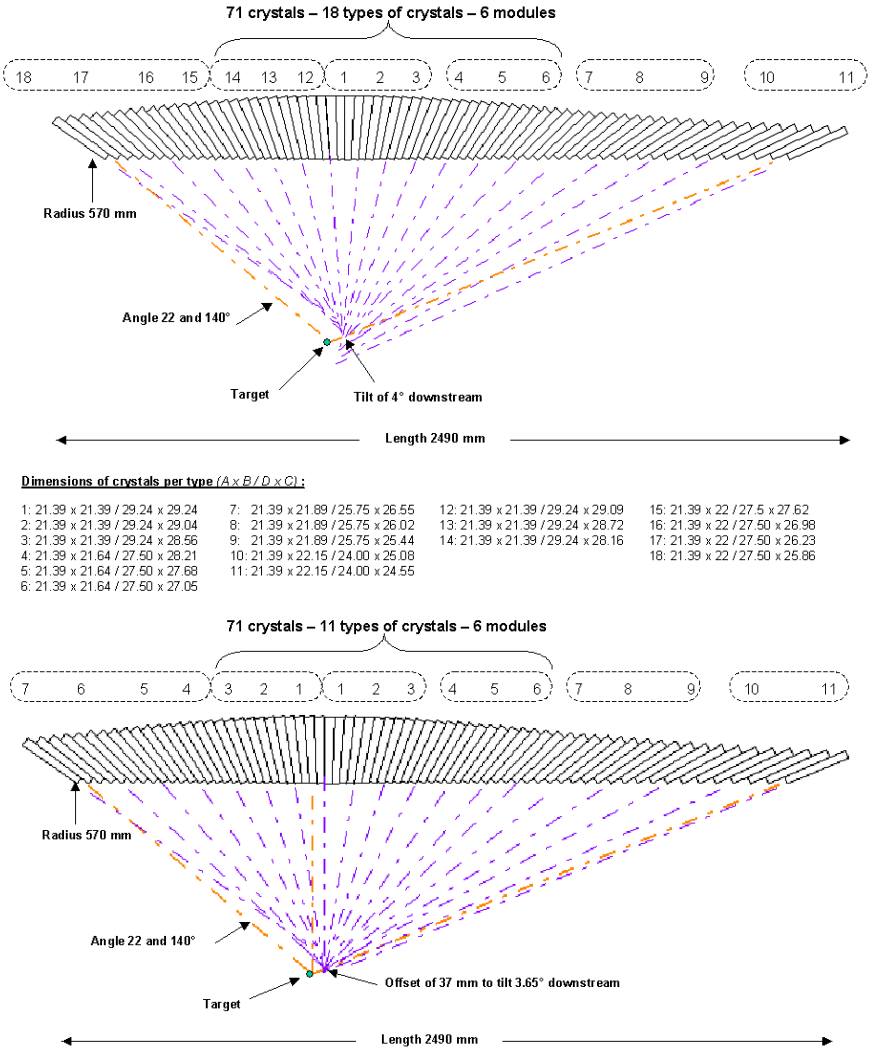

Figure 8.58: a) Geometrical arrangement of the crystals of the barrel in a cut along the beam axis. The definition of subgroups is indicated as well as the individual dimensions of the 18 different shapes according to the definition in Fig. 8.56. b) Geometrical arrangement of the crystals of the barrel in a cut along the beam axis based on a symmetric version reducing the number of different shapes to 11.

relative movement. This pack is inserted in one of the 10 alveoles which compose an alveole pack (40 crystals). It is glued to an insert made of the same carbon material to avoid a differential thermal expansion. This insert is the interface with the support elements. In front of the alveoles, a plate is added to avoid the movement of crystals.

8.6.1.3 Photosensor, Preamplifier and Electronic Boards

One or two Avalanche Photo Diodes (APD) will be glued on the back face of the crystal. The APDs are covered light tight by a plastic box in which an optical fiber for light injection is inserted in a corner. The APD is connected to a preamplifier with a KAPTON-cable. The preamplifier is placed above the thermal shield on the support elements. Due to the limited space in front of the calorimeter, LED- or LASER-light will be injected from the rear side of the crystals. In contrast to the severe radiation damage expected for the ECAL of CMS, which requires an online monitoring of the optical transmission change, the light pulser system is primarily intended for stability control of the complete readout chain including the APD. A first prototype is under construction based on a LED light source with optical fiber distribution (see Sec. 8.7.2.1).

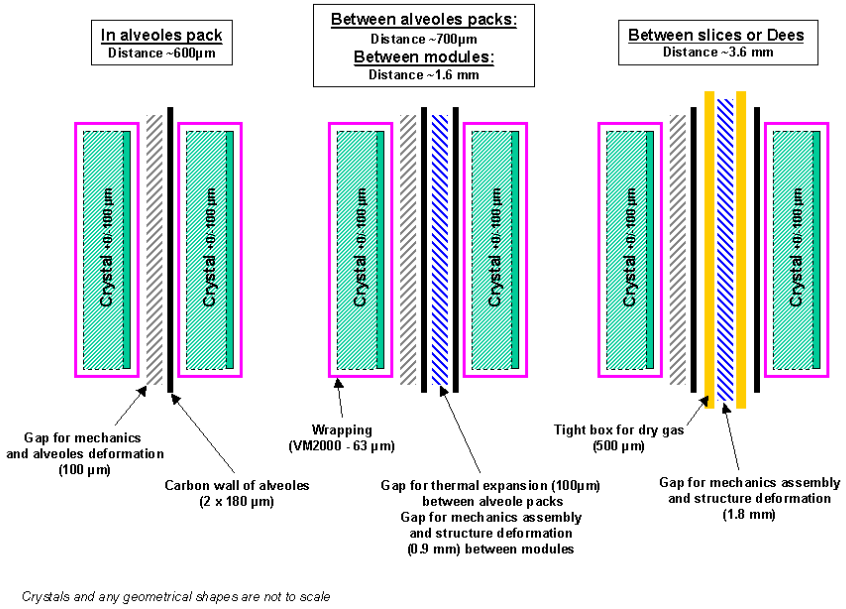

Figure 8.59: Estimate of the expected dead space between calorimeter elements.

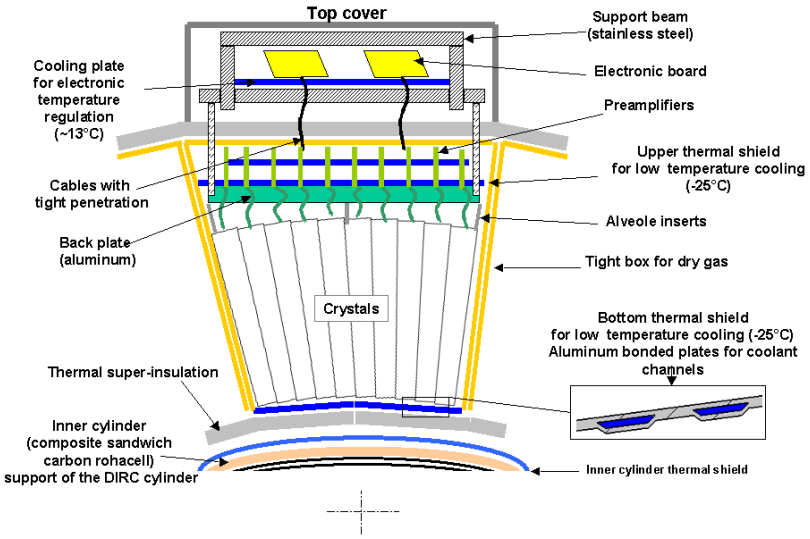

Figure 8.60: Schematic view of the concept and the major components of a barrel slice.

The electronic boards can be integrated into the support beam of the barrel slices or on the rear sides of the end caps, respectively.

8.6.2 Calorimeter Barrel

8.6.2.1 Crystal Arrangements along the Circumference

The barrel calorimeter including the mechanical structure is defined in the 22° to 140° acceptance between the radius from 570 to 950 mm. Fig. 8.57 shows the crystal arrangement on the ring based on the gap dimensions defined in Sec. 8.6.2.3. Choos-

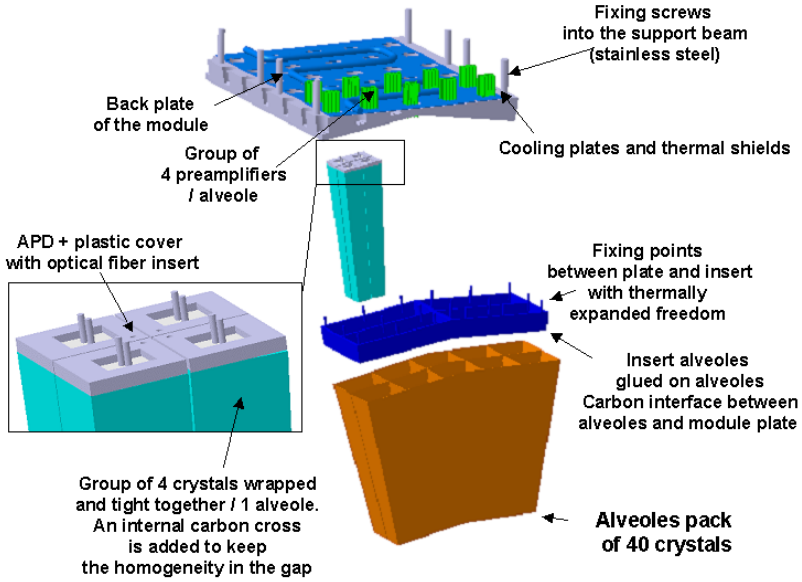

Figure 8.61: Schematic view of a single alveole pack housing 4 scintillator crystals.

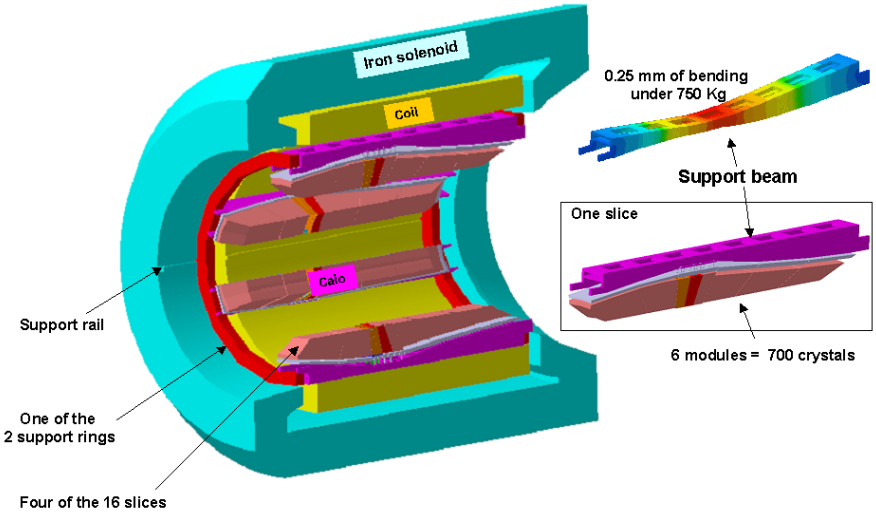

Figure 8.62: Illustrative view of the implementation of the barrel calorimeter within the PANDA detector.

ing the front size of an individual crystal close to 20 mm (21.39 mm exactly) at a radius of 570 mm, which corresponds to the Moliére radius, the ring divides into 160 crystals. The crystals are grouped into packs of 4×10 (one alveole pack) leading to 16 sectors of 22.5° coverage, which are termed slices.

A tilt of 4° is added on the focal axis of the slice to reduce the dead zone effect.

8.6.2.2 Longitudinal Crystal Positioning

Along the length of the barrel (beam axis) the crystal positions and individual geometries are shown in Fig. 8.58. In order to minimize dead space between crystals due to stacking, the proposed size of the alveole packs contains 40 crystals. In case of the arrangement shown in Fig. 8.58 18 different crystal shapes are necessary, shown at the upper part of the figure. The lateral sizes of the back faces vary between 24.0 mm to 29.24 mm. In total 71 crystals

are aligned at the radius of 570 mm. A tilt angle of 4° is introduced. In one slice, 3 or 4 alveoles packs are grouped together into 6 modules: 4 modules of 120 crystals, 1 module of 90 and 1 of 140 crystals, respectively. The entire barrel contains in total 11360 crystals. The barrel has a total length of 2490 mm.

Fig. 8.58b shows an alternative more symmetric arrangement, which is based on 11 different shapes only. It will reduce machining costs at the expense of a more tight packing (see next chapter).

8.6.2.3 Crystal Packing in the Barrel

The distance between two crystals is calculated from the thickness of materials, structure deformation and mechanical tolerances. Fig. 8.59 presents drawings of the different gaps which are explained in detail below. A conservative concept has been chosen, which can be considered as an upper limit of the expected dead space. Optimisation will require the construction of real size prototypes.

The basic distance between crystals inside a pack is set to 0.6 mm and represents the sum of :

- the double thickness of the carbon alveoles is 360 μm
- the double thickness of the wrapping material is 126 μm
- the free distance left for the alveole deformation and manufacturing tolerance of approximately 100 μm.

This is based on the nominal dimension of the crystal. There might appear an additional distance of < 0.2 mm between two adjacent crystals due to polishing tolerances.

Gaps due to the stacking can be minimized by the selection of 18 different shapes compared to the symmetric arrangement asking for 11 shapes only. But there is always left approximately 50μm close to the front and up to 500 μm near the rear side of the crystals. Between alveole packs, the thermal expansion of the module plate is about 100 μm and has to be added. Between modules, a distance of 0.9 mm has to be considered to take into account tolerances in the mechanical assembly and structure deformations, which are summing up to a total value of 1.6mm. Between adjacent slices, a gap up to 3 mm has to be assumed due to mechanical tolerances caused by the deformation of the whole structure. The distance between crystals in this area amounts to < 3.6 mm.

8.6.2.4 Mechanics around Crystals

One single slice is composed of 6 modules fixed on a support beam. Fig. 8.60 presents the design principle of one slice coping with all constraints: thermal, mechanics and electronics integration. Fig. 8.61 shows one module in more detail. The crystals are inserted into an alveole pack fixed to the module back plate, sufficiently rigid to keep planarity under load. The carbon insert is fixed on this back plate with special care to minimize movements between these two elements when the aluminium back plate is thermally expanding.

The support beam is a stainless steel U-reinforced structure of 20 mm thickness, which is fixed at both ends on 2 support rings. These rings (shown in Fig. 8.62), lay on a support rail fixed either to the inner cylinder of the coil cryostat or to the iron super-structure, depending on which of these two provide a more ridgid installation.

On the inner diameter, a cylinder encloses the whole barrel to act as a thermal shield and to provide a possible support for the DIRC detector. The cylinder walls could be made of a sandwich carbon / rohacell, strong enough to support the 150 kg load of the DIRC cylinder fixed to some rails placed on the inner skin.

8.6.2.5 Thermal Design

The crystals are to be cooled down to a temperature of -25°C stabilized to ± 0.1 K. To reach the temperature without condensation, the slices have to be tight boxes, in which dry and cool gas is circulated as indicated in Fig. 8.60. Two thermal shields are introduced:

- Above the crystals, the module plate is cooled via a copper plate and serpentine tubes attached to it. Additional cooling plates can be added cooling the electronics. Between preamplifiers and APDs, a kapton cable passing through an insulation panel is added in order to break the connection between the two elements.
- In front of the crystals, the thermal shield is composed of two aluminium plates of 1 mm thickness bonded together to create internal channels (Fig. 8.60).

The thermal shield is completed with 18 mm thick insulation material from the ambient temperature or an intermediate one as a thermal shield can be added (as shown on Fig. 8.60).

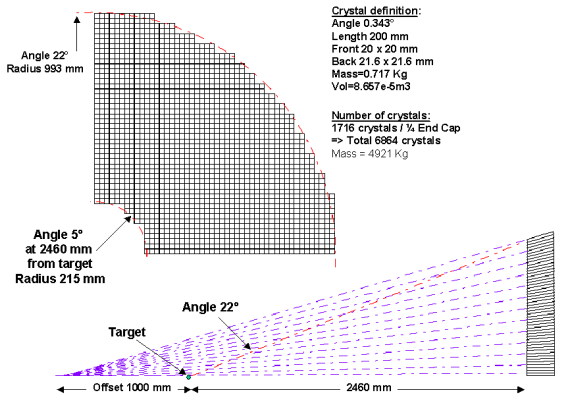

Figure 8.63: Geometry of the crystal elements in one quarter of the downstream end cap.

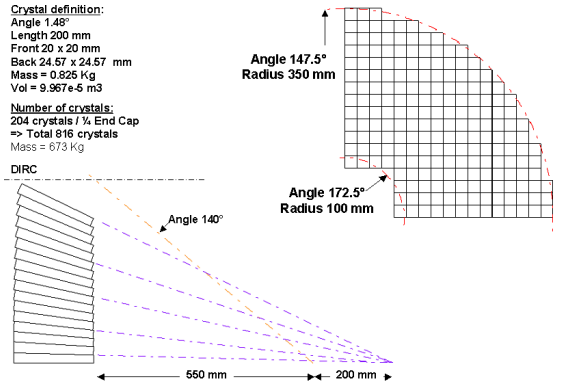

Figure 8.64: Geometry of the crystal elements in one quarter of the upstream end cap.

On the side, 0.5 mm thick aluminium plates close the gas tight box. The insulation between slices is achieved at the level of the thermal shields. In fact, no insulation can be introduced on the sides because no space is left for and it is assumed that the temperature is kept at -25°C.

The power needed to cool down the slices is estimated to be 1 200 W (further analysis has to be performed).

First simulations of the cooling process have been started based on R&D work for the CLAS-DVCS calorimeter [61]. In a first estimate under the assumption of cooling only via the front and rear side of the crystal arrays the final temperature can be reached within 2 days.

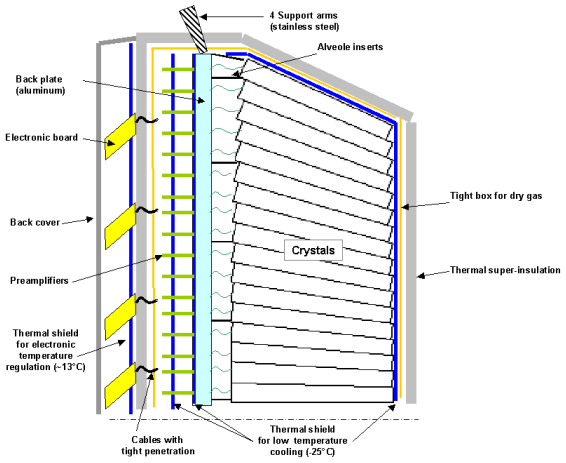

Figure 8.65: Schematic side view of the concept and the major components of one of the end caps.

8.6.3 End Caps of the Calorimeter

8.6.3.1 Crystal geometry

The acceptance of the end caps defines the opening angle where crystals have to be placed as straight walls as shown in Fig. 8.63 and Fig. 8.64, respectively. The upstream end cap is defined between 147.5° and 172.5° of acceptance between radii of 100 and 350 mm. The downstream unit covers the acceptance between 5° and 22° with respect to the beam and corresponding radii of 215 mm and 993 mm, respectively. The required number of crystals amounts to 816 and 6864 ones for the up- and downstream end caps, respectively.

8.6.3.2 General Layout

The principle for both end caps is presented on Fig. 8.65. The end caps are consisting of two symmetric parts called the "Dees" mounted on both sides of the beam axis. The alveole pack and insert principles are identical to the barrel, except for the outer diameter. Special packs are foreseen in order to reach as close as possible the circumference of a circle. The upstream end cap is fixed by its back plate on the DIRC support frame at some positions. The downstream can be fixed on the iron super structure. The thermal aspects are identical to the barrel part and have still to be studied in more detail, in particular, the position of the thermal shields and the overall layout of the tight box.

8.6.3.3 Distance between Crystals

It should be mentioned that the basic distances follow the same principle as for the barrel, and are presented in Fig. 8.59. A tolerance of 50 μm has been added because of the gaps created geometrically due to the stacking. To take into account the thermal expansion of the back plate, 0.1 mm is added between each alveole pack. A distance of 3.6 mm is expected between both Dees.

8.7 Calibration and Monitoring

8.7.1 Calibration

At this stage of detector development, the presently discussed options for energy and position calibration are based on the experience with running detector systems such as TAPS, Crystal Ball, Crystal Barrel and BaBar. The final concept will depend on the achieved prototype performance, reproducibility and stability of operation. There will be in-beam detector and calibration tests with full size prototypes, such as one out of the 16 slices comprising the barrel of the target section. Based on the present experience with the temperature sensitivity of the complete detector elements including the crystal and the photosensor, a final in-beam calibration of the whole calorimeter does not appear appropriate. All calibrations have to be performed using the complete set-up operating at the final temperature. A relative inter-calibration can be done using a light distribution system or cosmic muons. The absolute energy calibration has to rely on the correct reconstruction of neutral mesons via a shower reconstruction and determination of the invariant mass. The stability of the calibration parameters depends on the monitoring of the response function of each detector element. The absolute geometrical position of the individual calorimeter elements has to be deduced from the mechanical design. The point of impact of the photon relies on the reconstruction of the electromagnetic shower and primarily on the appropriate mathematical algorithm, which will be optimized for the prototype arrays.

8.7.2 Monitoring

The monitoring system should provide a reference to identify and record any changes of the coefficients for the energy calibration of all calorimeter cells. The response can shift due to changes of the luminescence process and the optical quality of the PWO crystals, the quantum efficiency and gain of the APD, and of the preamplifier/ADC conversion gain, for example. These effects can originate from temporary and permanent radiation damages and/or temperature changes. Due to extensive research on the radiation damage of PWO carried out during the last decade it was established that the luminescence yield of PWO crystals is not affected by irradiation, only the optical transmission. Any change of transparency can be monitored by the use of light injection from a constant and stabilized light source. The concept to be used depends on the time scale these deteriorations appear. As outlined in Sec. 8.2.4 the expected dose rate will stay well below the values expected for CMS operation. Therefore, one can assume that the possible degradation of the optical performance will evolve gradually and very slowly in time. In that case, trends and corrections can be deduced from kinematic parameters such as invariant masses calculated off-line. To avoid photon conversion in front of the calorimeter, the overall thickness of dead material has to be minimized. Mechanical structures for support or cooling should be installed as close as possible to the crystal front face. A system of optical fibers for light injection from the front side might be excluded due to the space needed to cope with the large bending radius of fibers. Injecting light from the rear might be less significant for the optical transmission due to enhanced multiple scattering before its detection in the photosensor. Both concepts have to be studied in detail when a first prototype is ready. The temperature gradient of the luminescence yield of PWO, which varies due to temperature quenching between 2 and 3 %/K requires a temperature stabilization of the whole system with a precision of $\sim$ 0.1° including a finely distributed temperature measurement. The requirements are less stringent in case of BGO. However, the intrinsic gain and the noise level of the APD photo sensors show similar temperature sensitivity. The thermal contact to the crystals should should be sufficiently reliable. However, an exptected slightly inhomogeneous temperature distribution within the whole calorimeter will require an individual adjustment and control of the APD bias voltage. The change of performance due to radiation damage will indirectly contribute to the integral performance. The separate control of the electronic readout chain can be calibrated and monitored by standard charge injection technique.

8.7.2.1 Concept of a Light Source and Light Distribution System

To maintain exact correspondence between observed changes of the measured amplitude of the light monitoring signal and the detector signal initiated by high energy photons, which is influenced by the variation of the optical transmission of PWO crystals it is necessary to meet two requirements: Optical emission spectrum of the light source should be similar to the radio-luminescence spectrum of PWO; effective optical path length for monitoring light in the crystal should be identical to the average path length of the scintillation light created by an electromagnetic shower in the crystal. Further technical requirements for the monitoring light source are: Number of photons per pulse should generate the output signal equivalent to about 2 GeV in each cell; the duration of the pulse should be similar to the decay time of the scintillation of PWO; a long-term pulse stability better than 0.1 % has to be achieved; minimal pulse height variation from pulse to pulse (determined only by photon statistics without any additional line broadening to keep the required number of monitoring events at the minimum). Nowadays available ultra-bright LEDs (brightness $>$ 10 cd) emitting at various wavelengths give the opportunity to create a system to meet most of the above requirements. In case of blue-violet LEDs the emission spectrum (centered at 420–430 nm) as well as the spectral width (approx. 70 nm FWHM) correspond exactly to those for PWO radio-luminescence. The number of photons per 20 ns pulse can be as large as 109 and can be further increased by more than one order of magnitude by combining optically many LEDs in one emitting block. Moreover, combining LEDs of different color allows fine-tuning to the entire scintillator emission spectrum. Even taking into account the light losses in the distribution system one might illuminate 1 000–1 200 calorimeter cells with one large LED block. Consequently 10 to 15 such stabilized blocks can provide the monitoring of the whole electromagnetic calorimeter. Such a concept allows the selective monitoring of different parts of the calorimeter by electronic triggering of the appropriate LED blocks without the necessity of optical switching

The distribution system should provide the light transfer to each cell with the option to fire selectively only $\sim$ 10 % all cells simultaneously to avoid interference problems in the front-end electronics and an overload of the data acquisition system. This can be implemented with optical fibers grouped into 10 bunches attached to the outputs of multi LED blocks. Each fiber bunch will contain additional fibers controlling possible losses in fiber transparency. Fiber material (quartz or plastic) will be finally chosen after specification of the irradiation environment.

8.7.2.2 Concept of the Light Monitoring System

The concept of the system should provide flexible control and redundancy in terms of measured parameters to distinguish between different sources of instability. Each emitting block will be equipped with an optical feedback and a thermo-stabilized PIN-photodiode as reference. Such a device has been successfully implemented for CMS ECAL [62]. A central sequencer will trigger all blocks with maximum frequency up to a few kHz. A separate unit is foreseen to measure the light amplitude of the reference fiber in each bundle. The system does not require regular maintenance. Fig. 8.66 and 8.67 show the schematic layout and the major components of a first functioning prototype.

8.8 Expected Performance

PWO has been proposed as scintillator material based on the experience obtained in several test measurements with crystals of standard CMS quality manufactured in Russia or China. In contrast to CMS requirements, the experiments have been concentrating on the response to photons and charged particles at energies below 1 GeV. Excellent energy and time resolutions have been obtained for single detectors and crystal arrays comprising up to 25 modules. Consistent test series have been performed with rectangular crystals of 150 mm length and a quadratic cross section of $20 \times 20\,\text{mm}^2$ with all sides optically polished. The read-out of the scintillation light was achieved with photomultiplier tubes and commercial electronics of NIM and CAMAC standard. In most of the cases the anode signals were carried via RG58 coaxial cables over a distance of 30-50 m outside the experimental area to the DAQ system. Therefore for practical reasons, energy and time informations are deduced and digitized after long passive delays, causing a significant signal attenuation and loss of high-frequency response. The compact detector arrays have been operated at a stabilized temperature, slightly below room temperature.

Beside the response to low energy γ-rays of radioactive sources tests have been performed using energy

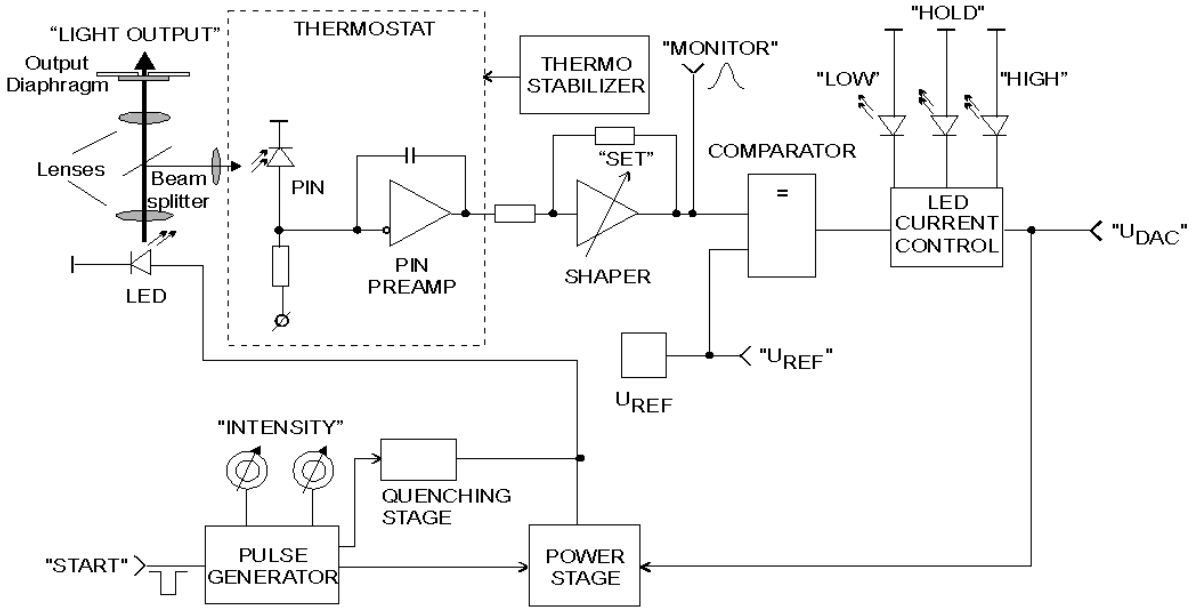

Figure 8.66: Schematic layout of the stabilized light pulser system.

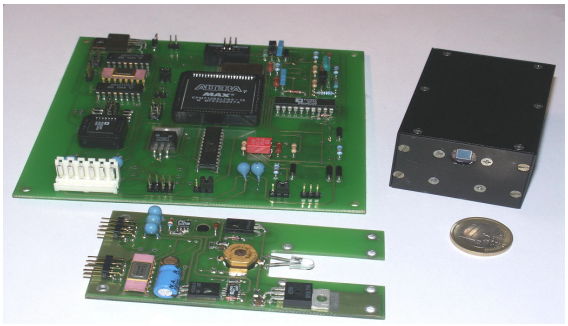

Figure 8.67: Major components of a first prototype of the monitoring system.

marked photons at the tagging facility of MAMI at Mainz between 50 and 850 MeV energy [3], [4], [5]. Additional experiments at KVI, Groningen and COSY at the FZ Jülich, Germany have delivered first results for low and high energy protons and pions [63]. For protons, which are completely stopped in a crystal of 150 mm length, an energy resolution of $\sigma/E = 1.44\,\%/\sqrt{E} + 1.97\,\%$ (E given in GeV) has been extracted as an upper limit, since the proton energy had to be deduced from the time of flight measured using a fast plastic start counter. For 90 MeV protons typical resolutions between 4 % and 5 % are achievable.

The response to monoenergetic photons shows an excellent energy resolution of $\sigma/E = 1.52\,\%/\sqrt{E} + 0.41\,\%$ (E given in GeV) for a matrix of 5 × 5 elements. Affected by the increased shower leakage, the resolution of a 3 × 3 matrix worsens to $\sigma/E = 1.78\,\%/\sqrt{E} + 0.58\,\%$.

In a later experiment with slightly improved crystal quality and more efficient light collection due to a tapered shape, a resolution of $\sigma/E = 1.41\,\%/\sqrt{E} + 0.90\,\%$ has been achieved for a 5×5 matrix. All measurements have been performed at $T = 10°\mathrm{C}$.

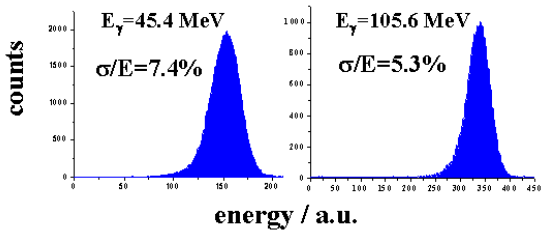

Figure 8.68: Response function of a 5×5 matrix of 15 cm long PWO crystals to mono-energetic photons of 45.4 and 105.6 MeV energy.

Fig. 8.68 shows the lineshape obtained for two selected energies at 45.4 MeV and 105.6 MeV, respectively. The intrinsic resolution of approximately 1.5 MeV of the tagger system has not been folded in. In all measurements excellent time resolutions have been achieved, in spite of the fact that the timing discriminators were located after long readout cables. A time resolution of $\sigma_t < 130$ ps was obtained

for energies above 25 MeV.

8.8.1 Energy Resolution

As outlined in the previous chapters the expected specifications of the electromagnetic calorimeter should be achievable by improvement of the crystal quality and the reduction of the thermal quenching by operation at lower temperatures of $\approx -25°C$, which delivers an additional increase of the light yield by a factor of 2–3.

In the past year the production of large size PWO-II crystals of 150 and 200 mm length has been successfully completed. Arrays comprising 3×3 crystals of 150 mm length, manufactured at BTCP and SICCAS, became available as well as a full size 5×5 matrix of 200 mm long scintillators from Russia. All crystals are rectangular parallelepipeds to allow a direct comparison to the measurements performed in the past and discussed in the previous section.

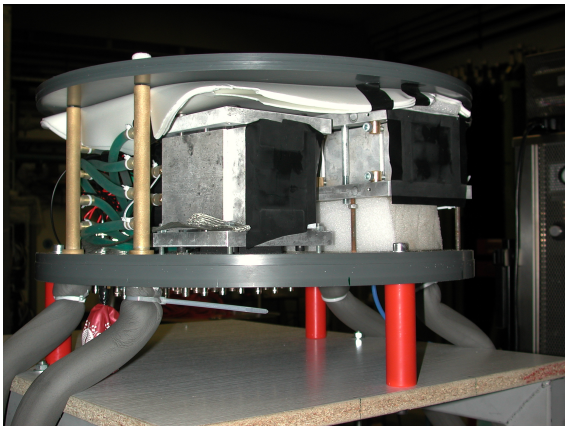

Figure 8.69: Experimental set-up of the first pilot experiment to operate a PWO matrix at low temperatures.

In a pilot experiment in February 2004, a first 3×3 subarray of 150 mm long crystals has been tested at −24°C. The low temperature of the crystals has been reached by conventional cooling of aluminum plates, which are directly attached to the crystal block and are cooled with the aid of a circulating liquid. The crystals had to be mounted and wrapped individually, causing an additional amount of dead material in between. Fig. 8.69 shows two detector arrays in a set-up, which was later on closed and filled with dry nitrogen to avoid water condensation.

Fig. 8.70 illustrates the achieved lineshapes for 8 selected photon energies between 64 and 715 MeV energy. In spite of the limited active volume of a

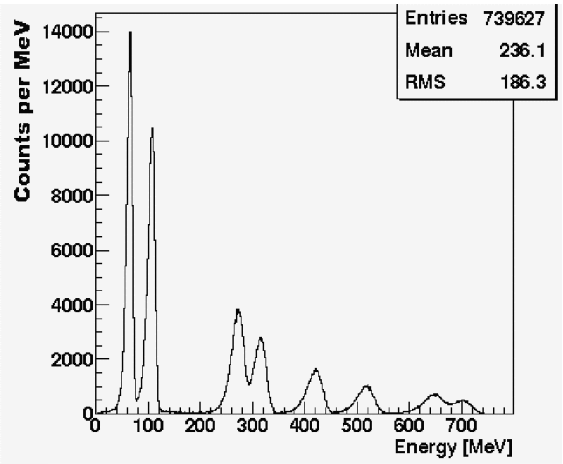

Figure 8.70: Energy response of a 3×3 crystal matrix to monoenergetic photons between 64 and 715 MeV energy, operated at −24°C. The scintillation light was read-out with photomultipliers.

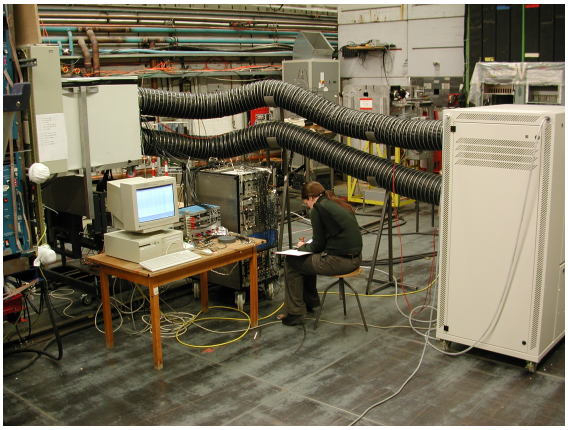

Figure 8.71: The experimental setup at the tagged photon facility comprising the cooling unit (right), the connection pipe to circulate cold dry air and the container for the test detectors (left).

3×3 matrix an improved energy resolution of $\sigma/E = 1.59\,\%/\sqrt{E} + 0.76\,\%$ was achieved but did not lead to the improvement of the resolution at energies below 200 MeV as it was hoped for. The quality of PWO-II crystals and the cooling should improve significantly the statistical term [64].

The temperature stabilization and the operation at low temperatures in an atmosphere free of moisture required the installation of a new experimental set-up, which comprises an insulated container with a large volume to house the different detector arrays with high flexibility. A completely computer controlled cooling machine, which circulates

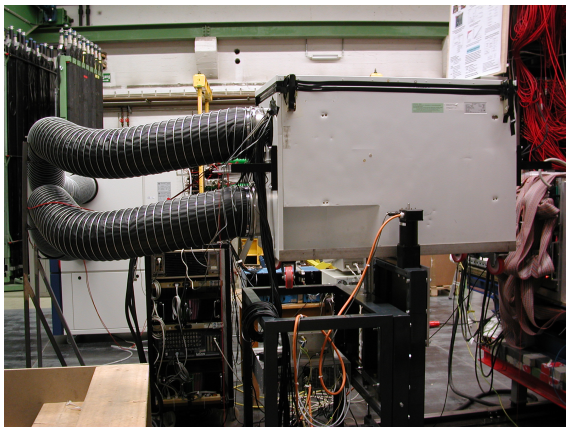

Figure 8.72: The insulated container to house the test detector arrays. The cold air is circulated via the connected two black pipes.

Figure 8.73: The 5×5 PWO matrix shown inside the insulated box including the photomultipliers and read-out cables.

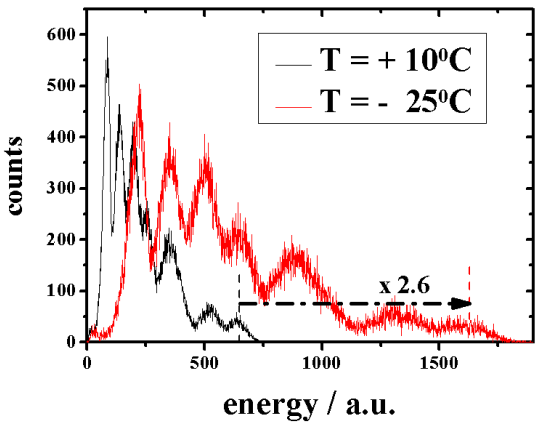

Figure 8.74: Overlay of the response function of the central detector to 8 selected photon energies between 64 and 520 MeV energy. The measurement at two temperatures indicates the gain of light output due to cooling.

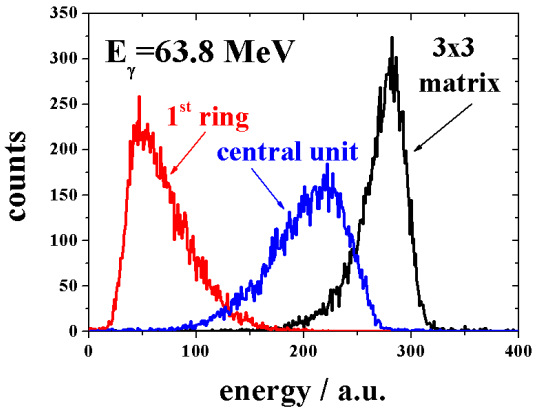

Figure 8.75: Response function of the 3×3 matrix to photons of 63.8 MeV energy measured at $T = -25°C$.

cold and dry air of predetermined temperature, has been purchased adapted to the required needs. It enables detector operation in an experimental volume either inside the machine or external to it by sending cooled gas through thermally insulated 5m long pipes with large diameter. Fig. 8.71, Fig. 8.72 and Fig. 8.73 present the experimental setup at the A2 hall at Mainz behind the CB/TAPS experiment.

In a very recent experiment middle of December 2004 the new set-up has been used to test the first 3×3 array of 200 mm long crystals from BTCP, again read-out via photomultipliers (Philips XP 1911) for comparison. The measurement was performed at $T = 10°C$ and $T = -25°C$, respectively, to show directly the effect of cooling. A very preliminary analysis indicates a break-through in detector development. Fig. 8.74 shows the response of the central detector for 8 different photon energies between 64 and 520 MeV, respectively, for the two operating temperatures. The light-output was measured under identical conditions of the photomultiplier bias and electronics settings and illustrates directly the gain factor of 2.6 of the overall luminescence yield. Fig. 8.75 and Fig. 8.76 show with reduced statistics the lineshape of the central detector, the total energy deposition in the surrounding ring of 8 crystals and the integral of the full array for the two extreme photon energies. The persisting low energy tail indicates the significant shower leakage, which limits the obtained resolution even at the lowest energy. To indicate the presently achievable energy resolution and partly

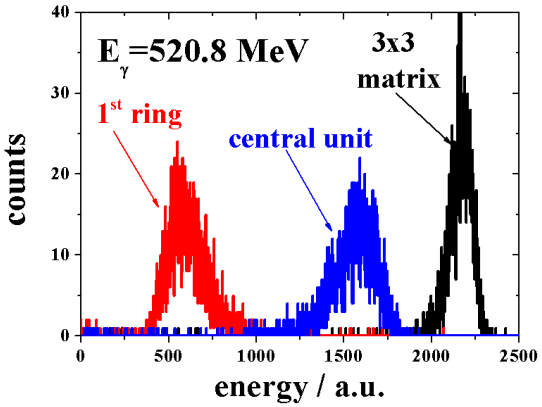

Figure 8.76: Response function of the 3×3 matrix to photons of 520.8 MeV energy measured at $T = -25°C$.

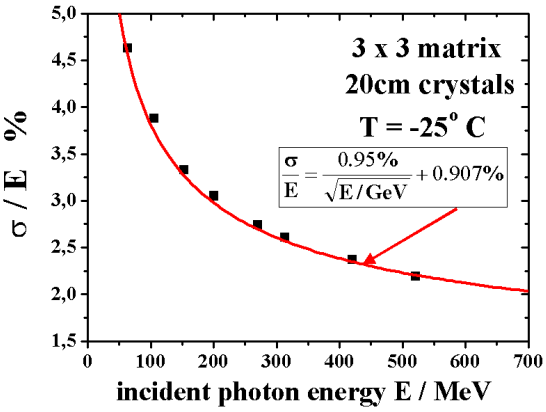

Figure 8.77: Energy resolution of a 3×3 PWO matrix of 200 mm long crystals measured at $T = -25°C$ read out with photomultipliers.

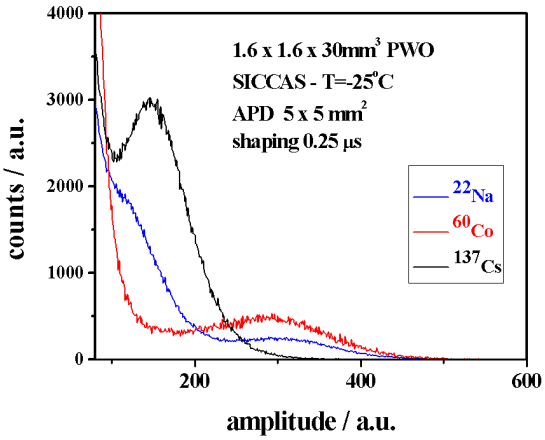

Figure 8.78: Response of a $(16 \times 16 \times 30)\,\mathrm{mm}^3$ PWO-II crystal to low energy γ-rays measured at a temperature of $-25°C$. The scintillation light collected with a $(5 \times 5)\,\mathrm{mm}^2$ APD.

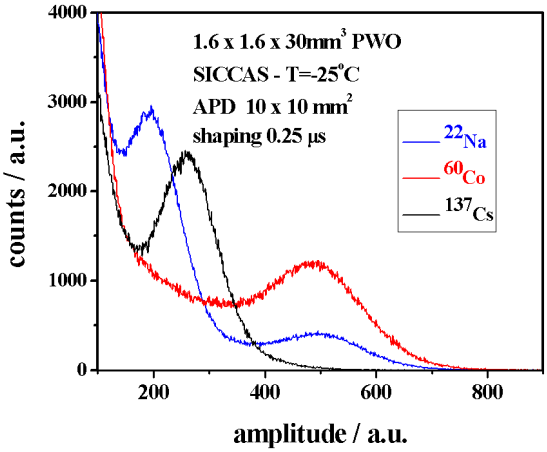

Figure 8.79: Response of a $(16 \times 16 \times 30)\,\mathrm{mm}^3$ PWO-II crystal to low energy γ-rays measured at a temperature of $-25°C$. The scintillation light collected with a $(10 \times 10)\,\mathrm{mm}^2$ APD.

correct for the leakage, the lineshapes have been fitted with a Gaussian. An excellent energy resolution of $\sigma/E = 0.95\,\%/\sqrt{E} + 0.907\,\%$ has been deduced, which represents the best resolution ever measured for PWO (see Fig. 8.77).

In an upcoming experiment it is foreseen to use the full 5×5 matrix and optimize the signal treatment by using the new VME-based TAPS electronics, which can be located close to the detector avoiding any deterioration due to long cables and increased noise pickup.

The operation of the calorimeter inside the solenoid will require a read-out with APDs or equivalent sensors not affected by strong magnetic fields. As outlined in a previous chapter, a new low noise and compact charge sensitive preamplifier has been developed and produced. First tests with small crystals of $(16 \times 16 \times 30)\,\mathrm{mm}^3$ volume and cooled down to $-25°C$ using low energy γ-sources have indicated a clean identification of the photopeak of energies down to 511 keV. Fig. 8.78 and Fig. 8.79 present typical spectra using small $(5 \times 5\,\mathrm{mm}^2)$ or large area $(10 \times 10\,\mathrm{mm}^2)$ APDs coupled to the new preamplifier and further integrated by a commercial Spectroscopic Amplifier with 0.25 μs shaping time.

During the beam test in December 2004 for the first a 3×3 matrix of 150 mm long crystals of PWO-II quality was operated at $T = -25°C$ and completely read-out with $10 \times 10\,\mathrm{mm}^2$ LAAPDs from Hamamatsu. The charge output was collected in

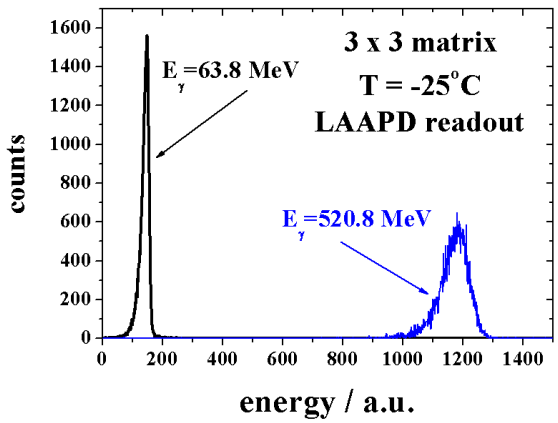

Figure 8.80: Response function of the 3×3 matrix to photons of 63.8 MeV and 520.8 MeV energy measured at $T = -25°$C. The 150 mm long crystals are read-out with LAAPDs.

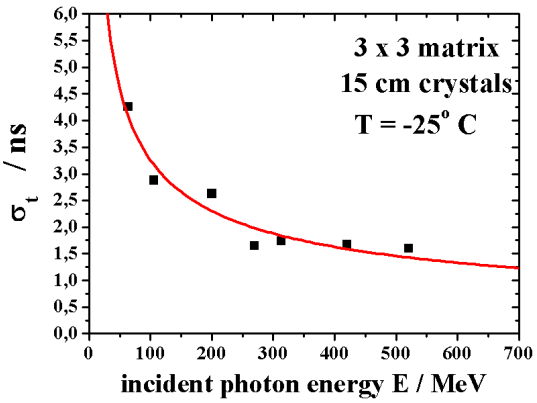

Figure 8.82: Time resolution of a 3×3 PWO matrix of 150 mm long crystals measured at $T = -25°$C read out with LAAPDs.

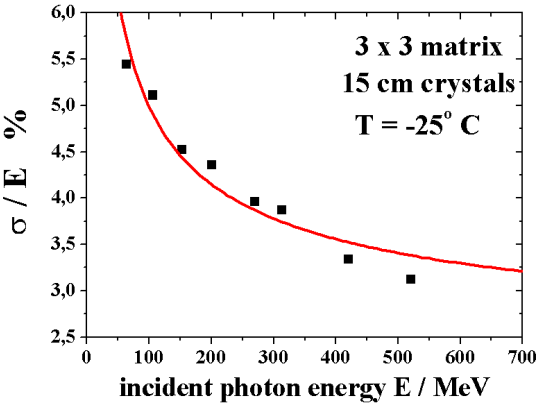

Figure 8.81: Energy resolution of a 3×3 PWO matrix of 150 mm long crystals measured at $T = -25°$C read out with LAAPDs.

the new charge sensitive preamplifier and passively split afterwards as well to integrate the signals in a Spectroscopy Amplifier as to deduce a timing information from a Constant Fraction Discriminator after shaping in a Timing Filter Amplifier (Integration 50 ns, Differentiation 50 ns). Both signals were transferred via 40 m coaxial cables to the DAQ system for digitizing.

In spite of the long transfer lines and the missing remote control and adjustment an excellent preliminary result has been achieved. Fig. 8.80 shows the obtained lineshape at 64 and 520 MeV photon energy, respectively, reconstructed from the electromagnetic shower deposition in the 3×3 array. It should be mentioned that one of the detector modules was not functioning at all. The deduced energy resolution is summarized in Fig. 8.81 and can be parametrized as $\sigma/E = 0.90\,\%/\sqrt{E} + 2.13\,\%$. This very first result is significantly superior to the measurements in the past with photomultiplier read-out operating slightly below room temperature. The low value of the statistical factor reflects the high statistics due to the significantly larger quantum efficiency of the APD. The overall statistics of e/h pairs is superior compared to the number of photoelectrons of the alternatively used photomultipliers. The large constant term can be related to the missing detector, the very preliminary analysis and the used commercial electronics. Therefore, the present status indicates several opportunities for substantial improvements in particular with respect to the treatment of the preamplifier output.

The first attempt to deduce a timing information can give a first impression of the time resolution. In order to identify off-line the photon energies the trigger signal of the responding scintillators of the tagger ladder were measured in coincidence and were recorded. A first estimate of the time resolution for different photon energies can be deduced using these tagger detectors as time reference, which have an intrinsic resolution of approximately 1.2 ns (FWHM). In spite of the by far not optimized timing measurement, a time resolution of < 2 ns can be reached above 200 MeV photon energy even with the present set-up and emphasizes the timing capabilities of PWO.

8.8.2 Position Resolution

The point of impact of the impinging photon can be reconstructed from the center of gravity of the

electromagnetic shower distributed over the cluster of responding detector modules. The experimental tests described in the previous section will provide in the further analysis detailed results on the achievable position resolution.

Based on experiments in the past with detector arrays of identical geometry but inferior crystal quality a position resolution of $\sigma < 2\,\text{mm}$ appears feasible [3], slightly depending on the reconstruction algorithm and assuming a final detector cross section and modularity similar to the present crystal shapes of $20 \times 20\,\text{mm}^2$ front face.

8.8.3 Particle Identification

The capabilities of particle identification, such as the different cluster size of detector modules responding to hadron or photon/electron induced events, have not been investigated recently. In previous experiments with 2.1 GeV proton induced reactions at COSY [63] a clean separation of hadrons and photons was possible even in a sub-array of 5×5 units. Further simulations and test measurements are foreseen in the near future. Due to the expected fast response sharp and selective coincidences with the other detector components of $\overline{\text{P}}$ANDA will provide additional criteria for particle identification and discrimination.

8.9 Organization and Responsibilities

The research and development of the electromagnetic calorimeter covering the target area has been focusing so far on the basic components, i.e. the scintillator material and the photosensors most likely to be used. A very active collaboration comprising 11 institutions has been formed so far. This collaboration is concentrating on the calorimeter aspects, and meetings are scheduled on a regular base both at and in between the general $\overline{\text{P}}$ANDA meetings.

The fields of interests are primarily given by the expertise and ongoing research programme at these institutions such as experimental activities at GSI or the operation of large scale experiments such as BaBar, TAPS/Crystal Ball/Crystal Barrel at several accelerator facilities. The future organization of the R&D and the final construction will be closely correlated to the present activities. It will, however, also strongly depend on the final funding from the national agencies for the institutions. In addition, we expect further groups to be joining the activity with special preferences in the future.

Presently, the main R&D activities are:

1. mechanical design and construction,
2. development of full size prototypes,
3. development and test of PWO crystals,
4. radiation hardness and defects in scintillators,
5. development of BGO crystals,
6. development of APDs,
7. development of alternative sensors,
8. development of FE electronics,
9. development of read-out electronics,
10. development of monitoring and quality control of crystals,
11. development of quality control of sensors,
12. simulations.

8.9.1 Institutional Responsibilities

The responsibilities are not strictly assigned to certain institutions, but several groups may collaborate in certain aspects but develop other topics separately. In Table 8.8 the currently involved institutions and their responsibilities are listed. This is including some activities, which are due to be started very soon in 2005 and where the participation is confirmed by the corresponding institution.

8.10 Planning

In Fig. 8.83 is shown the detailed timeline for the development phase, the production and commissioning of the central part of the electromagnetic calorimeter.

institution	activities						
University Basel	3	8	12				
GSI Darmstadt	1	2	8	9	12		
Ruhr University Bochum	5	6	8	9	11	12	
University Frankfurt	6	11					
Justus-Liebig-University Gießen	1	2	4	6	7	8	12
Forschungszentrum Jülich	7	12					
RINP Minsk	3	4	10				
SINS Warsaw	3	6	12				
Uppsala University	3	12					
University Valencia	3	7	12				
IPN Orsay	1	2	3	12			

Table 8.8: Institutions currently involved in the above listed activities (Sec. 8.9).

8.11 Forward Electromagnetic Calorimeter

8.11.1 Introduction

Photon and electron detection with high efficiency and high resolution is essential for the reconstruction of many of the discussed benchmark channels (see Sec. 2). In the forward region a Shashlyk-type calorimeter can meet those requirements at comparably moderate costs. These modules typically consist of layers of lead and scintillators sandwiched together subsequently. A characteristic feature of the Shashlyk design is the readout by wave length shifting (WLS) fibers passing through holes in the scintillator and lead layers. The various types existing may differ in the mechanical design and the optical properties of scintillators and fibers. The technique, however, is well established. It was successfully used in E865 at Brookhaven [65] and it has been adopted or is being considered by other experiments, like PHENIX [66], HERA-B [67], and LHCb [68]. The calorimetry in the new experiment KOPIO [69, 70] at BNL is also based on a Shashlyk-type EMC. Its properties were essentially improved during dedicated R&D studies [71]. The E865 Shashlyk module reached an energy resolution of $8\,\%/\sqrt{E}$, and a new prototype module which has been constructed for KOPIO achieved an energy resolution of even $4\,\%/\sqrt{E}$ [69].

8.11.2 Requirements

The forward EMC is located at a distance of 7 m downstream of the target. The face area is rectangular and is determined by the angular acceptance of the FS defined by the aperture in the Forward Spectrometer Dipole Magnet which is $\pm 5°$ and $\pm 10°$ in the vertical and horizontal plane respectively. Thus the area that must be covered by the forward EMC is about $3\,\mathrm{m}^2$ and it has the dimensions $L_y = 122\,\mathrm{cm}$ and $L_x = 247\,\mathrm{cm}$ in vertical and horizontal direction respectively. With the module size of $11\,\mathrm{cm} \times 11\,\mathrm{cm}$, this area is covered by an EMC with 11 rows and 23 columns. We add additionally 2 rows and 4 columns (1 and 2 on top and bottom and each side respectively) to handle the showers on the periphery of the calorimeter. Thus the forward EMC consists of $13 \times 27 = 351$ modules in total. The total depth of the forward EMC is $\approx 70\,\mathrm{cm}$ plus the size of the photon detector. The parameters which would fulfil the physics requirements are summarized in Table 8.9.

Energy resolution	$0.5\,\% \oplus 4\,\%/\sqrt{E}$
Time resolution	$< 100\,\mathrm{ps}/\sqrt{E}$
Active depth	$\sim 20\,X_0$
Photon detection inefficiency	$< 10^{-4}$
Granularity	$\sim 10\,\mathrm{cm} \times 10\,\mathrm{cm}$
Active area	$\sim 3\,\mathrm{m}^2$

Table 8.9: Parameters required for the forward EMC from the physics point of view.

8.11.3 Considered Solutions

Due to the relatively large dimensions of the Forward EMC, a compromise between the energy resolution and the cost has to be reached. Two solutions – (i) a lead-glass calorimeter such as for example the LEDA calorimeter from the CERN WA98

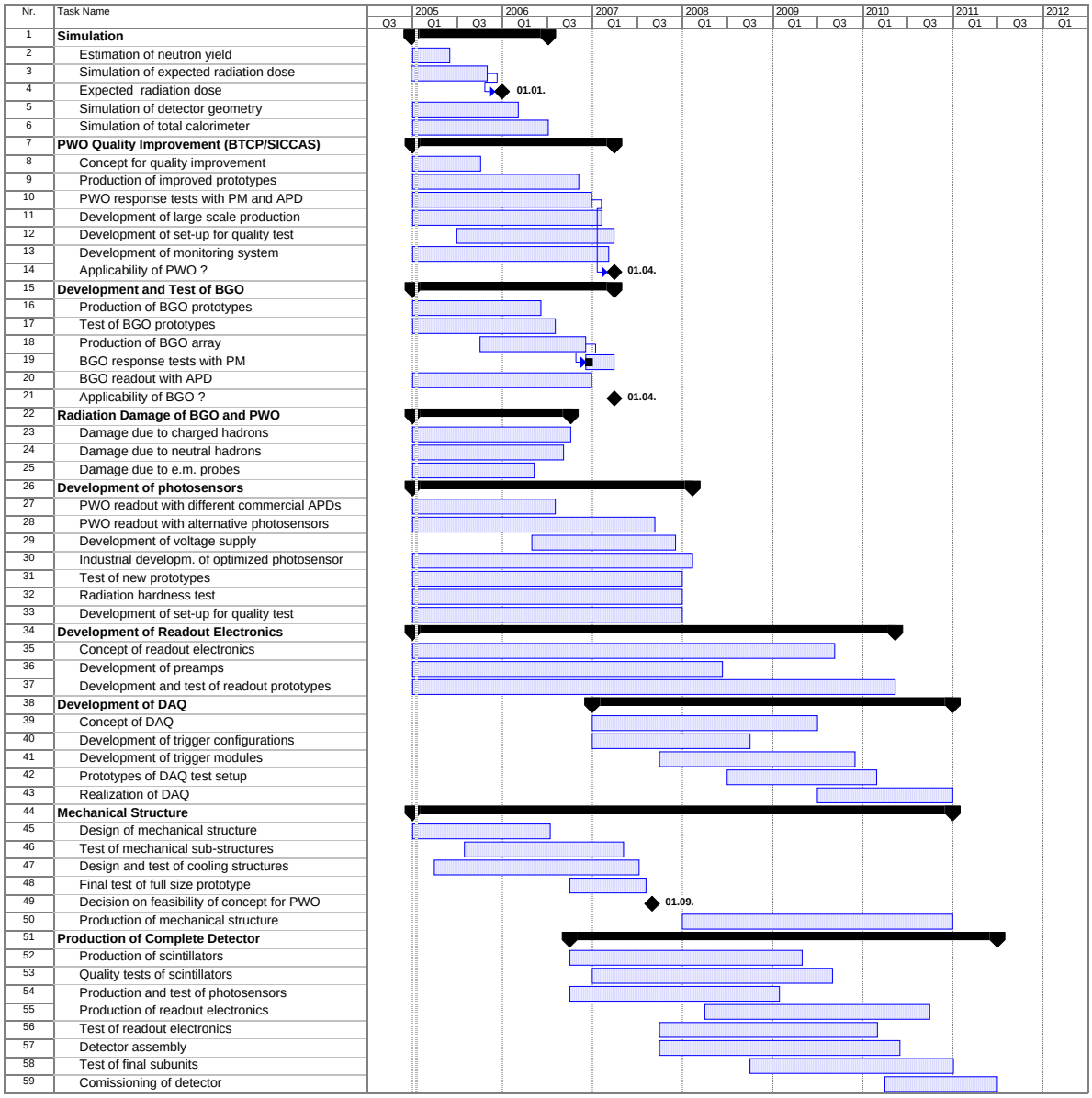

Figure 8.83: Timeline for the EMC.

experiment [72] and (ii) a Shashlyk calorimeter of the KOPIO type – seem to be optimal in this respect. They offer much better resolution than traditional sampling calorimeters such as for example the MIRAC[1] type. Both are about an order of magnitude cheaper than high resolution calorimeters build e.g. from PWO or CsI, and their resolution is only about a factor of two worse than those.

In order to check the rate of aging of the lead-glass and Shashlyk calorimeters in the high particle flux expected at the forward EMC, we performed simulations. The response to products of the $\overline{\mathrm{p}}\mathrm{p}$ reactions induced by a 10 GeV/c antiproton beam was studied. The largest energy deposits appear in the most central modules of the calorimeter (see Fig. 8.84). The longitudinal energy deposits in 65 cm long modules of the lead-glass calorimeter and in 70 cm long Shashlyk modules are shown in Fig. 8.85. In both cases the maximum occurs at a depth of about 20 cm corresponding roughly to $7X_0$. The radiation dose expected for one year of a continuous measurement at a $\overline{\mathrm{p}}\mathrm{p}$ interaction rate of $2 \cdot 10^7\,\mathrm{cm}^{-2}\mathrm{s}^{-1}$ is 2.8 krad for the central modules of the lead-glass calorimeter and 2.4 krad for the scintillator plates in the corresponding modules of the Shashlyk calorimeter. This level of radiation doses causes serious losses of transparency in typical

1. This type is described in detail in Sec. 8.12.

led-glasses such as TF1 [73], but is still acceptable for organic scintillators [74]. Therefore, we chose the Shashlyk type as the optimal solution for the forward EMC.

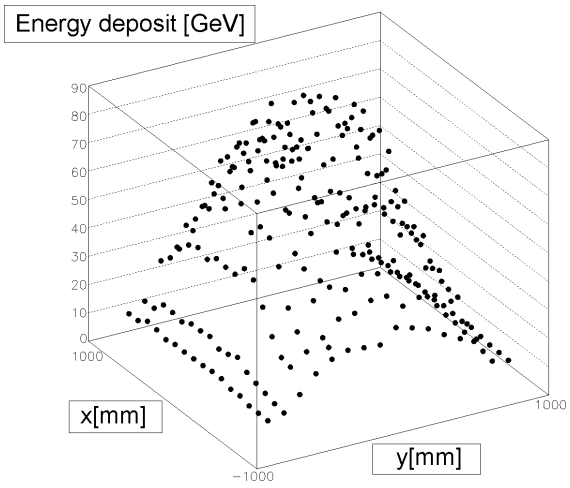

Figure 8.84: Energy deposit in the forward calorimeter as a function of the lateral coordinate (horizontal and vertical x and y respectively) from 10 000 simulated events. Used were $\overline{\mathrm{p}}\mathrm{p}$ reaction products induced from incident 10 GeV/c antiprotons.

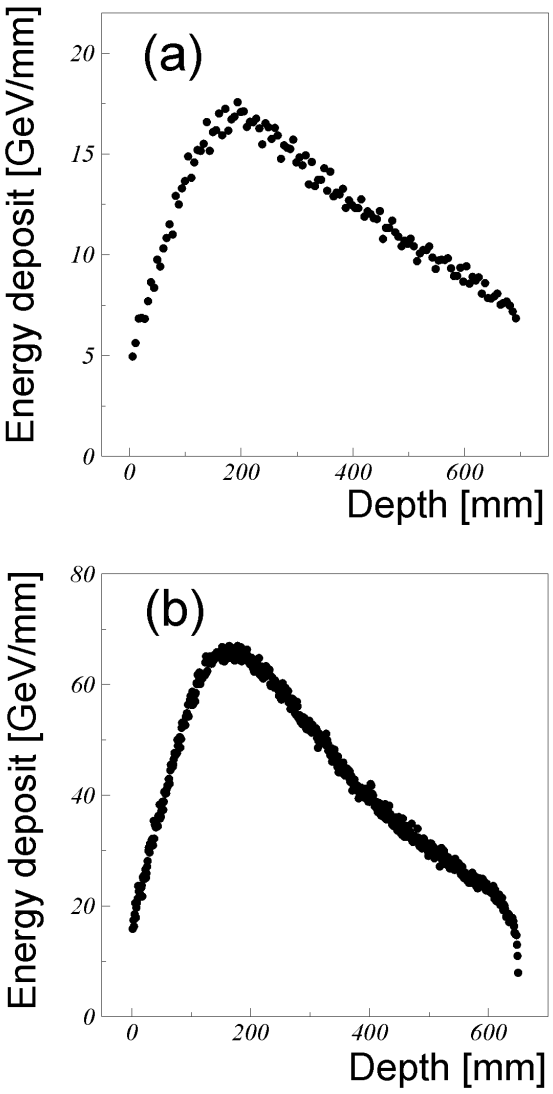

Figure 8.85: Longitudinal energy deposit in scintillation plates of a Shashlyk calorimeter (a) and in a lead-glass calorimeter (b). Simulated 10 000 events from $\overline{\mathrm{p}}\mathrm{p}$ reaction products induced from incident 10 GeV/c antiprotons were used.

8.11.4 Single Module Parameters

A view of a Shashlyk module is shown in Fig. 8.86. A new scintillator based on the BASF143E$^{\mathrm{TM}}$ polystyrene was manufactured at IHEP, Protvino. The most important property of the new scintillator tiles is a high efficiency of the light reflection from the surface of the scintillator of about 97 %. The parameters are listed in Table 8.10 for two versions of the KOPIO type and for the version suggested for $\overline{\mathrm{P}}$ANDA. The KOPIO versions achieve an energy resolution of $4.0\,\%/\sqrt{E}$ and $2.9\,\%/\sqrt{E}$ respectively.

8.11.5 Mechanical Setup

The module is a sandwich of stamped lead and polystyrene-based scintillator plates (see Fig. 8.87). The lateral size of a module is 110 mm × 110 mm; the thickness of plates is 0.275 mm for the lead tile and 1.5 mm for the scintillator tile. Each plate has 144 equidistant holes in a 12 × 12 matrix with the spacing between holes of 9.5 mm. The diameter of the holes is equal to 1.3 mm.

72 WLS fibers are inserted into these holes. The fibers do not end at the front of the module but is bend back there, such that both ends of a fiber are connected to the PMT. Such a loop (radius ∼ 3 cm) can be considered as a mirror with the reflection coefficient of about 90 %. The fiber ends are collected in one bunch, glued, polished, and connected to the PMT.

To increase the light collection, 60 mm of perforated white reflecting paper is put between lead and scintillator plates, and the edges of scintillator plates are aluminized as well. The complete stack of the all plates is compressed by four 50 mm stainless steel strips that are pre-tensioned and welded to both front and back end caps.

	KOPIO-1999 [69]	KOPIO-2004 [71]	$\overline{\text{P}}$ANDA
Radiation depth	$15.9\,X_0$	$15.9\,X_0$	$20\,X_0$
Lateral dimensions	$(110 \times 110)\,\text{mm}^2$	$(110 \times 110)\,\text{mm}^2$	$(110 \times 110)\,\text{mm}^2$
Scintillator thickness	1.5 mm	1.5 mm	1.5 mm
Scintillator material	NE110	IHEP scint.	IHEP scint.
Gap between scintillator tiles		0.350 mm	0.350 mm
Lead absorber thickness	0.350 mm	0.275 mm	0.275 mm
Number of absorber layers	240	300	378
Number of WLS fibers per module	72	72	72
Length of WLS fibers per module		108 m	136 m
Hole diameter (lead/scint.)	1.5 mm/1.4 mm	1.3 mm	1.3 mm
Diameter of WLS fiber Y11-200MS	1.0 mm	1.0 mm	1.0 mm
Fiber bundle diameter	14.0 mm	14.0 mm	14.0 mm
External wrapping (TYVEK$^{\text{TM}}$) thickness	$2 \times 60\,\mu$m	$150\,\mu$m	$150\,\mu$m
Effective radiation length, X_0	31.5 mm	34.9 mm	34.9 mm
Effective Moliere radius, R_M	54.9 mm	59.8 mm	59.8 mm
Effective density	$2.75\,\text{g/cm}^3$	$\approx 2.7\,\text{g/cm}^3$	$\approx 2.7\,\text{g/cm}^3$
Active depth	473 mm	555 mm	698 mm
Total depth (without photo-detector)	610 mm	650 mm	793 mm
Total weight		18 kg	22.5 kg
Photodetector	APD	APD	PMT
Energy resolution	$4.0\,\%/\sqrt{E}$	$2.9\,\%/\sqrt{E}$	$4.0\,\%/\sqrt{E}$
Time resolution	$\approx 100\,\text{ps}/\sqrt{E}$	$90\,\text{ps}/\sqrt{E}$	$\approx 100\,\text{ps}/\sqrt{E}$

Table 8.10: Relevant parameters of Shashlyk type calorimeters. The right column shows the suggested solution for $\overline{\text{P}}$ANDA with a depth of $20\,X_0$.

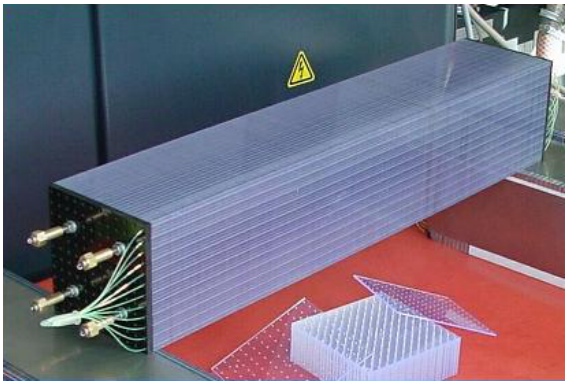

Figure 8.86: View of a single Shashlyk module [75].

8.11.6 Simulation

In order to optimize the Shashlyk parameters such as the thickness of the lead absorbers we simulated its performance using the GEANT4 package. In the simulations, the response of the calorimeter to a pencil-like beam of photons with energies up to 10 GeV has been investigated. In order to optimise combination of scintillators and lead tiles simulations were performed for four setups corresponding to four different values of the lead absorbers thickness specified in Table 8.11. For that reasonable values for the thickness of the scintillator layers and total calorimeter thickness were set to 1.5 mm and $20\,X_0$ respectively.

The photon energy was reconstructed by summing up energy deposits in adjacent modules. Only deposits exceeding the threshold of 15 MeV in a single module were taken into account. The sum was then multiplied by a calibration factor accounting for the fact that only part of the total energy of the particle is deposited in the scintillators. The calibration factor varies with energy as shown in Fig. 8.88. This factor was parametrized by a function $aE \times (b + cE)^{-d}$ where E denotes the energy deposit and a, b, c, d are parameters fitted to the data. A sample spectrum of the reconstructed energy for 1 GeV photons is shown in Fig. 8.89.

The energy resolution $\sigma(E)/E$ was determined in terms of σ for a Gaussian function fitted to the energy deposit measured (see e.g. Fig. 8.90. The energy resolution was parametrized using the function:

$$\frac{\sigma(E)}{E} = A + \frac{B}{\sqrt{E[\text{GeV}]}}\,, \qquad (8.3)$$

where E is the photon energy and the parameters

	Setup 1	Setup 2	Setup 3	Setup 4
Scintillator thickness	1.5 mm	1.5 mm	1.5 mm	1.5 mm
Lead absorber thickness	0.150 mm	0.200 mm	0.275 mm	0.400 mm
Number of absorber layers	654	506	378	266
Active depth	1 125 mm	896 mm	698 mm	524 mm

Table 8.11: Setups used to simulate the optimal configuration of the scintillator-lead layers.

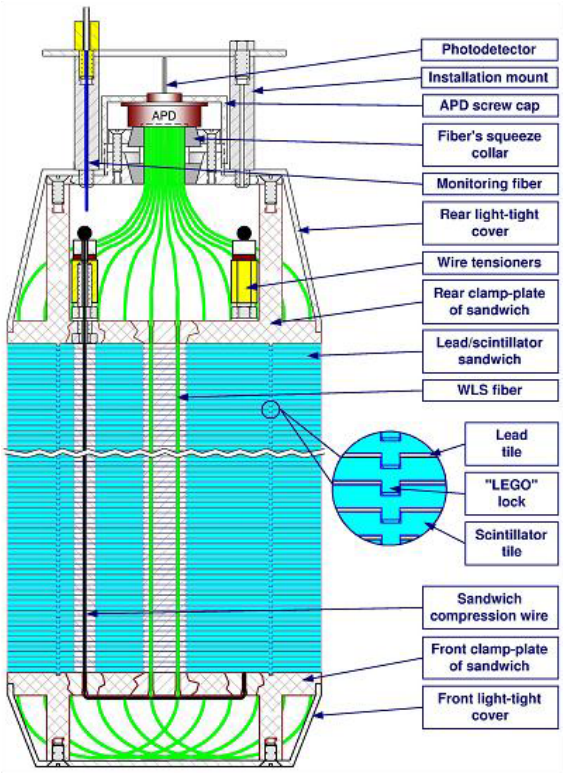

Figure 8.87: Design sketch of a Shashlyk module [75].

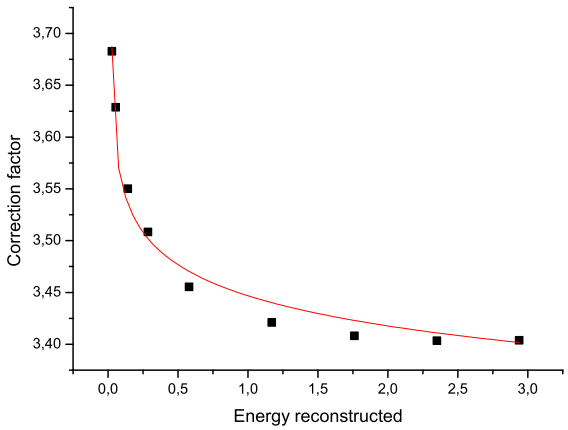

Figure 8.88: Energy dependence of the calibration factor for setup 3. The solid line indicates the fitted function (see text).

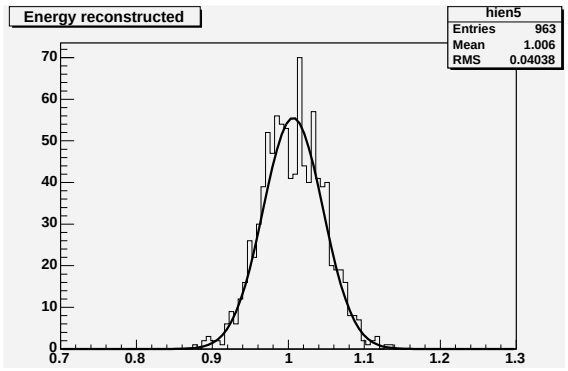

Figure 8.89: Reconstructed energy for 1 GeV photons.

A and B are fitted and their results given in Table 8.12.

	Setup 1	Setup 2	Setup 3	Setup 4
A	0.26 %	0.37 %	0.33 %	0.2 %
B	2.5 %	2.7 %	3.4 %	4.7 %

Table 8.12: Results for the parameters A and B when fitting the function in Eq. 8.3 to the energy distributions for mono-energetic photons as shown in Fig. 8.89.

Taking into account these results and cost estimates based on the amount of scintillator material needed, we consider setup 3 as an optimal solution. It provides a significantly improved energy resolution compared to setup 4 at a still affordable number of layers (see Table 8.11).

Test measurements with the KOPIO-2004 [71] calorimeter (see Table 8.10) were done using the LEGS setup and the photon beam at Brookhaven NSLS. The energy resolution was measured for two prototypes. The photon beam was directed to the centre of the arrays of 9 modules. The results are shown in Fig. 8.91. For the APD with wave form digitizer (WFD) readout, the fit gives:

$$\sigma(E)/E = (1.96 \pm 0.1)\% \oplus \frac{(2.74 \pm 0.05)\%}{\sqrt{E[\mathrm{GeV}]}} \,. \quad (8.4)$$

The latest KOPIO beam tests with 0.2-2.0 GeV/c

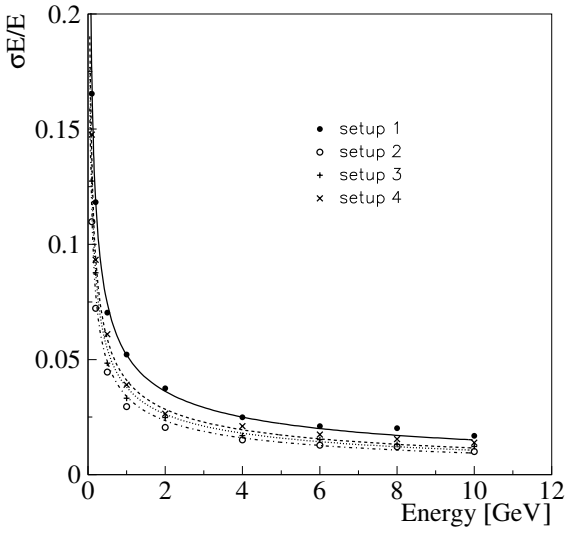

Figure 8.90: Energy dependence of the energy resolution for the four different setups (points and crosses as indicated in the figure). The functions (see Eq. 8.3) fitted to the data are shown as lines and the parameters obtained listed in Tab. 8.12.

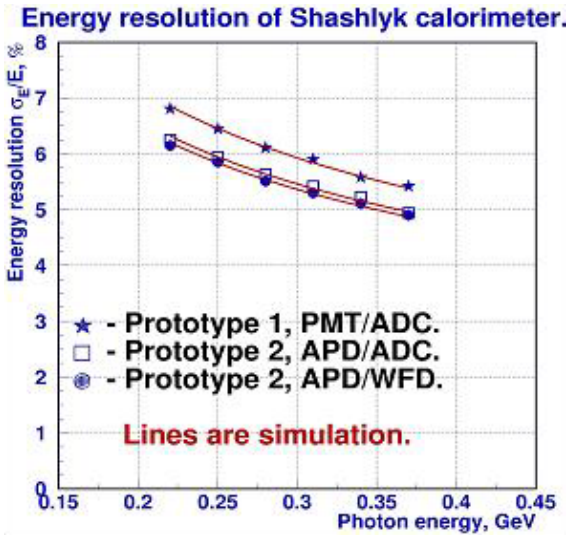

Figure 8.91: Energy resolution *versus* photon energy for a KOPIO type Shashlyk calorimeter using several readout options [75].

positrons were reported recently [75] for a prototype consisting of 33 modules. The results of the measurements performed for four types of light collection systems are shown in Fig. 8.92 together with the used parametrisations. A GEANT calculation in the limit of sampling and geometry alone is also shown. The best result was obtained for a Shashlyk structure made of 300 layers of 1.5 mm thick scin-

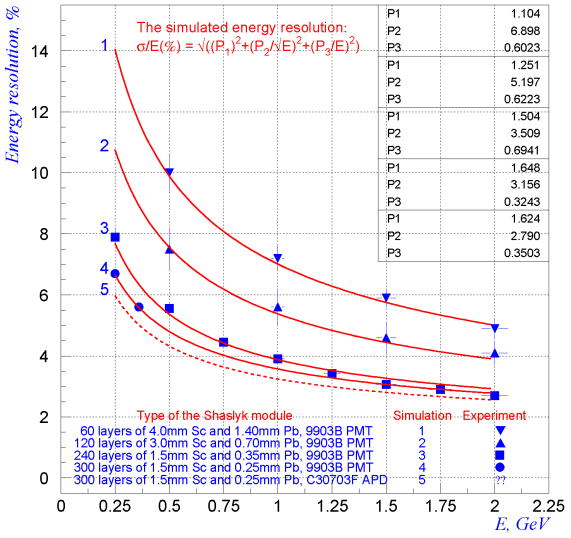

Figure 8.92: Energy resolution for an array of 9 modules *versus* momentum of the electron beam [75].

tillators and 0.25 mm thick lead absorbers. At an energy of 1 GeV, the energy resolution is then 3.5 %.

Time Resolution and Threshold Detailed time resolution studies of the Shashlyk modules were made by the PHENIX collaboration [66]. For 1 GeV electrons, the time resolution and the light yield was measured to be 100 ps and 1200 photoelectrons respectively. For the improved module designed at KOPIO, the experimental light yield was 3100 photoelectrons at 1 GeV. Since the time resolution is inversely proportional to the square root of the light yield, one can expect a time resolution of about $50\,\mathrm{ps}/\sqrt{E}$.

The detection threshold which has been obtained so far in tests with 4 MeV electrons is equal to 40 photoelectrons.

8.11.7 Prototyping and R&D Work

The prototype calorimeter is a block of 3×3 modules with an active depth of $22\,X_0$. The R&D programme includes beam testing at various electron energies and, in particular, in the energy range of a few GeV. In this energy range, the beam tests can be done at IHEP, Protvino. The EMC response at energies less than 1 GeV could be examined in Mainz.

We plan to test the performance with different types of PMT and readout components. The block of modules will be exposed to electron beams to study

temperature dependencies and leakage effects. The leakage of the initial electron energy and its influence on the energy resolution will be examined at different values of longitudinal thickness for modules in the range of $20\,X_0$ to $22\,X_0$.

Various design and geometry options will be studied for optimizing homogeneity and testing a prototype of the calorimeter modules. The duration of the R&D work is planned to be 24 months. The R&D specifications are given in the following.

8.11.8 Realization

Timelines and Milestones. The timeline of the Shashlyk project is summarised in Fig. 8.93. A first period of simulation studies will be made partially in the framework of the Shashlyk R&D work and in the framework of the overall $\overline{\mathsf{P}}$ANDA tracking. The R&D studies will relate to the uniformity and to the improvement of energy and time resolutions. To achieve optimised parameters for the experimental energy range, a comparison will be made for the performance of test modules equipped with several types of PMTs. A test device consisting of 3×3 Shashlyk modules will be constructed. The work load concerning simulations, R&D studies and tests will be shared between the institutes IHEP and JU in Cracow. The modules will be produced and equipped at IHEP, Protvino.

Responsibilities. The responsibilities are shared for the Shashlyk forward EMC for the Institute for High Energy Physics, Protvino, Russia (IHEP) and Jagellonian University, Cracow, Poland (JU) as given in Table 8.13.

8.12 Forward Hadron Calorimeter

8.12.1 Introduction

The antineutrons originating from $\overline{\mathrm{p}}\mathrm{p}$ reactions are mostly emitted at small angles with respect to the antiproton beam. Estimations made on the basis of the Dual Parton Model [76] indicate that for beam momenta larger than $5\,\mathrm{GeV}/c$ more than 50 % of antineutrons are confined in the solid angle of the forward spectrometer (see Fig. 8.94). In order to measure energies of antineutrons, but also of neutrons and of neutral kaons K_L, we plan to set up a hadron calorimeter (HC) as a component of the forward spectrometer.

The calorimeter, will be also used for a fast triggering on reactions with forward scattered hadrons. For the beam momentum above $6\,\mathrm{GeV}/c$ the rate of reactions with at least one neutral hadron reaching the HC is roughly one third of all reactions as it is shown in Fig. 8.95.

In addition, the hadron calorimeter will serve as an active filter for muons emitted in the forward direction. For this purpose, the information about the energy loss in the calorimeter will be used in addition to the information in the dedicated muon counters behind.

For the hadron calorimetry we plan to refurbish and adopt the mid-rapidity probing calorimeter (MIRAC) from the WA80 experiment. In the next four sections a description of the expected MIRAC performance, a plan of adaptation of this calorimeter to the $\overline{\mathsf{P}}$ANDA needs, and the foreseen realization of this plan is given.

8.12.2 MIRAC Calorimeter

8.12.2.1 Mechanical Setup

The MIRAC calorimeter is described in details in Ref. [77] and consists of 30 independent modules. A view and cross section of a single module is shown in Fig. 8.97 and a picture of a forward part of the module with removed housing is presented in Fig. 8.96.

Such a module has a cross section of $(22 \times 120)\,\mathrm{cm}^2$ and consists of an electromagnetic part and a hadronic part using stacks of scintillators with lead and steel respectively. The electromagnetic part contains 27 layers of 3 mm thick lead plates sandwiched between two 0.8 mm thick aluminum sheets and interlaced with 3.2 mm thick scintillator plates. The total thickness of the electromagnetic part is 22 cm which corresponds to 15.6 radiation lengths. The hadronic section consists of 119 stainless steel plates, each 8 mm thick, interlaced with 3.2 mm thick scintillator plates. The depth of the hadronic section is about 1.4 m which corresponds to more than 6 absorption lengths. In order to assure uniform light distribution in the scintillators a sheet of white Mylar is placed on each side of every scintillator. The main parameters for an original MIRAC module are listed in Table 8.14. The relative energy resolution for electromagnetic shower is $0.014 \oplus 0.11/\sqrt{E[\mathrm{GeV}]}$ and for hadronic shower is $0.034 \oplus 0.34/\sqrt{E[\mathrm{GeV}]}$. Due to a poor energy resolution of the electromagnetic part, only the hadronic part is planned to be used in the $\overline{\mathsf{P}}$ANDA setup.

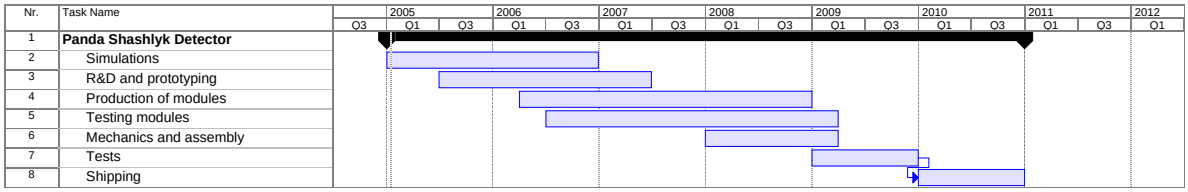

Figure 8.93: Timeline of realizing the forward Shashlyk EMC.

1.	Simulations	–	JU Cracow, IHEP Protvino,
2.	R&D and prototyping	–	IHEP Protvino, JU Cracow,
3.	Production and assembly of modules	–	IHEP Protvino,
4.	Beam tests	–	IHEP Protvino, JU Cracow,
5.	Mechanics, assembly	–	IHEP Protvino.

Table 8.13: Activities and responsibilities for the Shashlyk-type forward EMC.

Electromagnetic section	
Number of absorber plates	27
Size of absorber plates	$1200\,\text{mm} \times 205\,\text{mm} \times (0.8\,\text{mm}\ Al + 3\,\text{mm}\ Pb + 0.8\,\text{mm}\ Al)$
Number of scintillator plates	27
Size of scintillator plates	$1199 \times 206 \times 3.2\,\text{mm}^3$
Depth of electromagnetic section	224 mm
Number of radiation lengths	15.6
Hadronic section	
Number of steel plates	119
Size of steel plates	$1200 \times 198 \times 8\,\text{mm}^3$
Number of scintillator plates	119
Size of scintillator plates	$1199 \times 200 \times 3.2\,\text{mm}^3$
Depth of hadronic section	1390 mm
Number of absorption lengths	6.1

Table 8.14: Main parameters of a MIRAC module.

8.12.2.2 Optical Readout and Electronics

The scintillator used in the MIRAC calorimeter is PS-15A based on the polymethylmethacrylate (PMMA) with a 15 % naphtalene and 1 % butyl-PBD admixture. The scintillator plates are read out from both sides through twelve wave length shifters (WLS), six on the left and six on the right side of every module. The width of a WLS is 20 cm and they are placed one above the other, building a six level tower in height within one the module (see Fig. 8.97). In this way the optical readout divides the module in six independent sub-modules. Adjacent WLSs are separated by thin aluminum strips to improve the light collection and reduce light leaking into neighbouring sub-modules to the 5 % level. The BBQ (benzimidazo-benzisoquinoline-7-1) doped acrylic WLS were chosen, because its absorption spectrum matches well the emission spectrum of the PS-15A scintillator. The ends of WLSs opposite to the photo-tube were coated with a TiO_2-loaded epoxy to minimize the attenuation of light along the WLS. To assure a good light collection in the photo-tubes the WLS should be thick enough. On the other hand it should be sufficiently thin in order to reduce the effect of Cherenkov light produced by charged particles. As a compromise, 3 mm thick WLSs were chosen. Every ≈ 140 cm long WLS is separated from the edges of the module by two 1 mm diameter fishing lines, and is coupled to the photo-tube through a light guide.

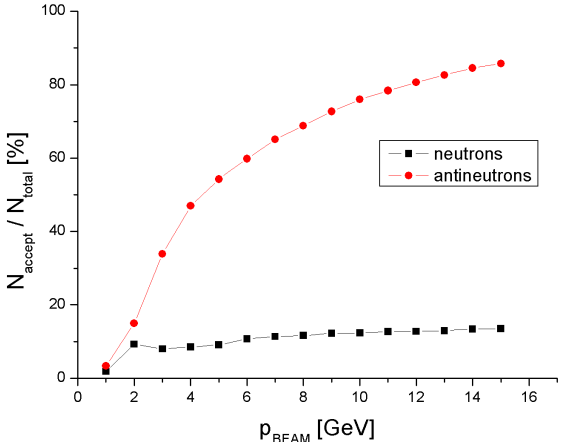

Figure 8.94: Percentage of neutrons and antineutrons accepted in the forward spectrometer as a function of beam momentum.

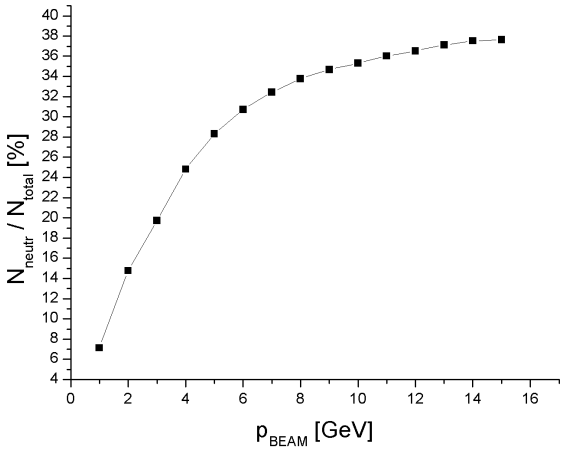

Figure 8.95: Percentage of reactions with at least one neutral hadron in the forward spectrometer acceptance.

8.12.3 Simulations on the Performance

8.12.3.1 Energy resolution

In order to optimize the HC thickness we performed "fast" simulations using the GEANT4 package. In the simulations, the HC setup was simplified in the way that every module had a rectangular shape with a cross section of 20 cm × 20 cm. The response of the calorimeter to a pencil-like beam of neutrons, protons and antineutrons was investigated for different numbers of layers of an absorber-scintillator sandwich in the range from 70 to 150. The energy was reconstructed by summing up energy deposits exceeding the threshold of 200 MeV in a single module. The sum was taken over firing modules forming continuous clusters and was multiplied by a calibration factor, taking into account the fact that only part of particle's energy ($\sim$ 4 %) is deposited in the scintillators. Sample energy spectra in the HC consisting of 120 layers are given in Fig. 8.98

The energy resolution was determined in terms of σ from a Gaussian function fitted to the energy deposit histogram. For protons, neutrons and antineutrons with momenta of 10 GeV/c, corresponding to an energy of 9 GeV, σ is of about 1.4 GeV and is in agreement with the value of 1.3 GeV obtained from a parametrization given in Ref. [77]. The energy resolution for 10 GeV/c antineutrons as a function of the calorimeter thickness is shown in Fig. 8.99.

For a thickness in the range of 100–150 layers the energy resolution changes only slightly while for a smaller thickness the resolution becomes significantly worse. Thus we come to the conclusion, that the thickness of the hadronic part of MIRAC can be reduced from 119 layers, used currently at WA80, to 100 layers at $\overline{\text{P}}$ANDA without essential deterioration of the energy resolution. This is also favourable due to the restrictions on the longitudinal extension of the forward spectrometer.

8.12.3.2 Hadron Detection Efficiency

The detection efficiency of the calorimeter was determined as a ratio of the number of events with exactly one cluster reconstructed to the number of all simulated events. This efficiency is roughly the same for neutrons, antineutrons and protons and amounts to about 80 %–90 %. Worse efficiency is obtained for high energy particles due to a higher energy leakage out of the clusters. The efficiency depends on the applied energy threshold but nearly does not change with the calorimeter thickness. A small threshold improves the efficiency for low energetic particles, but it leads to a reduction of the efficiency at high energies due to an increased number of "split-offs" from the clusters. As a compromise we select an energy threshold of 200 MeV.

8.12.3.3 Muon Filter

The hadron calorimeter will be used in combination with muon counters for an active muon filtering. This will allow for much better identification of muons compared to the case of a passive filter made of an absorber block. The active filtering will use the energy deposit in the calorimeter for distinguishing between muons reaching the muon counters and charged hadrons producing sec-

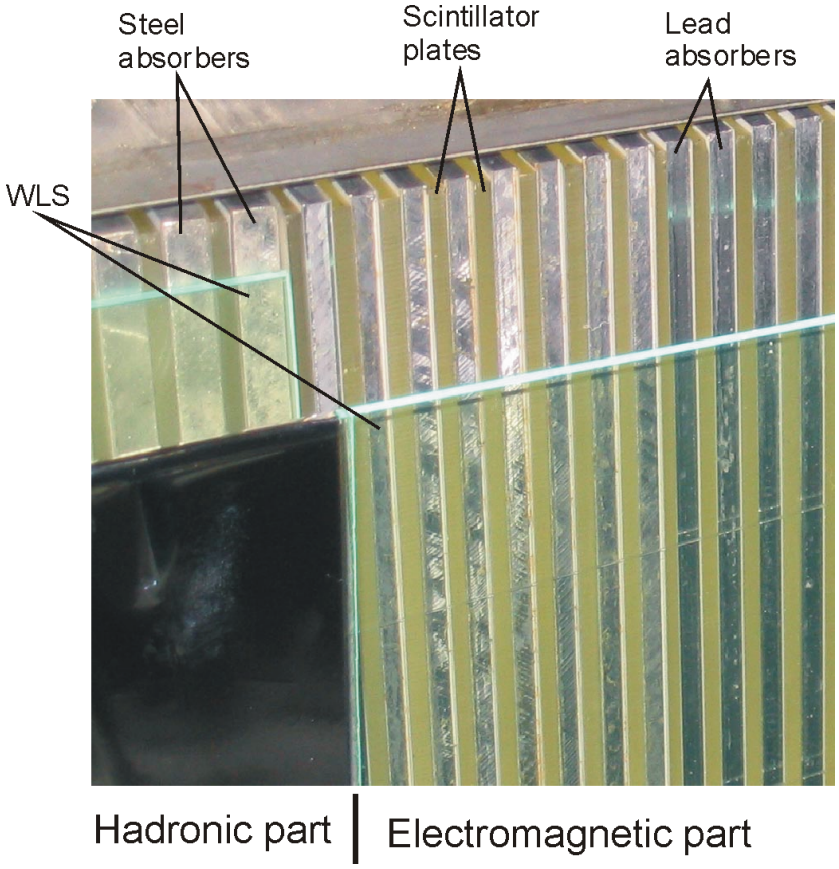

Figure 8.96: Photography of a forward part of the MIRAC module.

ondary particles, which may also reach those counters. The percentage of muons reaching the muon counters is given in Table 8.15 for several muon momenta and varying calorimeter thickness. For the considered thickness of 100 layers about 94 % of 3 GeV/c muons passes through the calorimeter and for 4 GeV/c muons the transparency of the calorimeter is close to 100 %.

Number of layers	2 GeV/c	3 GeV/c	4 GeV/c
70	91.4 %	99.8 %	100 %
100	85.2 %	94.6 %	99.7 %
120	83.3 %	89.0 %	99.9 %
150	72.7 %	90.1 %	98.3 %

Table 8.15: Transparency of the HC for 2, 3 and 4 GeV/c muons μ^+ for 70 to 150 layers of MIRAC modules.

The mean energy deposit of muons linearly decreases with decreasing calorimeter thickness (see Fig. 8.100) and, therefore, for a thinner calorimeter the energy window for muon detection will be shifted towards smaller values. In real measurements this window can be additionally adjusted to the muon momentum known from the deflection in the magnetic field of the PANDA dipole.

A comparison of the active and passive filtering of 2, 5 and 10 GeV/c muons from protons with the same momenta is presented in Fig. 8.101. The probability of misidentification of 10 GeV/c protons as muons is by more than an order of magnitude smaller for the active filtering than for the passive filtering. For 5 GeV/c protons the reduction is much smaller and in the case of 2 GeV/c protons no reduction is seen. This result indicates that below a certain energy it is not possible to distinguish between hadrons and muons on the basis of the energy deposit in the calorimeter only and that the active filtering is much more important at higher energies. As expected the thickest simulated setup (150 layers) filters high energy muons most efficiently. However, due to the high muon detection threshold, for smaller muon energies its performance becomes slightly worse than for the setups with moderate thickness (100–120 layers). In conclusion, again a setup consisting of 100 layers was chosen. This is

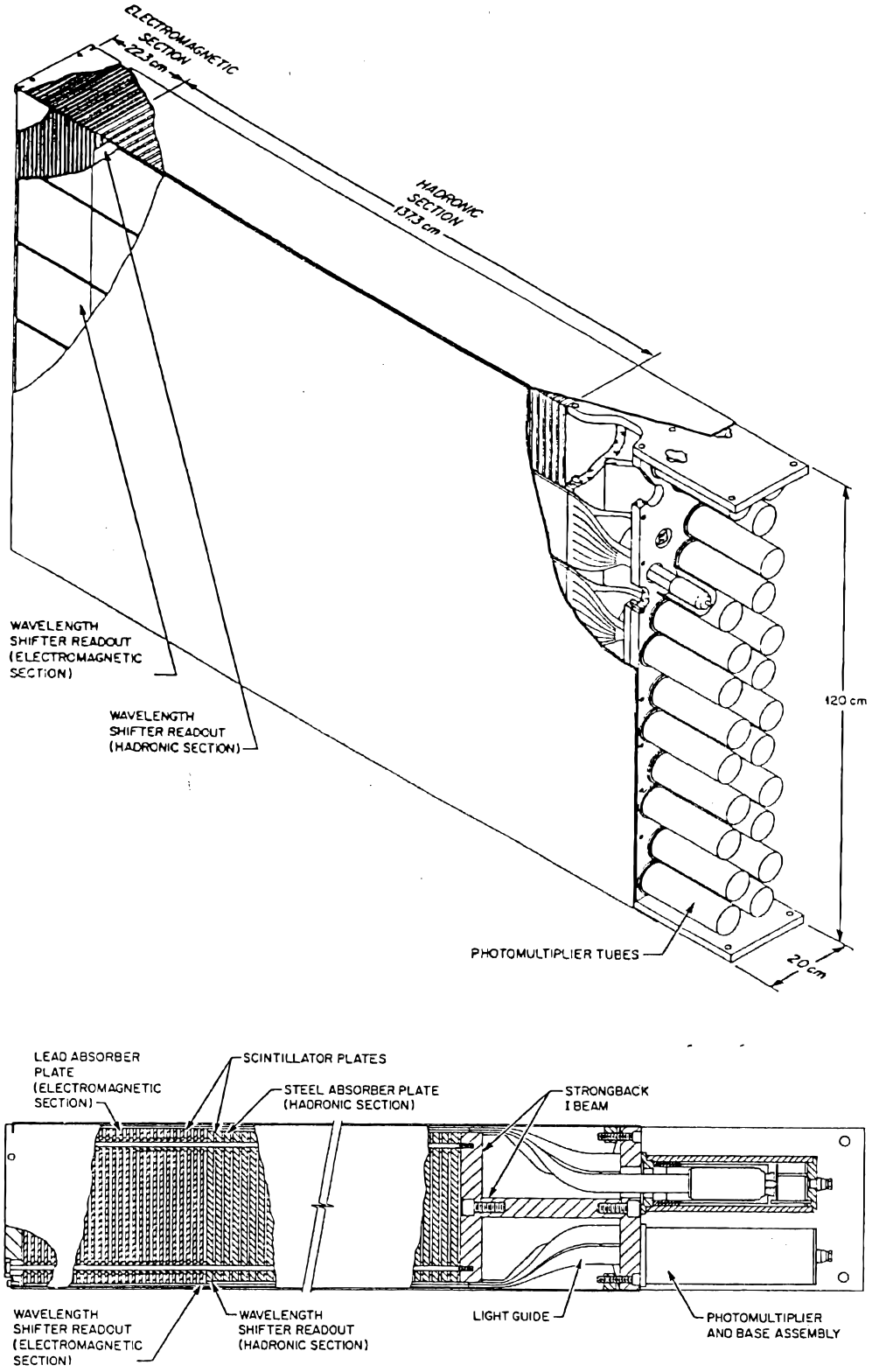

Figure 8.97: Isometric view and cross section of a MIRAC module. Figure taken from Ref. [77].

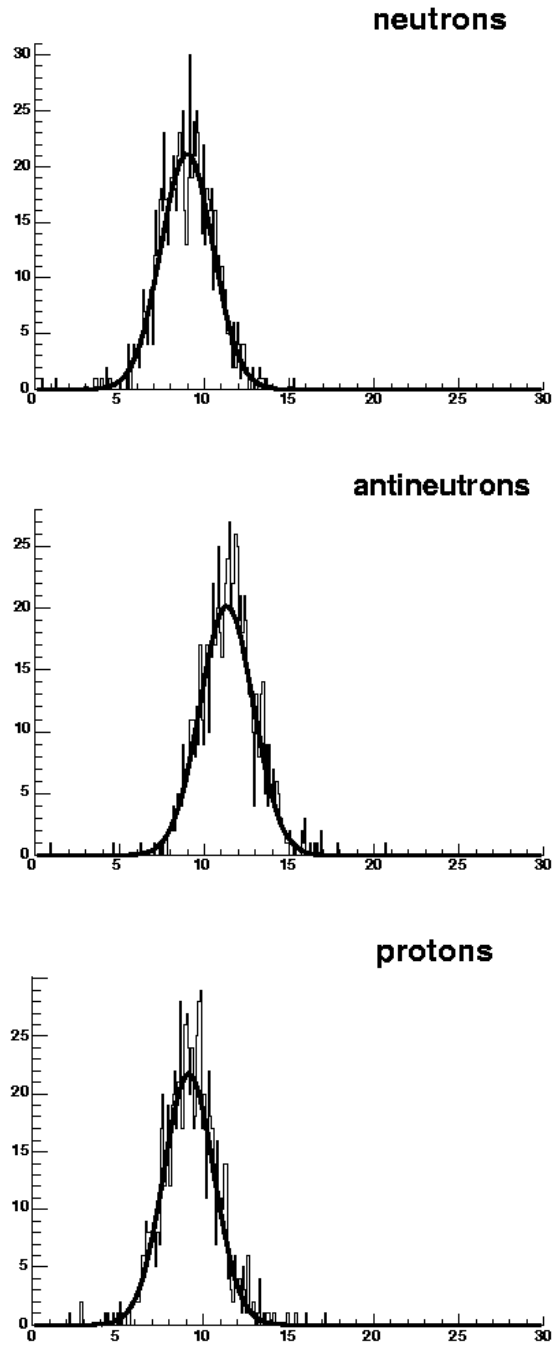

Figure 8.98: Reconstructed energy of 10 GeV/c neutrons, antineutrons and protons.

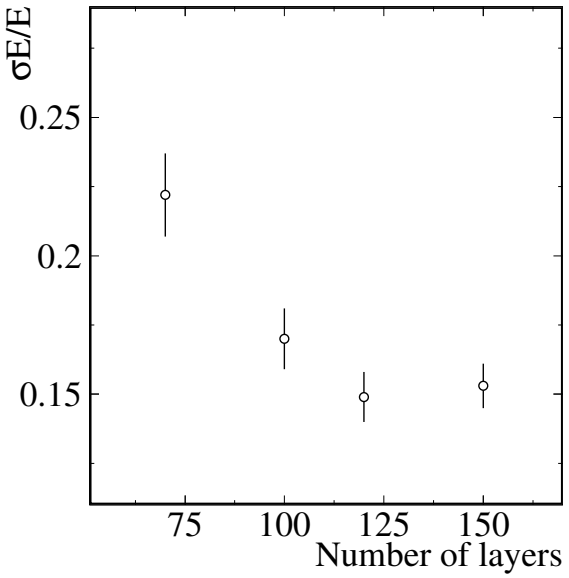

Figure 8.99: Energy resolution for 10 GeV/c protons as a function of calorimeter depth.

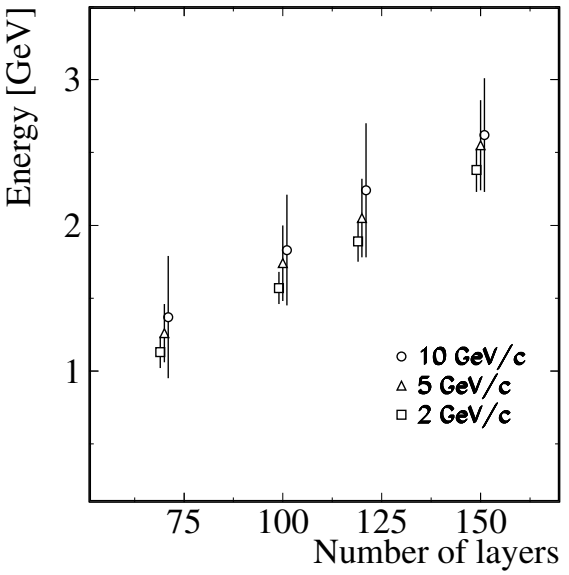

Figure 8.100: Mean energy deposit in the hadron calorimeter for of 2, 5 and 10 GeV/c muons μ^+ as a function of calorimeter depth. In order to make the points of the different measurements distinguishable in the figure, the number of layers were increased and decreased by 1 for the 10 GeV/c and for 2 GeV/c values respectively.

because its muon detection threshold is quite low and its performance as a muon filter is well suited for the energy range of interest.

8.12.4 Adaptation to the $\overline{\text{P}}$ANDA needs

The hadron calorimeter will be located about 8 m downstream from the target. It will consist of 40 modules arranged in two rows as shown in

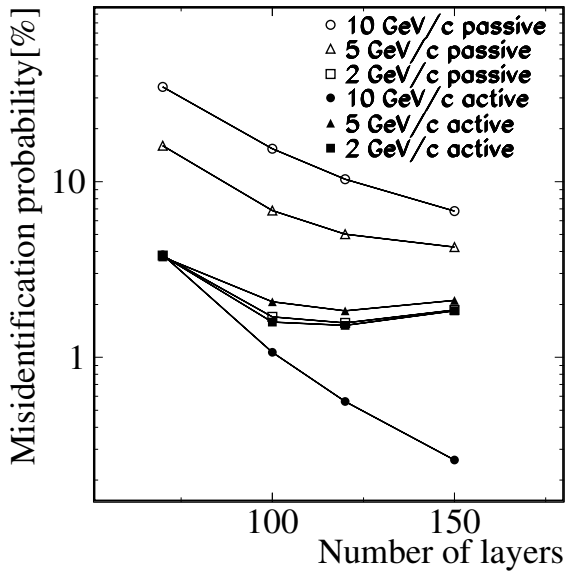

Figure 8.101: A comparison for the probability of misidentification of a hadron as a muon for a passive (open symbols) and active filter (full symbols) as a function of number of layers in the calorimeter.

Fig. 8.102. The modules in the lower row have the same transverse dimensions as the MIRAC modules. In turn, the modules in the upper row are only half in height compared with the MIRAC ones. They will be built using the steel and scintillator plates from the MIRAC modules cut into two equal parts. Each module will contain 100 steel-scintillator layers corresponding to a thickness of 112 cm. The total depth of the modules including the photo-detectors and light guides will be about 170 cm. The total number of modules corresponds to 360 readout channels. The active area of the calorimeter will be 440 cm horizontally and 180 cm vertically. In the central part an opening of 30 cm × 20 cm will be left for the beam pipe.

The steel and scintillater plates, the WLSs, as well as the light guides from the existing MIRAC modules will be used for building up the $\overline{\text{P}}$ANDA hadron calorimeter. In order to do this, new housings, assuring a proper rigidity of the modules, have to be designed and build. Also the PMs, voltage dividers, and cabling has to be exchanged. Prior to the installation at $\overline{\text{P}}$ANDA, the performance of the modules will be tested in dedicated measurements with proton or pion beams.

References

[1] CERN-LHCC-97-33.

[2] CERN-LHCC-95-71.

[3] K. Mengel et al., IEEE Trans. on Nucl. Sci. **45**, 681 (1998).

[4] R. Novotny et al., IEEE Trans. on Nucl. Sci. **44**, 477 (1997).

[5] R. Novotny et al., IEEE Trans. on Nucl. Sci. **47**, 1499 (2000).

[6] B. Adeva et al., Nucl. Instr. and Meth. **A289**, 35 (1990).

[7] E. Aker et al., Nucl. Instr. and Meth. **A321**, 69 (1992).

[8] E. D. Bloom et al., Ann. Rev. Nucl. Sci **33**, 143 (1983).

[9] A. A. Annenkov, M. V. Korzhik, and P. Lecoq, Nucl. Instrum. Meth. **A490**, 30 (2002).

[10] A. Annenkov et al., Nucl. Instrum. Meth. **A450**, 71 (2000).

[11] M. Kobayashi et al., volume A537, page 312, 2005.

[12] M. Korzhik, Talk at FEMC03, FZ Jülich, Germany, March 10-11, 1003.

[13] X.Liu, G.Hu, X.Feng, Y.Huang, and Y.Zhang, Phys. Stat. Sol. (a) **190**, R1 (2002).

[14] H. Chen et al., 1999.

[15] M. Ishii et al., page 402, 1999.

[16] L. Nagornaya et al., IEEE Trans. Nucl. Sci. **42**, 337 (1995).

[17] M. Nikl et al., Inorganic scintillators and their applications.

[18] I. Solskii et al., page 595, 1999.

[19] S. Baccaro et al., Nucl. Instrum. Meth. **A385**, 209 (1997).

[20] N. Cocozzella, *Quality control in scintillating crystals through interference fine pattern analysis: theoretical study, design and construction of a test bench*, PhD thesis, 1999.

[21] P. Richter, G. Kruger, and C. Pistorius, Acta Crystall **B32**, 928 (1976).

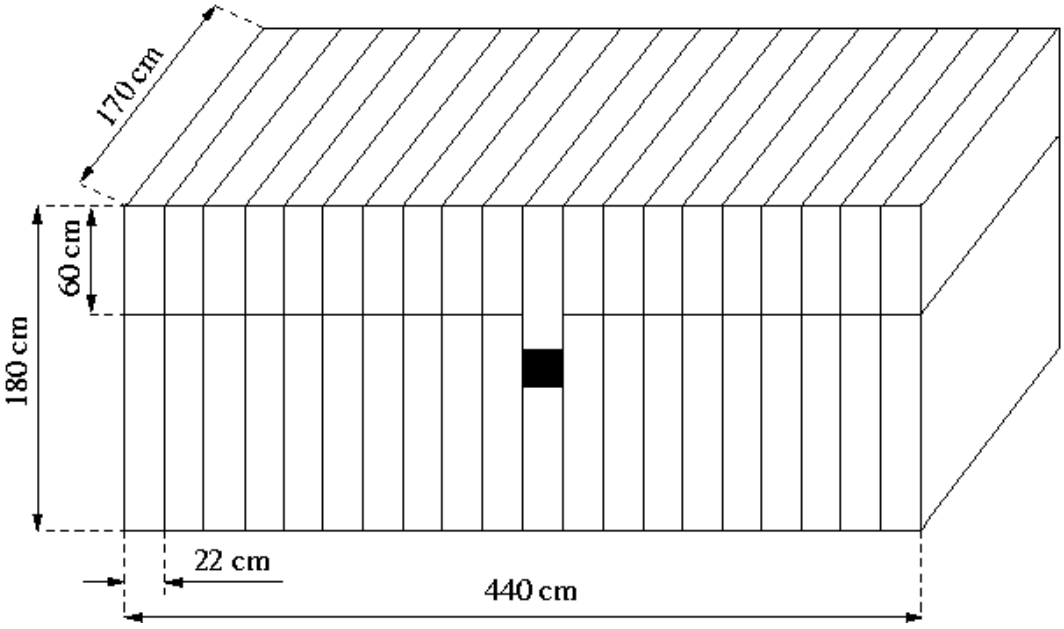

Figure 8.102: Arrangement of modules in the hadron calorimeter.

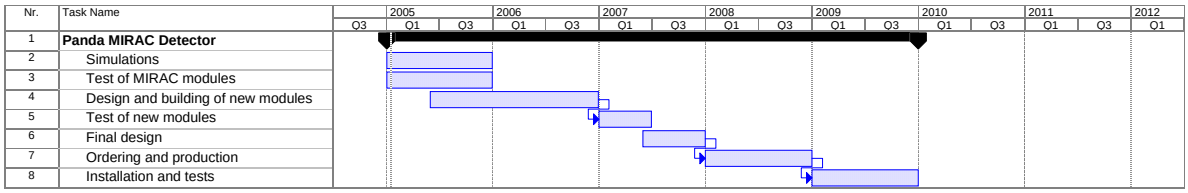

Figure 8.103: Timelines for the forward hadron calorimeter.

[22] T. Fujita, I. Kawada, and K. Kato, Acta Crystall **B33**, 162 (1977).

[23] J. Moreau, R. Gladyshevski, P. Galez, J. Peigneux, and M. Korzhik, J. of Alloys and Compound **284**, 104 (1999).

[24] R. Williams, Y. Zhang, Y. Abraham, and N. Holzwarth, 1999.

[25] A. Hofstaetter, A. Scharmann, D. Schwabe, and B. Vitt, Z. Phys. **B30**, 305 (1978).

[26] G. D. Böhm, A.E. Borisevich et al., (1997), LAPP-EXP-97. 13, LAPP, Annecy-le-Vieux.

[27] A. Annenkov et al., Nucl. Instrum. Meth. **A403**, 302 (1998).

[28] A. Alves et al., Radiation Measurements **33**, 641 (2001).

[29] B. Han, X. Feng, G. Hu, Y. Zhang, and Z. Yin, J. Appl. Phys. **86**, 3571 (1999).

[30] M. Böhm et al., page 139, 1998.

[31] M. Böhm et al., Rad. Effects and Defects in Solids **150**, 413 (1999).

[32] V. Laguta, J. Rosa, M. Zaritski, M. Nikl, and Y. Usuki, J. Phys. Condensed Matter **10**, 7293 (1998).

[33] A. Hofstaetter et al., Spectroscopic characterisation of defects in tungstate scintillators, 1999.

[34] A. Hofstaetter et al., Radiation Measurements **33**, 533 (2001).

[35] M. Nikl et al., Applied Phys. Lett. **71**, 3755 (1997).

[36] S. Baccaro et al., Phys. Stat. Sol. (a) **160**, R5 (1997).

[37] M. Korzhik et al., private communication.

[38] R. Y. Zhu, private communication.

[39] X. Qu et al., Nucl. Instr. and Meth. **A480**, 470 (2002).

[40] R. Mao et al., IEEE Trans. on Nucl. Sci. **51**, 1777 (2004).

[41] E. Lorenz, Nucl. Instrum. Meth. **A225**, 500 (1984).

[42] R. Sumner, Nucl. Instrum. Meth. **A265**, 252 (1988).

[43] J. A. Bakken et al., Nucl. Instrum. Meth. **A343**, 456 (1994).

[44] O. Adriani et al., Nucl. Instrum. Meth. **A302**, 53 (1991).

[45] W. W. Moses et al., Nucl. Instrum. Meth. **A353**, 189 (1994).

[46] S. Eidelman et al., Phys. Lett. **B592**, 1+ (2004), http://pdg.lbl.gov.

[47] G. J. Bobbink, A. Engler, R. W. Kraemer, J. Nash, and R. B. Sutton, Nucl. Instr. Meth. **A227**, 470 (1984).

[48] C. Laviron and P. Lecoq, Nucl. Instrum. Meth. **A227**, 45 (1984).

[49] S. K. Sahu et al., Nucl. Instrum. Meth. **A388**, 144 (1997).

[50] K. C. Peng et al., Nucl. Instrum. Meth. **A427**, 524 (1999).

[51] D. F. Anderson, IEEE Trans. on Nucl. Sci. **36**, 137 (1989).

[52] R. Novotny, Nucl. Instr. and Meth. **A486**, 131 (2002).

[53] J. Chen et al., presented at IEEE NSS 2004, submitted to Trans. on Nucl. Sci. .

[54] CMS Electromagnetic Calorimeter Technical Design Report, Technical report, 1997.

[55] D. Renker, Status of the avalanche photodiodes for the CMS Electromagnetic Calorimeter., Annecy, 2000, Prepared for 9th International Conference on Calorimetry in Particle Physics (Calor 2000).

[56] B. Patel et al., (1999), Prepared for 5th Workshop on Electronics for the LHC Experiments (LEB 99), Snowmass.

[57] BURLE INDUSTRIES, INC., 1000 New Holland Avenue, Lancaster, Pennsylvania 17601-5688, USA.

[58] H. Orth, private communication.

[59] B. Aubert. et al., Nucl. Instr. and Meth. **A479**, 1 (2002).

[60] CERN-LHCC-99-4.

[61] P. Rosier, R&D Detection - IPN Orsay, France, internal report RDD 2004-02, 2004.

[62] A. Fyodorov, M. Korzhik, A. Lopatik, and O. Missevitch, Nucl. Instr. and Meth. **A413**, 352 (1998).

[63] S. Ohlsson, Master Thesis, Uppsala University, Sweden, June 2004.

[64] M. Hoek et al., Nucl. Instr. and Meth. **A486**, 136 (2002).

[65] G. S. Atoyan et al., Nucl. Instrum. Meth. **A320**, 144 (1992).

[66] G. David et al., Performance of the PHENIX EM calorimeter, Technical report, PHENIX Tech. Note 236, 1996.

[67] A. Golutvin, (1994), HERA-B Tech. Note 94-073.

[68] LHCb Technical Proposal CERN LHCC 98-4, LHCC/P4, 1998.

[69] I.-H. Chiang et al., (1999), KOPIO Proposal.

[70] H. Morii, (2004), Talk at NP04 Workshop at J-PARC.

[71] G. Atoyan et al., Test beam study of the KOPIO Shashlyk calorimeter prototype, in *Proceedings of "CALOR 2004"*, 2004.

[72] T. Peitzmann et al., Nucl. Instr. and Meth. **A376**, 368 (1996).

[73] A. V. Inyakin et al., Nucl. Instrum. Meth. **215**, 103 (1983).

[74] V. G. Vasilchenko et al., Nucl. Instrum. Meth. **A369**, 55 (1996).

[75] KOPIO R&D reports, http://pubweb.bnl.gov/ users/ e865/ www/ KOPIO.

[76] V. V. Uzhinsky and A. A. Galoyan, hep-ph/0212369.

[77] T. C. Awes et al., Nucl. Instrum. Meth. **A279**, 479 (1989).

9 γ-ray Detector

9.1 Decay of Hypernuclei

9.1.1 γ-ray Detection

For the high resolution spectroscopy of excited hypernuclear states an efficient, position sensitive Germanium γ-array is required. To maximise the detection efficiency the γ-detectors must be located as close as possible to the target. Hereby the main limitation is the load of particles from background reactions. Most of the produced charged particles are emitted into the forward region. Since the γ-rays from the slowly moving hypernuclei are emitted rather isotropically the Germanium detectors will be arranged at backward axial angles $\theta \geq 100°$. Fig. 9.1 shows a γ-ray spectroscopy setup with 8 Germanium cluster detectors. The first ring of detectors is located at $\theta = 123°$, the second one at $\theta = 150°$.

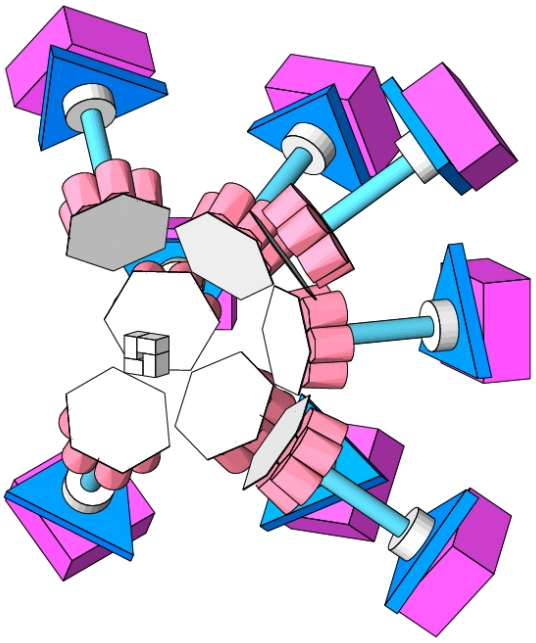

Figure 9.1: Setup with 8 Germanium cluster detectors for hypernuclei experiments at $\overline{\text{P}}$ANDA. The beam enters from right.

Presently, the use of the largest possible number of Euroball cluster detectors [1], partially owned by GSI, and in addition the use of the Vega detectors [2] of GSI are foreseen.

9.1.1.1 Required modifications of the Germanium detectors

Standard electronic readout systems are hardly capable of dealing with particle rates exceeding 10 kHz. However, the fully digital electronic system currently developed for the new generation of Germanium arrays like Vega [2] will – in connection with fast preamplifiers – allow the load of background particles at rates higher than 100 kHz for each detector element. Arranging several cluster detectors – each cluster contains in its present configuration 7 independent detector elements – and taking into account that most of the produced particles are emitted into the forward region not covered by the Germanium array an interaction rate of $10^7\,\text{s}^{-1}$ seems to be manageable.

Close to the $\overline{\text{P}}$ANDA main detectors the available space in radial direction is limited to the diameter of the tracking detector. Therefore, a practical mounting of the Germanium detectors inside the tracking detector is not feasible when including the present dewar into the setup. It is planned to replace the bulky storage tanks for liquid Nitrogen by a more compact cooling system. Presently two possible solutions are explored:

- A central Helium gas cooling system. Helium is a good heat conductor and the low condensation point makes it a good heat transfer mediator for the cryogenics. However, to achieve a good performance the cooler needs a special heat exchanger at the cold site which reduces the acoustic noise dramatically (no turbulent gas flow, only laminar flow) at the same time preserving the heat capabilities. A particular gas mixture (Ne, N, ...) may optimise the cooler performance and reduce the Helium losses. Nonetheless, since Helium easily penetrates welding lines the vacuum integrity of the dewar has to be considered.

- A mechanical cooling system based on the Stirling thermal cycle, like e.g. the X-COOLER II by ORTEC [3]. These systems have a good cooling power, however, acoustic noise and vibrations present a serious problem. Although, when using a fully digital readout system based on flash ADCs it might be possible to correct for these (periodic) distortions.

9.1.1.2 Particle background

At an average interaction rate of $5 \cdot 10^6\,\mathrm{s}^{-1}$ UrQMD calculations (Sec. 12.3.1.3) of $\overline{\mathrm{p}}$+Ni interactions at 3 GeV/c momentum predict in the backward hemisphere a total charged and neutral particle rate of $3.5 \cdot 10^7\,\mathrm{s}^{-1}$. Since most of the charged particles emitted into backward axial angles are very low in kinetic energy, most of them will be absorbed in the beam pipe and in the signal cables coming from the Silicon sensors of the secondary target. More critical are the neutrons emitted into backward axial angles.

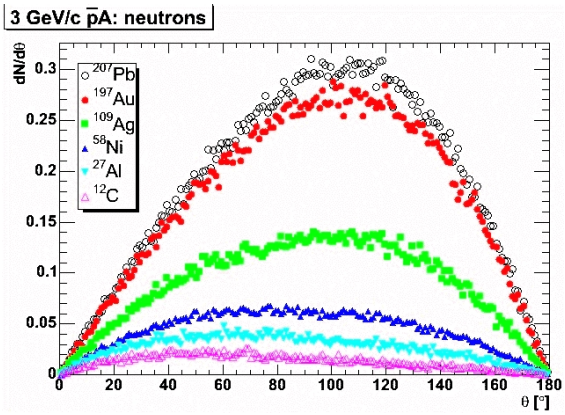

Figure 9.2: UrQMD predictions for the differential multiplicity of neutral particles per interacting antiproton for various targets at 3 GeV/c incident momentum.

Like for a Silicon detector, one expects that the major degradation of a Germanium detector is due to spatially extended disordered regions caused by the impact of fast neutrons in the MeV kinetic energy range [4, 5, 6]. Based on the known energy dependence of the displacement damage in Silicon [7] it is reasonable to assume that the damage done by neutrons with kinetic energies below 0.1 MeV is very small.

An n-type Germanium detector is expected to withstand a fast neutron fluence of about $4 \cdot 10^9/\mathrm{cm}^2$ without major degradation [5, 8, 9]. A reasonable operation may still be possible up to a neutron fluence of $10^{10}/\mathrm{cm}^2$. UrQMD calculations (Fig. 9.2) predict approximately 4.5 neutrons per reaction in the backward hemisphere for a target in the $Z = 30$ mass region. For a Au target this number increases by a factor of about 4 while the Ξ^- production factor increases only by about 60 %. Assuming a distance of approximately 30 cm between the primary target and the Germanium detectors and an interaction rate of $5 \cdot 10^6\,\mathrm{s}^{-1}$ one finds a load of fast neutrons on the Germanium detectors of about $4\,000\,\mathrm{ncm}^{-2}s^{-1}$. Taking no further precautions this would allow a continuous operation of about 30 days before an annealing procedure has to be performed.

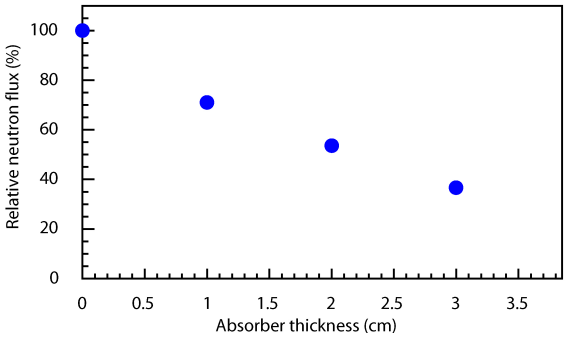

Figure 9.3: Relative yield of fast neutrons ($E >$ 100 keV) in the Germanium detectors predicted by GEANT simulations as a function of the thickness of a $(CH_2)_n$ moderator surrounding the beam pipe. The moderator covers the backward region beyond at axial angles $\theta > 100°$.

In order to reduce the number of fast neutrons entering the Germanium detectors a moderator will be placed close to the primary target surrounding the beam pipe. This moderator will be made out of $(CH_2)_n$. While γ-rays emitted by hypernuclei are only weakly effected by this absorber because of its low Z material, a 2 cm thick moderator reduces the fast neutron yield by about a factor of 2 (see Fig. 9.3).

9.1.1.3 Operation of Germanium detectors

One of the major challenges at PANDA is the operation of the Germanium detectors close to a strong magnetic field. The performance of Germanium detectors in a strong magnetic field has not been well investigated, and there are three problems expected: (i) break-down of FETs in preamplifiers, (ii) discharging and sparking in the crystals, and (iii) deterioration of the vacuum enclosing the crystals.

To verify that the proposed Germanium detectors can be safely and efficiently operated in a high magnetic field Euroball cluster detectors, being used by the RISING collaboration [10], and one Vega detector were tested. Before the measurements the energy resolution of the detectors were determined with a ^{60}Co source to be 2.2 keV (FWHM) at 1.333 MeV. Then the detectors were mounted inside the aperture of the ALADIN magnet at GSI. Three of the seven crystals of the cluster detector were activated and had full operating high-voltages.

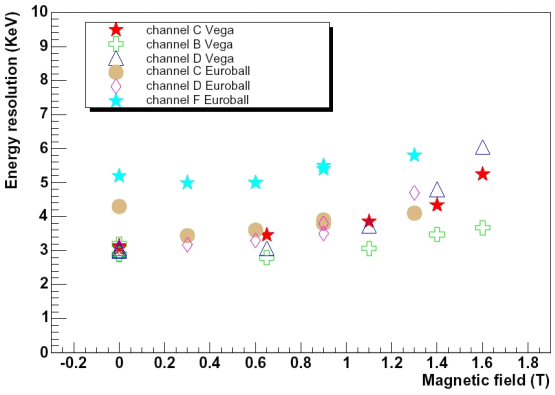

Figure 9.4: Measured energy resolution (FWHM) of Euroball cluster detectors and Vega detectors in a magnetic field.

Fig. 9.4 shows the energy resolution (FWHM) at 1.333 MeV of three crystals of each detector as a function of the magnetic field. Crystal no. F of the Euroball detector was found to have a worse energy resolution than the other crystals because of pick-up noises in its electronic readout, whereas two other crystals of the same detector, no. C and no. D, responded in a similar way to the magnetic field. Their energy resolution slightly exceeded 0.3 % at 1.2 T, however, a 0.3 % energy resolution is excellent enough to perform γ-ray spectroscopy on hypernuclei. A similar behaviour was found for the Vega detectors.

The measurements were performed over a period of two days, and we did not observe any problems with FETs, vacuum breaks or sparking of the crystals. After the measurements the original energy resolution was recovered. A pulse shape analysis with data taken by a FADC system is in progress, and details will be found in [11].

Finally, one has to consider the fact that the $\overline{\text{P}}$ANDA magnet is a super-conducting solenoid and that one cannot exclude a dramatic event like a quench. Of course we were not able to reproduce such a situation with a resistive magnet like ALADIN. Nevertheless, we monitored the behaviour of the Vega detectors during a fast decrease of the current from its maximum value (2400 A) to zero without observing any effect or detecting any damage.

9.1.1.4 Rate estimate

The diversity of detectors used for this experiment does not allow a full integration of the detection system into detailed GEANT simulations at the present stage. Based on calculations or – when available – on data we quantified the various steps of the double hypernucleus production process in order to derive an estimate of the final count rate.

Our rate estimate is based on an antiproton interaction rate of $5 \cdot 10^6\,\text{s}^{-1}$. At a $\overline{\text{p}}$ momentum of 3 GeV/c the $\overline{\text{p}}\text{p} \rightarrow \Xi^-\overline{\Xi}^+$ production cross section is about 2 μb [12], to be compared to the elastic cross section $\sigma_e(\overline{\text{p}}\text{p} \rightarrow \overline{\text{p}}\text{p}) \approx 23.7$ mb and the annihilation cross section of $\sigma_a(\overline{\text{p}}\text{p} \rightarrow X) \approx 26$ mb. Since no information on the mass dependence of the $\Xi^-\,\overline{\Xi}^{+,0}$ production cross section is available, we assume a $A^{2/3}$ dependence. This results in $\sigma(\Xi^-\,\overline{\Xi}^{+,0})/\sigma_{tot} = 4 \cdot 10^{-5}$. With these assumptions we expect approximately 126 $\Xi^-\overline{\Xi}^+$ pairs per second or 11 million per day. For a target in the Nickel mass region the "production factor" is of the order $6 \cdot 10^{-3}$. This provides us with about 104 000 stopped Ξ^- per day.

Recently, Yamada and co-workers studied within the framework of the doorway double Λ hypernuclear picture [13] the production of double Λ hypernuclei for stopped Ξ^- particles in ^{12}C [14]. Per stopped Ξ^- they predict a total double Λ hypernucleus production probability of 4.7 %. An even larger probability of 11.1 % was recently obtained by Hirata *et al.* within the Antisymmetrized Molecular Dynamics approach [15, 16]. In both calculations the ${}^{12}_{\Lambda\Lambda}$B, ${}^{12}_{\Lambda\Lambda}$Be, and ${}^{11}_{\Lambda\Lambda}$Be nuclei dominate the yield and are produced with comparable probabilities. As a conservative estimate we assume a $\Xi^-\text{p} \rightarrow \Lambda\Lambda$ conversion probability of only 5 %. This results in the production of about 5 200 double hypernuclei per day.

Individual excited states may be populated with up to 10 % of the total yield [13]. From the thickness of the secondary target and the neutron moderator we estimate for γ energies between 0.1 and 10 MeV an escape probability of a gamma ray from the target between 60 and 80 %. One cluster detector mounted at a distance of 30 cm covers 1.85 % of 4π. Since the decaying hypernuclei are at rest and assuming isotropic angular distributions, 8 cluster detectors will cover approximately 15 % of 4π corresponding to a full photo-peak efficiency of 3.5 % for 1.33 MeV γ-rays.

The proposed trigger scheme assumes a detection of hadrons containing the associated anti-strange quarks. The cleanest tag will be a high momentum $\overline{\Xi}^+$ at small angles. However, the majority of $\overline{\Xi}^+$ will annihilate in the primary nucleus. Assuming the $\overline{\Xi}^+$p absorption cross section to be close to the $\overline{\text{p}}$p annihilation cross section and averaging over

$\overline{\text{p}}$p interaction rate	$5 \cdot 10^6 \text{s}^{-1}$
$\overline{\text{p}}$ momentum	3 GeV/c
internal target	$Z \approx 30$
detector	see Sec. 2
reactions of interest	$\overline{\text{p}}\text{p} \rightarrow \Xi^-\overline{\Xi}^+$
	$\overline{\text{p}}\text{n} \rightarrow \Xi^-\overline{\Xi}^0$
cross section ($\overline{\text{p}}N$)	2 μb
rate	$200\,\text{s}^{-1}$
Ξ^- PF (see Sec. 4.6)	$6 \cdot 10^{-3}$
total stopped Ξ^-	104 000 per day
$\Xi^-\text{p} \rightarrow \Lambda\Lambda$ conversion probability	5 %
produced $\Lambda\Lambda$ hypernuclei	5 200 per day
probability of individual transition	10 %
target escape probability ($E_\gamma = 1$ MeV)	70 %
full energy peak efficiency	3.5 %
trigger efficiency	40 %
detected individual transitions	150 per month

Table 9.1: Rate considerations for hypernuclear physics with γ-ray spectroscopy.

the impact parameter we expect even in case of a carbon target a $\overline{\Xi}^+$ escape probability of only 20 %.

The reconstruction of a high momentum $\overline{\Xi}^+$ is straight forward [17] and will make use of the experience gained, for example, with the Fopi detector [18, 19] at GSI. In addition to the characteristic $\overline{\Lambda}$ vertex, the subsequent annihilation of the stopped antiprotons from the $\overline{\Lambda}$ decay may serve as a unique signature for the $\overline{\Xi}^+$. Taking branching ratios into account we expect a reconstruction efficiency of about 50 %. While two kaons will be produced in the annihilation process, the trigger will be based on the detection of only one K^+ in the forward region $\theta \leq 40°$ not covered by the secondary target. In order to reduce the single K^+ rate of about $5 \cdot 10^5\,\text{s}^{-1}$ to a rate acceptable by the DAQ, additional filters based, for example, on the vertex in the secondary target, the signals in the Germanium detectors or the missing energy in the forward region will be employed. Also in the kaon channel a trigger efficiency of 40 % seems feasible.

Putting all the numbers together we expect a rate of about 150 events per month for an individual transition. It should be stressed that the present consideration leaves still room for numerous improvements. For example, a lighter target material like Aluminium has only a slightly smaller Ξ^- production factor but would allow significantly higher interaction rates at similar neutron fluence at backward angles. Experience gained during the first experiments and subsequent optimisation of the experimental conditions may therefore allow to significantly increase the event rate.

9.1.2 Weak Decay

Single Hypernuclei weakly decay in two different ways [20]: Mesonic Weak Decay (MWD) and Non Mesonic Weak Decay (NMWD). The basic features of these decays are shown in Table 9.2.

The MWD proceeds through the conversion of the Λ into a nucleon with emission of a pion like in the free Λ decay. The nucleon (proton or neutron) is produced with a momentum of about 100 MeV/c (about 5.6 MeV kinetic energy), that is significantly less than the Fermi momentum in the nucleus (around 270 MeV/c). In accordance with the Pauli principle it should occupy a free energy level, but in general the lowest levels in a nucleus are occupied. In heaviest nuclei the first free levels are found at such high energies that MWD is forbidden. On the other hand the lightest nuclei have unoccupied low energy levels also in the ground state and MWD is sometimes observed.

The NMWD is based on the interaction of the hyperon with a nucleon producing two ordinary nucleons without any meson emission. The excess energy of this reaction gives both nucleons a momentum of about 400 MeV/c, significantly larger than the Fermi momentum, and they are emitted from the nucleus.

The study of the NMWD in single hypernuclei requires the detection of at least one decay nucleon

but the most appreciable results are obtained with those apparatuses which measure both neutron and proton in coincidence. In general this decay is sensitive to the hyperon-nucleon interaction. Moreover, information about the proton and neutron relative decay width and both with respect to the MWD width can be obtained. A considerable amount of new results are in sight in the next future concerning the mesonic and non mesonic decay of single hypernuclei because new facilities with new large-scale experiments like FINUDA@DAFNE are now operating.

In line with the decay of single hypernuclei, a double hypernucleus can decay in three ways due to the different combinations of mesonic and non mesonic decay: (i) both mesonic, (ii) both non mesonic and (iii) mixed mesonic and non mesonic decay. In the non mesonic decay the nucleon which induces the decay of one hyperon is different from that one which induces the decay of the other. But there exists another possibility for a non mesonic decay of a double hypernuclei, the so called hyperon induced non mesonic weak decay: $\Lambda\Lambda \rightarrow YN \rightarrow NN$, where Y denotes a Λ or a Σ hyperon. This novel weak decay [21, 22] occurs *exclusively* in the double hypernuclei and the decay depends on the hyperon-hyperon interaction. Studying this decay will be complementary to the study of double hypernuclei spectra for understanding the general baryon-baryon interaction. For example, the $\Lambda\Lambda \rightarrow \Lambda$n channel is especially intriguing since the dominant pion exchange is forbidden, thus forcing this reaction to proceed mostly via kaon exchange. One would therefore gain access to the weak $\Lambda\Lambda K$ and $\Lambda\Sigma K$ vertices. This decay has already been searched for by the Collaboration E373 at KEK [23] in the channel $\Lambda\Lambda \rightarrow \Sigma^-$p and an upper limit of 3 % for the double hypernucleus production from the Ξ capture at rest times the Σ^-p decay branching ratio has been determined. Predictions for the partial decay rates expressed in units of Γ_Λ are in the range of a few times 10^{-3} [21, 22], unless the H-di-baryon is formed inside the nucleus instead of the double hypernucleus.

The experimental apparatus should have both good energy resolution for pionic decay, good detection efficiency for protons (and neutrons) from the non mesonic decay and large (possibly full) angular acceptance. The pionic decay probability also in the intermediate nuclei like carbon is increased by the fragmentation. In general the pion spectrum consists of some discrete peaks coming from the direct first 2-body decay of the formed double hypernucleus or from the first 2-body decay of a double hyper-fragment (in this latter case the peak is slightly broadened by the recoil momentum of the hyper-fragment) and a continuum coming from the many-body decays of all single and double hypernuclei and hyper-fragments. The hyperon induced non mesonic weak decay of a double hypernucleus has a very unique fingerprint of two discrete peaks in the nucleon spectrum (c.f. Table 9.2).

The micro-tracker surrounding the hypernuclear target will detect the protons coming from the de-excitation and fragmentation of the hypernucleus. The main straw or TPC tracker will help to determine the momentum of the charged pions which come from the Λ particle's MWD. Neutral pions can be identified in the electro-magnetic calorimeter making use of the low energy threshold.

9.1.3 Ω Atom Production

It is planned to measure the hyperfine splitting in Ω^--Pb atoms [24, 25, 26] which is modified by the electric quadrupole moment of the Ω^- baryon according to $\Delta E \propto (\alpha Z)^4 Q_\Omega m_\Omega^3$. Like it was observed in antiprotonic [27, 28] and Σ^- atoms [29] and predicted for Ξ^- atoms [30] it is reasonable to assume that the main x-ray cascade will proceed via states with the radial quantum number $n_r = 0$, i.e. transitions of type $(n, l = n-1) \rightarrow (n-1, l = n-2)$. Since only for principal quantum numbers $n^2 > (\alpha m_\Omega) Z \cdot A^{1/3}$ the probability of radiative transitions exceeds the probability of nuclear capture for a lead nucleus n must be greater than six. Since also the x-ray energy shifts due to the interaction of the Ω^- hyperon with the nucleus should be kept small, it is in actual experiments necessary to deal with somewhat larger values of $n \approx 10$ [31, 29]. Assuming $Q_{\Omega^-} = 0.028\,\mathrm{fm}^2$ and the magnetic moment of the Ω hyperon to be $-2.5\,\mu_N$, Giannini and Krivoruchenko predicted [32] x-ray energies around 520 keV for $(n = 11, l = 10)$ to $(n = 10, l = 9)$ atomic transitions in the ^{208}Pb Ω^- atom. Fig. 9.5 shows the dominant transitions from $(n = 11, l = 10)$ to $(n = 10, l = 9)$.

Little is known on the production of $\overline{\Omega}^+\Omega^-$ pairs in $\overline{\mathrm{p}}N$ interactions. The quark-gluon string model predicts for $\overline{\mathrm{p}}$p collisions an $\overline{\Omega}^+\Omega^-$ production cross section of about 50 nb at an incident momentum of about 5.5 GeV/c [12]. Thus, we expect an $\overline{\Omega}^+\Omega^-$ rate of about $10\,\mathrm{s}^{-1}$ at an antiproton interaction rate of $10^7\,\mathrm{s}^{-1}$. Because of the slightly smaller lifetime of the Ω^- as compared to the Ξ^- and because of the higher momenta involved in this reaction we estimate the Ω^- production factor to be of the order of 10^{-4}. This results in the production of a few

decay	decay channel	N/π momentum [MeV/c]
free mesonic	$\Lambda \to \pi^- + \text{p}$ or $\pi^0 + \text{n}$	101 or 104
single hypernucleus mesonic	$\Lambda \to \pi^- + \text{p}$ or $\pi^0 + \text{n}$	≤ 101 or ≤ 104
single hypernucleus non mesonic	$\Lambda + N \to \text{n} + N$	≤ 416
double hypernucleus double mesonic	$\Lambda\Lambda \to \pi N + \Lambda \to \pi N + \pi N$	≤ 101 or ≤ 104
double hypernucleus non mesonic	$\Lambda\Lambda + NN \to \Lambda N + NN \to NN + NN$	≤ 416
double hypernucleus mixed	$\Lambda\Lambda + N \to \pi N + \Lambda N \to \pi N + NN$	≤ 104 and ≤ 416
hyperon induced non mesonic	$\Lambda\Lambda \to \Lambda N \to NN$	433 and ≤ 416
hyperon induced non mesonic	$\Lambda\Lambda \to \Sigma N \to NN$	325 and ≤ 416

Table 9.2: Weak decays of Λ particles in nuclei.

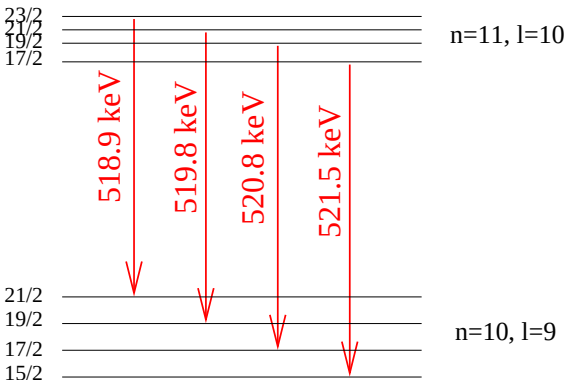

Figure 9.5: The Ω atomic levels of $(n = 11, l = 10) \to (n = 10, l = 9)$ transitions in ^{208}Pb, predicted by [32]. Favoured transitions are shown with arrows. $Q_{\Omega^-} = 0.028\,\text{e} \cdot \text{fm}^2$ and $\mu_{\Omega^-} = 2.5\,\mu_N$ are assumed.

hundred Ω^- atoms per day. Based on predictions for Ξ^-Pb atoms [30] the absolute yields of the relevant transitions are expected to be of the order of 20 %. With similar photo-peak and trigger efficiencies as discussed before, we will therefore be able to observe a few 10 transitions per month data taking.

Most likely the energy resolution of the Germanium array will not allow a separation of the expected transitions at 518.9, 519.8, 520.8 and 521.5 keV. Particularly interesting is, therefore, the $\Delta J = 0$ transition from the $J = 21/2$ level (see Fig. 9.5), despite the fact that the probability of this transition is reduced by about a factor of 50 [32]. This transition is shifted by 3.6 keV upwards, so that it is not masked by possible low energy tails of the dominant transitions, and is well separated from all other possible transitions by about 0.8 keV. Furthermore its position shows a large sensitivity to the Ω quadrupole moment. While the existing detector scheme will allow to observe the x-rays from the Ω atom, it is clear that further improvements and optimisation of the γ-detection system will be needed to identify the $J = 21/2 \to J = 21/2$ transition. Already today resolutions around 1.5 keV (FWHM) seem to be achievable with modern γ-ray tracking methods [33]. Furthermore, the fact that only a very narrow energy window around 520 keV is relevant for this measurement may also help to significantly improve the count rate capability.

9.2 Timelines

The timeline schedule for the installation and preparation of the hypernucleus experiment is shown in Fig. 9.6. The hypernucleus experiment requires two major technical developments:

1. modification of the cooling system of the Germanium detectors and the upgrade of the readout electronics for higher data rates. The modification of the cooling system necessary because of the limited space available within the field region of the $\overline{\text{P}}$ANDA detector.

2. design and construction of the Silicon tracker of the secondary target. While we hope to benefit from the developments at ATLAS, the compact arrangement needed for the present experiments will probably require major changes in the frontend electronics of the Silicon sensors.

The phase of the prototype development and the construction will be accompanied by detailed Monte Carlo calculations.

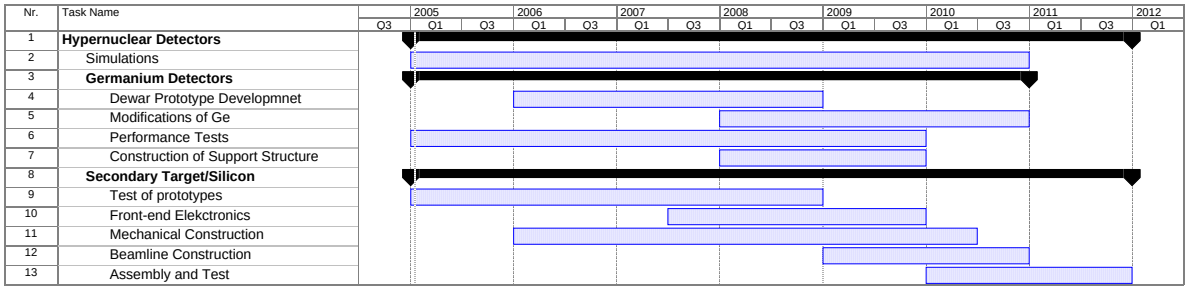

Figure 9.6: Timeline for the realization of the hypernuclear setup.

References

[1] J. Eberth et al., Nucl. Instr. Meth. **A369**, 135 (1996).

[2] G. Gerl and H. Grawe and E. Roeckl , 1998, http://www-gsi-vms.gsi.de/ eb/ html/ vegaproject.html.

[3] ORTEC, http://www.ortec-online.com/ detectors/ xcool.htm.

[4] H. W. Kraner, IEEE Trans. Nucl. Sci **NS-27**, 218 (1980).

[5] T. Raudorf and R. H. Pehl, Nucl. Instr. Meth. **A255**, 538 (1987).

[6] P. Leleux et al., Astronomy and Astrophysics **411**, L85 (2003).

[7] A. Vasilescu and G. Lindström, http://sesam.desy.de/ members/ gunnar/ Si-dfuncs.html.

[8] R. Pehl et al., IEEE Trans. Nucl. Sci **NS-26**, 321 (1979).

[9] J. Eberth et al., Nucl. Instr. Meth. **A369**, 135 (1996).

[10] H.-J. Wollersheim et al., Nucl. Instr. Meth. **A**, in print.

[11] A. Sanchez, PhD thesis, Institut für Kernphysik, Johannes Gutenberg-Universität Mainz.

[12] Kaidalov and Volkovitsky, Agenda of the Second Meeting of the Working Group: Physics with Secondary Beams, 1996.

[13] T. Yamada and K. Ikeda, Nucl. Phys. **A585**, 79c, 1995.

[14] T. Yamada and K. Ikeda, Phys. Rev. C **56**, 3216, 1997.

[15] Y. Hirata, Y. Nara, A. Ohnishi, T. Harada, and J. Randrup, Nucl. Phys. **A639**, 389c (1998).

[16] Y. Hirata, Y. Nara, A. Ohnishi, T. Harada, and J. Randrup, Prog. Theor. Phys. **102**, 89 (1999).

[17] M. Merschmeyer, PhD thesis, Universität Heidelberg, http:// www.ub.uni-heidelberg/ archiv/ 5061.

[18] A. Gobbi et al., Nucl. Instr. Meth. **A324**, 156 (1993).

[19] J. Ritman et al., Nucl. Phys. **B (Proc. Suppl.) 44**, 708 (1995).

[20] W. Alberico and G. Garbarino, Phys. Rep. **369**, 1 (2002).

[21] A. Perrero, A. Ramos, and C. Bennhold, Phys. Rev. **C65**, 015205 (2001).

[22] K. Sasaki, T. Inoue, and M. Oka, nucl-th/0306067, 2003.

[23] Y. Sato et al., Nucl. Phys. **A691**, 189c (2001).

[24] R. Sternheimer and M. Goldhaber, Phys. Rev. **A8**, 2207 (1973).

[25] A. Moskalev, N. Popov, and R. Ryndin, Yad. Phys. **29**, 138 (1979).

[26] S. S. Gershtein and Y. M. Zinov'ev, Yad. Fiz. **33**, 1442 (1981).

[27] J. D. Fox et al., Phys. Rev. Lett. **29**, 193 (1972).

[28] T. Yamazaki et al., Phys. Rep. **366**, 183 (2002).

[29] R. Powers et al., Phys. Rev. **C47**, 1263 (1993).

[30] C. Batty, E. Friedman, and A. Gal, Phys. Rev. **C59**, 295 (1999).

[31] R. Kunselman and R. Seki, Phys. Rev. **C8**, 2492 (1973).

[32] M. M. Giannini and M. I. Krivoruchenko, Phys. Lett. **B291**, 329, 1992.

[33] http://grfs1.lb.gov.

10 Magnet Systems

10.1 Introduction

The magnetic field is used for tracking charged particles, and is essential for many of the techniques used for particle identification. Ideally, the magnetic field should have a simple configuration and should look the same throughout the phase space of $\overline{\mathsf{P}}$ANDA.

At present the magnetic field is generated by a solenoid, which is co-axial with the incident anti-proton beam, in combination with a large aperture dipole – part of the forward spectrometer - which is downstream of the solenoid. Using a coordinate system for which the z-axis points along the incident beam direction, the xz plane is horizontal and the yz plane is vertical, the dipole field is along the y-direction. Since the dipole field does not preserve the azimuthal symmetry of the solenoidal field, the interaction of the solenoid and dipole fringing fields in the space between the two magnets gives rise to a non-uniform, asymmetric field in a region which is used for tracking forward going particles. This effect is particularly noticeable if the solenoid and dipole fields have no magnetic clamps.

Although the anti-proton beam is undeflected as it passes along the axis of the solenoid, it is deflected in the dipole field. This deflection can be compensated for if two additional dipoles, which together with the dipole are doubly achromatic, are placed downstream of $\overline{\mathsf{P}}$ANDA. An alternative solution would be a horizontal iron plate with a hole through it for the anti-proton beam, placed in the middle of the dipole. The plate acts as a magnetic shield for the beam and its thickness is chosen so that the residual magnetic field experienced by the beam as it passes through the hole produces a negligible deflection.

As an alternative to the dipole, a configuration of 6 superconducting coils arranged in a "spoke" geometry has been considered. A toroidal field, which preserves the azimuthal symmetry of the solenoid, is generated. Furthermore, there is no field along the axis, so that the anti-proton beam is unaffected. However, in this design the six coils meet in the middle and hence give rise to a dead region close to the axis. Some preliminary toroidal field calculations have been completed.

A third configuration of magnets for the forward spectrometer has also been proposed. This would consist of two wide aperture quadrupoles followed by a dipole. The quadrupoles would be used to collect forward going charged particles and partially focus them before they pass through the dipole, which would measure their axial momentum. Since there is zero magnetic field along the axes of the quadrupoles, they will not affect the anti-proton beam, and due to the focusing of the quadrupoles, the aperture of the dipole will be much smaller than that of the dipole being used in the solenoid-dipole configuration. Since the dipole will be further away from the solenoid, there will be essentially no interaction between the solenoid and dipole. At present, there have been no field calculations undertaken for a quadrupole-quadrupole-dipole configuration.

The following sections provide more details on the solenoid, the solenoid-dipole and the solenoid-toroid configurations.

10.2 Design Options

Currently the preferred solution for the magnet system consists of two large scale magnets which, in combination, would provide both an azimuthally symmetric almost 4π spectrometer and a zero-degree magnet spectrometer for forward emitted particles. This can be achieved using a solenoid with a variety of detectors inside its coils and a downstream dipole magnet together with additional detectors. At this stage, however, other design options are still being considered and compared to the default solution. Specifically, a configuration using the symmetric field of a toroid at forward angles is discussed, and field calculations are presented in Sec. 10.3.

10.2.1 Solenoid-Dipole Configuration

The configuration of a 2 T solenoid followed by a 2 Tm dipole is currently the default configuration for $\overline{\mathsf{P}}$ANDA. In this section the principal options on how to design this system are considered, whereas the detailed description of the components and their implementation are described in Sec. 10.4.

Taking into consideration the high costs of production and maintenance as well as the high level of reliability required, several different design options

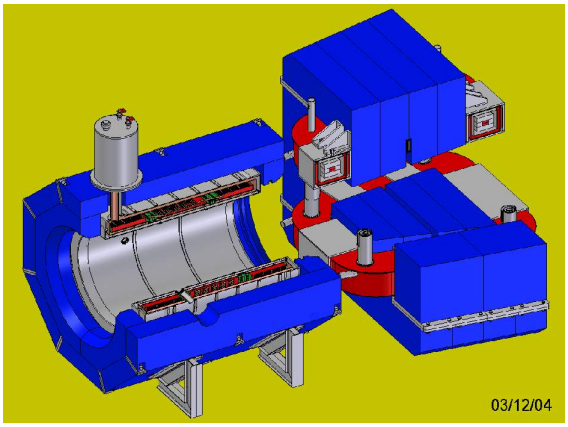

Figure 10.1: View of the superconducting solenoid and superconducting dipole magnet

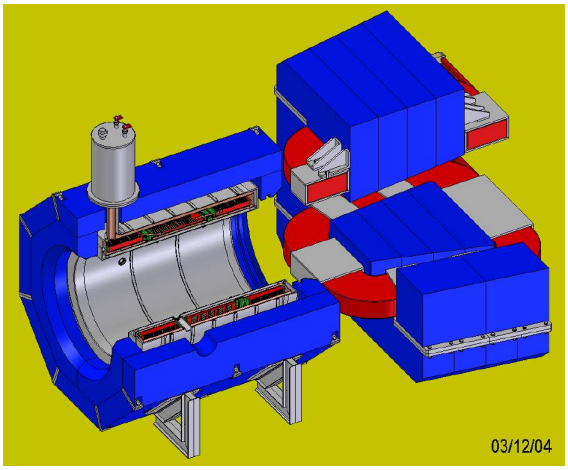

Figure 10.2: View of the superconducting solenoid and dipole magnet with water cooled racetrack winding.

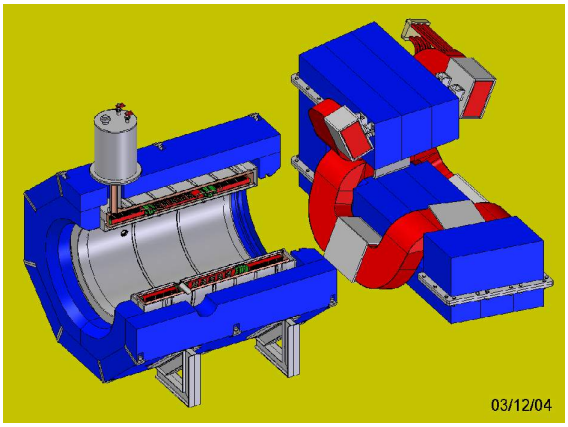

Figure 10.3: View of the superconducting solenoid and dipole magnet with water cooled bedstead winding.

for the PANDA magnet system have been considered within this document. Some of these options

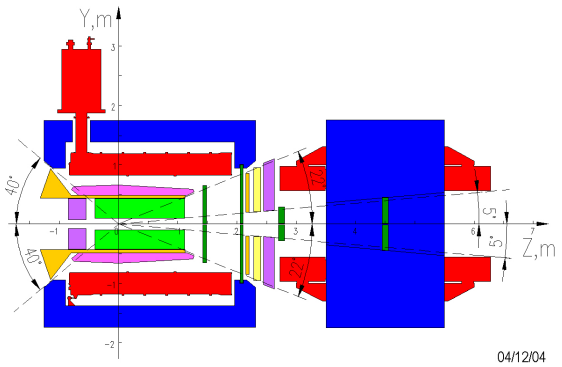

(a) side view

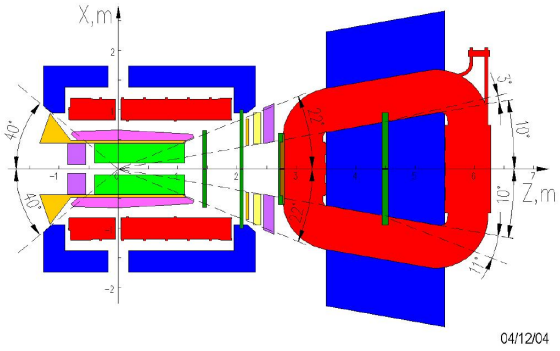

(b) top view

Figure 10.4: Layout of the water cooled dipole magnet with racetrack coils.

were omitted at an early stage, as they could be excluded using simple arguments. For example the use of High Temperature Superconductors (HTS) in the magnet windings was rejected because of high cost, low reliability, and currently insurmountable technological problems. Similarly options based on Nb_3Sn superconductor, operated at a temperature of about 6K, were excluded. It became evident that, while a marginal reduction in operation costs can be achieved, this cannot compensate for the higher costs of a superconductor solution involving a technologically complex coil.

Thus three options have been considered in detail:

- a superconducting solenoid and superconducting dipole magnet (see Fig. 10.1),
- a superconducting solenoid and water-cooled dipole magnet with racetrack coils (see Fig. 10.2),
- a superconducting solenoid and water-cooled dipole magnet with bedstead coils (see Fig. 10.3);

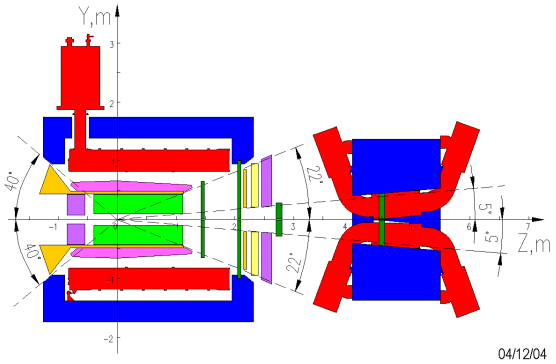

(a) side view

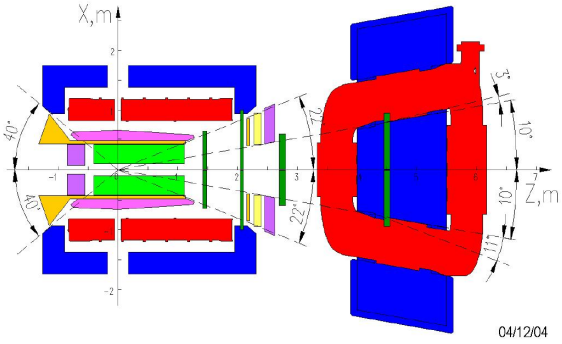

(b) top view

Figure 10.5: Layout of the water cooled dipole magnet with bedstead coils.

shown in 3D drawings in Figs. 10.1 to 10.3. 2D sketches, showing dimension scales, for the two solutions with a normal-conducting dipole are presented in Figs. 10.4 and 10.5. All of these options have been analysed in detail. These considerations, a scheme for implementation, and time lines are given in the following sections.

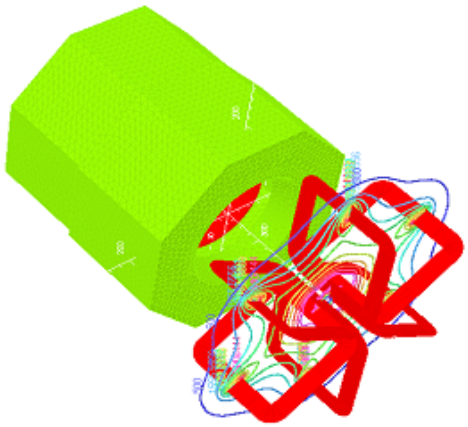

Figure 10.6: A 3-dimensional view of the solenoid-toroid configuration is shown below along with the magnetic field lines generated by the toroid. The toroid is a 6-spoke configuration of square superconducting coils.

each coil	
conductor winding cross sec.	$(0.5 \times 0.6)\,\mathrm{cm}^2$
area of conductor	$2 \times 30\,\mathrm{cm}^2$
turns per coil	200
conductor length per coil	1 600 m
current density	$7\,620\,\mathrm{Acm}^2$
total current per coil	4.57×10^5 A
6 coil assembly	
total conductor length	9 600 m
total current	2.74×10^6 A

Table 10.1: Parameters for the toroid configuration.

10.2.2 Solenoid-Toroid Configuration

In another scenario the solenoid would be kept as in the solenoid-dipole configuration, but the dipole would be exchanged by a toroid (see Figs. 10.6). The advantages are the conservation of an azimuthal symmetric field as shown in Sec. 10.3 at the cost of the ability to detect particles detected under zero degrees in polar angle. Six identical square coils of outside conductor length 2 m are arranged as a star around the beam pipe as shown in Fig. 10.6. The most important parameters for such a configuration are listed in Tab. 10.1.

The geometrical acceptance of the toroid with respect to the radial distance r from the axis at the entrance to the toroid, and also with respect to the polar angle θ from the target defined by r, are shown in Fig. 10.7.

The acceptance at the entrance to the toroid is given by the ratio: (area available to particles)/(total area.). The acceptance goes to zero at a radius $r = 10\,\mathrm{cm}$ from the beam, which is equivalent to an polar angle of $\theta = 1.6°$. However, the ends of the coils come together to form a hexagon, which could be designed to have a hole through its middle. Thus there is no need for there to be any material in the construction of the toroid for r less than $\sim 8.5\,\mathrm{cm}$. In principle the velocities of particles which go through the hole could be measured by time-of flight, and their 4-vectors obtained by using the exclusivity of $\overline{\mathrm{P}}$ANDA.

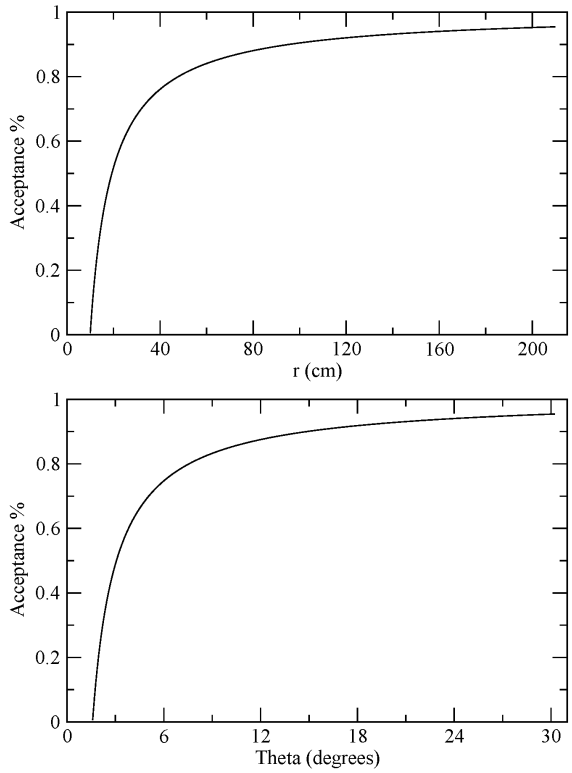

Figure 10.7: Geometrical acceptance *vs.* radial distance and polar angle for the toroid.

10.3 Field Calculations

In order to show the properties of the designs being considered, field studies have been performed for various configurations. The solution, considered presently as the default, of a solenoid in combination with a large gap dipole is compared to the combination with a toroid. The field inside the solenoid is governed mainly by its coils and its homogeneity may be crucial for the operation of Straw-Tube Trackers (STT)or Time-Projection Chambers (TPC). Details are discussed in Sec. 10.3.3

10.3.1 Solenoid-Dipole Configuration

In this section we present contour magnetic field maps of the axial and transverse field components in both the yz and xz planes for the solenoid-dipole configuration for:

- no iron plate in the dipole and no field clamps (Figs. 10.8a – 10.8d),
- no iron plate in the dipole, dipole field clamps and downstream solenoid field clamps (Figs. 10.8e – 10.8h),
- iron plate in the dipole and no field clamps (Figs. 10.9a – 10.9d) and
- iron plate in the dipole, dipole field clamps and downstream solenoid field clamps (Figs. 10.9e – 10.9h).

The use of an iron plate inserted into the dipole magnet has been discussed in order to decouple the optics of the HESR beam from the magnetic field strength applied at the dipole. This is, however, merely an option and, apart from its feasibility concerning the inhomogeneities in the magnetic field, simulations have to show whether this solution is acceptable from the tracking point of view.

Figs. 10.8a and 10.8b, which show the axial and transverse fields in the yz-plane when there is no iron plate in the dipole and no clamps on the solenoid or dipole, illustrate very clearly the interaction between the fringing fields from the solenoid and dipole. Above the xz-plane the fields add, whereas below the plane they subtract. This results in an asymmetric, non-uniform field in a region used for tracking. From Fig. 10.8b it is seen there is saturation in parts of the dipole yoke.

Due to the influence of the solenoid on the dipole, and vice versa, the combined field will not be the sum of the individual fields. This means that any field map will have to be measured with the two magnets in their correct relative position and both switched on.

Figs. 10.8c and 10.8d, which show the axial and transverse fields in the xz-plane when there is no iron plate in the dipole and no clamps on the solenoid or dipole, show that the fields between the solenoid and dipole are quite different from the corresponding fields in Figs. 10.8a and 10.8b. This means that there is no azimuthal symmetry to the field between the magnets.

Figs. 10.8e to 10.8h show the axial and transverse fields when there is no iron plate in the dipole. Clamps are attached on the downstream side of the solenoid and on both sides of the dipole magnet. The fields inside the magnets become well separated and more homogeneous in all components and in both the yz and xz planes. Also the field between the magnets seems to get less inhomogeneous. However, only simulations including possible field uncertainties will be able to show how much the track reconstruction would benefit from this configuration.

Figs. 10.9a and 10.9b, which show the axial and transverse fields in the yz-plane when there is an iron plate in the dipole and no clamps on the solenoid or dipole, are not significantly different

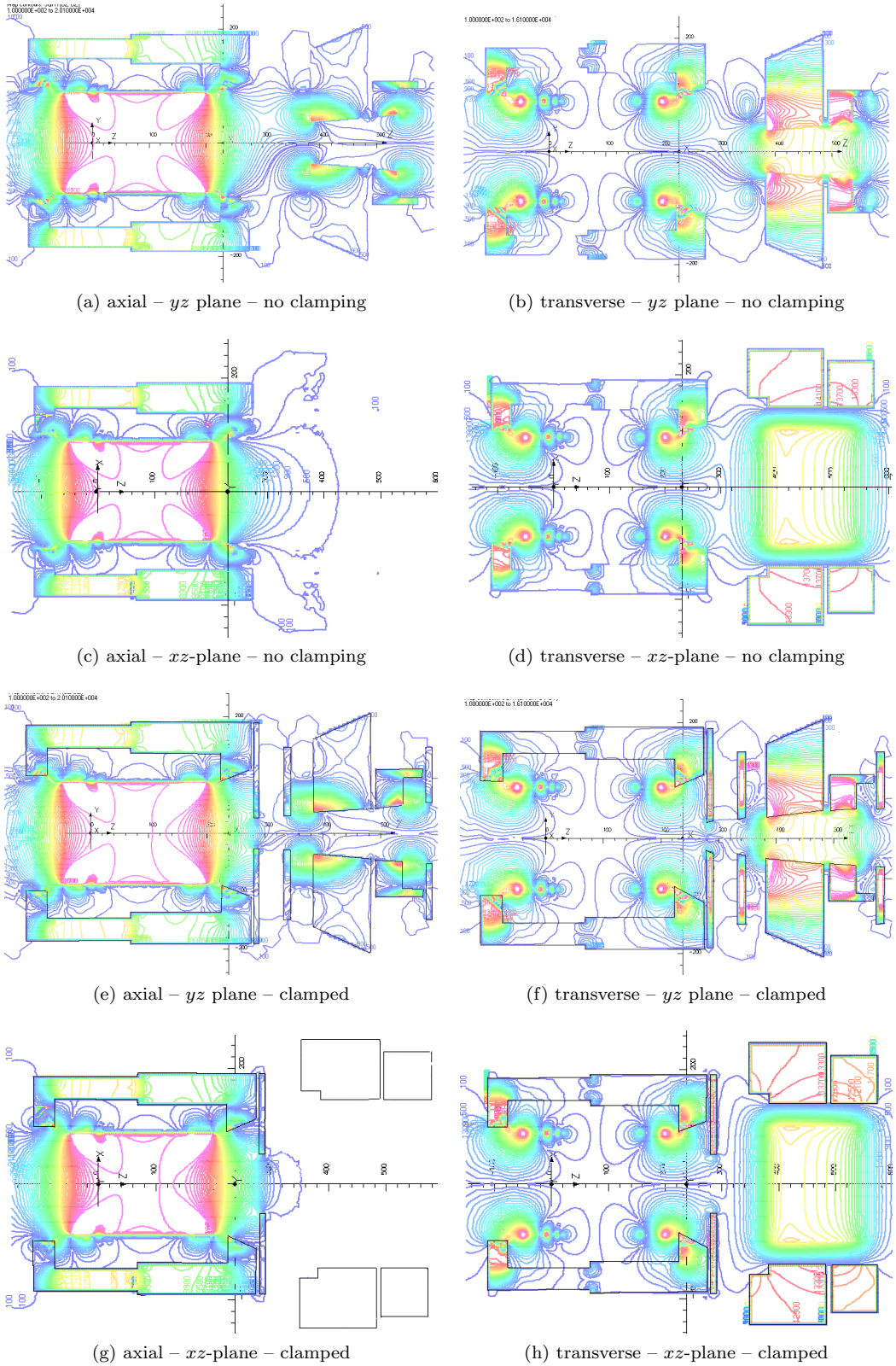

(a) axial – yz plane – no clamping

(b) transverse – yz plane – no clamping

(c) axial – xz-plane – no clamping

(d) transverse – xz-plane – no clamping

(e) axial – yz plane – clamped

(f) transverse – yz plane – clamped

(g) axial – xz-plane – clamped

(h) transverse – xz-plane – clamped

Figure 10.8: Contour plot of the field for the solenoid and dipole magnet for an open and clamped version (discussion see text). Lines ranging from blue to red indicate a field strength from 100 to 20100 and 16100 G for the axial and transverse fields respectively.

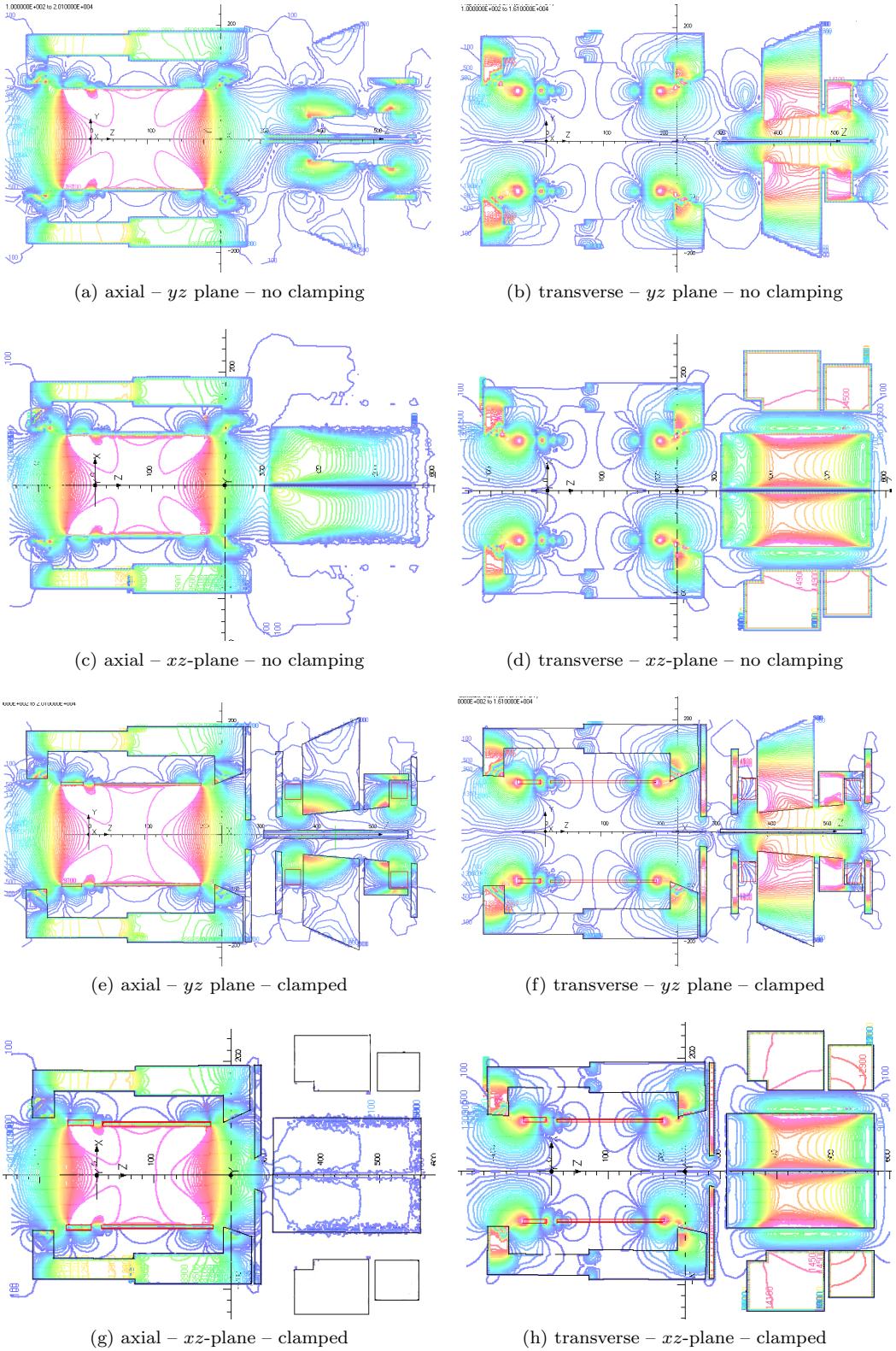

(a) axial – yz plane – no clamping

(b) transverse – yz plane – no clamping

(c) axial – xz-plane – no clamping

(d) transverse – xz-plane – no clamping

(e) axial – yz plane – clamped

(f) transverse – yz plane – clamped

(g) axial – xz-plane – clamped

(h) transverse – xz-plane – clamped

Figure 10.9: Contour plot of the field as in Fig. 10.8 but with an iron plate in the dipole. The plate would decouple the magnetic dipole field from the HESR beam optics but introduces strong field changes (see text).

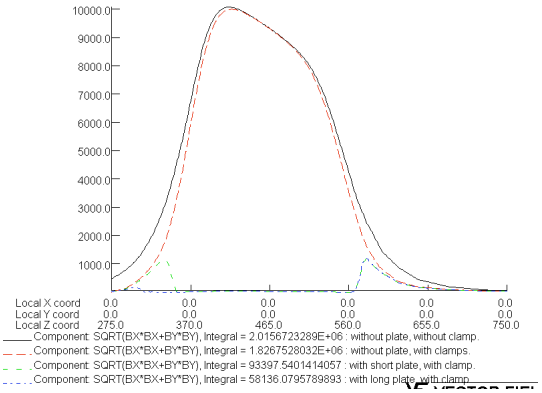

(a) Full scale: solid black line: without clamps, no plate. Red dashed line: with clamps, no plate. Green dashed line: with clamps and short plate. Blue dashed line: with clamps and long plate.

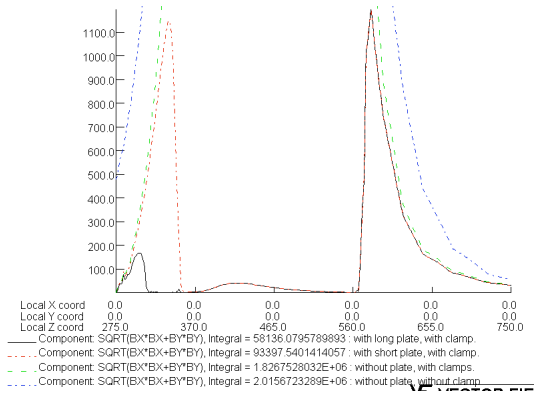

(b) Expanded scale: dot-dashed blue line: without clamps, no plate. Dash green line: with clamps, no plate. Dot/dash red line: with clamps and short plate. Solid black line: with clamps and long plate.

Figure 10.10: Transverse magnetic field along the z-axis of the dipole for various configurations.

from Figs. 10.8a and 10.8b, although the plate does perturb the field at its upstream end and the dipole transverse field shows more signs of saturation.

Figs. 10.9c and 10.9d, which show the axial and transverse fields in the xz-plane when there is an iron plate in the dipole and no clamps on the solenoid or dipole, show that the solenoid field is essentially unchanged, but that there is saturation from the transverse field in the plate. This is probably the cause of transverse field leaking through the plate into the central hole (see Fig. 10.10b).

Figs. 10.9e and 10.9f, which show the axial and transverse fields in the yz-plane when there is an iron plate in the dipole and clamps on the solenoid and dipole, show the field between the clamps on the solenoid and dipole is considerably reduced, although field lines are still being attracted from the solenoid into the upstream edge of the plate.

Figs. 10.9g and 10.9h, which show the axial and transverse fields in the xz-plane when there is an iron plate in the dipole and clamps on the solenoid and dipole, show that there is very little field between the clamps on the solenoid and dipole, but that the iron plate is saturated by the transverse field.

In Figs. 10.10a and 10.10b we show the transverse dipole field along the z-axis for the following:

1. without clamps and no plate,
2. with clamps and no plate,
3. with clamps and a long plate, and
4. with clamps and a short plate.

The figures show the effect of the clamps on the dipole fringing field at both the entrance and exit of the magnet, where the field is reduced. The peak field however remains unaltered.

Fig. 10.10b is the same as Fig. 10.10a, but with an expanded vertical scale. It is seen that for the short plate, there is a transverse field of ~ 1100 G at both the upstream and downstream edges of the plate. There is also a field rising to around 50 Gauss in the middle of the plate, probably caused by field saturation in the plate. If the plate is lengthened in an upstream direction, the field at the upstream edge of the plate is reduced to ∼170 Gauss.

10.3.2 Solenoid-Toroid Configuration

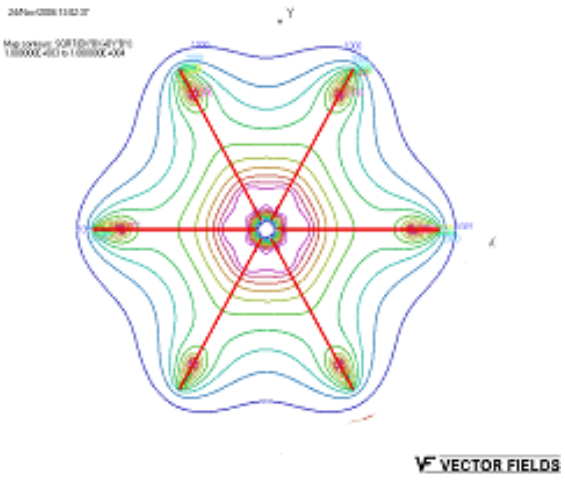

Figure 10.11: Front view of magnetic field lines generated by the toroid.

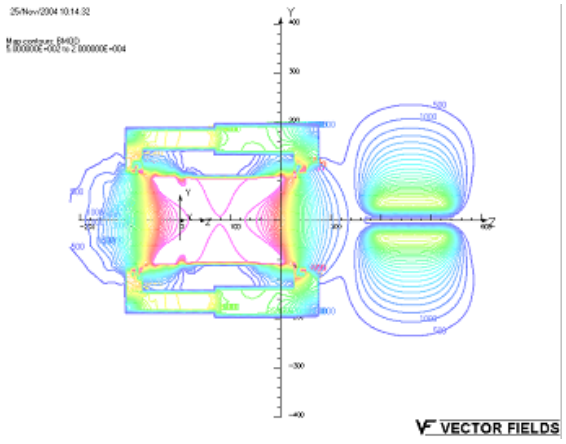

Figure 10.12: Contour map of the magnitude of the magnetic field for the solenoid/toroid in the yz-plane.

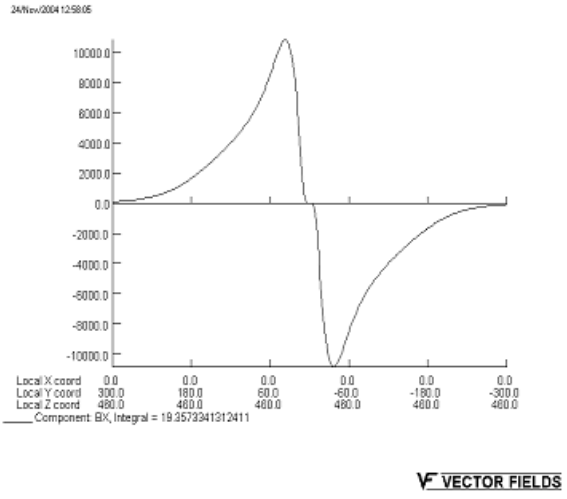

Figure 10.13: Variation of B_x along the y-axis at the centre of the toroid.

The following are general comments about the solenoid/toroid configuration.

1. The toroidal coil configuration has no iron in it at the moment, and hence there is a very clean separation between the solenoidal and toroidal fields.
2. From Fig. 10.11 it is seen that out to a radius of ~ 1 m, the field has very good azimuthal symmetry.
3. From Fig. 10.7 it is seen that at $\sim$5 degrees the acceptance is $\sim 60\%$, and falls to zero at $\sim 1.5°$, although the central hole through the coil configuration could be exploited.
4. At small angles, the acceptance of the toroid should be compared with the acceptance of the dipole with an iron plate.

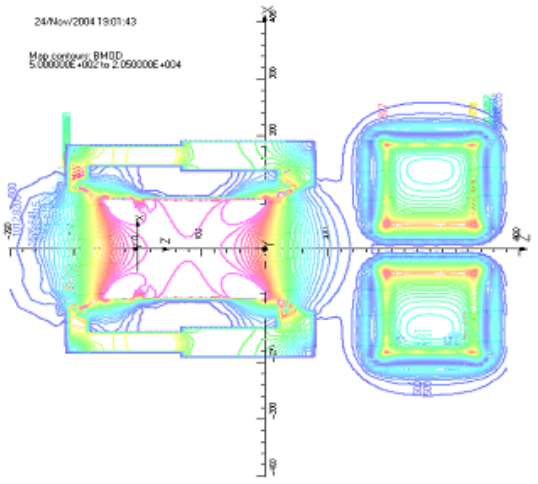

Figure 10.14: Contour map of the magnitude of the magnetic field for the solenoid/toroid field in the xz-plane.

5. Fig. 10.13 shows B_x along the y-axis for the magnetic field shown in Figs. 10.12 and 10.14. The field component reaches its maximum a distance of ~ 40 cm from the axis.
6. In operating the toroid, for a given current direction through the coils, particles of one sign of charge will be bent towards the axis, and particles of the opposite charge away from the axis. To exploit the full potential of the toroid, the direction of the current through the coils should be reversed.
7. The unoccupied volumes between the coils could be used for tracking detectors.
8. The effectiveness of the toroid will be enhanced if it operates in conjunction with a time-of-flight system.

10.3.3 Central Solenoid Field

The solenoid contains a variety of detectors. Close to the target there will be either a straw tube tracker (STT) or a time projection chamber (TPC). These tracking detectors require field homogeneities of $\pm 1\%$ throughout their volumes, and recently, studies have been carried out to investigate the effects of different solenoid conductor and yoke geometries on the field homogeneity.

The shape of the coils has been chosen considering:

- Only 3 coil sections in order to facilitate manufacturing,
- Minimum coil radius 1 010 mm,

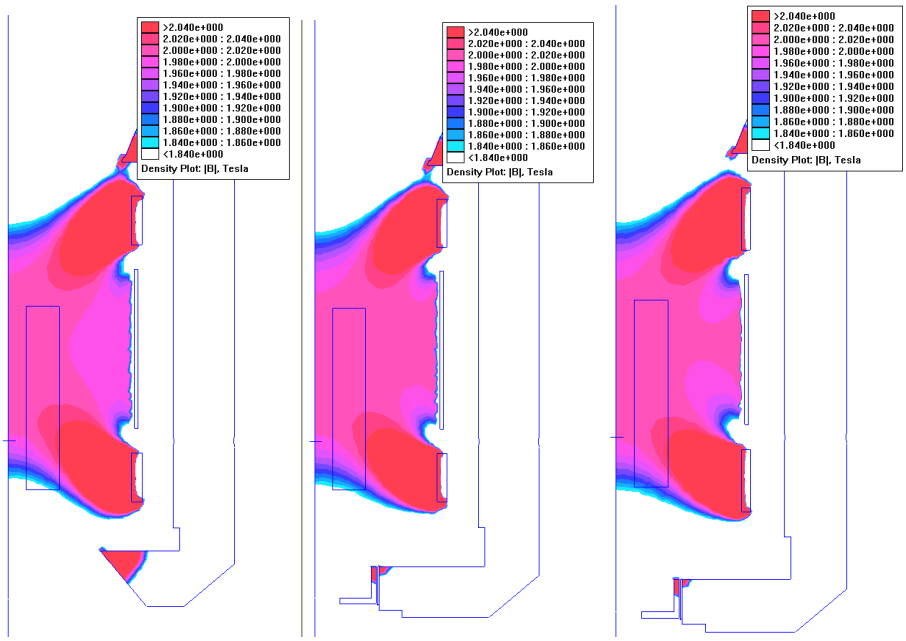

(a) small configuration (JL-A) (b) extended yoke (JL-B) (c) ext. coil and yoke (JL-C)

Figure 10.15: Contour plots of the magnetic field for several solenoid configurations. In these plots one half of the solenoid is shown and the HESR beam enters the figure from the bottom. Indicated as a box is the position of the straw-tube tracker STT or time-projection chamber TPC. Colours varying from white *via* blue to red indicate field strength changes from 0 to 2 T respectively.

- Average current density $50\,\mathrm{A/m^2}$,
- Gap of 200 mm for target warm bore (at $z = 0$ mm).

The z-position of the end cap of the yoke is determined by minimizing the axial forces on the coils.

Fig. 10.15 shows the field strength for a comparison of three different geometries in which both the current leading coil as well as the iron yoke have been varied. In Fig. 10.15a (JL-A) the radius of the coils is $R = 1010$ mm, the length is $L = 2500$ mm (from $z = -500$ mm to $z = +2000$ mm in the coordinate frame relative to the target position) and the backward opening angle of the yoke is 40°. For Fig. 10.15b (JL-B) the cylindrical yoke has been extended by 100 mm in backward direction. The upstream end cap is closed down to an opening of 500 mm (or 22°). An additional field clamp is added, which helps in two respects: first, to homogenize the field in the solenoid and secondly, to shield the field towards the outside. Finally, in Fig. 10.15c (JL-C) both the coil and the yoke respectively are extended by 100 (110) mm in the backward direction relative to Fig. 10.15b.

In all three cases the field is rather homogeneous over large parts of the tracker but becomes minimal

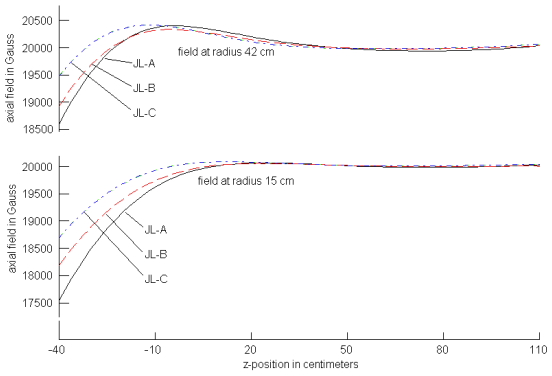

Figure 10.16: Longitudinal magnetic field B_z as a function of z for the three models.

at its backward end. Field gradients at this position of the tracker ($z = -400$ mm) at two radial positions are given in Table 10.2 It is here, where both the axial as well as the radial magnetic fields show the largest inhomogeneity. (see Fig. 10.16 and Fig. 10.17). There is about a factor of 2 improvement in $(B_{max} - B_{min})/B_{central}$ in going from model JL-A to JL-C.

Although the gradients (see Table 10.2) are of the order of 50 G/cm, the relative field changes over

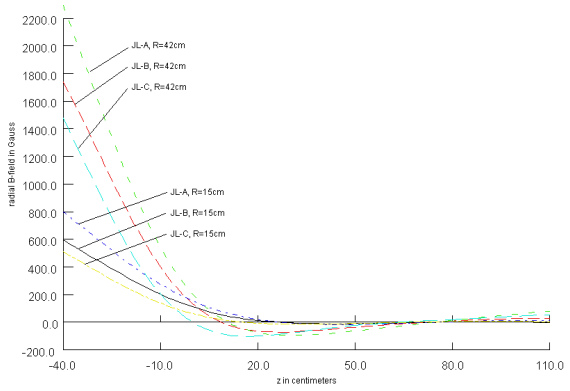

Figure 10.17: Radial magnetic field as a function of z for all three models.

	$R = 150\,\text{mm}$		$R = 420\,\text{mm}$	
	$\text{d}B_z/\text{d}z$	$\text{d}B_r/\text{d}z$	$\text{d}B_z/\text{d}z$	$\text{d}B_r/\text{d}z$
Model	G/cm	G/cm	G/cm	G/cm
JL-A	80	20	80	50
JL-B	60	15	70	45
JL-C	50	15	55	45

Table 10.2: Field gradients at the upstream end of the tracker, which is most severely dependent on a constant field. Here the field becomes weakest.

1 cm by only $\text{d}B/B = 0.3\%$ both for axial and transverse fields. The question whether these gradients can be tolerated needs further study.

The solenoidal field can be shaped in various ways such that the homogeneity over the tracking volume improves. The radical solution is making the magnet coils including the yoke longer. But before we settle for the expensive solution, we need a quantitative input for the sensitivity to field gradients for both the straw chamber and the TPC. For this analysis one has to take into account values for the radial and the axial field gradients separately.

10.3.4 Conclusion

The magnetic fields for all three configurations, solenoid with dipole, toroid or quadrupole-quadrupole-dipole, require further investigation before a final decision on the best configuration can be made, the chief criteria being:

- leaving space for detectors and mountings,
- providing a field for momentum reconstruction in almost 4π, and
- a minimum of field inhomogeneities,
- being cost-effective.

It is not unlikely that those conditions can only be fulfilled by using a combination of superconducting solenoid and water-cooled dipole (with bedstead coils), for which we find:

- The vertical field (yz-plane) between the solenoid and dipole becomes rather inhomogeneous. This may become unacceptable for the particle tracking if no clamping is introduced.
- With field clamps on both the solenoid and dipole the fields are in effect separated and significantly improved also in the region between the magnets. Dedicated simulations are to be done to study the effects on particle tracking. Further design work is required to optimise the clamp geometries and study how the introduction of clamps will affect the $\overline{\text{P}}$ANDA detector systems.
- The dipole yoke shows signs of saturation. This must be investigated further.
- For the option of an iron plate in the centre of the dipole the transverse field in it is saturating. This means that the hole in the plate has a transverse leakage field and the plate thickness may have to be increased. There is also a substantial field on the axis at the entrance to the hole in the plate, caused by the plate attracting field lines from the solenoid. The magnitude of this field is very sensitive to the length of the plate, and becomes smaller as the plate is extended towards the solenoid, which however increases the solid angle blocked by the plate.
- In terms of field homogeneity, the combination of a toroid with the solenoid may be favorable, but the acceptance gap at small angles might prove to be unacceptable.
- The field homogeneity inside the solenoid, especially in the region of the straw-tube trackers or the time-projection chamber, is not yet optimised fully. The straightforward solution of this problem is the prolongation of the solenoid which is, from the detector point of view, no principle problem, and foreseen in the current detector design. However, other cost saving options are still under study.

10.4 Design and Implementation

In this section a detailed plan for the design and implementation, including also some field calculations, is presented for the currently most likely configurations. That is a superconducting solenoid in combination with a dipole which may be either superconducting or normal conducting in two different mechanical designs.

10.4.1 Superconducting Solenoid

10.4.1.1 Magnetic field and solenoid parameters

The target solenoid consists of a superconducting coil with an inner radius of ~ 0.9 m and a length of 2.5 m. The maximum magnetic field in the operational area is 2 T. In order to minimize the amount of material in front of the electromagnetic calorimeter the calorimeter is placed inside the magnetic coil. The length forward of the target allows a reasonable momentum resolution even at the smallest polar angles (5°) detected only in the solenoid. This minimum angle of the solenoid acceptance is small enough to allow the dipole magnet to maintain a 1 m gap height. A 40 mm hole through the solenoid is foreseen for the pellet target tube [1]. To transport the solenoid from the operational area to the assembly a special carriage will be used. The superconducting solenoid of the Panda magnet system (Fig. 10.18 and 10.19) is of split type to provide a warm hole 100 mm in diameter between two unequal halves to accommodate the target system. Since the radiation transparency of the solenoid coil has not been included as a requirements for the $\overline{\text{P}}$ANDA experiment, the material of the superconductor was chosen to be NbTi in a Cu matrix because of the higher level of heat capacity of Cu with respect to Al. The materials of the coil mandrel and of the cryostat shells are stainless steel and copper. The dimensions of the cryostat and the iron yoke are shown in Fig. 10.20 and summarized in Table 10.3. Parameters of the coil sections of the solenoid winding are given in Table 10.4. A coil was designed with an average current density of 4.17×10^7 A/m^2 to achieve the desired magnetic field of 2.0 T at the operational area of the straw detector. To limit the helium consumption in the current leads the coil was designed with an operating current of 1 568 A.

To compensate for the local operational field inhomogeneity at the upstream end of the solenoid, arising from initial design constraints imposed on the solenoid length, an additional correction coil was used there. At the other end of the solenoid, a symmetrical correction coil was placed to equalize the axial force on the coil inside the iron yoke. The

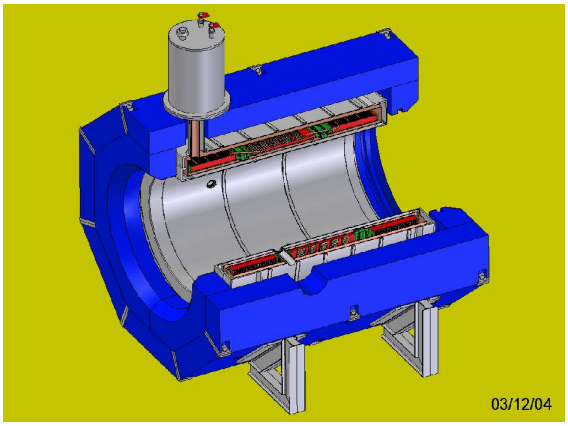

Figure 10.18: Solenoid magnet of the $\overline{\text{P}}$ANDA magnet system.

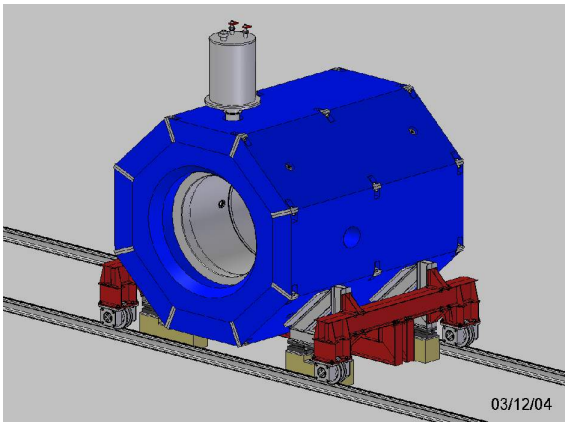

Figure 10.19: Solenoid magnet of the $\overline{\text{P}}$ANDA magnet system mounted on a carriage.

Cryostat	
Inner radius (ø of the warm hole)	0.81
Outer radius	1.2
Length	2.75
Forward length (z^-)	0.839
Backward length (z^+)	1.911
Iron Yoke	
Inner radius of the yoke	1.381
Outer radius of the yoke	1.884
Length of the yoke	3.572
Radius of the cap doors	0.942

Table 10.3: Main dimensions of the Cryostat and the Iron Yoke (all dimensions in meters).

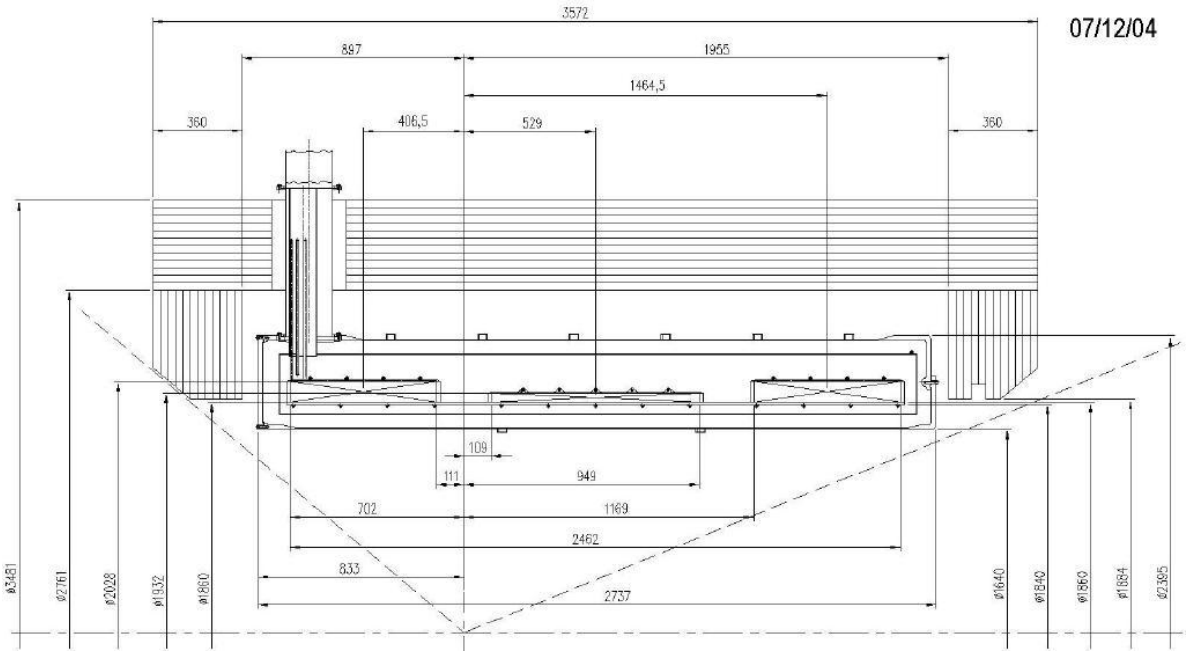

Figure 10.20: Cross section of the solenoid.

distance from the upstream side of the coil to the initial point was increased in comparison with the detector conceptual design, but the upstream side of the iron yoke was kept unchanged. The distance to the downstream boundary of the iron yoke was decreased a little bit since it does not influence on the field homogeneity at the operational area. The adopted design with two correction coils can achieve the required field homogeneity of $\leq$ |4.8|% relative to the average field.

Fig. 10.21 shows the coils configuration and Fig. 10.22 shows TOSCA calculations of the axial and radial magnetic field distribution in the solenoid operational region. Figs. 10.23 and 10.24 show the contour lines of the axial magnetic field and field homogeneity in the region of the detectors. The maximum field in the coil area is located on the inner surface of the correction coil (Fig. 10.25) and reaches $\sim$3,3 T. Stray fields $B_{\text{mod}}(x, y)$ of the solenoid in the sections at $z = 2.5$ m and 2 m are shown at Figs. 10.26 and 10.27. The stray field in the longitudinal vertical section of the magnet is shown at the Fig. 10.28. The maximal stray field at the radial distance 4 m is not higher than 0.003 T.

TOSCA calculations were used to calculate the forces acting on the solenoid coils and the iron yoke. There are asymmetrical forces on the solenoid coil of 8 kN in the y-direction and of approximately 45 kN towards the rear end cap (z-direction). Later on it is planned to decrease the asymmetry in the forces (in z-direction) by means of non-symmetrical placing of the coil relative to the iron yoke. The main parameters for the solenoid are summarized in Table 10.5.

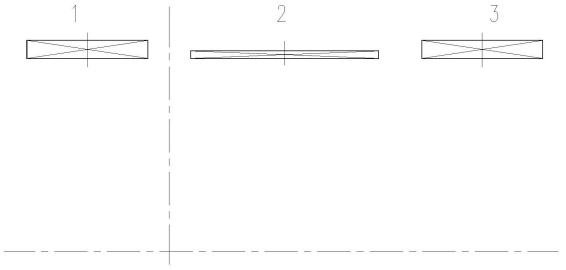

Figure 10.21: Coil configuration.

10.4.1.2 Cooling Modes and Coil Design Options

To minimize the mass of liquid helium in the winding area it would be useful to choose indirect cooling. This can be achieved by circulating liquid helium in pipes attached to the outer tape bandage-shunt resistor structures surrounding the coil and to the inner surfaces of the stainless steel spool (Fig. 10.29). However, it would be difficult to provide an effective thermal contact between the cooling conductor elements and the coil surface, when the coil is heated. Thus the option of a helium bath cooling seems preferable from the point of view of

	1	2	3
Inner diameter, mm	1 860	1 860	1 860
Outer diameter, mm	2 028	1 932	2 028
Distance from IP to a coil section centre along z-axis, mm	-406.5	529.0	1 464.5
Length, mm	591	840	591
Number of turns in a layer	76	108	76
Number of layers	17	7	17
Number of turns	1 292	756	1 292
Length of the conductor, m	7 899.1	4 504.1	7 899.1
Weight of the conductor, kg	1 968.5	1 122.4	1 968.5
Number of turns	3 340		
Length of the conductor of the coil, m	20 302.3		
Weight of the conductor of the coil, kg	5 059.4		

Table 10.4: Parameters of the coil sections. Coil numbering as in Fig. 10.21

Axial component of the magnetic field in the centre of the solenoid, T	2.0
Ampere-turn of the solenoid, MA	5.24
Nominal operational current, A	1 568
Design current density (without ground wall insulation), MA/m^2	41.7
Stored energy, MJ	16.3
Self inductance, H	13.3
Maximum field in the superconducting winding at operational current, T	3.3

Table 10.5: Main Parameters of the Solenoid.

reliability. This type of coil cooling will require a closed helium volume, where about 1–1.5 m^3 of liquid helium would be accumulated during operation. It is important to note, that this helium would act as a protection for the magnet against the interruption in cooling.

Two options of coil design have been considered depending on the type of cooling. In the case of indirect cooling it is planned that the coil would be wound and glued on the surface of a stainless steel mandrel. For the second option the coil is of a mandrel-less type.

10.4.1.3 Conductor Design

The conductor will be produced of high a purity copper C-form beam channel (4×7 mm) soldered into a superconductor flat cable insert of the Rutherford type (see Fig. 10.30). This would provide the operational current of $I = 1\,568$ A. Adequate safety factors have to be included in the conductor design for two reasons: firstly to decrease the possibility of cracking of the glue interfaces between the coil composite and the stainless steel mandrel in the case of the first coil option, and secondly to decrease the influence of friction between the coil surface and the flanges for the second option.

The cable will be braided from 11 superconducting strands, 0.6 mm in diameter, which contain 54 superconducting wires 54 μm in diameter. The Cu:Sc ratio is ~ 1.3. The critical current of the coil conductor has to be above 3 200 A to keep a suitable safety factor. At a temperature of 4.2 K and at a field of 3.3 T the critical current for a single wire is 385 A. The total current for 11 wire strands will be $11 \times 385\,\text{A} = 4\,235$ A. At the operational temperature of the solenoid (4.4 K) the critical current will be reduced to 3 970 A. This is sufficient to ensure that the safety factor is kept.

The dimensions of the flat cable before compression (defined according to Ref. [2]) are $a' = 2d$ and $b' = (n+1)d/2$ (see Fig. 10.30). After compression, the final dimensions of the cable are $a = 2d - \varepsilon_a$ and $b = (n+1)d/2 - \varepsilon_b$, where $\varepsilon_a = (0.3 \pm 0.1)d$ and $\varepsilon_b = (0.3 - 0.1)d$. So finally sizes of $a = 1.02 - 1.14$ mm and $b = 3.42 - 3.54$ mm were obtained. The fill factor of the metal in the flat cable is about 90%. The grove in the copper C-form channel, into which the flat cable has to be soldered, has the sizes $a = 1.22$ mm and $b = 3.62$ mm.

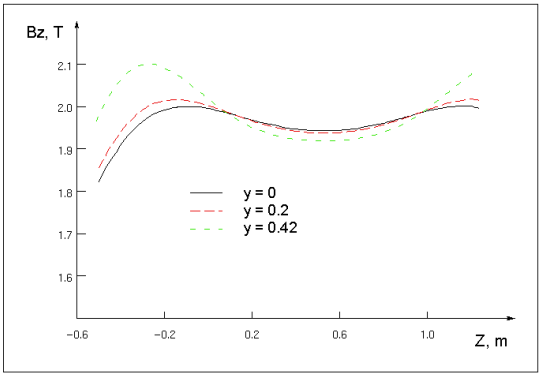

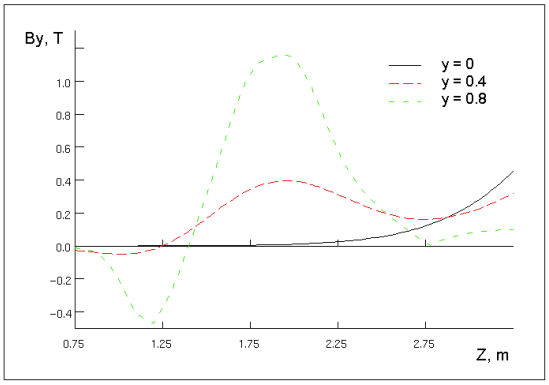

Figure 10.22: Axial and radial field distributions in the MDC region.

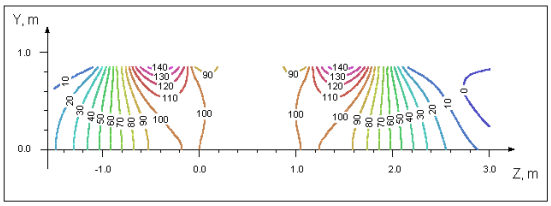

Figure 10.23: Equipotential lines of the axial magnetic field component (percentage of central field).

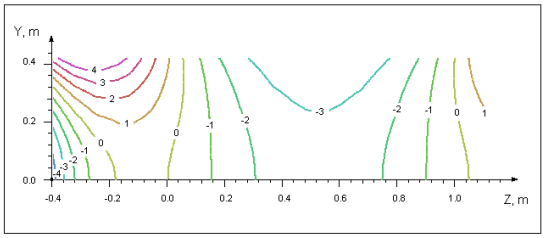

Figure 10.24: Equipotential lines of the inhomogeneity of the axial magnetic field (percent of central field).

The final dimensions of an array cell of the conductor are $4.75 \times 7.6)\,\mathrm{mm}^2 = 37.589\,\mathrm{mm}^2$. This includes turn-to-turn insulation and interlayer sheets

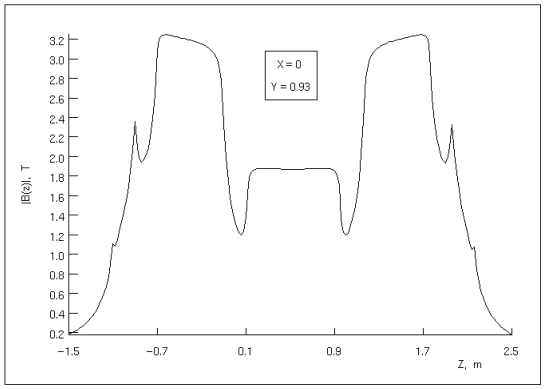

Figure 10.25: Magnetic field distribution along the coil inner surface.

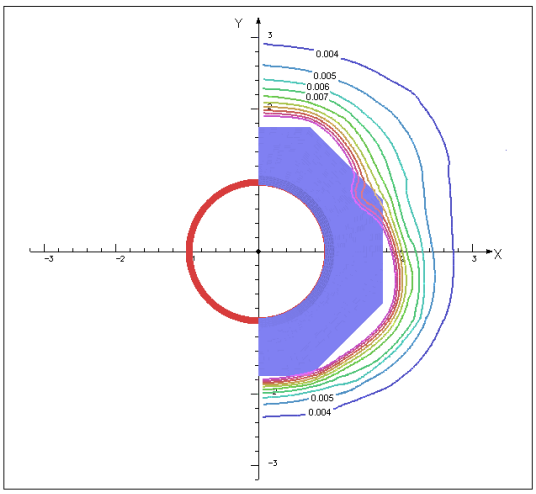

Figure 10.26: Stray field $B_{mod}(x, y)$ of the magnet system (solenoid and DM) at $z = 2.5\,\mathrm{m}$.

of thickness 0.3 mm and 0.15 mm respectively. The cross section of the copper in the conductor is $S_{cu} = 23.58 + 11x0.15973\,\mathrm{mm} = 25.34\mathrm{mm}^2$. The cross section of the insulation in the cell is $9.589\,\mathrm{m}^2$. The cross section of the soldering in the groove is $1.22 \times 3.62 - 3.11 = 1.306\,\mathrm{m}^2$.

The fill factors of the copper, insulation, superconductor and solder in the coil cell are $\lambda_{Cu} = 0.6741$, $\lambda_{sc} = 0.03596$, $\lambda_{sl} = 0.03474$ and $\lambda_{ins} = 0.2551$. The main design parameters of the copper matrix, the insulation and the superconducting insert are summarized in Table 10.6. The full length of the conductor in the coil is 20.6 km. The weight of the conductor is 5.14 t. This conductor could be produced according to the specifications by the American branch of the Outokumpu company [3].

Matrix: C-form channel	
Material	Cu (RRR 100)
Overall dimensions	4 x 7mm^2
Groove for flat cable	(1.22×3.62) mm^2
Insulation	
Material	Prepreg tape
Thickness of turn-to-turn ins.	0.3 mm
Thickness of interlayer ins.	0.15 mm
Thickness of ground wall ins.	1.0 mm
SC insert	
Material	NbTi/Cu
Cu/NbTi ratio	$\sim$ 1.3/1
Operational temperature	4.4 K
Critical current (B = 3.7(3.3) T, T = 4.2 K)	4 235 A
Critical current (B = 3.7 T, T = 4.4 K)	3 970 A
Number of filaments	60
Filament diameter	51 μm

Table 10.6: Main Parameters of the superconducting cable.

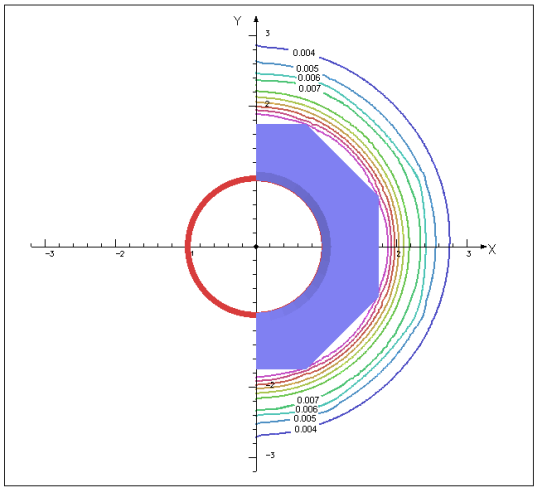

Figure 10.27: Stray field $B_{mod}(x, y)$ of the magnet system (solenoid and DM) at $z = 2\,m$.

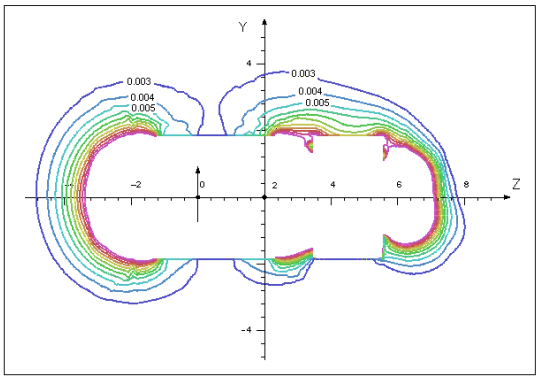

Figure 10.28: Stray field $B_{\mathrm{mod}}(x, y)$ of the magnet system (solenoid and DM). Longitudinal section.

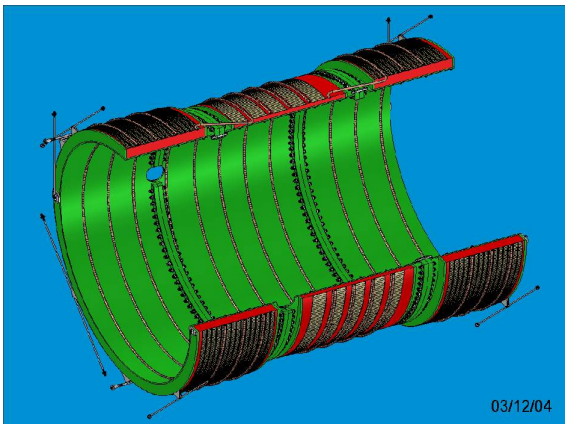

Figure 10.29: "Cold mass" of the solenoid.

10.4.1.4 Quench Protection and Power Supply

The stored energy in the Panda solenoid magnet and the current density in the windings are 16.3 MJ and 4.17 A/m^2 respectively. If after a quench the accumulated energy could be distributed in the coil conductor uniformly the maximal temperature rise would not exceed 37 K. Nevertheless, special measures have to be undertaken to protect the coil against destruction after a quench, because in case of an inhomogeneous distribution of the released energy the temperature parts in the coil material can

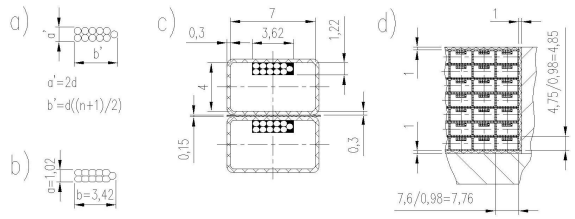

Figure 10.30: Cross section of the superconducting cable a) before pressing; b) after pressing. c) cross section of the insulated turns; d) cross section of the coil.

become much higher.

10.4.1.5 Hot-Spot Temperature

A passive protection method including a subdivision of the winding into sections and shunting them by cold resistors will be used for the PANDA solenoid coil. A sketch of the protection circuit is shown in Fig. 10.31. After a quench the current in the section will be damped by the corresponding shunt resistor. Additionally when a quench is detected by voltage taps in the coil, the protection switch will be opened to accelerate an entire winding quench (by means of whole winding heating with tape heaters located at the outside surface of the coil). Therefore it will eliminate cold shunt resistor current overloading and retain the advantages of a passive protection by subdivision. Furthermore, the shunt resistors are in thermal contact with the coil surface, and will hence heat the coils in the transaction process and accelerate the quench process.

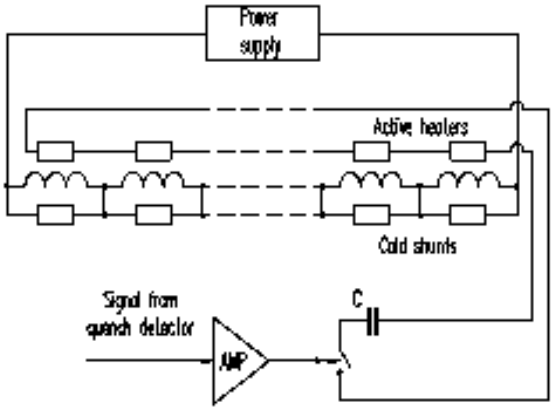

Figure 10.31: Protection circuit of the solenoid.

The total energy dissipated in the shunts in the transient process is 20% of the energy accumulated in the solenoid. The energy absorption sharing between the shunts is shown in Table 10.7. The energy

Shunt number	Dissipated energy (J)
1	2.04×10^6
2	2.38×10^5
3	1.13×10^6

Table 10.7: Dissipated energy in the various shunts.

dissipated into section 1 of the coil is about 80% of the total energy.

The temperature of the hottest point in the transient process for section 1 in is shown in Fig. 10.32. The maximal temperature in the coil after a quench is 85 K. This value does not include energy absorption by NbTi, soldering and insulation. In case it is required, the solenoid coil will be additionally divided into sections to decrease the maximal temperature. Moreover, the active heaters will initiate a spread of the normal zone into the coil.

The maximal over voltage in the coil will not exceed 300 V. This is an acceptable value from the point of view of the coil integrity in the transient process. The electrical insulation with a 1 mm layer ground wall insulation is 1 kV.

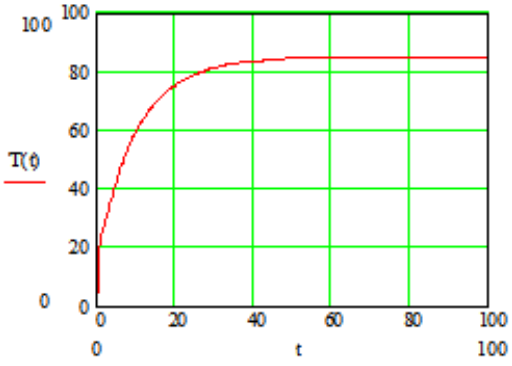

Figure 10.32: Temperature increase for the hottest point of coil section 1 after a quench.

10.4.1.6 Stainless Steel Shunts

Stainless steel resistors will be used to shunt the coil section and to evacuate the part of energy from the coil sections after a quench. These will be wound bifilar from a insulated flat wire on top of the superconducting coil sections. Additionally, the heating of wires during a quench process will be used to accelerate the quench of superconductors in the sections.

Magnet Current Control Parameters	Standard Model 420. Programmable Limits ±2 000 A
Measurement Resolution:	4.0 mA
Accuracy (% of $I_{\max}$):	0.005%
Minimum Ramp Rate:	1 mA/min
Maximum Ramp Rate:	100 A/s
Magnet Current Control	
Temperature Coefficient:	0.01% of I_{max}/°C
Stability:	Better than 0.01% (40 min. warm-up)
Programming Resolution:	15 digits[a]
Ramp Rate Resolution:	15 digits
Nominal Load Inductance Range:	0.5 to 100 H
Magnet Voltage Measurement	
Maximum Limits:	-20 to +20 VDC
Accuracy:	0.1% of V_{max}
Temperature Coefficient:	0.01% of V_{max}/°C
Resolution:	10 mV
Power Requirements	
Primary:	100–120 or 200–240 VAC ±10% 50–60 Hz, 50 VA max
Memory Backup Battery:	3.6 V AA Lithium Cell

Table 10.8: Specification of the Power Supply, AMI, Model 420, 2 000 A

10.4.1.7 Power Supply

The coil voltage drop will be 6.3 V, if a rise of the current of 0.47 A/s (3 830 $s \approx$ 1 h) is taking place at a coil inductivity of 13.3 H. The suggested power supply from of American Magnetics Inc. (AMI's High-Current Power Supply System) consist of an AMI Model 420 Programmer (configured for 2000 A operation), a Danfysik 860 Current Measuring System with a 2 000 A transducer head, and a 3rd party high-current DC power supply. The technical specifications of this power supply system is given in Table 10.8.

The power supply can operate with a stability of 0.01. It will be connected to the current leads by aluminium bars (cross section 2 000 mm^2, length 2×20m). The voltage drop at the bus bars is 2×0.5 V at an operational current of 1800 A.

10.4.1.8 Thermal Design

The coil is contained in the vacuum chamber and supported by high thermal resistance ties and struts. The coil is surrounded by a thermal shield, which is supported from the vacuum chamber and cooled with He gas (outlet temperature 60 K). Stainless steel foil plates, 50 μm in thickness and 400 mm in width, sputtered by high purity Al [4] are tack welded to the surfaces of the thermal shield and to the surfaces of the coil. They are used to reduce the heat loads both on the shield and on the coil. All ties and pillars, which support the coil, have heat intercepts connected to the thermal shield in order to reduce the heat load at 4.4 K. An evaluation of the heat loads on the coil and shield during stationary operation and during coil excitation has been carried out and the heat losses of the current leads have been estimated.

10.4.1.9 Vacuum Vessel

Since from the physics point of view a low radiation length is not required, stainless steel (12X18N10T) was chosen as the material for the cryostat. This assures mechanical stability of the cylindrical shells in the vacuum vessel. The design value for an overpressure in the cryostat is 0.7 bar. The minimum thickness of the outer shell of 4 mm is determined by the buckling limit. The thickness of the inner shell, which is subjected to internal pressure, is also 4 mm.

The ends of the shells are thickened to provide means for anchoring rods and pillars, which are used to support the coil. Furthermore, they will act as transition between the shells and the end caps (Fig. 10.33). Both shells of the cryostat have stiffening ribs (in groups of six) in radial direction.

The vacuum vessel has a chimney for the current leads, the liquid and gaseous helium inlets and outlets, the diagnostic wires and vacuum pumping (see

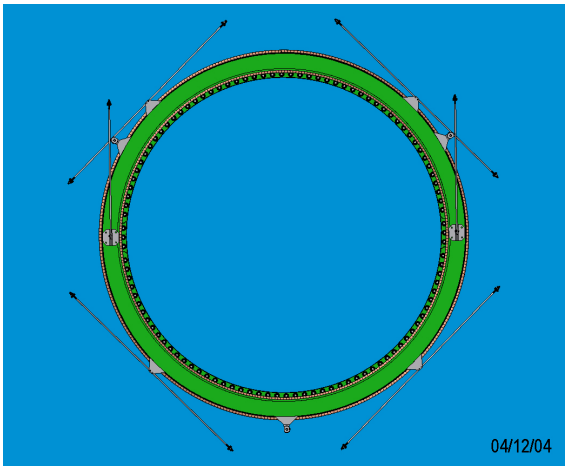

Figure 10.33: Cold mass support

in Fig. 10.20). It is coupled to the vacuum vessel by means of flanges and vacuum seals. All thickness values, which are presented here, will have to be checked with the Russian pressure vessel safety code.

10.4.1.10 Thermal Shield

The shield is made from a 3 mm thick Cu alloy. It is fixed to the vacuum vessel on the outer and inner shells using fiberglass supports. To reduce the heat load, stainless steel foils of 50 μm thickness and 400 mm in width, sputtered with high purity Al, are glued using Al adhesive tape (3M) to the surfaces of the thermal shield. At the surface of the thermal shield a cryo-getter panel is mounted to pump residual gas from the cryostat. It is consisting of a copper plate brazed to the shield surface, and small pieces of activated charcoal SKT-2B are glued on top.

10.4.1.11 Design of the Mandrel

The cylinder spool, apart from stiffening, must fix the coil in the cryostat against gravity and electromagnetic forces. Furthermore, it must provide indirect cooling. Assuming that the magnetic forces are supported completely by the conductor, the thickness of the stainless steel (12X18N10T) component was determined using constraints arising from small differential thermal contraction between the coil and the cylinder, and taking into account the lack of separation between the inner surface of the coil and the mandrel. The forces arise from the magnetic force to the inner surface of the coil during the energisation. The small separation can result in a spontaneous quench of the coil. A proper design is achieved using a correct value for the tension of the conductor during the process of coil winding. The choice of mandrel thickness is also crucial.

The coil is pre-stressed during the winding with a tensile stress of 3.5 kg/mm^2. A thickness of 10 mm is necessary due to the lack of separation previously mentioned (the differential thermal contraction between the coil and restraining cylinder is negligible). In Table 10.9 the results from calculations of the pressure at the surface of the coil mandrel are shown. These are arising from the different thermal coefficients of stainless steel in the coil mandrel and the composite material in the winding. P_{therm} is the equivalent magnetic force acting onto the coil inner surface, P_{magn} the pressure because of the tension of the superconducting wire in the process of winding, and $P_{winding}$ the resulting pressure at the mandrel surface in the operational conditions $P_{separation}$.

1^{st} coil	P_{therm}, kg/cm^2	-8.1
	P_{magn}, kg/cm^2	11.3
	$P_{winding}$, kg/cm^2	-10.5
	$P_{separation}$, kg/cm^2	-7.3
2^{nd} coil	P_{therm}, kg/cm^2	-6.0
	P_{magn}, kg/cm^2	8.4
	$P_{winding}$, kg/cm^2	-5.4
	$P_{separation}$, kg/cm^2	-3

Table 10.9: Pressure at the surface of the coil mandrel.

The numbering of the coils is equal to the one in Table 10.5. The integral coefficients for the stainless steel and composite material caused by coil shrinkage from 300 K to 4.2 K were found to be acceptable — 0.0031 and 0.0035 respectively. It is observed that for both coils the pressure at the mandrel surface is negative, which is desirable due to the lack of a separation under operational conditions.

After the winding of the superconductor, the maximum stress in the mandrel is 2 000 kg/cm^2, and the maximum hoop stress in the composite material of the coil is 1 120 kg/cm^2. These values are acceptable from the point of view of material strength. Because of the difference in thermal coefficients, the mandrel pre-stress is a necessary condition arising from the lack of separation. A smaller value for this difference could imply an additional bandage for the coil.

10.4.1.12 Coil Supports

The forces acting on the coil are: its own weight (68 kN) and the magnetic axial force (122 kN) arising from the asymmetry of the magnetic system. For this reason a simple structure for the coil supports was proposed: 20 stainless steel pillars of 400 mm^2 cross section, fixed at the ends of the outer vacuum shell, support the weight of the coil and support cylinder. These supports assure the alignment of the solenoid within the tolerances. The axial magnetic forces in the negative z-direction are taken up by 3 titanium rods, 13 mm in diameter, which are fixed to the outer vacuum shell and to the restraining cylinder (Figs. 10.20, 10.33).

10.4.1.13 Coil Construction

It is planned to build a dedicated winding facility in the clean area at Dubna. This facility will include a winding machine, an alignment device, a controlled tension machine (electromagnetic break), a cleaning unit, a taping unit and a device for passing the conductor. In the winding process a tension of about 50% of the yield stress will be applied to guarantee the integrity of the conductor during pancake winding. The conductor will be aligned and straightened under tension. Turn-to-turn insulation will be carried out during the winding process.

10.4.1.14 Test of the Coil Materials

Mechanical, thermal and electrical tests of the superconducting cable samples will have to be carried out at room temperature and at liquid helium temperatures.

10.4.1.15 Electrical Joints

With a total conductor length, exceeding 19 km, it will be necessary to have several joints (up to 10) inside the coil. The exact number of joints will depend on the design requirements and available lengths of the superconductor. A joint must have a resistance lower than $10^{-8}\,\Omega$ to limit the power loss to 4 mW at the maximum current. A simple well known method will be used, to solder overlapping cables across the full length of the turn near a spool flange.

10.4.1.16 Solenoid Dummy Model Coil and Tests of the Materials

To verify the most critical points of the project a model of the solenoid, about 1 m in diameter and about 1 m in length (the exact dimensions will depend on the accessible test cryostat), has to be constructed. The same superconducting cable, the same winding and insulation procedure will be used for this model.

The operation of the model will give important information on the following issues:

- RRR measurement of the magnet,
- measurement of the resistance of the cable joint,
- measurement of the temperature profile from the coil during indirect cooling as a function of helium flow,
- measurement of the temperature profile following a cool-down stop,
- heat losses during current changes,
- magnet temperature as a function of the liquid nitrogen shield temperature,
- measurement of mechanical strains in the winding,
- measurement of the temperature distribution during quenching,
- measurement of the induced current in the thermal shield,
- control of the separation between the coil inner surface and the mandrel.

The second dummy coil will be constructed to model the axial shear forces between the coil composite and the coil stainless steel mandrel. This has to be performed to validate the mechanical stability of the solenoid. The shear forces will be induced at this boundary using a SC electromagnetic press at the Kurchatov Institute (Moscow). The maximum force, which can be provided by this electromagnetic press, amounts to 10.2 t. It is planned to apply a shear stress at the inner surface of the dummy coil of up to 0.25 MPa with uniform cylindrical spacers and up to 15 MPa for non symmetrical arranged spacers. The main characteristics of the model and press coils are given in Table 10.10.

	Dummy coil	Power drive coils		Background field coil
		1	2	
Length, m	0.031	0.0285	0.0285	0.0525
Inner diameter, m	0.4	0.374	0.374	0.488
Outer diameter, m	0.449	0.450	0.450	0.588
Number of turns	4×4	90×6	90×6	
Current, A	2 200	800	800	800

Table 10.10: Main characteristics of the model and press coils.

Nominal steel 10 plate thickness	30
Number of plates	12
nominal block thickness	0.360m
(octagon and end cap modules)	
Weight of an octagon module, t	12.7
Weight of end cap modules, t	9.43
Overall dimensions of the yoke, m	
Length × Width × Height, m^3	3.572
	×3.481
	×3.481
Weight of the yoke, t	119.7

Table 10.11: Parameters of the iron yoke.

10.4.1.17 Iron Yoke

The yoke has an octagonal shape, which is closed by an end cap on both sides (see Figs. 10.18 and 10.20). The main parameters of the yoke are summarized in Table 10.11. The total weight of the yoke is 120 t.

The yoke is built of modules, which are bolted together. The octagonal cylinder splits into eight blocks. Each end cap module is split into two 4.7 t blocks. All blocks are constructed from steel sheets of 30 mm nominal thickness, welded together through the holes under pressure. The heaviest single piece of the yoke is 12.7 t to facilitate handling and transportation. An iron yoke carriage is intended for transportation of the solenoid from the parking position to the operational position.

Four rests support the bottom yoke parts. The assembly of the yoke is planned to be carried out *in situ*. After assembly of the cylindrical part of the yoke the upstream end cap will be mounted. The cryostat has to be placed into the yoke and initially fixed there. Then the downstream end cap will be inserted and the cryostat aligned relative the beam. The material of all modules consists of a low carbon steel (Steel 10). The chemical properties of this type of steel are shown in Table 10.12, its mechanical properties in Table 10.13, and the magnet properties in Table 10.14.

10.4.1.18 Timelines.

The timelines are given in Fig. 10.34.

10.4.2 Dipole

The dipole magnet (DM) of the forward spectrometer is planned to provide a bending power of 2 Tm. The "H-type" magnet will have a rectangular aperture, which opens up conically to the beam-downstream side. Three options have been considered in detail:

1. a conventional magnet with water-cooled winding with flat trapezoidal coils,
2. a conventional magnet with water-cooled winding with bedstead coils,
3. a superconducting magnet.

Option 1 is in construction the cheapest solution, the second option, however, provides much more space which may be needed to mount and service the detectors . Furthermore the field at the detectors generated by the ends of the coils is better for option 2. These disadvantages apply also to option 3, where the additional costs for building a superconducting system cannot be compensated due to lower operational costs during an operation period of 10 years. Though the conventional system with bedstead coils (option 2) seems favorable, the final choice will be made after a comprehensive analysis.

10.4.2.1 Conventional Type

Magnetic Field and Parameters. The winding of the conventional dipole magnet (Fig. 10.35) consists of two identical flat trapezoidal coils surrounding the magnet poles. A cross section of a coil

C	Si	Mn	S	P	Cr	Ni	Cu	N_2
0.07-0.014	0.17-0.37	0.35-0.65	0.04	0.035	0.15	0.25	0.25	0.08

Table 10.12: Chemical composition of Steel 10.

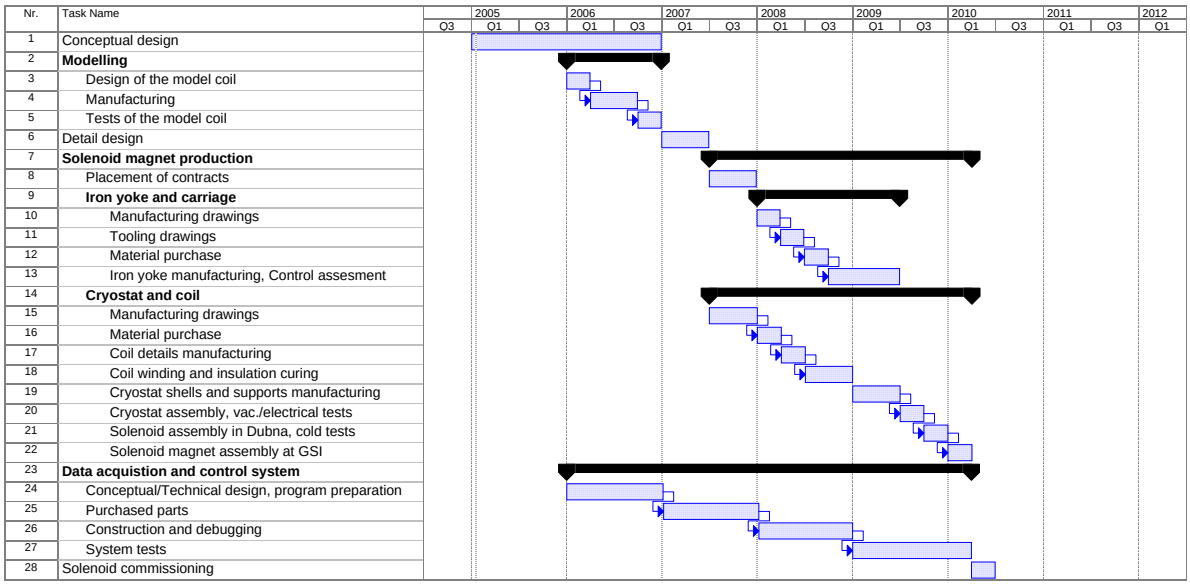

Figure 10.34: Time schedule for the superconducting solenoid magnet.

Item	Value
Coefficient of thermal expansion at 18°C, /°C	$13{\cdot}10^{-6}$
Young's module, Gpa	198
Tensile strength (annealed), MPa	340
Yield stress (annealed), MPa	210
Elongation, %	29

Table 10.13: Mechanical properties of Steel 10.

Induction, T	Magnetizing Field [A/m]
1.55	$<$ 2 179
2.01	$<$ 23 881

Table 10.14: Magnetic properties of Steel 10.

is shown in Fig. 10.36. Each coil includes 3 double pancakes. The pancakes are vacuum impregnated and therefore a coil behaves as a rigid unit whenever magnetic forces or thermal stresses are present. The coils, rigidly connected to the iron yoke by means of stainless steel brackets, are fixed at the bottom and top beams. The fixing construction does not require additional machining of the block surfaces.

The vertical magnetic field component distributions along straight lines with origin at $(x, y, z) = (0, 0, 0)$ are shown in Fig. 10.37. The maximum magnetic field B_y at the central axis of the dipole is 0.87 T. Field integrals of B_y along straight lines with origin at $(x, y, z) = (0, 0, 0)$ are given in Table 10.15. The average field integral in the aperture is 2.01 Tm. Approximate dipole magnet parameters are listed in Table 10.16. Distributions of the absolute value of the magnetic field induction for $z = 3.6$ m, 4.5 m and 5.4 m are presented in Figs. 10.38 – 10.40. The distribution of the field in the longitudinal section is presented in Fig. 10.41. The maximum field in the "back" of the yoke is about 1.4–1.5 T. The small pole area is saturated with a field of 2.1 T. So the iron yoke can be considered as unsaturated and its weight may be decreased later on.

The stray field distribution in the plane of the DM for $z = 4$ m is shown in Fig. 10.42. The maximal value of the stray field does not exceed 0.002 T at a radius > 4 m.

Power Supply. The winding will be powered by a DC power supply (Thyristor rectifier 5 kA 100 V).

φ_x φ_y	0°	2.5°	5°	7.5°	10°
−5°	1.863	1.868	1.895	1.970	2.012
−2.5°	1.955	1.951	1.935	1.868	1.595
0°	2.050	2.041	2.002	1.876	1.599
2.5°	2.158	2.153	2.135	2.063	1.785
5°	2.269	2.273	2.296	2.367	2.392

Table 10.15: Field integrals of the B_y component along straight lines with origin at $(x, y, z) = (0, 0, 0)$.

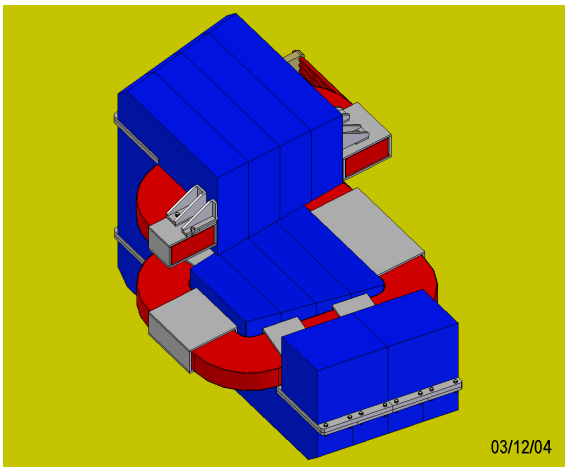

Figure 10.35: Dipole Magnet with aluminium water-cooled winding.

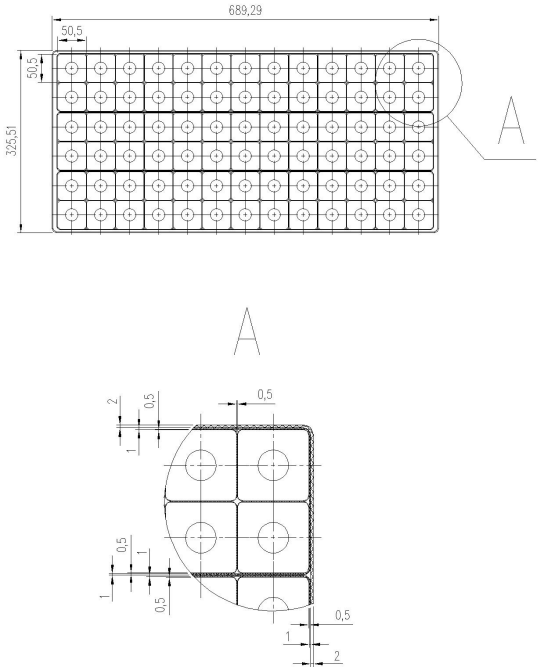

Figure 10.36: Cross section of the aluminium winding.

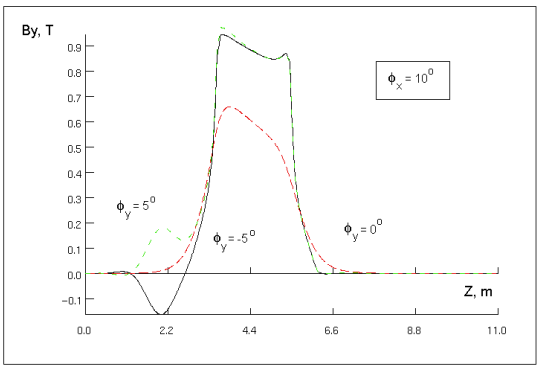

Figure 10.37: Magnetic field distributions of the B_y component along straight lines with origin at $(x, y, z) = (0, 0, 0)$.

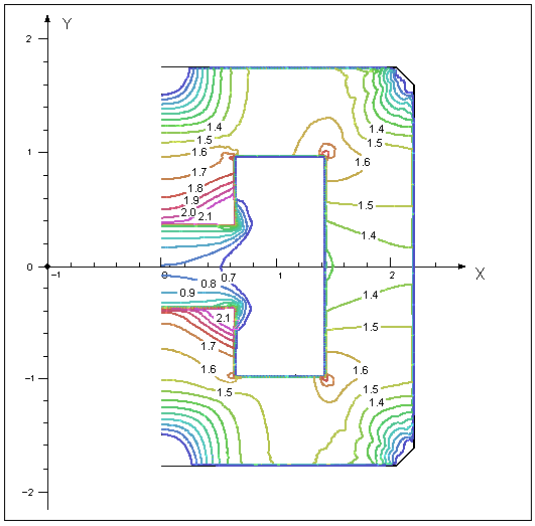

Figure 10.38: Distribution of the absolute value of the magnetic field induction at $z = 3.6\,\mathrm{m}$

Conductor. The material of the conductor is extruded aluminium AD0 with a purity of 99.5%. Impurities are: Fe $\leq 0.3\%$, Si $\leq =0.3\%$, Cu $\leq 0.015\%$. The total amount of impurities for this material must be $\leq 0.5\%$, according to GOST 4784-74. The main properties of the conductor material are

Item	Unit	Value
1. Magnetic field		
1.1 Maximum flux density on the magnet axis	T	0.87
1.2 Average Field Integral in the aperture	Tm	2.01
1.3 Winding inductivity	H	0.209
2. Electric consumption		
2.1 Amp-turns total RMS	kA	2×275
2.2 Operation current	kA	3.525
2.3 Winding Resistance at 40°C	Ω	0.020145
2.4 Power consumption	kW	250
3. Winding		
3.1. Conductor weight	t	9.25
3.2 Turn-to-turn Insulation thickness	mm	1
3.3 Inter-pancake insulation thickness	mm	2
3.4 Ground insulation thickness	mm	5
3.5 Average length of a turn	m	9.438
3.6 Conductor length	km	1.472
3.7 Number of double pancakes in a coil		3
3.8 Number of turns per a pancake		2×13
3.9 Number of turns per winding		156
4. Conductor		
4.1 Material, Al		AD0
4.2 Conductor cross section	mm^2	50.5×50.5
4.3 Channel diameter	mm	16.5
4.4 Radius of edges	mm	3
4.5 Al cross section area	mm^2	2 328.7
5. Cooling		
5.1 Cooling water flow rate	l/s	1.99
5.2 Cooling water pressure drop	Bar	5.4
5.3 Water temperature drop, (max)	°C	30
6. Magnet yoke		
6.1 Length of the iron yoke	mm	2 000
6.2 Pole gap (at z=3.5m)	mm	713
6.3 Pole gap (at z=5.5m)	mm	1 063
6.4 Yoke weight	t	189
7. Overall dimensions of the magnet		
7.1 Length	mm	3 551
7.2 Width	mm	5 318
7.3 Height	mm	3 504
7.4 Distance up to the centre of the DM	mm	4 500

Table 10.16: Main characteristics of the dipole magnet with flat trapezoidal coils.

shown in Table 10.17.

The conductor dimensions are in accordance with TU-1-5-027-77 for hollow extruded aluminium conductor of Verchnyaya Salda Metallurgical Production Association (VSMPO Joint Stock Co., Russia). The corners of the conductor are to be rounded with a radius of (3±0.4) mm.

Conductor Cooling. The turns of one section form a single water circuit. Concerning the cooling water all sections will be connected in parallel. The water circuits of the magnet will be designed according to Fig. 10.43. The coils should be cooled by circulating de-mineralized water. The inlet water temperature can vary between $15 - 25$°C. Within the coils a maximum rise of temperature of the cooling water will be 30°C. Under these condi-

Item	Value
Max. Electrical resistance at 20°C, Ω×m	$< 2.95\times10^{-8} > 2.92\times10^{-8}$
Temperature coefficient of resistance at 20°C, Grad^{-1}	4.0×10^{-3}
Coefficient of thermal expansion at 20°C, /°C	23.5×10^{-6}
Young's module, GPa	71
Tensile strength of annealed sample, Mpa	70
Strength yield stress of annealed sample, MPa	40
Elongation, %	> 15

Table 10.17: Main properties of the aluminium AD0 used as conductor.

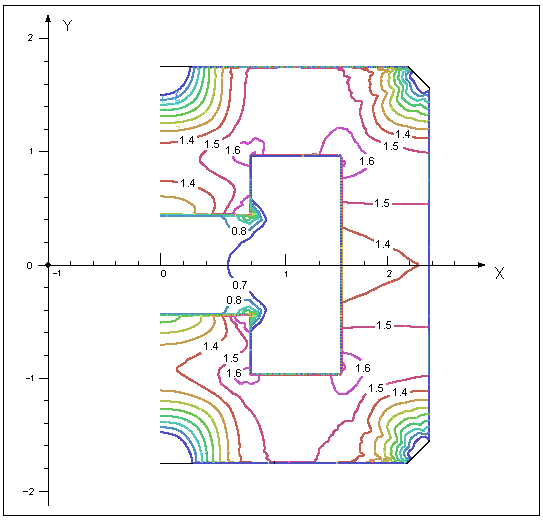

Figure 10.39: Distribution of the absolute value of the magnetic field induction at $z = 4.5\,\text{m}$

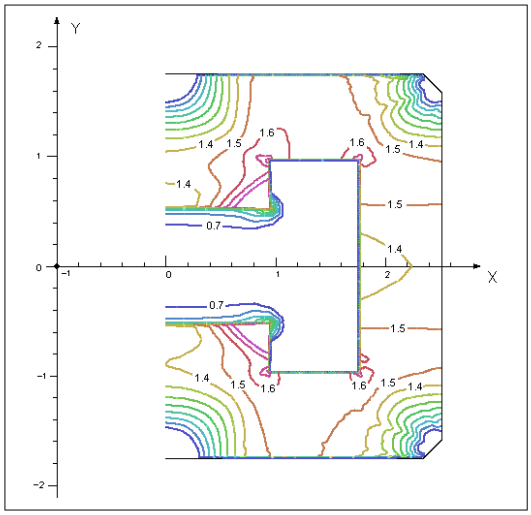

Figure 10.40: Distribution of the absolute value of the magnetic field induction at $z = 5.4\,\text{m}$.

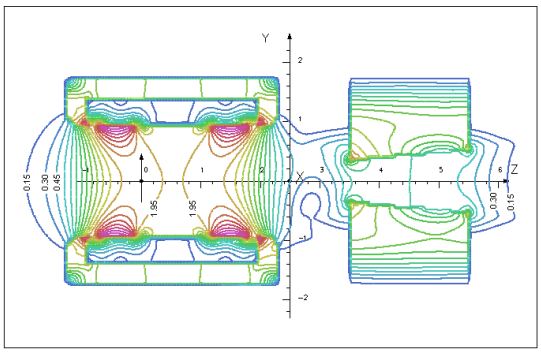

Figure 10.41: Distribution of the absolute value of the magnetic field induction (longitudinal cross section).

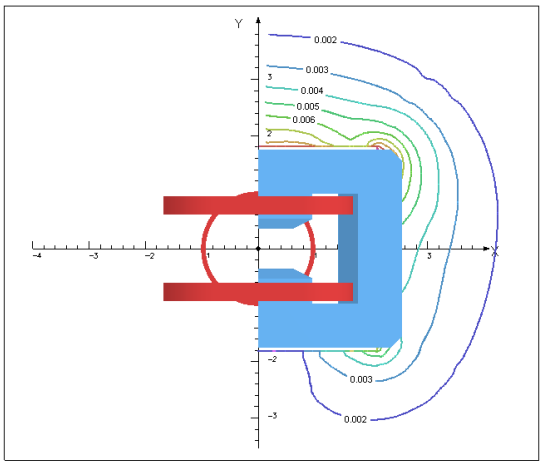

Figure 10.42: Stray field distribution at $z = 4\,\text{m}$.

tions the maximum coil temperature will be about 55°C. The cooling water flow rate will be 21/s, and the maximum pressure drop in the cooling water will be 5.4 bar.

Insulation. The turn-to-turn, interlayer and ground plane insulation of the magnet is made of glass-fibre reinforced plastic. In the process of the

coil production dry glass-fibre tapes are applied and then the coils have to be vacuum impregnated with epoxy resin and cured at a temperature of about 130°C. The insulation system must withstand repeated thermal cycling and radiating doses without mechanical or electrical failure. The CIBA epoxy resin is chosen such that the coil behaves as a rigid unit whenever magnetic forces or thermal stresses are applied or released.

Electrical connections. Pancake-to-pancake electrical connections are realised by means of welding air-cooled aluminium bars to current leads. All pancakes and both of the coils should be electrically connected in series.

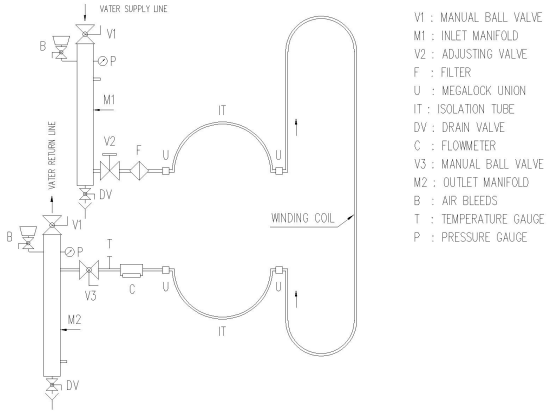

Figure 10.43: Water circuits of the dipole magnet.

Design. Front, top and side views of the dipole magnet with water-cooled coils are shown in Figs. 10.44, 10.45, and 10.46.

Coils. The manufacturing procedure involves the winding of flat double pancakes with one continuous length of a hollow aluminium conductor. After the final assembly of all the double pancakes, the package has to be pressed and wrapped with a ground wall insulation. After the epoxy vacuum impregnation, the coil package will be compressed vertically and the epoxy compound cured at a temperature of about 130°C.

For the welding of the pancake-to-pancake connections SV.A5 or SV.A97 (*GOST 7871-75*), aluminium and aluminium alloys welding wire, or equivalent, will be used. The installation of the water connections will be carried out using screw joint transitions with rubber seals, which will be fixed in the cooling channels. The water joints will be connected to manifolds through rubber tubes. Individual testing of the pancakes must precede the assembly of every coil.

After curing the insulation, the coils will be subjected to thermal cycles by letting current flow through them and simultaneously adjusting the water flow to obtain a temperature rise of 35°C between inlet and outlet. The current will then be reduced to zero while the cooling water flow will be increased to its nominal value. No cracks, fissures, delaminating *etc.* should occur during this procedure. The coolant circuits will also be tested for flow and pressure drops and shall be subjected to a hydrostatic pressure test. The DC resistance at each coil will be measured and recorded continuously. A voltage spike will be employed to the coil to control short turns. Furthermore, measurements of the ground plane insulation resistance will be performed.

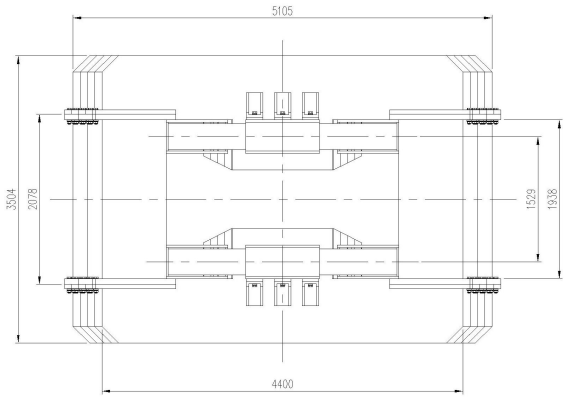

Figure 10.44: Front view of the dipole magnet with water-cooled winding.

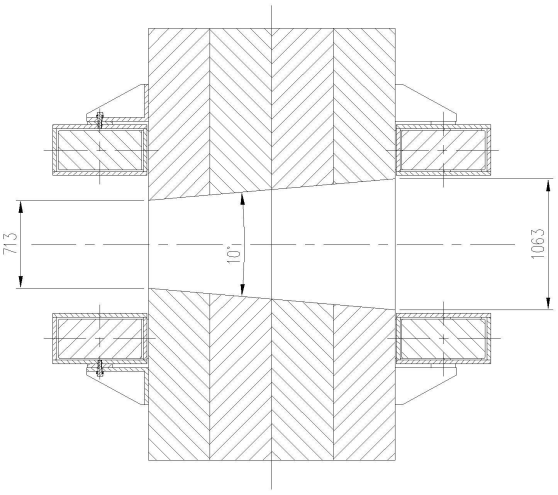

Figure 10.45: Side view of the dipole magnet with water-cooled winding.

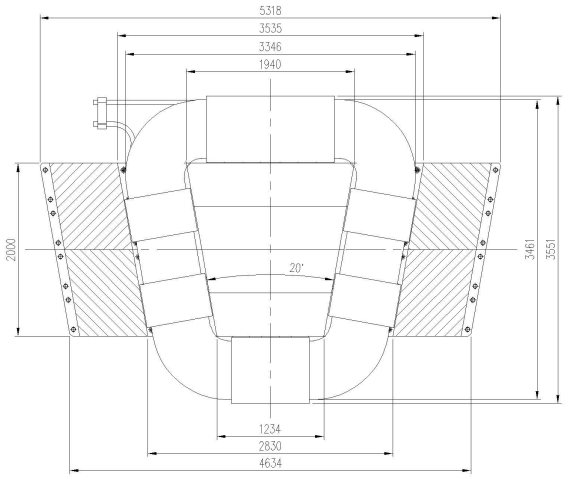

Figure 10.46: Top view of the dipole magnet with water-cooled winding.

Iron Yoke. The yoke consists of four blocks made from low carbon steel: bottom and top beams, and two uprights. Each bottom and top block consists of four modules; each of the vertical blocks consists of four modules. All blocks include a set of 30 mm steel sheets, welded under pressure through their holes. The sidewalls and poles of the yoke follow the angular acceptance of the magnet - 5° in the vertical plane and 10° in the horizontal plane.

Tension rods will be used to consolidate the horizontal beams and the uprights. Adequately positioned dowel pins will guarantee the alignment between sub-units. To guarantee a precise match at the junction between those parts, flanges should be welded at the outer ends of the sub-units and machined simultaneously with the mating surfaces. The mechanical connection will then be achieved with tension bolts between the flanges. The mutual positioning of the reference surfaces of the side blocks on the assembled yoke has to be reproducibly repeated.

The material of the modules is low carbon steel – Steel 10, like the material for the iron yoke of solenoid. Chemical, mechanical and magnetic properties of this steel are shown in Tables 10.12 to 10.14. The maximum weight of one yoke module is about 18 tons.

An assembly at the producer will be necessary to test the magnetic circuits, correct the geometry, establish all reference surfaces, and locate the reference and alignment dowels. Subsequent reassemblies will not require realignment of the subunits.

Assembly of the Complete Dipole Magnet will proceed with individual tests of the coils and the assembled yoke. There will be two stages for the assembly:

1. assembly of the magnet for acceptance tests at JINR (Dubna),
2. final assembly of the magnet for commissioning in the experimental hall at FAIR.

To mount the coils, elastic pads of adequate thickness inserted between the coil surfaces and clamps will be used to correct the position of the coils, to take up surface irregularities, and to allow for thermal expansion of the coil.

The sequence of the assembly is foreseen in the following order:

- The modules of the bottom part of the iron yoke will be assembled on the aligned surface plate, clamped together by means of tension rods and fixed by dowel pins.
- Upright modules will be erected on the bottom part, clamped together and fixed to each other at the bottom part.
- Top modules will be mounted, clamped together and fixed by dowel pins.
- All bolt connections will be tightened.
- The space frame with the upper coil will be mounted in the yoke aperture, in order to make the upper coil mounting and fixing easier. The upper coil will be mounted and fixed to the pole.
- The space frame will be extracted from the aperture.
- The bottom coil will be fixed onto the pole by means of a hoisting device and then clamped.
- Electrical and water coil interconnections will be mounted.

The first assembly of the dipole magnet and the first tests will be carried out in building 205 at JINR. After this, the magnet will be disassembled and dispatched to Germany, and set up at FAIR.

Acceptance Tests of the Magnet. Electrical tests on the complete magnet will include the application of a DC voltage between the terminal of the winding and the yoke. The leakage resistance should be less than 1 000 MΩ.

The operation test of the complete magnet will include powering it up to the operating current for a period of at least two hours. Local hot spots or other faults during this period would be recorded.

Transport Fixtures. It is planned to bring all parts of the magnet to FAIR on land (i.e. lorry or railway). In the past, the most difficult constraint proved to be the European restrictions for road transport limiting the unit weight to about 25 tons. With a maximum weight of a yoke module of about 18 tons, this problem should not arise. Special arrangements will be required for the transport of the coils. The design of the yoke modules includes lifting brackets adequate for assembly and for splitting the yoke for the transport.

Timelines. The timelines are given in Fig. 10.47.

10.4.2.2 Dipole Magnet with Bedstead Coils

Magnetic Field and Parameters. The winding of the Conventional Dipole Magnet with bedstead coils consists of two identical coils surrounding the magnet poles. The individual coil sections are similar in shape to the coils shown in Fig. 10.3. Each coil includes 3 double pancakes. The pancakes are vacuum impregnated and therefore behave as rigid bodies whenever magnetic forces or thermal stresses are applied. The coils, rigidly connected to the iron yoke by means of stainless steel brackets, are fixed to the bottom and top beams. The fixing construction does not require additional machining of block surfaces.

The vertical magnetic field component distributions along straight lines with origin at $(x, y, z) = (0, 0, 0)$ are presented in Fig. 10.50. The maximum magnetic field B_y at the central axis of the dipole is 0.87 T. Field integrals of the B_y component of the magnetic field along the straight lines with origin at $(x, y, z) = (0, 0, 0)$ are given in Table 10.18. The average field integral in the aperture is 1.99 Tm. Approximated Dipole Magnet parameters are listed in Table 10.19. The distributions of the absolute value of the magnetic field induction in the sections at $z = 4$ m, and 4.75 m are presented in Figs. 10.48a and 10.48a. Fig. 10.48c shows that the poles are saturated. The distribution of the field in a longitudinal section is presented in Fig. 10.48d. The small pole area near the sharp ends of the poles is saturated with a field of about 2.6 T. The maximum field in the "back" of the yoke is about 2 T, so the iron yoke can be considered as saturated, too.

The current density dependence of the average field integral in the dipole magnet aperture is shown in Fig. 10.53. The operation point $J = 1.52{\cdot}10^6$ A/m^2 lies in the saturated area. This requires further investigation.

The stray field distributions in the cross sections of the magnet at $z = 5$ m and 6 m are shown in Fig. 10.51 and Fig. 10.52. The maximum value of the stray field does not exceed $2.5{\cdot}10^{-3}$ T at a radius > 5m.

The changes in the y component of the magnetic field in the area between the solenoid and dipole magnet can be observed in Fig. 10.54 and compared with the alternative racetrack coil design in Fig. 10.22.

The magnetic forces between the solenoid and dipole magnets are smaller than those of the racetrack coil design - as one would expect given the increased distance between the magnets for the bedstead design. The accumulated energy of the dipole magnet is higher than for the previous design option: 2.7 MJ, instead of 1.3 MJ.

$$\text{Average value} \left(\int_0^\infty B_y \, dl \right) = 1.987 \, \text{Tm}$$

Power Supply. The winding will be powered by a DC power supply (Thyristor rectifier 5 kA 100V) for a constant magnetic field.

Conductor. See Sec. 10.4.2.1. The level of resistive losses can be kept below 300 kW, if the material of the conductor is hollow Cu.

Conductor Cooling. The Dipole Magnet water circuits will be built as shown in Fig. 10.43. The cooling water flow rate will be 3.7 l/s, the maximum cooling water pressure drop 8 bar.

The insulation and electrical connections are done as described in Sec. 10.4.2.1.

Dipole Magnet Design. Top, side and front views of the water-cooled DM with bedstead coils are shown in Figs. 10.55, 10.56, and 10.57.

DM Coils. The manufacturing procedure for the bedstead coil involves the winding of flat double pancakes, shaping the pancakes, staging of the pancakes in a package, wrapping around by dry ground wall insulation, impregnation of the coil with an epoxy compound and curing of the compound.

Nr.	Task Name
1	Conceptual design
2	**Modelling**
3	Tests of the materials
4	Design of the model coil
5	Manufacturing
6	Tests of the model coil
7	Detail design
8	**Dipole magnet production**
9	Placement of contracts
10	**Iron yoke**
11	Manufacturing drawings
12	Tooling drawings
13	Material purchase
14	Iron yoke manufacturing, Control as
15	**Aluminium coil**
16	Manufacturing drawings
17	Material purchase
18	Tooling manufacturing
19	Coil pancake winding
20	Coil assembly and insulation curing
21	Dipole magnet assembly in Dubna
22	Dipole magnet commissioning at GSI

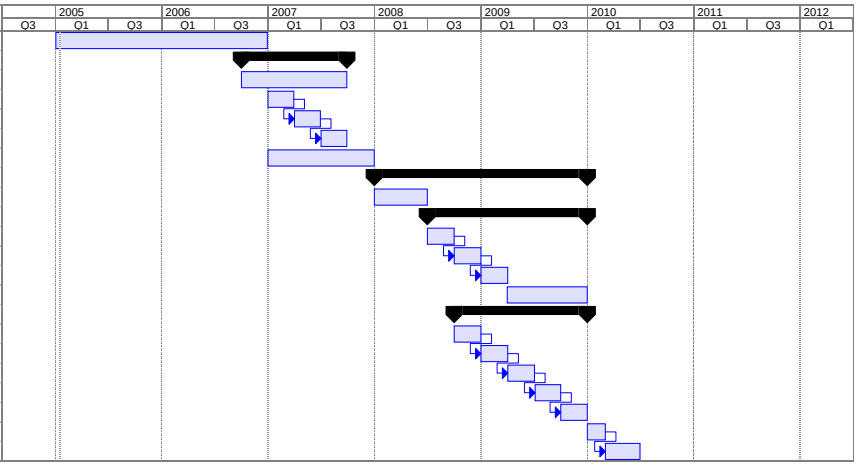

Figure 10.47: Time schedule for the conventional dipole magnet.

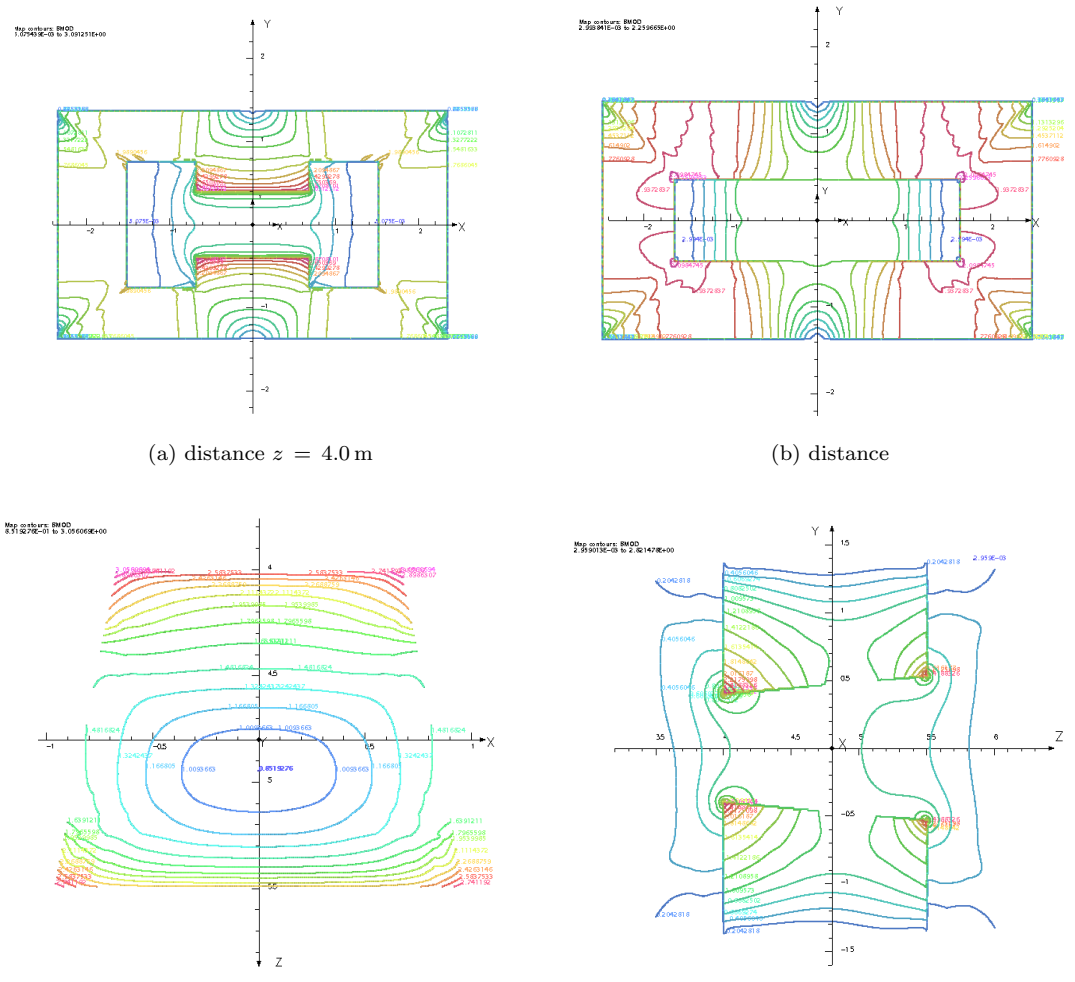

(a) distance $z = 4.0\,\mathrm{m}$

(b) distance

(c) pole surface

(d) longitudinal section

Figure 10.48: Distribution of the absolute value of the magnetic field induction.

The winding of the flat double pancakes is similar to the process described in Sec. 10.4.2.1. The bending

φ_x \ φ_y	0°	2.5°	5°	7.5°	10°
- 5°	1.839	1.840	1.843	1.862	1.738
- 2.5°	1.925	1.921	1.905	1.864	1.790
0°	2.017	2.010	1.987	1.929	1.789
2.5°	2.120	2.115	2.099	2.055	1.979
5°	2.229	2.229	2.231	2.246	2.116

Table 10.18: Field integrals of the B_y component along straight lines starting at $(x, y, z) = (0, 0, 0)$.

Item	*Unit*	*Value*
1. Magnetic field		
1.1 Maximum flux density on the magnet axis	T	0.87
1.2 Average Field Integral in the aperture	Tm	1.99
1.3 Winding inductivity	H	0.283
2. Electric consumption		
2.1 Amp-turns total RMS	kA	2×341
2.2 Operation current	kA	4.37
2.3 Winding Resistance at 40 °C	Ω	0.024037
2.4 Power consumption	kW	459
3. Winding		
3.1 Conductor weight	t	10.12
3.2 Turn-to-turn Insulation thickness	mm	1
3.3 Inter-pancake insulation thickness	mm	2
3.4 Ground insulation thickness	mm	5
3.5 Average length of a turn	m	10.777
3.6 Conductor length	km	1.681
3.7 Number of double pancakes in a coil		3
3.8 Number of turns per a pancake		2×13
3.9 Number of turns per winding		156
4. Conductor		
4.1 Material, *Al*		AD0
4.2 Conductor cross section	mm^2	50.5 x 50.5
4.3 Channel diameter	mm	20
4.4 Radius of edges	mm	3
4.5 Al cross section area	mm^2	2228.4
5. Cooling		
5.1 Cooling water flow rate	l/s	3.66
5.2 Cooling water pressure drop	bar	7.9
5.3 Water temperature drop, (max)	°C	30
6. Magnet yoke 6.1 Length of the iron yoke	mm	1 500
6.2 Pole gap (at $z = 4.0$ m)	mm	800
6.3 Pole gap (at $z = 5.5$ m)	mm	1 063
6.4 Yoke weight	t	120
7. Overall dimensions of the magnet		
7.1 Length	mm	2 833
7.2 Width	mm	5 219
7.3 Height	mm	3 334
7.4 Distance up to the centre of the DM	mm	4 750

Table 10.19: Main characteristics of the dipole magnet with water cooled bedstead coils.

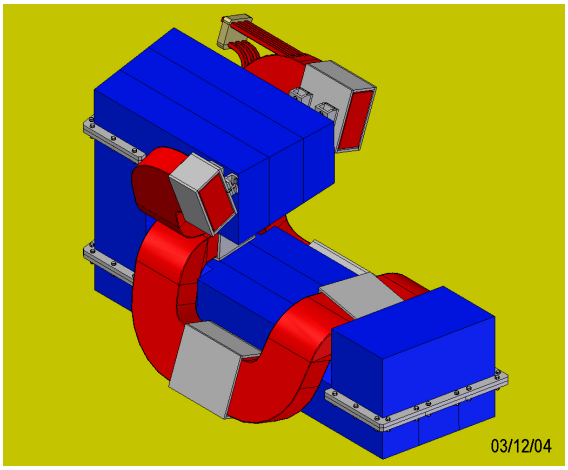

Figure 10.49: Dipole Magnet with aluminium water-cooled bedstead winding.

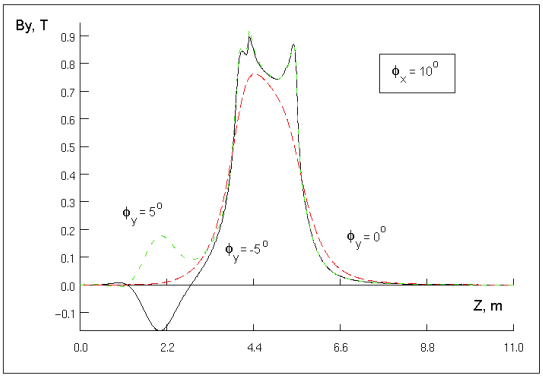

Figure 10.50: Magnetic field component B_y distributions along straight lines starting at the origin.

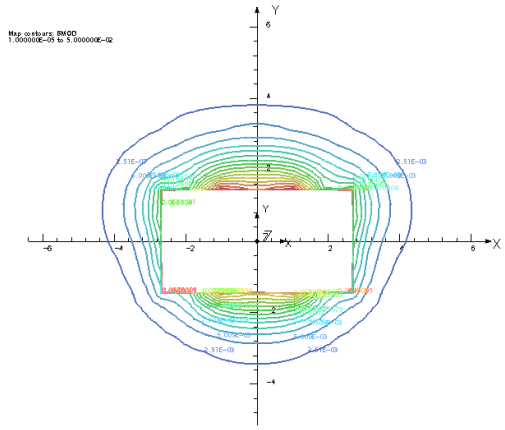

Figure 10.51: Stray field distribution at $z = 5\,\mathrm{m}$.

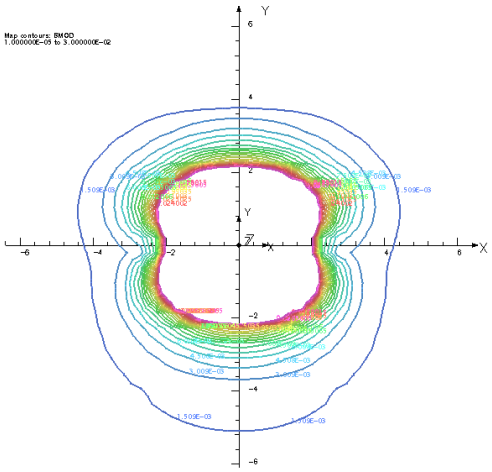

Figure 10.52: Stray field distribution at $z = 6\,\mathrm{m}$.

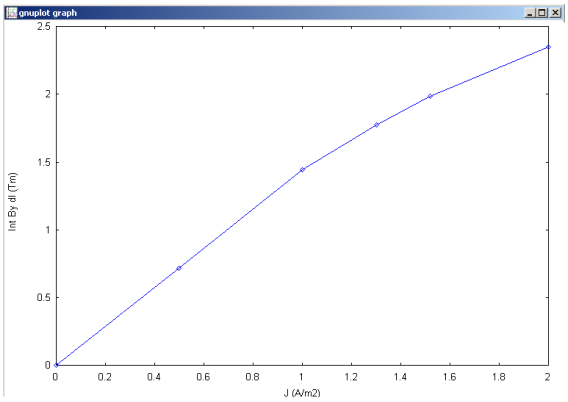

Figure 10.53: Current density dependence of the average field integral in the dipole magnet aperture.

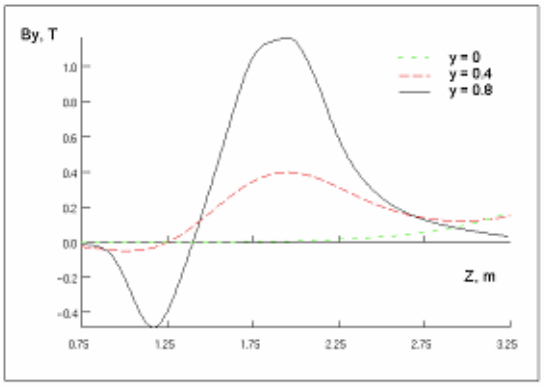

Figure 10.54: Magnetic field induction (y component) in the area between solenoid and dipole magnets.

of the flat pancakes could be done as for the ALICE dipole coil prototype (Fig. 10.58) made in JINR or for the coils at SigmaFi (France). Again, individual testing of the pancakes must precede the assembly of every coil.

Thermal test of the coils, pressure and flow mea-

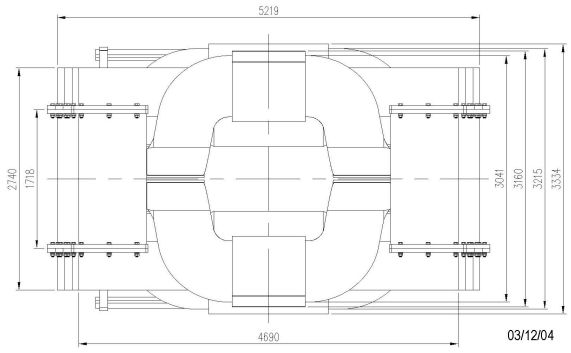

Figure 10.55: Front view of the dipole magnet with water-cooled bedstead winding.

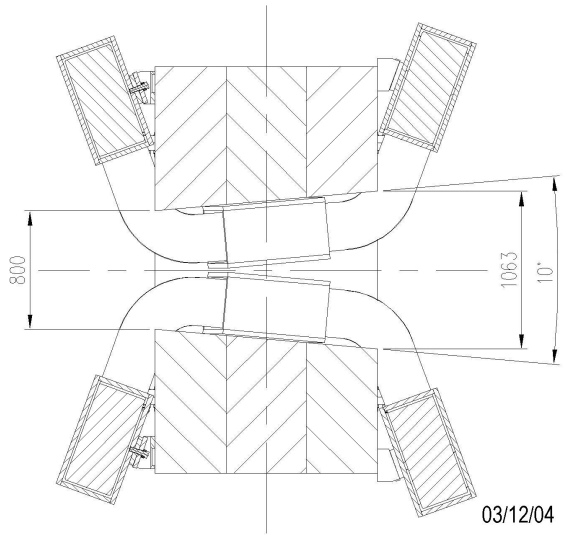

Figure 10.56: Side view of the Dipole Magnet with water-cooled bedstead winding.

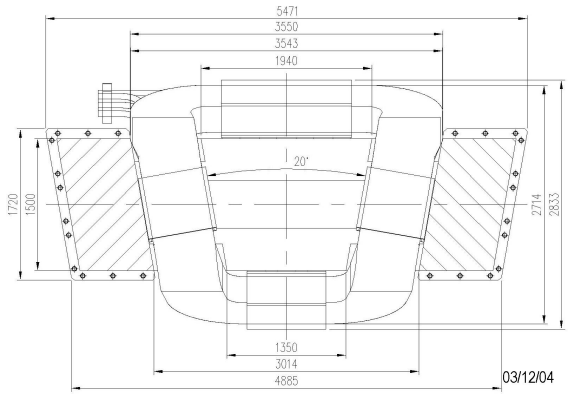

Figure 10.57: Top view of the Dipole Magnet with water-cooled bedstead winding.

surements for the coils, electrical tests and measurements for the coils will be prepared according to Sec. 10.4.2.1.

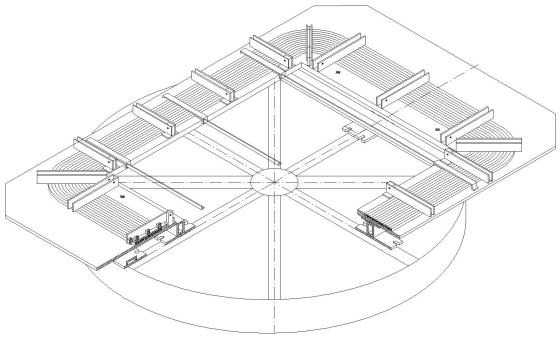

Figure 10.58: The jig for the winding of flat pancakes.

Iron Yoke. The weight of the yoke will be 120 t. The main features of the yoke are similar to those of the yoke with flat trapezoidal coils (see Sec. 10.4.2.1. The maximum weight of a yoke module is about 18 t.

Assembly of the Complete Dipole Magnet. The assembly of the yoke is similar to that of the racetrack coil magnet. (see Sec. 10.4.2.1) Acceptance tests of the magnet the transport fixings will be handled as described in Sec. 10.4.2.1.

Timelines. The timelines are given in Fig. 10.59.

10.4.2.3 Dipole Magnet with Superconducting Windings

The winding of this dipole magnet (Fig. 10.60) would consist of two identical flat superconducting coils of trapezoidal form surrounding the magnet poles. A cross section of the coil is shown in Fig. 10.61. Each coil includes two pancakes. The coils will be using a NbTi/Cu conductor, which is identical to the conductor used for the solenoid winding. The coils will be of core-less type and vacuum impregnated with epoxy resin. They will be indirectly cooled by a flow of liquid helium trough cooling pipes, which will be welded to the Al case surface or included in the winding pack to ensure effective cooling. The coil pancakes will be supported in aluminium support frames, which are likely to have cold supports between the straight sections of the coils in order to resist the tendency of the coil to become round. Four adjustable ties will join both coil frames.

Nr.	Task Name
1	Conceptual design
2	**Modelling**
3	Tests of the materials
4	Design of the model coil
5	Manufacturing
6	Tests of the model coil
7	Detail design
8	**Dipole magnet production**
9	Placement of contracts
10	**Iron yoke**
11	Manufacturing drawings
12	Tooling drawings
13	Material purchase
14	Iron yoke manufacturing, Control assesment
15	**Aluminium coil**
16	Manufacturing drawings
17	Material purchase
18	Tooling manufacturing
19	Coil pancake winding
20	Coil pancake shaping
21	Coil assembly and insulation curing
22	Dipole magnet assembly in Dubna
23	Dipole magnet commissioning at GSI

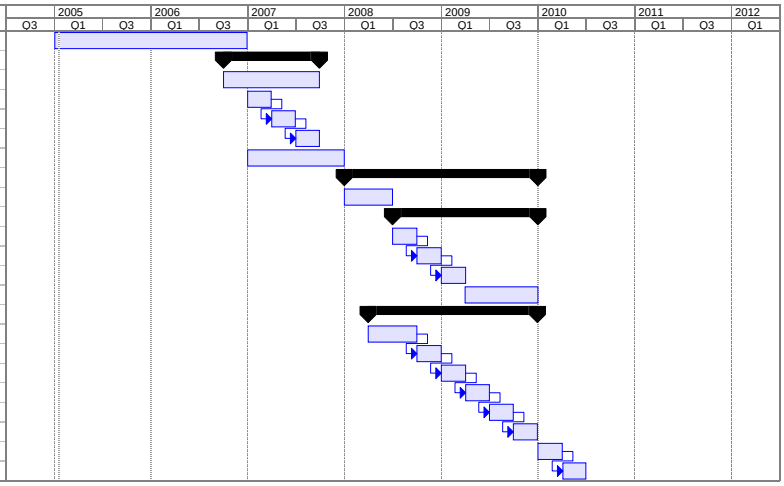

Figure 10.59: Time schedule for the dipole magnet with bedstead type coils.

The cold mass will have a 60 K radiation screen in between formed from rigid panels and the inner and outer vacuum case vessels. The cold mass will be supported from the outer and inner vacuum cases by a number of tension ties.

Magnetic Field and Parameters. The magnetic field distribution and the field integrals of the DM with superconducting winding are very similar to the magnetic field and the integrals for the conventional dipole magnet with water cooled winding (see Sec. 10.4.2.1).

The main parameters of the magnet are given in Table 10.20. The coil pancakes were designed with an average current density of $5.27{\cdot}10^7$ A/m^2. This density corresponds to an operating current of 1 919 kA. The stored energy in the winding is 1.8 MJ.

TOSCA calculations were used to calculate the forces acting on the coils and the iron yoke. The forces acting on the components for different operational regimes of the PANDA magnet system are shown in Table 10.21 — very large forces act on some magnet parts in different regimes. Further design work is required to investigate this. The forces that act on different parts of the coil are listed in Table 10.22.

Cooling Mode and Conductor Design. Indirect cooling was chosen for the superconducting winding. Cryogenic aluminium pipes will be welded to the Al support structure. The full length of the conductor in the coils is 3.67 km. The weight of the conductor is 0.917 t.

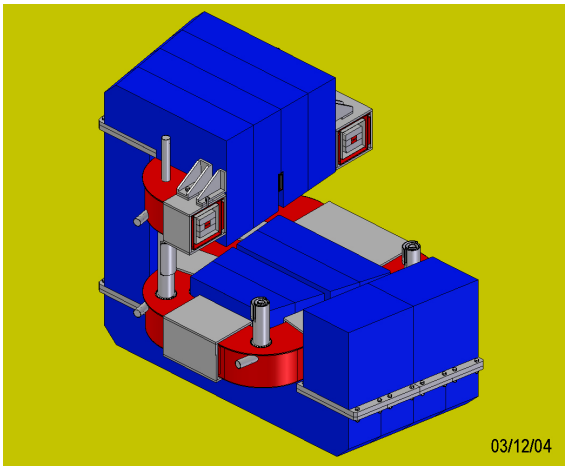

Figure 10.60: Dipole magnet with superconducting winding.

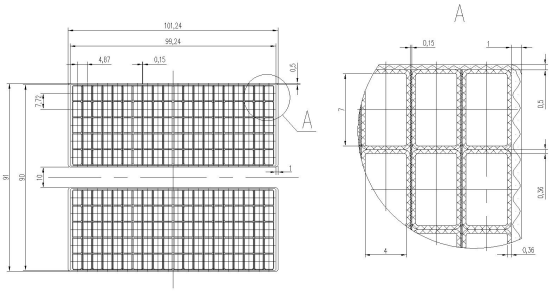

Figure 10.61: Cross section through a superconducting winding.

Item	*Unit*	*Value*
1. Magnetic field		
1.1 Maximum flux density on the magnet axis	T	0.87
1.2 Average Field Integral in the aperture	Tm	2.1
1.3 Maximal magnetic field in the coil	T	1.2
2. Electric parameters		
2.1 Amp-turns total	kA	2×307
2.2 Operation current	kA	1.920
2.3 Design current density in a coil pancake	A/m^2	$5.27 \cdot 10^7$
2.4 Self inductance	H	0.98
2.5 Stored Energy	MJ	1.8
3. Winding		
3.1 Turn-to-turn Insulation thickness	mm	0.3
3.2 Layer-to-layer insulation thickness	mm	0.15
3.3 Ground insulation thickness	mm	1.0
3.4 Average length of a turn	m	11.47
3.5 Conductor length	km	3.67
3.6 Weight of the conductor	t	0.917
3.7 Number of pancakes in a coil		2
3.8 Number of turns per a pancake		4×20
3.9 Number of turns per winding		320
4. Conductor		
4.1 Material		NbTi/Cu
4.2. Conductor cross section (without insulation)	mm^2	4 x 7
5. Magnet yoke		
5.1 Length of the iron yoke	mm	2 000
5.2 Pole gap (at $z = 3.5$ m)	mm	713
5.3 Pole gap (at $z = 5.5$ m)	mm	1 063
5.4 Yoke weight	t	200
6. Overall dimensions of the magnet		
6.1 Length	mm	3 399
6.2 Width	mm	5 110
6.3 Height	mm	3 866
6.4 Distance up to the centre of the DM	mm	4 500

Table 10.20: Main characteristics of the dipole magnet with superconducting winding.

	Fx, kN	Fy, kN	Fz,kN
Solenoid switched on, DM switched on			
Coil	0	44.04	175,5
Yoke	0	-86.3	-27.1
Solenoid switched off, DM switched on			
Coil	0	0.5	17.6
Yoke	0	-0.5	-18.3
Solenoid switched on, DM switched off			
Yoke			-12.5

Table 10.21: Forces acting on parts of the dipole magnet (DM).

N	Fx (kN)	Fy (kN)	Fz (kN)
1	0	66.17	-13.71
2	28.61	196.6	-5.044
3	0	77.31	73.6
4	-28.61	196.6	-5.044
5	-11.57	22.45	-14.67
6	11.57	22.45	-14.67
7	21.08	46.02	21.97
8	-21.09	46.02	21.98
$\sum$	-0.01	673.62	64.412
1'	0	-18.15	15.92
2'	25.14	-200.9	-4.432
3'	0	-84.42	73.5
4'	-25.14	-200.9	-4,432
5'	-6.542	-13.97	-6.767
6'	6.542	-13.97	-6.767
7'	21.21	-48.62	22.05
8'	-21.21	-48.62	22.05
$\sum$	0	-629.6	111.122
Grand Total	0	44.04	175.5

Table 10.22: Forces acting on parts of the coil when the solenoid and dipole magnet are switched on.

Quench Protection and Power Supply. The energy stored in the Panda solenoid magnet and the engineering current density in the winding are 1.8 MJ and $5.27{\cdot}10^7$ A/m^2 respectively. If, after a quench, the accumulated energy could be uniformly distributed in the coil conductor, the maximal temperature rise would not exceed 20 K. Special measures have, however, to be taken to protect the coil against destruction after a quench, because the energy released at the hottest point in the coil can be significantly higher than average. A passive protection method includes the subdivision of the winding by sections and shunting by cold resistances. It is considered to use active heaters in order to accelerate the quench. A sketch of the protection circuit is shown in Fig. 10.31. When a quench is detected by voltage taps in the coil, the protection switch is opened to accelerate the entire winding quench (by heating the winding). Therefore it prevents the cold resistor to overload, while retaining the advantages of the passive protection by subdivision.

Power Supply. The winding will be powered by a DC power supply identical to the power supply for the solenoid winding. The power supply will be connected to the current leads by aluminum bars (cross section 2 000 mm^2, length 2×20 m). The voltage drop at the bus bars will be 2×0.6 V at the operational current of 1 919 A.

Thermal Design. The coils will be contained in vacuum chambers and supported by high thermal resistance ties and struts. The coils will be packed in a thermal shield supported by the vacuum chamber and cooled with helium gas (outlet temperature 60 K). Stainless steel foil plates (50 μm in thickness and 400 mm in width, sputtered by high purity aluminium [2]) will be tack-welded to the surfaces of the thermal shield and to the surfaces of the coil. This will reduce the heat load both on the shield and on the coil. All ties and pillars supporting the coil have heat intercepts connected to the thermal shield in order to reduce the heat load at 4.4 K. An estimate of the heat load on the coil and the shield during stationary operation as well as during coil excitation are shown in Table 10.23, together with estimated heat losses for the current leads.

Coil and Cryostat Design. Front, side and top views of the dipole magnet with superconducting winding are shown in Figs. 10.62, 10.63, and 10.64. Each cryostat contains two pancakes. The pancakes operate under heavy-duty conditions — they are exposed to gravity and electromagnetic forces (including the interaction forces with the solenoid magnet). The coils are cased in an aluminium mandrel to prevent large deformations of the superconductor. The calculation of the sags for the coil straight parts are shown in Fig. 10.65.

In the production process, each coil will be externally wound on a dummy mandrel having the same dimensions as the finished coil. The surface of the mandrel will be coated with a release agent in order to allow the easy release of the coil after impregnation. Then the ground plane insulation (a precured epoxy strip) will be put in place. (Optionally the rectangular copper cooling channels could first be wound onto the mandrel bottom, secured and aligned to continue the coil winding). Next, the coil turns will be wound. The layer to layer transitions will be made near the mandrel flanges. The spaces in the transition areas will be filled by fibreglass. The dry glass fibre cloth will be placed at the flanges to create the ground plane insulation after the impregnation process. The turn-to-turn insulation will be prepared as dry Dacron and glass fibre braiding. Then a layer of outside ground plane insulation strips on the external coil surface will complete the coil. The coil will be impregnated by epoxy compound in a vacuum oven. The epoxy will be cured at approximately 100°C. After this, the coil will be removed from the cold mandrel, the

	Stationary Operation	Coil excitation
Coil (T = 4.6 K safety factor 2)		
Radiation	0.3 W	0.3 W
Support conduction	3.8 W	3.8 W
Residual gas conduction	0.14 W	0.14 W
Conductor joints and wires	2 W	2 W
Losses in the Al frame		20W
Current leads Conduction (T = 4.6 K–64 K)	1.5 W	1.5 W
Total	7.74 W	20.74 W
Shield (T = 60 K safety factor 2)		
Radiation	420 W	420 W
Shield support	114 W	114 W
Heat intercepts of the coil supports	16 W	16 W
Eddy currents		10 W
Current leads (T = 60 K–300 K, safety factor 2)		
Operational current (T = 64 K–300 K)	280 W	280 W
Total:	830 W	840 W

Table 10.23: Heat Load on the cryostat units.

coil surfaces cleaned and inserted into the coil support structure.

Temperature sensors will be fitted to the outside of each coil support structure to measure the temperature of each individual coil during cool down and quench. In addition, temperature sensors will be also fitted to the pipes to monitor the temperature of the helium coolant flow. Voltage taps will be fitted to the coil to monitor the onset of possible quenches. The magnet will however also be protected passively. If a quench should start in any of the coils the heaters on the inter-coil joints will be switched on and start a fast propagation of the normal zones in all coils.

Each cryostat will consist of the cold mass described above, inner and outer radiation screens and an outer vacuum case.

Thermal Shield. The radiation screen will consist of prefabricated panels on each flat face with cooling pipes filled with liquid nitrogen or gaseous helium at some suitable temperature 50–80 K. The plates will be supported by the cold mass support, providing a heat intercept on them. Around the curved ends of the coils, copper strips will be laid out that will be soldered to the radiation screen-cooling pipe and then laid over the curve of the cold mass in order to intercept radiant heat from the vacuum case. Stainless steel foil plates (50μm in thickness and 400 mm in width, sputtered from high purity Al) will be tack-welded to the surfaces of the thermal shield to reduce the heat load.

Design of the Mandrel. The coil pancakes will be secured in the Al support structure. In the cool-down process some radial and vertical pressure will act upon them due to different temperature coefficients of the coil composite material and aluminium. Cryogenic Al pipes will be welded to the Al support structure.

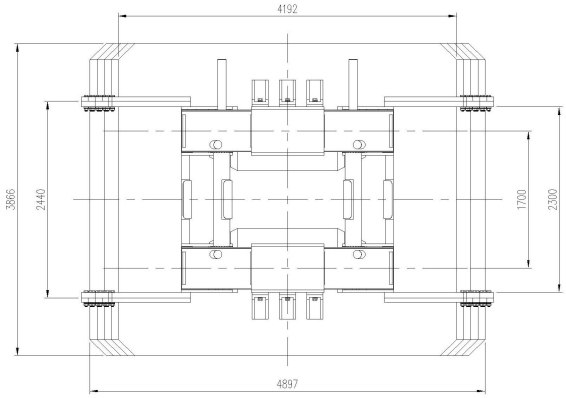

Figure 10.62: Front view of the dipole magnet with superconducting winding.

Vacuum Vessel. The cryostat will be fabricated from stainless steel 12Ch18N10T with nominally 10 mm plates. It includes two halves (top and bottom). They are connected by four flange tubes, which include adjustable connections. Stiffening sections will be welded to the outside of the cases in order to support the electromagnetic load between the coil and the iron yoke. The design value for overpressure in the cryostat is 0.7 bar.

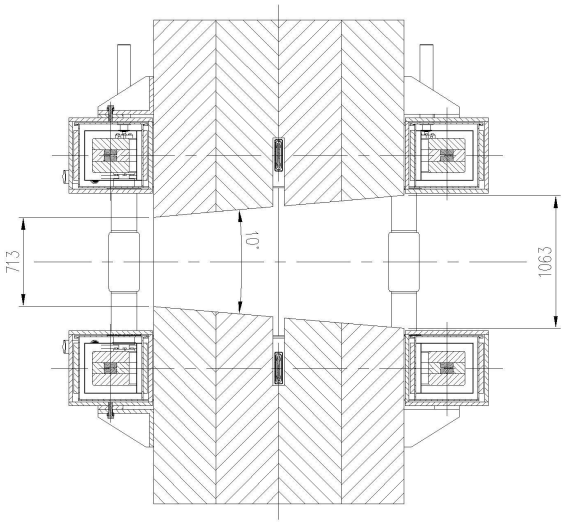

Figure 10.63: Side view of the dipole magnet with superconducting winding.

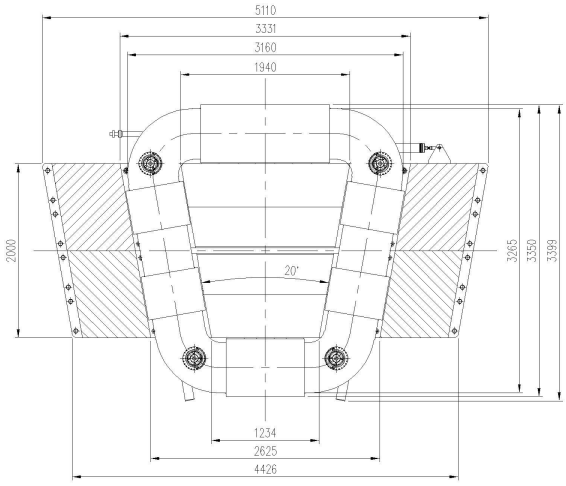

Figure 10.64: Top view of the dipole magnet with superconducting winding.

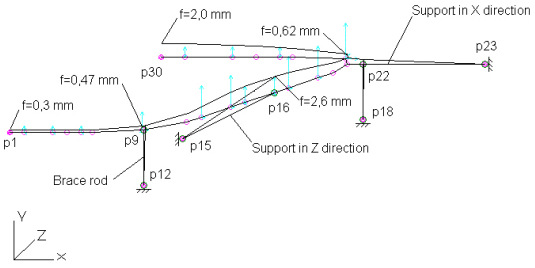

Figure 10.65: Coil section displacement with solenoid switched on.

The vacuum vessel has manifolds for the current leads, the LHe and GHe inlets and outlets, the diagnostic wires, and vacuum pumping as shown in Figs. 10.62 and 10.64. They are coupled to the vacuum vessel by means of flanges and vacuum seals. All values presented here will have to be checked against the Russian pressure vessel safety code.

Cold Mass Supports. The cold mass will be supported by a number of supports, which will be designed both to support the cold mass (4.67 t) against gravity and the forces that exist between the coils (DM and Solenoid) and the iron, and to centre the coil. The tie rods supporting the cold mass of the dipole will be made from stainless steel 12X18N10T. There are 4 ties acting in vertical direction, 4 ties acting in the beam direction, and 2 ties acting in transverse direction (see Fig. 10.66).

Electrical Joints. With a total conductor length in the coil pancakes in excess of 3.7 km it will be necessary to have several joints (up to 10) inside the coil. The exact number of joints will depend on the design requirements and the available lengths of superconductor. A joint must have a resistance lower than $10^{-8}\,\Omega$ to limit the power loss at the maximum current to 4 mW. A simple well known method will be used to solder the overlapping, to be connected cables across the full length of a turn near a spool flange.

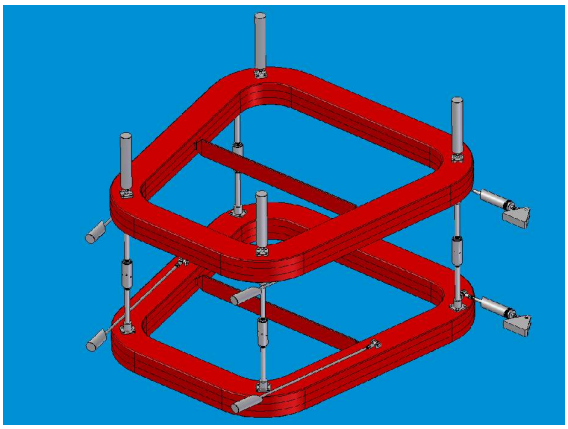

Figure 10.66: Cold mass supports, bottom coil suspension rods and straight section connections.

Dipole Magnet Model Coil. To verify the most critical points of the project, a model of the Dipole Magnet trapezoidal coil has to be constructed. The same superconducting cable, winding technique and insulation procedure as for the solenoid will be used for the superconducting DM prototype.

Iron Yoke. The yoke design is very similar to the yoke design of the DM with water-cooled coil (see Sec. 10.4.2.1). The main parameters of the yoke are summarized in Table 10.20. The total weight of the yoke is 200.1 t. The heaviest single piece of the yoke is only 18.7 t to facilitate handling and transport.

Timelines. The timelines are given in Fig. 10.67.

10.4.3 Cryogenic System

10.4.3.1 Operational Conditions

In order to maintain the operational conditions for the magnets, the refrigerator has to provide the magnets with streams of circulating Nitrogen and Helium as follows:

- helium at 4.4 K and appropriate pressure to guarantee stable operating conditions for both superconducting magnets;
- helium gas at an intermediate temperature ($\sim$ 60 K) to run the thermal radiation shields and current leads of the magnets;
- nitrogen gas at 77 K to run the thermal shields of the magnets;
- helium gas at room temperature ($\sim$ 300 K) to warm up the magnet coils and shields to prevent condensation of water.

In the event of coolant loss the system must survive several minutes releasing the energy from the solenoid and dipole.

10.4.3.2 Operation Modes

In case of a magnet "quench" (a superconductor suddenly returning to normal conductivity) a very fast overheating of the superconducting winding and evaporation of all the Helium contained in the magnet must take place. In this situation the thermal status requires a partial re-cooling and the full re-energisation. So the expected operating modes for the cryoplant are the following:

- Both magnets are operating at full capacity. This is the normal operation mode.
- One of the devices is being cooled down or in a scheduled warming up period while the other device is operating at full capacity.
- Recovery to normal operation mode after quenches or fast discharge of one or two devices.

10.4.3.3 Cryogenic System Features

The chief considerations for choosing a specific cryogenic system are:

1. Combination of low consumption of refrigeration capacity in operating conditions and a large cooling capacity when cooling down the magnet coils.
2. It is preferable to use for both magnet elements (dipole and solenoid) only one standard industrial helium liquefier.
3. At the beginning of the cooling down process, the maximum permissible cooling rate of the coils must be taken into account. The cooling down rate is limited by the thermal stress caused by the temperature difference between the inlets and outlets of the dipole and solenoid.
4. A very important issue is the reliability of the device and the possibility of a fast restoration of the operating conditions after a quench.

Two-phase helium cooling is suggested. The helium compressor will supply two-phase helium flow through heat exchangers of satellite refrigerators and the J-T circuit. Two-phase cooling avoids an increase in temperature along the flow circuit. This is found in supercritical or single-phase gas cooling circuits. The operating temperature of the magnets is close to the temperature of the helium in the liquid helium vessel (0.1 to 0.2 K difference only). The advantages of two-phase helium cooling are as follows:

1. The cool down of the magnet is well controlled because the helium in the tube flows along a well-defined path.
2. The total helium mass in the cooling system is less than the mass of the helium in a bath cooled cryostat.
3. The amount of helium in direct contact with the magnet coil is limited to the helium within the coil cooling tube. This has positive safety implications for the magnets and their cryogenic vacuum vessels.

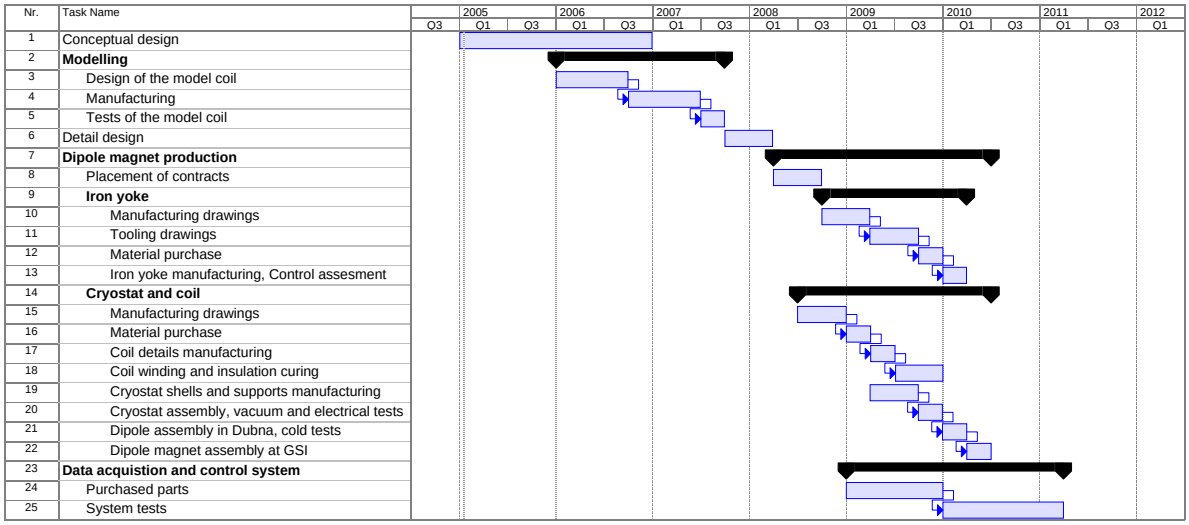

Figure 10.67: Time schedule for the superconducting dipole magnet.

Concerning refrigeration plants for large-scale accelerators with superconducting magnets, cryogenic systems consisting of refrigerators uniformly distributed around the ring perimeter with excess back flow (satellites) are sometimes preferred. They operate using liquid helium obtained from a central liquefier, which makes it possible to manage with a minimum amount of equipment in each of these refrigerators. In this case the refrigerator, which usually consists only of heat exchangers and a liquid-helium collector, is highly reliable and requires no maintenance, because the least reliable cryogenic elements requiring the largest amount of maintenance are concentrated in the central liquefier. An important feature is that the high thermodynamic efficiency is preserved. Since the heat capacity (the product of the flow rate and the specific heat) of the back flow is always somewhat higher than that of the forward flow, the optimal temperature distribution is established independently in the heat exchanger, when the temperature difference of the flow varies in proportion to the temperature of the back flow.

Many authors have studied the use of refrigerators with excess back flow, but the most detailed thermo-dynamical analysis was published in [5]. Therein information is given about the optimal parameters of the satellite refrigerators, the specific consumption of the energy, and the required surface areas of the heat exchangers. These results are used here, to define the principal criteria of the PANDA magnet cryogenic system.

A general view of the basic design of the solenoid refrigeration is given in Fig. 10.68. The refrigeration device for the dipole magnet would be the same. The cryogenic system employs a helium liquefier, a liquid helium vessel, a compressor, and a liquid nitrogen vessel. Each of the magnet elements (solenoid and dipole) has its own cryostat with build-in satellite refrigerators. The satellite refrigerator consists of two- and three-flow heat exchangers, vats of liquid nitrogen and liquid helium, and adjusting valves V1, V2 and V3. The cooling down process does not involve the use of any additional equipment, except the satellite refrigerators. During this process the forward and backward flows are in the same directions as in the nominal mode, i.e. in the refrigeration of the magnets at helium temperatures. However, to regulate and speed up the cooling, the satellite refrigerators are equipped with bypass lines *via* the valves V4 and V5.

For the PANDA magnets described above, there are constraints on the cooling time arising from thermal gradients and stresses in the structural elements. Up to now, it is envisaged that the entire magnet system is cooled down as fast as possible. An analysis shows that the optimum time is about 100 hours. The schematic solution (Fig. 10.68) uses a forced flow of gaseous helium, cooled in the satellite refrigerators by the evaporation of about 7 m^3 of previously supplied liquid nitrogen.

To store that quantity of liquid nitrogen, a liquid nitrogen vessel and cryogenic tubes would be needed. It seems worth considering to set up a nitrogen liquefier. The cryogenic system has been designed according to such a scheme. The total liquid nitrogen consumption at operating conditions will be about 18.2 kg/h.

The buffer liquid helium vessel shown in Fig. 10.68 not only increases the system reliability but also helps in achieving the required cooling down time of no more than 100 hours. At operating temperatures of the magnets of $4.6 < T < 77\,\mathrm{K}$, cooling of the magnets requires extra evaporation of liquid helium exceeding the capacity of a typical helium liquefier. The volume of the additional liquid helium vessel will be about 1 000 liter.

Each magnet is powered by a pair of electrical leads which consist of two parts. The first part is made of a high temperature superconductor and does not need cooling. The second part will be cooled by gas drawn from the satellite refrigerator at a temperature of 60 K. Table 10.24 shows the main parameters of the cryogenic system.

Cryogenic Transfer Lines The cryogenic system consists of different elements. The lines connecting the refrigerator with the magnets is assembled in a "four in one" layout (a vacuum insulated line containing four cryogenic lines), where the warmer of the four cryogenic lines (the 60 K return) is used to create a thermal shield for the other colder lines. For the magnets a total of four lines are necessary, two cryogenic lines and two room temperature lines. They are:

- 4.2–4.6 K liquid helium supply/return
- 60 K helium gas supply/return
- 300 K helium gas supply/return.

The design values of the transfer lines heat loads are:

- 0.22 W/m for the 4.6 K lines
- 1.5 W/m for the 60 K lines

10.4.4 Vacuum System

After the installation of the coils (solenoid or dipole magnet) in the cryostat they will be cooled down to liquid N_2 temperature and leak tested. The cryostat and the feed box of the satellite refrigerators must be evacuated down to 10^{-5} torr (at room temperature) to provide an insulating vacuum around the cold masses that reduces the cryogenic losses. This pumping has also the task to minimise the danger of condensed vapours trapped in the cryostats.

To ensure a good quality each cryostat must be connected to an independent pumping system, which consists of a forepump and a turbo molecular pump (with a final pressure of $\sim 10^{-5}$ mbar at room temperature). The pressure will go down to $\sim 10^{-7}$ mbar when the coils and cryogetter panels are cool. The pressure drop is due to cryogenic pumping of the vapours on the cryogetter charcoal surfaces.

The cryogetter panel is mounted on the surface of the thermal shield. It is a copper plate brazed to the shield surface. Small pieces of activated charcoal SKT-2B are glued to its degreased surface by means of a mix of glue PVA-40 (TU-6-05-1593-77) and fine-dispersed Cu powder with 4–6 hours postheating at 350–400°C.

To avoid pressurising the cryostat when a quick temperature rise occurs, a relieve valve for an overpressure of 0.2 bar will be be inserted in the vacuum system. When a vacuum failure occurs, the coils are discharged. After 2 or 3 minutes the coils are energized at the maximum current allowed by the power supply for a uniform warm up, which also reduces condensation on the vacuum shells.

10.4.5 Control, Diagnostics and Instrumentation

To ensure a proper operation of the solenoid and dipole magnet, a diagnostic system will be built. The following magnet systems will be monitored

- **Quench detection.** To protect the superconducting winding in the event of a quench, the resistive zone must be detected. A detached electronic system will be used that is insensitive to spurious signals and interferences, and is protected against voltage drops across the coil.
- **Current control** is used to monitor the magnetic field intensity and the stability of the solenoid and the dipole magnet.
- **Control parameters of the cryogenic system** are the pressure, flow rate, and temperature parameters of the cryogenic fluids, as well as the gate valve state.
- **Current lead control.** The potential drop and the temperature of the current leads at both sections (Cu and HTS) will be monitored continuously to provide protection against a quench in the HTS current lead section under normal conditions or overheating of the Cu section with subsequent burn-out.
- **Temperature control.** The temperature of the solenoid mandrel and bandages as well as

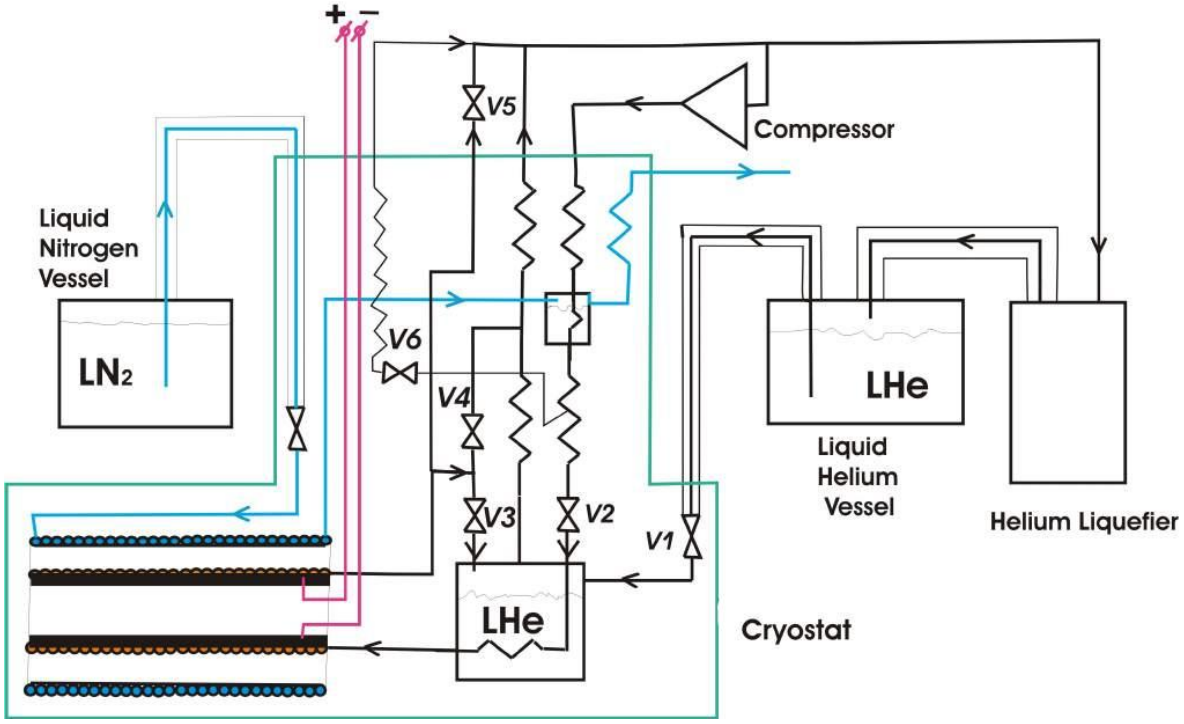

Figure 10.68: Simplified flow diagram of the cryogenic system for the PANDA magnets.

Satellite refrigerators:	
Refrigeration consumption of the solenoid at 4.5 K, W	10
Refrigeration consumption of the dipole at 4.5 K, W	10
Total refrigeration capacity at 4.5 K, W	20
Capacity of helium liquefier, l/h	3.22
Coefficient of surplus return,	0.08
Compressor of the satellite refrigerators:	
Inlet pressure, MPa	0.102
Outlet pressure, MPa	1.5
Capacity of the compressor, g/s(Nm^3/h)	1.4 (28)
Total power expense per unit refrigeration capacity, W/W	460
Total power expense for refrigeration at 4.5 K, W	9 200
Thermal load to screens:	
Thermal screen of the solenoid (at 77 K), W	500
Thermal screen of the dipole (at 77 K), W	500
Total liquid nitrogen consumption for thermal screens, kg/h	18.2
Cool down:	
Average cool down speed of the magnets, K/h	3.6
Total cool down time of the magnets, h	100
Liquid nitrogen consumption during cool down , kg/h	54.6
Total cool down consumption of liquid nitrogen, kg	5 460

Table 10.24: Main parameters of the cryogenic system. (Some numbers apply only for the solution including a superconducting dipole magnet.)

the temperature of the case of the aluminium coil of the DM will be controlled by several thermo-resistors. The thermal shield temperature will be controlled by linear temperature

sensors.

- **Control of stresses and forces.** Strain gauges will be mounted on the coil cylinder of the solenoid to control the stress levels during the solenoid energization. Several strain gauges will be mounted on the tie rods of the solenoid and the dipole, which counteract the magnetic force.
- **Vacuum pressure control.** Couple pressure gauges will control the normal operation of the vacuum system of the cryostats of the solenoid and the dipole magnet. These pressure signals will also be used as an interlock to discharge the solenoid or DM after a vacuum failure.

The chief task of the diagnostic system is as follow:

1. signal processing to generate alarm and interlock signals for magnet safety in emergency situations,
2. control parameters of the normal operation regime,
3. data display at the operator's console and remote control of the parameters,
4. data logging and,
5. signal processing to generate control responses for optimizing the magnet systems.

The magnet and auxiliary equipment control system will incorporate a distributed computer control system composed of commercially available components.

This computer system will be created on the basis of VXI or PXI plug&play instrumentation. The VXI (IEEE 1155) standard is considered most promising for the creation of trusted DA systems. At the present stage of development the standards of electromagnetic compatibility and noise immunity (EN 55011, EN 50082-1) were applied. Hardware interface VXI modules are produced by all world leading manufacturers (Hewlett-Packard, Tektronix, Racal, Colorado Data Systems, National Instruments, Fluke, Agilent Technology, VXI Technology, Inc.) which are amalgamated in the VXI plug&play System Alliance. The distributed system on the basis of C-type crates which are controlled by embedded computers will be used to provide a high level of efficiency. The measurement and control modules of the crates are directly connected with measuring converters, gauges and process execution elements. The crates will be located in the vicinity of the sensors to minimize the cable length and thus improve noise immunity. A detached server will provide data-logging and remote control. The operator will interact with the system through PC workstations, Ethernet joint crates, fileserver, and an operator console.

The VXI instrumentation specification has proven to be very robust and successful. The other option with the same architecture is a crate according to the PXI standard. PXI defines many of the same extensions for instrumentation as the VXI specification. The standard PXI (PCI eXtention for Instrumentation) has been developed by National Instruments in 1997 as an extension of the CompactPCI standard. All modules of this standard have been designed for Plug&Play technology. The only producer of this standard is National Instruments for the time being. It looks as if the final cost of the DAS would be lower for PXI standard hardware. However, using the PXI standard one has to take special measures to provide an adequate level of electromagnetic compatibility and noise immunity.

There is a new system development on the basis of a distributed system of input/output, which prevails in industrial monitoring and control systems. To date the best-known and functional system is the FieldPoint system of National Instruments. The FieldPoint system enables a wide choice of analog and digital Input/Output modules, as well as communication modules for the connection with industrial nets and modular terminal blocks. The great advantage of the FieldPoint system is the possibility to minimise the analog signal circuit lengths. In addition, the cost for this distributed system is much lower than for VXI or PXI.

The final choice of the electronic standard will be made at the stage of the technical design report, after a careful analysis of the requirements concerning the algorithm, number of channels, system reliability, electromagnetic compatibility, interference immunity, etc.

10.4.6 Quality Assurance

A written Quality Assurance (QA) Manual has to be provided, generally in accordance with the requirements of ISO 9001. The manual shall describe the QA organisation, authorities and responsibilities, requirements for design and procedural documentation, requirements for control of manufacturing, procurement, and inspection operations, as well as the requirements for record keeping.

FAIR should investigate where the power supplies,

cooling water supply and other engineering systems can be accommodated. To maintain compatibility with this work the Interface Document will define minimum and maximum limits for many of the engineering parameters or indicate fixed parameters. The first version of this document has been drafted by JINR.

The supplier will provide a written Manufacturing Plan which describes the overall process sequence and details critical process steps in fabrication, assembly and inspection of the coils.

As a minimum requirement, the supplier will supply the following records:

- materials input test reports;
- inspections reports during the coils manufacturing;
- acceptance test reports.

10.4.7 Conclusion

On the basis of the previous Conceptual Design, further simulations and the ongoing optimisation of the $\overline{\text{P}}$ANDA Detector [6], a preliminary design of the $\overline{\text{P}}$ANDA magnet system consisting of a target solenoid and a forward dipole magnet can be presented.

The solenoid, placed on a movable carriage, consists of a superconducting NbTi coil with an inner radius of 0.93 m and a length of 2.5 m. The coil is cooled indirectly by liquid helium. The maximum magnetic field in the operational area is 2 T. The coil has an outside iron yoke. The total weight of the solenoid including the cryostat, iron yoke and carriage is approx. 140 t.

The dipole magnet of the forward spectrometer provides a bending momentum of 2 Tm. This magnet has an "H-type" iron yoke with a rectangular conical aperture. The total weight of the dipole magnet is approx. 210 t. Three options were considered; a conventional magnet with water cooled Al winding (racetrack or bedstead form), and a magnet with superconducting NbTi winding. All options were evaluated according to reliability, complexity of implementation and cost.

10.5 Timelines

Based on the proposed design in Sec. 10.4 time schedules have been prepared for all the scenarios discussed in detail, i.e. a superconducting solenoid and the three options for the dipole (see Figs. 10.34, 10.47, 10.59, and 10.67).

Based on the design previously discussed, a budget offer was given by Ansaldo company, Genoa [7]. A complete system consisting of a superconducting solenoid and a conventional dipole magnet as in the default solution above is offered. The item "Components" comprises for the:

- **solenoid:** a cryostat with turret, thermal shields, a containment cylinder, a yoke in ferromagnetic material, a support and handling trolley, a pumping group, a feeder, QD, DAQ, valves, sensors, pipe fillings, and vacuum instrumentation;
- **dipole magnet:** bus bars, valves, a impregnation plant, an assembly tool, a magnetic measurement system, and a transportation device;

and "Tooling": winding lines, impregnation tools, assembly tools, tooling for magnetic measurements and transport devices. Furthermore a transfer line for the testing at Ansaldo is included for the solenoid. The offer (number 20427) was made in November 2004.

References

[1] M. Kotulla et al., Strong Interaction Studies with Antiprotons, Darmstadt, 2004, Letter of Intent.

[2] H. Hillman, Supercon. Mat. Sc. , 275 (1981).

[3] Outokumpu Advanced Superconductors, Inc, 2004, Offer n° 4643.

[4] M. Larin et al., J. Vac. Sci. Technol. **A.ser.2, v13, N5**, 2579 (1995).

[5] N. Agapov et al., Adv. Cryog. Eng. **43**, 557 (1998).

[6] J. Ritman, Preprint Elsevier Science. 18 July 2003.

[7] Ansaldo Superconduttori S.p.A., Genoa, Italy, 2004, Budget Offer n° 20427.

11 Trigger and Data Acquisition

11.1 System Overview

In many contemporary experiments the trigger and data acquisition system is based on a two layer hierarchical approach. A subset of especially instrumented detectors is used to evaluate a first level trigger condition. For the accepted events, the full information of all detectors is then transported to the next higher trigger level or to storage. The time available for the first level decision is usually limited by the buffering capabilities of the front-end electronics. Furthermore, the hard-wired detector connectivity severely constraints both the complexity and the flexibility of the possible trigger schemes.

In our approach all detector channels are self triggering entities. They autonomously detect signals and pre-process them to extract and transmit only the physically relevant information. The data related to a particle hit substantially reduced in the pre-processing step are marked by a precise timestamp and buffered for further processing. The trigger selection finally occurs in so called compute nodes which access the buffers via a high bandwidth network fabric.

11.1.1 Key Requirements

Since the physics of $\overline{\mathsf{P}}$ANDA is frontier physics, high statistics is needed to detect rare processes or small deviations in physical distributions. Therefore the $\overline{\mathsf{P}}$ANDA experiment plans to operate at interaction rates of the order of 10 MHz (with increases up to 20 MHz at a later stage). Even with pre-processing on the detector electronics for a substantial reduction of the data volume, typical event sizes are in the range of 4 to 8 kB. This amounts to total raw data rates in the order of 40 GB/s and up to 200 GB/s later on.

Furthermore $\overline{\mathsf{P}}$ANDA has a rich physics program with many different topics based on varying physical selection criteria. This means that different detectors contribute to the selection process for the measurements, which in turn should be performed in parallel wherever possible, to maximize the physics yield.

A conventional approach to read out the experimental data is not sufficient to match both criteria – high flexibility and selectivity on one side and very high data rates on the other – at the same time. Therefore the concept of a continuously sampling data acquisition in which event selection takes place in programmable processing units is planned for $\overline{\mathsf{P}}$ANDA.

11.1.2 Major Components

Key technologies to be exploited within the DAQ framework are high speed serial links (10 Gb/s per link and beyond) and high-density FPGA with large numbers of programmable gates and more and more advanced embedded features. There are three major ingredients of the new architecture:

The basic building blocks of the hardware infrastructure, which can be combined in a flexible way to cope with varying demands, are the following:

- Intelligent front-end modules capable of autonomous hit detection and data preprocessing (clustering, hit time reconstruction, pattern recognition ...) are needed.
- A very precise time distribution system is mandatory to provide a clock normal from which all timestamps can be derived. Without this, data from subsystems can not be correlated.
- Concentrators/buffers provide point-to-point communication, typically via optical links, buffering and on-the-fly data manipulation.
- Compute nodes aggregate large amounts of computing power in a specialized architecture rather than through commodity PC hardware. They may employ FPGAs, DSPs or other computing units and have to deal with feature extraction, association of data fragments to events and finally event selection.

A major component providing the glue between all others is the network fabric. Here special emphasis lies in cascadable switches which can be reconfigured to reroute traffic for different physics selection topologies.

Finally, the various algorithms for front-ends and selection levels have to be developed and tested. It should be attempted to develop a common high level programming environment for all components so that algorithms can be coded by physicists rather

than engineers in more abstract programming languages than HDL and DSP assembler.

11.1.3 Data Flow Overview

The detector front-end electronics reads and digitizes the data and performs the first level of data reduction by determining valid hits, combining them to physical information like clusters, energies or even tracklets.

Each group of data are marked by a precise timestamp which allows the association of information belonging to one interaction. This data association has to proceed in a detector specific way allowing for different signal characteristics (length, delay, ...) and some data may have to be assigned to multiple interactions. Thus, each interaction corresponds to a detector specific time slice in the data stream.

According to the settings of the respective physics measurements, the data of a detector are either buffered or passed directly to a network of compute nodes. These are supposed to extract a first simple physical signature which allows a decision on which time slices have to be transferred to the next processing level. The decision is broadcast through the network so that the next level's compute nodes can address the relevant buffered data of other detectors. Some detectors with a particularly difficult reconstruction may buffer data across several levels, contributing only at the last event selection step.

The first processing level and the concentrators/buffers are attached to a configurable cascaded high speed network. This means that some parts of the data stream bypass the processors at lower aggregate bandwidth while others feed into the processors with high bandwidth. Which detectors send to how many processing units and which ones wait for the first selection broadcasts is fully programmable and requires no hardware intervention. Like this computing power can be assigned dynamically based one the computing requirements of the respective physics measurements.

The last network level is attached to the online reconstruction farm which performs the final event selection based on the reconstruction of complete events and applying a comprehensive set of selection criteria. This network can be more traditional and just has to provide the required aggregate bandwidth.

11.1.4 Benefits of the Concept

The new concept provides a high degree of *flexibility* in the choice of trigger algorithms. It makes trigger conditions available which definitely are outside the capabilities of the standard approach, an obvious example being displaced vertex triggering.

In addition, all sub-detectors can contribute to the trigger decision on the same footing, and there are no restrictions due to a hard-wired trigger setup. Different physics can be accessed either in parallel or after software reconfiguration of the system with the same hardware setup.

Apart from these fundamental advantages the system offers some further benefits. Its *modularity* allows to connect building blocks in different ways through network interfaces and to realize small test systems as well as large high-rate systems.

Furthermore the system is *scalable*, both by implementing more components and by providing more powerful ones, e.g. faster processors, higher bandwidth interfaces, larger buffers *etc.*.

In addition, the system should be *cost efficient* since it is largely based on mass market components and consists of a small number of different building block designs which are used in large quantities. After all, using the same setup for a large number of measurements allows the most efficient usage of the equipment.

11.2 Requirements for DAQ and Trigger

11.2.1 Design Goals

11.2.1.1 Data Acquisition

The DAQ system must provide electrical and logical interfacing to front-end electronics and collect the data produced by the $\overline{\text{P}}$ANDA detector front-end systems. Tight but flexible integration of trigger and data acquisition ensures adaptation to the entire range of the $\overline{\text{P}}$ANDA physics programme. The processed data will be assembled into event-correlated data streams (event building).

Tagging of subsystem data will ensure proper event building at all levels. The final output stream will be archived for further offline analysis. Multiple event data streams will be provided for online analysis. Integration with slow control will ensure that no detector parameters are modified during archiving runs. Flow control with propagation of

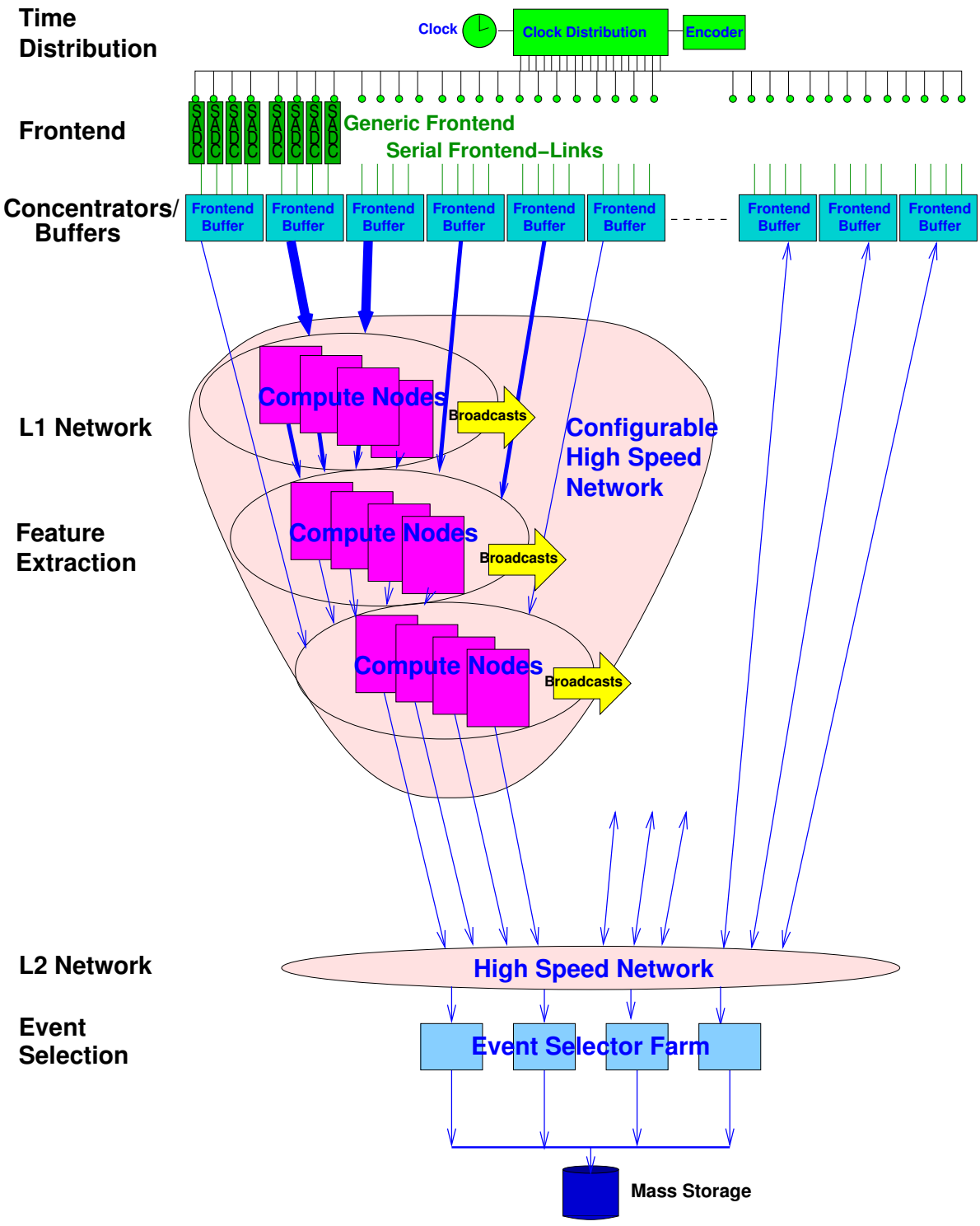

Figure 11.1: Scheme of the DAQ system

busy signals throughout the chain of DAQ/Trigger components is provided. The system has to be able to run in different modes including normal running with/without archiving, calibration runs, test/debugging modes. Flexible partitioning will support parallel debugging/calibration of detector subsystems. The system must guarantee high availability which can be achieved via techniques such as fault tolerance and self monitoring.

The system has to operate at an interaction rate of $10^7\,/s$. Data produced by the detector subsystems which is below predetermined thresholds will be suppressed by the detector front-end electronics. Moreover, dedicated feature extraction at the front-end level reduces the raw data rate down to a maximum of $3 \cdot 10^{11}$ bits per second which must be processed by the data acquisition system. Event selection in the trigger system will further reduce the data rate down to 10^{10} bits per second which need to be archived online.

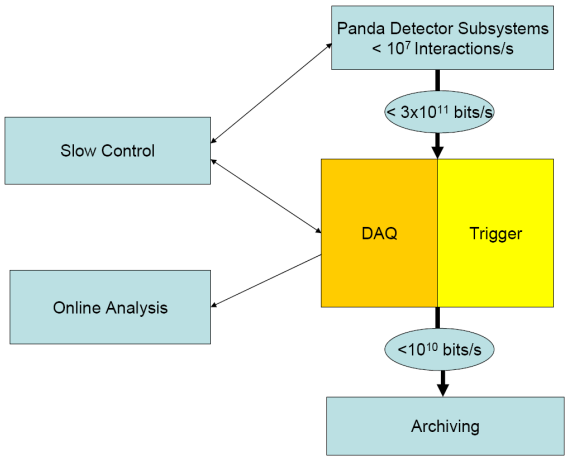

Figure 11.2: Schematic view of the data flow to/from the data acquisition and trigger system.

11.2.1.2 Trigger System

The trigger system will select a subset of the primary data stream based on physics signatures. The ability of the trigger system to reduce the primary event rate is strongly dependent on the physics to be studied. A significant part of the PANDA physics programme involves rare channels such as open charm production. Here, selective trigger algorithms such as the search for displaced vertices in the silicon pixel tracker can be devised which lead to a reduction of the primary event rate by more than 2 orders of magnitude. In contrast, other parts of the programme focus on channels with large cross sections. Here, the trigger system will be much less selective, requiring a reduction of the primary rate. This is compensated by the fact that channels with large cross sections can be investigated with sufficient statistics at reduced event rates.

The diversity of the physics programme requires a very flexible approach to triggering. Thus, conventional solutions with hard-wired trigger decisions are not optimal. Instead, massively parallel processing based on FPGA and DSP technology interconnected by a configurable high speed network is foreseen.

Data produced by the detector which is below predetermined thresholds will be suppressed by the detector front-end electronics. Moreover, dedicated feature extraction at the front-end level reduces the raw data rate down to a maximum of $3{\cdot}10^{11}$ bits per second which must be processed by the data acquisition system. Event selection will further reduce the data rate down to 10^{10} bits per second which need to be archived online.

11.2.2 Rate Requirements

In order to estimate the expected data rates, we have assumed operation at 10^7 interactions per second at a beam momentum of 15 GeV/c. GEANT4 simulations have been performed employing the actual detector geometry and a realistic event generator for the dominant annihilation channels (see Sec. 12.3.1 for details). The data rate will strongly depend on the choice of the central tracker. Two options are currently discussed which include a straw tube tracker (STT) and a TPC. A comparison of the expected data rates for both tracking solutions is shown in Table 11.1. For the TPC solution (bottom table), the resulting data rate is larger by a factor of 3 as compared to the STT solution (top table). In this estimate, front-end zero suppression and feature extraction as well as data compression using Huffman encoding for the TPC was assumed. Resulting data rates of 15 and 41 GB/s are obtained for the STT solution and the TPC solution, respectively.

This does not include electronics noise, pileup and background particles. Although the intelligent front-end electronics should be capable to distinguish unwanted hits from good ones, a safety factor of two should be foreseen giving an upper limit of about 80 GB/s.

11.2.3 Trigger System

Triggering is most effective for rare channels with clear physics signatures. A significant fraction of the physics channels of interest does allow very selective triggering. As an example, the decay of J/ψ into lepton pairs can be considered. A selective trigger would combine information from tracking and particle identification to reconstruct the invariant mass of lepton pairs. Candidates within the J/ψ mass region can be used as trigger signature for

15 GeV/c	Multiplicity	#DataBits/hit	#HeaderBits/hit	B/event	MB/s
FSMDC	45	20	16	203	2 025
FSEMC	102	24	14	485	4 845
FSHC	9	10	14	27	270
MVD	16	16	20	72	720
EMC	90	24	14	428	4 275
STT	69	16	20	311	3 105
					15 240

15 GeV/c	Multiplicity	#DataBits/hit	#HeaderBits/hit	B/event	MB/s
FSMDC	45	20	16	203	2 025
FSEMC	102	24	14	485	4 845
FSHC	9	10	14	27	270
MVD	16	16	20	72	720
EMC	90	24	14	428	4 275
TPC	850	12	16	2 975	29 750
					41 885

Table 11.1: Expected $\overline{\mathsf{P}}$ANDA data rates from GEANT4 simulations. Events representing the dominant annihilation channels at 15 GeV/c are considered for the two different tracking options (top: straw tube tracker, bottom: TPC). The primary interaction rate is 10^7/s.

events relevant to charmonium spectroscopy. The implementation of such triggers requires a highly parallel architecture which allows independent lepton candidate searches in the relevant subsystems. In a second stage, lepton candidates of opposite charge can be combined to calculate the pairs' invariant mass.

As another example for a highly selective trigger signature, we consider the decay of D mesons. Here, the signature is a displaced secondary vertex. Due to the small $c\tau$ of a few 100 μm, the relevant tracking information can only be obtained from the silicon tracker. As a second step, a calculation of the invariant mass of the decay products can be performed to further suppress background.

In order to efficiently utilize allocated beam time, it is crucial that the trigger system is able to handle multiple trigger conditions in parallel. The triggers should provide high selectivity without introducing a physics bias within the channels selected. In a typical run, triggers might be applied which differ in rate by several orders of magnitude. In order to avoid dead-time due to bandwidth limitations and archiving, appropriate downscaling factors for the individual triggers have to be introduced.

Moreover, effective methods for online evaluation of the trigger efficiency have to be available. It should be noted that trigger operation is strongly correlated to detector performance and stability.

Trigger processing will occur mainly on 3 levels. A first level, where only local information of a single subsystem is considered, will be able to identify signatures of rare events based on the local particle identification properties of the subsystem. Examples include pattern recognition for the Cherenkov detectors or the search for displaced vertices in the tracking detectors. Depending on selectivity, efficiency and fake rate of the local trigger, reduction factors between 3 and 10 could be expected. The second level will utilize the information derived from local trigger processing. Here, the aim is to reconstruct the invariant mass of rare particles using fast tracking methods which have limited momentum resolution. Reduction factors of the order of 10 can be expected. The third level trigger would then utilize more sophisticated tracking algorithms and could take into account other global observables such as kinematic constraints, depending on the reaction. This could further reduce the accepted event rate by one order of magnitude.

11.2.4 Data Handling

Latency and buffer sizes will strongly depend on the hardware implementation of the various algorithms under consideration. The First Level Buffers must be capable of holding data until a first level trigger decision is made. Assuming a latency of 3 μs for first level decisions, buffer space for 30 events must

be made available to cope with the interaction rate of $10^7\,/s$. This latency depends on the underlying algorithm and may extend up to $100\,\mu$s.

The data volume to be processed per event is approximately 4 kB (TPC scenario). In order to estimate the required processing power, we assume that on average 100 operations per byte are required. As a result, $4 \cdot 10^5$ operations per event or $4 \cdot 10^{12}$ operations per second are required for the first level trigger. This can be realized by implementing parallel algorithms in compute nodes based on large FPGAs, each assumed to operate at 0.5–1 Tops/s. Several hundred FPGAs will be required. The total number of FPGAs does not only depend on the desired processing power but also on boundary conditions imposed by data transfer. Modern FPGAs with high speed serial links are very well suited to implement such architectures. Moreover, the local topology of the subsystems has to be considered when designing the compute nodes.

Assuming a reduction of 3 by the first level trigger, the data rate to be handled by the second level trigger is approximately 14 GB/s. For the second level trigger, a latency of $100\,\mu$s is assumed, assuming FPGA - based compute nodes. After further reduction by one order of magnitude, the third level trigger has to handle a data rate below 2 GB/s. Here, larger latency of the order of several 10 ms for sophisticated trigger decisions including calibrations and sophisticated tracking are required.

11.3 System Design

11.3.1 Integrated Concept of Sampling DAQ

As lined out in the overview, the requirements should be met by a continuously sampling data acquisition system. This concept can only work, if massive parallel processing of the digitized data is performed on the way throughout all levels of data transport from the detector front-end to the final event selection. One has to achieve a sufficient data reduction and physics selectivity to arrive at a tolerable data rate to mass storage. In this section we outline the various levels of processing on the data path and which tasks and algorithms have to performed.

11.3.1.1 Data Reduction

This term denotes all the processing on the detector side which is aiming at the effective reduction of data by treating locally available information. It may include physics based data processing but not yet active selection of time slices across the experiment, i.e. beyond the local noise reduction.

First step in any detector readout is the noise reduction and zero suppression. This step includes of course the conversion of analog detector signals to digital data.

The second step is the evaluation of the signal time from data. Depending on the detector type a fitting of detector signals across several clock cycles can be necessary. Other detectors with intrinsically good time resolution are read e.g. by TDCs to give directly hit times. This is an important step in the preparation of event association, i.e. the combination of overlapping timeslices throughout all detectors belonging to one physical interaction.

Clusterisation of hits is performed in most detectors. In this way information is grouped and even improved (by calculating centroids) to minimize data size. Here overlapping signals from pileup have to be distinguished correctly, best by using refined hit times.

Pattern recognition is the last step in the preprocessing phase in which actual physical patterns are extracted from the digitized detector data. This includes e.g. track segments in tracking subsystems, energies in calorimeters or ringlets in Cherenkov detectors.

In the end, data concentrators with buffers store the preprocessed data which is reduced to the physically relevant information, ready for transport to more global processing levels.

At the same time, processing power on these concentrators can already group and address data according to the timing information as a further preparation for the event association. Here, the higher levels of data reduction (e.g. pattern recognition, clusterisation) can be performed as well.

On receiving broadcasts with data requests from the next processing levels the specified time slices are passed on to the indicated destination.

For the effective treatment of data on the front-end side, with respect to an accurate description of physical signatures, a constantly updating online calibration including alignment *etc.* is a prerequisite. The logical consequence is, that front-end processors perform this calibration autonomously and save their constants in regular intervals in a persistent database. Typically two modes can be distinguished, one where a fresh calibration database is built from some starting values and a sec-

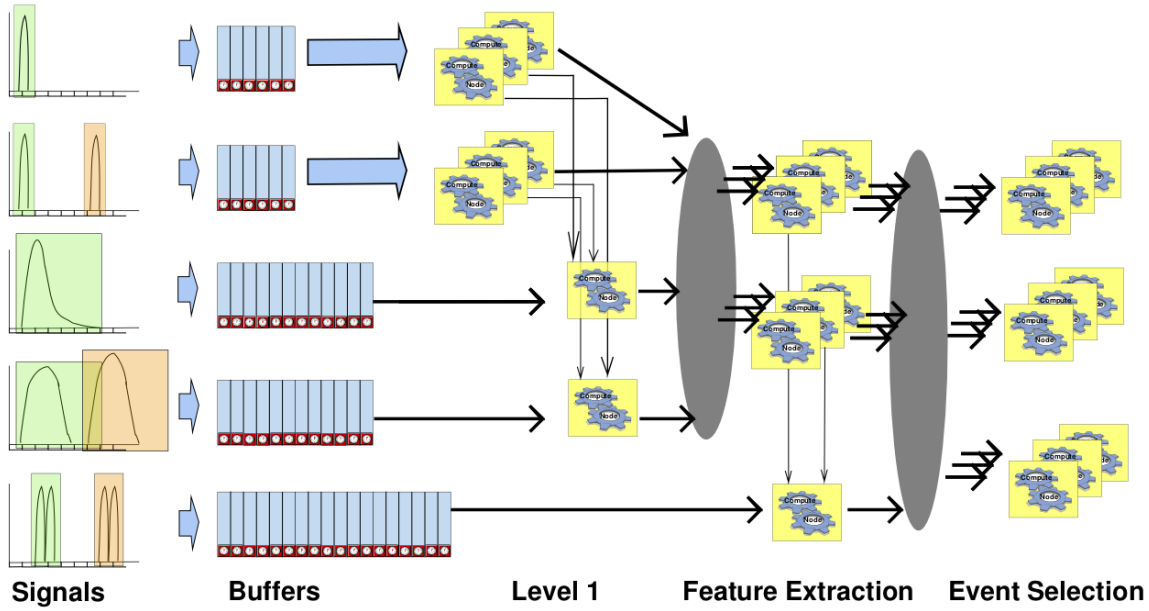

Figure 11.3: Different view of the data flow and selection.

ond one performing calibration updates throughout the measurement during actual physics data taking. The first mode needs feedback from more powerful processing levels e.g. including full track reconstruction which precludes physics data taking.

11.3.1.2 Feature Extraction

The next step in processing the data is to combine detector information to extract physical signatures relevant for the actual measurement of interesting processes. Examples are the fast determination of a muon track, the combination of two calorimeter clusters to find neutral pions and the verification of calorimeter clusters against tracking data to distinguish neutral and charged particles. Other examples are a fast determination of time-of-flight, the detection of tracks with large impact parameters w.r.t. the interaction point and the enrichment of kaons using PID detectors.

The various selection tasks can be grouped internally in several levels, for simplicity we consider here only two. The first level is based on signatures which are fastest to extract and require the smallest fraction of the total data stream. The corresponding detector front-ends deliver these data at very high bandwidth to processing nodes. These nodes determine interesting time slices from the signatures and broadcast the corresponding timestamps to the next processing level. This second level combines already processed data with still buffered data to achieve a more refined selection which then is the base for the final event building. The decision at which level a selection takes place is based among other criteria on the complexity of the selection algorithm, the amount of data to process and the number of detectors involved.

As described in the overview the feature extraction is embedded in a configurable cascaded network. This allows to change dynamically the bandwidth assignments between detector front-ends and compute nodes for different physics measurements.

11.3.1.3 Event Selection

The last step in the data processing before mass storage is the event selection based on completely assembled event data blocks. Here, the goal is to achieve the highest possible level of selectivity by performing a nearly complete event reconstruction with momentum information, invariant mass determination of decaying particles, vertex reconstruction and particle identification. This level can be performed at a large processor farm connected to the previous levels through an ordinary (i.e. static) high bandwidth network. The event reconstruction should be greatly facilitated by the fact, that front-end preprocessing already provides physically relevant information so that data decoding is trivial at this level and most processing power can be spent

for physics reconstruction.

11.3.2 Data Flow

In this subsection the flow of data is described. Two issues are important in this context, on one hand the actual architecture of the network and on the other hand the management of data flow.

11.3.2.1 Data Network

There are essentially two network classes present in the DAQ structure. A fairly low bandwidth class serves the need of controlling and programming the readout system. This comprises both detector control and programming networks as well as the time distribution network. Depending on the choice of the underlying hardware these two may be combined or not as explained in more detail in the section on network implementation (see Sec. 11.4.2).

The further focus in this paragraph however is the class of high bandwidth networks for data distribution. The total bandwidth as follows from the requirements is in the order of 40–200 GB/s. The data flow is governed by the respective physics selection scheme. This scheme implies the selection algorithm and along with it buffer latencies and maximum storage times. The buffers are located on the concentrator modules and are dimensioned big enough to hold event data for a maximum of 10 s, corresponding to a full reconstruction. If lower latencies can be kept by a faster selection this figure may be reduced. The processing nodes of the first selection level receive data from a specific subset of detectors, e.g. with 10% of the data volume. The transfer blocks are grouped in larger time frames to have bigger block sizes and thus more efficient transfers, which are assigned to single processing units. In addition this facilitates the combined analysis of adjacent, potentially overlapping time slices. The processing units of the first level must provide buffer and processing power to process the received data in a short time of the order of up to 1 s. This amounts to buffer sizes of around 50 GB. Once a node has processed a time frame it broadcasts the interesting time slices to the next processing level via a scheduler keeping track of which time slice is processed by which second level node. The reduction factor of the first level is in the order of 10 and with the same amount of buffering 10 s processing latency can be covered. Here a higher selectivity can be achieved, but a conservative estimate of the reduction is again 10. The final step is to transmit all remaining data blocks of selected time slices to the final level where a full reconstruction and high level selection is performed before mass storage so that in the end the desired 100–200 MB/s are reachable.

11.3.2.2 Flow Management

The flow of data through the processing network has to be controlled in order to avoid congestion and direct it to available processing nodes. In our system we consider several different options which shall be briefly discussed here.

In general one can distinguish between two classes, "pull" and "push" schemes of data transfer. In the pull-scheme a decision is taken which destination takes care of which part of the data and requests this from the data sources when it is ready. This scheme is especially attractive for the higher filtering levels since here the corresponding compute node just requests the time slice it has to process from the concentrators. The disadvantages of this scheme are, that in total more messages are sent and that some central intelligence ("scheduler") has to direct the assignment of slices to nodes. The information on available nodes can come from notifications of the nodes to the scheduler or from a modified round robin trial and error scheme, in which the scheduler asks certain nodes for their availability.

In the push-scheme data sources send data to the destination assuming that the destination is in principle always ready to receive data. They may be some buffering available on the source side and XON/XOFF signals can control, when the destination is ready to receive. But in average the destination has to digest the full rate.

A third way is a push-scheme where the destination is not a single compute node but a chain of nodes where each node either processes a data block or forwards it to another member of the chain. The chain can be constructed either physically from nodes with two interfaces connected one after another or logically by defining the passing of unprocessed data. The advantage is, that no scheduler is needed but an excess of compute nodes has to be made available to ensure the processing of all data and nodes later in the chain may be idle for a larger fraction of time then the first nodes. A variation of this would be a collection of star configurations with a central node keeping track of the availability of processing nodes assigned to it and distributing data accordingly. The hub node should be able to buffer data and reset processing nodes to overcome processing time-outs.

Finally, an additional aspect is the management of

buffers. A compute node broadcasts information on selected time slices to all concentrators/buffers, which mark the corresponding buffer areas for further processing. Unmarked buffers are erased or overwritten after a programmable time-out corresponding to the processing latency plus some safety margin.

11.3.3 Definition of Time Slices and Events

In a traditional track-and-hold system a detector is read out after a hardware trigger signal has arrived. Only after everything has safely been read, the system is cleared and ready for a new trigger input. More modern pipelined systems are able to process new triggers while previous ones are still being read. Here, a unique event number is needed to distinguish data blocks belonging to different events. Triggers are nevertheless - as in the old-fashioned way - read in a strict sequential order. However, in the concept of a continuously sampling data acquisition system this notion of trigger is lost. As a consequence it is not any more trivial to define which data belongs to each other.

However, this is not simply a feature (or weakness) of the sampling DAQ, but has its physical reason in the large rate of interactions and consequently detector pulses following one another. In fact, they may not even follow nicely any more but be smeared and overlapping. The problem outlined here has to be solved in the process of what we call event association. This process has in its realization two steps, first, the grouping of data into time slices, and second, the association of time slices to events, i.e. single primary interactions, which should be measured by the experiment.

The definition of time slices as the first step is a detector specific task. Here it has to be taken into account how the signal is generated in the detector and which are its characteristics. The crucial parameters are signal shape, signal duration, propagation or delay, amplitude and noise. It is also important to consider features of the specific readout electronics like double pulse resolution and deadtime. Based on these items a processing module on or close to the front-end electronics should characterise the (zero-suppressed) detector signals and group them into appropriate time slices. A detector with very good time resolution like a scintillator may have very short time slices whereas e.g. a gas-based detector might need to define longer and thus potentially overlapping time slices. This is graphically represented in the left part of Fig. 11.3.

The second step is even more elusive than the first: While one detector specific timeslice should correspond to one single physical signal it is likely that more than one time slice or physical signal can be created from one single primary interaction. Disentangling potentially correlated physical signals from background and other reactions can therefore depend also on the respective physics selection scheme. This means that, depending on the signature a selection of primary interactions is based on, more or fewer time slices might have to be selected for further processing and analysis.

This may then also lead to a non-unique assignment of time slices to events, to potential retransmissions of data and to the necessity of a wider latency window within which data cannot yet be safely discarded. A physical reason can again be overlapping physical pulses or too close primary interactions.

The proper way to deal with these issues in the design of the system is to come to the concept of time-addressed buffers which are typically located on the data concentrators. After the detector-specific assignment of time slices the data can be stored in buffers which can be addressed by external processing resources for feature extraction and event selection on the basis of time. The selection based addressing is then simply mapped on the proper definition of address ranges to access during a selection cycle. In this way the detector part and the selection part are decoupled logically, and may be so also physically (being handled by different processing units).

11.3.4 Data Filtering Stages

After processing on the front-end level the data are reduced to the minimum corresponding to the physically relevant information. This fact was already considered in the estimation of event sizes in Sec. 11.2. This still amounts to raw rates in the order of 40–80 GB/s (at 10 MHz), which is far too much for any storage system. However, up to now no selection of specific physics processes has been done. The storage requirement was set to 100 MB/s, so in total a reduction factor of 1 000 has to be achieved. A second constraint is the number of nodes per level, which has to be in a manageable order of magnitude. Furthermore the latency of selection algorithms determines the total buffer size. Here the fraction of data rate needed to be processed at one level multiplied by the latency gives the buffer size per level.

11.3.4.1 Bandwidth

Starting at a safe value of 100 GB/s and assuming that about 10% of all detector data has to be considered at the first level, 10 GB/s have to be transferred to the first processing level. Possibly less data would be required in case of simpler, cleaner signatures. With a latency of 100 μs per event 1 000 processing nodes would serve to digest the required input event rate of 10 MHz.

Similarly at a latency of 1 ms in the second level another 1 000 nodes would fit to read a first level rate of 1 MHz. Here data bandwidth is not an issue, since only at maximum only 10% of the initial events are selected plus a possible overhead of pileup. At the final step before event building 10 ms per event match to a 1% input from the second level.

However the description given here should not be taken literally, but only as an example of the evolution of rates. Different physics runs may require a different assignment of rates and levels and moreover different selection paths could be operated concurrently, e.g. a very clean signature leading to a big reduction factor may need only two levels whereas more difficult patterns may require more processing steps. Another issue is the possibility to combine two fairly simple signatures arising from two separate selection trees. This can be done already at the transfer level, e.g. by requiring in the scheduler that time slices are transferred only then to the second level if two subsystems from the first level have both marked them as interesting.

11.3.4.2 Processing Nodes

The various options for processing platforms are discussed in more detail in Sec. 11.4.3. Here the logical structure of nodes should be discussed. Basic features of the nodes are as follows:

- The basic network fabric of the DAQ system, e.g. Ethernet, is the common interface to all processing cards. Furthermore the nodes have to adhere to the common scheduling protocol in which processed time slices are marked by one level, assigned to the next level and addressed on the buffers.

- A common control and programming environment should be available. This comprises on one hand an (embedded) platform on which control software is executed and on the other hand a common high level language to describe the algorithms. In this way building blocks of a chain of algorithms can be assembled in a consistent way.

Beyond these common points the choice of the platform may depend on the actual type of algorithm. A simple pattern matching algorithm which has to digest a big amount of data at high speed is best implemented in FPGAs whereas more complicated floating point calculations are better represented in CPUs or DSPs. Therefore a possible scenario is a mixed pool of processing nodes based on FPGAs and DSPs/CPUs to which assignments are adapted according to the respective processing profiles.

11.3.4.3 Algorithms

In the following a brief overview of possible physical signatures and their implementation in algorithms is given.

Decay vertices. In the case of open charm decays, the most powerful signature is the observation of a decay point clearly separated from the interaction point. A reconstruction of a such a secondary vertex can give a reduction factor in the order of 100 or more. However to achieve this it might be more convenient to first simply require the presence of tracks not pointing to the interaction point as a first selection. The combination of all tracks for the actual vertex reconstruction is then performed at a higher level so that the total event rate for this more complicated task is reduced. At yet a higher level momentum assignments to the tracks would allow the determination of invariant masses.

J/ψ decays. A very clean signature already employed in many experiments are the decays of $J/\psi \to \mu^+\mu^-$ or $\to e^+e^-$. Easiest to realize is the trigger on muons because of the characteristics in the interaction with matter. But also electrons when combining to high energy clusters in the calorimeter and making an invariant mass cut provide a clean selection. Both can be done at the first selection level.

Lepton tags are more general signatures which are simple to realize but which have to be seen in conjunction with other filters to achieve appropriate reduction factors. Here triggering on muons from Charm decays, but also high energy electrons may provide an enrichment of D decays.

PID tags. A very important signature is the occurrence of a specific type of charged particle. This signature is covered by the Cherenkov detectors and the $\mathrm{d}E/\mathrm{d}x$ measurements, most notably in the TPC. Since there single detector systems are concerned, a preprocessing of ring patterns (RICH) or hit train curvatures and energies (TPC) would provide an early enrichment of interesting particles like kaons or electrons.

V^0 decays and hyperons. A whole class of interesting particles is based on the detection of V0 decays, i.e. the decay of neutral strange hadrons into two charged tracks. The V-shaped decay signature is easy to detect. The TPC hit pattern algorithm is well adapted to this task, but also other trackers can give reveal these decays with reasonable data processing. Based on this signature mother particles like Ξ can be reconstruction by adding further pions to Λ candidates at a higher processing level.

EMC correlations. Final states with photons or electrons are detectable by the electromagnetic calorimeter. The task of selecting physical signatures here is concerned with the combination of data from two opposite hemispheres. Since in $\overline{\mathsf{P}}\mathsf{ANDA}$ the hit multiplicity is fairly low simple combinatorial tests of photon or e^+e^--pairs can give an enrichment of there mother states (e.g. η, π^0 or $J\!/\!\psi$). Again, this should be feasible at the first processing level dealing with single detectors.

Missing energy. A more complex example is the detection of missing energy. First of all, this requires a good hermiticity of the detector. To extract this signature several detectors have to be considered and even a momentum balance of tracks has to be calculated to a certain accuracy.

If enough processing power is available, many of these selection tasks can be performed in parallel and more complex *selection masks* combining several criteria can yield high reduction factors at high efficiency.

The second level will then combine the signatures (particles) and perform computations like vertices or invariant masses. The bottom of the line is, that our system is flexible enough to achieve very high selectivity simply by anticipating typical data analysis steps in an act of processed data transmission. In this way a large number of detectors can participate in the extraction of the actually looked for physics at an early stage.

11.3.5 Discrete Event Simulations

In the proposed scheme of a continuously sampling data acquisition system with multiple layers for processing, proper buffering will play a crucial role in places where sampled and partially processed data have to wait for further processing steps before being finally stored or discarded. First of all we plan to use discrete event simulations to obtain indications on the amount of buffering needed at various stages and the optimal location where the buffers should be installed. As the amount of buffering is a function of available throughput and speed of implemented algorithms, we plan to construct models of various interconnections between buffers and processing nodes and use them to find the optimal architecture with indications on the placement of various components and required parameters (like processor speed or link throughput).

The placement of buffers has a direct impact on system latency, traffic patterns and congestion points. Modelling gives us a possibility to look into the internals of the architecture, usually not easily accessible with other tools, and follow the dynamics of the data flow. During the analysis of various buffering topologies we plan to monitor all aspects of data flow and look for an optimal combination leading to a stable, working system. The results from these models should be considered when taking a decision on the final architecture.

The type of behavioural simulation used here is known as "discrete event simulation". Basically, the simulation program maintains a time-ordered list of "events" i.e., points in time at which the simulated system changes state in a way implied by the type of "event" occurring. Only when an event occurs the modelled system is allowed to change its state. In most cases only a small part of the states of the simulated system needs to be updated. The state change can result in the generation of new events for a later time. These events are then entered at the correct position in the event list. The simulation program executes a loop in which the earliest event is fetched from the event list and then handled. We plan to organize modelling efforts around four activities in the sequence described below, with possible iterations of some or all steps in case we encounter significant discrepancies in demonstrating the feasibility of our model:

Parametrization: The components of the designed architecture may be quite complex. In our approach we will identify a limited set of parameters to keep the model as simple as possible but which

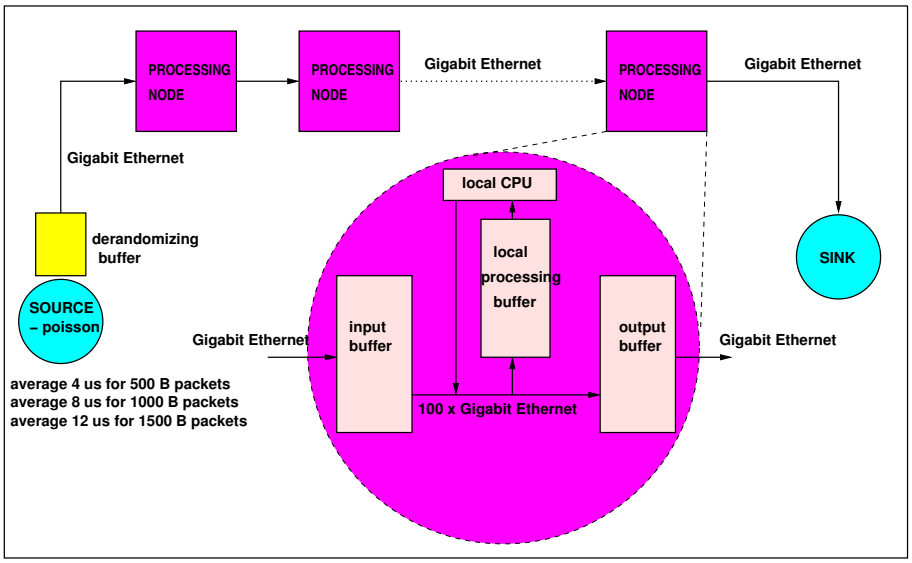

Figure 11.4: Schematics of a simple test case for discrete event simulations.

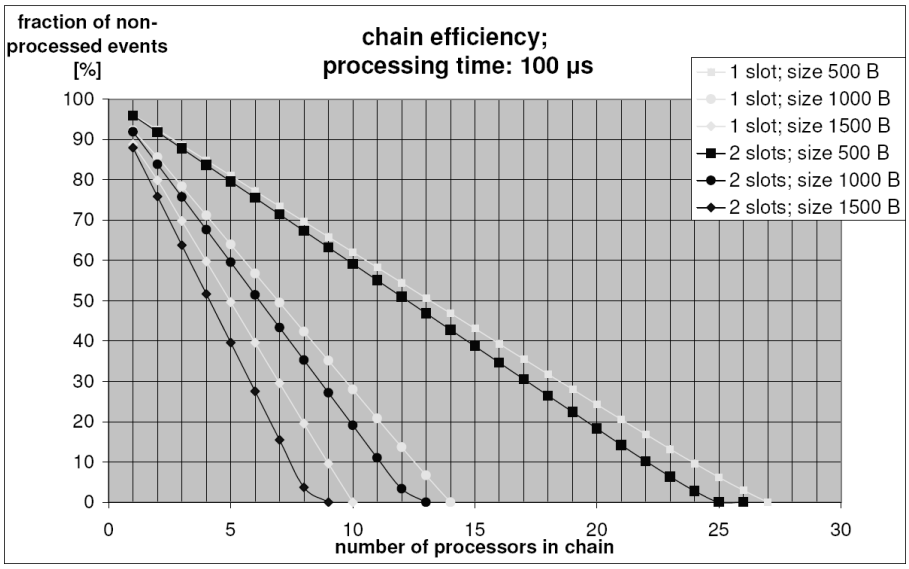

Figure 11.5: Efficiency of different chain architectures.

is sufficiently detailed to reproduce behavioural aspects relevant to the issues studied.

Calibration: The values for the identified parameters will be measured in dedicated setups. Hardware prototypes will be monitored using electronic equipment. Models of software will be calibrated by introducing timestamps into the code and taking measurements during the software execution.

Validation: Calibrated, parametrised models will be used to simulate small-scale test-beds where various prototypes of the components of the designed architecture will be put together to test the inter-operation and measure the performance. The capability to reproduce with our model the same results as measured in the test-bed will give credibility to modelling the full scale system.

Prediction: This is the final step of our modelling effort where models of various architectures

will be run and produce results (throughput, latencies) which will be the base for making architectural decisions for the final system. We considered and evaluated two tools (modelling environments) as platform for our model development. The Ptolemy environment, developed by the University of Berkeley, which has been closed and now becomes obsolete and the SystemC, developed by OSCI (Open SystemC Initiative) which offers free access to a set of libraries supporting hardware-oriented constructs implemented as the C++ classes. We selected SystemC for our development as it offers the same performance as Ptolemy in terms of memory usage and modelling speed but has now much better support.

A simple test architecture of daisy chained processing nodes, depicted in Fig. 11.4, has been used as example to demonstrate applicability of discrete event simulation for behavioural analysis. This is one model addressing the problem of handling busy nodes and data flow management in a simple way (s. Sec. 11.3.2). The links interconnecting nodes provide Gigabit throughput. The source of data (for example detector front-ends) produces packets of raw data according to the Poisson distribution with an average depending on the packet size in order to keep the Gigabit Ethernet link saturated. The packets are put into a de-randomizing buffer and stay there during the time the output link is occupied by the previous packet. Once placed on the output link they travel through the chain to reach the sink. If the processing node at which a packet arrives has free processing power, it uses the processing power for a fixed time and changes its contents from raw data into processed data. Upon conversion from raw to processed data, the size of the packet shrinks by half. Once processed, data packets do not need to be processed any more by the downstream compute nodes. In our model we investigated how the distribution of buffers within the processing nodes improves the performance of the architecture. We compared the performance of two chains: One with processing nodes having only one buffering slot for the local CPU and the other with 2 slots, where an additional packet can wait for the local CPU if it is busy. The rate at which the packets were generated follows a Poisson distribution with an average equal to the time a given packet size is being transferred over the Gigabit link (a 64 B packet takes 0.512 μs whereas 1500 B takes 12 μs).

Fig. 11.5 shows efficiency of the two architectures for three data sizes measured as a fraction of non-processed data arriving at the sink for a given length of the chain. The architecture with processing nodes having two buffering slots for the local processing requires a shorter chain to reach the same level of non-processed packets than the architecture with only one slot for the local processing. This observation is confirmed in Fig. 11.6, where CPU usage is plotted for the shortest chain with all data packets arriving at the sink as processed. A single additional buffering slot allows to use the CPU very efficiently – close to 100% and more slots are not necessary. In both cases processors close to the chain's end are used less efficiently as most of the traffic passing through these nodes is already processed, and the simple relaying of processed packets between input and output becomes the main task of these nodes. A possible optimization would be to use shorter chains with the possibility to re-direct non-processed packets from the sink back to the chain at some place close to the chain's end.

11.4 Implementation

11.4.1 Guidelines for Front-end Design

The concept of a continuously sampling data acquisition has major implications on the design of any detector front-end electronics. While in pipelined, but triggered systems a small dead-time can still be accommodated by regulating the minimum time between triggers, in a sampling DAQ dead-time is translated directly into detector inefficiency. Therefore any dead-time should not exceed the length of physical signals so that inefficiencies are only of the same order as pileup and signal overlap. Naturally, pipelines and buffering have to be implemented at all levels to avoid congestion and allow maximum de-randomization so that only bandwidths and transport and processing latencies have to be considered.

11.4.1.1 Data Reduction Levels

Throughout the front-end electronics several levels of data reduction have to be implemented. The first level concerns the zero suppression of raw detector pulses. This comprises noise reduction by common mode noise suppression and threshold comparison after proper pedestal subtraction. Furthermore, pileup, delta electrons and secondary interactions should be dealt with at this level. This first level has to be performed on the detector front-end. It may

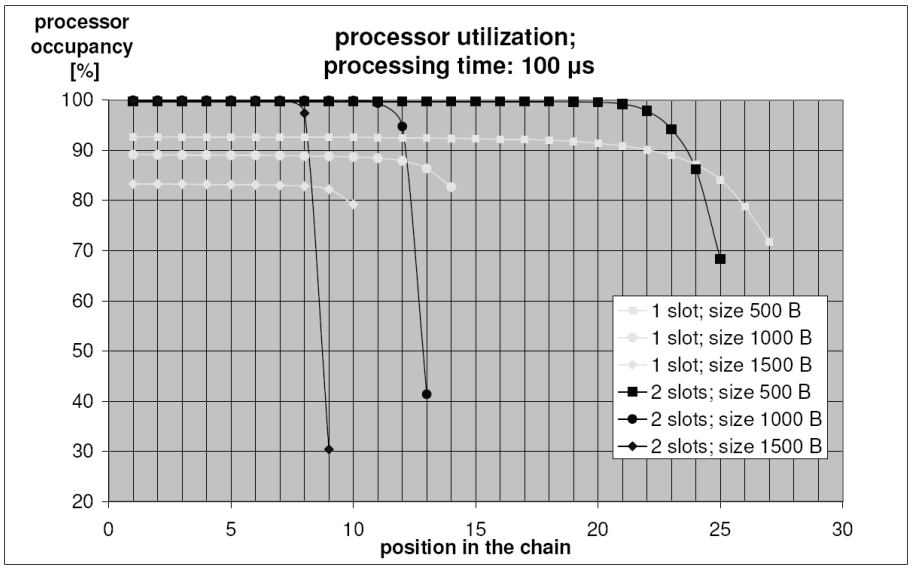

Figure 11.6: CPU usage for different chain architectures.

be located on the readout card directly connected to the detector channels or on a readout driver multiplexing several readout cards at a small distance.

On the next level, digitized data is treated to extract first physical signal features. Here clusterisation and time reconstruction take place. Amplitudes are treated to combine channels in a weighted summary information (cluster centroids, cluster amplitude sums). This level can be either performed on the detector front-end or on a subsequent processing unit.

On the third processing level, physical information is extracted from the data. Here amplitudes and centroids are converted into energies and coordinates. A first step in pattern recognition to form tracklets, rings, *etc.* can be performed at this level as well. It also requires access to online calibration constants. The proper place for the processing are data concentrator/buffer modules with attached processing units which interface between the detector level and the general cascaded high speed network.

11.4.1.2 Standard Interfaces

For the integration in the overall processing and data transport infrastructure several standardized interfaces have to be defined.

Time Distribution Network: The time distribution system described in Sec. 11.4.4 provides a stable clock to all readout systems with a jitter in the order of 25 ps. The signal is generated by a single source and transported via optical fibers and a network of passive optical splitters to all readout boards. From this clock normal all clocks relevant for timing and digitization are derived in order to achieve a synchronous readout with consistent timestamps.

Control and Configuration Network: Simple Ethernet will be employed as control and configuration network. Readout concentrators must have a small embedded CPU and an electrical Ethernet interface. Through this interface they receive asynchronous control signals and data for programming and configuration of readout processors attached to them. Local network switches will have optical uplinks to ensure electrical decoupling to avoid ground loops and limit noise.

Serial Data Interface: Wherever practical a standardized serial interface for data transmission should be implemented. This would be the standard input to default concentrator boards. The serial link should also implement a backwards direction for setup and programming of the attached front-end boards. Depending on detector requirements and cost an electrical or an optical version can be selected.

Data Network: The concentrators send their output to a cascaded high-speed network. This can

be (10-)Gigabit Ethernet or another switching network as will be specified during the design phase. If detector-specific concentrators are needed this interface must be implemented as this would be the last level where deviations from general purpose components may be allowed for special detectors. The $\overline{\text{PANDA}}$ Front-end Committee will define the standards for these interfaces which must be implemented by all types of front-end electronics. The strict adherence to these interfaces is mandatory to achieve a homogeneous infrastructure minimizing losses and ensuring data coherence.

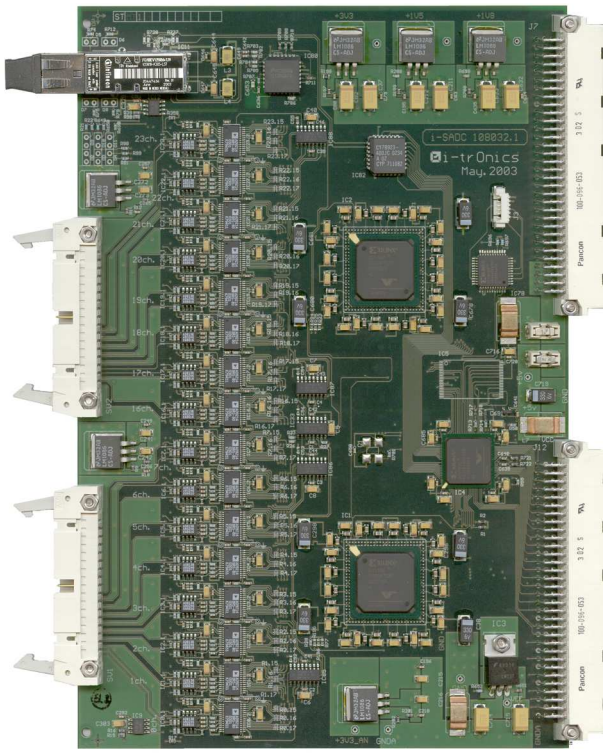

Figure 11.7: Sampling ADC VME module from TUM.

11.4.1.3 Example Front-ends

The goal of an early standardization of readout components is to reduce overhead by multiple parallel developments both in the design phase and the operation phase. With a standard set of front-end boards only the actual coupling to the detector including proper pre-amplification and shaping are open detector-specific tasks. The Front-end Committee will define a minimal set of front-end boards. Example front-ends are given as examples in the following, but the detector- specific parts are described in the detector chapters.

The first implementation of a small scale sampling DAQ is the Sampling ADC (SADC) from TU Munich. The SADC comprises on one VME card 32 differential analog to digital converters and some FPGAs as a first processing stage. The input range and impedance for each channel can be adapted to different detector signals by preamplifiers preceding each ADC. The ADC resolution can also be changed between 8, 10 and 12 bits to meet different precision and power requirements. The selectable sampling frequency up to 100 MHz, allows also an ideal adaptation to either raw detector signals or already preprocessed signals from a front-end ASIC. A first processing of the raw ADC data is then performed in FPGAs on the SADC module. This can include for example data buffering, pedestal subtraction, noise suppression, peak detection or signal time reconstruction. As the FPGA firmware can be reloaded during operation, it is possible to run different physics programmes with ideal matched firmware versions. The preprocessed data are transmitted to the next readout level via a bidirectional optic fibre link. To ensure also a precise time information between different SADC cards and channels, the fibre uplink to the SADC is used to distribute a low jitter clock signal to the module which then drives the ADCs synchronously.

Certain classes of detectors require a readout with very good time resolution rather than analog amplitude measurement. These are high time definition devices like scintillators or RPCs on one hand and detectors where time is a measurement defining coordinate like drift chambers on the other. For these detectors traditionally TDCs are used for readout. To avoid the necessity of a custom sampling TDC an alternative is the conversion of time into charge with subsequent analog-to-digital conversion. Like this only a pre-stage to the sampling ADC is needed. The time resolution that can be achieved in this way is with few tens of picoseconds quite excellent and beats most high frequency PLL devices. A design-critical issue is however the conversion dead-time at the first step. This can be reduced by fast switching parallel input stages.

Nevertheless where large channel counts and very low noise requirements are stringent, ASICs are unavoidable. To minimize the number of different front-end classes it is desirable to find a device that can serve many detector systems. For future experiments at CERN and GSI an initiative is under way to design a multi-purpose ASIC for TRDs, calorimeters, RICH detectors and TPCs. Its purpose is an accurate dead-time-free measurement of charge and time. It includes signal filters and

shapers, analog-to-digital conversion, noise reduction and signal processing for data reduction. It shall be able to run in a trigger-less as well as in triggered mode.

11.4.2 Network Infrastructure

The DAQ system utilizes a number of different networks to transmit the various types of information needed during full scale operation having different requirements on bandwidth, flexibility, stability and added functionality.

In general there are several possible choice in each case and the final decision will be based on design criteria as well as the market situation. The basic choices are between more customized networks with additional functionality and off-the-shelf high-bandwidth networks where functional overheads are simply absorbed by extra bandwidth.

In the following we outline the different network topologies for the required networks.

The simplest network is the control and configuration network. It serves to program components of the DAQ system, upload run condition data, upload or download calibration data and monitor the operation. This can easily be taken over by simple Ethernet.

The next task is the distribution of a precise clock normal along with short synchronous messages and potentially some additional asynchronous information. There are various options to implement this time distribution network:

The first option is a custom optical network as used in COMPASS and at LHC. This is unidirectional and can therefore be operated best by using passive optical splitters which provide a natural method to broadcast messages and deliver a very low time jitter in a simple and stable manner. The bandwidth of asynchronous information is however limited as data addressed to subsystems is received by all connected devices and has to be filtered according to a tag identifying the actual destination.

Another option is the usage of slightly standard optical networks, potentially even Ethernet. The essential modification here is the implementation of a standard clock used by all emitters and passed on from level to level with proper phase recovery. In this way a bidirectional link is possible and data can actively be routed to single destinations. The distribution of a stable clock is however a more complicated task and has not yet been done in such a framework. Nevertheless more economic components could be used and the number of different networks may be reduced by merging control and time distribution.

An intermediate way is the use of a passive optical distribution system with the capability of allowing directed back-links from receivers to the controller.

The most demanding network is the data processing network. The requirement is to be able to assign at full raw front-end data rate (after data reduction) processing nodes to any detector, to be able to configure arbitrary first level selection schemes. Of course, processing power and buffer sizes must match the latencies of the respective selection algorithms and the resources are limited within the full network. To achieve this, two roads can be chosen.

The brute force method is to over-assign bandwidth to all attached nodes in a away that almost all possible connection requirements can be met in any selection scheme. Then the limiting resources are only buffers and processing units, but bandwidth should not play a role any more.

The second approach requires a configurable network hierarchy. Here switches are connected in several layers and only the actual connections to processing nodes and concentrators/buffers have full physical bandwidth. The network itself is not a full cross-bar but switches have to be assigned to different levels to have sub-networks with higher bandwidth for first level selection and others with more nodes but less traffic for higher levels. This is depicted in Fig. 11.1.

The final network connection the feature extraction network with the event building network where the last selection step is performed after assembly of complete event blocks. This network is also hooked up to the storage network. Here standard computer center technology is fully sufficient.

For the time distribution network some customization is needed in any case. If this is done based on standard (Ethernet) components or with simpler (partly passive) optical networks is a choice to be made.

For the more demanding task of the high-speed processing network the selection of network technologies at hand or at least predictable now is given in the following.

Clearly the most obvious choice is to follow the evolution of Ethernet. As of now Gigabit Ethernet is fully mass-market, and even optical components for this become cheap. The standardisation of electrical 10-Gigabit Ethernet is at hand, the optical standard is in production in computer centres and network backbones. The formulation of 40-Gigabit

Ethernet is on the way and will be certainly available when $\overline{\text{P}}$ANDA turns on. Thus Ethernet offers a rather safe road to higher bandwidths at reasonable prices.

A new emerging technology is the advanced switching layer for PCI-express. Initially being a serial high-speed replacement of PCI and meant for usage only within computers the serial interface as such offers the possibility to have point-to-point connections over longer distances. With the introduction of advanced switching of PCI-express more complex networks are feasible at very high bandwidths. The new technology offers high scalability and the possibility to achieve high integration of large bandwidths. Clearly the aim of this technology is a high-performance mass market with strong interconnection of communication and computing infrastructures. On top of PCIe-AS multiple protocols can be implemented by means of encapsulation offering added functionality for a custom DAQ network.

Other network technologies in the high-performance sector are Infiniband and GSN (aka HIPPI-6400). They are both targeted at future high performance data centers and offer scalability and separability of I/O and processing resources. At the moment Infiniband has the broader industry base and bandwidths up to 100 Gb/s are under development.

11.4.3 Computing Infrastructure

The computing infrastructure of the DAQ system has to provide the necessary resources to treat in real-time data generated and distributed at all levels of the readout and selection process. In the implementation of the full system there are two competing tendencies: On one side, processing power has to be localized as close as possible to the place where data treatment is required at a specific level in order to reduce data traffic and bandwidth requirements. On the other side, the full system should have a reasonably homogeneous structure to be able to move single tasks from one level to another without having to surmount big architecture dependencies.

11.4.3.1 Processing Levels

A number of separate processing levels can be identified throughout the DAQ system. Boundary lines are of course not sharp but are defined by requirements as well as platform choices.

Front-end Board: The first processing step concerns the efficient data reduction on the detector front-end. After zero suppression the signal time has to be determined, hit clusters have to be found and online decoding with preloaded calibration constants should take place. These steps take place at the front-end board level.

Detector Processing Unit: At the next level data is formatted and may be buffered on concentrator modules. A processing unit attached to a concentrator/buffer module performs more complex cluster algorithms and first steps in pattern recognition. It also performs the grouping of data into timeslices for time addressed access.

Compute Node: General purpose processing units placed in the cascaded high speed network take part in the feature extraction, filtering physically relevant event signatures for further processing.

Farm Node: The final high level event selection and online reconstruction takes place in powerful computer farms attached to the storage network.

11.4.3.2 Platform Options

The collection of useful platforms depends very much on the evolution of the IT sector with time. However, different architectures, their advantages and disadvantages can be outlined and at the time of implementing a prototype architecture it will crystallize, which platform is used at which levels. Here we describe the options in a hierarchy supposedly going from devices closest to the detector to the end of the processing chain.

Only the very first level in the readout system, if at all, has to be implemented in ASICs. Here careful electrical design not to deteriorate analog signals, radiation tolerance and highly optimized designs are crucial issues.

Modern FPGAs offer a large flexibility and power and implement more and more additional features like integrated DLLs or even PLLs for highly stable clock pulses and time measurement. On the other hand, embedded CPU cores (MIPS, PowerPC, ARM, ...) allow for standardized communication and control. In addition, having ample amounts of gates available, complex functionalities previously deemed too costly like e.g. arithmetic units can be implemented in custom designs. Chip road-maps indicate that these devices are getting

more and more powerful. However, up to now proprietary tools for programming and even software development are needed.

DSPs allow to parallelise complex arithmetic operations of digital signals. As such they provide high but specialized processing power. Their drawbacks are the need for custom software development tools and specific interfaces to the computing and network environment. Most DSPs have high-performance serial or parallel data interfaces but with vendor-specific designs and protocols making it more difficult to communicate in a standardized, platform-independent manner. A powerful solution is their usage as co-processors for high-speed processing. As processing device attached to a standard platform they can perform simple but time-consuming and frequently routines.

A very promising platform are System-on-Chip devices, i.e. systems which implement all necessary peripheral interfaces, memory controller and bootstrap devices on the same chip as the CPU itself. These devices are more fault-tolerant and power-efficient than ordinary computers and can therefore be embedded on smaller form factors and at larger numbers. Their application can be seen in two directions, coupling to more specialized hardware to provide a control and programming platform or in massively parallel computing. They may supersede in future a large amount of more standard computing platforms.

The domain of high-performance multi-purpose CPUs will be the highly computing-intense tasks where multi-Gigahertz processing with fast floating point and integer pipelines is required as well as high-speed mass-storage interfaces and other high-level periphery.

Clearly, the choice of the platform for each level not only depends on performance and flexibility but also on economic boundary conditions. General market trends can therefore play an important role outside of pure design considerations.

11.4.3.3 Operating Environment

Since our system will comprise many thousands of processing nodes at the various levels, there is basically no alternative to royalty-free operating environments. The goal of a homogeneous environment across all levels can be best achieved by using Linux wherever possible: Linux is available as embedded variant on small scale micro-controllers as well as full fledged networked operating system on almost all standard types of CPUs.

An interesting strategy in the field of reconfigurable logic is the use of Linux on CPUs embedded on-chip to program FPGA resources on the same die. The FPGA is driven by Linux as a "device".

In addition there are Linux ports for most System-on-Chip devices. A seamless integration from front-ends to compute nodes to high level farms is therefore feasible and a common environment can be achieved allowing the interoperability of tasks and processes across all levels. In addition the development can start at an early stage on less powerful standard platforms and then be migrated at the time of deployment.

11.4.3.4 Programming Tools

By using standard tools like high level programming languages and compilers, algorithms can be ported across the system. Moreover, non-engineering personnel can participate in the development and implementation of algorithms making the direct use of physics based know-how possible.

Promising tools in the context of simulation and synthesis of FPGA based algorithms are e.g. HandelC and SystemC. In particular SystemC on one hand is connected to a growing Open Source community and has a strong industry base on the other.

In both cases a high-level language interface via C/C++ is provided with additions and libraries specific to hardware implementations. Core algorithms can - in an ideal case - be simply translated into hardware code to run on an FPGA or DSP.

11.4.4 Timing and Fast Control

Timing and synchronisation are common problems of high rate experiments in the field of particle physics. In order to synchronize the data and provide a time reference for high precision timing measurements the Time Distribution System (*TDS*) is needed. The system provides an absolute time by distributing the reference clock down to the level of the front-end electronics, i.e. very close to the detectors. The front-end electronics measures the timing of the detector signal respectively to the clock, adds an absolute timestamp and sends this information to the next level of the DAQ.

11.4.4.1 Requirements

- The maximum jitter of the time reference is 20 ps.

- The system is scalable from few hundred to few thousand destinations.
- The components of the TDS are mounted on the front-end modules very close to the detectors where radiation conditions exceed normal radiation level, therefore the components should be radiation tolerant.
- The time distribution system is flexible in order to follow the development and new requirements of the experiment.

11.4.4.2 Architecture

The architecture of the proposed Time Distribution System is based on existing systems like the TTC for LHC experiments [1], and the TCS [2], built for the COMPASS experiment at CERN [3]. The precise time reference is provided by distributing an encoded clock and data from a single source via a passive optical network to a large number of destinations. The basic architecture of the TDS is shown in Fig. 11.8 and includes only unidirectional data transfer, but we plan to study the possibility of using passive optical networks with a bidirectional interface. The bidirectional network will allow to combine the functionality of the time distribution system with the front-end interface.

We are considering two exploit one of two possible methods to implement the bidirectional network using the TDS architecture:

- One can use passive splitters as a concentrator to transfer the light signals from all destinations back to the central master module. This is possible because the light splitter has an asymmetric attenuation parameter depending on the direction of light propagation. The disadvantage of this method is that only one TDS receiver at a time may power its laser diode and switching from one TDS receiver to another requires extra time and a safe protocol.
- One can use active concentrators which combine information from e.g. 32 sources to one destination. This solution is certainly feasible but the reliability of the system has to be evaluated.

The Time Distribution System includes three main components:

- TDS master module with integrated laser transmitters;

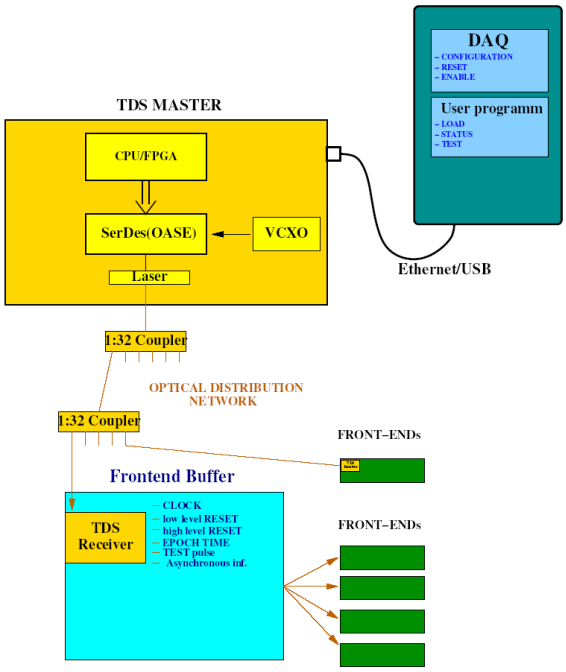

Figure 11.8: The TDS system, functional diagram.

- passive optical network with e.g. 1:32 splitters;
- TDS receivers.

The TDS master module is a central module of the system which includes:

- the processor and/or an FPGA to control the system;
- the temperature compensated oscillator crystal,
- OASE serializer/deserializer chip,
- the interface to the control software, DAQ and user programs;
- the control signal inputs,
- input/outputs for extending the system to a bigger number of destinations.

The TDS receiver can be a small mezzanine card with the OASE chip and an FPGA. The pin and laser diodes are integrated into the SerDes chip. The FPGA receives data from the SerDes chip, extracts control signals and provides asynchronous information to the destination module via the serial link. Every TDS receiver has its own unique ID for addressing and configuration via the optical link.

11.4.4.3 Clock and data Encoding

The clock and data are encoded in a single serial line by using standard 8 bit/10 bit encoder. Using a serializer/deserializer (SerDes) at a high speed of 2 Gb/s, which becomes a standard in these days, will eliminate the problem of clock jitter.
The most suitable candidate for the SerDes chip is the OASE chip which is being developed by the University of Mannheim in cooperation with the company ULM Photonics (Ulm). The functional diagram of the chip is shown in Fig. 11.9. The development of the OASE chip is part of the FutureDAQ project and gives the possibility to implement features which are specific for the time distribution system:

- radiation tolerant behaviour of digital electronics by designing the state machines and data transfer interfaces with a single bit error recovery logic;
- clock phase adjustment to compensate the fibre length and the position of the detector respectively to the target;
- clock divider to provide the front-ends with desired clock frequency;

11.4.4.4 Synchronous and asynchronous information

The TDS distributes two classes of information: synchronous and asynchronous. The synchronous information is a time critical control information, which is distributed with fixed latency. The synchronous information is decoded at the destination and provided as control signals to the front-end modules.

The synchronous information or control signals:

- low level RESET- reloads FPGAs, resynchronises PLL and DLL ;
- high level RESET - resets all data buffers, counters and state machines, it also defines the TIME ZERO in the experiment;
- GLOBAL ENABLE - enables/disables data taking in all front-ends ;
- EPOCH TIME - the signal is distributed with a fixed time interval, generates the EPOCH TIME information on the data stream and allows to verify the synchronisation of the destination module;
- TEST PULSE - initiate generation of the test pattern on the data stream, the test patterns allow to verify the integrity of the front-end DAQ interfaces.

The asynchronous information is distributed for configuration of the TDS receivers.

11.4.5 Control Software

To operate a high speed readout system it is necessary to have control over all aspects of the experiment to ensure stable measurement conditions and good data quality. To achieve this a control system must address several issues discussed here briefly.

Run Control. Data taking conditions have to be defined by means of a graphical user interface. These conditions comprise the setup of detector front-ends to read, triggering and selection conditions, run types (physics data taking, alignment, calibration, test, ...). Data flow should be controllable from this interface to view data rates and buffer levels to detect congestion or other problems at an early stage. It should be controllable which nodes or node-networks are participating in the readout monitoring host load (network, CPU, buffer) and responsiveness. Furthermore one has to define which types of data are to be recorded on mass storage and the state of the storage resources should be monitored.

Monitoring. During data taking the quality of the data has to be monitored constantly. This monitoring system extends not only to detector channels (wire maps). It also has to report readout errors (data inconsistency, missing front-ends, ...) and give access to online detector calibration constants. It should monitor physical signals, e.g. by means of showing standard particle yields and filter efficiency. Furthermore the beam has to be monitored to obtain its quality and keep record of the integrated luminosity.

Detector Configuration. Important running conditions are the proper configuration of the detectors and their readout. This includes thresholds and other parameters for data reduction. Of relevance is also the programming of front-ends with firmware, calibration constants, algorithms and lookup tables.

Detector Control. Finally, the control of detector parameters like high voltage, low voltage and

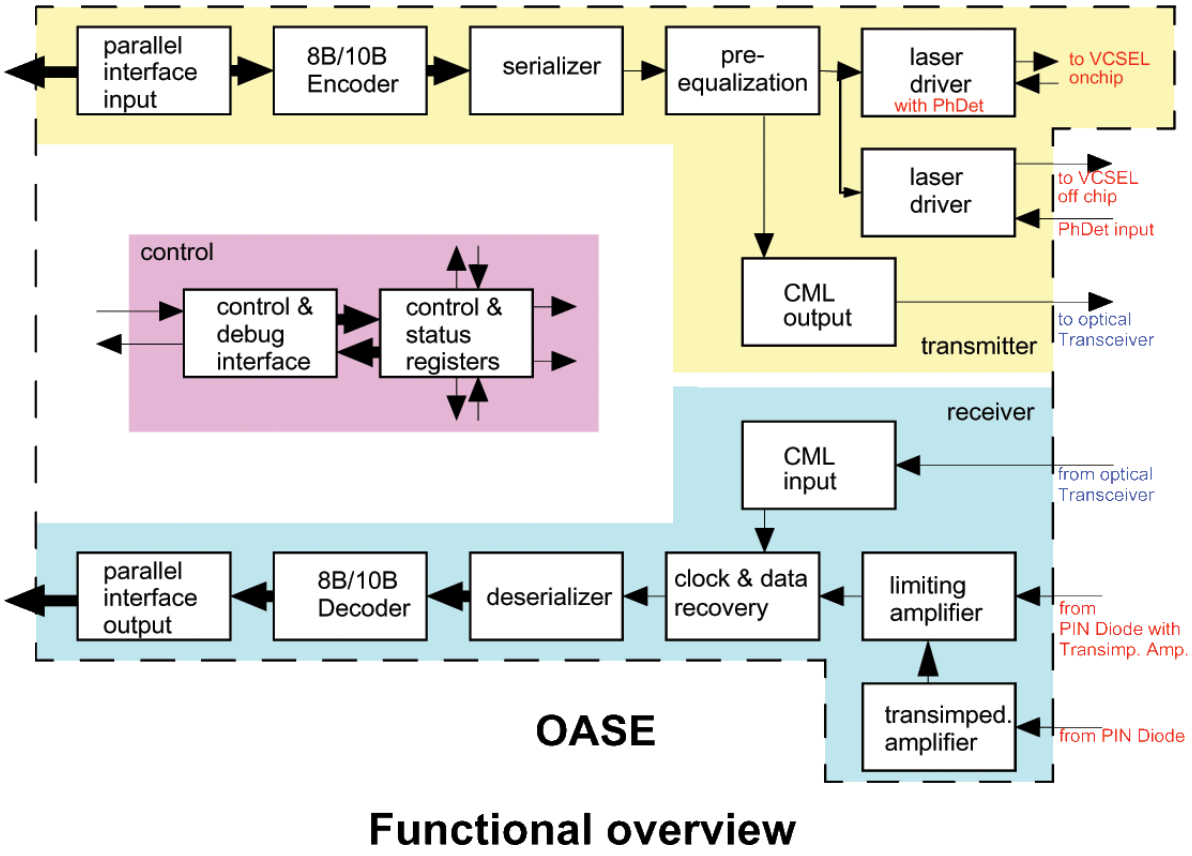

Figure 11.9: OASE chip, functional diagram.

currents, gas pressures, flows and mixtures has to be performed by the system. In addition environmental conditions like temperatures, atmospheric pressure and the readout of various probes (magnetic fields, switches and relays, ...) have to be monitored. At last, critical conditions have to be detected and announced and emergency procedures have to be executed.

A common database for all issues described above is desirable as is a unified user interface covering all aspects of experiment control. A joint experiment controls group at GSI shall work out the framework of software and hardware with which each experiment can realize its goals.

11.5 Planning

The development of the DAQ/Trigger system for $\overline{\text{P}}$ANDA is characterized by the fact that it is operating on the technological frontier in IT. To achieve the desired results not only technical aspects have to be addressed but the evolution of the IT market has to be taken into account, since it is impossible to develop all necessary base technology within experimental physics alone. For this reason even though general concepts and specifications have to be spelled out early enough to allow for a proper interfacing with all parts of the $\overline{\text{P}}$ANDA detector most feasible technical options should be kept open until the final prototyping starts.

11.5.1 Relation to FutureDAQ JRA

The key technologies of the relevant components will be explored within FutureDAQ, a Joint Research Activity within the EU 6th Framework Integrated Infrastructure Initiative on Hadron Physics (I3HP) aimed at the development of a data acquisition concept which is much better matched to the high data rates and to the complexity of the next generation of experiments.

The deliverables of FutureDAQ include the prototyping of a data concentrator, a time distribution system, a cascadable switch, compute and filter nodes and various algorithms. Since FutureDAQ is a joint project of the $\overline{\text{P}}$ANDA and CBM experiments not all results may suite our needs one-to-one but

may have to be adapted for reasons of functionality or budget.

FutureDAQ is supposed to finish at the latest at the end of 2007 assuming a one year prolongation due to the late start of funding.

After FutureDAQ is completed, a final evaluation and selection of designs shall take place and a prototype design for the PANDA DAQ and Trigger system will start. This prototype will be tested extensively and then the designs are updated for the subsequent initial production and deployment phase.

.

11.5.2 Responsibilities

Table 11.2 represents expressions of interest of groups involved in PANDA concerning the realisation of the DAQ/Trigger system is given. This implies that the corresponding institutes apply for funding for manpower, R&D and later on the construction of the system. Since this funding is however not yet guaranteed at this time, no legal commitment can be made yet.

Item	**Person/Institute**
Time distribution system	TU Munich
Concentrator/Buffer	Krakow
Data reduction	Torino
Compute Nodes	Gießen
Cascaded high-speed network	GSI & FZJ
Control Network	FZJ & GSI
Algorithms	Gießen, TUM, GSI
	Katowice, Pavia, Warsaw
Event filter farm	GSI

Table 11.2: Expressions of interest in work for the DAQ/T system.

References

[1] B. Taylor et al., IEEE Tran. Nucl. Sci. **45**, 821 (1998).

[2] I. Konorov et al., The trigger control system for the COMPASS Experiment, in *IEEE Nuclear Science Symposium Conference Record*, IEEE, 2002.

[3] L. Schmitt et al., IEEE Tran. Nucl. Sci. **51**, 439 (2004).

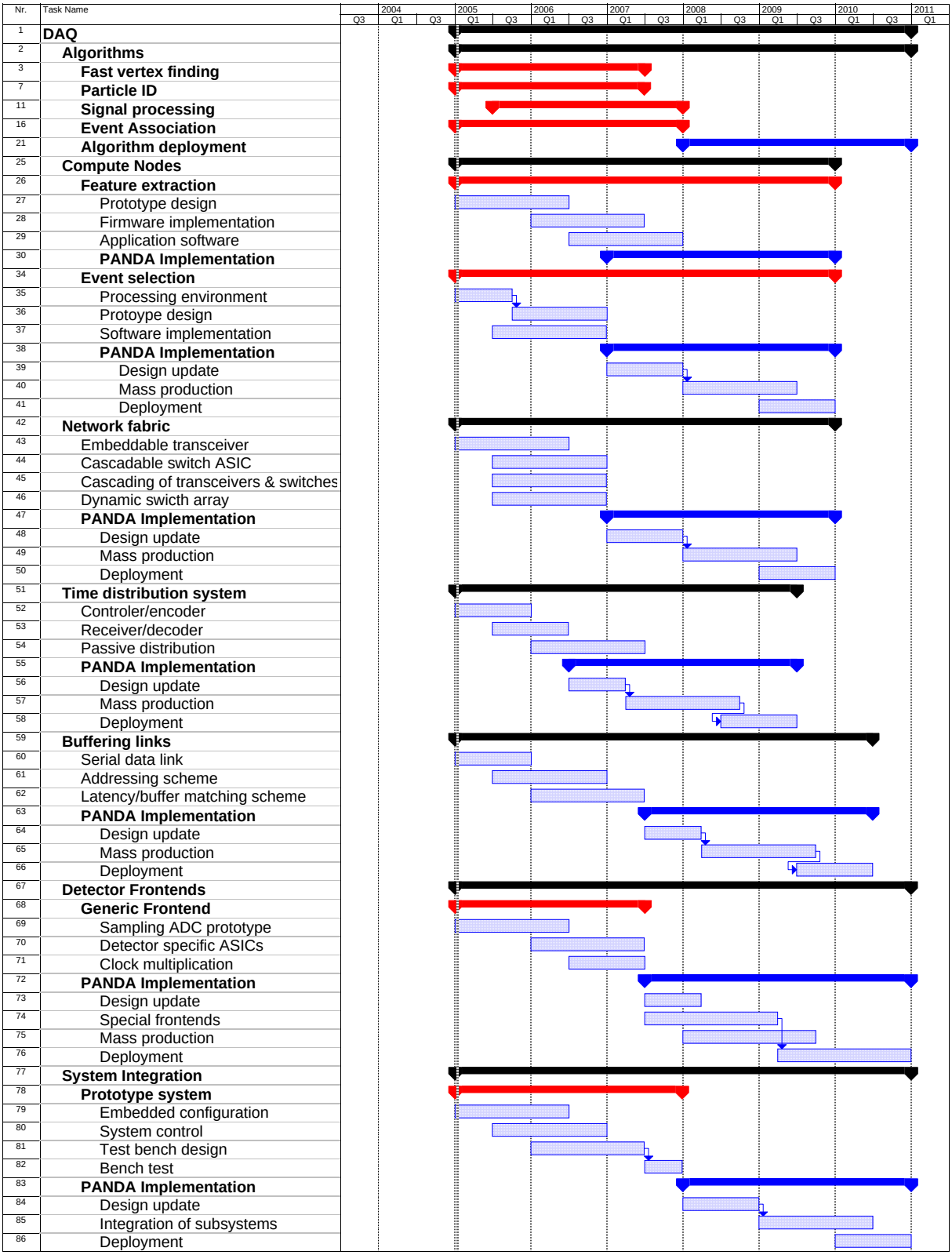

Figure 11.10: Estimate of timeline for development and deployment of the $\overline{\text{P}}$ANDA DAQ.

12 Computing

12.1 Introduction

There are a number of challenges for the computing requirements of the $\overline{\text{P}}$ANDA experiment. As already mentioned in Sec. 11.1 it is planned to operate at interaction rates of the order of 10 MHz which results in a raw data rates of approximately 100 GB/s. After online event selection 100–200 MB/s are put to mass storage. This large data quantity must be stored and analysed within a reasonable timeframe. Therefore very high computing power and large data storage is needed. This requires an infrastructure with computing resources at several different places of the world which must be used in parallel.

The planned $\overline{\text{P}}$ANDA setup is subdivided into several individual detectors. Each sub-detector consists, in general, of a large number of modules. Thus, the event simulation, the event reconstruction and the analysis as well require a very extensive offline programming code. Therfore a software environment is needed which allows code development at different sites in parallel.

The following chapter will describe the present software components as well as the code development and distribution in detail. Furthermore a proposal for an ideal computing model for the $\overline{\text{P}}$ANDA experiment will be presented.

12.2 Software development and distribution

The $\overline{\text{P}}$ANDA offline software will follow an object oriented approach, and most of the code will be written in C++. Wherever possible proved software tools and packages that are common in HEP computing will be used and adapted to the $\overline{\text{P}}$ANDA needs to limit the necessary amount of manpower in the software development. E.g. we will use

- GEANT4 for geometry modulation and particle tracking in the Monte Carlo simulations
- ROOT I/O for object persistency
- ROOT histogramming in framework applications as well as in the final analysis steps
- ROOT for interactive access to the analysis relevant levels of the event data
- Perl for job control and the automatization of data production processes
- MySQL as relational database for bookkeeping and conditions and configuration storage
- CVS for version control of the source code

All external packages will be interfaced to the offline software by OO techniques to allow an easy replacement by new developments and new techniques which for sure will become available until $\overline{\text{P}}$ANDA starts and during the time it will take and analyse data.

In addition to the external packages that are commonly used in HEP computing, we will take over and adapt concepts, ideas and parts from the experiment software of other HEP experiments like BaBar and the LHC experiments, because on one side $\overline{\text{P}}$ANDA does not have yet the necessary resources of qualified manpower to develop every part of the offline software by its own, and on the other side experiences with offline and analysis software of other experiments are available.

During the development of the code used to produce the data shown in this report, a number of design flaws showed up, and the $\overline{\text{P}}$ANDA computing group decided to start now the development of a new offline software. In this new software parts of the BaBar offline code will be incorporated. I.e. we plan to use the BaBar application framework, to adapt the tracking code, or to use the BaBar Kanga eventstore. Reusing elaborated parts of the BaBar offline software should allow to build a complete and working system with limited manpower in a reasonable time.

12.2.1 Development environment

The software development was done in the past and will be done in the future as well in a distributed manner. Up to now there's no $\overline{\text{P}}$ANDA computing infrastructure at GSI that could be used by the developers to login, edit, compile and run, but the contributing developers work at their home institutes, and the institutes function as $\overline{\text{P}}$ANDA computing sites. Releases of the $\overline{\text{P}}$ANDA software get build centrally in Bochum, and get imported by the contributing sites, as a base for further development work.

For release administration and release import we use the BaBar SoftRelTools (SRT). SRT furthermore provide structured makefiles, tools for package and release administration, dependency control, etc.

Currently the $\overline{\text{P}}$ANDA software supports just one platform, the most cost effective combination of Linux on Intel compatible CPUs, though SRT supports the usage of multiple platforms. Developing on at least two independent platforms is of large benefit, because more errors show up already at compile time, and the debugging efforts can get reduced. Therefore we aspire to support a second platform in the future.

12.3 Software components

The software framework used for the studies presented in this report has been devised with four major applications for events generation, simulation, reconstruction and final analysis.

Several different event generators depending upon the process of interest are available. In order to determine the feed-through from the remaining annihilation channel, the Dual Parton Model is used as a background generator. Similarly, the feed-through from background events in $\overline{\text{p}}A$ annihilation reactions is calculated using the UrQMD model. A further application can generate specific signal channels from $\overline{\text{p}}\text{p}$ annihilation as well as single particles.

The second main application of the software framework is the simulation part. The generated particles and all subsequently produced secondaries are tracked through the detector volume using GEANT4 [1]. In the next step the simulated output informations are reconstructed to composite informations such as particle energy deposits in the EMC, tracks in the MVD, STT, TPC and MDCs or PID in DIRC and RICH. Finally this information is combined to particle candidates which are available in the analysis application.

12.3.1 Event Generators

12.3.1.1 Overview

The major interests of computer simulations for the $\overline{\text{P}}$ANDA experiment are the following:

- Simulation of s-channel resonance production (J/ψ, *etc.*) and decay into various particles ($\mu^+\mu^-$, e^+e^-, *etc.*).
- Simulation of 2, 3 and 4 particles final states ($\mu^+\mu^-$, e^+e^-, *etc.*) for estimation of background of signal reactions, and study of benchmark channels.
- Simulation of multi-particle final states.
- Simulation of single particles for detailed detector studies.

We use known properties of decay channels for known resonances solving the first task. For undiscovered resonances we assume at the beginning a uniform population of phase-space. We are going to use theoretical predictions in the following.

The uniform phase-space hypothesis is applied for second class simulations, although there can be

anisotropy in angular distributions of reaction products connected with the physics of the reactions. The study physics requires good particle detection in various phase-space regions. Thus the hypothesis of uniform phase-space population is useful for the detector design. Its simulation algorithm is well known [2] and is implemented in the $\overline{\text{P}}$ANDA framework.

The first question to the simulations of the third class is the rate of events with various multiplicities. The second question is the particle composition of the events. At given multiplicity and particle composition, the kinematic properties of particles can be found using the hypothesis of the uniform phase-space. It is obvious, that like this the well known angular anisotropy can not be reproduced.

There are two ways to find a solution to these questions: parametrize known experimental data or apply a theoretical model. The parametrization was very popular in the past when it was assumed that light meson production gave the main contribution to the multiplicity. The point of view changed after the recognition of the large role of resonances in multi-particle production (about 70% of the light mesons are decay products of heavy mesonic states). Because it is very heavily to parametrize production properties of various resonances, the simulations of multi-particle states using theoretical models are more popular now. The simulations are performed with the help of so-called Monte Carlo event generators. Each generator is a set of routines written in a high programming language.

In the $\overline{\text{P}}$ANDA framework we use Dual Parton Model [3] based event generator (DPM) and Ultra-relativistic Quantum Molecular Dynamic model [4, 5] generator (UrQMD). They are described below. Both randomly generate various final states with particle composition and kinematic properties of the states determined according to physical ideas implemented in the models. After that, decays of short-living resonances are simulated.

12.3.1.2 Dual Parton Model

The Dual Parton Model [3] is a synthesis of the Regge theory, topological expansions of QCD $1/N_f$ or $1/N_c$ in terms of, and ideas from the parton model. The Regge theory gives the energy dependence of hadron-hadron cross sections assuming various exchanges of particles between projectile and target in the t-channel. The cross sections are in a correspondence with diagrams of $1/N$ expansion. The diagrams describe creation of unstable intermediate s-channel states – quark-gluon strings or color tubes.

The main objects of the theory are constituent quarks having masses $\sim$300–350 MeV, strings, and string junctions for baryons. It is assumed that mesons consist of a quark and an anti-quark which are coupled by color forces. The vortex lines of the field are concentrated in a small space region forming a string-like configuration. So, mesons are considered as strings with small masses.

Baryons are assumed to consist of three quarks. Two possible string configurations in baryons were considered: triangle and Mercedes star configurations [6, 7, 8, 9, 10, 11, 12]. Three strings are joined in the central point in the Mercedes star case.

Various processes are possible in baryon-antibaryon interactions. Some of them are shown in Fig. 12.1 where string junctions are presented by dashed lines. The diagram of Fig. 12.1a represents a process with string junction annihilation and creation of three strings. The diagram 12.1b describes quark-antiquark annihilation and string creation between diquark and anti-diquark. Quark-antiquark and string junctions annihilation is shown in Fig. 12.1c. At last, one string is created in the process of Fig. 12.1 e. After fragmentation of the strings, hadrons appear in the same way as in e^+e^--annihilation. One can assume that excited strings with complicated configuration are created in processes 12.1d and 12.1f. If the collision energy is sufficiently small glueballs can be formed in the process 12.1f. Mesons with constituent gluons can be created in the process 12.1d.

The pomeron exchange is responsible for 2 strings formation and diffraction dissociation (Fig. 12.1g and 12.1h). They are dominant at high energies.

In the simplest approach it is assumed that the cross sections of the processes have an energy dependence depicted in Fig. 12.1 where s is the total CMS energy squared. Calculation of cross sections of binary reactions is a rather complex procedure (see [13]) because there are interactions in initial and final states. The interactions reflect also on cross sections of other reactions [14]. As first step in order to reproduce the main properties of inelastic $\overline{\text{p}}$p-interactions we have parametrised the cross sections of Fig. 12.1 in the following form:

$$\begin{aligned}
\sigma_a &= 51.6/s^{0.5} - 58.8/s + 16.4/s^{1.5}, \\
\sigma_b &= 77.4/s^{0.5} - 88.2/s + 24.6/s^{1.5}, \\
\sigma_c &= 93/s - 106/s^{1.5} + 30/s^2, \qquad (12.1) \\
\sigma_e &= 0, \\
\sigma_g &= 18.6/s^{0.08} - 33.5/s^{0.5} + 30.8/s, \\
\sigma_h &= 0.
\end{aligned}$$

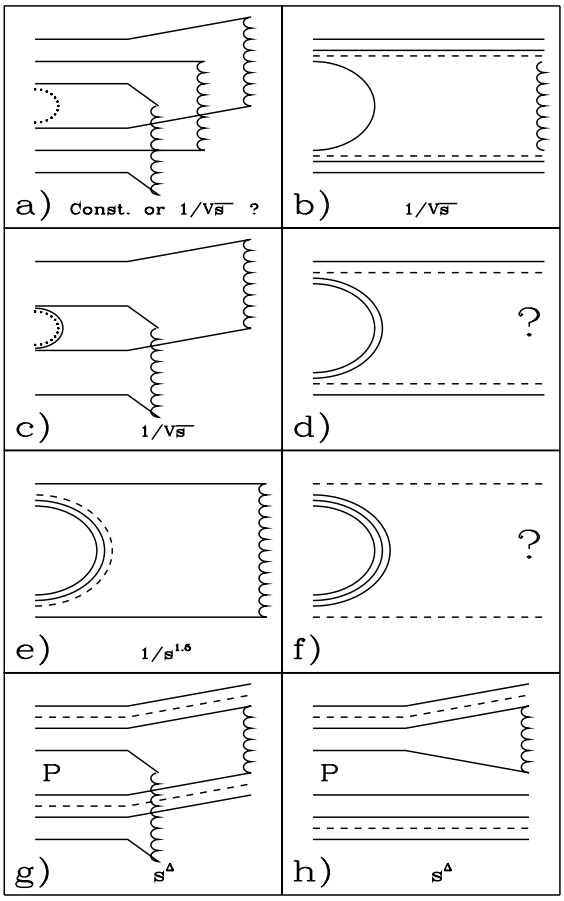

Figure 12.1: Possible processes in $\overline{\text{p}}$p-interactions.

All cross sections are given in mb. There can be another set of cross sections (see for example Refs. [15, 16]). We are going to improve the cross sections in the future.

String masses are determined by kinematic properties of quarks and anti-quarks at their ends. According to Ref. [3] we assume:

$$\begin{aligned} dW_a &\propto x_+^{-\alpha_R(0)} dx_+ \\ dW_b &\propto x_+^{-\alpha_R(0)} (1-x_+)^{-\alpha_R(0)} dx_+ \\ dW_{g,h} &\propto x_+^{-\alpha_R-(0)} (1-x_+)^{\alpha_R()-2\alpha_N(0)} dx_+ \end{aligned}$$

where x_+ is the light-cone momentum fraction of quarks, and $\alpha_R(0)$ is the intercept of the non-vacuum reggeon trajectory.

The transverse momentum distribution of quarks has been chosen in the form:

$$d^2W = B^2 e^{-Bp_T} d^2p_T, \qquad B = 4.5/\text{GeV}/c. \tag{12.2}$$

The strings fragment into hadrons. The mechanism of the fragmentation is like the one applied in the LUND model [17, 18]. Here we use a code proposed by S. Ritter [19] with fragmentation functions (hadron distributions on light-cone momentum) taken from Refs. [20, 21]. Strings with small masses are considered as hadrons, and we put them on the mass-shell.

After the string fragmentation all unstable hadrons decay. We simulate the processes with a help of the code DECAY [22].

12.3.1.3 UrQMD

The Ultra-relativistic Quantum Molecular Dynamic model (UrQMD) [4, 5] is a microscopic model based on a phase space description of nuclear reactions. It describes the phenomenology of hadronic interactions at low and intermediate energies ($\sqrt{s} < 5\,\text{GeV}$) in terms of interactions between known hadrons and their resonances. At higher energies, $\sqrt{s} > 5\,\text{GeV}$, the excitation of colour strings and their subsequent fragmentation into hadrons are taken into account in the UrQMD model. The model was proposed mainly for a description of nucleus-nucleus interactions. Note, that up to now there is no unique theoretical description of the underlying hadron–hadron interactions, with their vastly different characteristics at different incident energies and in different kinematic intervals. Perturbative quantum chromodynamics (pQCD) can be applied to describe hard processes, i.e. processes with large four-momentum transfer, Q^2. But pQCD is formally inappropriate for the description of the soft interactions because of the absence of the large Q^2-scale. Therefore, low-p_T collisions are described in terms of phenomenological models. A vast variety of models for hadronic- and nuclear collisions have been developed. The UrQMD model is the most appropriate one for the energy range of the $\overline{\text{P}}$ANDA experiment.

The model is based on the covariant propagation of all hadrons considered on the (quasi-)particle level on classical trajectories in combination with stochastic binary scattering, colour string formation and resonance decay. It represents a Monte Carlo solution of a large set of coupled partial integro-differential equations for the time evolution of the various phase space densities of particle species $i = N$, Δ , Λ, etc.. The main ingredients of the model are the cross sections of binary reactions, the two-body potentials and decay widths of resonances.

In the model, as in other Quantum Molecular Dynamics (QMD) models (see [23, 24, 25, 26]), each nucleon is represented by a coherent state of the

form ($\hbar c = 1$)

$$\phi_i(\vec{x};\vec{q}_i,\vec{p}_i,t) = \left(\frac{2}{L\pi}\right)^{3/4} \exp\left\{-\tfrac{2}{L}(\vec{x}-\vec{q}_i(t))^2 + \tfrac{1}{\hbar}\mathrm{i}\vec{p}_i(t)\vec{x}\right\} \quad (12.3)$$

which is characterized by 6 time-dependent parameters, $\vec{q}_i$ and $\vec{p}_i$, respectively. The parameter L, which is related to the extension of the wave packet in phase space, is fixed. The total n-body wave function is assumed to be the direct product of coherent states (Eq. 12.3)

$$\Phi = \prod_i \phi_i(\vec{x},\vec{q}_i,\vec{p}_i,t) \quad (12.4)$$

The equation of motion of the many-body system is calculated by means of a generalized variational principle. The Hamiltonian H of the system contains a kinetic term and mutual interactions V_{ij} ($H = \sum_i T_i + \frac{1}{2}\sum_{ij} V_{ij}$). The time evolution of the parameters is obtained by the requirement that the action is stationary under the allowed variation of the wave function. This yields an Euler-Lagrange equation for each parameter.

$$\dot{\vec{p}}_i = -\frac{\partial\langle H\rangle}{\partial\vec{q}_i} \quad \text{and} \quad \dot{\vec{q}}_i = \frac{\partial\langle H\rangle}{\partial\vec{p}_i}\,. \quad (12.5)$$

$$\dot{\vec{q}}_i = \frac{\vec{p}_i}{m} + \nabla_{\vec{p}_i}\sum_j\langle V_{ij}\rangle = \nabla_{\vec{p}_i}\langle H\rangle \quad (12.6)$$

$$\dot{\vec{p}}_i = -\nabla_{\vec{q}_i}\sum_{j\neq i}\langle V_{ij}\rangle = -\nabla_{\vec{q}_i}\langle H\rangle \quad (12.7)$$

$$\langle V_{ij}\rangle = \int d^3x_1\, d^3x_2\, \phi_i^*\phi_j^* V(x_1,x_2)\phi_i\phi_j \quad (12.8)$$

These are the time evolution equations which are solved numerically. The equations have the same structure as the classical Hamilton equations.

The interaction is based on a non-relativistic density-dependent Skyrme-type equation of state with additional Yukawa- and Coulomb potentials. Momentum dependent potentials are not used – a Pauli-potential, however, may be included optionally. The Skyrme potential consists of a sum of two- and a three-body interaction terms. The two-body term, which has a linear density-dependence models the long range attractive component of the nucleon-nucleon interaction, whereas the three-body term with its quadratic density-dependence is responsible for the short range repulsive part of the interaction. The parameters of the components are connected with the nuclear equation of state. Only the hard equation of state has been implemented into the current UrQMD model.

A projectile or target nucleus is modelled according to the Fermi-gas ansatz. The wave-function of the nucleus is defined as the product wave-function of the single nucleon Gaussians. In configuration space the centroids of the Gaussians are randomly distributed within a sphere with radius $R(A)$,

$$R(A) = r_0\left(\frac{1}{2}\left[A + \left(A^{\frac{1}{3}}-1\right)^3\right]\right)^{\frac{1}{3}}$$
$$r_0 = \left(\frac{3}{4\pi\rho_0}\right)^{\frac{1}{3}}. \quad (12.9)$$

ρ_0 is the nuclear matter ground state density used in the UrQMD model.

The phase-space density at the location of each nucleon is evaluated after its placement. If the phase-space density is too high (i.e. the respective area of the nucleus is already occupied by other nucleons), then the location of that nucleon is rejected and a new location is randomly chosen.

The initial momenta of the nucleons are randomly chosen between 0 and the local Thomas-Fermi-momentum:

$$p_F^{max} = \hbar c\left(3\pi^2\rho\right)^{\frac{1}{3}}, \quad (12.10)$$

with ρ being the corresponding local proton- or neutron-density.

A disadvantage of this type of initialization is that the initialized nuclei are not really in their ground-state with respect to the Hamiltonian used for their propagation. The parameters of the Hamiltonian were tuned to the equation of state of infinite nuclear matter and to properties of finite nuclei (such as their binding energy and their root mean square radius). If, however, the energy of the nucleons within the nucleus is minimized according to the Hamiltonian in a self-consistent fashion, then the nucleus would collapse to a single point in momentum space because the Pauli-principle has not been taken into account in the Hamiltonian. One can use a so-called Pauli-Potential [27] in the Hamiltonian. Its advantage is that the initialized nuclei remain absolutely stable whereas in the conventional initialization and propagation without the Pauli-Potential the nuclei start evaporating single nucleons after approximately 20–30 fm/c. A drawback of the potential is that the kinetic momenta of the nucleons are not any more equivalent to their canonic momenta, i.e. the nucleons carry the correct Fermi-momentum, but their velocity is zero. Furthermore, the Pauli-Potential leads to a wrong

specific heat and changes the dynamics of fragment formation.

The impact parameter of a collision is sampled according to the quadratic measure ($dW \sim bdb$). At given impact parameter, the centres of projectile and target are placed along the collision axis in such a manner that the distance between the surface of the projectile and the target is equal to 3 fm. Momenta of nucleons are transformed in the system where the projectile and target have equal velocities directed in different directions of the axis. After that the time propagation starts. During the calculation each particle is checked at the beginning of each time step whether it will collide within that time step. A collision between two hadrons will occur if $d < \sqrt{\sigma_{\text{tot}}/\pi}$, where d and σ_{tot} are the impact parameter of the hadrons and the total cross section of the two hadrons, respectively. After each binary collision or decay the outgoing particles are checked for further collisions within the respective time step.

In the UrQMD model the total cross section σ_{tot} depends on the isospins of colliding particles, their flavour and the c.m. energy. The total and elastic proton-proton and proton-neutron cross sections are well known [28]. Since their functional dependence on $\sqrt{s}$ shows a complicated shape at low energies, UrQMD uses a lookup-table for those cross sections. The neutron-neutron cross section is treated as equal to the proton-proton cross section (isospin-symmetry). In the high energy limit ($\sqrt{s} \geq 5$ GeV) the CERN/HERA parametrization for the proton-proton cross section is used [28].

Baryon resonances are produced in two different ways, namely

i) *hard production*: N+N$\rightarrow$ ΔN, $\Delta\Delta$, N*N, etc.

ii) *soft production*: π^-+p$\rightarrow$ Δ^0, K$^-$+p$\rightarrow$ Λ^* ...

The formation of s-channel resonances is fitted to measured data. Partial cross sections are used to calculate the relative weights for the different channels.

There are six channels for the excitation of non-strange resonances in the UrQMD model, namely $NN \rightarrow N\Delta_{1232}$, NN^*, $N\Delta^*$, $\Delta_{1232}\Delta_{1232}$, $\Delta_{1232}N^*$, and $\Delta_{1232}\Delta^*$. The Δ_{1232} is explicitly listed, whereas higher excitations of the Δ resonance have been denoted as Δ^*. For each of these 6 channels specific assumptions have been made with respect to the form of the matrix element, and the free parameters have been adjusted to the available experimental data.

Meson-baryon cross sections are dominated by the formation of s-channel resonances, i.e. the formation of a transient state of mass $m = \sqrt{s_{hh}}$, containing the total c.m. energy of the two incoming hadrons. On the quark level such a process implies that a quark from the baryon annihilates an antiquark from the incoming meson. Below 2.2 GeV c.m. energy intermediate resonance states get excited. At higher energies the quark-antiquark annihilation processes become less important. There, t-channel excitations of the hadrons dominate, where the exchange of mesons and Pomeron exchange determine the total cross section of the MB interaction [29].

To describe the total meson-meson reaction cross sections, the additive quark model and the principle of detailed balance, which assumes the reversibility of the particle interactions are used.

Resonance formation cross sections from the measured decay properties of the possible resonances up to c.m. energies of 2.25 GeV/c^2 for baryon resonance and 1.7 GeV/c^2 in the case of MM and MB reactions have been calculated based on the principle. Above these energies collisions are modelled by the formation of an s-channel string or, at higher energies (beginning at $\sqrt{s} = 3$ GeV), by one or two t-channel strings. In the strangeness channel elastic collisions are possible for those meson-baryon combinations which are not able to form a resonance, while the creation of t-channel strings is always possible at sufficiently large energies. At high collision energies both cross section become equal due to quark counting rules.

A parametrization proposed by Koch and Dover [30] is used in the UrQMD model for the baryon-antibaryon annihilation cross section. It is assumed that the antiproton-neutron annihilation cross section is identically to the antiproton-proton annihilation cross section.

The total and elastic proton-antiproton cross sections are treated according to the CERN/HERA parametrization:

$$\sigma(p) = \text{A} + \text{B}\,p^n + \text{C}\ln^2(p) + \text{D}\ln(p) \qquad (12.11)$$

with the laboratory-momentum p in GeV/c. The parameters are listed in [5].

For momenta $p_{lab} < 5$ GeV/c, UrQMD uses another parametrisation to obtain a good fit to the data:

$$\sigma_{\text{tot}}(p) = \begin{cases} 75.0 + 43.1p^{-1} + 2.6p^{-2} - 3.9p \\ \quad : \quad 0.3 < p < 5 \quad \text{GeV}/c \\ 271.6\exp(-1.1\,p^2) \\ \quad : \quad p < 0.3 \quad \text{GeV}/c \end{cases} \qquad (12.12)$$

$$\sigma_{\rm el} = \begin{cases} 31.6 + 18.3p^{-1} - 1.1p^{-2} - 3.8p \\ \quad : \quad 0.3 < p < 5 \quad \text{GeV}/c \\ 78.6 \\ \quad : \quad p < 0.3 \quad \text{GeV}/c \end{cases} \tag{12.13}$$

For low lab-momenta the annihilation cross section is dominant. The sum of annihilation and elastic cross section, however, is smaller than the total cross section:

$$\Delta\sigma = \sigma_{\rm tot} - \sigma_{\rm el} - \sigma_{\rm ann} \tag{12.14}$$

This difference is called "diffractive" cross section in UrQMD, $\sigma_{\rm diff} = \Delta\sigma$, and is used to excite one (or both) of the collision partners to a resonance or to a string. In the string case the same excitation scheme as for proton-proton reactions is used. For high energies the "diffractive" cross section is the dominant contribution to the total antiproton-proton cross section.

The final state of a baryon-antibaryon annihilation is generated via the formation of two meson-strings. The available c.m. energy of the reaction is distributed in equal parts to the two strings which decay in the rest frame of the reaction. On the quark level this procedure implies the annihilation of a quark-antiquark pair and the reordering of the remaining constituent quarks into newly produced hadrons (additionally taking sea-quarks into account). This model for the baryon-antibaryon annihilation thus follows the topology of a *rearrangement*-graph.

The hadron-hadron interactions at high energies are simulated in 3 stages. According to the cross sections the type of interaction is defined: elastic, inelastic, antibaryon-baryon annihilation etc.. In the case of inelastic collisions with string excitation the kinematic characteristics of strings are determined. The strings between quark and diquark (antiquark) from the same hadron are produced. The strings have the continuous mass distribution $f(M) \propto 1/M^2$ with the masses M, limited by the total collision energy $\sqrt{s}$: $M_1 + M_2 \leq \sqrt{s}$. The rest of $\sqrt{s}$ is equally distributed between the longitudinal momenta of two produced strings.

The second stage of h-h interactions is related to string fragmentation. The string break-up is treated iteratively: String $\rightarrow$ hadron + smaller string. A quark-antiquark (or a diquark-antidiquark) pair is created and placed between leading constituent quark-antiquark (or diquark-quark) pair. Then a hadron is formed randomly on one of the end-points of the string. The quark content of the hadron determines its species and charge. In case of resonances the mass is determined according to a Breit-Wigner distribution. Finally, the energy-fraction of the string which is assigned to the newly created hadron is determined: After the hadron has been stochastically assigned a transverse momentum, the fraction of longitudinal momentum transferred from the string to the hadron is determined by the fragmentation function. The conservation laws are fulfilled. The diquark is permitted to convert into mesons via the breaking of the diquark link.

This iterative fragmentation process is repeated until the remaining energy of the string gets too small for a further fragmentation.

The fragmentation function $f(x, m_t)$ represents the probability distribution for hadrons with the transverse mass m_t to acquire the longitudinal momentum fraction x from the fragmenting string. One of the most common fragmentation functions is the one used in the LUND model [31]. In UrQMD, different fragmentation functions are used for leading nucleons and newly produced particles, respectively:

$$f(x)_{\rm nuc} = \exp\left(-\frac{(x-B)^2}{2\,A^2}\right) \quad \text{for leading nucleons} \tag{12.15}$$

$$f(x)_{\rm prod} = (1-x)^2 \quad \text{for produced particles} \tag{12.16}$$

with $A = 0.275$ and $B = 0.42$. The fragmentation function $f(x)_{\rm prod}$, used for newly produced particles, is the well-known Field-Feynman fragmentation function [32, 33].

The fragmentation scheme determines the formation time of created hadrons. Although there are various possibilities (for details see Ref. [4, 5]).

After the fragmentation, decay of the resonances proceeds according to the branching ratios compiled by the Particle Data Group [34]. The resonance decay products have isotropic distributions in the rest frame of the resonance. If a resonance is among the outgoing particles, its mass must first be determined according to a Breit-Wigner mass-distribution. If the resonance decays into $N > 2$ particles, then the corresponding N-body phase space is used to calculate their N momenta stochastically.

The Pauli principle is applied to hadronic collisions or decays by blocking the final state if the outgoing phase space is occupied.

The UrQMD collision term contains 55 different baryon species (including nucleon, delta and hyperon resonances with masses up to 2.25 GeV/c^2)

and 32 different meson species (including strange meson resonances), which are supplemented by their corresponding anti-particle and all isospin-projected states. The states can either be produced in string decays, s-channel collisions or resonance decays. For excitations with higher masses than $2\,\mathrm{GeV}/c^2$ a string picture is used. Full baryon/antibaryon symmetry is included: The number of implemented baryons therefore defines the number of antibaryons in the model and the antibaryon-antibaryon interaction is defined via the baryon-baryon interaction cross sections.

Elementary cross sections are fitted to available proton-proton or pion-proton data. Isospin symmetry is used when possible in order to reduce the number of individual cross sections which have to be parameterized or tabulated.

The UrQMD model reproduces nicely various properties of hadron-hadron and nucleus-nucleus interactions.

A very important improvement of the UrQMD model was proposed in Ref. [35] where the model was coupled with the Statistical Multifragmentation (SM) Model [36]. According to the Ref. [35] the UrQMD calculation is carried out up to a time scale referred to as the transition time $t_{tr} \sim 100$fm. The position of each nucleon is then used to calculate the distribution of mass and charge numbers of pre-fragments. In determining the mass and charge numbers of the pre-fragments, the minimum spanning tree method [37] is employed, a pre-fragment is formed if the centroid distances are lower than $R_{clus} = 3\,\mathrm{fm}$. The total energy of each pre-fragment is determined in its rest frame by the Lorentz transformation. The excitation energy (e^*) of the hot pre-fragments is calculated as the difference between the binding energy of the hot pre-fragments and the binding energies of these pre-fragments in their ground state.

The ensemble of pre-fragments is characterized by excitation energy e^*, nucleon A_0, and proton Z_0, numbers. The decay of the residual nuclei is described by the SM model. The SM model assumes that a hot nucleus expands to a freeze-out volume where it splits into primary hot pre-fragments and nucleons in thermal equilibrium. Obviously, the volume is a free parameter of the model. The volume is generally defined as $V_b = (1 + k)V_0$, $k = 2$, and V_0 is the volume of A_0 nucleon system in the ground state. The breakup channels are constrained by the total mass, charge, and energy of the system. All pre-fragments (and nucleons) are considered as Boltzmann particles while Fermi gas approximation is used for their internal excitation. The probabilities of different breakup channels are calculated according to their statistical weights. After primary breakup excited pre-fragments propagate independently under mutual Coulomb field and undergo secondary decay. This secondary disintegration of large fragments ($A > 16$) is described by an evaporation model [38], for smaller fragments the Fermi breakup model [39] is used.

We use the combination of the models for estimation of neutron production in $\bar{\mathrm{p}}$-interactions with nuclear targets. We are going to improve the models parameters in the future.

12.3.1.4 PANDA event generator

A special software package was developed for the purpose to generate individual decay chains of the $\bar{\mathrm{p}}$p-annihilation. This Monte-Carlo based PANDA event generator is completely written in C++ and uses important tools of the ROOT-library and CLHEP-library, respectively. Decay channels can defined with particles which are available in the ROOT particle database. Also other particles decaying in secondaries with desired momenta can also be created. One can change the beam momentum as well as the location and smearing of the annihilation vertex. Moreover single particles such as muons, pions or photons can be generated for detailed detector resolution and acceptance studies.

12.3.2 Detector Simulation

The present PANDA simulation consists of an executable which reads setup parameters via ASCII files, implements the defined geometry of all individual detector modules, propagates particles through the detector and stores all hit informations of each sub-detector module in ROOT trees. For this purpose the code is using the GEANT4-library and is completely written with the object-oriented programming language C++. For each component of the PANDA detector classes were created which are responsible for the implementation of the corresponding passive and active volumes as defined in GEANT4.

Messenger classes read the geometry input file and steer the procedure for the implementation of the individual components of the PANDA setup. It is possible to disable and enable sub-detectors and one can also change the most important setup parameters like module sizes, materials, *etc.* without any recompilation. This allows an easy handling for the simulation of a lot of detector options and is

therefore an important tool for detector optimization studies.

Particles generated with DPM, UrQMD or $\overline{\text{P}}$ANDA event generator are propagating through the detector. The corresponding hit informations of each individual detector module getting from GEANT4 interface are stored in ROOT output files without any persistence. For this I/O the ROOT library is used.

12.3.3 Event Reconstruction

The reconstruction application reads the setup configuration and all hit information for each event via the simulation output file. Since a proper digitisation is not implemented yet the hits are smeared with the expected detector response. Through several reconstruction algorithms which are described below, these information are combined to particle energy deposits and to track candidates with PID probabilities, respectively.

12.3.3.1 Photon Reconstruction

Reconstruction Algorithm. The main detector parts for the reconstruction of photons are the EMC components in the target and forward spectrometer as well. If a photon hits the EMC it produces an electromagnetic shower which, in general, extend over several crystals. Such an area of contiguous EMC modules is called a cluster.

The available informations of position and energy deposit of each crystal hit allow a determination of the four vector of the initial photon. Most of the photon reconstruction code used in the $\overline{\text{P}}$ANDA framework is based on the particle energy deposit (PED) algorithm which was developed and successfully applied by the Crystal Barrel experiment.

The first step of this algorithm is to find a continuous area of fired crystals. In order to suppress contributions of crystal noise only modules with an energy deposit above the threshold E_{sc} are considered. The second step is to find a local maximum within this area. This requires at least one module which deposits more energy than E_{max}. All direct neighbour crystals must contain smaller energy deposits. Finally a cluster is found if the total energy is above the third threshold E_{cl}. A Cluster with only one local maximum is called a PED and is identified with a particle. In this case the corresponding energy deposition is exactly the cluster energy E_{cluster}.

If there are more than one local maximum inside the cluster the global maximum is in any case identified as a PED. An additional PED is found if the energy sum of the deposit of the local maximum crystal together with the deposits of the direct neighbour crystals E_9 has got at least 50% of the E_9-sum of the global maximum. The total energy of the cluster is then shared between the PEDs according to the relative magnitude of the E_9-sums. The jth PED is calculated in the following way:

$$E_{PED_j} = \frac{E_{j9}}{\sum_{i\,\epsilon\,PEDs} E_{i9}} \cdot E_{\text{cluster}} \quad (12.17)$$

For the reconstruction of the spatial coordinates of the PEDs each crystal is associated with a weight. The PED position with regard to the target point is calculated via the sum of all weighted crystal positions:

$$(\Theta,\Phi)_{PED} = \sum_{\text{crystals},i} \frac{w_i \cdot (\Theta,\Phi)_i}{\sum_{\text{crystals},j} w_i} \quad (12.18)$$

with:

$$w_i = max(0, 4.5 + ln(\frac{E^i_{cr}}{E_{\text{PED}}})) \quad (12.19)$$

The reason for this chosen logarithmic weight is the fact that the radial energy distribution decreases exponentially.
A PED is identified as a photon if it does not match with charged particles. This requires a minimum distance between the PED position and the position of a charged track extrapolated to the front face of the EMC.

Crystal Resolution. As explained before the hit information getting from the simulation output are smeared with reasonable detector responses within the reconstruction application. For the EMC target spectrometer two different crystal materials, PWO and BGO respectively, are under discussion and investigated. Since the crystal resolution depends on the material and, in general, on the operation temperature rough estimates are used which are listed in Table 12.1. The smearing is done with a Gaussian distribution for the electronic noise and with a Poisson distribution which considers the statistical fluctuations of the number of photoelectrons reached the APDs.
For the EMC forward part two different detector options, the KOPIO-LEDA setup and the EMC part of the MIRAC calorimeter, are under investigation. The same resolution mentioned in Sec. 8.11 for KOPIO-LEDA and in Sec. 8.12.1 for the MIRAC version are used.

Material	Temperature [°C]	σ_{noise} [MeV/c^2]	p.e./MeV/c^2
PWO	-25	1.3	50
BGO	20	0.4	150

Table 12.1: Energy resolution used for the materials PWO and BGO crystals.

Reconstruction Thresholds. For detailed studies of the EMC target spectrometer the reconstruction processes are performed by using different thresholds. Since the crystal noise depends on the material reasonable values for BGO and PWO are used. Table 12.2 summarises the applied thresholds for this EMC part as well as for the EMC setup of the forward spectrometer as well.

Leakage Correction. Because of shower leakages in particular inside the crystal gaps the reconstructed energy differs from the real photon energy. An energy correction function depending on the Θ-angle and the energy is necessary. The following parametrisation is used:

$$\begin{aligned} E_\gamma &= E_{PED} \cdot exp(c_1(\Theta_i) \\ &+ c_2(\Theta_i) \cdot ln(E_{PED}) \\ &+ c_3(\Theta_i) \cdot ln^2(E_{PED}) \\ &+ c_4(\Theta_i) \cdot ln^3(E_{PED})) \end{aligned} \quad (12.20)$$

with: Θ_i = ring index of the EMC setup.
The determination of these parameters was done by Monte Carlo studies. For this purpose single particles decaying in two photons were generated homogeneously in space and momentum range between 0–6 GeV/c. With the minimisation tool MINUIT the parameters were varied until the least square between the invariant mass of the two reconstructed photons and nominal mass of the generated particle is reached.
Fig. 12.2 shows the result for the ring parameters $c_1(\Theta_i)$. The huge correction values getting in the ending regions of the barrel (index around -22 = overlap region with end cap; index around 30 = overlap region with forward wall) are an indication for an extremely high shower leakage.

Misidentifications. In some cases the number of reconstructed photons does not correspond with the real photon multiplicity. One reason is that the $\overline{\text{P}}$ANDA detector does not cover the complete solid-angle of 4π so that not all photons can be detected. The other reason is that the described reconstruction method can result in the following mis-identifications:

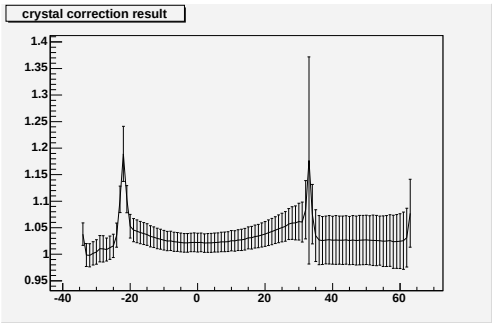

Figure 12.2: This example for the setup with constant crystal length and BGO crystals shows the fitted result for the parameter c_1.

- The photon hits in the EMC produce electromagnetic showers which do not always proceed in a geometrically regular way. It is possible that statistical fluctuations can also generate local maxima. Such secondary local maxima are called *electromagnetic splitt-offs* and may be misidentified as photons. Detailed studies done by the Crystal Barrel experiment show that the number of splitt-offs increases dramatically by decreased splitt-off energies. In order to get rid of most of these mis-identifications the settings of the reconstruction thresholds plays an important role.

- The interaction of hadrons, usually charged pions and kaons, hitting the EMC can result in so called *hadronic splitt-offs* produced by secondary particles.

- For high momentum π^0's decaying in two photons it is possible that only one PED-cluster appears. The reason is that the opening angle of the two photons is getting smaller by increased π^0 momenta in the laboratory frame. If the opening angle is too small in comparison to the crystal granularity of the EMC setup only one misidentified photon is reconstructed.

- Some primary photons do not reach the crystal calorimeter since they interact already with other detectors located in front of the EMC.

EMC part	Setup	Material	E_{cl} [MeV/c^2]	E_{max} [MeV/c^2]	E_{cluster} [MeV/c^2]
TS	see	BGO	3	15	20
	section		3	15	30
	13.2		3	15	50
		PWO	5	20	25
			10	35	50
FS	KOPIO-LEDA	lead/scint.-leadglass	10	20	20
	MIRAC	lead/scintillator	20	40	40

Table 12.2: Reconstruction thresholds for different setups and materials.

Especially pre-showers from DIRC and RICH may produce untidy clusters.

Outlook: Possible Improvements A simple solution to get rid of most of electromagnetic split-offs is a usage of photon reconstruction thresholds above approximately $50 MeV/c^2$. The disadvantage of this approach is that also low energetic photons get lost, and some gools of the PANDA physics program are not reachable. Therefore elaborated split-off recognition tools are needed and have to be developed. Crystal Barrel for example already developed and used successfully such tools based on a artificial neuronal networks [40].

For more detailed studies of channels with charged particles hadronic split-off recognition [41] has to be provided.

In addition the identification and proper reconstruction of DIRC pre-showers should yield in a better reconstruction performance.

12.3.3.2 Reconstruction of Charged Particles

Tracking in the Target Spectrometer The track recognition and reconstruction is based on the information from all tracking devices inside the target spectrometer: Micro-Vertex Detector (MVD), Straw Tube Tracker (STT) or Time Projection Chamber (TPC) and Mini-Drift Chambers (MDC). Their setups are described in chapters 5 and 6.

The whole process of the track reconstruction can be split in two stages: *track finding* and *track fitting*.

Track finding. The present track finder for charged tracks in the target spectrometer (TS) is very simple and based on assigning the hits to the tracks, using the Monte Carlo truth information. Because of that an efficiency of such a track finder is 100%. To make it more reasonable 5% of the STT hits are randomly rejected. Of course, such solution was accepted only on temporary basis. A track finder, based on the Hough[42] or Kalman[43] algorithm will be developed in the future.

Track fitting. At present time, in the simulation, the magnetic field in the target spectrometer is assumes to be a constant. It means, that in first approximation, a particle trajectory is considered as a cylindrical helix with the constant radius along the z-axis. This helix parametrization uses 5 parameters:

$$\begin{aligned} x &= (D_0 + qR)[-\sin(\phi) + \sin(\phi_0)] \\ y &= (D_0 + qR)[\cos(\phi) - \cos(\phi_0)] \\ z &= Z_0 - qR(\phi - \phi_0)\cot(\theta) \end{aligned}$$

where D_0 is the distance of the closest approach of the helix to the straight line going through the track origin, parallel to the beam axis, Z_0 is z-coordinate of the helix in the closest approach point to the track origin, ϕ_0 is the azimuthal angle of the helix tangent in the closest approach point to the track origin, R is the helix radius, θ is the polar angle of the helix and q is a sign of the particle.

Than track fit is performed by the MINUIT package using the five aforementioned parameters to estimate χ^2 between hit positions and the fitted helix. To get the correct χ^2 value the distance of the closest approach between the hit and the helix is normalized by the correspondent sub-detector resolution. One should notice that multiple scattering in the MVD is taken into account by reducing the weight of the measuring points by adding to the measurement precision a momentum and polar angle dependent contribution. At present, the energy loss in the detector elements is not taken into account at all.

In principle, the starting values for the helix fit should be taken from the track finder, but since the track finder is based now on the Monte Carlo truth information, they are also taken from there.

In case of the Time Projection Chamber the global χ^2 fitter is not an ideal option because the algorithm has to loop several times over a huge amount of data. (The TPC produces in the order of thousand

data points per track.) For the complete TPC data this approach would not have been feasible with the available resources. To be able to run the TPC in the given computing framework only 2% of the hits of each track have been used for the track-fit. This of course will not exploit the possible resolution potential of this detector!

Tracking Efficiency. The tracking efficiency depends on the angular distribution and momentum of decay products. On average it is rather high, in spite of the simplicity of the track fitter, for example, for the reaction $D^* \rightarrow D^0\pi \rightarrow K\pi\pi$ the efficiency is about 95%.

Outlook: Future Improvements. In the near future the existing "track finder" should be replaced with the real one. Also the existing simple tracking algorithm should be replaced or modified using ideas, like Kalman filtering[44] and [45], which include the multiple scattering and the energy losses in the natural way and can also be used on huge data samples (as in the TPC case) with good performance.

Tracking in the Forward Spectrometer. Reconstruction algorithm. The dipole of the forward spectrometer is simulated with an idealized magnetic field of 1.5 Tm perpendicular to the beam axis (y-axis). Charged particles passing this field are deflected in the xz-plain on an orbit. The radius of this orbit is completely defined by the charge and the p_{xz}-momentum of the particle and by the constant magnetic field, respectively.

Because of very low manpower in the computing group a simple tracking reconstruction is implemented which is only based on the hit information from the two MDCs in front and the two MDCs behind the dipole (see 13.2.2). In the first step of the reconstruction all fired wires within the drift chambers are combined to hit points defined by the three pairs of inclined wires. Then all possible combinations of one hit in each chamber are considered to find track candidates. Such a candidate is found if the four hit entries are nearby not deflected in the y-direction. With two hit points in front and behind the dipole the track positions entering and exiting the magnetic field are extrapolated. Also the corresponding tangents of the possible track orbit are available. With this information the calculation of the radius in the xz-plain of the track candidate is overdetermined. This allows the determination of the p_{xz}-momentum in two different ways and results in an improved momentum resolution. Finally the track will be extrapolated to the target location. With the rough determination of the helix track within the solenoid fields of the target spectrometer one gets also the initial direction and momentum of the particle. **Efficiency and resolution.** For these studies single muons with total momentum of 1 GeV/c were generated homogeneously in the forward region between $\Theta = 1^\circ - 5^\circ$. With the algorithm described above a reconstruction efficiency of about 99% and a σ-resolution of the total momentum of 1.1% are reached. In case of three generated muons within this solid angle (μ-momenta: 0.9 GeV/c, 1.3 GeV/c and 1.7 GeV/c) the reconstruction efficiency drops to 88.8%.

Outlook: Future Improvements. To take all information in consideration it is necessary to get rid of the separation between the tracking reconstruction of the target spectrometer and the simple tracking reconstruction of the forward spectrometer. Also an improvement of efficiency and resolution is expected by using the Kalman filter [44] and [45].

12.3.3.3 Particle Identification

The main sub-detectors for the reconstruction of charged particles are the ring imaging Cherenkov counters and the muon detectors. While the Cherenkov counters positively identify kaons and protons and the muon counters the muons, the pions are the remaining unidentified particles. A positive identification of pions within the Cherenkov counters is only possible in a restricted way.
The TPC tracker can also provide particle identification especially at low momenta where the Cherenkov counters are not efficient any more. The details of this method which is also implemented in the reconstruction software are described in Sec. 6.5.7.

DIRC Reconstruction. A charged particle travelling with a velocity faster than the speed of light in the radiator slabs emits Cherenkov photons with a certain relative angle to the particle's trajectory. The photons are transported towards one end of the radiator slab consisting of fused quartz by internal reflections and by a mirror on the other end of the slab. Since all neighbouring surfaces where this reflections occur are perpendicular to each other, the geometric properties of the Cherenkov cone is preserved in a four-fold symmetry. Depending where the last reflection occurred, a photon with a certain direction can leave a slab

with directions up, down, left, or right. In the simulation, the positions of the hit photon detectors and the knowledge of the hit slab from the tracking devices yield the directions of the photons leaving the slab. Reflecting the photon directions in one quadrant of the photons momentum space produce a unique pattern independent on the last reflection.

We use in the simulation the DIRC setup as described in 7.2.1. Realistic optical properties of the radiator slabs are taken into account. The number of photons was generated depending on their wavelength with a $1/\lambda^2$ probability. An exponential absorption length of 10 m for the photons in the bulk and an internal reflection probability of 0.9999 at the radiator surface were taken. The quality of the surface was simulated by changing the direction of the photon after each refection by 0.005 mrad from the ideal reflection. Photons closer than 50 μm to an edge were absorbed, in order to describe the quality of the edges. Dispersion is not taken into account, however only photons with a wavelength $\lambda > 300$ nm are recorded by the photomultiplier array with an efficiency of 20%.

In the reconstruction four hypotheses of the particle being an electron, muon, kaon, or proton are tested. Knowing the momentum of the particle from tracking and the mass from the hypothesis, allows to generate a Cherenkov cone of photons, which directions are also reflected in one quadrant, and allows to compute the χ^2. Here, a minimum of five photons in the photon detector is required, in order to get enough information from the Cherenkov cone. For the sake of simplicity, each particle is treated separately and neglects, therefore, effects of overlapping Cherenkov images from double hits. Since the DIRC detector itself has no information which slab is hit where, each particle from the tracking detectors is combined with the hits of the DIRC. The combination with the lowest χ^2 is later on taken and the χ^2 for the different hypotheses stored. The χ^2-distributions per degree of freedom of right identified particles are not centred around one and have to be rescaled. After that, the correlation of χ^2 and the probability of the particle being e.g. a kaon allows in the kaon selector to treat all particles with a probability higher than a certain threshold as reconstructed kaons.

RICH Reconstruction. In forward direction between angles of 5–10° and 22° a RICH detector performs the particle identification. Contrary to the various setup options described in 7.3.1, we use in the simulation a simplified setup. A radiator consisting of 4 cm of C_6F_{14} generates Cherenkov photons which are measured in a photon detector plane at a distance of 10 cm.

The number of photons was generated depending on their wavelength with a $1/\lambda^2$ probability. A bulk transmission probability of

$$p = p_0 \exp\left[\frac{-L}{(C(\lambda/400)^4)}\right] \tag{12.21}$$

was used, with L the path length of the photon and an absorption length of $C = 10$ m. The transmission coefficient p_0 was assumed to be 1.

The reconstruction is performed similar to the DIRC, however a reflection in one quadrant of the momentum space of the photons is not necessary. With the information from the tracking detectors and with the help of five particle hypotheses, a χ^2 test with the photon directions of the particle and the photon directions generated with above assumptions is performed. After rescaling of the χ^2 distributions per degree of freedom to make them centred around one, all particles with probabilities of being e.g. a kaon above a certain threshold, are treated as kaons.

Muon Reconstruction. In the simulation the muon counters of the target and forward spectrometer were used. Their setup is described in 7.4.2. All charged particles which penetrate the iron yoke and hit the muon-scintillator strips are treated as muons. However, they have to be distinguished from secondary charged particles which are generated within the material in front of the muon counters: the strips are read out from both sides by photomultipliers. Their hit position is determined by the time difference of the photons hitting both photon detectors, and the time resolution of the photomultipliers were assumed to be $\tau = 0.5$ ns. The difference between the muon position from the tracking detectors and the measured position were used to perform a χ^2 test and to compute the probability of the particle to be a muon and not a secondary particle created in the iron yoke. Particles with probabilities to be muons larger than an adjustable threshold were then taken for the reconstruction.

12.3.4 Analysis Tools

The analysis programming code is based on the concept used by the BaBar experiment. For each event the informations of the reconstruction output are combined to particle candidates such as kaons, pions or photons and are stored in corresponded particle lists. For the identification of complete decay chains selector applications can be developed

with the possibility to get access to the candidate lists and to extract all important informations such as number of particles, total event energy or four vectors of each particle. One can combine particle candidates to mother particles and can also calculate secondary vertices via vertex refitting routines. The I/O control as well as the settings of cut parameters for the selection are specified by tcl-scripts. This allows the modification of tcl-files without any recompilation of the analysis code.

12.4 Computing Model

12.4.1 Current Model

In the current $\overline{\text{P}}$ANDA computing model several points are missing which are mandatory for large scale Monte Carlo productions or running a real experiment. Therefore the computing group will start to implement a new computing model in January 2005. Due to limited person power a heavy reuse of components of the BaBar offline software is planned, and concepts of the BaBar computing model will be adapted as a starting point for the next $\overline{\text{P}}$ANDA computing model.

Currently $\overline{\text{P}}$ANDA computing provides a GEANT4 based Monte Carlo application, an application that does the event digitization and reconstruction, and a number of analysis applications adapted to the needs of the various benchmark channels. For the I/O ROOT files are used; object relations don't get persisted. Because the applications are not based on a common framework, it is not possible to make an applications that combines simulation and reconstruction, and after each step all objects have to be stored. This yields to a relatively large amount of needed storage capacity.

All output files are stored in a directory tree on file servers in Bochum and Glasgow. Applications can read data from this simple event store via the rootd protocol, or for production runs the files get copied to the site that provides the computing resources for a higher performance multiple access. Because $\overline{\text{P}}$ANDA does not possess the necessary storage capacities at the main production sites GridKA and GSI, the bandwidth of the network file access limits the achievable MC production rate.

The physics analysis code as well as the event reconstruction make heavy use of the ROOT tool kit, and it is possible to access all data interactively.

12.4.2 Proposed Model

To run an experiment of a complexity like $\overline{\text{P}}$ANDA, more computing power and more data storage capacity is needed than a single laboratory or computer center can provide. Resources in different countries on different continents have to be used in parallel. The experiences of running experiments like BaBar, Belle, COMPASS or DØ have shown, that distributed computing is necessary and feasible at all stages of the event processing, like event reconstruction, Monte Carlo production or physics analysis. While the currently running experiments

are following more conventional approaches, the LHC experiments decided to contribute to the development and implementation of the GRID, and to use the GRID technologies to run a distributed offline computing in an effective manner. Though the today available GRID implementations did not reach the reliability and completeness which are needed to run the event processing of an experiment like $\overline{\text{P}}$ANDA in production mode, this situation will change in the next years. Therefore it seems to be the natural solution for $\overline{\text{P}}$ANDA computing to make use of the GRID implementation which will be the standard in HEP computing when the data production environment for the first $\overline{\text{P}}$ANDA data challenges gets set up around 2007.

It is common use in HEP computing to structure the event data in components of different levels of detail. The proposed event components are

- Simulation data (SIM): The result of the particle tracking in the simulation.
- Raw data (RAW): The output of the DAQ and of the digitization step of the MC simulation.
- Reconstructed data (RECO): The result of the event reconstruction that contains all reconstruction objects like detector hits, calorimeter clusters, fitted particle tracks, *etc.*.
- Event Summary Data (ESD): A subset of the reco data that contains all objects which are needed in physics analysis, and in addition all objects necessary for track refitting, detector alignment and calibration studies, *etc.*.
- Analysis Object Data (AOD): All objects that are needed for physics analysis, like particle candidates, vertex information, error matrices, *etc.*.
- MC Truth data (TRU): For simulated data this component holds the Monte Carlo truth information that is associated with analysis objects.

The DAQ will produce raw data events of 8 kB at a rate of $25 \cdot 10^3 s^{-1}$, what corresponds to $2.16 \cdot 10^9$ events/day. To decouple data taking and event processing a disk buffer of 53 TB is needed. This ensures that the data taking can continue for three days though the event processing system is down. To archive the raw data for future reprocessings a tape storage system has to be foreseen that is able to write 20 TB/day.

The raw data will be used for a fast monitoring and quality assurance (QA), running on ≈ 20 processors. In the first step of the event processing calibration constants have to be deduced. The number of events needed to calculate calibration constants with the necessary accuracy does not scale with luminosity. Therefore it should be sufficient to run the calibration on a subset of the events on a small processor farm of about 48 CPUs. The calibration data are written to a (relational) database, from where they can be accessed in the subsequent processing stages.

For an event reconstruction that can keep track with incoming data and that takes 1 s CPU time on a today's CPU, about 625 CPUs are necessary if Moore's law is still valid in 2012.

The output of the event reconstruction are the RECO, AOD, and ESD event components. Running experiments have shown that it is sufficient to persist the AOD and ESD data in the bulk data production. RECO data objects are needed just in detector studies for small subsets of the events. The table shows estimations for the sizes of the event components.

component	size [kB/event]
RAW	8
SIM	200
RECO	60
ESD	6
AOD	3
TRU	10

Additional computing power is needed for the reprocessing of all accumulated data once a year. If $\overline{\text{P}}$ANDA will take data 6 months per year, the extra resources are of the same amount per year as for the the initial processing. If these CPUs are distributed over 5 computing sites, this goal can be reached with CPU farms of a still manageable size.

A large part of the computing power will go to physics analysis. Experiences in running experiments show that at least 1 000 CPUs will be necessary when analysis is running in the various fields of $\overline{\text{P}}$ANDA physics. In the GRID approach users do not have to login at computer centers where computing resources and the necessary input data are available, but they run their analysis jobs from any desktop computer or from a laptop. The GRID takes care that the jobs will run at a place where they get all necessary resources. Therefore for physics analysis it is not necessary to build up clusters of login server, but to provide computing and storage elements for the GRID at the contributing computing centers and institutes.

For physics analysis a number of MC events that is

larger than the number of corresponding real events are needed. Therefore and because a detailed detector simulation always needs a lot of computing time, the MC production needs more computing power than the event processing. Taking into account PANDA's runtime duty cycle, 1 000 CPUs distributed over all collaborating institutes may be adequate.

Today ROOT I/O is the persistence technology commonly used in HEP computing. This may change at some point in the future, but the actual developments of the PANDA event store will be ROOT based. A clear separation of transient and persistent objects in the PANDA software will allow a change of the persistence technology.

When the GRID will reach production status it will provide a file catalogue whose functionality can be used to build an event store. By then an event store like the BaBar event store without central file catalogue based on xrootd and ROOT I/O will be used.

The storage capacity needed for the event data of one year of data taking plus the corresponding MC data up to the ESD component adds up to $14 + 30 = 44$ PB. This storage capacity has to be provided by the contributing computing centers as a tape background storage with a large disk buffer. For performance reasons it may be necessary to have more than one disk copy of the data that will be accessed by a large number of physics analysis jobs in parallel. A disk storage of 20 PB/year may be adequate.

Data from older reprocessings have to be stored just on tape. For this additional 100 PB of tape storage are needed.

12.5 GRID Computing

12.5.1 Introduction

From a computing resources standpoint, hadron physics experiments such as PANDA, with a projected acquisition rate of several PB/year, have similar requirements to large scale high energy physics projects, both in terms of data acquisition rate and size of data files. Such an amount of data requires a huge reconstruction effort and large scale simulations during the running of the experiment. Even during the detector design stage (where we now stand), there are advantages in adopting an HEP model of distributing computing. PANDA will have heavily distributed processing and event storage, with 50 participating institutions and more than 300 collaborating physicists. Hence, the amount of data also poses logistical problems with regard to:

- consistent distributed data cooking[1];
- locating the optimal site for analysis code execution;
- avoiding duplicate analyses;
- locating inputs and outputs of the analysis code;
- organizing (partial/final) results;
- maintaining a file catalogue.

This functionality must be provided while users are shielded from the GRID machinery by sophisticated user interfaces.

12.5.2 Framework

The PANDA GRID is built upon the AliEn [46] software written by the ALICE collaboration at CERN, and which is the base of the new EGEE gLite [47] framework. AliEn was adopted by PANDA before the EGEE initiative was launched in 2003. AliEn (which stands for **Ali**ce **En**vironment) was build on top of available public domain and open source components and standards, aiming to remain operational even if underlying technologies change.

AliEn uses SASL/OpenSSL/OpenCA as authentication protocols. Additionally, it can use Globus/GSS for authentication compatible with other Grid projects. CONDOR ClassAds language

1. cooking means processing of the raw data and obtaining higher-level information such as 4-vectors and PID

is used for job description (although $\overline{\text{P}}$ANDA has now a slightly modified implementation of this) and OpenLDAP for configuration management. Apache provides a Web Portal user interface while MySQL is used as relational database backend. AliEn is 99% open source with more than 90% of the AliEn software package is written in perl [48] which enormously simplifies development and bug fixes.

Summary of $\overline{\text{P}}$ANDA GRID features:

- Authentication module - supports several authentication methods
- Distributed file catalogue - with user interface that mimics a UNIX file system
- Secure file transport and replication services
- Task/Transfer queues - managed by a resource broker
- Site resources organized using computing and storage elements (referred to herein as CE and SE)
- Metadata catalogue
- C/C++/perl APIs
- Very descriptive and easy to use web portal interface [49] besides the text-only command interface

Although a full evaluation of our GRID framework will be possible only at full scale production - first data challenge in 2007 - we have already achieved very promising results.

12.5.3 Current Status

As of December 2004, $\overline{\text{P}}$ANDA GRID has five sites more or less running. The Glasgow site is the most advanced - it contains the server, database, CE and SE - and the NPE group is the most knowledgeable in GRID usage. The $\overline{\text{P}}$ANDA GRID has already been employed locally to run tens of thousands (more than 25 000 run as of December 2004) of simulation and data analysis jobs besides tests of actual $\overline{\text{P}}$ANDA design simulation jobs.

A large amount of software development effort has been put in already. The original CERN AliEn package has been modified in accordance with the needs and constraints of the $\overline{\text{P}}$ANDA collaboration.

12.5.3.1 $\overline{\text{P}}$ANDA GRID Sites

The GRID is composed of one (or few [2]) central server(s) and a set of remote computing clusters that we will call herein *sites*. In general, the sites can be identified geographically with the participating member institutions.

The $\overline{\text{P}}$ANDA GRID sites as of December 2004 are listed in Table 12.3.

12.5.4 Future Development

Future evolution of the $\overline{\text{P}}$ANDA grid can be envisioned as development of tailored code within the collaboration, while keeping informed of progress within other GRID frameworks. Even if EGEE were to provide ready-to-use tools for GRID computing, and our collaboration were to decide to switch to the new software once it proves itself reliable, continual development of the present $\overline{\text{P}}$ANDA GRID framework is important for two reasons:

1. Anything that EGEE will provide has at its core the same software as $\overline{\text{P}}$ANDA GRID; being able to develop the code will ensure that the group will have the necessary expertise if gLite were to need customization or new features implemented
2. GRID computing is a different approach to running large scale computations compared to more traditional cluster computing. Familiarising users and simulation/analysis code developers with the GRID philosophy and features and basically is crucial

New features can and most likely will be implemented as the $\overline{\text{P}}$ANDA project evolves. Manpower for code development should be allocated.

12.5.4.1 Manpower

The are the two aspects of the GRID computing effort: development and maintenance. Maintenance will require part-time work from the site administrators (probably not more than 10% person/year) and will imply tasks like: package upgrades, fixes after site-specific OS upgrades, job environment and package dependencies set up, batch queue set up and occasionally rebooting nodes.

On the other hand, development would require a more dedicated effort. Our experience with AliEn

2. for example MySQL database and job control can run on separate servers if necessary

Site	CPUs	Linux Flavor	Storage [GB]	Installation Status
Glasgow	50	RH9	500	Done
GSI	60	Debian	50	In progress
Bochum	2	SuSe	1 000	Done
Frascati	2	RH9	50	Needs updates
FZK	200	Scientific		In progress
Gießen		SuSe		Started

Table 12.3: Grid sites status as of December 2004.

tells us that GRID software will not work out-of-the-box and is most likely better tailored for HEP purposes than for our particular needs and constraints. Hence it might be necessary to modify the GRID code and tailor for $\overline{\text{P}}$ANDA, adding features or simplifying protocols. Dedicated manpower needs to be assigned to this task since code development within $\overline{\text{P}}$ANDA can bring many obvious advantages.

What must also be considered is the more mundane, but nonetheless important tasks such as:

- installing and configuring packages on new sites;
- initial training of local GRID administrators;
- administering the substructure of computer clusters on the sites.

We estimate that a core group of three or four persons (working 50% person-year) would be enough for the code development described above. However, there will be a permanent need of (probably 10% person-year) administrators for every site.

References

[1] S. Agostinelli et al., Nucl. Instrum. Meth. **A506**, 250 (2003).

[2] F. James, CERN Program Library W505 (1970).

[3] A. Capella, U. Sukhatme, C.-I. Tan, and J. Tran Thanh Van, Phys. Rept. **236**, 225 (1994).

[4] M. Bleicher et al., J. Phys. **G25**, 1859 (1999).

[5] S. A. Bass et al., Prog. Part. Nucl. Phys. **41**, 225 (1998).

[6] X. Artru, Nucl. Phys. **B85**, 442 (1975).

[7] G. C. Rossi and G. Veneziano, Nucl. Phys. **B123**, 507 (1977).

[8] L. Montanet, G. C. Rossi, and G. Veneziano, Phys. Rept. **63**, 149 (1980).

[9] T. T. Takahashi, H. Matsufuru, Y. Nemoto, and H. Suganuma, Phys. Rev. Lett. **86**, 18 (2001).

[10] G. S. Bali, Phys. Rept. **343**, 1 (2001).

[11] D. S. Kuzmenko and Y. A. Simonov, Phys. Atom. Nucl. **64**, 107 (2001).

[12] D. S. Kuzmenko and Y. A. Simonov, Phys. Atom. Nucl. **66**, 950 (2003).

[13] A. B. Kaidalov and P. E. Volkovitsky, Z. Phys. **C63**, 517 (1994).

[14] V. V. Uzhinsky and A. S. Galoyan, hep-ph/0212369 (2002).

[15] N. S. Amelin and L. V. Bravina, Sov. J. Nucl. Phys. **51**, 133 (1990).

[16] N. S. Amelin, L. V. Bravina, L. I. Sarycheva, and L. N. Smirnova, Sov. J. Nucl. Phys. **51**, 535 (1990).

[17] B. Andersson, G. Gustafson, and C. Peterson, Zeit. Phys. **C1**, 105 (1979).

[18] B. Andersson, G. Gustafson, and T. Sjostrand, Zeit. Phys. **C6**, 235 (1980).

[19] S. Ritter, Comput. Phys. Commun. **31**, 393 (1984).

[20] A. B. Kaidalov, Yad. Fiz. **45**, 1452 (1987).

[21] A. B. Kaidalov and O. I. Piskunova, Z. Phys. **C30**, 145 (1986).

[22] K. Hanssgen and S. Ritter, Comput. Phys. Commun. **31**, 411 (1984).

[23] J. Aichelin, Phys. Rept. **202**, 233 (1991).

[24] J. Aichelin, A. Rosenhauer, G. Peilert, H. Stocker, and W. Greiner, Phys. Rev. Lett. **58**, 1926 (1987).

[25] J. Aichelin and H. Stocker, Phys. Lett. **B176**, 14 (1986).

[26] G. Peilert et al., Phys. Rev. **C39**, 1402 (1989).

[27] L. Wilets, E. Henley, M. Kraft, and A. McKellar, Nucl. Phys. **A282**, 341 (1977).

[28] R. M. Barnett et al., Phys. Rev. **D54**, 1 (1996).

[29] A. Donnachie and P. V. Landshoff, Phys. Lett. **B296**, 227 (1992).

[30] P. Koch, B. Muller, and J. Rafelski, Phys. Rept. **142**, 167 (1986).

[31] B. Andersson, G. Gustafson, and B. Soderberg, Z. Phys. **C20**, 317 (1983).

[32] R. Field and R. P. Feynman, Phys. Rev. **D15**, 2590 (1977).

[33] R. Field and R. Feynman, Nucl. Phys. **B136**, 1 (1978).

[34] S. Eidelman et al., Phys. Lett. **B592**, 1+ (2004), http://pdg.lbl.gov.

[35] K. Abdel-Waged, Phys. Rev. **C67**, 064610 (2003).

[36] J. P. Bondorf, A. S. Botvina, A. S. Ilinov, I. N. Mishustin, and K. Sneppen, Phys. Rept. **257**, 133 (1995).

[37] C. Hartnack et al., Eur. Phys. J. **A1**, 151 (1998).

[38] V. F. Weisskopf, Phys. Rev. **52**, 295 (1937).

[39] E. Fermi, Prog. Theor. Phys. **5**, 570 (1950).

[40] T. F. Degener, *A Feed Forward Neuronal Network for Recognition of Fluctuations in Electromagnetic Showers*, New Computing Techniques in Physics Research III, World Scientific, Singapure (1994).

[41] M. B. et al., *Split-Off recognition in data with charged tracks. The TAXI logics*, Crystal Barrel Internal Note 280, unpublished.

[42] T. Burghardt, Circle Detection in Images, http://www.cs.bris.ac.uk/home/burghard/ImageProcessingReport.pdf.

[43] P. Billoir and S. Qian, Nucl. Instrum. Meth. **A294**, 219 (1990).

[44] R. Djilkibaev and R. Konoplich, (2003).

[45] R. Frühwirt, Nucl. Instrum. Meth. **A262**, 444 (1987).

[46] AliEn CERN Website, http://alien.cern.ch/.

[47] EGEE gLite Project Website, http://glite.web.cern.ch/glite/.

[48] L. Wall, T. Christiansen, and J. Orwant, *Programming Perl, 3rd Edition*, O'Reilly, 2000.

[49] PANDA GRID Web Portal, http://panda.physics.gla.ac.uk/.

13 Monte Carlo Simulation Results

13.1 Introduction

The main purpose of the following Monte Carlo studies is to demonstrate if the proposed detector setups can fulfil the discussed physics cases. Furthermore acceptance, resolution, and background rejection power have been estimated. Comparisons between some detector configurations should give a rough indication for an optimal detector design. Studies of several benchmark channels are presented which either covering the most relevant physical topics or allow a comparison with well known results getting from other experiments.

All benchmark results are based on studies without the use of kinematic fitting routines. Such routines will improve efficiencies and resolutions and require a precision knowledge of spatial and energy resolution of all reconstructed particles obtained from the informations of individual sub-detectors or detector combinations. Since several different detector options are under investigation it was not possible so far to determine the detector resolutions for each option.

It is also important to keep in mind that there is a lot of space for improvements of photon reconstruction, tracking reconstruction and fitting as well as particle identification. Therefore the comparison between the different detector options has to be taken with a grain of salt.

Before the results of the benchmark channels are presented the simulated detector configurations and the procedure of the mass production will be described in detail.

13.2 Simulated Detector Setups

The overall detector setup implemented in the simulation is based on the conceptional design already discussed in the chapters before. Since alternative scenarios for many sub-detectors are under discussion it is not possible to take all options into account. The simulation studies are concentrating on the most favourite designs. Since the mechanical designs of the sub-detectors are in progress and modifications as well as improvements are regularly necessary the simulated detector setup is not completely in agreement with the detector descriptions in the chapters before. Therefore a brief discussion about the simulated detector setups will follow.

13.2.1 Target Spectrometer

13.2.1.1 Target

Only the target pipe is implemented into the simulation. The most realistic scenario for the pellet target is used with an aluminium-beryllium alloy (30% of aluminium) and a minimum wall thickness of 0.2 mm. The upper part as well as the lower part of the pipe is divided in several different cones with a radius variation between 0.95 cm and 2.5 cm. The position resolution of the pellets and of the beam as well can be considered with the event generators by smearing the annihilation vertex.

13.2.1.2 MVD

The version which is already discussed in Sec. 5.5 is used. It consists of a barrel section with five layers of silicon pixel sensors (pixel size $(50 \times 300)\,\mu m^2$) and five forward disk structures (pixel size $(100 \times 150)\,\mu m^2$). However, neither readout components and cables nor support structures are implemented.

13.2.1.3 STT

Also this sub-detector is fully in agreement with the description of Sec. 6.4.1. 11 double layers of straws are placed at radial distances between 15 cm and 42 cm to the beam axis. The overall length is 150 cm.

13.2.1.4 TPC

This alternative tracking device is also integrated into the simulation with the same setup as described in Sec. 6.5. One can switch between the STT and the TPC without any re-compilation of the simulation and reconstruction code. The comparison between these two tracking devices should allow a rough assessment of the quality of reconstruction and identification of charged particles.

13.2.1.5 MDC

For a proper reconstruction of charged particles in forward direction below 22° two drift chambers are placed within the target spectrometer 1.4 m and 2.0 m downstream with respect to the target location. Also the same layout described in Sec. 6.6.1.1 is used. The detector planes are grouped in four pairs with the same orientation of wires and the chambers are filled with a gas mixture of 90% argon and 10% ethane.

13.2.1.6 DIRC and RICH

The purpose of these two sub-detectors is the identification of charged particles in the momentum range between approximately 0.5 GeV/c and 3 GeV/c. The DIRC is placed directly in front of the EMC barrel and covers also the polar angular range between 20° and 140°. It is equipped with quartz bars as described in Sec. 7.2.1.

The RICH device is placed in front of the EMC forward wall with a circular hole of 5°. The chosen radiator material is per-fluoric hexane (C_6F_{14}).

13.2.1.7 Muon Counters

Plastic scintillator counters are placed behind the iron yoke of the solenoid magnet of the target spectrometer. They cover a polar angle between 5° and 80° which allow a proper muon identification of reconstructed charged tracks.

13.2.1.8 EMC

For the EMC of the target spectrometer two different setups and in addition two different crystal materials, PWO and BGO, are used. The purpose of these options is on one hand a rough investigation for the optimisation of the EMC detector geometry and on the other hand a study of the comparison between the two different crystal materials which are under discussion. Besides the resolution of the reconstructed photons the background rejection of some neutral benchmark channels is one of the main interests for these comparisons.

Each of the two setups consists of three different detector parts. The barrel has a cylindrical geometry with an inner radius of 50 cm and a length of 1.2 m in downstream and 0.6 m in upstream direction. This requires 33 different types of crystals placed in 55 rings of 120 modules each. To take the construction of the target pipe into account it was necessary to create two holes by removing four crystals in the first forward and in the first backward ring, respectively. The barrel covers a range of polar angles from 22° to 141°. Contrary to the real mechanical detector design (Sec. 8.6) for this part of the EMC the so called pointing geometry towards the target location is used.

For the other two detector parts, the forward wall and the end cap, the crystals are placed in parallel to the beam axis. The end cap covers polar angles between 140°–170° and is placed 0.7 m in front of the target location. The wall is divided in 12 different rings which requires also 12 different crystal types. The forward wall covering the polar angle between 5°–22° is placed 2.5 m behind the target location and is subdivided in 31 rings.

For each setup the size of the crystal front face is $(2.5 \times 2.5)\,\text{cm}^2$. The gap between the crystals is set to 0.5 mm and is completely filled with carbon fibres which is one realistic scenario for the support structure. This setup results in a total number of 11896 crystals.

The two geometries differ only in the crystal length. For the first setup a constant crystal length with a radiation thickness of 18 X_0 is used. The second version takes also the kinematical requirements into account. The consequence of fixed target measurements is a Lorentz boost in the beam direction of all produced particles. This causes the necessity to detect high energy gammas in the forward direction and only low energy gammas in the backward region. Therefore the crystal length is extended linearly in the forward part from 18 X_0 up to 22 X_0. The backward part of the barrel as well as the end cap consist of constant crystal length and are identical to the first version.

13.2.1.9 Magnet and Yoke

The same dimensions and materials as described in Chap. 10 are implemented in the simulation. The superconducting coil has a radius of 90 cm and a length 2.5 cm. An idealised solenoid field of 2.0 T in beam direction is used. This field starts at 0.6 m in front and ends 2.0 m behind the target point.

13.2.2 Forward Spectrometer

13.2.2.1 Dipole magnet

For the superconducting dipole magnet in the forward spectrometer a window frame with 1 m gap and 2 m aperture is implemented. The magnet

yoke occupies the space between 4 m and 6 m downstream of the target location. In the simulation an idealized magnetic field of 1.5 Tm perpendicular to the beam axis is used.

13.2.2.2 MDC

The deflection of particle trajectories within the dipole field is measured with a set of 4 drift chambers, 2 placed before and 2 behind the magnet. The chambers consist of rectangular frames with an active area of $1.3\times0.7\,m^2$ in the first two chambers and $2.4x1.2\,m^2$ in the second chamber pair. Each chamber contains three pairs of detection planes: One pair with vertical wires and two pairs with wires inclined +45° and -45°.

13.2.2.3 Calorimeter

As calorimeter the MIRAC version as already described in 8.12 is implemented. This detector part is subdivided in 30 independent stacks with dimensions of 22 cm horizontally and 120 cm vertically. Each stack consists of a lead-scintillator electromagnetic section 15 X_0 long, and a steel-scintillator section 6 X_0 long. The energy resolution of the modules can be modified which allows also a comparison with the second EMC calorimeter option KOPIO-LEDA.

13.2.2.4 Muon Detection

Behind the calorimeter as well as behind the yoke of the dipole magnet a wall of counters for muon identification similar to the ones in the target spectrometer are placed.

13.2.2.5 Particle Identification

Neither the time-of-flight detector nor the ring imaging Cherenkov counter which are the favourite devices for the particle identification in the forward spectrometer are implemented yet.

13.2.2.6 Radiation Length of Individual Detectors

Fig. 13.1 shows the radiation length of all individual sub-detectors with respect to the target location. All devices placed in front of EMC parts are taken in consideration. The frames of the MDCs of the target spectrometer cause the narrow enhancement in the overlapping region between the EMC barrel and the EMC forward wall ($\Theta \simeq 22°$).

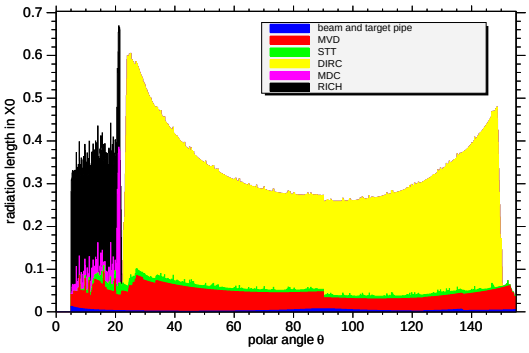

Figure 13.1: Radiation length of individual subdetectors versus Θ with respect to the target location.

13.3 Benchmark analysis

All benchmark channels with the corresponding backgroud events and the simulated detector setups are listed in table 13.1.

13.4 Mass Production

To check the feasibility of the various detector options which are currently under discussion, extensive Monte-Carlo simulations, and a reconstruction and analysis of the simulated data are necessary. Especially for a statistically significant test of the background suppression in the order of 10^8 events are needed. This needs more CPU time and more disk storage than one of the institutes which contribute to Panda computing has. Therefore at multiple sites the infrastructure for a MC production was set up.

13.4.1 Production Model and Sites

The original plan to make use of the Alien Grid implementation to run the data production with a minimal amount of manpower, could not be finished in time. To run jobs at GridKa [1] at FZ Karlsruhe, the iwarp cluster [2] at the IWR at FZ Karlsruhe, and the GSI batch farm, a number of perl scripts were developed, which handle the automatic import of input data, the export of the output to the event store, the generation of configuration and setup files, and the submission of the jobs to the local batch queues. For the MC production we had access to the computer clusters listed in Table 13.2.

benchmark channel	background channel	number of events	$\overline{\text{p}}$ mom. [GeV/c]	setup EMC(TS)	setup EMC(FS)	setup Tracking	major tasks
$\overline{\text{p}}\text{p} \to \pi^0\pi^0\eta$		200 k	3.6755	PWO1,2^{a,b}	KL	STT	EMC
	$\pi^0\pi^0\pi^0 \to 6\gamma$	200 k	15.1528	BGO1,2^{c,d,e}	KL	STT	study
	$\pi^0\eta\eta \to 6\,\gamma$	200 k		PWO1,2^{a}	M	STT	
	$\omega\pi^0\pi^0 \to 7\gamma$	200 k		BGO1,2^{c}	M	STT	
$\overline{\text{p}}\text{p} \to \phi\phi \to 4K$		10 k	3.6755	BGO2^{c}	KL	STT	tracking
	DPM	1 M		BGO2^{c}	KL	TPC	PID
$\overline{\text{p}}\text{p} \to \eta_c \to \gamma\gamma$		20 k	3.6755	PWO1,2^{a,b}	KL	STT	EMC
	$\pi^0\gamma \to 3\gamma$	1 M		BGO1,2^{c,d,e}	KL	STT	study
	$\pi^0\pi^0 \to 4\gamma$	10 M					
	DPM	1 M					
$\overline{\text{p}}\text{p} \to K^0_S K^{\pm}\pi^{\mp}$		10 k	3.6755	BGO2^{c}	KL	STT	tracking
	4π	100 k		BGO2^{c}	KL	TPC	PID
	$2\pi 2K$	100 k					
	DPM	1 M					
$\overline{\text{p}}\text{p} \to \gamma\gamma$		10 k	3.605	PWO1^{f}	KL	STT	EMC
	$\pi^0\gamma \to 3\gamma$	10 k					study
	$\pi^0\pi^0 \to 4\gamma$	10 k					
$\overline{\text{p}}\text{p} \to D\overline{D}$		10 k	6.5686	BGO2^{c}	KL	STT	tracking
	DPM	1 M		BGO2^{c}	KL	TPC	PID
$\overline{\text{p}}\text{p} \to D^*\overline{D^*}$		10 k	7.7025	BGO2^{c}	KL	STT	tracking
	DPM	1 M		BGO2^{c}	KL	TPC	PID
$\overline{\text{p}}\text{p} \to \Lambda\overline{\Lambda}$		10 k	4.0	BGO2^{c}	KL	STT	tracking
			6.0	BGO2^{c}	KL	TPC	PID
			7.7025				
$\overline{\text{p}}\text{p} \to \psi_g\eta$		10 k	15.1528	PWO1,2^{a,b,f}	KL	STT	EMC
				BGO1,2^{c,d,e}	KL	STT	study
				PWO1,2^{a,b,f}	M	STT	
				BGO1,2^{c,d,e}	M	STT	
$\overline{\text{p}}A \to J/\psi X$		10 k	4.05	BGO2^{c}	KL	STT	μ-
	UrQMD	5 M					reco

Table 13.1: List of all benchmark channels with the corresponding simulated setups and thresholds.
The following abbreviations for the EMC(TS) setup are used: PWO(BGO)1=setup with constant crystal length and PWO(BGO) crystals, PWO(BGO)2=setup with extended crystal length in the forward region and PWO(BGO) crystals and the reconstruction thresholds:
^{a}: E_{sc}=5 MeV, E_{max}=20 MeV, E_{cl}=25 MeV
^{b}: E_{sc}=10 MeV, E_{max}=35 MeV, E_{cl}=50 MeV
^{c}: E_{sc}=3 MeV, E_{max}=15 MeV, E_{cl}=20 MeV
^{d}: E_{sc}=3 MeV, E_{max}=15 MeV, E_{cl}=30 MeV
^{e}: E_{sc}=3 MeV, E_{max}=15 MeV, E_{cl}=50 MeV
^{f}: E_{sc}=10 MeV, E_{max}=20 MeV, E_{cl}=20 MeV.
For the FS tracking KL=KOPIO-LEDA or M=MIRAC are used.

The simulated events were reconstructed with up to four settings for energy thresholds and resolutions in the calorimeters.

1.6 TB of simulated, reconstructed and analysed events are stored in a simple event store on file servers at Ruhr-Universität Bochum and at Glasgow University.

13.4.2 Generated Events

During the reconstruction in the mass production and for development and test of the reconstruction and analysis software, the event data can be read via the *rootd* protocol. This makes all data accessible for everybody and avoids expensive data duplication. The actual contents of the event store and the status of the mass production can be inspected

Cluster	CPUs available	CPUs used	# of simulated events
GridKa	1070	250	$165 \cdot 10^6$
iwarp	20	20	$50 \cdot 10^6$
GSI	72	72	$41 \cdot 10^6$

Table 13.2: Mass production sites for the Technical Progress Report 2005.

anytime on a web page.

For background channels that need 10^7 events per setup just 10^6 simulated events were stored in the event store. The rest was produced just in time before the reconstruction jobs started, because the export and re-import of the GEANT4 output data would need more time than the production of the data if a large number of CPUs are used in parallel. A second reason is that we do not have the storage capacity to keep all intermediate data on disk.

13.5 Results

13.5.1 All-Neutral: $\overline{\mathrm{p}}\mathrm{p} \rightarrow \pi^0\pi^0\eta \rightarrow 6\gamma$

13.5.1.1 Introduction

The objective of the study of the reaction $\overline{\mathrm{p}}\mathrm{p} \rightarrow \pi^0\pi^0\eta \rightarrow 6\gamma$ is to test and optimize the electromagnetic calorimeter. Good energy resolution and large detector acceptance is necessary to separate this channel from background channels with pure photon final states. At high beam momenta the angle between the two photons from high-energetic pions is very small, so high granularity is needed to reconstruct these pions. In figure 13.2 the momentum distribution of pions generated at $\sqrt{s} = 5.5\,\mathrm{GeV}/c^2$ is shown. One can see that the pions at low polar angles can have momenta larger than 10 GeV/c.
Monte Carlo simulations have been done at $\sqrt{s} = 2.98\,\mathrm{GeV}/c^2$ and $\sqrt{s} = 5.5\,\mathrm{GeV}/c^2$ for several detector setups and different energy thresholds in the γ-reconstruction. The different setups are listed in Table 13.1. 200k signal events have been analyzed for each setup. These events are generated isotropically over the phase space. Additionally 200 k background events of following reactions have been studied:

- $\overline{\mathrm{p}}\mathrm{p} \rightarrow \pi^0\pi^0\pi^0 \rightarrow 6\gamma$
- $\overline{\mathrm{p}}\mathrm{p} \rightarrow \eta\,\eta\,\pi^0 \rightarrow 6\gamma$
- $\overline{\mathrm{p}}\mathrm{p} \rightarrow \pi^0\pi^0\omega \rightarrow 7\gamma$

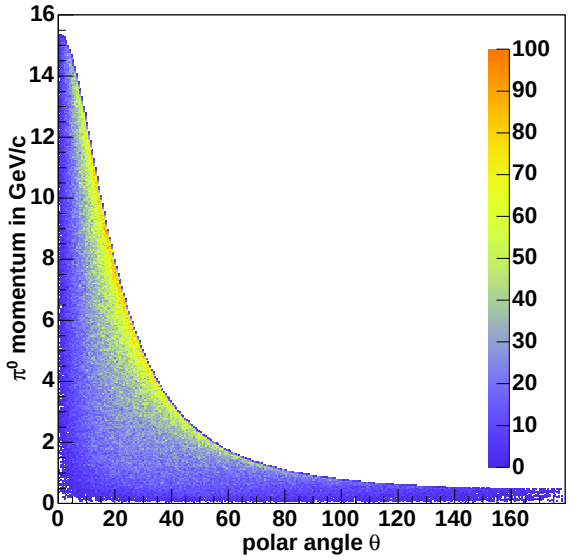

Figure 13.2: π^0 momentum of generated $\overline{\mathrm{p}}\mathrm{p} \rightarrow \pi^0\pi^0\eta \rightarrow 6\gamma$ events at $\sqrt{s} = 5.5\,\mathrm{GeV}/c^2$

To estimate the relative branching ratios 10^7 events at $\sqrt{s} = 2.98\,\mathrm{GeV}$ and $5{\cdot}10^7$ events at $\sqrt{s} = 5.5\,\mathrm{GeV}/c^2$ have been produced with the DPM generator. Events with $2\pi^0\eta, 3\pi^0, 2\pi^0\omega, \pi^0 2\eta$ in final state have been extracted. From the number of the extracted events the relative branching ratios are calculated. The feed through from other channels will be investigated with the DPM event generator in future studies.

channel		rel. BR $\sqrt{s} = 2.98\,\mathrm{GeV}/c^2$	$\sqrt{s} = 5.5\,\mathrm{GeV}/c^2$
$\overline{\mathrm{p}}\mathrm{p} \rightarrow 2\pi^0\eta$	$\rightarrow 6\gamma$	1	1
$\overline{\mathrm{p}}\mathrm{p} \rightarrow 3\pi^0$	$\rightarrow 6\gamma$	2.6	2.5
$\overline{\mathrm{p}}\mathrm{p} \rightarrow 2\eta\pi^0$	$\rightarrow 6\gamma$	0.13	0.12
$\overline{\mathrm{p}}\mathrm{p} \rightarrow 2\pi^0\omega$	$\rightarrow 7\gamma$	0.16	0.09

Table 13.3: Rough relative branching ratios at $\sqrt{s} = 2.98\,\mathrm{GeV}/c^2$ and $\sqrt{s} = 5.5\,\mathrm{GeV}/c^2$.

13.5.1.2 Selection

The selection is done without a kinematic fit. Kinematic fitting routines which would improve the energy and angular resolution of photons are under investigation. Nevertheless as many constraints as possible are used to get a good background suppression.
A $\overline{\text{p}}\text{p} \to \pi^0\pi^0\eta \to 6\gamma$-event has to fulfill following selection criteria:

- exactly six reconstructed γ
- no track reconstructed
- momentum and energy cuts
  for $\sqrt{s} = 2.98GeV$:
  - $|E_{6\gamma} - E_{6\gamma}^{reco}| < 0.4\,\text{GeV}$
  - $|P_{6\gamma} - P_{6\gamma}^{reco}| < 0.3\,\text{GeV}/c$
  - $|Pz_{6\gamma} - Pz_{6\gamma}^{reco}| < 0.3\,\text{GeV}/c$
  - $Px_{6\gamma}Px_{6\gamma}+Py_{6\gamma}^{reco}Py_{6\gamma}^{reco} < 0.04\,\text{GeV}/c^2$

  for $\sqrt{s} = 5.5\,\text{GeV}$:
  - $|E_{6\gamma} - E_{6\gamma}^{reco}| < 1\,\text{GeV}$
  - $|P_{6\gamma} - P_{6\gamma}^{reco}| < 1\,\text{GeV}/c$
  - $|Pz_{6\gamma} - Pz_{6\gamma}^{reco}| < 1\,\text{GeV}/c$
  - $Px_{6\gamma}Px_{6\gamma}+Py_{6\gamma}^{reco}Py_{6\gamma}^{reco} < 0.09\,\text{GeV}/c^2$

There are 45 possibilities to combine a $\overline{\text{p}}\text{p} \to \pi^0\pi^0\eta$ event from six photons. For each combination the mass difference is calculated:

$$\begin{aligned} m_{diff} =& m_{6\gamma} - m_{\gamma_{k1},\gamma_{k2}} - m_{\gamma_{k3},\gamma_{k4}} - m_{\gamma_{k5},\gamma_{k6}} \\ &+ m_{\pi^0}^{PDG} + m_{\pi^0}^{PDG} + m_{\eta}^{PDG} \end{aligned} \tag{13.1}$$

By using only the three mass constraints a χ^2 for $\overline{\text{p}}\text{p} \to 2\pi^0\eta$,$\overline{\text{p}}\text{p} \to \pi^0 2\eta$ and $\overline{\text{p}}\text{p} \to 3\pi^0$ hypothesis is calculated for each combination. The reconstructed masses $\text{m}_{\pi^0}, \text{m}_{\eta}$ and the reconstructed mass widths σ_{π^0} and σ_{η}, depending on the detector setup are taken from a gaussian plus polynomial fit of the invariant $\gamma\gamma$-mass spectrum(see figure 13.3 and Table 13.4).

$$\begin{aligned} \chi^2_{2\,\pi^0\eta} =& \frac{(m_{\gamma_{k1},\gamma_{k2}} - m_{\pi^0})^2}{\sigma^2_{\pi^0}} + \frac{(m_{\gamma_{k3},\gamma_{k4}} - m_{\pi^0})^2}{\sigma^2_{\pi^0}} \\ &+ \frac{(m_{\gamma_{k5},\gamma_{k6}} - m_{\eta})^2}{\sigma^2_{\eta}} \end{aligned}$$

$$\begin{aligned} \chi^2_{\pi^0 2\eta} =& \frac{(m_{\gamma_{k1},\gamma_{k2}} - m_{\pi^0})^2}{\sigma^2_{\pi^0}} + \frac{(m_{\gamma_{k3},\gamma_{k4}} - m_{\eta})^2}{\sigma^2_{\eta}} \\ &+ \frac{(m_{\gamma_{k5},\gamma_{k6}} - m_{\eta})^2}{\sigma^2_{\eta}} \end{aligned}$$

$$\begin{aligned} \chi^2_{3\,\pi^0} =& \frac{(m_{\gamma_{k1},\gamma_{k2}} - m_{\pi^0})^2}{\sigma^2_{\pi^0}} + \frac{(m_{\gamma_{k3},\gamma_{k4}} - m_{\pi^0})^2}{\sigma^2_{\pi^0}} \\ &+ \frac{(m_{\gamma_{k5},\gamma_{k6}} - m_{\pi^0})^2}{\sigma^2_{\pi^0}} \end{aligned} \tag{13.2}$$

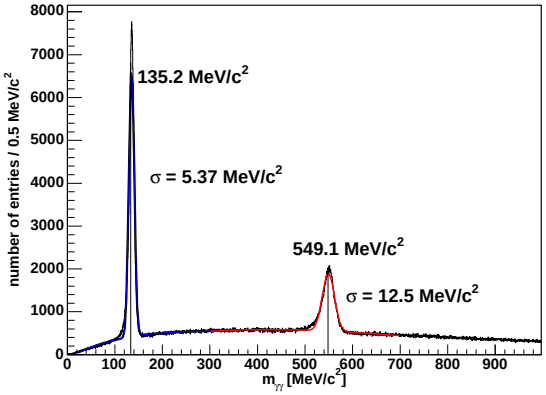

Figure 13.3: Invariant mass of $\gamma\gamma$ pairs of 200 k $\pi^0\pi^0\eta$-events at $\sqrt{s} = 2.98\,\text{GeV}/c^2$. setup: PWO V2 (5,20,25) MeV KOPIO-LEDA.

setup	σ_{π^0}	σ_{η}
PWO V1 (5,20,25) MeV	5.6	13.5
PWO V2 (5,20,25) MeV	5.4	12.5
PWO V1 (10,35,50) MeV	5.8	15.0
PWO V2 (10,35,50) MeV	5.6	13.9
BGO V1 (3,15,20) MeV	5.5	12.3
BGO V2 (3,15,20) MeV	5.4	11.5

Table 13.4: σ_{π^0} and σ_{η} for different setups at $\sqrt{s} = 2.98\,\text{GeV}/c^2$

For the final selection we demand:

- for $\sqrt{s} = 2.98\,\text{GeV}$:
  -at least one combination has to fulfill
  $|m_{diff} - 2.98\,\text{GeV}/c^2| < 0.2\,\text{GeV}/c^2$
  -for the combination with the lowest $\chi^2_{2\pi^0\eta}$ following cuts have been applied
  $\chi^2_{min,2\pi^0\eta} < \chi^2_{min,3\pi^0}$
  $\chi^2_{min,2\pi^0\eta} < \chi^2_{min,\pi^0\,2\eta}$
  $\chi^2_{min,2\pi^0\eta} < 11.35$
  $\chi^2_{min,3\pi^0} > 50$

- for $\sqrt{s} = 5.5\,\text{GeV}$:
  $|m_{diff} - 5.5\,\text{GeV}/c^2| < 0.3\,\text{GeV}/c^2$

$\chi^2_{min,2\pi^0\eta} < \chi^2_{min,3\pi^0}$
$\chi^2_{min,2\pi^0\eta} < \chi^2_{min,\pi^0\,2\eta}$
$\chi^2_{min,2\pi^0\eta} < 16.11$
$\chi^2_{min,3\pi^0} > 50$

13.5.1.3 Results

The results achieved with these simple selection methods are listed in Table 13.5. At $\sqrt{s} = 2.98\,\mathrm{GeV}/c^2$ we got good efficiencies and a background feedthrough less than 1% for all setups. Using EMC version 2 (extended crystal lengths in forward direction) the number of selected signal events increased, while the background could be further reduced. Figure 13.4 shows a Dalitz plot of phase space distributed events using the EMC setup PWO V2 setup at $\sqrt{s} = 2.98\,\mathrm{GeV}/c^2$. No significant structures nor regions of poor efficiency are visible.

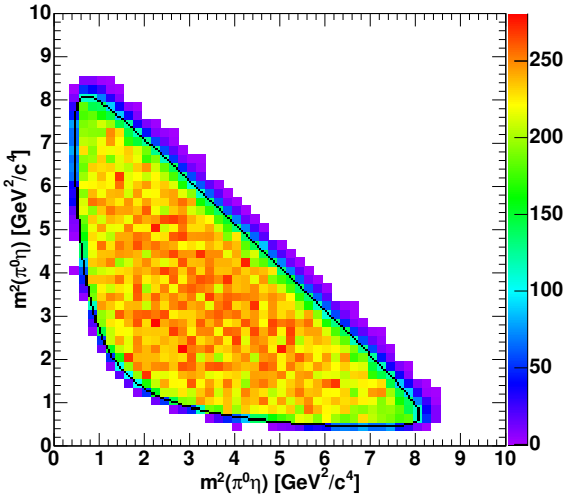

Figure 13.4: Dalitz plot of reconstructed $\pi^0\pi^0\eta$ events, which are generated isotropically over the phase space. setup: PWO V2 (5,20,25) MeV KOPIO-LEDA.

The results at $\sqrt{s} = 5.5\,\mathrm{GeV}/c^2$ have to be treated with care. Because up to now there is no electromagnetic split-off recognition available in the offline software, the efficiency decreases due to the cut on exact six photons. This cut is mandatory for a efficient background suppression. The efficiency can also be improved by adapting the energy threshold in the photon reconstruction to improve the detection efficiency of merged pions. This will be done in future studies.

13.5.2 ϕ-dominated Charmonium Decay: $\bar{p}p \rightarrow \eta_c \rightarrow \phi\phi$

13.5.2.1 Introduction

The decay through two ϕ resonances into four kaons provides a very clean signature for charmonium events. The particles in the final state are highly correlated which allows the efficient application of kinematic fits to reach high resolution in the physical observables.

The η_c undergoes an S-wave 2-particle decay into two ϕ, which immediately decay into two kaons each. $\phi \rightarrow K^+K^-$ happens just above the threshold with a $Q_{\phi\rightarrow 2K} = 32\,\mathrm{MeV}$. The resulting signature for the channel is two pairs of kaons which are strongly boosted in the direction of the decaying ϕs. The kinematics of the final state kaons are shown in fig. 13.5.

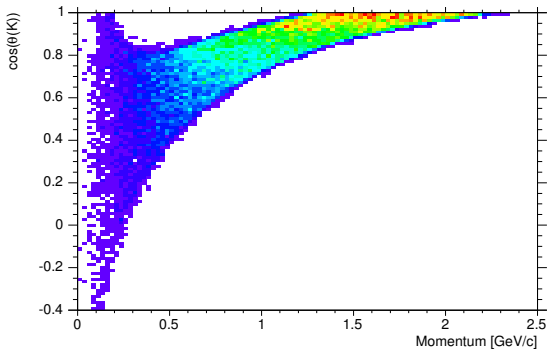

Figure 13.5: Angle vs. momentum of final state kaons from $\eta_c \rightarrow \phi\phi \rightarrow K^+K^-K^+K^-$.

The final state particles mainly occupy the region between 0.2 and 2 GeV/c. Since the ϕ are produced back to back in the CMS there is a strong angular correlation between them. To illustrate this in Fig. 13.6 the reconstructed angles against the beam axis are plotted in the CMS.

This channel has an extremely small cross section. Data from experiments [3][4] together with the $\eta_c \rightarrow \gamma\gamma$ branching ratio [5] lead to this value for the η_c peak[1] production cross section:

$$\sigma(\bar{p}p \rightarrow \eta_c) \simeq 450\,\mathrm{nb}$$

The branching ratios are [5]:

$$BR(\eta_c \rightarrow \phi\phi) \simeq 7.1 \cdot 10^{-3}$$

$$BR(\phi \rightarrow K^+K^-) \simeq 0.491$$

1. the cross section is measured at the resonance peak with a beam spread (r.m.s) of 0.3MeV [4]

at $\sqrt{s} = 2.98\,\text{GeV}/c^2$					
setup		$\pi^0\pi^0\eta$	$\pi^0\pi^0\pi^0$	$\pi^0\pi^0\omega$	$\eta\eta\pi^0$
PWO V1	5,20,25 KL	79174 (39.6%)	79 ($2.6 \cdot 10^{-3}$)	1025 ($2.1 \cdot 10^{-3}$)	129 ($2.1 \cdot 10^{-4}$)
PWO V1	10,35,50 KL	71035 (35.5%)	65 ($2.4 \cdot 10^{-3}$)	1918 ($4.3 \cdot 10^{-3}$)	108 ($2.0 \cdot 10^{-4}$)
PWO V1	5,20,25 M	78517 (39.3%)	70 ($2.3 \cdot 10^{-3}$)	1021 ($2.1 \cdot 10^{-3}$)	133 ($2.2 \cdot 10^{-4}$)
PWO V2	5,20,25 KL	82449 (41.2%)	69 ($2.2 \cdot 10^{-3}$)	981 ($1.9 \cdot 10^{-3}$)	102 ($1.6 \cdot 10^{-4}$)
PWO V2	10,35,50 KL	73680 (36.8%)	64 ($2.6 \cdot 10^{-3}$)	1891 ($4.1 \cdot 10^{-3}$)	105 ($1.9 \cdot 10^{-4}$)
PWO V2	5,20,25 M	81406 (40.7%)	64 ($2.0 \cdot 10^{-3}$)	982 ($1.9 \cdot 10^{-3}$)	102 ($1.6 \cdot 10^{-4}$)
BGO V1	3,15,20 KL	77227 (38.6%)	64 ($2.2 \cdot 10^{-3}$)	773 ($1.6 \cdot 10^{-3}$)	123 ($2.1 \cdot 10^{-4}$)
BGO V1	3,15,30 KL	76440 (38.2%)	55 ($1.9 \cdot 10^{-3}$)	1008 ($2.1 \cdot 10^{-3}$)	110 ($1.9 \cdot 10^{-4}$)
BGO V1	3,15,50 KL	69886 (34.9%)	50 ($1.9 \cdot 10^{-3}$)	1418 ($3.2 \cdot 10^{-3}$)	97 ($1.8 \cdot 10^{-4}$)
BGO V1	3,15,20 M	76537 (38.3%)	61 ($2.1 \cdot 10^{-3}$)	767 ($1.6 \cdot 10^{-3}$)	126 ($2.1 \cdot 10^{-4}$)
BGO V2	3,15,20 KL	80242 (40.1%)	66 ($2.1 \cdot 10^{-3}$)	737 ($1.5 \cdot 10^{-3}$)	108 ($1.7 \cdot 10^{-4}$)
BGO V2	3,15,30 KL	79050 (39.5%)	57 ($1.9 \cdot 10^{-3}$)	935 ($1.9 \cdot 10^{-3}$)	103 ($1.7 \cdot 10^{-4}$)
BGO V2	3,15,50 KL	71948 (36.0%)	50 ($1.8 \cdot 10^{-3}$)	1392 ($3.1 \cdot 10^{-3}$)	93 ($1.7 \cdot 10^{-4}$)
BGO V2	3,15,20 M	79244 (39.6%)	64 ($2.1 \cdot 10^{-3}$)	746 ($1.5 \cdot 10^{-3}$)	108 ($1.8 \cdot 10^{-4}$)

at $\sqrt{s} = 5.5\,\text{GeV}/c^2$					
setup		$\pi^0\pi^0\eta$	$\pi^0\pi^0\pi^0$	$\pi^0\pi^0\omega$	$\eta\eta\pi^0$
PWO V1	5,20,25 KL	33156 (16.6%)	221 ($1.7 \cdot 10^{-2}$)		131 ($4.7 \cdot 10^{-4}$)
PWO V1	10,35,50 KL	37343 (18.7%)	139 ($0.9 \cdot 10^{-2}$)		172 ($5.5 \cdot 10^{-4}$)
PWO V1	5,20,25 M	35983 (18.0%)	225 ($1.6 \cdot 10^{-2}$)		107 ($3.6 \cdot 10^{-4}$)
PWO V2	5,20,25 KL	39237 (19.6%)	160 ($1.0 \cdot 10^{-2}$)		107 ($3.3 \cdot 10^{-4}$)
PWO V2	10,35,50 KL	43799 (21.9%)	117 ($0.7 \cdot 10^{-2}$)		138 ($3.8 \cdot 10^{-4}$)
PWO V2	5,20,25 M	40333 (20.2%)	152 ($0.9 \cdot 10^{-2}$)		87 ($2.6 \cdot 10^{-4}$)
BGO V1	3,15,20 KL	28610 (14.3%)	178 ($1.6 \cdot 10^{-2}$)		125 ($5.2 \cdot 10^{-4}$)
BGO V1	3,15,30 KL	29336 (14.7%)	191 ($1.6 \cdot 10^{-2}$)		119 ($4.9 \cdot 10^{-4}$)
BGO V1	3,15,50 KL	28553 (14.3%)	159 ($1.4 \cdot 10^{-2}$)		145 ($6.1 \cdot 10^{-4}$)
BGO V1	3,15,20 M	30927 (15.5%)	227 ($1.8 \cdot 10^{-2}$)		109 ($4.2 \cdot 10^{-4}$)
BGO V2	3,15,20 KL	33556 (16.8%)	152 ($1.1 \cdot 10^{-2}$)		120 ($4.3 \cdot 10^{-4}$)
BGO V2	3,15,30 KL	34093 (17.0%)	139 ($1.0 \cdot 10^{-2}$)		109 ($3.8 \cdot 10^{-4}$)
BGO V2	3,15,50 KL	32872 (16.4%)	108 ($0.8 \cdot 10^{-2}$)		115 ($4.2 \cdot 10^{-4}$)
BGO V2	3,15,20 M	34439 (17.2%)	167 ($1.2 \cdot 10^{-2}$)		111 ($3.9 \cdot 10^{-4}$)

Table 13.5: Number of events reconstructed as $\pi^0\pi^0\eta$ (reconstruction efficiency and corresponding background levels) The simulation of the background channel $\pi^0\pi^0\omega$ at $\sqrt{s} = 5.5\,\text{GeV}/c^2$ could not be finished in time for this report.

So for the complete branching ratio of this channel one gets:

$$BR(\overline{\text{p}}\text{p} \rightarrow \eta_c \rightarrow \phi\phi \rightarrow K^+K^-K^+K^-) =$$
$$BR(\eta_c \rightarrow \phi\phi) \cdot BR(\phi \rightarrow K^+K^-)^2 \simeq 1.7 \cdot 10^{-3}$$

The total cross section follows to be

$$\sigma(\overline{\text{p}}\text{p} \rightarrow \eta_c \rightarrow \phi\phi, \rightarrow 4K) \simeq 0.77\,\text{nb}$$

This has to be compared to the total cross section for $\overline{\text{p}}$p annihilations which in this region is $\simeq 25\,\text{mb}$ [5]. The raw signal to noise ratio which one has to overcome is:

$$\frac{\sigma(\text{signal})}{\sigma(\overline{\text{p}}\text{p} \rightarrow X)} \simeq 3.1 \cdot 10^{-8}$$

Although kinematic constraints alone already re-

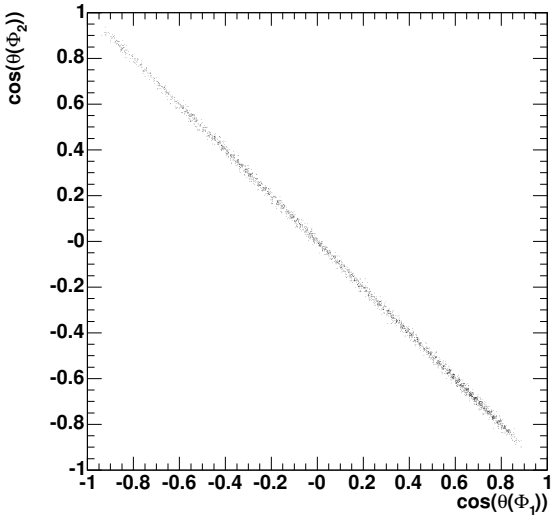

Figure 13.6: Angular correlation of the reconstructed ϕ s in the CMS.

duce the background by several orders of magnitude, one still needs good particle identification to separate a clean sample of signal events.

Comparison of tracker options
In the low momentum region which is populated by the kaons in this channel the particle identification by Cherenkov radiation (DIRC and RICH) is not possible any more (see Sec. 7). The TPC can provide PID in this low momentum range. In addition momentum reconstruction at low p_t gets difficult due to rising energy losses and multiple scattering. For this reason this channel is a good test for the two tracking options. (See Sec. 6.5 and Sec. 6.4)

13.5.2.2 Selection

The initial data sample consists of 10^4 signal events and 10^6 background events from the DPM event generator. The $\eta_c \rightarrow \phi\phi$ event generator does not reproduce the shape of the η_c resonance. The width is assumed to be zero. So the reconstruction should directly give the achievable mass resolution.

The analysis proceeds in three steps:

1. kaon selection
2. reconstruction of $\phi \rightarrow K^+K^-$
3. reconstruction of $\eta_c \rightarrow \phi\phi$

The selection of the η_c signal is obtained by applying several kinematical and geometrical cuts and cuts on the PID information. The four kaons are subjected to a vertex fit, which tries to find a common vertex. This vertex has to be near the interaction point (IP). The reconstruction of one ϕ requires 2 kaons with opposite charge. A cut is applied on the resulting mass of the ϕ-candidate. A kinematic fit, which would not only improve the resolution but also put strong restrictions on the selection, has not been used – this has to be investigated in future studies.

The channel has been analysed with two different setups: TPC tracker option and STT option. Two slightly different sets of cuts have been used (see Table 13.6) the main difference being the particle identification.

The DIRC is only sensitive at momenta higher than approx. 0.6 GeV/c. It's efficiency is about 40ϕ s it is very unlikely that all four kaons have momenta in a region which allows an identification with the DIRC. Consequently the requirement to have four identified kaons reduces the statistics dramatically if only the DIRC is used for PID (see Table 13.6 values in brackets) as would be the case with the STT option. To be able to reconstruct the channel anyway in this setup one has to include those particle candidates for which no clear identification can be done. In this case the reconstruction algorithm assigns an equal likelyhood of 0.2 is to every PID hypothesis. By including the range of accepted likelyhoods down to this value the statistics can be recovered (compare Table 13.6). However one has to keep in mind, that this will also increase the background contamination.

Table 13.7 shows the impact these cuts have on the data. It lists the number of surviving events after each cut. For the STT signal the numbers in brackets are the results with the same stricter PID cut as has been applied in the TPC setup (kaon likelihood $\geq$ 0.25 instead of 0.20). It is apparent, that the channel cannot be reconstructed with this setting without TPC PID.

The roughly 42% efficiency for the TPC after the kaon cut corresponds to a single particle PID efficiency (at this cut-level) of about 80%.

In the STT case on the 25% level the value (97 events) corresponds to a single particle PID efficiency of about 30% reached with the Čerenkov detectors in this momentum region alone.

We observe a comparatively large cut on the signal data with the cut on the vertex fit quality. This might be due to multiple scattering which up to now is not accounted for at any place in the reconstruction.

Cut	TPC	STT
4 kaons with likelihood	≥ 0.25	≥ 0.20
vertex fit: reduced χ^2	≤ 5	
distance of vertex from IP	$\leq 0.3\,\text{mm}$	
ϕ mass window	$\lvert m_\phi - m_\phi^{reco}\rvert \leq 0.02\,\text{GeV}/c^2$	
η_c momentum in CMS	$< 0.2\,\text{GeV}/c$	

Table 13.6: Cut parameters for the TPC and the STT option.

Cut	TPC		STT	
	signal	DPM	signal	DPM
	10^4	10^6	10^4	10^6
kaon ID	4 226	14	5 565 (97)	78 058
vertex fit: reduced χ^2	3 059	6	3 311 (97)	19 358
vertex position	3 041	6	3 284 (86)	14 705
ϕ mass window	3 000	0	3 213 (86)	1 080
η_c momentum in CMS	3 000	0	3 200 (85)	3

Table 13.7: Cut yields for the TPC and the STT option. In brackets are for comparison the values one gets when using the same kaon likelihood cut for the STT as for the TPC (25%).

13.5.2.3 Results

η_c reconstruction

Fig. 13.7 shows the η_c mass peak reconstructed from 10 000 signal events without background. From a gaussian plus linear background fit to the peak the achieved mass resolution is found to be

$$\sigma_{\eta_c}^{TPC} = 11\,\text{MeV}/c^2$$

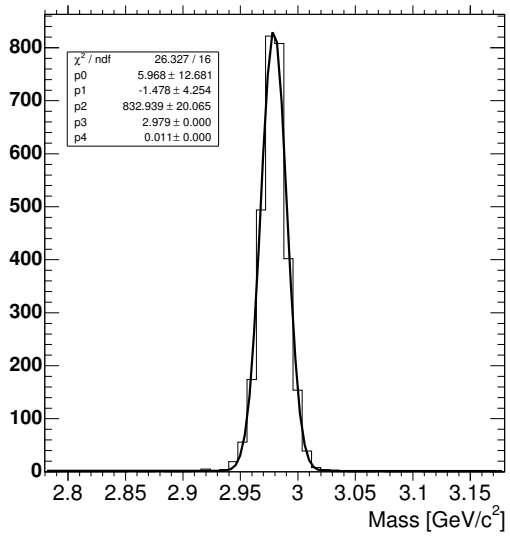

Figure 13.7: Reconstructed η_c mass (TPC).

To calaculate the total reconstruction efficiency only those η_c candidates were counted, that are within 3σ of the reconstructed mass peak. The result for the TPC is:

$$\epsilon_{\eta_c}^{TPC} = \frac{N_{\text{reco}}}{N_{\text{sim}}} = 29,8\%$$

Fig. 13.8 shows the analogues results for the straw tube tracker.

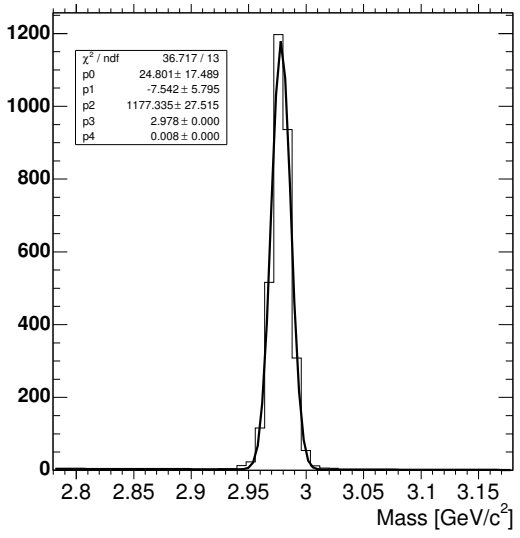

Figure 13.8: Reconstructed η_c mass (STT).

$$\sigma_{\eta_c}^{STT} = 8\ \text{MeV}/c^2$$

$$\epsilon_{\eta_c}^{STT} = \frac{N_{\text{reco}}}{N_{\text{sim}}} = 31.5\%$$

Background suppression
As can be seen from the list of the cut-results (Table 13.7) with the kaon identification provided by the TPC together with the kinematic cuts a good background suppression is achieved. Due to the limited statistics which were available for this study we can only give a limit for the reachable signal to noise level. An upper limit for the contamination of this channel is

$$\lambda = \frac{N_{\text{ghost}}}{N_{\text{background}}} < 1.08 \cdot 10^{-6} \quad 66\,\%\,\text{CL}$$

which (taking 30% reconstruction efficiency into account) corresponds to a signal to noise level of

$$S/N > 2.9 \cdot 10^{-2}$$

If one looks a bit closer to Table 13.7 one sees from the STT data, that the last kinematic cut (on the η_c residual momentum in the CMS) reduces the background by a factor of about 300. If one assumes, that this cut will do the same if it is invoked at higher statistics on TPC data a signal to noise ratio better than 1/1 seems feasible with the TPC. With the straw tube tracker the channel will probably not be discernible from the background.

It must be pointed out, that this statement has to be taken with care. Further investigations with higher statistics are necessary to clarify the point since one cannot rule out correlations between the used cuts.

13.5.3 Electromagnetic Charmonium Decay: $\overline{\text{p}}\text{p} \rightarrow \eta_c \rightarrow \gamma\gamma$

13.5.3.1 Introduction

In consideration of physical questions within the QCD-model, an accurate determination of the mass, width, and the decay behaviour of the $\eta_c(1^1S_0)$ charmonium is necessary to understand and test the models of the QCD. Especially a better knowledge of the central production of the η_c in the $\overline{\text{p}}$p-annihilation with the electromagnetic decay mode into two photons can give important contributions to answer these questions.
Up to now only the E835 experiment could observe the reaction $\overline{\text{p}}\text{p} \rightarrow \eta_c \rightarrow \gamma\gamma$ significantly [4]. Since further investigations are needed $\overline{\text{P}}$ANDA also foresees the measurement of this decay chain. The intention of this benchmark study is to roughly estimate if the proposed detector scenarios can fulfill this physics case.

The following two topics are under investigation within these simulations:

- Comparison with E835: The signal has been observed with a maximum peak to background ratio of about 1 to 1 in the kinematic range $|cos\Theta^*| < 0.25$. (Θ^* being the angle between the direction of the photon in the CM frame and the beam). The main sources for background are the reactions $\overline{\text{p}}\text{p} \rightarrow \pi^0\gamma$ and $\overline{\text{p}}\text{p} \rightarrow \pi^0\pi^0$. Their production cross section in this kinematic range are $\sigma_{\pi^0\,\gamma} \simeq 2.5\,\text{nb}$ and $\sigma_{\pi^0\,\pi^0} \simeq 25\,\text{nb}$. For the η_c signal a cross section of $\sigma_{\eta_c} \simeq 50\,\text{pb}$ can be assumed.
- Variation of the kinematic range $\cos\Theta^*$: The purpose of this study is to figure out the maximum acceptance region, in which η_c still can be detected with tolerable background suppression.

The experimental challenge is to separate the η_c signal from the two main background channels, which show a high occurrence of low energetic photons (see Fig. 13.9). Especially photons below 50 MeV/c^2 may remain undetected and due to this, the background is identified as a two photon final state incorrectly. Also high momentum pions can result in a misidentification of two photon final states (merged pions (see Sec. 12.3.3.1)).

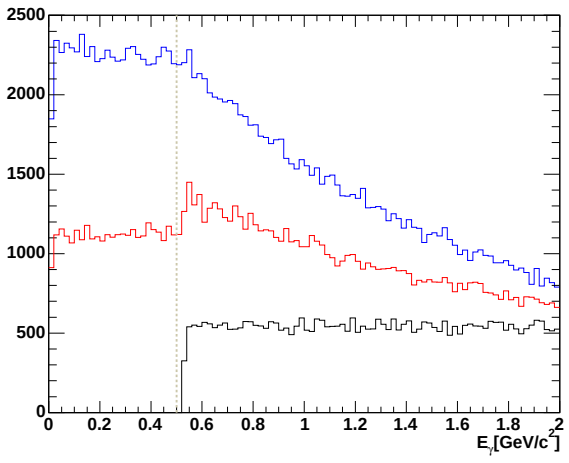

Figure 13.9: γ energy distribution of generated events taken from MC data. The black line indicates the generated events of η_c, the red line the $\pi^0\pi^0$- and the blue line the $\pi^0\gamma$ events.

On the basis of the assumed cross sections within the angular region mentioned above, the ratio of events to be simulated is 1:50:500. Therefore 20 000 events for the η_c-reaction, 1 000 000 events for the $\pi^0\gamma$- and 10 000 000 events for the $\pi^0\pi^0$ reaction

with different EMC setups and materials and associative energy thresholds were simulated. A reasonable approximation is to assume a flat decay distribution of the background events in the same kinematic range as E835. Therefore each channel was generated isotropically over the phase space.

13.5.3.2 Selection

To get a clean sample of the η_c it has been required, that no charged particles have been detected and that there are exactly two PED entries in the EMC.

The energy difference between the known CM energy of the $\overline{\text{p}}$p system and the energy of the η_c-candidate was set to be smaller than 0.4 GeV/c. Furthermore the difference of the magnitudes of the photon momenta in the CM frame was set to be smaller than 0.4 GeV/c.

An event was rejected, if the invariant mass of the two photons does not fit the mass window between approximately 2.85 MeV/c^2 and 3.1 MeV/c^2 (values depending on the resolution of the simulated detector setup).

The signal to background ratio depends on the cuts applied to the angle between the two photons in the CMS frame. In previous $\overline{\text{P}}$ANDA simulations the cosine of the angle was set to be smaller than -0.9999 in the strictest case. Because of an improved spatial and energy resolution of the EMC, based on more precise energy correction functions, it is now possible to set this parameter to $\cos\theta_{\gamma\gamma} < -0.99995$ without losing much of the signal. This can be seen in figure 13.10 (see also Table 13.8).

By means of the cluster shower mass (M_s) it is possible to identify and finally to get rid of merged pions. This cut is reasonable as can be seen in figure 13.11. In the region of $|M_s - M_{\pi^0}| > 30\,\text{MeV}/c^2$ the signal contains almost no entries contrary to the $\pi^0\gamma$- and $\pi^0\pi^0$ events. This cut reduces the misidentification of the $\pi^0\gamma$ background approximately one order of magnitude.

To scan the acceptance region of the detector, the cut on $|\cos\Theta^*|$ is varied from 0.2 to 0.4.

In summary, the following cuts were applied to the dataset:

1. Exactly two photons and no charged tracks
2. Angle between the two photons (in CM frame): $\cos\theta_{\gamma\gamma} < -0.9995...0.99995$
3. Missing energy (in CM frame): $\Delta E = E_{\overline{\text{p}}\text{p}} - E_{\eta_{ccand}} < 0.4 GeV$
4. Missing momentum (in CM frame): $\Delta P = |P_{\gamma_1} - P_{\gamma_2}| < 0.4\,\text{GeV}/c$
5. Angle of momentum: $|\cos\Theta^*| < 0.2...0.4$
6. Mass window: $2.85\,\text{GeV}/c^2 < M_{\gamma_1\gamma_2} < 3.1\,\text{GeV}/c^2$
7. Showermass of of each candidate $|M_s - M_{\pi^0}| > 30\,\text{MeV}/c^2$

13.5.3.3 Results

Comparison with E835.

Applying the $\cos\theta_{\gamma\gamma} < -0.99995$ cut in the angular region of $|\cos\Theta^*| < 0.25$ to the dataset of EMC V2 BGO with (3, 15, 20) MeV threshold, the invariant $\gamma\gamma$ mass distribution is obtained as shown in figure 13.12. Detected events of the $\pi^0\gamma$ decay contribute to most of the background. The signal to background ratio is calculated to be 1.193 with this setup threshold combination and thus shows an agreement with the results of the E835 experiment. The resolution of the reconstructed η_c mass shows a σ of approximately 33 MeV/c^2.

The η_c efficiency results of the $\cos\theta_{\gamma\gamma}$ variation within this kinematic range are shown in Table 13.8. It can be seen, that the efficiency stays at about 18.5% until $\cos\theta_{\gamma\gamma}$ is getting smaller than -0.99985.

$\cos\theta_{\gamma\gamma}$	η_c-efficiency [%]
-0.9995	18.945
-0.99965	18.925
-0.9998	18.74
-0.99985	18.50
-0.9999	17.465
-0.99995	14.445

Table 13.8: Efficiency of the signal depending on the cuts applied to the angle between the two photons. (Values of EMC V2 BGO-setup with (3, 15, 20) MeV-threshold and $|\cos\Theta^*| < 0.25$)

In addition to different simulated EMC setups, the energy thresholds which are of decisive importance for the suppression of the concurring channels are varied. The efficiencies and the signal to background ratios depending on the simulated setup are given in Table 13.9. The DPM background was also simulated with all these setups (1 000 000 events), but no events survived the selection cuts.

As can be seen in Table 13.9, the η_c efficiency increases by using higher reconstruction thresholds for each investigated EMC-option. This happens

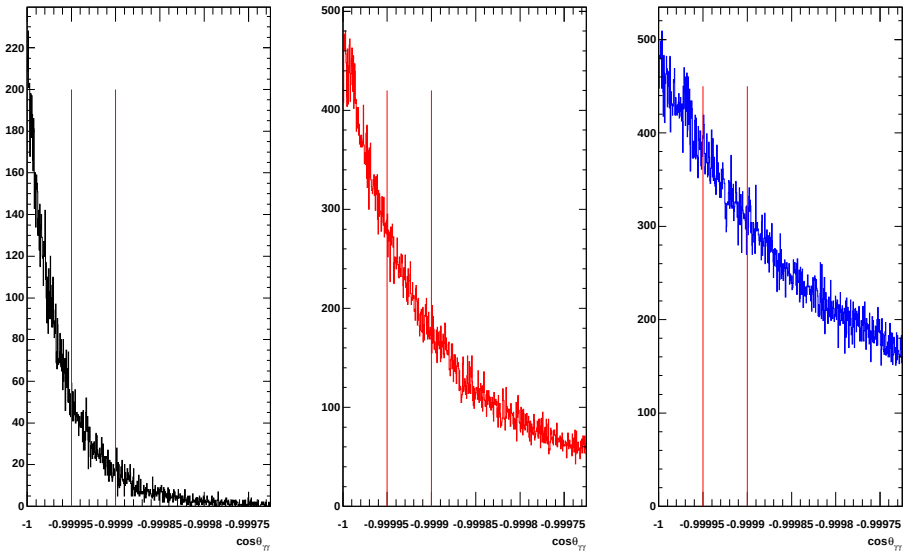

Figure 13.10: Cosine of the angle between two photons in the CMS frame for η_c events (black), $\pi^0\gamma$ events (red) and $\pi^0\pi^0$ events (blue)

EMC-setup	Thresholds	η_c-eff. [%]	π^0 mis-id. [%]	$\pi^0\pi^0$-mis-id. [%]	S/BG
EMC V1BGO	B (3, 15, 20) MeV	13.795	0.1903	0.0035	1.224
	B (3, 15, 30) MeV	13.895	0.2376	0.00504	0.964
	B (3, 15, 50) MeV	14.465	0.3225	0.0101	0.683
EMC V2BGO	B (3, 15, 20) MeV	14.445	0.2073	0.00347	1.193
	B (3, 15, 30) MeV	14.6	0.2579	0.00533	0.938
	B (3, 15, 50) MeV	14.72	0.342	0.01054	0.658
EMC V1PWO	P (5, 20, 25) MeV	13.57	0.2284	0.0049	0.978
	P (10, 35, 50) MeV	14.12	0.3387	0.01234	0.611
EMC V2PWO	P (5, 20, 25) MeV	15.17	0.2574	0.00522	0.979
	P (10, 35, 50) MeV	15.475	0.3767	0.01345	0.605

Table 13.9: Efficiencies and signal/background-ratios for all simulated detector setups and corresponding energy thresholds for cuts on the angle between the two photons $\cos\theta_{\gamma\gamma} < -0.99995$ and the acceptance region $|\cos\Theta^*| < 0.25$

due to an improved split-off suppression (see 12.3.3) by changing the thresholds to higher values. The minimum energy of the photons of the η_c-decay does not fall below $500\,\mathrm{MeV}/c^2$ as can be seen in Fig. 13.9 in contrast to the main background channels. Since a lot of low energetic photons occur below the threshold, the misidentification of $\pi^0\gamma$- and $\pi^0\pi^0$ events increases simultaneously with the η_c efficiency, so that the signal to background ratio gets worse.

A comparison between the different used setups proved to be difficult. It can be seen, that the efficiency of the signal improves by using EMC setup version 2 in contrast to version 1. To give a proper statement about the background rejection within these geometrical settings, it is essential to have an improved reconstruction code.

Variation of the kinematic range $|\cos\Theta^*|$.

The results of the $|\cos\Theta^*|$ scan (in case of the EMC V2 BGO setup version in combination with (3, 15, 20) MeV thresholds and $\cos\theta_{\gamma\gamma} < -0.99995$) can be seen in Table 13.10. The η_c efficiency and also the misidentification of the background grows approximately linear by increasing $|\cos\Theta^*|$. With the currently available reconstruction code it is not yet possible to give a clear estimate of the maximum of the kinematic range, in which a proper η_c reconstruction is still feasible.

$\cos\Theta^*$	η_c-eff. [%]	π^0 mis-id. [%]	$\pi^0\pi^0$-mis-id. [%]
0.2	11.63	0.1651	0.00272
0.25	14.445	0.2073	0.00347
0.3	17.32	0.2515	0.00422
0.35	20.33	0.2917	0.00489
0.4	23.535	0.3331	0.00567

Table 13.10: Efficiencies for the signal and the main background channels in case of EMC V2 BGO, (3, 15, 20) MeV thresholds and $\cos\theta_{\gamma\gamma} < -0.99995$.

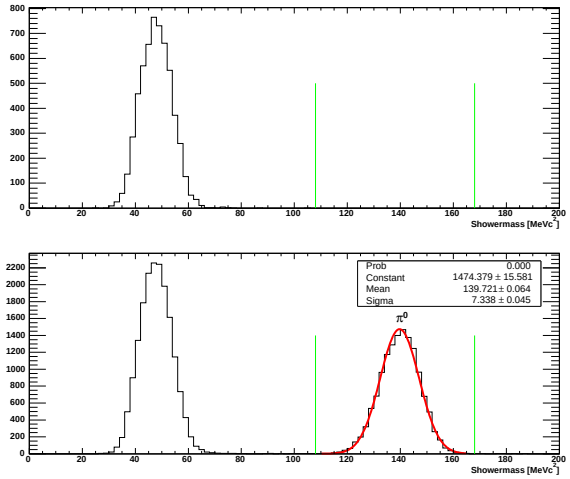

Figure 13.11: Shower-mass of η_c (top) and $\pi^0\gamma$ events (bottom) with $\cos\theta_{\gamma\gamma} < -0.99995$ and $|\cos\Theta^*| < 0.25|$ cut applied to the dataset of EMC V2 BGO with (3, 15, 20) MeV thresholds. The result of fitting the subrange around the π^0 signal is a σ of approximately 7.3 MeV/c^2. The range of 30 MeV/c^2 cutted out around the π^0-mass is marked by lines.

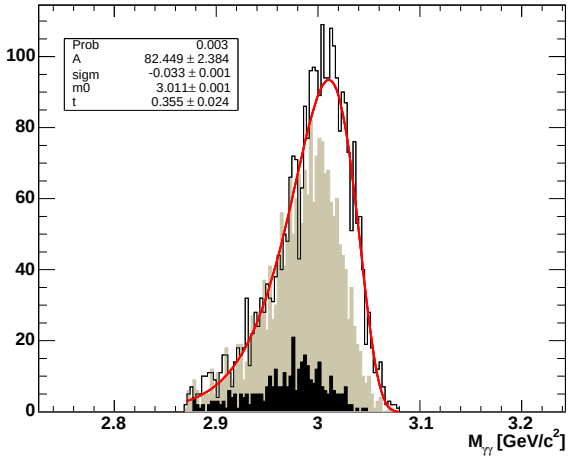

Figure 13.12: Invariant $\gamma\gamma$ mass of all selected events. The solid line denotes events of the η_c decay, the hatched area corresponds to events of the $\pi^0\gamma$- and the black filled area to events of $\pi^0\pi^0$ type. A Novosibirsk fit is applied to the η_c signal (red line).

13.5.3.4 Outlook

The presented results show a clear accretion of the signal to background ratio by reducing the reconstruction thresholds. A disadvantage of doing this is that the electromagnetic split-offs will rise whereby it is a necessity to introduce an elaborated split-off recognition to the current code (based on artificial neural networks for example). Applying a kinematic fit in addition it can be expected, that these modifications would result in a significant improvement of the resolution and background rejection.

13.5.4 Hadronic Charmonium Decays: $\overline{\text{p}}\text{p} \to \eta_c \to K^0_S K^\pm \pi^\mp$

13.5.4.1 Introduction

We generated 10^4 $\overline{\text{p}}\text{p} \to K^0_S K^\pm \pi^\mp$ annihilation events at the η_c energy (antiproton momentum $p = 3.6755\,\text{GeV}/c$), 10^5 $\overline{\text{p}}\text{p} \to 2\pi^+2\pi^-$ and 10^5 $\overline{\text{p}}\text{p} \to K^+K^-\pi^+\pi^-$ events as specific background channels and 10^6 events of generic background.

In the first general selection, we require for each event the reconstruction of 4 charged prongs connected to a vertex, with a charged kaon, a pair of pions with invariant mass in the K^0_S region, and the total invariant mass in the η_c region.

Since the cross section of the $\overline{\text{p}}\text{p} \to \eta_c \to \gamma\gamma$ channel around 3–5 GeV is about 200–300 pb [3, 4] and the branching ratio $\text{BR}(\eta_c \to \gamma\gamma) = (4.4 \pm 1.5)\ 10^{-4}$ [5], it results that

$$\sigma(\overline{\text{p}}\text{p} \to \eta_c) \simeq 500 \text{ nb}. \qquad (13.3)$$

This cross section has been obtained from exper-

imental data measured with a beam spread of 0.3 MeV/c (as also described in Sec.13.5.2.1). It is orders of magnitude larger than the η_c indirect production in e^+e^- annihilation; for example, the $\sigma(e^+e^- \to \psi X \to \eta_c)$ or $\sigma(e^+e^- \to e^+e^-\gamma\gamma \to e^+e^-\eta_c)$ cross sections at 3–5 GeV are of the order of pb [6, 7].

Nevertheless, the $\sigma(\overline{\mathrm{p}}\mathrm{p} \to \eta_c)$ cross section is swamped by the hadronic interaction background: the $\overline{\mathrm{p}}\mathrm{p}$ annihilation cross section at 3.5 GeV is $\simeq$ 25 mb[5], to be compared with the much smaller cross section of η_c production (Eq. 13.3).

Using the branching ratio $\eta_c \to K\overline{K}\pi = 5.7 \pm 1.6\ 10^{-2}$ [5] from (Eq. 13.3) we obtain:

$$\sigma(\overline{\mathrm{p}}\mathrm{p} \to \eta_c \to K^0_S K^\pm \pi^\mp) \simeq 10 \pm 3 \ \text{ nb} \ . \quad (13.4)$$

Knowing the annihilation branching ratios around 3.6 GeV/c momentum of the antiproton [8, 9, 10, 11] the contamination due to the annihilation channels competing with the $\eta_c \to K^0_S K^\pm \pi^\mp$ decay can be evaluated. The results are shown in Table 13.11. In particular, we note the rather uncertain and high value of the direct $\overline{\mathrm{p}}\mathrm{p} \to K^0_S K^\pm \pi^\mp$ production [9]:

$$\sigma(\overline{\mathrm{p}}\mathrm{p} \to K^0_S K^\pm \pi^\mp) = 11 \pm 6 \ \mu\text{b} \ . \quad (13.5)$$

13.5.4.2 Selection

The final selection of the η_c signal is obtained by applying kinematical cuts on total energy and momentum, geometrical cuts on both primary and secondary vertices and the kinematical fit. The cuts are the following:

- particle identification: kaon probability ≥ 0.25
- mass window around the reconstructed η_c peak: $\mid M \mid \leq 0.05\,\mathrm{GeV}/c^2$
- missing energy: $\mid dE \mid \leq 0.1\,\mathrm{GeV}$
- CM momentum of the reconstructed η_c: $p \leq 0.15\,\mathrm{GeV}/c$
- reduced χ^2 of the fit of $K^\pm$ and $\pi^\mp$ to a common vertex: $\chi^2_r \leq 5.0$
- z coordinate of the primary vertex: $\mid Z \mid \leq 0.4\,\mathrm{mm}$
- radial distance between the beam axis and the primary vertex: $d \leq 0.4\,\mathrm{mm}$
- z coordinate of the secondary vertex: $z \geq 2.0\,\mathrm{mm}$
- distance between the primary vertex and the K^0_S trajectory: $D \leq 1.5\,\mathrm{mm}$

The simulations have been made with two different setups: the STT and the TPC. In the simulation with the STT setup the particle identification is provided only by the Cherenkov (DIRC and RICH), while in the TPC setup both Cherenkov counters and TPC have been used for PID.
The η_c signal obtained from the selected events is shown in Fig. 13.13 (STT setup) and Fig. 13.14 (TPC setup). In Table 13.12 a summary of the effect of the cuts on the data is shown.

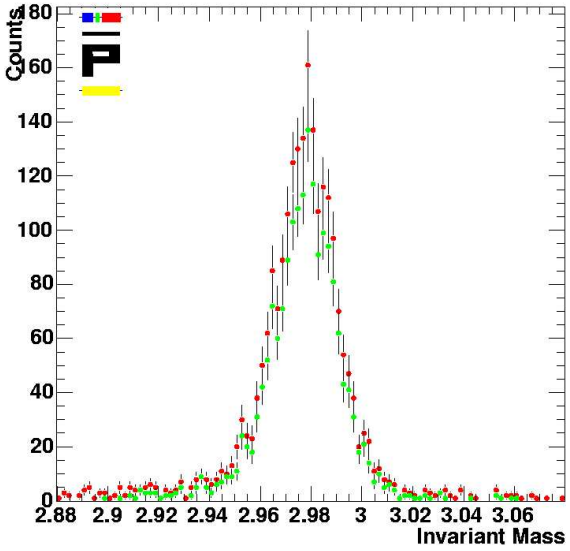

Figure 13.13: The red histogram shows the invariant mass without any cut, the green one shows the invariant mass with all the cuts applied (STT).

13.5.4.3 Results

The final number of events passing our selection criteria is shown in the last column of Table 13.13, where we see that, apart from the non resonant $K^0_S K^\pm \pi^\mp$ background, no $K^+K^-\pi^+\pi^-$ and $2\pi^+2\pi^-$ event survives after the cuts over a total of 10^5 generated events. This corresponds to a $CL = 90\%$ upper limit of $2.3 \cdot 10^{-5}$ for the contamination probability by these two background reactions. Considering the cross sections of Table 13.11, it results that their contribution to the total background is less than $2 \cdot 10^{-3}$.
Concerning the reconstruction efficiency, it is higher with the TPC because it is able to provide particle identification for low energy kaons.

Therefore, the background consists almost completely by the non-resonant $\overline{\mathrm{p}}\mathrm{p} \to K^0_S K^\pm \pi^\mp$ chan-

reaction	cross section	ratio S/N	$\overline{\text{p}}$ Mom. GeV/c	ref.
$\sigma_S \equiv \sigma(\eta_c \to K^0_S K^\pm \pi^\mp)$	10 ± 3 nb	-	$\simeq 3.6$	–
$\sigma_B \equiv \sigma(\overline{\text{p}}\text{p} \to K^0_S K^\pm \pi^\mp)$	11 ± 6 μb	1/1100	3.66	[9]
$\overline{\text{p}}\text{p} \to 2\pi^+ 2\pi^-$	430 ± 30 μb	1/40000	3.59	[10]
$\overline{\text{p}}\text{p} \to K^+ K^- \pi^+ \pi^-$	240 ± 30 μb	1/24000	2.90	[11]

Table 13.11: Comparison between the $\overline{\text{p}}\text{p} \to \eta_c \to K^0_S K^\pm \pi^\mp$ channel to other background final states.

Cut	STT	TPC
no cut	2 638	6 046
cuts on energy and momentum	2 216	4 837
cuts on primary vertex	2 015	4 244
all cuts	1 802	2 922

Table 13.12: Summary of the effect of the cuts applied on the signal data (10^4 generated events). The table shows the number of reconstructed events after each cut.

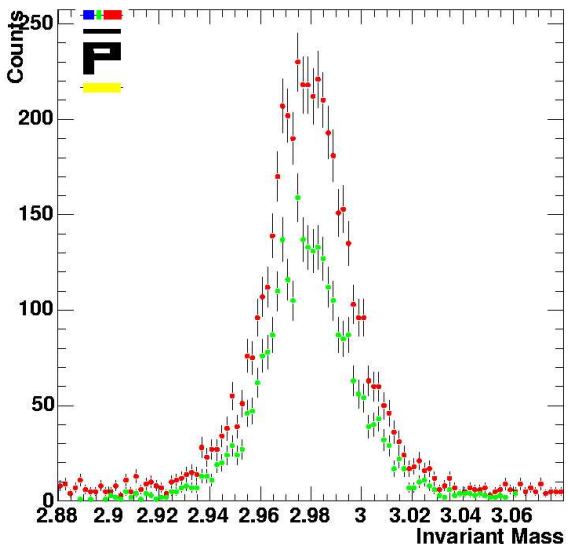

Figure 13.14: The red histogram shows the invariant mass without any cut, the green one shows the invariant mass with all the cuts applied (TPC).

nel. To evaluate the time necessary to have a significant η_c peak over this background, we use the formula

$$n_\sigma = Lt\epsilon\sigma_S / \sqrt{Lt\,\epsilon\sigma_S + Lt\,\epsilon\sigma_B}\ ,$$

where n_σ is the significance level, σ_S and σ_B are from Table 13.11, $L \simeq 10^{32}$ cm^{-2} s^{-1} is the luminosity, t is the run time and ϵ indicates the reconstruction efficiency for this reaction. With $n_\sigma = 5$ we obtain:

$$t = \left[25 \frac{\sigma_S + \sigma_B}{\sigma_S^2} \frac{1}{L}\right] \frac{1}{\epsilon} \simeq \frac{8 \text{ hours}}{\epsilon}\ . \qquad (13.6)$$

The simulation shows a $K^0_S K^\pm \pi^\mp$ reconstruction efficiency of at least about 20%. Neglecting the trigger efficiency it results that a clear peak over the background can be obtained in 40 hours of beam time.

13.5.5 Crossed-channel Compton Scattering: $\overline{\text{p}}\text{p} \to \gamma\gamma$

13.5.5.1 Introduction

As described in Chap. 2.6.2, crossed-channel wide angle Compton scattering (WACS) $\overline{\text{p}}\text{p} \to \gamma\gamma$ is one of the prime QCD processes to study Generalized Parton Distributions in $\overline{\text{p}}\text{p}$ annihilation. The two photon final state has a unique signature which in principle can be easily triggered and selected in the $\overline{\text{P}}$ANDA experiment. The only difficulty is the smallness of the cross section which makes it difficult to sufficiently suppress the large competing background.

The trigger of the process can be composed from two energy deposit signals in the electromagnetic calorimeter which sum up to about the total beam energy and a veto for any charged track in any of the tracking detectors. This trigger will already suppress any events with charged particles and most of the background with π^0's in the final state. Due to the abundance of π^0's in $\overline{\text{p}}\text{p}$ collisions, the two processes $\overline{\text{p}}\text{p} \to \pi^0\gamma$ and $\overline{\text{p}}\text{p} \to \pi^0\,\pi^0$ are the dominant background sources which have to be suppressed by additional cuts. There are three most important cuts to distinguish $\gamma\gamma$ events from pion background:

1. There are exactly two energy clusters in the electromagnetic calorimeters,
2. those two clusters are collinear in the CMS frame,

Events	generated	general selection	kinematical selection
STT:			
Signal (final state)			
$\overline{\mathrm{p}}\mathrm{p} \to K_S^0 K^{\pm}\pi^{\mp}$	10^4	2 638	1 802
Background			
$\overline{\mathrm{p}}\mathrm{p} \to K^+K^-\pi^+\pi^-$	10^5	3	0
$\overline{\mathrm{p}}\mathrm{p} \to 2\pi^+2\pi^-$	10^5	0	0
DPM	10^6	2	0
TPC:			
Signal (final state)			
$\overline{\mathrm{p}}\mathrm{p} \to K_S^0 K^{\pm}\pi^{\mp}$	10^4	6 046	2 922
Background			
$\overline{\mathrm{p}}\mathrm{p} \to K^+K^-\pi^+\pi^-$	10^5	3	0
$\overline{\mathrm{p}}\mathrm{p} \to 2\pi^+2\pi^-$	10^5	0	0
DPM	10^6	1	0

Table 13.13: Number of particles surviving after the selection procedures discussed in the text with the two different setups.

3. and each of the two clusters has an energy in the CMS frame which is equal to half of the total CMS energy.

From the physics point of view an additional cut has to be applied: $\gamma\gamma$ events can only be interpreted in perturbative QCD when there is a large transverse momentum transfer from the quarks to the photons. This is equivalent to requiring a cut of about $45° < \theta^* < 135°$ on the polar angle in the CMS frame. The interesting quantities to measure are the angular and energy dependences of the absolute $\overline{\mathrm{p}}\mathrm{p} \to \gamma\gamma$ cross sections.

13.5.5.2 Selection

For the Monte Carlo simulation an energy of $s = 13\,\mathrm{GeV}^2$ has been selected, as for this energy there exist measurements of the background processes [12]. The signal $\overline{\mathrm{p}}\mathrm{p} \to \gamma\gamma$ is simulated using the model as described in Ref. [13], however the cross section is scaled with a factor of 22.1 according to the fits to e^+e^- data in Ref. [14]. The background processes $\overline{\mathrm{p}}\mathrm{p} \to \pi^0\gamma$ and $\overline{\mathrm{p}}\mathrm{p} \to \pi^0\,\pi^0$ were simulated according to the cross section measurements from [12]. In the simulation a calorimeter cluster is identified with an energy threshold of 20 MeV. The following cuts were applied:

- number of reconstructed elm. clusters $N_{Cl} = 2$
- relative angle of the 2 clusters (in CMS) $\theta^*_{\gamma\gamma} > 179.28°$
- total energy $E^*_{\gamma\gamma} > 3.45\,\mathrm{GeV}$
- individual energy $E^*_{\gamma} > 1.7\,\mathrm{GeV}$
- polar angle $|\cos(\theta^*_{\gamma})| < 0.6$

13.5.5.3 Results

The results of a first the MC simulation are listed in Table 13.14. These preliminary results yield a signal which is contaminated by 45% from $\pi^0\gamma$ and $\pi^0\pi^0$ background. There is a large uncertainty in the relative cross sections and therefore the results are still uncertain. More sophisticated cuts have to be applied to improve the ratio of signal/background. One option is to assign to each calorimeter cluster an invariant mass and reject the cluster if it is equal to the pion mass. Another option is to refine the cluster algorithm to reduce the number of cluster splits for individual photons and to reduce the number of cases where two photons are reconstructed as one photon. The count rates for a 15 pb $\gamma\gamma$ cross section correspond to $\dot{N} = 0.003/\mathrm{s} = 7\,776$ events/month at a luminosity of $L = 2 \cdot 10^{32}\mathrm{cm}^{-2}\mathrm{s}^{-1}$. At larger beam energies, the count rates will decrease, but the signal/background ratio is expected to improve significantly as the cross sections of the background processes fall faster with energy than the one of the signal process. This has to be verified by Monte Carlo.

To conclude, it appears that WACS cross sections can be separated from background processes for en-

	$\gamma\gamma$	$\pi^0\gamma$	$\pi^0\pi^0$
generated events	10 000	10 000	100 000
events with 2 clusters	7 081	982	1 404
events after all cuts	5675	91	17
surviving yield	56.7%	0.9%	0.017%
estimated cross section (pb)	15	420	17 500
accepted cross section after cuts (pb)	8.5	3.78	2.98
relative contributions	55%	25%	20%

Table 13.14: The simulation of WACS events shows that the background can be efficiently suppressed without loosing the signal events.

ergies larger than $s \geq 13\text{GeV}^2$ with the set-up used in the current Monte Carlo version. Most important for the identification of WACS events is a fast electromagnetic calorimeter with good energy and angular resolution and a low energy threshold. The good energy and angular resolution and the low energy threshold is important for separating asymmetric pion decays from photon signals. The calorimeter has to be fast as due to the large luminosity of $\overline{\text{P}}$ANDA a slow calorimeter adds signals from previous events to the current trigger which jeopardize the cluster cuts.

13.5.6 Open Charm Production: $\overline{\text{p}}\text{p} \rightarrow \psi(3770) \rightarrow D\overline{D}$

13.5.6.1 Introduction

The study of the charmonium spectrum above the $D\overline{D}$ breakup threshold at 3.73 GeV/c^2 is the one important part of the $\overline{\text{P}}$ANDA physics program. The capability of the current $\overline{\text{P}}$ANDA design to detect the reaction $\overline{\text{p}}\text{p} \rightarrow \psi(3770) \rightarrow D\overline{D}$ has been studied for the decay channel $D \rightarrow K\pi\pi$.

One should notice, that this reaction was already studied in details as reflected in [15]. The call for a repetition of this studies is imposed by the changes in the detector implementation and an improvement in the particle identification. The scenario of this analysis generally repeats what is given in that note.

The dominant channel for the $\psi(3770)$ decay is a s-wave 2-body decay into $D\overline{D}$ pair [5], where both D mesons have a momentum of 276 GeV/c in CMS. D mesons has a relatively long lifetime of $c\tau = 311.8\,\mu$m. Therefore special emphasis has been placed on the MVD, since this is the most selective detector component in this analysis.

D mesons have many possible decay channels, some of them are listed in Table 13.15. For the further analysis only the channel $D^{\pm} \rightarrow K^{\mp}\pi^{\pm}\pi^{\pm}$ has been chosen ,because it can be reconstructed using only the tracking and PID information. Channels with a $\overline{K}^0$ have a much smaller reconstruction efficiency and because of that they will be analyzed in the future.

Decay channels	Branching ratio
$K^-\pi^+\pi^-$	9.2%
$\overline{K}^0\pi^+$	2.9%
$\overline{K}^0\pi^+\pi^0$	9.7%
$\overline{K}^0\pi^+\pi^+\pi^-$	9.7%

Table 13.15: Decay modes with branching ratio for the D^+ meson decays.

The yield of this channel can be estimated using Breit-Wigner formula [4] for the resonance cross section:

$$\sigma_R(s) \equiv \frac{4\pi(\hbar c)^2}{(s - 4m_p^2c^4)} \frac{B_{in}B_{out}}{1 + [2(\sqrt{s} - M_Rc^2)/\Gamma_R]^2} \tag{13.7}$$

where M_R and Γ_R are the mass and the full width of the resonance, m_p is the proton mass and the amplitude proportional to the product of $B_{in} \equiv B(\psi(3770) \rightarrow \overline{\text{p}}\text{p})$ and $B_{out} \equiv B(\psi(3770) \rightarrow D^+D^-)$. The branching ratio $B(\psi(3770) \rightarrow \overline{\text{p}}\text{p})$ can be estimated as follows:

$$\begin{aligned} B_{in} &\equiv B(\psi(3770) \rightarrow \text{p}\overline{\text{p}}) = \\ &= B(J/\psi \rightarrow \text{p}\overline{\text{p}}) \cdot \Gamma_{J/\psi}/\Gamma_{\psi(3770)} = \\ &= 2.12 \times 10^{-3} \times \frac{91\,\text{keV}}{23\,\text{MeV}} = 8.4 \times 10^{-6}, \end{aligned}$$

$$B_{out} \equiv BR(\psi(3770) \rightarrow D^+D^-) \simeq 44\%$$

For the condition $\sqrt{s} = M_Rc^2$ that results in:

$$\sigma(\overline{\text{p}}\text{p} \rightarrow \psi(3770) \rightarrow D^+D^-) \simeq 3.25\,\text{nb}$$

The branching ratio is [5]:

$$BR(D^{\pm} \rightarrow K^{\mp}\pi^{\pm}\pi^{\pm}) \simeq 0.092$$

and the total cross section of this channel is:

$$\sigma(\overline{\mathrm{p}}\mathrm{p} \to \psi(3770) \to D^+D^- \to K^\mp\pi^\pm\pi^\pm) \simeq 27.5\,\mathrm{pb}$$

Finally the signal to background ratio, which one has to refine, equals:

$$\frac{\sigma(signal)}{\sigma(\overline{\mathrm{p}}\mathrm{p} \to X)} = \frac{2.75\cdot 10^{-11}}{4.5\cdot 10^{-2}} = 6.1 \times 10^{-10}$$

with supposed a $\overline{\mathrm{p}}\mathrm{p}$ inelastic cross section of 45 mb, and a 100% suppression of elastic events.

13.5.6.2 Selection

Single D meson selection.
The performance of the $D^\pm \to K^\mp\pi^\pm\pi^\pm$ selector has been studied by simulating 1 000 events with exactly one D meson. The setup with the STT as tracker has been used in the simulation. These mesons were generated with 3.3 GeV/c momentum, which corresponds to half the beam momentum for a formation experiment of the $\psi(3770)$. In the Monte Carlo the physical parameters of the D mesons were modified to force a decay in every event to occur at the location (0.1, 0.1, 0.4) mm with respect to the nominal target position. The invariant mass of $D^\pm$ has been calculated using the standard selector.

The resolution for the three particle tracks vertex is presented in Figs. 13.15 and 13.16. In Fig. 13.15 the transverse distance of the vertex to the beam axis is given. The mean location of 0.152 mm is in good agreement with the expected value of $\sqrt{2} \times 0.1$ mm. The longitudinal vertex distribution is presented in Fig. 13.16. Here it is apparent, that the vertex location is systematically shifted backwards from the expected location of 0.4 to 0.38 mm. This results from the small angle scattering, that is not yet correctly accounted for in the single track fit. The resolution of the vertex is about 49 μm in the transverse and 49 μm in the longitudinal directions.

An efficiency of 27% for reconstruction with PID is determined from this analysis. The efficiency with the TPC as the main tracker should be significantly higher.

D^+D^- pair selection.
The next step was the analysis of the data samples with 50 000 signal events. The incoming antiproton beam momentum was 6.56863 GeV/c. The beam momentum spread and the width of the $\psi(3770)$ were assumed to be zero. Because of that the width of the D^+D^- invariant mass distribution should directly give detector mass resolution.

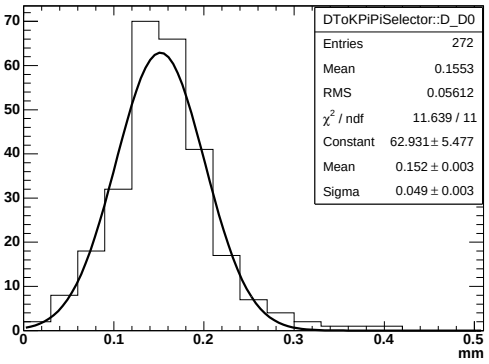

Figure 13.15: Distribution of the transverse distance (mm) of the vertex location to the beam axis.

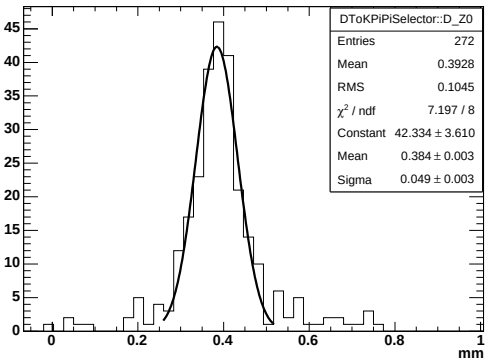

Figure 13.16: Distribution of the longitudinal distance (mm) of the vertex location to the target location.

Several cuts on kinematics and geometry together with the PID cut have been applied to obtain the $\psi(3770)$ invariant mass distribution.

The vertex location of the D meson candidate was determined by refitting the single tracks from an one kaon and two pions under the condition that they have a common vertex. After selecting D candidates that have $|M_{inv,K\pi\pi} - M_D| < 0.015\,\mathrm{GeV}/c^2$ and $0.1 < V_z < 2.0$ mm, a cut at $\chi^2/dof < 10$ is imposed, which together with the V_z cut strongly suppresses background events. One should notice that, despite of the good spatial resolution, the cut in the displacement the D vertex in that direction will not be very useful, because of the very low transverse momentum of the produced D mesons. Finally, the condition that at least two D candidates with opposite charge are required for the reconstruction of the $\psi(3770)$ have been applied to reduce the background. All cuts are listed in details in Table 13.16.

¿From the vertex location and the D meson momentum, the proper lifetime distribution can be calculated. An exponential fit to the distribution results

Cut	Value
1 kaon with likelihood	≥ 0.4
D mass window	$\lvert M_{inv,K\pi\pi} - M_D \rvert \leq 0.015\,\text{GeV}/c^2$
distance of vertex from IP	$0.1 < V_z < 2.0\,\text{mm}$
vertex fit: reduced χ^2	≤ 10

Table 13.16: Cut parameters for the $D\overline{D}$ pair selection.

in a lifetime of $294 \pm 3\,\mu$m, compared to the input of $311\,\mu$m. This systematic error is a result of small angle scattering, as mentioned in the previous subsection in the longitudinal vertex location of D mesons.

13.5.6.3 Results

D^+D^- pair reconstruction.
In Figs. 13.17 and 13.18 the invariant mass distributions for the $\psi(3770)$ are shown reconstructed from 50 000 signal events without background. The invariant mass resolutions for the STT and TPC options of the tracker from the Gaussian fit are found to be:

$$\sigma^{STT}_{\psi(3770)} = 10\,\text{Mev}/c^2$$

$$\sigma^{TPC}_{\psi(3770)} = 14\,\text{Mev}/c^2$$

The invariant mass resolution for the TPC option is significantly worse due to the fact that only about 2% TPC cluster have been used for the track fit to speed up the reconstruction (see Sec. 12.3.3.2).

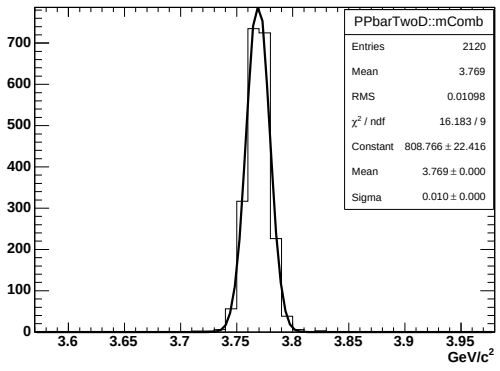

Figure 13.17: Reconstructed $\psi(3770)$ mass (STT).

The total reconstruction efficiencies for the $\psi(3770)$ are:

$$\epsilon^{STT}_{\psi(3770)} \simeq 4.2\%$$

$$\epsilon^{TPC}_{\psi(3770)} \simeq 4.6\%$$

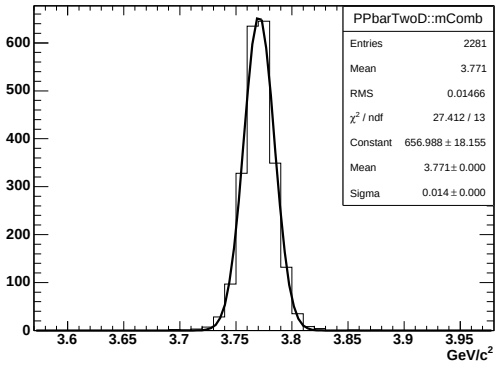

Figure 13.18: Reconstructed $\psi(3770)$ mass (TPC).

Background suppression.
To estimate the signal to background ratio for the $\psi(3770)$ reconstruction, one million background events have been calculated with the DPM code, and then tracked through the detector. Unfortunately these data are only available for the STT tracker option, so one can't judge about the background suppression using TPC. The results of the cuts applied to the data are shown in Table 13.17.

The fact that no events in this background sample contain a valid D^+D^- pair is unfortunately not very significant, since there will be many orders of magnitude more background events per signal event than included in this data sample. To examine the effect of the additional selection criteria, the D meson identification criteria have been relaxed. First, the invariant mass window has been widened to $\lvert M_{inv,K\pi\pi} - M_D \rvert \leq 0.5\,\text{GeV}/c^2$, then the vertex condition to $0 < V_z < 2.0\,\text{mm}$ has been changed. As a result, in total of 4 483 D meson candidate are found and two events have both a D^+ and D^- candidate.

Thus, a conservative estimate of the peak to back-

Cut	STT		TPC
	signal	DPM	signal
	5×10^4	10^6	5×10^4
kaon ID	71 618	13 488	105 893
D mass window	30 455	1 220	32 577
distance of vertex from IP	237 681	246	25 250
vertex fit: reduced χ^2	22 416	199	23 247
$\psi(3770)$ momentum in CMS	2 120	0	2281

Table 13.17: Cut yields for the TPC and the STT option.

ground ratio can be estimated as follows:

$$\begin{aligned}\frac{signal}{background} &= \frac{\sigma_{signal}}{\sigma_{background}} \times BR^2 \times \frac{\epsilon_{signal}}{\epsilon_{background}} \\ \frac{signal}{background} &= \frac{3.25 \times 10^{-9}}{45 \times 10^{-3}} \times (0.091)^2 \times \\ &\times \quad 0.042 / \left[\frac{2}{1\,000\,000} \times \left(\frac{199}{4\,483} \right)^2 \right] \\ &= 6.4 \times 10^{-3}\end{aligned}$$

In addition one can get a factor of 500 if a missing mass cut will be applied $|(M^{DD}_{miss})^2| < 0.002\,\mathrm{GeV}^2/c^4$ [15]. Therefore, finally one can get:

$$\frac{signal}{background} \simeq 3$$

This results must be treated with upmost care, due to the assumptions involved in determining $\sigma_{background}$ and $\epsilon_{background}$. Further studies with larger data samples are needed to get a more reliable result.

Finally, from this equation one can also estimate that only about 1 out of 10^{12} events will contain a reconstructed D^+D^- pair, and thus an extremely selective trigger is needed.

13.5.7 Open Charm Production: $\overline{\mathrm{p}}\mathrm{p} \rightarrow \psi(4040) \rightarrow D^{*+}D^{*-}$

13.5.7.1 Introduction

Another interesting state above the $D\overline{D}$ breakup threshold at $3.73\,\mathrm{GeV}/c^2$ is $\psi(4040)$. It has been discovered by the DASP detector at DESY in 1978 in e^+e^- collision, but later was not confirmed by the BES Collaboration. Presumably, this resonance should mostly decay into D and D^* mesons. The decay mode $\psi(4040) \rightarrow D^*(2010)^+D^*(2010)^-$ has been chosen for this analysis.

The $D^{*\pm}$ meson can decay into $D^\pm\pi^0$ or $D^0\pi^\pm$ pairs. The decay mode $D^{*\pm} \rightarrow D^0\pi^\pm$ has a branching ratio of 67.7%. A clear signature for this decay is the presence of slow charged pions, as shown in the Fig. 13.19. These pions have a very small transverse momentum and are emitted within a cone with an opening angle $< 30°$. As a result their detection is based only on the information from the forward MVD part. One should remember that D^0 mesons have a lifetime of $c\tau = 123\,\mu$m, which is three times shorter than for $D^\pm$. All that imposes especially high demands on the MVD performance.

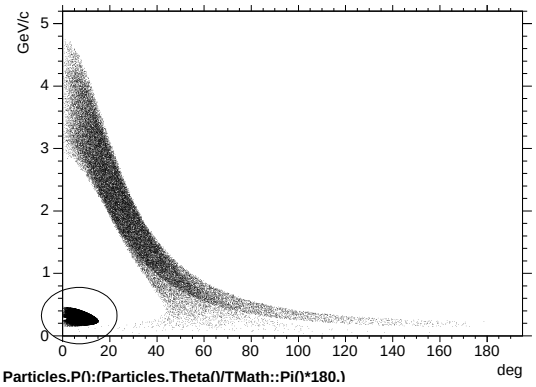

Figure 13.19: The distribution of momentum vs. polar angle of the final state kaons and pion from reaction $\psi(4040) \rightarrow D^{*\pm} \rightarrow D^0\pi^+\overline{D}^0\pi^- \rightarrow K^\mp\pi^\pm\pi^\pm$. The slow pions from D^* decays concentrate into the lower left corner (outlined by the ellipse).

Decay channels	Branching ratio
$K^-\pi^+$	3.8%
$K^-\pi^+\pi^-\pi^+$	7.46%
$\overline{K}^0\pi^+\pi^-$	5.97%
$K^-\pi^+\pi^0$	13.0%

Table 13.18: Decay modes with branching ratio for the D^0 meson decays.

Furthermore, D^0 has a lot of decay modes, but only a few of them can be used for the analysis(see Ta-

ble 13.18). The first two decays are chosen for the further studies. The cross section for this process can be estimated, using the same Eq. 13.7 as for $\psi(3770)$. The B_{in} and B_{out} can be estimated as:

$$\begin{aligned} B_{in} &\equiv B(\psi(4040) \to \mathrm{p\overline{p}}) = \quad (13.8)\\ &= B(J/\psi \to \mathrm{p\overline{p}}) \cdot \Gamma_{J/\psi}/\Gamma_{\psi(4040)} = \\ &= 2.12 \times 10^{-3} \cdot 91\,\mathrm{keV}/52\,\mathrm{MeV} \\ &= 3.7 \times 10^{-6}, \\ B_{out} &\equiv BR(\psi(4040) \to D^{*\pm} \to D^0\pi^+\overline{D}^0\pi^-) \simeq \\ &\simeq 0.5 \times 0.67 \simeq 0.33 \quad (13.9) \end{aligned}$$

Based on Eq. 13.8 and Eq. 13.9 the result is:

$$\sigma(\mathrm{\overline{p}p} \to \psi(4040) \to D^{*\pm} \to D^0\pi^+\overline{D}^0\pi^-) \simeq 0.47\,\mathrm{nb}$$

Taken into account the summary branching ratios for the chosen decays one can get:

$$\sigma(\mathrm{\overline{p}p} \to \psi(4040) D^{*\pm} \to D^0\pi^{\pm}) \simeq 6\,\mathrm{pb}$$

The resulting signal to background ratio is:

$$\frac{\sigma(signal)}{\sigma(\mathrm{\overline{p}p} \to X)} = \frac{6 \cdot 10^{-12}}{4.5 \cdot 10^{-2}} = 1.3 \times 10^{-10}$$

where a $\mathrm{\overline{p}p}$ inelastic cross section of 45 mb and a 100% suppression of elastic events are supposed.

13.5.7.2 Selection

The selection algorithm for the $\psi(4040)$ is similar to the $\psi(3770)$ (see Sec. 13.5.6.2). The selection algorithm includes following steps:

1. kaon selection,
2. reconstruction of D^0,
3. reconstruction of D^*,
4. reconstruction of $\psi(4040)$.

Several cuts on invariant masses and geometry together with the PID cut were applied during analysis. All of them are listed in the Table 13.19.

A sample of 5×10^4 signal events have been processed to tune this cuts. The results of these cuts applied to the 10^6 background events from the DPM event generator are shown in Table 13.20.

13.5.7.3 Results

Slow π reconstruction.
The ability of the MVD to reconstruct slow high ionizing particles has been tested using the slow pions from D^* mesons decays (see Fig. 13.19). In spite of the relatively high multiple scattering, the momentum resolution is good as can be seen on Fig. 13.20. The peak asymmetry on this figure is most likely due to the relatively high energy loss and the small angle scattering which is not yet taken into account.

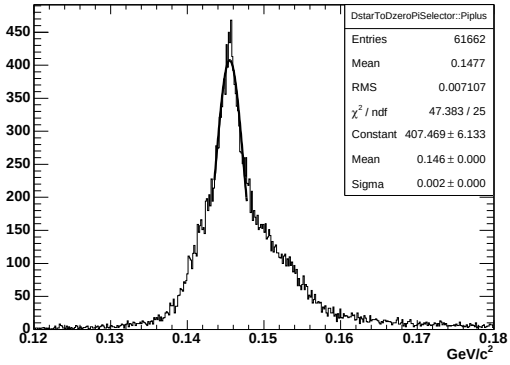

Figure 13.20: The difference between the invariant masses of D^{*+} and D^0 mesons. This difference is proportional to the momentum resolution of the MVD for the slow pions from D^* decays.

$D^{*+}D^{*-}$ pair reconstruction.
In Figs. 13.21 and 13.22 the invariant mass distribution for the $\psi(4040)$ are shown reconstructed from 50 000 signal events in the $D^0 \to K^-\pi^+$ channel without background. The invariant mass resolutions for the STT and TPC options of the tracker from the Gaussian fit are found to be:

$$\sigma^{STT}_{\psi(4040)} = 19\,\mathrm{MeV}/c^2$$
$$\sigma^{TPC}_{\psi(4040)} = 24\,\mathrm{MeV}/c^2$$

which are comparable with the natural width of this resonance. The invariant mass distributions for the $D^0 \to K^-\pi^+\pi^-\pi^+$ channel are shown on the Figs. 13.23 and Fig. 13.24. The visible peak asymmetry is most likely due to the combinatorial background, which is much higher for this channel. The invariant mass resolution for the TPC option is significantly worse due to this fact that only about 2% of the TPC clusters have been used for the track fit to speed up the reconstruction (see Sec. 12.3.3.2). The total reconstruction efficiencies for the $\psi(4040)$ in the $D^0 \to K^-\pi^+$ channel are:

$$\epsilon^{STT}_{\psi(4040)} \simeq 10.4\%$$

Cut	Value
1 kaon with likelihood	≥ 0.4
D^0 mass window	$\lvert M_{inv} - M_{D^0}\rvert \leq 0.05\,\mathrm{GeV}/c^2$
distance of vertex from IP	$0.1 < V_z < 2.0\,\mathrm{mm}$
reduced χ^2 of the vertex fit	≤ 4
D^* mass window	$\lvert M_{inv} - M_{D^*}\rvert \leq 0.07\,\mathrm{GeV}/c^2$

Table 13.19: Cut parameters for the $D^{*+}D^{*-}$ pair selection.

Cut	STT			TPC		
	signal		DPM	signal		DPM
	$K\pi$	$K3\pi$	total	$K\pi$	$K3\pi$	total
	5×10^4	5×10^4	10^6	5×10^4	5×10^4	10^6
kaon ID	102 422	733 539	213 626	104 386	771 390	602 932
D^0 mass window and distance of vertex from IP	33 022	85 804	5 899	37 658	73 705	12 787
vertex fit: reduced χ^2	32 414	47 233	4 053	37 383	35 780	7 360
D^* mass window	48 990	46 252	1 626	59 708	70 044	4 598
$\psi(3770)$ momentum in CMS	5 185	555	0	8 398	4 368	0

Table 13.20: Cut yields for the TPC and the STT option.

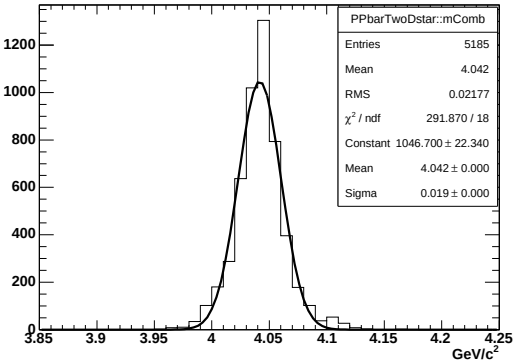

Figure 13.21: Reconstructed $\psi(4040)$ mass in the $D^{*+} \to D^0\pi^+ \to K^-\pi^+\pi^+$ channel (STT).

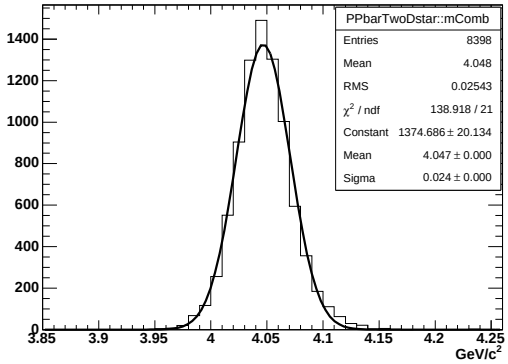

Figure 13.22: Reconstructed $\psi(4040)$ mass in the $D^{*+} \to D^0\pi^+ \to K^-\pi^+\pi^+$ channel (TPC).

$$\epsilon^{TPC}_{\psi(4040)} \simeq 16.8\%$$

The efficiencies for the $D^0 \to K^-\pi^+\pi^-\pi^+$ channel are:

$$\epsilon^{STT}_{\psi(4040)} \simeq 1.1\%$$

$$\epsilon^{TPC}_{\psi(4040)} \simeq 8.7\%$$

The significantly higher efficiency for TPC can be explained by the higher kaon PID efficiency.

Background suppression.

Due to the limited statistics available for the background studies one can set only upper limits for the signal to background ratio:

$$\frac{signal}{background} = \frac{\sigma_{signal}}{\sigma_{background}} \times BR^2 \times \frac{\epsilon_{signal}}{\epsilon_{background}}$$

$$\frac{signal}{background} > \frac{0.47 \times 10^{-9}}{45 \times 10^{-3}} \times (0.112)^2 \times \times \quad 0.04/10^{-6} = 5.5 \times 10^{-6} \quad \text{(STT)}$$

$$\frac{signal}{background} > \frac{0.47 \times 10^{-9}}{45 \times 10^{-3}} \times (0.112)^2 \times \times \quad 0.12/10^{-6} = 1.5 \times 10^{-5} \quad \text{(TPC)}$$

One also should keep in mind the additional factor of 500 provided by the missing mass cut (see Sec. 13.5.6.3). So one can expect:

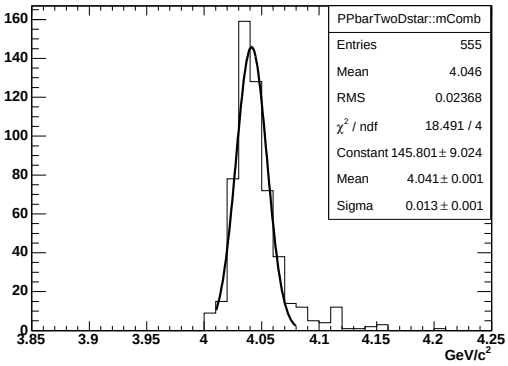

Figure 13.23: Reconstructed $\psi(4040)$ mass in the $D^{*+} \to D^0\pi^+ \to K^-3\pi^+\pi^-$ channel (STT).

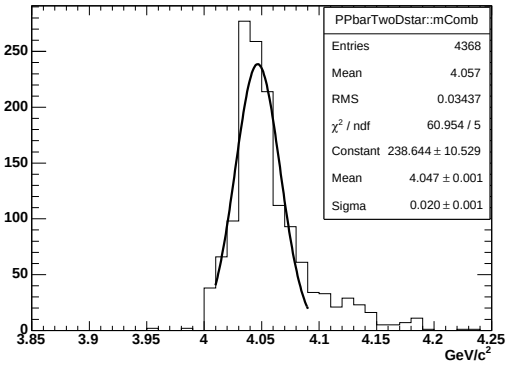

Figure 13.24: Reconstructed $\psi(4040)$ mass in the $D^{*+} \to D^0\pi^+ \to K^-3\pi^+\pi^-$ channel (TPC).

$$\frac{signal}{background} > 2.7 \times 10^{-3} \quad \text{(STT)}$$

$$\frac{signal}{background} > 7.5 \times 10^{-3} \quad \text{(TPC)}$$

These results should be taken only as a lower limits. Higher statistics are needed to provide more reliable results.

13.5.8 Strange Baryon Production: $\overline{\text{p}}\text{p} \to \Lambda\overline{\Lambda} \to \text{p}\pi^-\overline{\text{p}}\pi^+$

13.5.8.1 Introduction

The reaction $\overline{\text{p}}\text{p} \to \Lambda\bar{\Lambda}$ with beam momenta of 4.0,6.0,7.7 GeV/c was simulated. Two setup scenarios were investigated: one setup used the straw tube trackers (STT) and the other one used the time projection chambers (TPC). The Λ and the $\overline{\Lambda}$ particles were produced isotropically in the CM frame, without any decay asymmetry.

The decays $\Lambda \to \text{p}\pi^-$ and $\overline{\Lambda} \to \overline{\text{p}}\pi^+$ were studied. Possible background arises from a wrong particle ID assumption of $\text{p}\pi^+$ and $\overline{\text{p}}\pi^-$ respectively. The PID information was used for proton and pion identification.

At the beam momenta considered, Λ and $\overline{\Lambda}$ were emitted in the laboratory frame at angles between 0° and 35° for the lowest beam momentum and between 0° and 55° for the higher momenta.

13.5.8.2 Selection

The following cuts have been applied for the selection of $\Lambda\overline{\Lambda}$ events:

- χ^2 of the refitted decay vertex $<$ 5.0 ($\sim$5% event reduction)
- Λ $\bar{\Lambda}$ decay vertex Z coordinate between -2.0 mm and 350.0 mm ($\sim$5% event reduction)
- Angle between Λ and $\overline{\Lambda}$ momentum and the direction of the vector between primary and secondary vertex $< 1°$ ($\sim$5% event reduction)
- Λ, $\overline{\Lambda}$ mass window of 0.003GeV/c^2 ($\sim$1% event reduction)

13.5.8.3 Results

The Λ proper lifetime was studied. The reconstructed $c\tau$ value is found to be (70 ± 5.9) mm while the PDG one is 78.9 mm. Although in the retracking the energy loss in every detector is taken in account, there is still some discrepancy that needs to be studied.

The Λ invariant mass for the beam momentum of 4.0 GeV/c, normalized to 10 000 generated events, is presented in fig.13.25, obtained with the STT setup, and Fig. 13.26 obtained with the TPC setup, respectively.

With the STT setup, currently the reconstruction efficiency is only of the order of 25%, which might be due to a loss of low momentum pions in the reconstruction procedure. Clearly, further optimization needs to be done. Using the STT setup, the reconstruction efficiency of $\overline{\Lambda}$ is lower by 10% as compared to Λ reconstruction. This effect is not present when using the TPC. However, the overall reconstruction efficiency using the TPC reaches only 35%. Mass resolutions of (0.71 ± 0.02) MeV/c^2 for STT and (1.10 ± 0.02) MeV/c^2 for TPC trackers are obtained, independent of beam momentum.

For the $\Lambda\overline{\Lambda}$ pair reconstruction with the STT setup it is possible to reach an efficiency of 10%. Using the

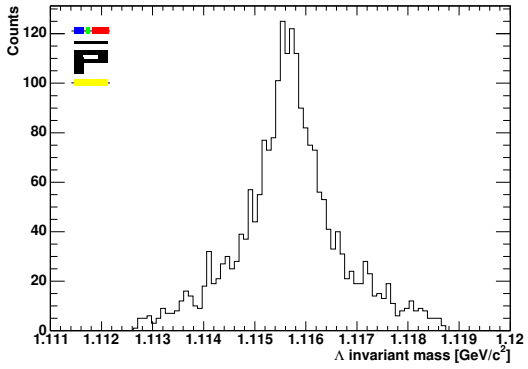

Figure 13.25: Λ invariant mass spectrum with at a beam momentum of 4 GeV/c^2 using the STT. Mass resolution: (0.71 ± 0.02) MeV/c^2.

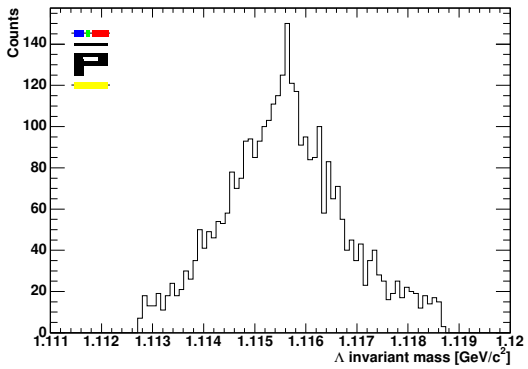

Figure 13.26: Λ invariant mass spectrum with at a beam momentum of 4 GeV/c^2 using the TPC. Mass resolution: (1.10 ± 0.02) MeV/c^2.

TPC setup, instead, the reached efficiency is around 25%, which clearly needs to be improved. The missing momentum, the missing energy and the missing mass were studied for the different beam momenta. In Table 13.21 the resolutions obtained with a beam momentum of 4.0 GeV/c for both setups are shown. It should be noticed that the missing momentum resolution is higher in transverse direction as compared to longitudinal direction. Comparing the STT and the TPC trackers, the STT setup offers a better resolution, but a lower reconstruction efficiency. With both setups, the resolution of the longitudinal missing momentum is worst at the highest beam momenta. There is also a reduction of the missing energy in the negative region of about 20 MeV/c^2.

Background studies based on the DPM model are in progress. Furthermore, we plan to study the decay asymmetry reconstruction of the Λ and the $\overline{\Lambda}$ particles.

	STT σ	TPC σ
Missing Energy [MeV]	19.98±0.88	39.54±0.88
Missing Mass [MeV/c^2]	46.43±2.12	80.48±2.95
Missing Transverse Momentum [MeV/c]	9.26±0.33	13.70±0.20
Missing Longitudinal Momentum [MeV/c]	20.28±0.79	35.25±1.05

Table 13.21: Resolution of missing energy, missing mass and missing momentum for a $\Lambda\overline{\Lambda}$ couple at a beam momentum of 4.0 GeV/c.

13.5.9 Exotic Charmed Hybrid: $\overline{\mathrm{p}}\mathrm{p} \rightarrow \psi_g\eta \rightarrow \chi_c\pi^0\pi^0\eta$

13.5.9.1 Introduction

The lowest charmonium hybrid is generally believed to be a $J^{PC} = 1^{-+}$ state, which is particularly interesting due to its exotic spin quantum numbers. LQCD predicts masses in the range 4.1–4.4 GeV/c^2, this study uses a mass of 4.29 GeV/c^2 and a width of 20 GeV/c^2 [16, 17, 18]. Particles with exotic spin quantum numbers can be reached only in production in $\overline{\mathrm{p}}$p-collisions. Here we assume production in association with a light meson, a π^0 or an η.

Non-relativistic flux-tube calculations predict suppression of decays into open charm for hybrid masses below the $D^0\overline{D}_1^0$-threshold [19]. Non-relativistic OZI-allowed decay into hidden charm would give a χ_{c1} state reached through emission of light hadrons, where scalar particles are preferred to isoscalars [20], the lightest scalar being composed of two neutral pions in an s-wave.

	BR
$\overline{\mathrm{p}}\mathrm{p} \rightarrow \psi_g\eta$	
$\psi_g \rightarrow \chi_{c1}(\pi^0\pi^0)_{s-wave}$	
$\chi_{c_1} \rightarrow J/\psi\gamma$	$31.6 \pm 3.2\%$
$J/\psi \rightarrow e^+e^-$	$5.93 \pm 0.1\%$
$\pi^0 \rightarrow \gamma\gamma$	98.8%
$\eta \rightarrow \gamma\gamma$	39.4%
Total χ_{c_1} decay BR	3.6%

Table 13.22: Decay channel for the simulation of the reaction $\overline{\mathrm{p}}\mathrm{p} \rightarrow \psi_g\eta$ with branching ratios (BR).

In Tab. 13.22 the investigated reaction is listed with branching ratios for the individual decays. The

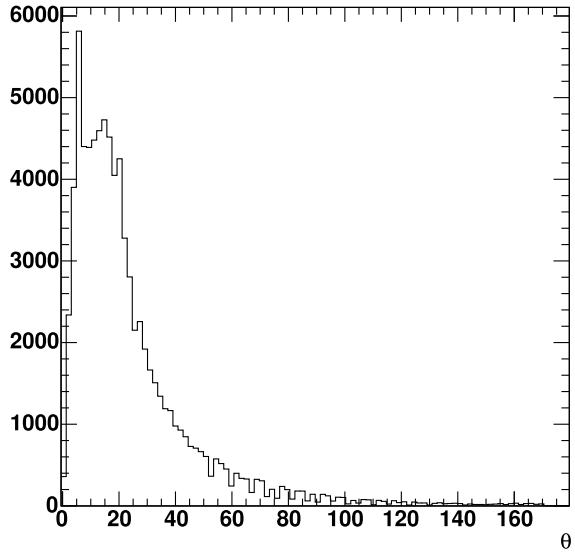

Figure 13.27: Detected photons *vs* θ for 10 000 events.

total branching ratio is calculated under the optimistic assumption of having BR($\psi_g \to \chi_{c1}\pi^0\pi^0$).

The final state has a restrictive signature and trigger in the e^+e^--pair at the narrow J/ψ-resonance. Possible background channels all contain a J/ψ and a large number of photons; single photons, photons from neutral pions, η mesons, ω mesons or from electromagnetic interactions within the detector material.

Production in association with a π^0 instead of an η as well as other decay channels, as for example $J/\psi \to \mu^+\mu^-$, are subject of ongoing investigation, as is background misidentification into the hybrid channel.

Having a final state with seven photons, it is clear that the EMC plays the major role. With high multiplicities, it has to cover almost completely 4π to enable detection and reconstruction of this reaction.

Fig. 13.27 shows that most photons are detected in the forward end cap, that covers the region $5° < \theta < 22°$ of the EMC, and a fraction of 8.6% is detected in the forward spectrometer. Other important parameters are the energy threshold, energy- and angular resolution of the EMC. The overall efficiency and background reduction, however, also depends on geometries of other detectors and materials which may degrade the photon energy or produce showers. Hence, full Monte Carlo studies with different setups have been done and further investigations are to follow.

13.5.9.2 Selection

The spectra in this section are produced with the setup in Tab. 13.23. To reconstruct the intermediate particles and eventually the hybrid candidate a number of cuts, listed in Tab. 13.24, are applied during the analysis. The particle identification (PID) of electrons and positrons is still under development and could not yet be used.

EMC version	1
Crystal length	15.0 cm(16.7 X_0)
EMC material	PWO
Forward calorimeter	KOPIO-LEDA
Single crystal threshold	10 MeV
Cluster threshold	20 MeV
$E_{\max}$-threshold	20 MeV

Table 13.23: Detector setup used for the study in section 13.5.9.2 and 13.5.9.3. Results from other setups are compared in the end of this section.

13.5.9.3 Results

Figs. 13.28 to 13.31 contain the invariant masses with full combinatorial background. For the mass plots of the χ_{c1} and the ψ_g the nominal masses for the constituent particles were used rather than the masses determined during the analysis. This provides a preliminary substitution for a kinematical fitting procedure that is still under development. The reconstructed masses and widths of the intermediate states are listed in Table 13.5.9.3.

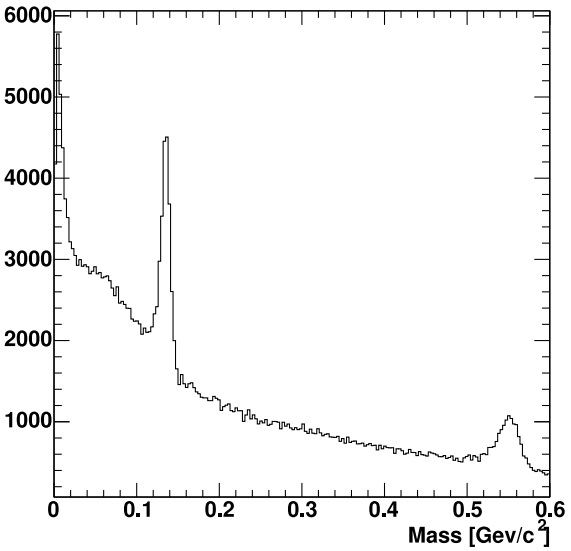

Figure 13.28: Mass distribution of all $\gamma\gamma$ pairs.

Cut	Particle	Applied cuts	Events after cuts
1		7γ and 2 charged tracks	2 061
2	π^0	$\lvert m_{\pi^0} - m_{\gamma\gamma}\rvert < 20\,\mathrm{MeV}/c^2$	7 439
3	J/ψ	$\lvert m_{J/\psi} - m_{e^+e^-}\rvert < 0.2\,\mathrm{MeV}/c^2$	7 045
4	χ_{c1}	$\lvert m_{\chi_{c1}} - m_{J/\psi\gamma}\rvert < 0.035\,\mathrm{GeV}/c^2$	6177
5	ψ_g	$\lvert m_{J/\psi_g} - m_{\chi_{c1}\pi^0\pi^0}\rvert < 0.4\,\mathrm{GeV}/c^2$	4 089
6	η	$\lvert m_\eta - m_{\gamma\gamma}\rvert < 40\,\mathrm{MeV}/c^2$	8 949
	$\psi_g\,\eta$	Cuts $1-6$, no overlap	1 107
		Additionaly $\cos\theta(\psi_g,\eta) \leq -0.99$	1 038

Table 13.24: Cuts applied in the analysis and the number of events which remain after those cuts are applied (from originally 10 000 events).

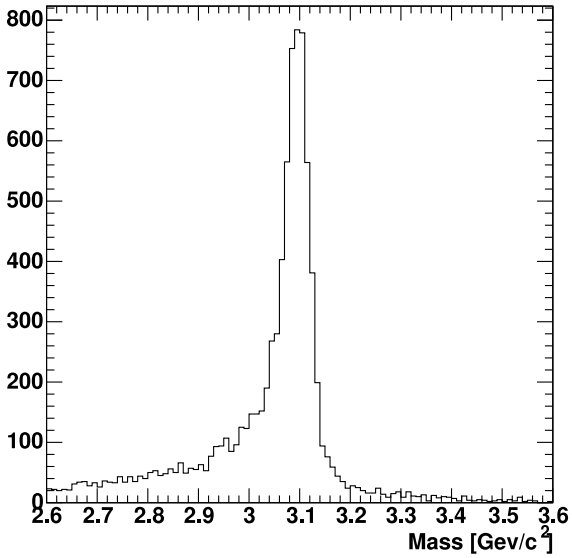

Figure 13.29: Mass distribution of all e^+e^--pairs with J/ψ-peak.

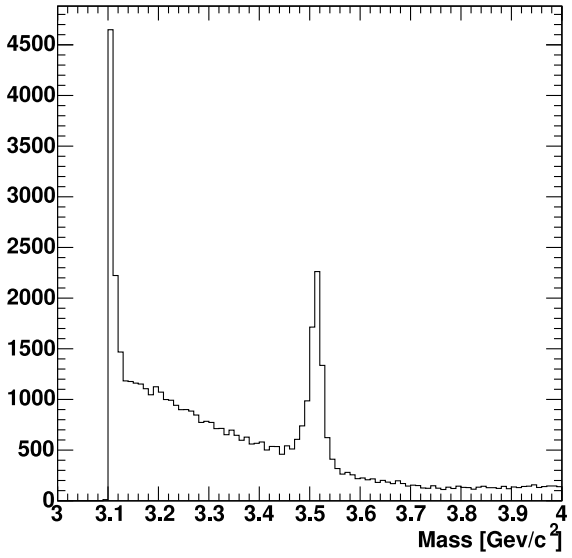

Figure 13.30: Mass distribution of all $J/\psi\gamma$-pairs.

Particle	Reconstructed mass	Width
π^0	$134.7\,\mathrm{MeV}/c^2$	$4.5\,\mathrm{MeV}/c^2$
η	$547\,\mathrm{MeV}/c^2$	$15\,\mathrm{MeV}/c^2$
J/ψ	$3.091\,\mathrm{GeV}/c^2$	$0.025\,\mathrm{GeV}/c^2$
χ_{c1}	$3.512\,\mathrm{GeV}/c^2$	$0.015\,\mathrm{GeV}/c^2$
ψ_g	$4.282\,\mathrm{GeV}/c^2$	$0.027\,\mathrm{GeV}/c^2$

Table 13.25: Reconstructed masses and widths of the intermediate states.

13.5.9.4 Comparison using different EMC setups

As this channel is highly dependent on the EMC, the event reconstruction was done using different setups and thresholds to investigate the reconstruction efficiency. The forward spectrometer could be chosen to include either a MIRAC or a KOPIO-LEDA EMC and the barrel EMC could have either a constant crystal length over the whole detector or a length adapted to the energy ranges expected, i.e. longer crystals in the forward direction. Crystal quality, readout and electronics determine the energy thresholds for the crystals. For each setup the energy thresholds, which differ from the central mass production, were varied as listed in Table 13.26. It seems, that the dependencies of the reconstruction efficiency on the different thresholds are not yet fully understood. This is subject to ongoing investigation. Split-offs and the variation of other thresholds may, however, explain the effects visible.

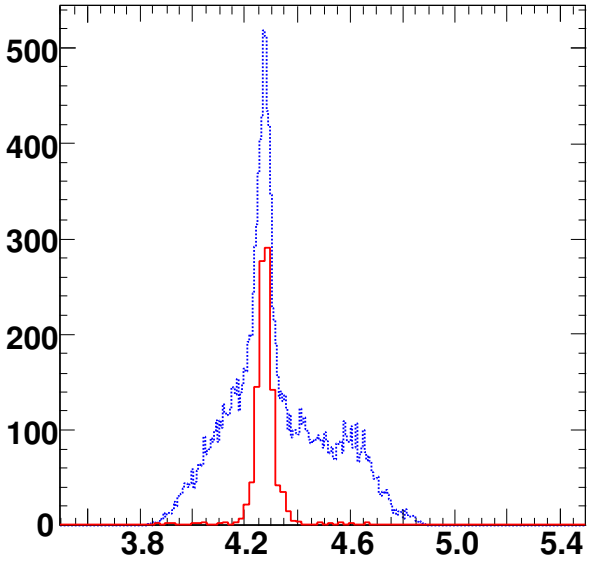

Figure 13.31: Mass distribution of all reconstructed charmed hybrid candidates (dotted blue) and of unambiguously reconstructed events only — as in Tab. 13.24 (solid red). Please note that the binning differs by a factor of 3.

Material	E_{sc} [MeV]	E_{max} [MeV]	E_{cl} [MeV]
BGO	3	15	20
	3	15	30
	3	15	50
PWO	10	20	20
	5	20	25
	10	35	50

Table 13.26: Thresholds for the different setups.

13.5.9.5 Conclusion

We made an analysis based on a very simple reconstruction taking into account only events, where 7 photons and 2 electrons have been unambiguously detected. As we can see from Tab. 13.24 in 80% a different multiplicity is actually found. As the analysis is not yet tuned to deal with split-offs and alike effects, we donnot use these events at all in the final step of the analysis. Thus we expect the amount of events which could be reconstructed, with a refined analysis, to be significantly higher than the values of about 12% found here. As an indication one may note that about 21% of all events survive the given cuts, if all multiplicities are allowed.

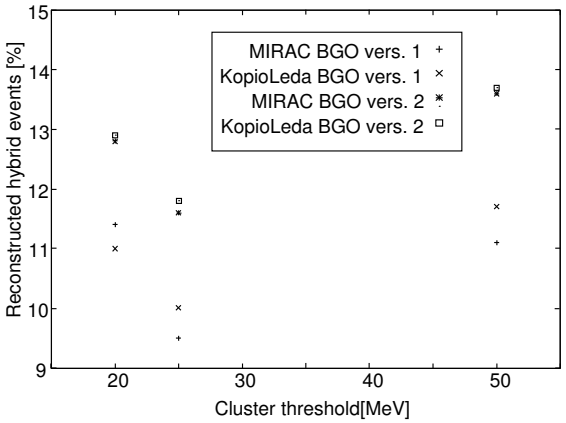

Figure 13.32: PWO: percent of fully reconstructed events *vs.* cluster threshold, E_{cl}. Based on a most conservative approach (see text). Note, that also other thresholds have been varied simultaneously (see Tab. 13.26).

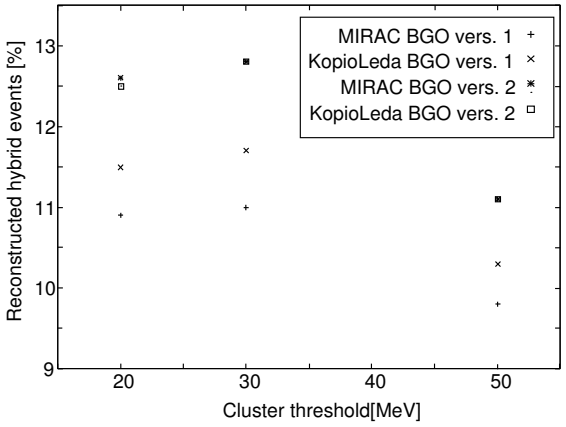

Figure 13.33: BGO: percent of fully reconstructed events *vs.* cluster threshold, E_{cl}. Based on a most conservative approach (see text).

13.5.10 Charmonium Absorption in Nuclei: $\bar{\mathrm{p}}\,A \rightarrow J/\psi X \rightarrow \mu^+\mu^- X$

One of the basic trigger concepts of the PANDA detector is based on the decay of heavy resonances in light particles with large transverse momenta, e.g. the decay of J/ψ in two muons. This enables triggering on two muons with large transverse momenta in the presence of muons from hadronic background. The detection of J/ψ mesons produced in $\bar{\mathrm{p}}$N collisions on nuclear targets serves here as an example to study the production of J/ψ in nuclear matter.

In Fig. 13.34 the invariant mass of two muons detected solely in the muon counters of the target

spectrometer is plotted for an integrated luminosity of $180\,\mathrm{nb}^{-1}$. These results have been produced for the LoI. For all muon candidates, track parameters and hit locations within the detectors are required to fulfil the condition of having a muon probability of more than 95 %. The signal peak at the invariant mass of the J/ψ represents calculations from [21] for $\overline{\mathrm{p}} + ^{63}Cu$ at $4.05\,\mathrm{GeV}/c$ after a filter procedure.

The target spectrometer alone detects 45 % of the originally produced J/ψ. This peak is well separated from nuclear background events which were calculated using the UrQMD [22, 23] event generator. These entries are the combinatorical background of muons coming from the decay of resonances of light quark mesons, especially from misidentified pions. The selection of muons with transverse momenta $p_t > 1\,\mathrm{GeV}/c$ leads to a complete suppression of the background shown in Fig. 13.34 without affecting the J/ψ signal.

In the present framework only ten J/ψ at lower invariant masses could be reconstructed using the same statistics of UrQMD generator events. They are not shown since for the shape of the background spectrum several orders of magnitude more events have to be simulated. It is interesting to note, that the difference between the background calculation presented in the LoI, which was performed for the same statistics, arises from the use of different versions of UrQMD event generators in the LoI [22, 23] and in this report (improvements described at end of Chap. 12.3.1.3). However, we show in the insert of Fig. 13.34 the result for the signal for the present framework. Clearly, the different predictions for the expected background distributions need more analysis work.

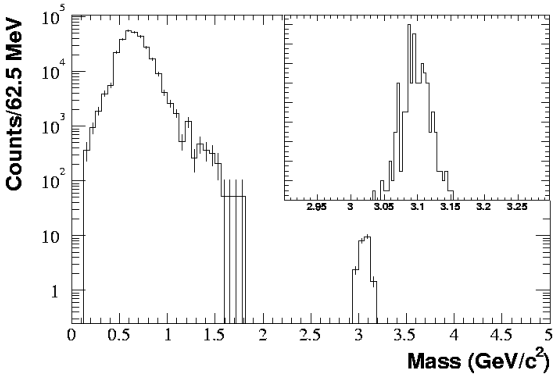

Figure 13.34: Invariant mass spectrum of J/ψ decaying in two muons. The signal at $3\,\mathrm{GeV}/c^2$ is from calculations in [21], the combinatorical background at lower invariant masses is taken from UrQMD calculations [22, 23].

References

[1] Grid Computing Centre Karlsruhe, http://www.gridka.de.

[2] Infiniband IWARP Cluster, http://savannah.fzk.de/projects/iwarp.

[3] T. Armstrong et al., Phys. Rev. **D52**, 4839 (1995).

[4] M. Ambrogiani et al., Phys. Lett. **B566**, 45 (2003).

[5] S. Eidelman et al., Phys. Lett. **B592**, 1+ (2004), http://pdg.lbl.gov.

[6] B. Aubert et al., Phys. Rev. Lett. **87**, 162002 (2001).

[7] G. Brandenburg et al., Phys. Rev. Lett. **85**, 3095 (2000).

[8] R. Armenteros and B. French, *High Energy Physics*, volume 4, Academic Press, 1969.

[9] C. Baltay et al., Phys. Rev. **142**, 932 (1966).

[10] J. Debray et al., Nucl. Phys. **B62**, 13 (1973).

[11] P. Eastman et al., Nucl. Phys. **B51**, 29 (1973).

[12] T. Armstrong et al., Phys. Rev. **D56**, 2509 (1977).

[13] A. Freund, A. Radyushkin, A. Schäfer, and C. Weiss, Phys. Rev. Lett. **90**, 092001 (2003).

[14] M. Diehl, P. Kroll, and C. Vogt, Eur. Phys. J. **C26**, 567 (2002).

[15] J. Ritman, Study of the reaction $\overline{\mathrm{p}}\mathrm{p} \to \psi(3770) \to D\bar{D}$, http://www-new.gsi.de/Documents/, 2003.

[16] C. Bernard and J. Hetrick, Phys. Rev. **D56**, 7039 (1997).

[17] F. Close, Phys. Rev. **D57**, 5653 (1998).

[18] P. Page, Acta Phys. Polon. **B29**, 3387 (1998).

[19] P. Page, Phys. Lett. **B402**, 183 (1997).

[20] C. Michael, Beyond the quark model of hadrons from lattice QCD, 2002, International Conference on Quark Nuclear Physics.

[21] A. Sibirtsev, K.Tsushima, and A. Thomas, Phys. Rev. **C63**, 044906 (2001).

[22] S. Bass et al., Prog. Part. Nucl. Phys. **41**, 255 (1998).

[23] S. Bleicher et al., J. Phys. **G25**, 1859 (1999).

14 Organisation and Infrastructure

14.1 Experimental Hall

The target for antiproton physics is located in the straight section at the east side of the HESR. At this location, an experimental hall of 36 m × 28 m floor space and 14.5 m height is planned (see Fig. 14.1). The hall is directly connected to an operation building which would extend to the left in the figure and connect this building to the electron cooler at the opposite straight section of the HESR. A concrete radiation shield of 2 m thickness on both sides along the beam line is covered by bars of 1 m thickness to suppress the neutron sky shine. Within the elongated concrete cave, the $\overline{\text{P}}$ANDA detector together with auxiliary equipment, beam steering, and focusing elements will be housed. The roof of the cave can be opened and heavy components hoisted by crane.

The shielded beam line area for the $\overline{\text{P}}$ANDA experiment including dipoles and focusing elements is foreseen to have 31.5 m × 9.4 m floor space and a height of 7 m. The height of the beam line is 2.5 m. The floor level of the HESR is 1 m higher. This level will be kept for a length of 4.5 m in the north of the hall (upper part in Fig. 14.1), to facilitate transport of heavy equipment from the central buildings.

The target spectrometer with electronics and supplies will be mounted on a carriage retractable to a parking position outside the HESR beam line (i.e. into the left part of the hall in Fig. 14.1). The experimental hall provides additional space for delivery of components and assembly of the detector parts. In the south corner of the hall, a counting house complex with two or three floors is foreseen. A crane (20 t) spans the entire area with a hook at a height of about 10 m.

Sufficient (300 kW) electric power will be available. Liquid helium coolant may come from the main cryogenic liquefier for the SIS rings. Alternatively, a separate small liquefier (50 W cooling power at 4 K) can be mounted. The temperature of the building will be moderately controlled. The more stringent requirements with respect to temperature and humidity for the detectors has to be maintained locally.

It is requested to provide for 600 m^2 additional laboratory and office space located in the nearby operations building as well as a conference room.

Radiation safety of the experimental cave has extensively been studied with the FLUKA code[1]. It could be shown that shielding along the beam line with 1 m thickness of concrete is sufficient. The sky shine can be suppressed covering this area with concrete plates of 0.5 m thickness.

1. see http://www.fluka.org

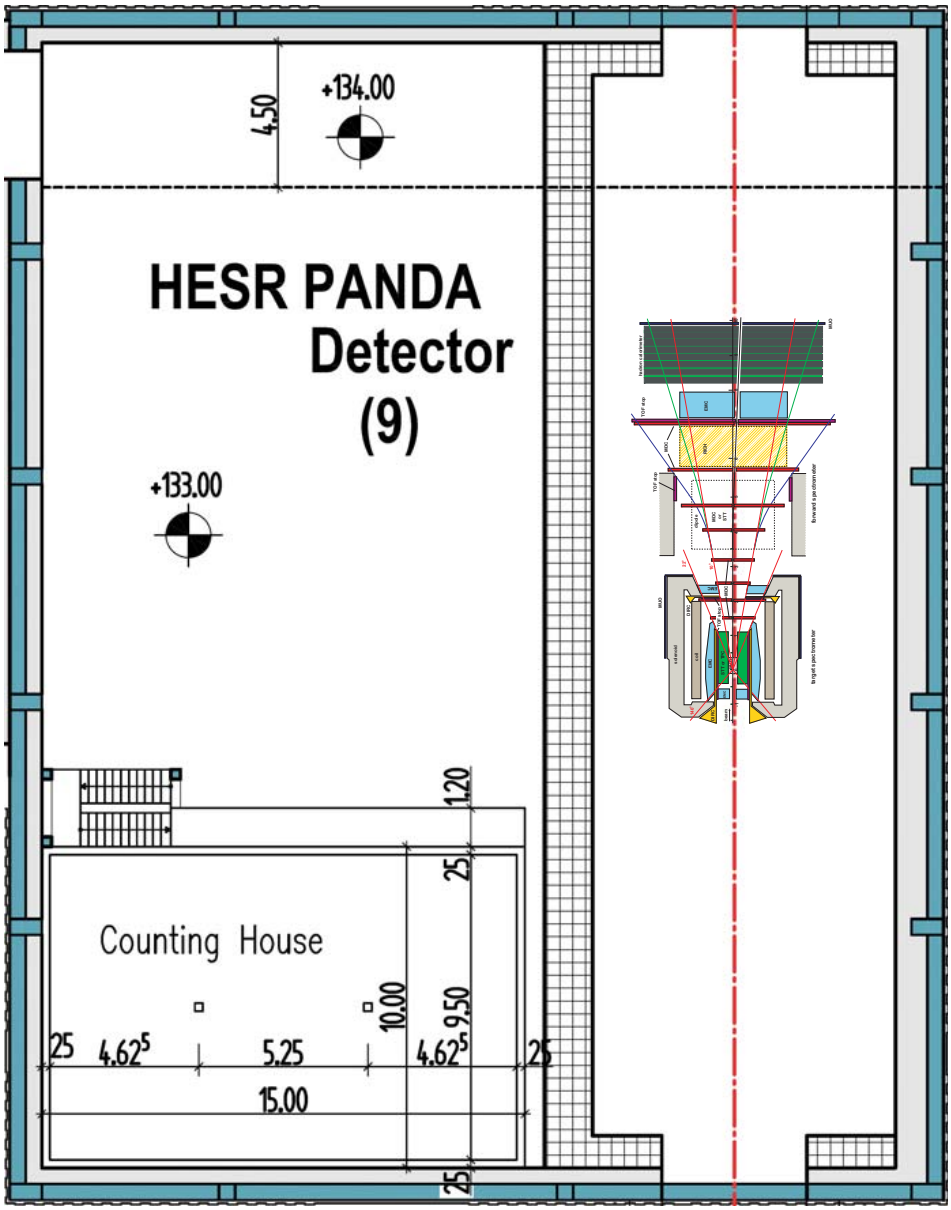

Figure 14.1: Top view of the experimental area indicating the location of PANDA in the HESR beam line (indicated as vertical dash-dotted line). North is to the top right. The beam enters from the bottom. The roll-out position of the detector will be in the left part of the Hall.

14.2 Structure and Responsibilities

14.2.1 Resources

The workload of the development and building of the components of the PANDA detection system, including the readout electronics and data acquisition system, is shared among the institutions of the collaboration. Each participating group has committed to a sizeable contribution to the PANDA setup. For some of the participating institutions, this requires a redefinition of the priorities within their research program, and a major rearrangement of their resources in terms of investment and personnel. The process of defining the longer term research activities related to the PANDA project is presently not completed, partially due to open questions concerning financial support in the intermediate future. The list of institutions associated with the various detector components has to be understood as an expression of interest in the respective technical issues on the basis of the existing ex-

Figure 14.2: Work breakdown schedule for the interaction region (target, vertex detector), and the charged particle tracker of the $\overline{\mathsf{P}}$ANDA detector.

pertise and infrastructure. The commitment of of the participating institutions concerning its contribution to the $\overline{\mathsf{P}}$ANDA project will be defined in a Memorandum of Understanding in the near future. A preliminary distribution of tasks is given below:

Pellet Target

FZ Jülich, TSL Uppsala, U Uppsala

Cluster-jet Target

GSI, U Münster, U/INFN Genova, IMEP Vienna

Superfluid He-target

U Frankfurt

Nuclear Targets

FZ Jülich

Micro Vertex Detector

U Catania, TU Dresden, U Edinburgh, FZ Jülich, U Mainz, IHEP Protvino INFN Torino, U Torino ("Dep.Exp.Phys.")

Cylindrical Tracker - STT/TPC

JINR Dubna, LNF Frascati, INFN Ferrara, FZ Jülich, IMP Lanzhou, TU München, U Tübingen, U Uppsala

Particle Identification - DIRC/RICH/TOF

U Catania, JINR Dubna, U Gießen, U Glasgow, GSI, FZ Jülich, IMEP Vienna

Electromagnetic Calorimeter - EMC

U Basel, U Bochum, U Frankfurt, U Gießen, GSI, FZ Jülich, IMP Lanzhou, U Minsk, IPN Orsay, U Uppsala, U Valencia, SINS Warsaw

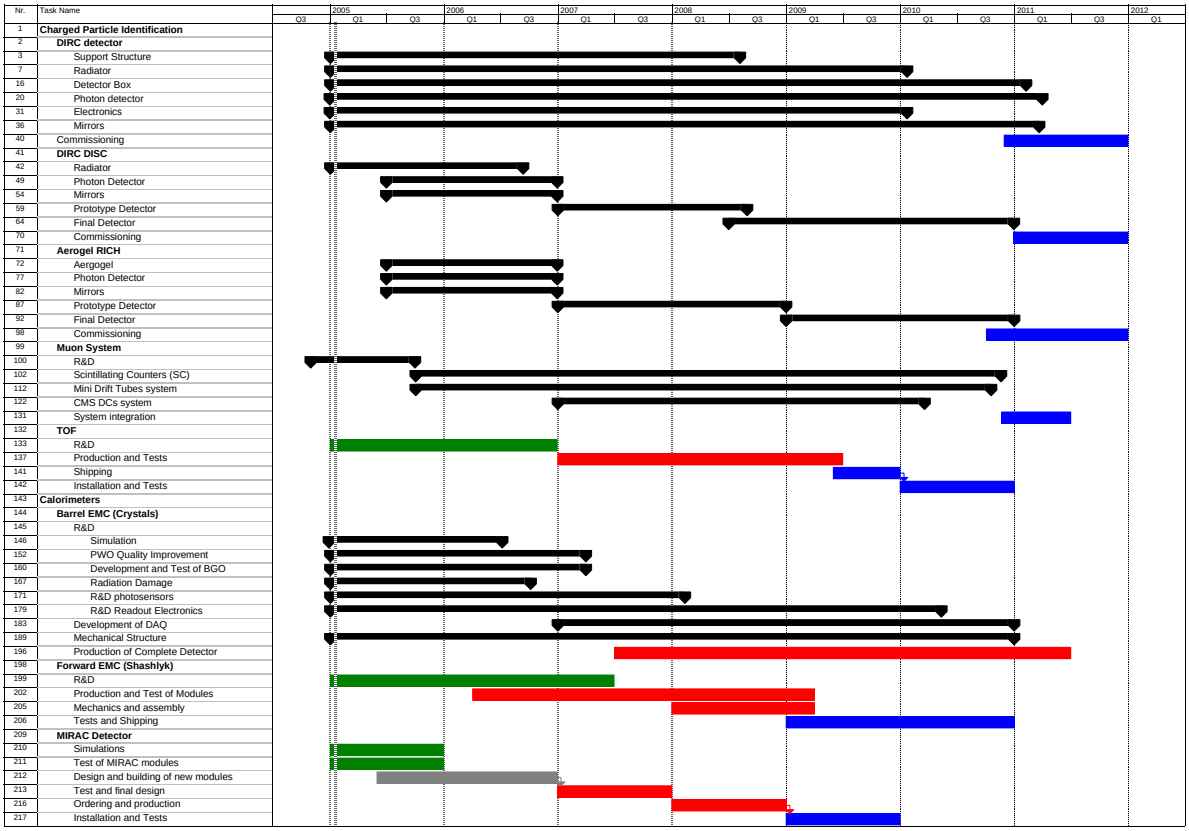

Figure 14.3: Work breakdown schedule for the PID detectors and calorimeters of the PANDA detector.

Magnets

U Cracow, JINR Dubna, U/INFN Genova, U Glasgow, IMP Lanzhou

Muon Chambers - MUD

JINR Dubna, U Piemonte Orientale, INFN Torino, U Torino ("Dep.Gen.Phys.")

Forward spectrometer - FS

U Cracow, JINR Dubna, GSI

Ge-Detector

U/INFN Catania, Politecnico Torino, U Mainz, KTH Stockholm, INFN Torino , U Torino ("Dep.Exp.Phys.")

DAQ/Trigger/Fast electronics

U Cracow, U Gießen, GSI, FZ Jülich, U Katowice, U Milano, TU München, U Pavia, INFN Torino, U Torino ("Dep.Gen.Phys."), SINS Warsaw

Computing

U Bochum, U Bonn, U Glasgow, GSI, FZ Jülich, U/INFN Pavia, TU München, Politecnico Torino, SINS Warsaw

14.2.2 Structure

Presently, the PANDA collaboration operates with a provisional structure but will soon closely follow the structure of existing international collaborations of similar size. Details will be worked out for the *Memorandum of Understanding* (MoU) with the participating institutes and the host institution.

14.3 Timelines

An overview for the R&D, construction, manufacturing, assembly, test, and commissioning of the various parts of the PANDA detector is shown in Figs. 14.2–14.4. More detail is provided in the detector chapters with more detailed timelines.

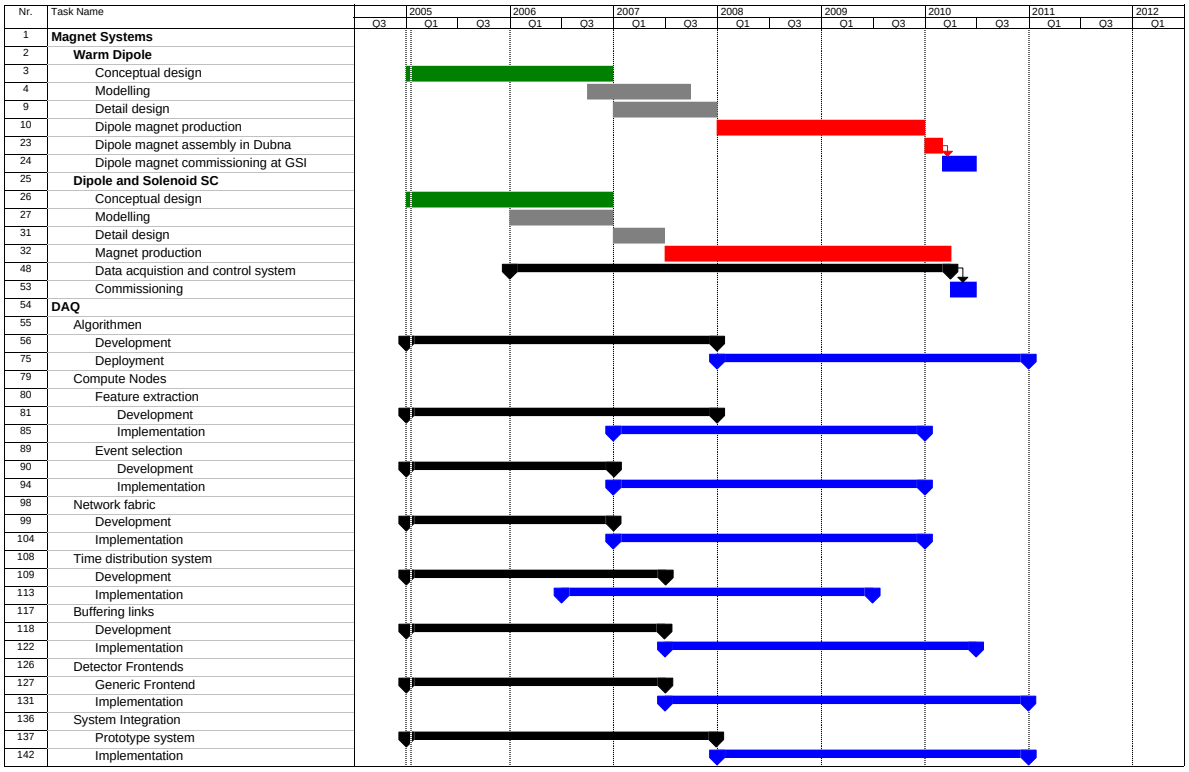

Figure 14.4: Work breakdown schedule for the magnets and the DAQ of the $\overline{\mathsf{P}}$ANDA detector.

Several detector implementations and/or concepts are under investigation in extensive R&D programs. Presently, a final layout of the overall detector cannot be decided upon. Therefore, we give timelines for all components discussed in the report. However, as soon as a decision is taken the declined subproject will no longer be pursued.

We will not provide a detailed timeline for the computing since the computing model and its implementation can only be designed 2–4 years prior to data taking. The computing costs are scaled from experience elsewhere.

14.4 Beam Time Considerations

One run period is considered to have a length of 6–9 months ($\approx 1.5\times10^7$s). Depending on the nature of the experiment (slow or quick changes of beam momenta), the different filling/cooling-cycle schemes, and other dead-times during data-taking the overall data-taking efficiency is expected to vary between 50 % (several changes a day) and 80 % (continuous running).

The hadron spectroscopy experiments (charmonium studies and search for gluonic excitations), charm in nuclei, and hypernuclear physics are mutually exclusive and will require dedicated running for more than one (most probable two) full run period each. For the spectroscopy experiments, this number is deduced from typical cross sections in the order of 10–100 pb and the minimum number of 1 k (per charmonium state) and 10–100 k (charmed hybrid) signal events for a conclusive analysis. The required luminosity for this time estimate is $2 \cdot 10^{32}\,\mathrm{cm}^2 s^{-1}$. Hypernuclear physics experiments require two run periods as well. The time estimate takes into account that the detector setup has to be changed and recalibrated and is based on assumptions concerning the cross sections for the production of double hypernuclei and their spectroscopy. For the study of charmed hadrons in matter, an efficient trigger on D mesons is required. In addition, a trigger on leptonic decays could be envisaged albeit at a low rate due to the cross sections. First estimates show that a running time between one and two run periods has to be foreseen for this program.

For the electromagnetic part of the program, we give hereafter the expected counting rates for the reactions $\overline{p}p \rightarrow \mu^+\mu^- X$ (the Drell-Yan process) for and a beam luminosity $\boldsymbol{\mathcal{L}} = 2 \cdot 10^{32}\ cm^{-2}\,s^{-1}$

For the $\overline{p}p \rightarrow \mu^+\mu^- X$ reaction we take the cross section value of 0.1 nb/nucl., given in [1] for a dimuon mass M falling in the "safe" region, that is for $4 \leq M \leq 9$, and for an antiproton beam momentum of 125 GeV/c. We scale down that value as $1/s$ and get $\sigma = 0.3\,\text{nb/nucl.}$ at $\sqrt{s} = 10\,\text{GeV}$ for a dimuon mass falling in the same "safe" region. The counting rate per second will be then $\boldsymbol{\mathcal{R}} = 2 \cdot 10^{32} \times 3 \cdot 10^{-34} \times A = 6 \cdot 10^{-2} \times A \approx = 15 \cdot 10^{-3}\, ev.\, s^{-1}$ for the acceptance $A = 0.25$.Simulation studies for the acceptance are in progress [2] Assuming for 20 useful hours in a day for data taking, one gets about 1 000 events/ day. In two periods of 100 days, 200 000 dimuons events in the continuum with masses larger than 4 GeV will be collected, that is 10 times more events with respect to previous experiments[1, 3] . Such a statistics remembering the M dependence of the cross-section that decreases by about two order of magnitude from $M = 4\ GeV$ to $M = 9\,\text{GeV}$ will allow to inspect the $x \rightarrow 1$ region where higher twist contributions are expected.

Other measurements can be performed simultaneously together with the key experiments with identical beam and detector settings. For instance, the long data-taking run for charmed hybrids at the highest beam momentum will allow for measurements on electromagnetic processes in parallel.

Including a full start-up run period to tune and understand the detector and to measure unknown cross sections the initial program adds up to eight years of data taking. Most likely this number will change, since most measurements are explorative with badly known cross sections. One may also keep in mind that this is an active research field and the relevance of some of the proposed topics may have altered while others may come up in addition.

References

[1] E. Anassontzis et al., Phys. Rev. **D38**, 1377 (1988).

[2] N.Skachkov and A.Skachkova, hep-ph/0412279.

[3] J. Conway et al., Phys. Rev. **D39**, 92 (1989).

Acknowledgments

We would like to thank the technical staff of the machine groups from the Gesellschaft für Schwerionenforschung mbH and the Forschungszentrum Jülich and of all the participating institutions for their invaluable contributions to the preparatory work on the experiment.
We acknowledge financial support from the Bundesministerium für Bildung und Forschung (bmb+f), the Gesellschaft für Schwerionenforschung mbH (GSI), the Deutsche Forschungsgemeindschaft (DFG), the Schweizerischer Nationalfond, the Swedish Research Council (VR) and the Polish Committee for Scientific Research (KBN).
This research is part of the EU Integrated Infrastructure Initiative Hadron Physics Project under contract number RII3-CT-2004-506078. It is also part of the EU Design Initiative on Internal Target experiments with highly energetic stored and cooled beams at the International Facility for Antiproton and Ion Research (FAIR). under contract number 515873.

ADC Analog to Digital Converter

AGATA Advanced Gamma Tracking Array

AGS Alternate Gradient Synchrotron

APD Avalanche Photo Diode

API Application Programming Interface

AS Advanced Switching

ASIC Application Specific Integrated Circuit

BGO Bismuth Germanate

BNL Brookhaven National Laboratory

BTCP Bogoroditsk Techno-Chemical Plant

CA Certification Authority

CAD Computer Aided Design

CCE Charge Collection Efficiency

CDR Conceptual Design Report

CERN Conseil European pour la Recherche Nucleaire

CLAS Cebaf Large Acceptance Spectrometer

CKM Cabbibo-Kobayashi-Maskawa

CLAS CEBAF Large Acceptance Spectrometer

COMPASS Common Muon Proton Apparatus for Structure and Spectroscopy

COSY Cooler Synchrotron

CT Central Tracker

CVS Code Versioning System

DAQ Data Acquisition

DESY Deutsches Elektronensynchrotron

DIRC Detector for Internally Reflected Cherenkov Light

DLL Delay Lock Loop

DPM Dual Parton Model

DSP Digital Signal Processor

DVCS Deeply Virtual Compton Scattering

EGEE Enabling Grids for E-science in Europe

ELT Enclosed Layout Transistors

EMC Electromagnetic Calorimeter

ENC Equivalent Noise Charge

Eoc End-of-Column

EPR Electron Paramagnetic Resonance

EU European Union

FADC Flash ADC

FAIR Facility for Antiproton and Ion Research

FE Front-End

FEE Front-End Electronics

FET Field-Effect Transistor

FNAL Fermi National Laboratory

FPGA Field Programmable Gate Array

FS Forward Spectrometer

FZJ Forschungszentrum Jülich

GEM Gas Electron Multiplier

GPD Generalized Parton Distribution

GSI Gesellschaft für Schwerionenforschnung

GSS Generic Security Service, an authentication API aka Kerberos V5

HC Hadron Calorimeter

HESR High Energy Storage Ring

HFG Hermann von Helmholtz-Gemeinschaft Deutscher Forschungszentren

HTS High Temperature Superconductors

HV High Voltage

IBP In-Beam Polarimeter

IP Interaction point

IHEP Institute for High Energy Physics

INFN Istituto Nazionale di Fisica Nucleare

KVI Kernfysisch Versneller Instituut

LAAPD Large Area APD

LEAR Low Energy Antiproton Ring

LEC Liquid Encapsulated Czrochalski

LED Light Emission Diode

LEGS Laser Electron Gamma Source

LHC Large Hadron Collider

LNP Low Noise Preamplifier

LOI Letter of Intent

LP Low-Pass

LQCD Lattice QCD

MAPS Monolithic Active Pixel Sensor

MDC Mini Drift Chamber

MIP Minimum Ionizing Particle

MIRAC Mid Rapidity Calorimeter

MUD Muon Detector

MVD Micro Vertex Detector

NIEL Non-Ionizing Energy Loss

NMR Nuclear Magnetic Resonance

PCB Printed Circuit Board

PCI Peripheral Component Interconnect

PDR Preliminary Design Report

PED Particle Energy Deposit

PID Particle Identification

PLL Phase Lock Loop

PMT Photomultiplier

PSI Paul Scherrer Institute

PTS Pellet Test Station

PWO Lead Tungstate

QA Quality Assurance

QCD Quantum Chromo Dynamics

QED Quantum Electrodynamics

RICH Ring Imaging Cherenkov Counter

RPC Resistive Plate Chambers

SASL Simple Authentication and Security Layer

SCT Semiconductor Tracker

SI Semi-insulating

SICCAS Shanghai Institute of Ceramics, Chinese Academy of Sciences

SLAC Stanford Linear Accelerator Center

SMD Surface Mount Device

SSL Secure Socket Layer

STT Straw Tube Tracker

TCS Trigger Control System

TDC Time to Digital Converter

TDS Time Distribution System

TJNAF Thomas Jefferson National Accelerator Facility

TOF Time-of-Flight Detector

TOP Time-of-Propagation

ToT Time-over-Threshold

TPC Time Projection Chamber

TRD Transition Radiation Detector

TS Target Spectrometer

TSL Thermostimulated luminescence

TSL The Svedberg Laboratory

TTC Time Trigger and Control

UrQMD Ultra-relativistic Quantum Molecular Dynamic

VEGA Versatile and Efficient Gamma Detector

VME Versa Module Eurocard

WLS Wave Length Shift(er/ing)

List of Figures

List of Tables